Deliverable 2.7: Final technical report on the steel/clay material interactions

Work Package 2

This project has received funding from the European Union's Horizon 2020 research and innovation programme under grant agreement N°847593.

Document information

Project Acronym	**EURAD**
Project Title	**European Joint Programme on Radioactive Waste Management**
Project Type	**European Joint Programme (EJP)**
EC grant agreement No.	**847593**
Project starting / end date	**1st June 2019 – 30 May 2024**
Work Package No.	**2**
Work Package Title	**Assessment of Chemical Evolution of ILW and HLW Disposal Cells**
Work Package Acronym	**ACED**
Deliverable No.	**2.7**
Deliverable Title	**Final technical report on the steel/clay material interactions**
Lead Beneficiary	**IRSN**
Contractual Delivery Date	**M46**
Actual Delivery Date	**M60**
Type	**Report**
Dissemination level	**PU**
Authors	**María Jesús Turrero (CIEMAT), Elena Torres (CIEMAT), Paloma Gómez (CIEMAT), Antonio Garralón (CIEMAT), Belén Notario (CENIEH), Marina Sanmiguel (CENIEH), Jaime Cuevas (UAM), Carlos Mota (UAM), Ana Isabel Ruiz (UAM), Raúl Fernández (UAM), Almudena Ortega (UAM), Javier Samper (ENRESA-UDC), Alba Mon (ENRESA-UDC), Luis Montenegro (ENRESA-UDC), Jebril HADI (UniBe), Mirjam Kizcka (UniBe), Andreas Jenni (UniBe), Jules Goethals (Subatech), Jean-Marc Greneche (IMMM), Karine David (Subatech) and Paul Wersin (UniBe)Václava Havlová (UJV), Angela Mendoza Miranda Norma (UJV), Martin Klajmon (UJV), David Dobrev (UJV), Petr Večerník (UJV), Margit Fabian (MTA EK), Diederik Jacques (SCK CEN)**

To be cited as:

Wittebroodt C., Turrero M.J., Torres E., Gómez P., Garralón A., Notario B., Sanmiguel M., Cuevas J., Mota C., Ruiz A.I., Fernández R., Ortega A., Samper J., Mon A., Montenegro L., Hadi J., Kizcka M., Jenni A., Goethals J., Greneche J.M., David K., Wersin P., Havlová V., Miranda Norma A.M., Klajmon M., Dobrev D., Večerník P., Fabian M., Jacques D. (2024): Final technical report on the steel/clay material interactions. Final version of deliverable D2.7 of the HORIZON 2020 project EURAD. EC Grant agreement no: 847593.

Disclaimer

Acknowledgement

This document is a deliverable of the European Joint Programme on Radioactive Waste Management (EURAD). EURAD has received funding from the European Union's Horizon 2020 research and innovation programme under grant agreement No 847593.

Status of deliverable		
	By	Date
Delivered (Lead Beneficiary)	Charles Wittebroodt (IRSN)	October 2023
Verified (WP Leader)	Diederik Jacques (SCK CEN)	January 2023 (after revision)
Reviewed (Reviewers)	Guido Deissmann (FZJ)	February 2024
Revised (Lead Beneficiary)	CharlesWittebroodt (IRSN)	April 2024
Verified (WP Leader)	Diederik Jacques (SCK CEN)	May 2024
Approved (PMO)	Tara Beattie	May 2024
Submitted to EC	Andra (Coordinator)	16 May 2024

Executive Summary

Subtask 2.1 of the ACED work package of EURAD relied upon a combined modelling-experimental approach to provide key information on carbon steel/clay material interface interactions that are important for understanding the long-term evolution of engineered barrier systems for a deep geological repository (DGR). The results obtained provide basic data for the upscaling from component/interface process level models to waste package scale models (Task 3) and disposal cell (Task 4) models.

FEBEX (Full-scale Engineered Barrier Experiment) was a demonstration and research project for the engineered bentonite barrier of a HLW repository, which replicates the crystalline host-rock environment at different scales (*in situ* full-scale, *mock-up* and laboratory tests). The FEBEX bentonite is made of montmorillonite (> 90 %) and contains quartz, plagioclase, potassic feldspar, calcite and trydimite as accessory minerals. It has up to 15 % illite/smectite interstratifications. Its cation exchange capacity is > 100 meq/100g and main exchange cations include: Ca (42 %), Mg (33 %), Na (23 %) and K (2 %). Geochemical processes occurring at the iron/FEBEX compacted bentonite interface under simultaneous hydration and heating were investigated thanks to long-term laboratory experiments. Results showed the impact of temperature on both water distribution inside the bentonite and salts precipitation that can impact corrosion processes initialization. Non saturated conditions seem to favour potential oxidizing conditions but dry conditions limited the extent of the reactions producing new minerals. Corrosion is restricted to zones close to the interface (≈ 2 mm) and the calculated corrosion rate is less than 0.5 µm/year under simultaneous hydration and heating processes that provided a realistic approximation of the expected geochemical conditions during the unsaturated state of a HLW repository. Corrosion products consist of iron oxides, mainly hematite, and magnetite – maghemite and/or goethite. After 15 years of interaction, the maximum thickness of corrosion products formed is about 10 µm, and the maximum thickness of bentonite interface material affected by iron mineral formation is about 200 µm. Geochemical interactions occurring for such iron powder/FEBEX compacted bentonite interface have been modelled with a THCM reactive transport model that considers bentonite swelling, evaporation and initially unsaturated conditions in the bentonite, and uses an assumed geochemical conceptual model. Conclusions arising from FB (F: iron powder layer, B: bentonite compacted block) test simulations showed that in contrast to experimental observation, magnetite is the only corrosion product observed and it precipitated in the whole iron powder, but only in a small amount in the first 2 mm into the bentonite (magnetite observed at iron powder/bentonite interface). To improve results, sensitivity runs were performed to change values of vapor tortuosity (i.e., tortuosity of the porous medium with respect to gas phase), Fe powder thermal conductivity, initial sorption site concentrations or initial mineral volume fraction composition. Even if the computed sorbed iron reproduces the measured data better than that of the base run, there are still some discrepancies between numerical representation and experimental data. The reactive transport model of FB tests has uncertainties which could be overcome by accounting for several parameters as (i) an initial aerobic corrosion stage and the associated Fe(III) oxides, hydroxides and oxyhydroxides precipitation, (ii) a time-varying corrosion rate depending on pH and saturation index, (iii) some kinetic aspects (magnetite precipitation or smectite dissolution) and (iv) some changes in porosity, permeability and diffusion coefficients caused by mineral dissolution/precipitation. FeMo (iron mobility) tests simulations showed that results obtained for different iron particle sizes are similar. Magnetite is the main corrosion product computed and it precipitated with siderite, greenalite and saponite-Mg at the Fe powder/bentonite interface. pH values increased in the metallic sinter, the iron powder (up to pH 9.5) and also in bentonite (more slightly) with small changes in smectite, quartz and calcite contents. The model exhibits uncertainties which could be overcome by accounting for a more complex 2D vertical model considering non uniform conditions along the vertical direction, and by taking into account the precipitation of other corrosion products (hematite, maghemite, lepidocrocite and akageneite).

The FEBEX *in situ* experiment has also been modelled using two alternative approaches thanks to two different models (UDC and UniBern models). The reactive transport model presented by UDC uses a simplified corrosion approach by considering a source of iron and oxygen to trigger goethite precipitation. The main conclusions associated to this model showed that both goethite precipitation in

the bentonite (mostly near the iron source, d < 50 mm) and measured total iron data are well reproduced. The modelled fronts of dissolved, exchanged and sorbed iron penetrate 150 mm into the bentonite. The model also showed that goethite precipitation induced pH and Eh decrease. This model exhibits uncertainties which could be overcome by accounting for a more realistic corrosion model considering an initial aerobic corrosion stage and the associated Fe(III) oxides, hydroxides and oxyhydroxides precipitation, and also by taking into account the precipitation of other corrosion products (magnetite, siderite, hematite, maghemite, lepidocrocite, akaganeite and Fe-phyllosilicates).

Anaerobic Fe(II)/montmorillonite interactions have also been investigated, with a focus on the possible redox processes (electron transfers between dissolved Fe and structural Fe). Various sets of batch experiments on dispersions were conducted, as well as diffusion experiments on compacted clay cores. Analytical methods including colorimetry, ion chromatography, ^{57}Fe Mössbauer spectrometry and isotopic analysis were used to distinguish between the different Fe(II) uptake processes. Fe(II) uptake by clay depends on multiple factors, especially the pH and the relative dissolved iron (Fe_{aq}) and structural iron (Fe_{str}) concentrations. Cation exchange dominates at low pH (below pH 5.0) but other processes (involving electron transfer and presumably Fe precipitation) are more prominent at higher pH (above pH 6.0). Such processes can lead to high Fe uptake by the clay, and two new mechanisms are proposed to explain the Fe uptake processes. Results of the diffusion experiments (pH 7.3) clearly show that the redox process between in-diffusing Fe(II) and structural Fe(III) in the compacted clay core does not occur, except at the vicinity of the filter (interfaces between the compacted core and the ferrous solutions). The interaction of dissolved Fe with compacted clay seems to be limited to cation exchange (planar sites) and surface complexation on edge sites, in contrast to dispersed clay.

The chemical evolution of several iron–bentonite–water systems was studied thanks to modelling of existing experiments. The geochemical modelling approach was based on a three-step procedure: (i) a simple equilibrium model for iron/bentonite/water systems, (ii) a kinetic model considering kinetic effects and time-dependence of geochemical processes and (iii) 1D reactive-transport models including kinetic effects and transport phenomena. This modelling includes the consideration of the simulation of the development and transfer of the corrosion products that evolved under the experimental conditions. Equilibrium modelling results showed that the main corrosion product identified at 25°C is siderite and that temperature increase (70°C) favors the formation of Fe- phyllosilicates (neither magnetite nor chukanovite calculated as equilibrium corrosion products). An impact of CO_2 partial pressure has been observed (supports siderite formation instead of Fe-phyllosilicates), particularly at lower temperatures. Parallelly, a partial dissolution of bentonite primary minerals (montmorillonite) has been noticed. Kinetic modelling results suggested that siderite is the only corrosion product to be formed (regardless of bentonite material and pCO_2 considered, no magnetite formation predicted). Some Fe(II)-illite phases induced by bentonite alteration caused by dissolved FeII ions from corrosion processes are also observed very locally. It has been noticed that bentonite underwent relatively minor and slow changes throughout the considered timescale of 10 years. Overall, kinetic modelling demonstrated that different considerations regarding the model parameters (adapted corrosion rate, higher pCO_2 and suppression of the secondary phyllosilicate minerals) provided quantitatively different results. Results of reactive transport modelling studies were generally consistent with those of the kinetic model in most cases but allowed for a more detailed insight into the spatial location of the geochemical changes. Siderite was the main corrosion product (precipitation on metallic surface, not in bentonite) and a very small amount of FeII-illite was formed in the bentonite at the interface iron/bentonite, especially when temperature increases. Finally, it appears that the dissolution of bentonite primary minerals was an insignificant process.

Table of content

List of figures

List of tables

Glossary

AAS	Atomic absorption spectroscopy
ABM1, ABM2	Alternative Buffer Material Tests performed at Äspö Hard Rock Laboratory (S)
ACED	Assessment of Chemical Evolution of ILW and HLW Disposal Cells
B_{HF}	Hyperfine field
BC	Base Case
BPW	Bentonite Pore water
CEC	Cation exchange capacity
CE	Cation exchange
CIEMAT	Centro de Investigaciones Energéticas, Medioambientales y Tecnológicas, Spain
DGR	Deep Geological Repository
EBS	Engineered Barrier System
EDX	Energy Dispersive X-ray spectroscopy
ES	Edge sorption
EURAD	European Joint Programme on Radioactive Waste Management
FB experiment	Fe/Bentonite interface cells
FEBEX	Full-scale Engineered Barriers Experiment
Fe_{aq}	Dissolved iron
Fe_{str}	Structural iron
FMHW	Full width at half height
Goe	Goethite
GGW	Grimsel groundwater
GTS	Grimsel test site
hem	Hematite
HLW	High Level Waste
HS	High Spin
ICP	Inductive coupled plasma
Ill	Illite
ILW	Intermediate Level Waste
IS	Isomer shift
LA-ICP-MS	Laser ablation-induced coupled plasma-mass spectrometry
mmt	Montmorillonite
MX-80	Bentonite of Wyoming
NRG	Nuclear Research and Consultancy Group, Netherlands
Oct	octahedral
P_S	Swelling Pressure
PEBS	Long-term performance of Engineered Barrier Systems EU project
QS	Quadrupolar splitting
RH	Relative Humidity
RS	Redox sorption
RT	Room Temperature
SCK-CEN	Belgian nuclear research centre in Mol, Belgium
SEM/TEM	Scanning electron microscopy / Transmission electron microscopy
SWy-3	Na-montmorillonites (Wyoming) from source clay repository

THCM model	Thermo-hydro-chemical-mechanical model
UAM	Autonomous University of Madrid, Spain
UDC	University of A Coruña, Spain
ÚJV	Nuclear Research Institute, Czech Republic
UOS	Disposal container project (Abbreviation for experiments performed at ÚJV)
X, N-CT	X-ray, neutron-computed tomography
XRD	X-ray diffraction
XRF	X-ray fluorescence
WP	Work package
2ε	Quadrupolar shift

1. General introduction

The work presented in this report is part of the EURAD work package "**A**ssessment of **C**hemical **E**volution of ILW and HLW **D**isposal **C**ells", short ACED. The broader scope of this work package is the assessment of the chemical evolution at the disposal cell scale involving interacting components/materials and thermal, hydraulic and/or chemical gradients by considering ILW and HLW disposal concepts representative for different concepts throughout Europe. The main objective is to improve methodologies to obtain multi-scale quantitative models for the chemical evolution at disposal cell scale based on existing and new experimental data and process knowledge and to improve the description of the most relevant processes driving the chemical evolution into robust mathematical frameworks.

An important basis for the work package is state-of-the-art scientific knowledge and experimental evidence on chemical processes acting at the interface of two materials. The investigation of the interface processes is dealt with in Task 2 of the ACED WP. **The general objective of this task is to provide geochemical and coupled reactive transport models for assessing the geochemical evolution at steel/clay material and steel/cement material interfaces in terms of corrosion rates, geochemical alterations and physical alterations.** These models will provide the bases for the up-scaling to waste package (Task 3) and disposal cell (Task 4) modelling (see Figure 1).

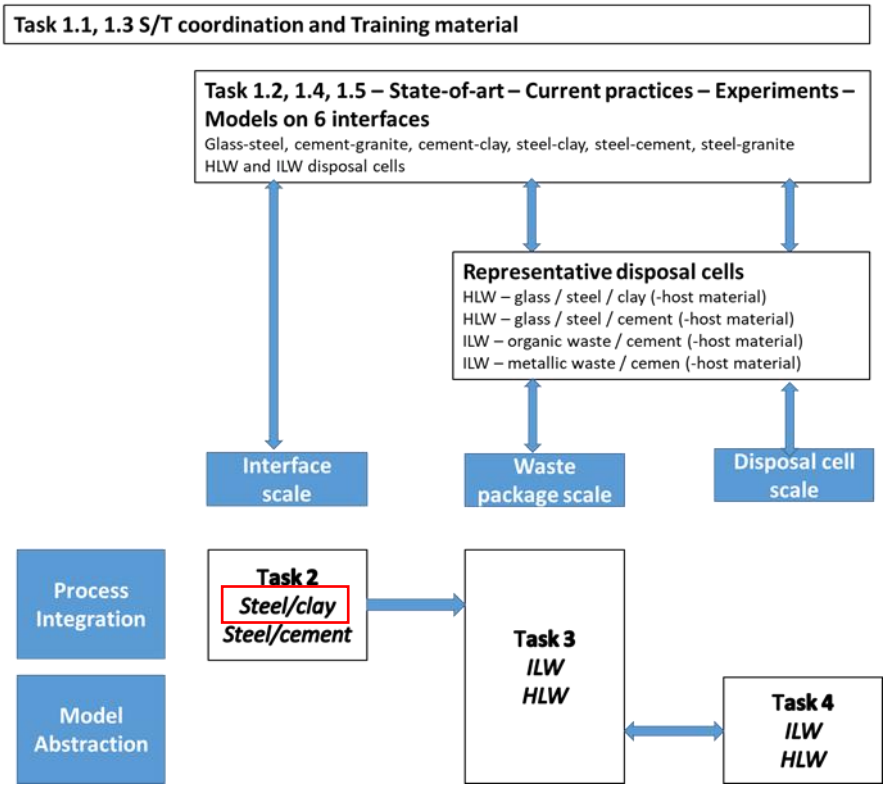

Figure 1 - Overall scope of the ACED project with its (sub)tasks and required information exchange between the different tasks. The red rectangle highlights the subtask dealt with in this report (source: WP proposal)

Task 2.1 focusses on the steel-clay interface and follows a combined modeling-experimental approach in order to increase confidence and decrease uncertainty of model simulations. Key factors and parameters for the conceptual description of steel/material interactions in reactive transport models and for model validation such as corrosion rates, physicochemical evolution and mineralogical evolution are determined using existing experiments and new experimental studies (Figure 2).

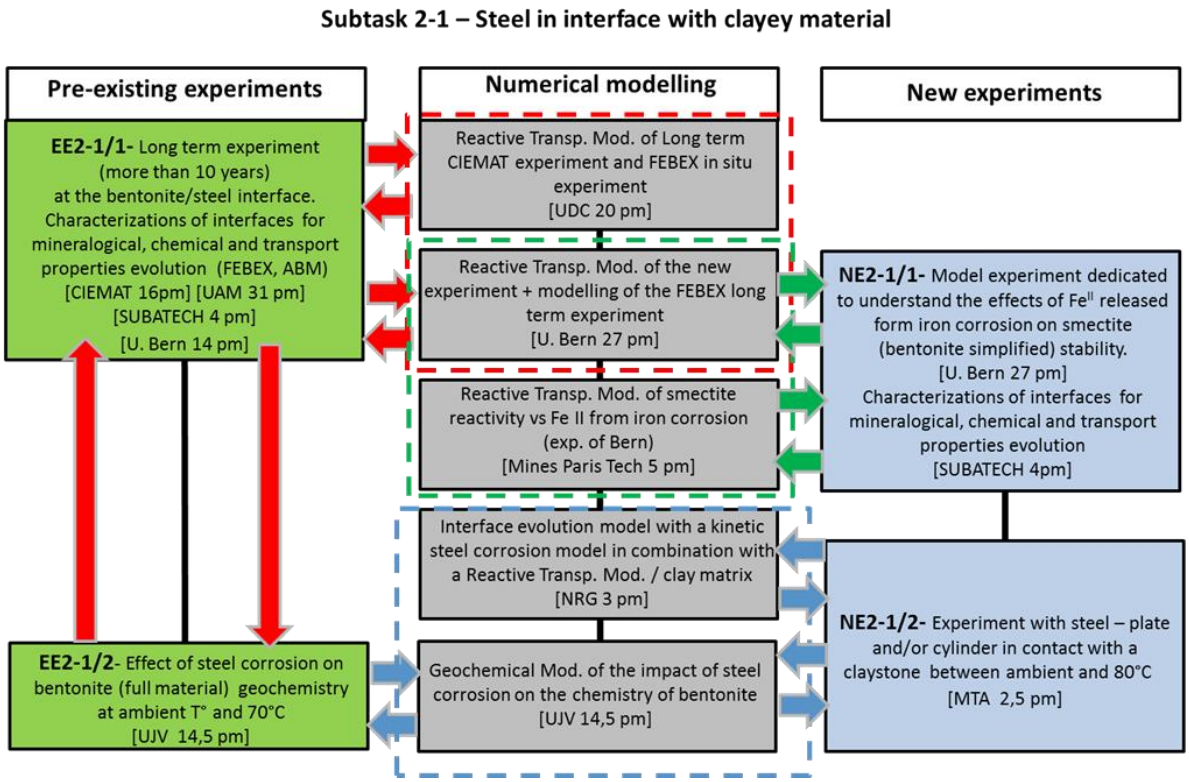

Figure 2 - Scheme of the subtask 2.1 organization with rectangles in dotted lines representing interactions between partners in the modelling group (source: WP proposal)[1]

This deliverable D2.7 - ACED Task 2.1 (Final technical report on the steel/clay material interactions) synthesizes the key results, identifies the difficulties and differences between the models and the experimental results, and proposes detailed outlooks in terms of experimental and modelling approaches to overpass the remaining gaps.

The report is structured as following:

Chapter 2 investigates the interactions of steel corrosion products with compacted FEBEX bentonite thanks to both experimental (FB and FeMo tests and FEBEX *in situ* experiment) and numerical (THCM reactive model – corrosion model) approaches (FEBEX Working Group);

Chapter 3 presents the experimental (batch and diffusion tests) and numerical (reactive transport model) work done to investigate the interactions between ferrous iron ions and purified montmorillonite to understand and quantify Fe migration (retention and diffusion) in compacted bentonite (Fe II Working Group);

Chapter 4 firstly details the modelling work done to better understand the chemical evolution of several iron–bentonite–water systems experimentally observed and secondly the experimental/modelling activities done to characterize carbon steel/clay rock interactions occurring at high temperature (80°C) in a surrounding clayey geochemical environment representative of one of the Hungarian DGR concept options (High Concentration Working Group);

Chapter 5 recaps the main information regarding steel/clayey material interfaces geochemical evolution that have been gathered within Subtask 2.1 and that would be useful for up-scaling modelling. An outlook of the possible improvement and work planned to cover the relevant knowledge gaps and missing processes is also presented.

[1] NRG task is replaced by SCK CEN.

2. FEBEX Working Group

This chapter includes steel/clay experimental and modelling work considering Spanish FEBEX bentonite as engineered barrier material for high-level radioactive waste disposal. Work with this bentonite started in the framework of the FEBEX project for studying the transient state of the near field for a HLW repository in crystalline rock according to the Spanish Reference Concept (ENRESA, 1995, 2000, 2006a). An extensive experimental program has been developed over the years to obtain information on the thermo-hydro-mechanical and geochemical processes occurring in the bentonite during the non-isothermal and unsaturated period. It included the geochemical processes at the different interfaces of the bentonite with the engineered barrier components, as the iron/bentonite interface. The experiments with interfaces included different space and time scales in the laboratory, and also a real scale *in situ* test at the Grimsel Test Site in Switzerland, which provides an incomparable upscaling opportunity.

The groups that have worked on the analysis and modeling of the FEBEX iron/bentonite interface based on laboratory and *in situ* experiments during the EURAD-ACED project have been:

- CIEMAT and UAM in the dismantling and analysis of the main geochemical processes that occurred in steel/FEBEX bentonite long-term laboratory tests, and contribution for modeling (section 2.1).
- UDC modeled the laboratory tests analyzed by CIEMAT and UAM, including a sensitivity analysis (sections 2.2 and 2.3).
- UDC and UniBern developed steel/bentonite corrosion models considering the data of the FEBEX in situ test dismantled in 2015 (sections 2.4 and 2.5).

2.1 CIEMAT / UAM experiments

2.1.1 Purpose of the investigation

The chemical interaction between the carbon-steel container (CSC) and the bentonite is one of the aspects to investigate regarding the long-term safety of a Deep Geological Repository (DGR), since failure of the container and alteration of the bentonite could compromise the safety of the site concerning radionuclide migration. The combined effect of the heat generated by radioactive decay and the influx of groundwater from the surrounding rock through the bentonite will control the chemical and moisture conditions at the canister surface and therefore, will condition the corrosion behaviour of the CSC. In turn, the interaction of CSC's corrosion products with bentonite could lead to the formation of new iron-rich minerals that alter the bentonite's basic properties (Guillaume et al., 2004; Charlet and Tournassat, 2005; Montes et al., 2005; Bildstein et al., 2006; Savage et al., 2010).

Modifications near the CSC-bentonite interface vary as environmental conditions change during the life of the repository (e.g., degree of saturation, temperature, redox, pH and dissolved species) from the initial operational and post-closure stages until the system reaches equilibrium. A detailed phenomenological description of the system and its evolution can be found in deliverables 2.1 (Neeft et al., 2022[2]) and 2.5 (Deissmann et al., 2021[3]) of the European EURAD-ACED project.

In general, the studies reported in these two reports show the results of corrosion rates, corrosion products, Fe-bentonite interaction and bentonite transformation under unique specific experimental conditions. Furthermore, reactive transport models can predict corrosion rates and products if a number of variables such as humidity, pH, and concentration of dissolved salts, organic carbon and oxygen are included. However, most experiments and models do not consider the timing and evolution of the system from the dry-out stage up to equilibrium conditions. This implies to address the coupling between the thermal and hydraulic gradients during the transient state, when oxygen is not yet completely consumed and the interface is not saturated. In fact, even the timing of ingress of oxygen until reaching completely

[2] https://www.ejp-eurad.eu/publications/eurad-d21-aced-initial-state-art-assessment-chemical-evolution-ilw-and-hlw-disposal
[3] https://www.ejp-eurad.eu/publications/eurad-d25-experiments-and-numerical-model-studies-interfaces

reducing conditions is not yet well defined. Considering this transient stage in long-term numerical modelling is crucial to minimize existing differences between experimental and model data. Upscaling approaches are not always consistent and uncertainties in the long-term predictions may be related to the fact that the models just count initial and final products but not the intermediate phases related to the transient stage. The purpose of CIEMAT-UAM work in EURAD-ACED is to better understand and delimit the processes that occur during the transient stage until saturation and equilibrium are reached to help to a better definition of long-term models.

The general objective of the experiments is to investigate the iron-bentonite interface to improve the description of the most relevant processes that influence the chemical evolution at the scale of the final disposal cell. The results should help to improve mathematical models that allow long-term predictions about the evolution in the near field of a DGR.

The specific objective of the iron-bentonite interface investigation is to obtain information on chemical variables and alteration in the composition of the solid phase at a detailed scale (µm to cm) and to contribute to the description of the integrated chemical evolution at the final disposal cell scale. On the other hand, the evolution of the microstructure of the material depends on the degree of saturation and on the chemical evolution of the interface, determining the potential exchange of chemical species.

The investigation focused on several aspects considered representative of a transient stage of a DGR: (i) estimation of corrosion rates, (ii) analysis of chemical gradients, (iii) identification of mineralogical changes, and (iv) examination of the microstructural modifications. The results provide a data set for use in reactive transport models.

2.1.2 Experimental set-up

In the context of the past European NF-PRO project (Sneyers, A. (Coordinator), Final Report, 2008[4]), we conceived a laboratory-scale experimental design to analyse the geochemical processes occurring at the iron-bentonite interface under conditions as close as possible to those of the real emplacement, mainly concerning thermal and hydraulic gradients. It consisted of columns containing a 13mm-thick iron powder layer (F) and a 87mm-thick bentonite compacted block (B) that were heated to 100°C from the iron side and hydrated from the bentonite side (coupled thermal-hydraulic processes) (Figure 3). In 2006, 5 cells of these characteristics were started-off (FB1 to FB5) with the aim of dismantling them sequentially, from 6 months to 14 years, and analysing the geochemical evolution of the interface. A sixth experiment without hydration (FB6) started-off at the same time to focus on the processes in the very early phases of post-closure when the degree of saturation is low. Cells FB1 (6 months), 2 (12 months) and 3 (18 months) were dismantled and analysed during the NF-PRO project (ENRESA, 2008; Torres et al., 2009). We dismantled cell FB4 (4.5 years) during the European PEBS project (Torres et al., 2014). The last two cells, FB5 (14 years) and FB6 (15 years) have been analysed in the context of the European EURAD-ACED project.

Also in the context of the NF-PRO project, we started a single iron-bentonite interaction experiment with the aim of evaluating the iron mobility (FeMo) and the bentonite alteration considering a conservative scenario: (i) saturated conditions, (ii) aerobic initial conditions, (iii) high corrosion rates, and (iv) room temperature. FeMo has been analysed in the context of the European EURAD-ACED project after 15 years of operation.

The bentonite used in the experiments comes from the Cortijo de Archidona deposit (Almería, Spain), which was selected by ENRESA as suitable material for the backfilling and sealing of HLW repositories (ENRESA, 1998). It is the same clay material used in the FEBEX Project (“Full-scale Engineered Barriers EXperiment for a deep geological repository for high-level radioactive waste in crystalline host rock”) to manufacture the blocks of the large-scale tests (ENRESA, 1998). From now on, the bentonite will be referred to as FEBEX bentonite. Main characteristics of FEBEX bentonite are (ENRESA, 1998):

[4] https://cordis.europa.eu/docs/publications/1039/103938551-6_en.pdf

(i) the montmorillonite content is above 90 wt.% (92 ± 3 wt.%), (ii) the smectite phases are actually formed by a smectite-illite disordered (R0) mixed layer (10-15 wt.% illite layers), (iii) bentonite contains variable amounts of quartz (2 ± 1 wt.%), plagioclase (2 ± 1 wt.%), K-feldspar (trace), calcite and cristobalite-tridymite (2 ± 1 wt.%), (iv) cation exchange capacity (CEC) equal to 97.5 meq/100 g and the exchangeable cations are Ca (35 ± 3 cmol(+)/kg), Mg (31 ± 3 cmol(+)/kg), Na (27 ± 1 cmol(+)/kg) and K (2.6 ± 0.4 cmol(+)/kg), and (v) the water content of the clay under laboratory conditions is approximately 13.7 ± 1.3 wt.% (Villar et al., 1997).

The use of iron powder instead of bulk carbon steel enhances corrosion phenomena. Such a conservative approach to the unsaturated and oxidizing conditions expected during the post-closure stage had a double purpose; on one hand, maximizing the corrosion rate since the high specific surface of the iron particles help to overcome kinetic constrains and on the other hand, decreasing the O_2 fugacity because of the consumption of residual oxygen during the corrosion process. Goodfellow iron powder with a particle size of 60 µm and 450 µm, and a purity higher than 99% (Typical Analysis: Si < 1400 ppm, C < 200 ppm, H-Loss < 3000 ppm, P < 150 ppm, S < 150 ppm) was used to contact with bentonite in all the experiments.

Parallel to the EURAD-ACED project, the UAM is guiding a PhD thesis that aims to study the interaction of three different bentonites with carbon steel (Na-bentonite (MX-80), Ca-Mg-Na-bentonite (FEBEX) and Mg-bentonite (FEBEX pre-treated with $MgCl_2$)). For this, UAM assembled a series of small-scale short-term steel-bentonite reactivity experiments heated to 100°C from the C-steel side and hydrated from the bentonite side (coupled thermal-hydraulic processes). Although these investigations were not included as part of the original project, some of the main results complement and help the discussion of the results obtained from the FB and FeMo cells and for this reason are summarized in this report.

2.1.2.1 Description of the tests

2.1.2.1.1 FB tests – long-term, thermo-hydraulic gradients, unsaturated

The tests were performed in cells specifically designed for the project NF-PRO (ENRESA, 2008). They comprised cylindrical cells with an internal diameter of 70 mm and an inner length of 100 mm made out of Teflon to prevent as much as possible lateral heat conduction. Externally, stainless steel 316 L rings avoid the deformation caused by the swelling of bentonite. The upper closing of the cells was made by means of a stainless steel plug. Inside this plug, water circulated at room temperature (25 °C) in a deposit. The bottom part of the cells was a plane stainless steel heater set at a temperature of 100 °C, which is the maximum temperature expected on the surface of the waste container in the Spanish concept (ENRESA, 1997). In this way, a constant temperature gradient between top and bottom of the sample was imposed. The hydration occurred through the upper plug of the cell with water taken from a stainless steel pressurized deposit. A schematic diagram of the setup and a picture of the cells, named from now on as FB5 (referring to Fe-Bentonite interface), is shown in Figure 3.

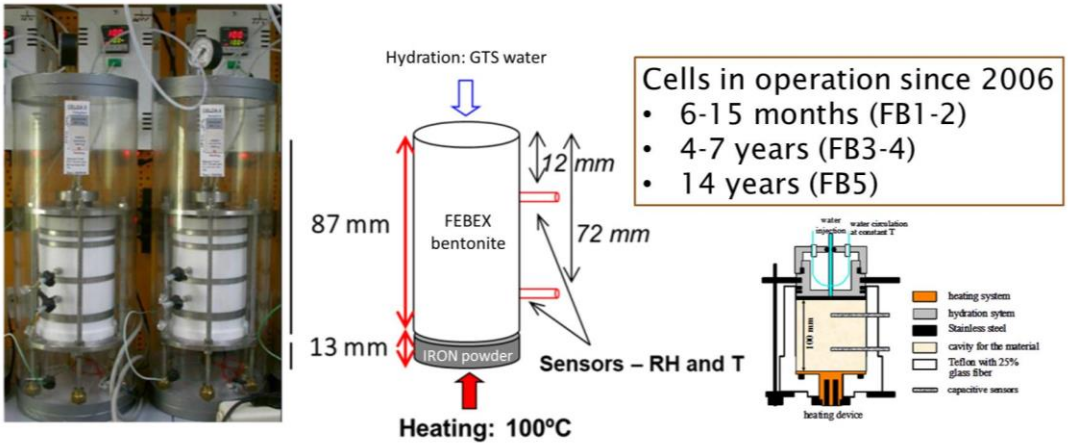

Figure 3 -On the left a photograph of the cells in operation is shown. On the right a schematic diagram of the cells used to make the Fe/Bentonite interaction tests, with the location of sensors measuring relative humidity and temperature. Note that the diagram is not at scale. GTS: Grimsel Test Site.

The FB-cells were instrumented with capacitive-type sensors placed inside the clay at two different levels, at 15 and 75 mm from the heater (Figure 3). The transmitters used are Sensirion STH75, which include a relative humidity (RH) sensor and a temperature-sensing element. A uniaxial pressure of 43 MPa was applied to 613.4 g of bentonite to manufacture 86.8-mm long compacted FEBEX bentonite blocks with its hygroscopic water content (14 wt.%) at a nominal dry density of 1.65 g/cm^3. At the bottom of the cell, in contact with the heater, 143.4 g of Fe powder were placed, giving rise to an iron layer thickness of 13.0 mm. On top of this, the bentonite block was inserted with a porous filter over it.

Once the assemblage mounted and the sensors connected, the temperature of the heater was initially set to 100 °C. The upper cooling was set at room temperature (25 ˚C). Finally, hydration from the deposit started immediately after assembling the whole system. The deposit was initially pressurized with nitrogen at five bars. The water injected to hydrate the iron/bentonite cells was Ca-Na-HCO_3^- granite-type water collected every year at the Grimsel Test Site (Garralón et al., 2017) (GTS in Figure 3). The borehole used for water sampling is close to the already dismantled in situ FEBEX experiment to study the processes influencing clay barrier evolution in a granite formation (ENRESA, 2006a).

2.1.2.1.2 FeMo test – long-term, isothermal-low temperature, saturated

The FeMo experiment was performed in a 120 x 120 mm square container 16 mm-high, made out of methacrylate and stainless steel 316L (Figure 4). FEBEX bentonite was compacted to a dry density of 1.6 g/cm^3 and placed into the cell with its hygroscopic water content (14 wt.%). Six holes were drilled into the bentonite (see distribution in Figure 4), and a 0.45 µm porous sintered steel tube was introduced inside. The gap between the sintered tube and the bentonite was filled with powdered iron with a grain size of 60 µm filling three holes and 450 µm filling the other three, in order to see if the differences in the reactive surface influence the corrosion process. Hydration was done through the sintered steel tubes using syringes fitted with O-rings to the system. The syringes were filled with Ca-Na-HCO_3^- granite-type water (Grimsel Test Site water, as FB cells). The test ran at room temperature for the whole experiment duration (15 years).

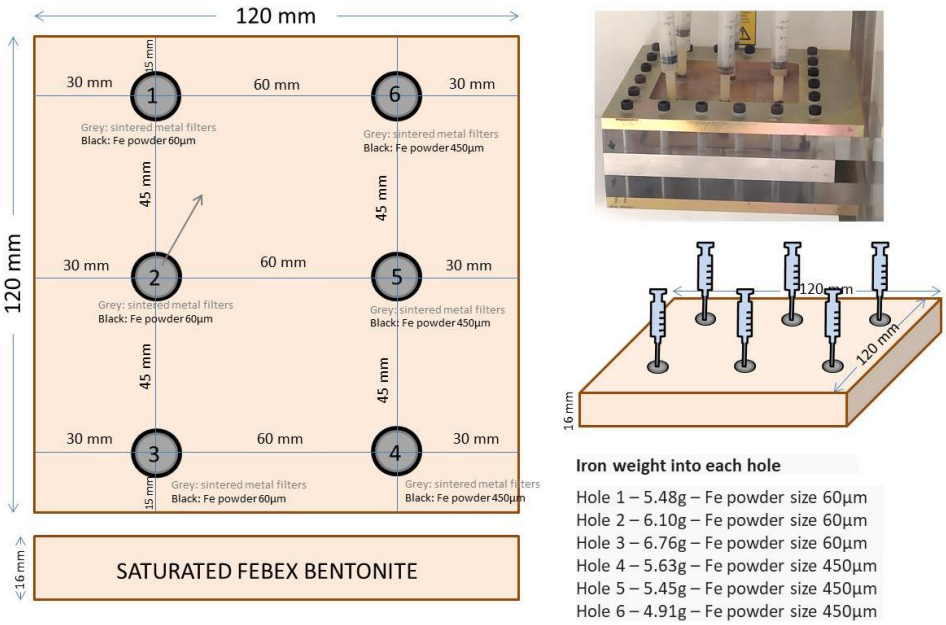

Figure 4 - Schematic illustration of the FeMo experimental set-up; (Right-up) Picture of the cell once assembled.

2.1.2.1.3 C-steel-bentonite tests (PhD) – short-term, thermo-hydraulic gradients, saturated

The experiments are performed using hydrothermal cells (Figure 5). Bentonite blocks, uniaxially compacted to a dry density of 1.65 g/cm^3, are faced to a disc of C-steel, which is heated to 100 °C. In the opposite side, the bentonite is hydrated with a saline solution of Na-Cl-SO_4 type (Mota-Heredia et al., 2023), as representative of a clay host rock. The experiments lasted approximately 1, 6 and 24 months. After six months, the samples were almost fully water-saturated. Additionally, there were two extra experiments with $FeCl_2$ instead of C-steel, to enhance reactivity in the system. In total, 11 cells were prepared.

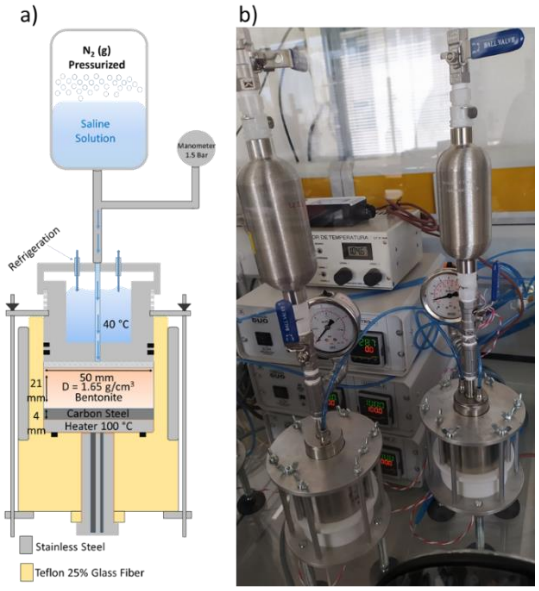

Figure 5 - (a) Scheme of a hydrothermal cell. (b) Photograph of the experimental set-up showing two cells and the electronic temperature controls at the back.

To study the evolution of the system, changes in the physical (water content and specific surface area) and chemical (cation exchange capacity and element distribution) properties of the bentonite were determined, as well as the formation of a corrosion layer on the steel.

2.1.2.2 Dismantling and Sampling

2.1.2.2.1 FB tests

Experiments FB5 and FB6 were dismantled inside a specific chamber assembled at the UAM laboratories for this purpose (hermetic and with an oxygen poor (sub-oxic) atmosphere (<2% vol.)). The chamber is large enough to dismantle the cell and to extract the column of bentonite and iron powder. As the sample was extracted, it was introduced into a cylindrical PVC housing with a spring occupying the entire space. The spring was compressed as the sample came out, thus avoiding a sudden fall of the sample inside the PVC housing and the breakage of the interface. This housing was previously filled with an Araldite 2020™ epoxy resin combined with a hardener to isolate the column from the environment, proceed to its study by micro-tomography and take samples in a controlled atmosphere (Figure 6). During dismantling of cell FB5, the capsule in which the sensor closest to the interface was inserted broke and one of the fragments remained inside the bentonite. In the micro-tomography image of Figure 6 (bottom right), the metallic fragment appears darker than the bentonite, near the interface. The image also shows the compressed spring (bottom of the image) and the powdered iron (upper part of the image).

Figure 6 - Pictures of dismantling operations and resin embedment of cell FB5. (Down-right) Micro-CT image of the whole cell showing the iron powder cap, the metallic sensor lost inside and the compressed spring at the base of the cell.

The column of bentonite and iron powder was cross-sectioned at the UAM laboratories according to the scheme shown in Figure 7. The cuts were made with a Well 2000™ diamond wire cutter, which allows a precise cut without producing frictional heat. For the cutting of the samples located in the proximity of the iron-bentonite interface, a special chamber was made to be able to section under controlled atmosphere, always protecting the sample with paraffin paper and adhesive tapes. Column samples were cut into circular sections retaining section FB5-1 (Figure 7) for specific sampling of the iron-bentonite interface. A similar sampling was carried out for cell FB6.

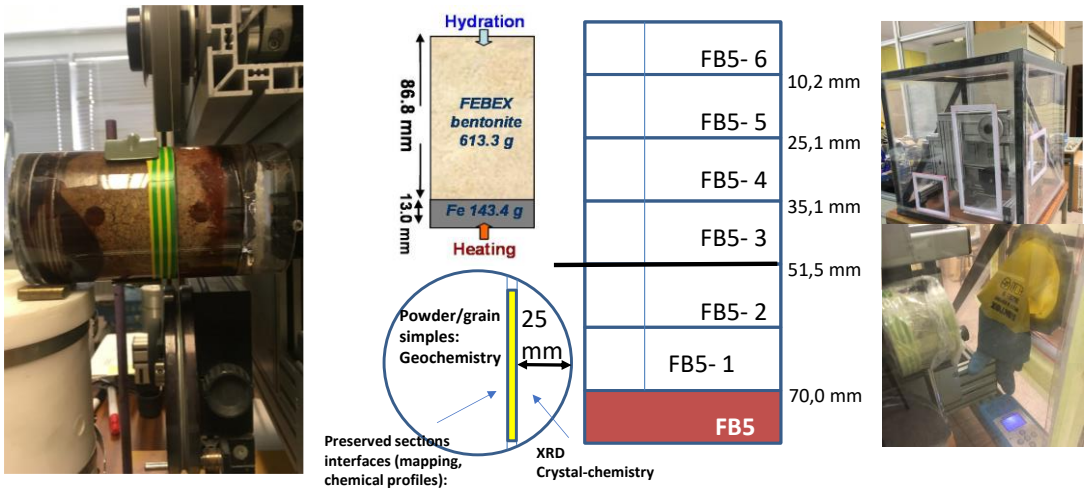

Figure 7 - Pictures of sectioning of cell FB5 inside a globe box under suboxic conditions. In the middle, schematic diagram of the sampling sections of FB5. The compacted bentonite block was sliced at different distances from the Fe/Bentonite interface. Sampling of FB6 cell was similar.

Sections FB5-6 to FB5-2 were split for the following analyses: (i) mineralogical, crystal-chemical, and geochemical analysis (X-ray diffraction (XRD), (ii) thermal analysis (thermogravimetric (TG) and differential thermogravimetric (DTG)), (iii) elemental analysis (C, H, S, N), (iv) chemical composition of the fraction smaller than 0.5 µm, (v) extraction and analysis of soluble salts and (vi) analysis of exchangeable cations and cation exchange capacity (CEC). In section FB5-1, a detailed study of the mineralogy of the bentonite samples at the iron-bentonite interface (microdiffraction, Mössbauer and Raman spectrometry, imaging study and variation of the chemical composition (Energy Dispersive X-Ray (EDX) profiles by Scanning Electron Microscopy (SEM)) was carried out.

Prior to sectioning and sampling, images of the column inside the cell were obtained by X-ray computed micro-tomography (examples of some images are shown in Figure 8). Micro-fissures observed in the unaltered column were also observed in the circular cross sections of the cut samples. Circular slices were done immediately after tomography and within a maximum of two weeks after dismantling to minimize salt and cation diffusion. Sampling of the iron-bentonite interface was carried out in a nitrogen atmosphere (evaporated liquid nitrogen). The samples were ground under these conditions for their study by XRD (airtight sample holder), and Mössbauer spectroscopy (Figure 9).

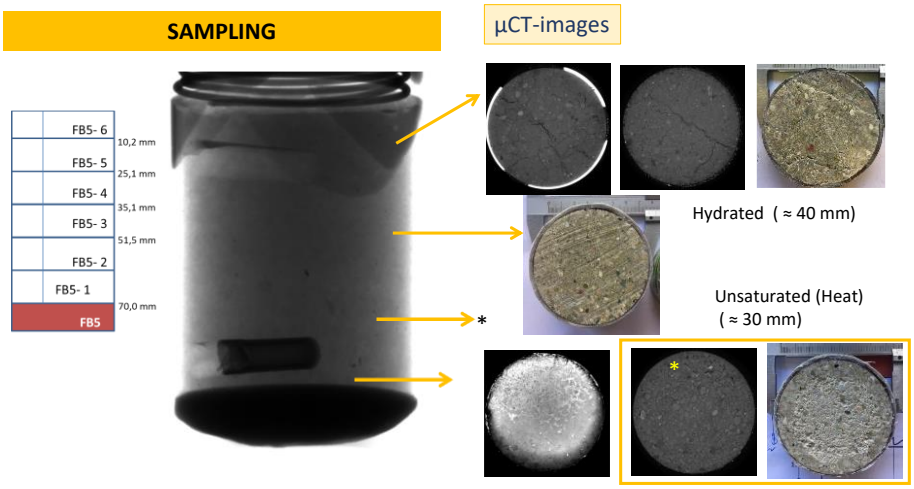

Figure 8 - Detail of circular sectioning of FB 5 sample. Visualization of microfissures and retraction cracks in different sampled sections.

Figure 9 - Preparation of FB-5 interface sample for mineralogical study. The transversal cut shown was performed also under suboxic conditions for the SEM-EDX study.

2.1.2.2.2 FeMo test

The experiment was dismantled inside a chamber with an oxygen poor (sub-oxic) atmosphere (<1% vol.). The sample was divided into six sections, each of which includes bentonite-iron powder-sintered with its corrosion halo (Figure 10). Each section was preserved embedded in resin. Section 3 was sealed with Araldite 2020 resin and cut under anoxic conditions to check the extent of the black and brown halo surrounding the iron powder between the bentonite and sintered steel cylinder. The 1 cm oxide halo extended to the cell surface. The thickness of the black-brown halo was inferior to 5 mm inside the cell (Figure 11 - cut details).

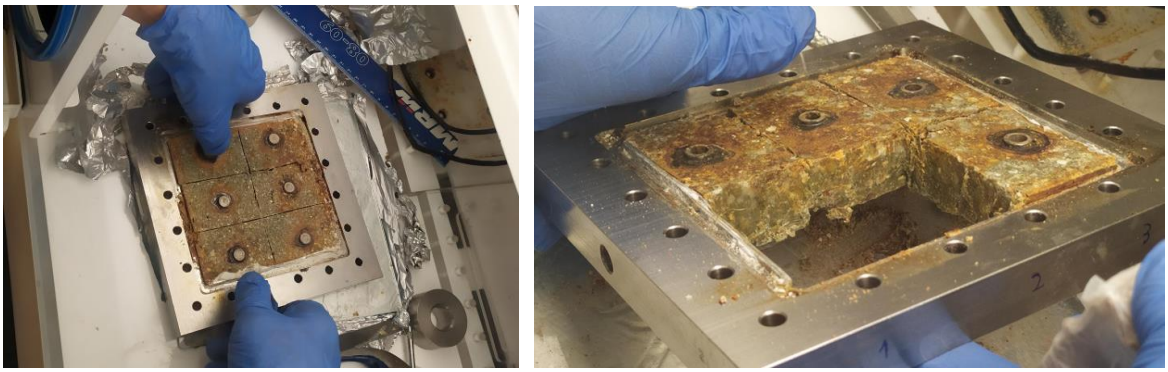

Figure 10 - Pictures of dismantling of FeMo test inside a suboxic chamber. (Left) Sectioning of the sample in six 40 x 60 mm blocks. (Right) Once two of the blocks were extracted, a cross section of the sample can be seen.

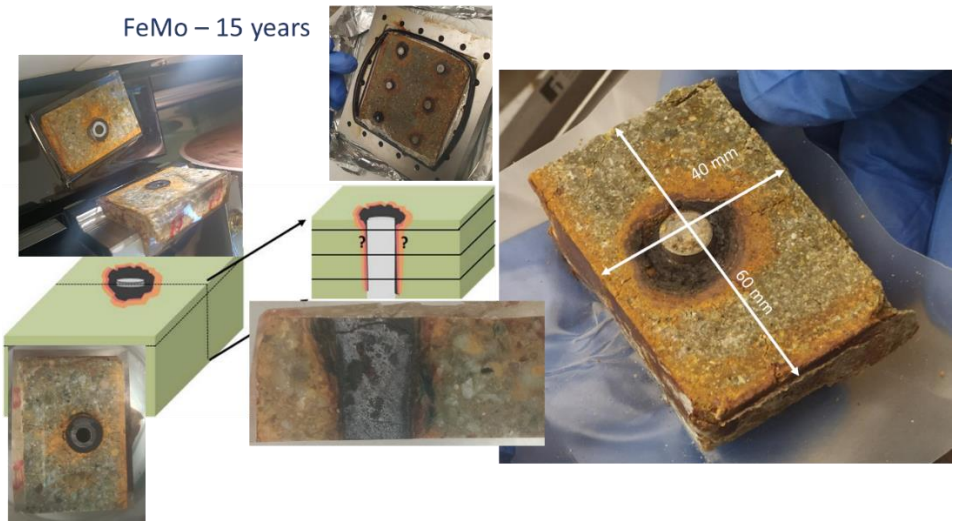

Figure 11 - Details of FeMo sampling of section 3. Black-brown halo transverse and cross cut is shown.

2.1.2.3 Methods of analysis

2.1.2.3.1 Water content

The gravimetric water content (*w*) was determined as the ratio between the mass of the sample and its mass after oven drying at 110 ºC for 48 hours (weight of solid). Measurements of gravimetric water content were made in FB5 sections. Duplicates were made for all the samples and unaltered FEBEX bentonite was used as reference.

2.1.2.3.2 Microstructure by µ-computed tomography

X-ray microcomputed tomography (micro-CT) is a non-destructive technique that was used to create cross-sections of the embedded FB5 sample to study the microstructure of the sample (e.g., porosity, volume of pores, microfissures, connectivity, etc). The inspection of the cell was done at the National Research Center of Human Evolution (CENIEH, Burgos, Spain) before sampling. The equipment used was a MicroCT V|Tome|X s 240 by GE Sensing & Inspections Technologies Phoenix X-Ray, with 1-micron spatial resolution. Because different material features and phases often have different X-ray absorption properties, we can easily identify the different features from the images. Pore sizes, pore orientation and interconnectivity were analysed in collaboration with CENIEH using both Dragonfly ORS (version 2022.2, software available at https://www.theobjects.com/dragonfly) and FIJI visualization and image analysis software (Schindelin et al., 2012).

2.1.2.3.3 Chemical characterization

Soluble elements

Soluble elements were analysed in aqueous extract solutions. pH and Eh were not determined in the extracts because they do not represent reliable environmental conditions regarding the actual cell system, but the method is assumed to give a useful indicator for the content of soluble ions. Bentonite samples were dried overnight in an oven at 105 °C. They were ground and placed in contact with deionised and degassed water at a solid to liquid ration of 1:8 (5 g of clay in 40 mL of water), shaken end-over-end and allowed to react for 24 hours. Separation was made by centrifugation (30 minutes at 12500 rpm) and the supernatant was filtered by a 0.45-µm pore size filter. Cations in supernatant were analysed by Inductive Coupled Plasma - Optical Emission Spectrometry (ICP-OES) in a Spectro ARCOS spectrometer after acidification of the samples to pH<2 with HNO_3 (8 ml/L). Anions were analysed using ion chromatography (Dionex DX-4500i). Duplicates were made for all the samples. Unaltered FEBEX bentonite was used as reference to compare and detect chemical perturbations.

Total cation exchange capacity and exchangeable cations

The method used to determine the CEC follows the procedure described by Meier and Kahr (1999), based on the substitution of the exchange cations of the clay by the Cu^{2+} cation and the capacity of the latter to absorb electromagnetic radiation of 620 nm wavelength. Measurements were made with a UV-visible spectrophotometer. Duplicates were made for all the samples. Unaltered FEBEX bentonite was used as reference to compare.

The distribution of exchangeable cations was determined using a $CsNO_3$ solution to displace the exchangeable cations (Sawhney, 1970). The concentration of the major cations was analysed by ion chromatography and ICP-OES. Duplicates were made for all the samples. Unaltered FEBEX bentonite was used as reference to compare.

Adsorbed iron

The samples remaining after soluble salt extraction were used to extract the adsorbed iron. The method employed was a modification of the one used by Aguilera and Jackson (1953) using 0.3 M citric acid as extraction solution. This type of chelating agent removes only the more reactive sites of the clay surface but does not dissolve the amorphous Fe oxides and magnetite/ilmenite. Neither structural Fe nor exchangeable Fe is affected by citric acid, so it was assumed that Fe determined by this method was mainly Fe absorbed in reactive surface sites of montmorillonite. Duplicates were made for all the samples. Unaltered FEBEX bentonite was used as reference to compare.

Free iron oxides

A citrate-bicarbonate-dithionite protocol was used for the removal of free iron oxides in clay samples (Mehra & Jackson, 1960). This treatment has almost no destructive effect on iron silicate clay minerals and has little impact on cation exchange capacity. Therefore, iron measured by this method would correspond mainly to iron oxides, as no alteration of bentonite is expected. Fe concentration was analysed by ICP-OES. Duplicates were made for all the samples. Unaltered FEBEX bentonite was used as reference to compare.

2.1.2.3.4 Mineralogical and crystal-chemical analysis

X-Ray Diffraction, powder samples

X-Ray Diffraction (XRD) was used to study the mineralogical changes along the bentonite block and at the interface with iron powder. Samples of around 5 g were dried in a desiccator (silica gel) avoiding atmosphere contact during drying. Then they were ball-milled in a MM200 RETCH™ device using Zircon vessels and balls. A final hand mortar milling in agate was used to homogenize sample grain size (< 5 µm). Prior to the measurements, the powder was equilibrated in an atmosphere of 55% RH in order to homogenize the water content of the samples. The analyses were performed using a Bruker D8 Discover diffractometer with a Ge monochromator and a lynxeye XE-T fast detector. The patterns were measured in a range of 3–70° θ/2θ, with angular increments of 0.02 and times of 1s. The device operated at 40 kV and 40 mA. For the samples taken near to the interface (<1 mm from the heater) and the iron powder and bentonite, an airtight holder (Figure 9) was used. The identification of mineral phases in X-ray diffractograms was performed by using the software X'Pert HighScore Plus® of PANalitycal™. The RIR semi-quantification method was used for interface samples. The International Centre of Diffraction Data (ICDD) powder diffraction files (PDF) standards supported in High Score Expert Plus© software (version 2.1.b 2005) was used for mineral checking (Table 1). Iron powder was sampled at the iron/bentonite interface and was put in an airtight holder for XRD analyses. Unfortunately, the obtained XRD patterns were not of sufficient quality to be treated with the refinement method of the RIETVELD software.

Table 1 - Mineralogical phases and modified RIR ratios (Cuevas et al., 2014) used for the identification and semi-quantification of minerals in bentonite. Iron interface ICDD PDF2 standards (2001) used as references are included.

Mineralogical phases	PDF standard reference	RIR[a]
Montmorillonite (Mont)	00-013-0135 [b]	0.2
Illite-mica (ill-Mca)	00-026-0911	2.0
Quartz (Qz)	01-079-1910	3.1
Cristobalite (Crs)	00-039-1425	1.0
Calcite (Cal)	00-024-0027	2.5
Tridymite (Trd)	00-001-0378	1.0
Sanidine (Kfs: Sa)	00-010-0353	0.6
Plagioclase, anorthite (Pl: An)	00-041-1486	0.6
Goethite (Gt)	00-029-0713	4.0
Hematite	00-024-0072	0.6
Maghemite-\ITC\RG	00-039-1346	1.4
Magnetite	01-075-1372	5.2
Iron	01-087-0721	10.8
Albite	00-001-0739	0.6

[a] RIR modified in High Score Expert Plus© (version 2.1.b 2005)

[b] Illite-2M_1 Muscovite

Microdiffraction

Some oxide grains detached from FB5 interface were examined immersed in oil and filled in a glass capillary in a Bruker Kappa Apex II single-crystal X-ray diffractometer with Mo Kα radiation (λ = 0.71073 Å). The microdiffraction analysis was performed with an exposure time of 60.00 s. The measurements were processed with the APEX4 software package (Bruker©2021).

FT-IR analysis

FT-IR spectra of corrosion products and bentonite samples were obtained in the middle-IR region (4000-400 cm^{-1}) with a Nicolet 6700 with a DTGS KBr detector (resolution 4 cm^{-1}, 40 scans) on KBr-pressed discs in transmission mode.

μ-Raman spectroscopy

μ-Raman spectroscopy was performed with a Jobin Yvon LabRAMHR800 instrument (HORIBA Scientific), with an Olympus BX41 confocal microscope. The laser beam (He-Ne laser) (nominal power 20 mW) was focused onto the sample through the 100× objective of the microscope with an excitation wavelength of 632.81 nm, and the Raman signal was collected in reflection mode. Spectra were measured in Raman shift intervals of 150 to 1400/2300 cm^{-1}. All acquired spectra were recalibrated using a Neon emission light.

The preserved iron particles of the interface sample were loaded in a Linkam stage inside an anoxic globe box to preserve it from oxygen while being manipulated. The stage is coupled with the BX4 Olympus microscope of the spectrometer. Nitrogen circulation prevented oxygen ingress while analyses were made.

Thermal Analysis (TA)

The thermal analysis of the bentonite sections for each cell was performed by TGA with 0.5 g of the bulk sample as prepared for bulk powder analysed by XRD. They were tested in a DSC/DTA/TGA Q600 TA Instruments R module from 25 to 1000°C at a temperature increment rate of 10°C/min. DSC data are not shown in this report.

Elemental analysis

The determination of the percentage of carbon, hydrogen, nitrogen and sulphur was performed in samples treated identically to XRD and TA measurements, in LECO CHNS-932™ equipment (Model NO: 601-800-500). The minimum quantified content is 0.2 wt.%, and the quantity of sample used was 1 mg (triplicated for each sample).

Mössbauer spectroscopy

Measurements were performed on airtight preserved samples for both bentonite and iron powder interface to check the Fe^{+2}/Fe^{+3} ratio. Mössbauer spectra were recorded in triangular mode using a conventional spectrometer with a 50-Ci ^{57}Co (Rh) gamma-ray source mounted on an electromagnetic transducer in transmission mode. The data obtained at room temperature were analysed with the NORMOS program (Brand, 1995). The spectrometer was calibrated for each velocity using an alpha-Fe (6 µm) foil.

Electron Microscopy

Scanning electron microscopy with energy dispersive X-Ray detector (SEM-EDX) was used to study the iron-bentonite interface, either to observe fresh fracture specimens (mineral morphologies identification) or polished flat surfaces with attention to the corroded grains and the distribution of elements at the interface (elements chemical profiles identifying chemical gradients).

Surface images and morphologies were captured using a Hitachi S-3000 N scanning electron microscope (SEM) coupled with an EDX XFlash® 6130 Bruker detector. To prepare samples for SEM, a thin layer (5mm) containing a transverse section of pressed iron powder (previously embedded in resin during the dismantling) and part of the FB bentonite section labelled 1 (Figure 7) was cut under anoxic atmosphere using a diamond wire cutting machine Well2000™. Once sectioned, FB interface chips were scrapped from one of the faces adjacent to the layer for vacuum drying and SEM observation. The remaining water content in the iron-bentonite thin layer was removed by immersing it in liquid nitrogen for 30 minutes to freeze water before applying vacuum for 2-3 days until the pressure dropped below $1.3x10^{-4}$ Pa (10^{-6} Torr). Once dried, the samples were embedded in Araldite 2020™ resin to create rigid pieces that could be easily cut with a saw to fit in the microscope chamber. Subsequently, the samples were polished using sandpaper of various grain sizes. This was done to achieve flat surfaces suitable for microscopic studies, with a specific focus on preserving the iron-bentonite interfaces as alterations in these regions are expected to occur within a narrow extent. To complete the preparation, the samples were coated with gold using a Q150T-S Quorum sputter coater system.

Corrosion rate and corrosion thickness estimation from back-scattered electron (BSE) images

The overall thickness of corrosion products was measured from multiple BSE images of the FB5 and FB6 iron samples. We converted images to false colour to help distinguish subtle variations not easily distinguishable in the original greyscale. Thicknesses were measured in lines perpendicular to the iron particle surface (see Figure 12) and averaged for each particle. An average value of the corrosion rate (µm/year) was estimated calculating the ratio average thickness/number of years that the experiment has been operating.

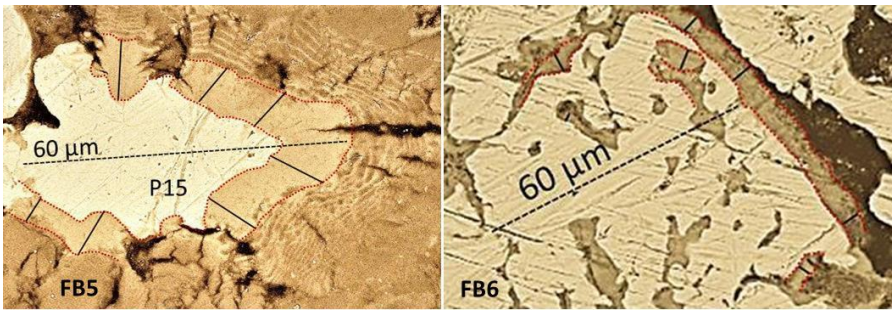

Figure 12 - Examples of false-colour back-scattered electron images showing the FB5 (left) and FB6 (right) iron particles (brighter colour) surrounded by an oxide rim (darker colour; surface between red

spotted lines). The thickness of the oxide rim was obtained from the average value of several lines drawn perpendicular to the surface of the iron particles.

XRF-Chemical analysis in <0.5 µm size fraction

The structural formulae of the smectite was calculated using analyses on the Ca-homogenised <0.5-µm fraction obtained by sample dispersion and centrifuging (Fernández et al., 2014). 0.5 g of the dried sample was fused with lithium tetraborate (0.3:5.5 sample:flux) in a PerlX'3 automatic bead preparation system (PANalytical™ B.V., Almelo, The Netherlands). The quantity of sample used was statistically significant for the analysis and a unique sample procedure was preferred instead of splitting the sample in smaller portions to obtain replicated analyses. The major elements were determined by means of wavelength dispersive XRF analysis in a ZETIUM (PANalytical™) instrument using a rhodium X-ray tube (Malvern PANalytical™ Ltd, Malvern, UK).

2.1.3 Results

2.1.3.1 FB tests

2.1.3.1.1 Heating-Hydration records and Water content

During the tests, temperature and relative humidity were measured at two positions, near the hydration end and near the interface end (heater). The sensors were read by connecting a specific device to the sensor output and then disconnecting it and connecting it to another sensor and so on until all available sensors were read. The data set was manually logged almost daily for two years. After that there was no continuous logging, but spot and random logging. Figure 13-A shows the evolution of temperature and relative humidity during sensor operation of cell FB5. The sensor close to the hydration in cell FB5 gave a failure after 2 years of operation and the sensor close to the heater registered an increase of temperature after around 2 years (when the other sensor failed) and then stabilized. The temperature at 28 mm from the heater (15 mm from the iron-bentonite interface) stabilized around 80 °C and at 12 mm from the hydration stabilized around 40 °C. Figure 13-B shows the cumulative curve of water inlet into the cell FB5 measured by weighing the injection bottle. The water input is progressive and the last recorded measurements after 3.8 years (about 1400 days) of operation are almost 60 grams of water, which would correspond to approximately 25% of gravimetric water content in the bentonite.

Figure 14 shows the data of the sensors of cell FB6 during operation, which gave indication of a correct functioning during the 15 years of operation. Temperature is quite similar to that measured in FB5; at 23mm from the heater (10mm from the iron-bentonite interface) it stabilized around 75 °C and at 12mm from the opposite side it stabilized around 45 °C. Relative humidity is much lower than measured in FB5, as expected in a cell with no hydration.

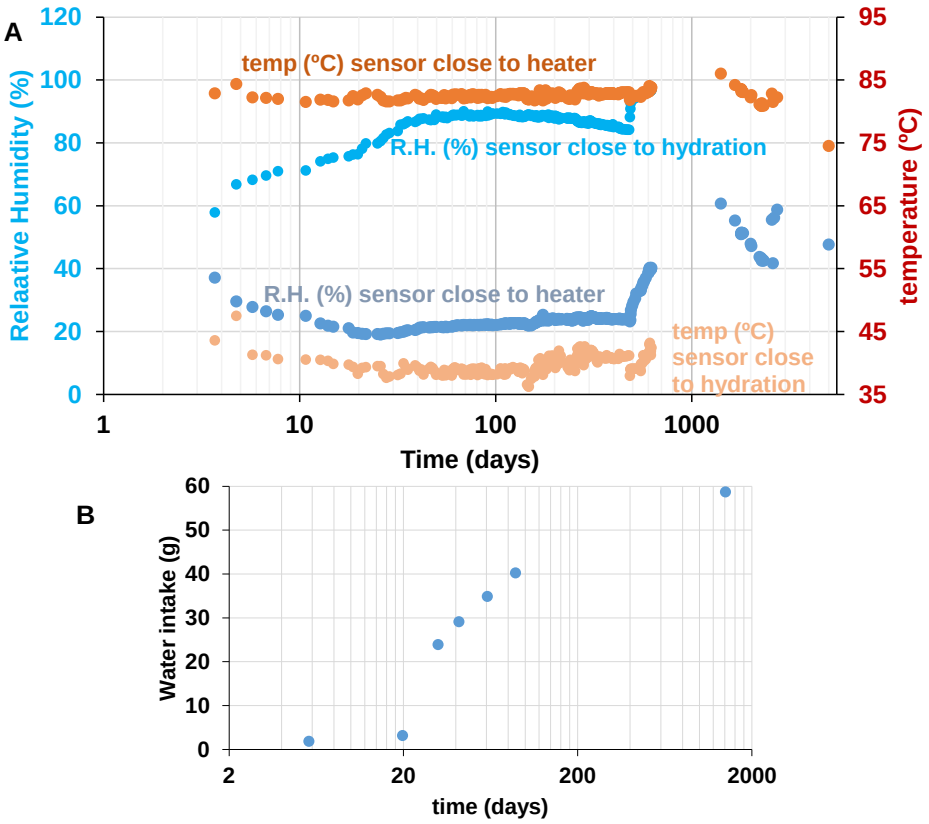

Figure 13 - (A) RH and temperature measured by sensors (near the hydration and the heater) in cell FB5. (B) Water intake in cell FB5

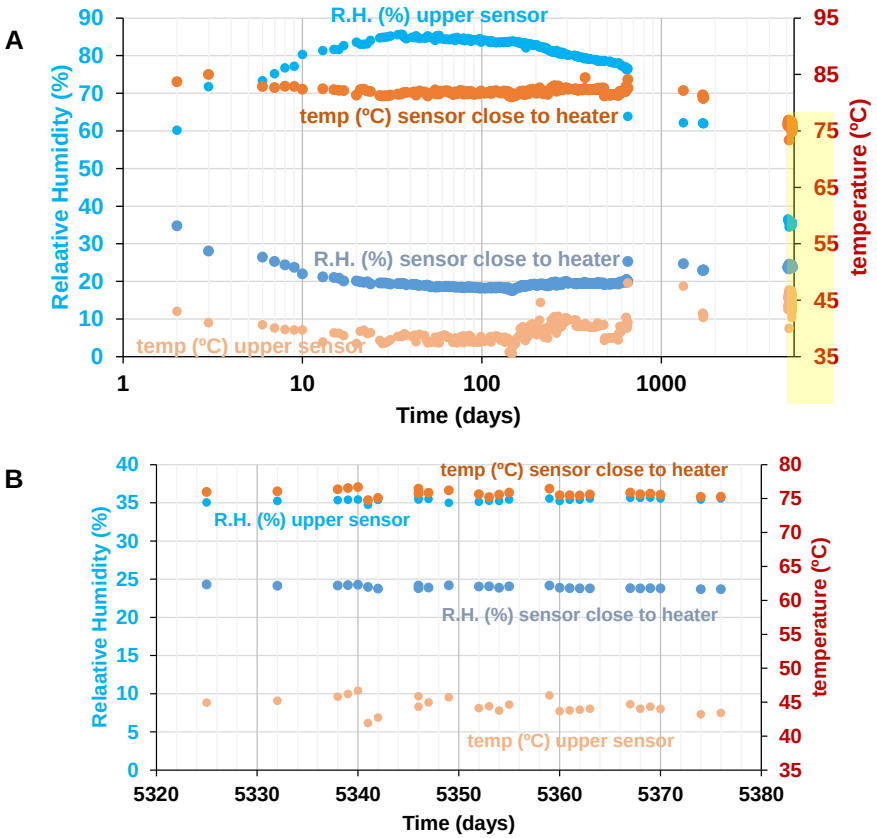

Figure 14 - (A) RH and temperature measured by sensors (near the upper part of the cell (without hydration) and the heater) in cell FB6. (B) Detail of the records of the last weeks of operation of FB6.

Figure 15-A shows the gravimetric water content (*w*) for each section of the FB5 cell. The distribution of the final water content is related to the thermal gradient and the hydration front. The water content near the heater is lower than the initial hygroscopic water content (14 wt.%). That indicate that desiccation (i.e., water vapour movement) was quick and persistent and liquid water did not reach the half of the bentonite column closest to the interface with the heater. The water content measured near the hydration was close to 20 wt.%. Figure 15-B shows the average temperature recorded by sensors during operation of FB5, and the values at the extremes are the set-temperature of the heater (100 °C) and the mean room temperature at the laboratory (25 °C).

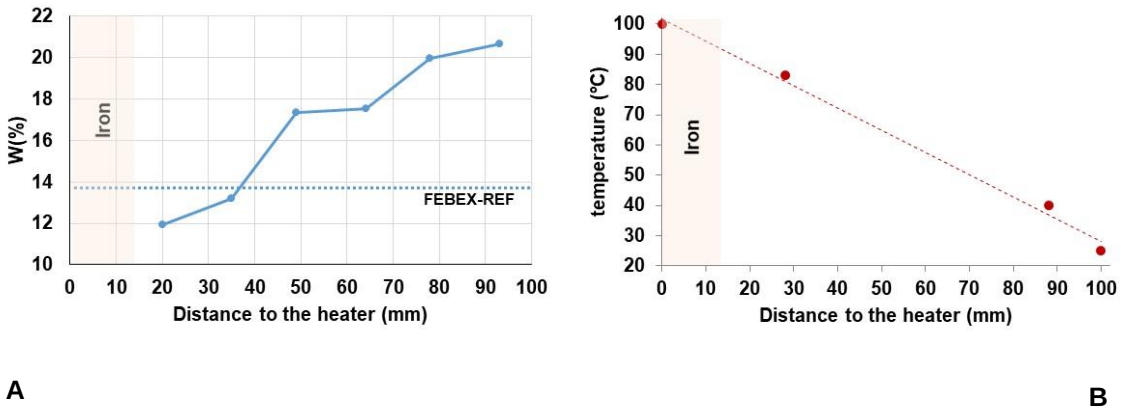

Figure 15 - (A) Plot with the gravimetric water content of bentonite in FB5 measured after dismantling. (B) Plot showing the average distribution of temperature in cell FB5 during operation.

2.1.3.1.2 Microstructure - X-ray microtomography

X-ray microtomography was performed on cell FB5. Results revealed the presence of microfissures perpendicular to the interface and to the sensors insertion holes, probably related to desiccation due to temperature at the interface combined with unsealed microcracks around the sensors formed during insertion as the bentonite is not saturated (Figure 16-A).

Dragonfly ORS software was used to segment the volume of the iron-bentonite interface. Once the volume is segmented, it is possible to analyse iron particle penetration (Figure 16-B). Thus, it is possible to obtain a diagram with a large number of points with different penetration thicknesses along an XY section. Then a mesh is created that contains at each point the thickness value of the object (iron particle) (Figure 17). The colour indicates the thickness of penetration (red colour representing the areas with greater Fe penetration and blue colour representing the areas with less Fe penetration).

To analyse the porosity (orientation of pores, porosity (voids) and connectivity), and pore size (as volume, mm^3), the bentonite cylinder was segmented into 2 sections parallel to the main axis and 3 sections parallel to the interface (Figure 18). For the analyses, the areas with distortion due to the holes left by the sensors were avoided. For P1 and T2 (see Figure 18) an area between the two sensors that contains the hydration front was selected. In all cases the edges of the cylinder were avoided to prevent

distortion of the data by the edge effect. On the one hand, the intrinsic porosity (the voids) was calculated as well as connectivity of pores. On the other hand, the orientation of the pores was analysed.

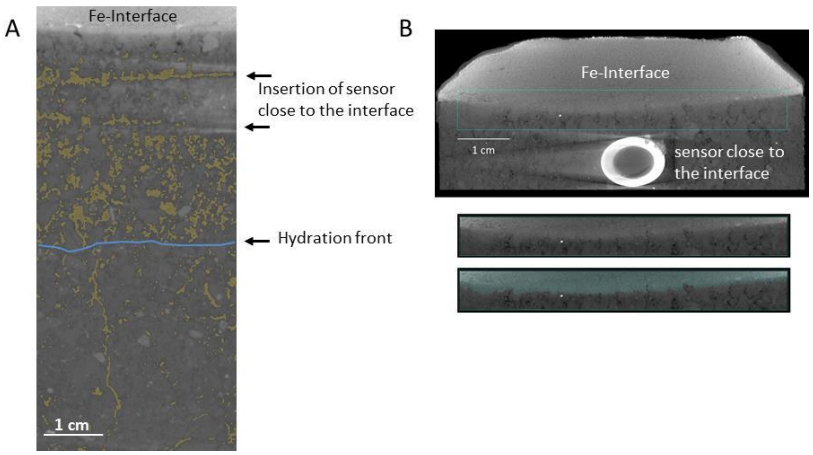

Figure 16 - A. X-ray microtomography stack showing a cross-section of FB5 including the interface, the insertion of upper sensor and the hydration front. B. Segmentation of the interface to obtain a representation of iron penetration thickness, as shown in Figure 17.

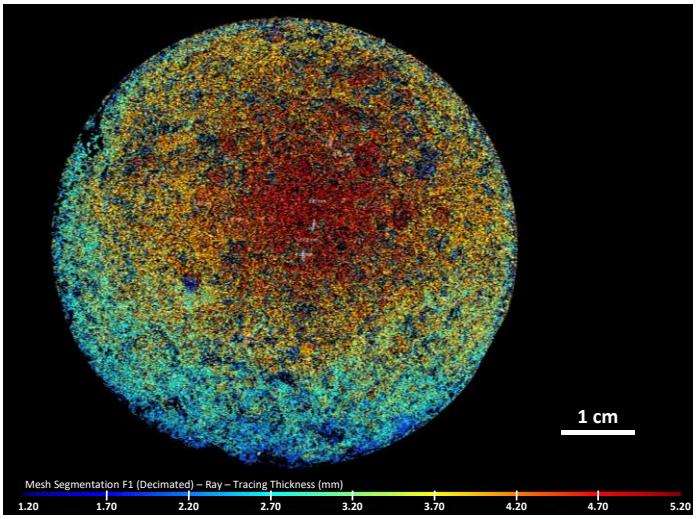

Figure 17 - Microtomographical surface of the iron-bentonite interface of FB5 showing the segmented iron-bentonite section (as shown in Figure 16-B) and the penetration thickness of iron particles into the bentonite.

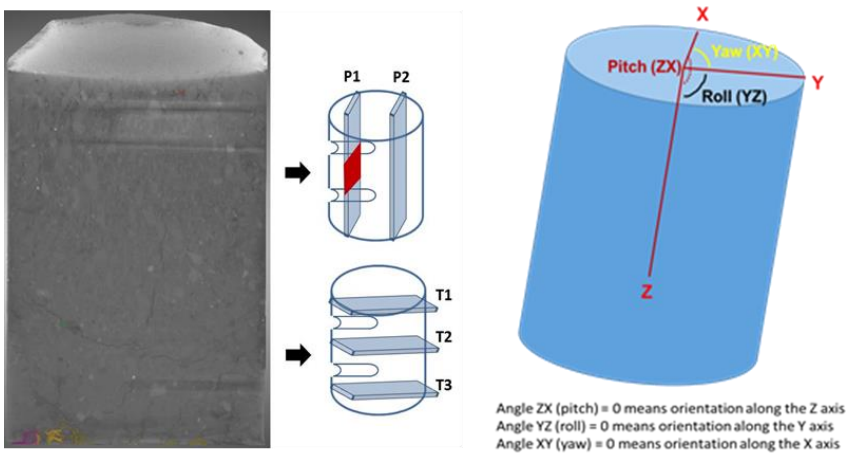

Figure 18 - Bentonite cylinder of FB5 was segmented into 2 sections parallel to the main axis (P1 – in red the section used for calculations to avoid holes left by the sensors and edges - and P2) and 3 sections parallel to the interface (T1 to T3).

The orientation results show that the pores are preferably oriented in the direction parallel to the axis of the cylinder (Z) since most of the pores give values of pitch = 0 for all sections (pitch → ZX = orientation Z if pitch = 0) (Figure 19).

For the calculation of porosity, the volume of pores with respect to the total volume was analysed in each of the sections shown in Figure 18. The results are shown in Table 2. It is observed that the highest values correspond to the section closest to the heater, which is the driest area. The connectivity values are also shown in Table 2. A value of zero indicates that there is no connectivity. Although the values are all very small (indicating little connectivity), some differences are observed along the sample, with the highest values corresponding to the interface (driest zone) and the hydration zone. Approximately 90% of the pores have sizes less than 0.5 mm^3 (Figure 20).

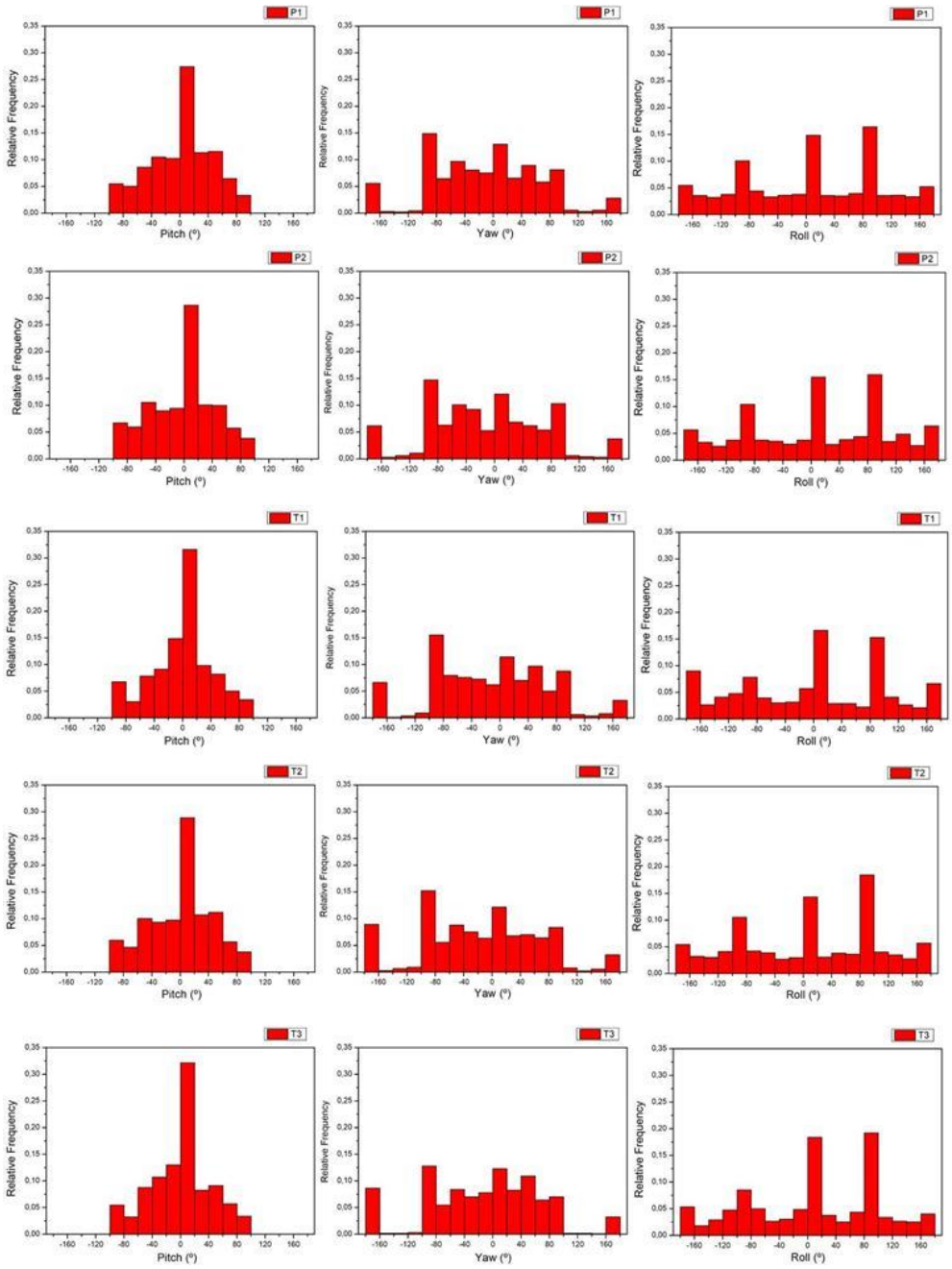

Figure 19 - Micro-CT of FB5. Pore orientation results in each of the sections shown in Figure 18. Pitch →ZX means preferential orientation along the Z-axis if pitch = 0. Roll →YZ means preferential orientation along axis Y if roll = 0. Yaw →XY means preferential orientation along axis X if yaw = 0.

Table 2 - Micro-CT results of porosity and connectivity in FB5 calculated for each of the sections represented in Figure 18.

SECTION	POROSITY (%)	CONNECTIVITY
P1	0.18	0.0006
P2	0.09	0.0022
T1	0.28	0.0034
T2	0.07	0.0002
T3	0.16	0.0183

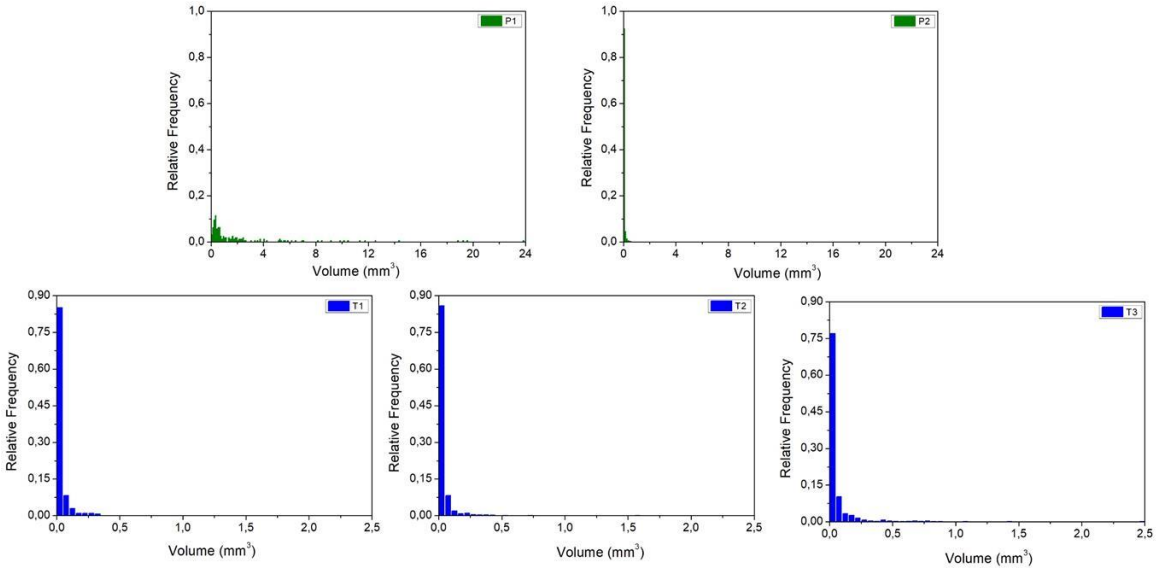

Figure 20 - Micro-CT of FB5. Pore size (as volume, mm³) results in each of the sections shown in Figure 18.

2.1.3.1.3 Chemical gradients

Soluble salts determination

The most relevant transport processes occurring in the FB cells can be determined from the behaviour of conservative ionic species such as chloride and sulphate. Figure 21 displays values obtained from the analysis of chloride and sulphate in the different sections of cell FB5 (thermal and hydraulic gradient) and FB6 (thermal gradient).

The chloride and sulphate distribution in the bentonite is closely related to the thermal gradient and the water redistribution process, advective-diffusive transport from wet to dryer sections. The mechanism was already described by Cuevas et al. (1997) and Fernández and Villar (2010) from shorter-term cells designed to investigate the thermo-hydro-mechanical (THM) behaviour of bentonite subjected to thermal and hydraulic gradients. Chloride behaves as a conservative anion, leached from the wetter sections that have concentrations lower than the ones measured for original FEBEX bentonite (FEBEX-REF) and transported towards the hotter, dryer zone (interface), where it is concentrated. This occurs in both cells FB5 and FB6, although more slowly in the latter, possibly due to the difference in the wet-dry boundary in the bentonite column. Sulphate concentration also increases towards the hotter zones in cells FB5 and FB6, but compared to chloride, sulphate moves more slowly. The behaviour of sulphate is complex and is related to its solubility, which decreases above 40 °C, coincident with the average temperature measured in section 5 in both cells. The maximum sulphate concentration of cell FB5 is found in section FB5-2 (27-36 mm from the iron-bentonite interface), and in section FB6-4 (52-62 mm from the iron-bentonite interface) in cell FB6. The difference in the position of the maximum sulphate concentration front in both cells may be due to the different position of the wet-dry boundary in the bentonite column.

Measurements of soluble salts in the iron powder in the FB5 cell result in a chloride content of 3 mmol/100 g in the first 5 mm of the iron layer from the interface with the bentonite, and below the detection limit from 5 to 13 mm, up to the heater. The sulphate content is below the detection limit in the 13 mm layer of iron powder. EDX analyses confirmed the presence of trace concentrations of chloride in the oxide layers and in the bentonite just at the iron-bentonite interface (Figure 23).

The cations also move towards the hotter areas of the bentonite block, and the dissolution/precipitation processes along the bentonite column condition their distribution. The concentrations of sodium, magnesium, calcium and potassium increased in the heated zone compared to those found in the colder zone, which is especially true in cell FB5 (Figure 22). Sodium concentration increases towards hotter zones following the trend of chloride although cation exchange reactions also influence its concentration.

The solubility of sulphates also conditions the calcium, magnesium and sodium behaviour, which increase in the intermediate zones of the bentonite block and close to the interface.

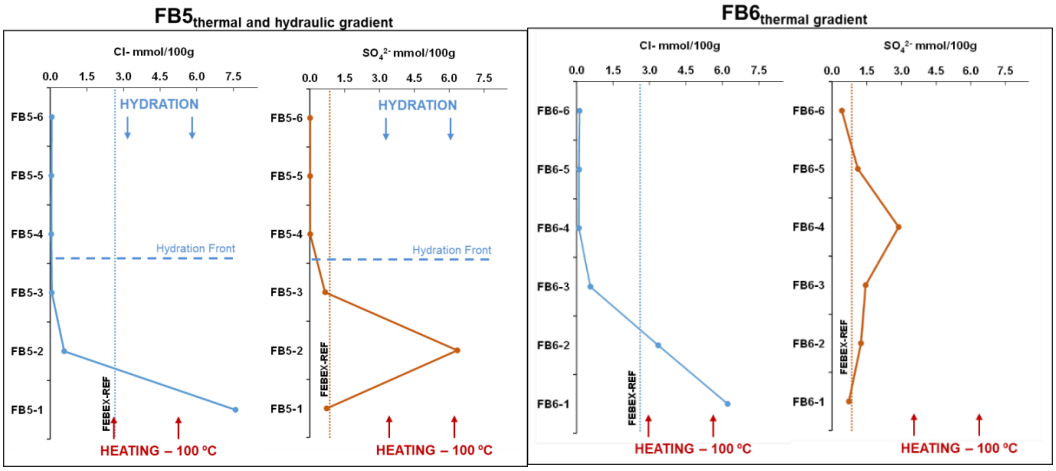

Figure 21 - Concentration profiles of chlorides and sulphates along the bentonite block from aqueous extracts at a solid:liquid 1:8 ratio.

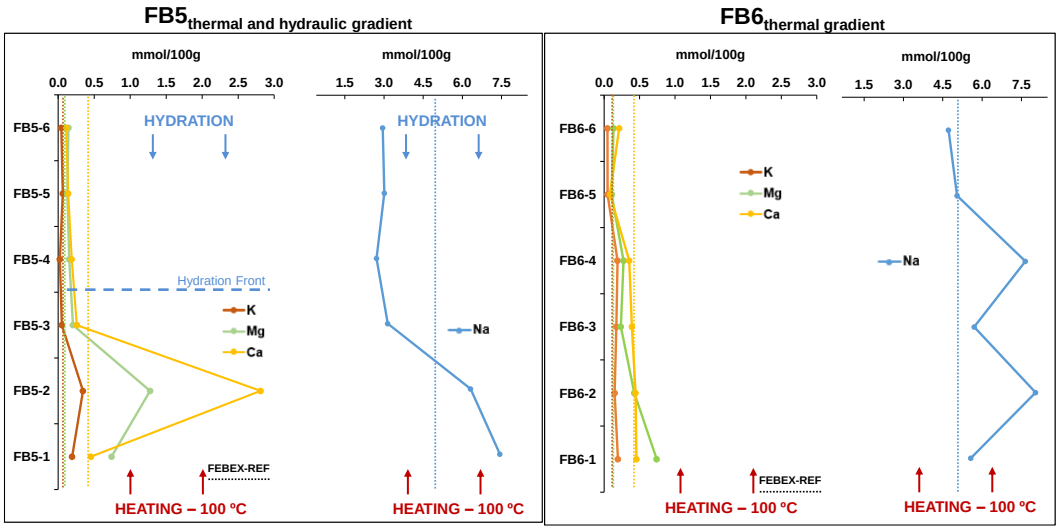

Figure 22 - Concentration profiles of cations along the bentonite block from aqueous extracts at a solid:liquid 1:8 ratio.

A

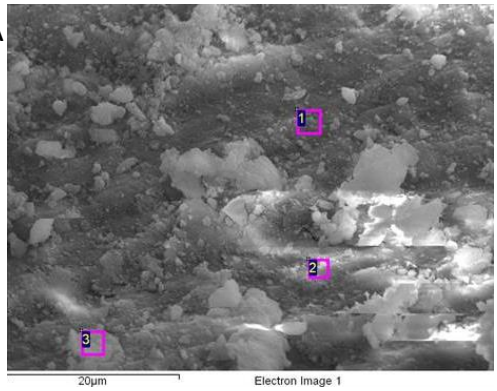

B

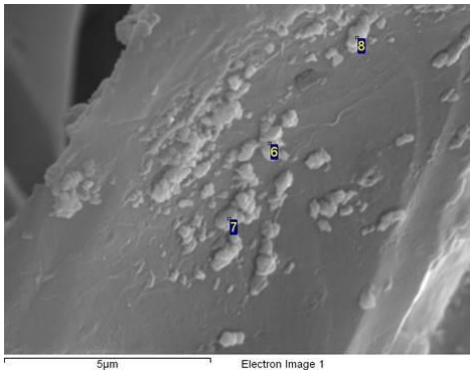

Spectrum	C	O	Na	Mg	Al	Si	Cl	K	Ca	Fe
1	11.08	53.17	0.74	2.91	7.8	21.69	0.52	0.25	0.49	1.35
2	19.23	53.13	0.54	2.72	5.91	16.75	0.41		0.29	1.02
3	18.74	54.75	0.54	2.35	5.85	15.44	0.5	0.18	0.46	1.2

Spectrum	C	O	Cl	Fe
6	63.43	28.77	0.37	7.43
7	65.06	26.65		8.29
8	72.72	23.67		2.98

Figure 23 - SEM micrographs and EDX analysis (wt. %) of the bentonite (A) and the iron oxide layer (B) just at the iron-bentonite interface in cell FB5.

Cation Exchange Capacity

A subtle decrease (< 2 cmol(+)/Kg) in the total cation exchange capacity is observed in the section closest to the heater (Figure 24) in both the FB5 and FB6 cells, and also a subtle increase (with respect to FEBEX reference) in the hydrated zones in FB5 and in the zones far from the heat source in FB6. However, these changes are not considered relevant if we take into account the reference values of the CEC of FEBEX bentonite (102 ± 4 cmol(+)/Kg, Fernandez et al., 2004). These data would indicate that there is no or very limited alteration of the bentonite.

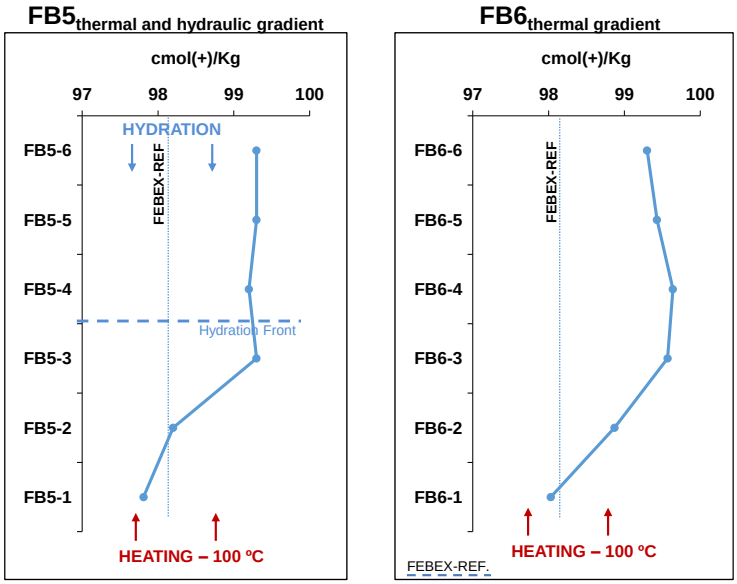

Figure 24 - Cation exchange capacity profiles along the bentonite block.

Exchangeable cations

Exchangeable cations vary as the thermal gradient does. Magnesium dominates the exchange complex in the hottest areas, near the interface, and decreases in saturated zones. Sodium seems to follow a opposite trend, it decreases towards the interface and increases close to the low-temperature hydration area (Figure 25). Cuevas et al. (1997, 2002) reported a change in the selectivity coefficients as a function of temperature from lab-tests with FEBEX bentonite. According to that study, the selectivity coefficient of magnesium increases with temperature, whereas, in the case of sodium, it decreases at higher

temperature. Magnesium is released from the interlayer to pore water in the coolest zone and is transported to the hottest zone. Near the heater, magnesium released in saturated areas enters the exchange complex. Magnesium–complexes seem to be more stable at high temperatures than the complexes formed by the other exchangeable cations. Calcium decreases slightly in the hot zone near the interface, due to substitution by magnesium. The average value of potassium is fairly constant. Similar results are described in Fernandez and Villar (2010) from THM experiments with FEBEX bentonite in large-scale cells (60 cm) that lasted 10 years and in the FEBEX in situ test (Torres et al, 2017; Wersin and Kober, 2017).

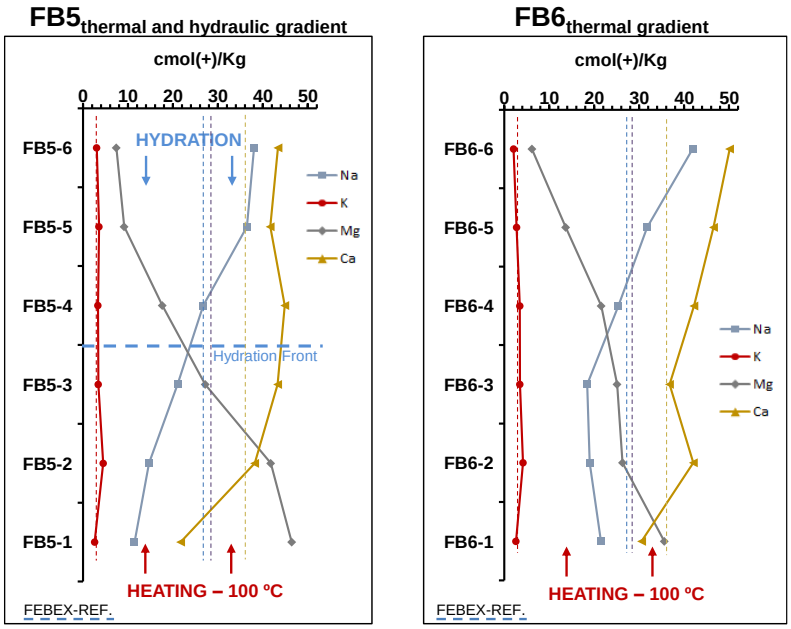

Figure 25 - Distribution of exchangeable cations (expressed in cmol(+)/kg of bentonite)along the bentonite column of FB5 (14 years, thermal and hydraulic gradients) and FB6 (15 years, thermal gradient), quantified by the $CsNO_3$ 0.5 N method.

Silica and Iron

Increase of silica towards the heater occurs in cell FB5 but not in cell FB6 (Figure 26), which seems to indicate that hydration may be relevant in silicate (quartz, feldspar, etc.) dissolution processes, and the temperature gradient in silica mobilization. A faster increase from the hydration front towards the heater is observed in FB5.

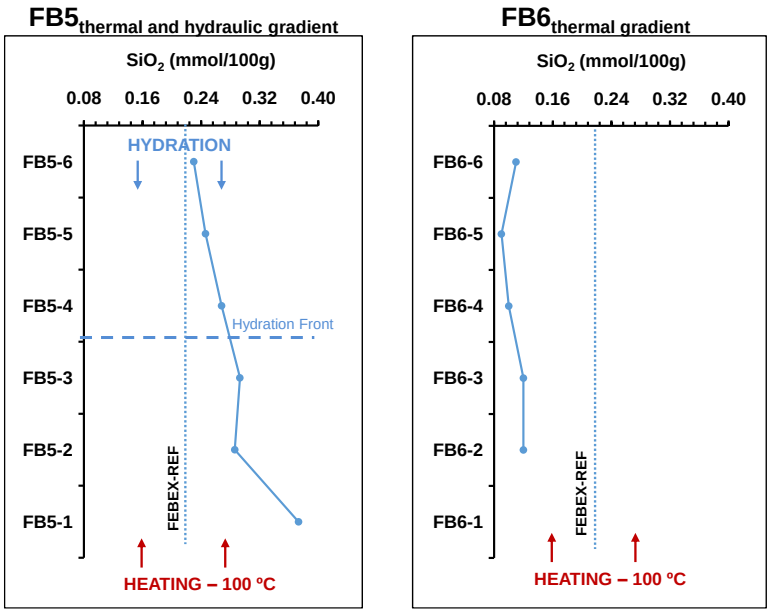

Figure 26 - Distribution of silica in cells FB5 and FB6.

The values of Fe adsorbed onto bentonite (smectite or accessory mineral external surfaces, or in exchangeable sites) range between 0.6-2.0 mmol/100 g in cell FB5 (Figure 27-A) and between 0.4-1.0 mmol/100g in cell FB6 (Figure 27-B). The plot of FB5 indicates a rather random distribution that is difficult to interpret, since we do not know the form and distribution in which iron is found in the bentonite column. Still, apparently, below the hydration front (i.e., the bentonite zone closest to the heater, where the degree of water saturation of the bentonite is low) the amount of adsorbed iron is lower than above the hydration front (more hydrated zone). The migration of iron in this zone is very limited, although occasionally nanocrystals of insoluble iron (III) oxides formed at the interface may be adsorbed on the surface of the bentonite particles. Data from cell FB6, which has no hydration and is overall dry, would confirm this.

The extractable iron (amorphous iron) content remains close to that of the original FEBEX in the hydrated zone in cell FB5 (Figure 27-B) and increases from the hydration front towards the heater. The increase in Fe content seems to be related to the precipitation of anhydrous Fe oxides at the interface, in the hot zone. The pattern in cell FB6 is similar but the values are lower.

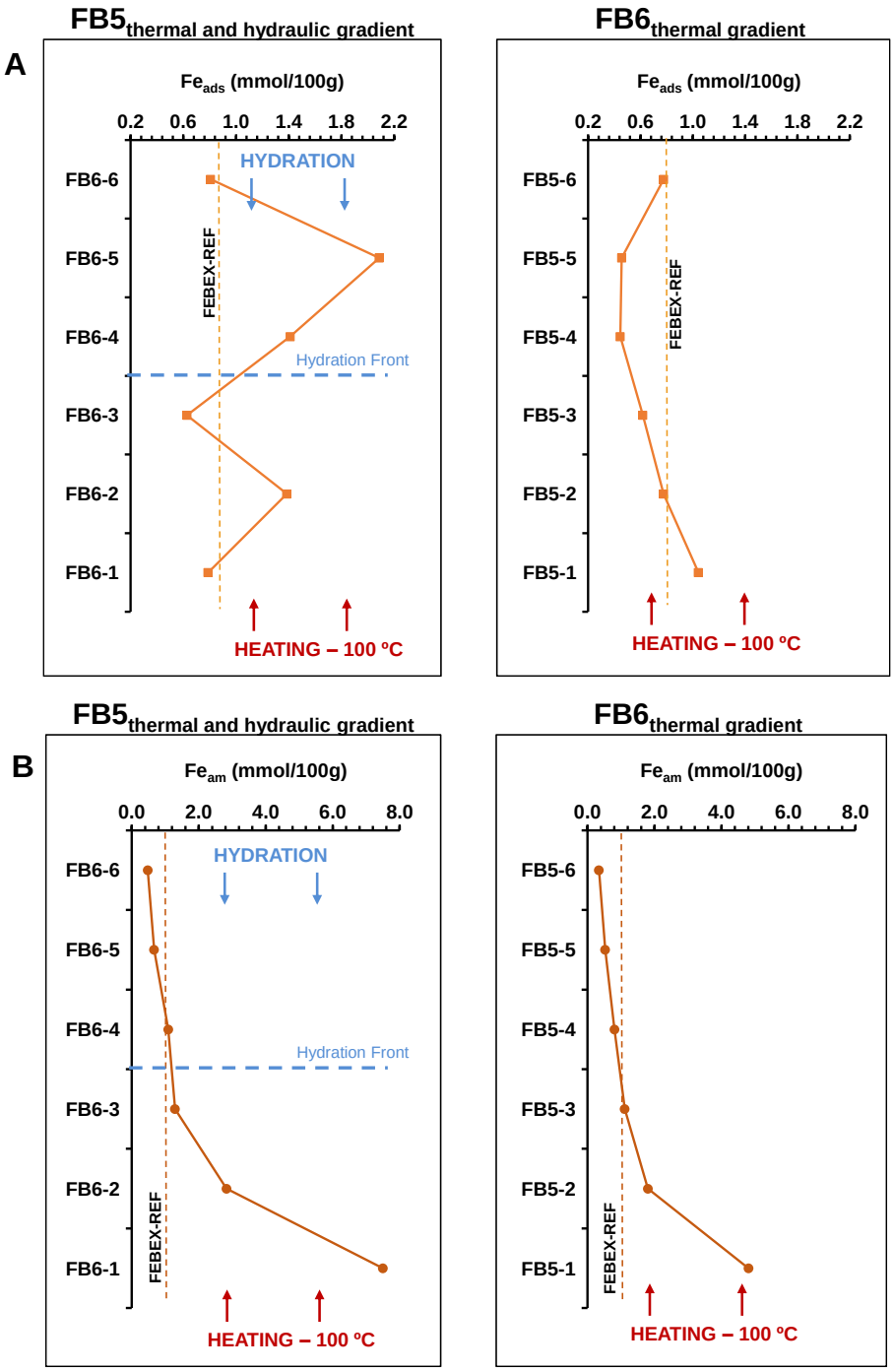

Figure 27 - Distribution of adsorbed iron (A) and amorphous iron oxides (B) in FB5 and FB6.

2.1.3.1.4 Mineralogy

The mineralogical and chemo-structural characteristics of corrosion products and bentonite were determined by the methods described in section 2.1.2.3.4, which apply specifically to corrosion products or/and bentonite at the interface as described below. In this section "*iron-interface*" refers to the analysis of the iron that is "faced" to the bentonite and "*bentonite-interface*" refers to the analysis of the bentonite in contact with the iron.

Iron-interface

The mineralogy of the altered iron rich material scrapped at the iron-bentonite interface reveal the predominance of hematite and metallic iron (Figure 28). FB5 interface material contains higher relative proportions of iron oxides compared to FB6. Maghemite (Mgh) and magnetite (Mag) are present

because reflections near 2.5 Å showed higher intensities than the highest relative intensity reflection of hematite at 2.70 Å. Maghemite characteristic XRD powder pattern contains common reflections with either magnetite and hematite and it is not distinguished unambiguously. The semi-quantification of iron phases Mag and Mgh has been calculated assuming the 2.53 Å shoulder in 2.52 Å peak (maghemite and minor hematite) to be magnetite (detail on top of Figure 29).

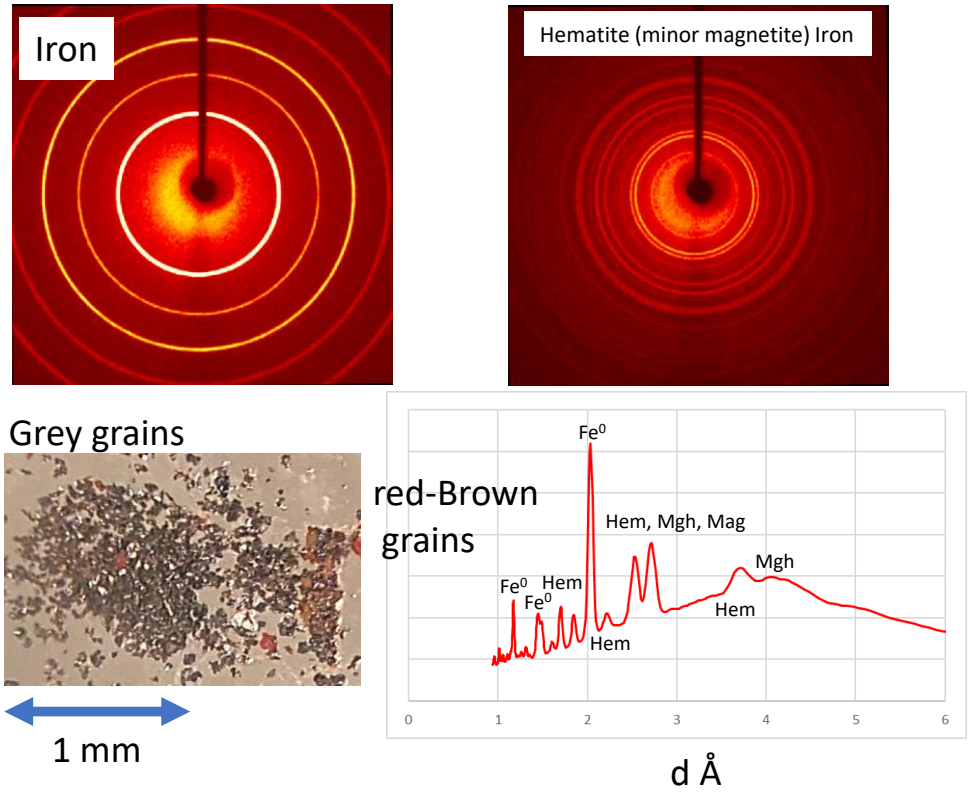

Figure 28 - Microdiffraction analysis of iron particles obtained at the interface by scrapping (bottom left - image of scrapped particles). Powder- ring polycrystal aggregates diffraction images obtained in a monocrystal microdiffraction device from two types of grains. Diffraction line pattern of red-brown grains obtained using a line scan of brightness intensity from the center of the images. Solid angle has been calculated as d distance using Bragg's law.

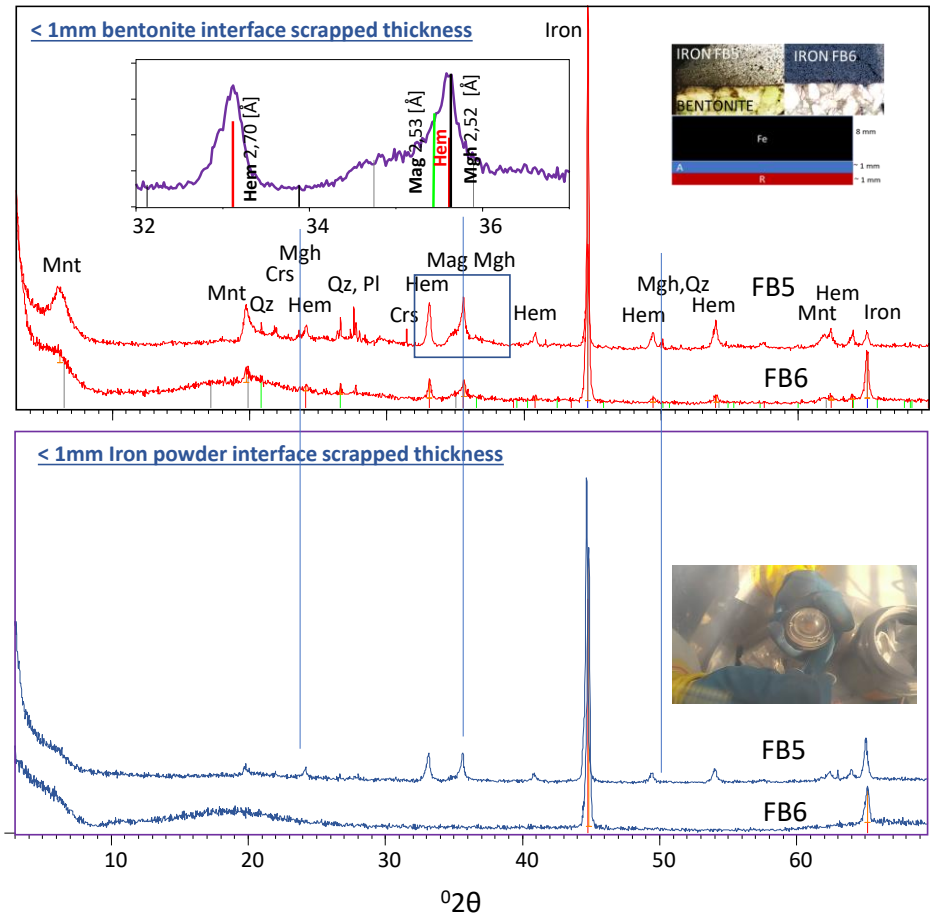

Figure 29 - XRD patterns of iron powder-bentonite interface samples in FB5 and FB6 cell experiments, taken within the first mm in the bentonite side (top) and the first mm in the iron side (bottom). Crs: cristobalite; Hem: hematite; Mag: Magnetite; Mgh: maghemite; Mnt: montmorillonite; Pl: plagioclase; Qz: quartz. Grey bars in the 32-37 $^{0}2\theta$ detail pattern zone correspond to Mnt. Aspects of polished sections of FB6 and FB5 are shown on top.

Raman spectroscopy was used to identify iron oxides and assess the presence of maghemite and magnetite identified by XRD.

Figure 30 *- Raman spectra of iron particles sampled at the iron-bentonite interface of the FB5 experiment lasting for 14 years. (Left) Hematite particles. (Right) Result of Lorentzian fits in the region 550-725 cm-1, highlighting the 610 cm-1 mode of hematite and the presence of characteristic peaks of magnetite and maghemite.*

Figure 30 and Figure 31 show the Raman results of iron particles extracted from the iron-bentonite interface of cell FB5.

Figure 30 *- Raman spectra of iron particles sampled at the iron-bentonite interface of the FB5 experiment lasting for 14 years. (Left) Hematite particles. (Right) Result of Lorentzian fits in the region 550-725 cm-1, highlighting the 610 cm-1 mode of hematite and the presence of characteristic peaks of magnetite and maghemite.*

Figure 30 shows two spectra of hematite particles with typical strong peaks at 225, 292 and 409 cm^{-1} according to the literature (Table 3). Meanwhile, the smallest peaks located around 661 cm^{-1} can be assigned to mixed magnetite-maghemite.

Figure 30 *- Raman spectra of iron particles sampled at the iron-bentonite interface of the FB5 experiment lasting for 14 years. (Left) Hematite particles. (Right) Result of Lorentzian fits in the region*

550-725 cm-1, highlighting the 610 cm-1 mode of hematite and the presence of characteristic peaks of magnetite and maghemite.

Figure 30 (right) shows deconvolution of the 600-720 cm^{-1} region allowing to differentiate the typical peaks of magnetite-maghemite in the same particles. Figure 31 shows two spectra of mixed magnetite-maghemite particles with deconvolution (Figure 31 (right)) showing typical peaks at 663 cm^{-1} (magnetite) and 678 cm^{-1} and 692 cm^{-1} (maghemite) according to the literature (Table 3).

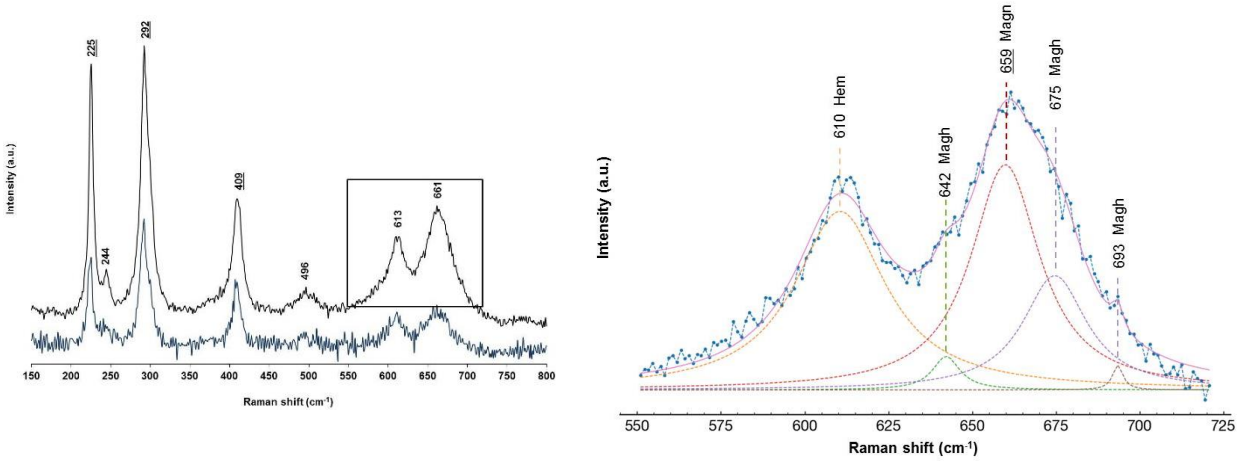

Figure 30 - Raman spectra of iron particles sampled at the iron-bentonite interface of the FB5 experiment lasting for 14 years. (Left) Hematite particles. (Right) Result of Lorentzian fits in the region 550-725 cm^{-1}, highlighting the 610 cm^{-1} mode of hematite and the presence of characteristic peaks of magnetite and maghemite.

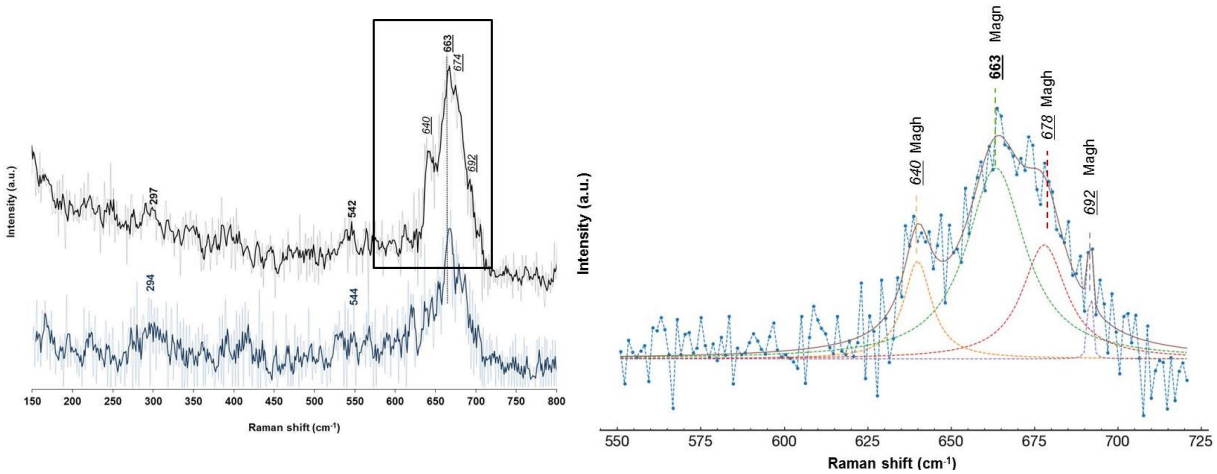

Figure 31 – Raman spectra of iron particles sampled at the iron-bentonite interface of the FB5 experiment lasting for 14 years. (a) Magnetite-maghemite particles. (b) Result of Lorentzian fits in the region 550-725 cm^{-1}, highlighting the typical peaks of the two mineral phases.

Table 3 - Peak positions of Raman bands measured for the iron particles sampled at the iron-bentonite interface of the FB5 experiment, lasting for 14 years. The peak positions are characteristic of individual iron oxides hematite, maghemite and magnetite. The most significant bands are underlined.

Mineral phase	Band positions (strong underlined)	Source
Hematite	225, 244, 292, 409, 496, 610	i.e., Faria et al., 1997, Chernishova et al., 2007, Faria and Lopes, 2007
Magnetite	542, 663	i.e., Schwaminger et al., 2020, Jubb and Allen, 2010
Maghemite	297, 640, 678, 692	i.e., Ruiz-Gómez et al., 2017, Hanesch, 2009

The FT-IR spectra did not shed new light on the mineral phases already detected. A spectrum of hematite is presented in Figure 32.

In cell FB6 (without hydration), the first millimeter of iron powder in contact with bentonite is practically pure iron, with no corrosion products. However, in cells FB5 and FB4 (with hydration), iron powder contains corrosion products in a thickness of about 2 mm from the contact with bentonite (Table 4) (see details on FB4 in Torres et al., 2014). Powders and grains obtained from these layers were examined by Mössbauer spectroscopy (Figure 33) and in a monocrystal microdiffraction device (Figure 28). Mössbauer spectroscopy detected oxidation state of octahedral iron in montmorillonite (Mnt). FEBEX Mnt shows 15 % of iron as Fe (+2), whereas iron of Mnt sampled near and at the contact of iron powder is in a fully oxidized state (Fe^{3+}). Microdiffraction data confirm the predominance presence of iron (Fe^{+3}) oxide at iron powder interface.

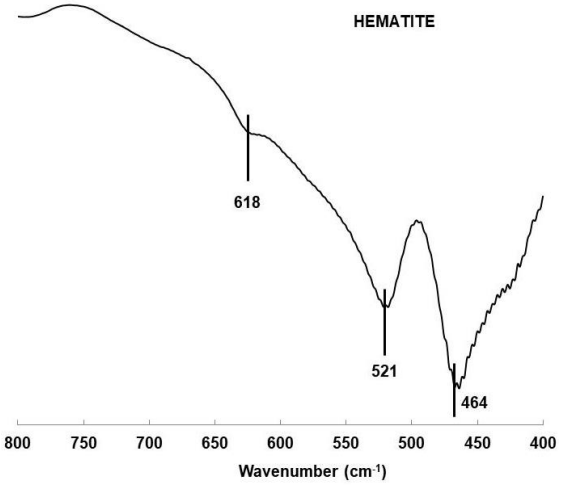

Figure 32 - Infrared spectra of iron particles at the iron-bentonite interface of FB5.

Table 4 - Semi-quantification of relative proportions of iron phases at the iron-powder bentonite interface. FB4 cell was dismantled at 4.5 years during European PEBS project (Torres et al., 2014).

	Weight % semi-quantification X'PERT High Score Plus (2005) RIR method

Sample/phase	Goethite	**Hematite**	Maghemite	Magnetite	**Iron**
FB6 A	n.d	n.d.	n.d.	n.d.	**100**
FB6 R	<5	**40**	10	<5	45
FB5 A	<5	20	10	<5	**65**
FB5 R	<5	**50**	15	10	25
FB4 A	n.d.	10	20	<5	**70**
FB4 R	<5	**70**	20	5	<5

A: bluish zone after red stained zone (R) corresponding approximately to 1mm near bentonite and 1mm towards iron powder.

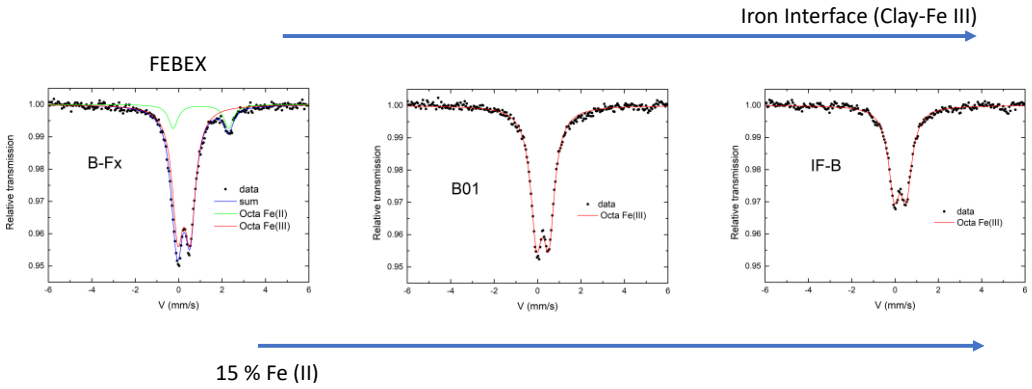

Figure 33 - Mössbauer spectra. From left to right: the initial FEBEX bentonite (B-Fx), bentonite at 1mm from the iron powder contact (B01) and scraped clay at the iron-powder contact (IF-B).

Microstructure (SEM-EDX analysis, corrosion mechanism and rates, altered thickness)

The electron microscopy images obtained from the emission of backscattered electrons (Figure 34) reveal how the intergranular pores of the iron particles are filled with materials that, due to their chemical composition, are iron oxides. The difference in thickness in which these pores are seen to be occupied by oxides at the interfaces of the FB5 and FB6 experiments is evident. Interface FB5 contains oxide fillers up to around 2 mm and partially filled up pores to around 3 mm thickness, while FB6 contains oxides less than 100 µm thickness of partially filled pores. The variation of the chemical composition measured every 50 microns near the interface shows in detail the concentration gradients that have been generated towards the interface with the iron powder. Considering that Al is a relatively immobile element, Fe/Al, Mg/Al, Ca/Al and Si/Al have been represented to show the relative variation in concentration of these elements (Figure 35). FB5 showed a clear relative increase of Mg and Cl towards the interface in a 2 mm region. Ca is also enriched (< 500 µm). Si is also progressively increased towards the interface, decreasing in a 500 µm region at the contact. Iron concentration is high in a 100-150 µm interface thickness. From this region Fe shows the same relative values of the bentonite up to 1 cm (10,000 µm). These gradients are not clearly observed in FB6 iron interface as well as the chloride gradient, as far as in FB6 this element is not currently detected. Then hydration conditions provide mechanisms of ion transport that are not significantly pronounced when the cell was not hydrated.

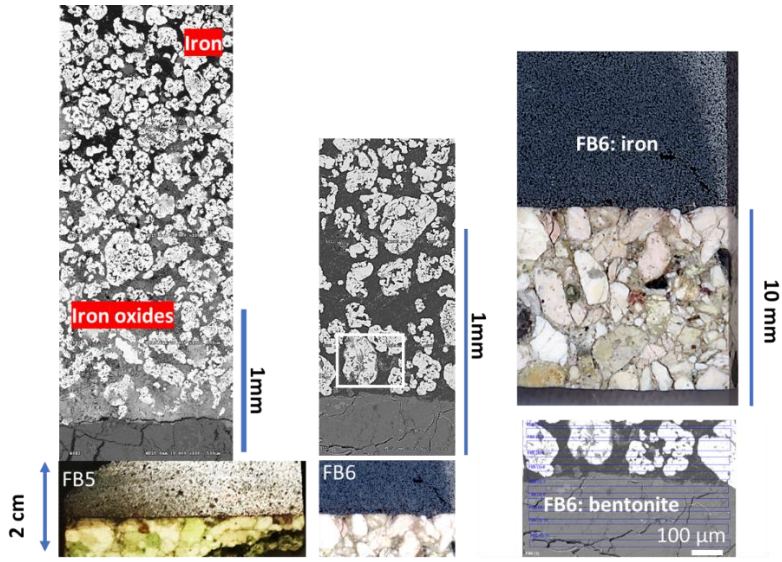

Figure 34 - Backscattered and real color polished sections images of FB5 and FB6 iron-bentonite interfaces. Intergranular oxide filler appears in light gray in electron microscopy backscattered images.

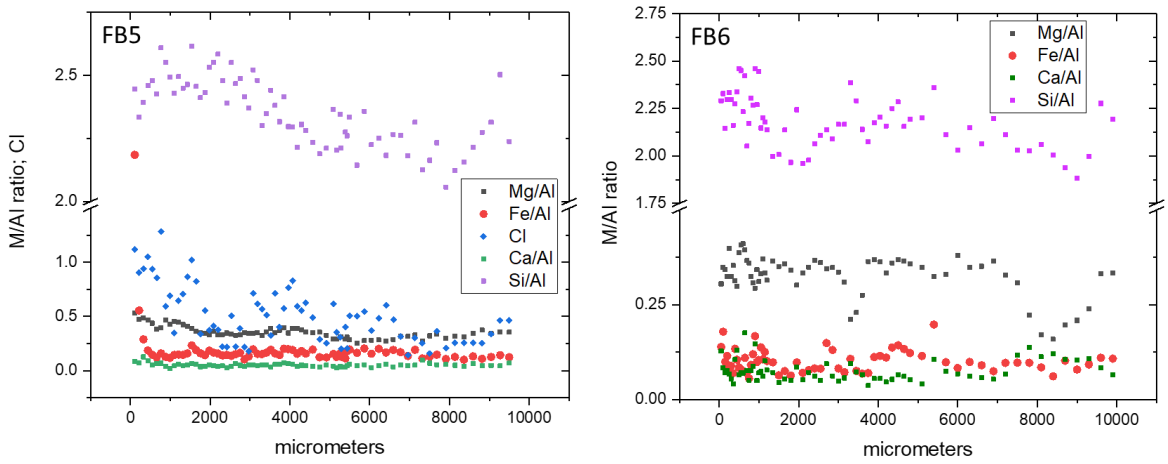

Figure 35 - Relative proportion of elements (atomic ratio) referenced to immobile Al. Chloride in FB5 (left) is at. % excluding C and O for the percentage normalization.

Iron oxides are the main corrosion products of elemental iron grains at the bentonite interface. A compact micrometric rim is developed at the border of the grains, whereas intergranular pores are filled with less dense porous precipitates. These precipitates are characterized by the presence of chloride, more clearly observed in FB5 cell (Figure 36). Nevertheless, chloride was also detected in FB6 within the partially filled pores observed in the less oxidized iron grains. This fact probes that even under non-forced hydration conditions, as in FB6, there was presumably movement of water vapour, and there were evidences of chloride at the interface, which acted as corrosion catalyst. This process is much more relevant in the FB5 cell.

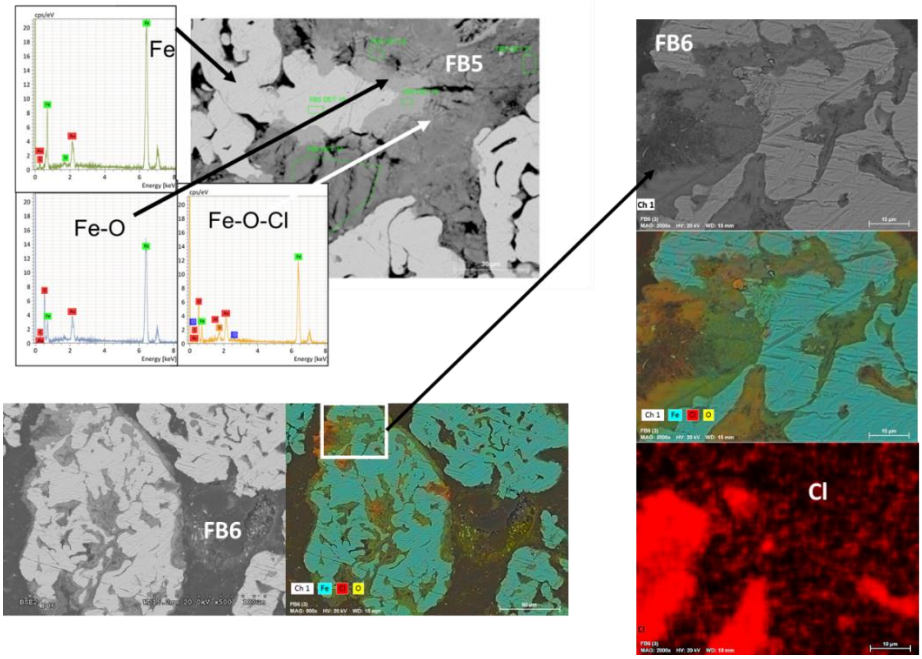

Figure 36 - Electron microscopy detailed backscattered electrons images of altered iron grains in FB5 and FB6 iron powder interface zone. Localised analysis and elemental mapping.

The corroded thickness was determined by measuring the corrosion rim of corroded grains from BSE images as described in section 2.1.2.3.4. Figure 37 displays BSE images of a cross section of the first 7 mm from the interface of the iron layer of the FB5 experiment. Figure 38 shows BSE images of a cross section of the first milimiter of the iron layer from the interface of the experiment FB6. The corrosion products present in FB5 are visible in the images as a darker rim on the surface of the particles and filling pores, being the unaltered particles ligther and brilliant. In the cross section of Figure 37, 3 zones are differentiated:

- Zone 1: it is a corroded zone around 2 mm deep from the interface, with the appearance of a compact layer with corrosion products occupying the pore space. The surface of the iron particles is inhomogenously corroded, although the thickness of corrosion products in corroded particles is quite similar.
- Zone 2: intermediate-transition zone (≈ 700 µm) with some voids between particles and less corroded particles than in zone 1, giving an appearance of a less compact layer.
- Zone 3: the deepest zone (≈ 3 to 13 mm - heater) is mainly composed of bare iron particles, without corrosion products and with large pores, although rare corroded particles can be also observed.

Average corrosion thickness and corrosion rate are measured on particles of zone 1 of FB5 and in the scarcely corroded zone of FB6. The results are presented in Table 5 and are summarized below:

- Average corrosion thickness of particles in FB5 is around 6.09 ± 0.97 µm and averaged corrosion rate is 0.44 µm/year (0.37 – 0.50 µm/year). Corrosion is inhomogeneous as shown in the histogram on the right side of Table 5.
- Average corrosion thickness of particles in FB6 is around 2.37 ± 0.92 µm and averaged corrosion rate is 0.16 µm/year (0.10 – 0.20 µm/year).

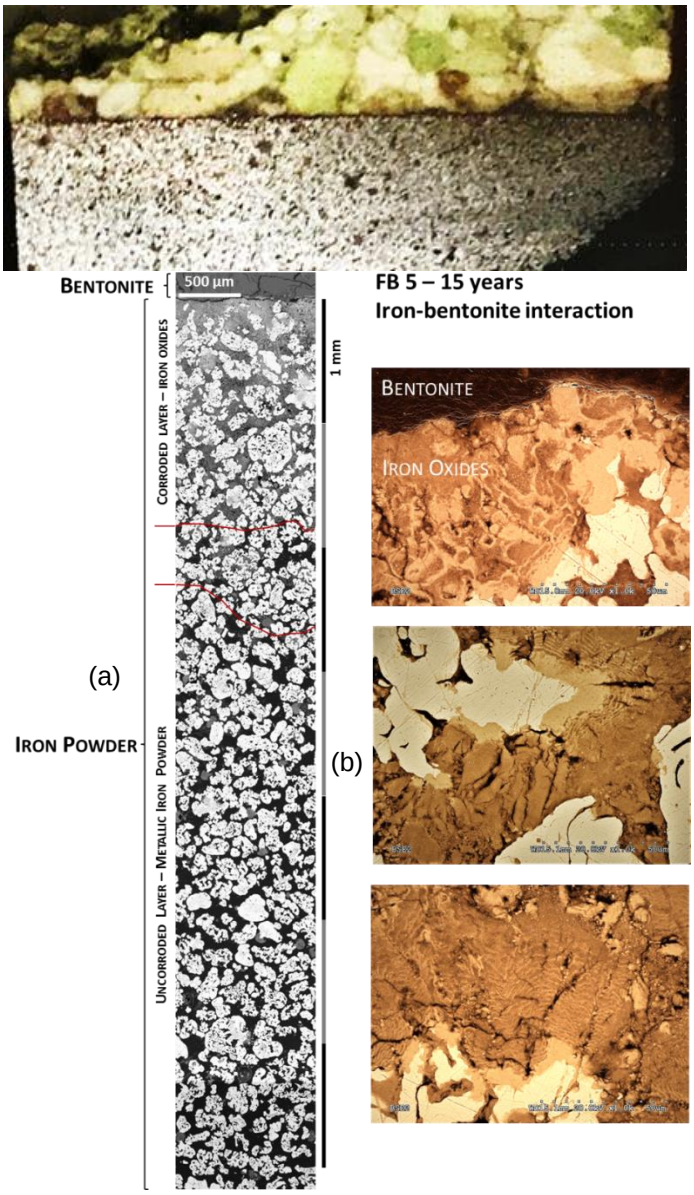

Figure 37 - *(a) BSE images showing a cross section from the iron-bentonite interface up to a depth of 7 mm of the iron layer of the FB5 experiment. (b) BSE images with false color showing details of the surface morphology and corrosion products rims of the iron particles.*

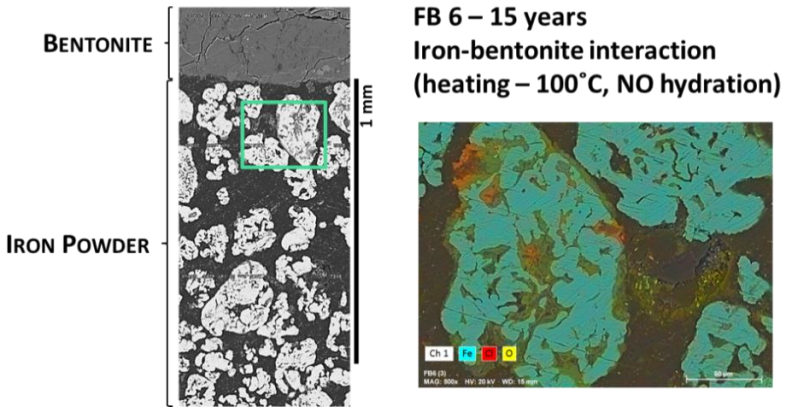

Figure 38 - *(a) BSE images showing a cross section from the iron-bentonite interface up to a depth of around 1 mm of the iron layer of the FB6 experiment. (b) BSE images showing a detail of the surface morphology and corrosion products rims of the iron particles.*

Table 5 - Average thickness of the corrosion products measured in BSE images of the FB5 experiment and calculated average corrosion rate. (Right) Figure showing the thickness ranges of corrosion rims in FB5.

	FB5 - 14 years corrosion rim (µm)		FB6 - 15 years corrosion rim (µm)	
	average	st. Dev.	average	st. Dev.
P1	8.00	0.00	3.58	1.15
P2	3.60	0.55	2.80	1.55
P3	1.90	0.21	2.56	1.19
P4	2.37	0.55	1.46	0.15
P5	3.67	0.76	1.46	0.15
P6	3.17	1.26		
P7	3.69	1.72		
P8	2.27	0.81		
P9	6.33	1.15		
P10	10.05	2.02		
P11	10.50	0.71		
P12	7.00	0.00		
P13	7.17	1.57		
P14	8.00	0.00		
P15	9.56	2.18		
P16	11.00	1.41		
P17	5.26	1.56		
Total	**6.09**	**0.97**	**2.37**	**0.84**

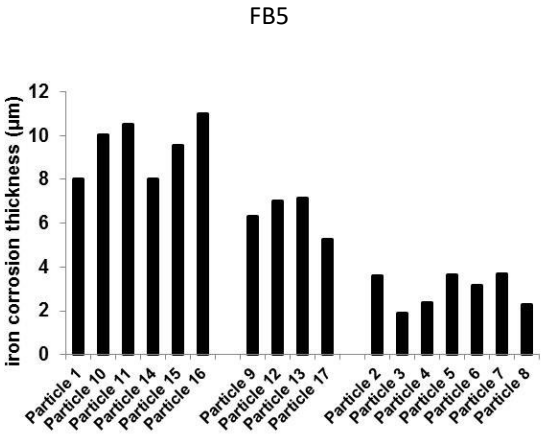

Bentonite-interface

Bentonite mineralogy has been quantified by random powder XRD in FB6 and FB5 (Table 6) by means of Rietveld refining. Smectite and disordered muscovite (1Md polyyipe illite-like) are the predominant clay minerals. The use of both crystallographic models was needed to achieve a good profile fitting of hk reflections (Cuevas et al., 2022). They sum to a quantity of 82 ± 4 wt.% out of the total composition in average, which is a value close to the one determined by a separation and weighting method for quantification of clay minerals in FEBEX bentonite and other Rietveld refined results published (80 wt.%; Cuevas et al., 2022; 87 ± 3 wt.%; Sudheer Kumar et al., 2021). Deviations in major components in the quantified mineralogy are attributed to intrinsic variability of the samples. Minor components as calcite in FB5 are concentrated in intermediate locations in the cell, near the interface where the hydration front saturated the bentonite. Calcite in FB6 seems to be dissolved in the extreme opposite to the heater. Variations in composition are shown graphically in Figure 39.

Table 6 - Quantification of the mineralogy of bentonite in FB5 and FB6 cells by BGMN-Profex Rietveld refinement

Phase	FEBEX	FB5_1	FB5_2	FB5_3	FB5_4	FB5_5	FB5_6
Plagioclase	7.7	11.8	14.8	9.5	13.0	9.7	16.6
Cristobalite	-	0.5	0.3	0.3	0.3	0.3	0.4
Calcite	0.9	0.6	1.8	0.6	3.9	1.1	2.2
Goethite	0.5	0.0	0.6	0.5	1.4	2.2	-
Halite	-	-	0.1	0.1	0.1	0.1	-
Hematite	-	-	-	-	-	-	-

Maghemite	-	-	-	0.1	-	0.2	-
Magnetite	0.4	-	-	-	-	0.1	-
Illite	12.7	1.3	9.5	11.9	11.0	8.1	7.1
Orthoclase	2.4	2.5	1.8	1.8	1.8	1.3	2.5
Quartz	2.5	1.3	1.1	2.5	1.0	1.0	1.5
Smectite	73.0	82.1	70.0	72.6	67.5	75.9	69.2
c2	2.9	3.6	3.6	2.6	2.9	2.5	4.8
Phase	**FEBEX**	**FB6_1**	**FB6_2**	**FB6_3**	**FB6_4**	**FB6_5**	**FB6_6**
Plagioclase	7.7	10.2	6.8	17.1	15.8	8.6	11.8
Cristobalite	-	0.4	0.3	0.4	0.2	0.6	0.3
Calcite	0.9	0.6	1.2	1.7	2.3	2.0	2.3
Goethite	0.5	0.7	0.1	1.2	-	-	-
Halite	-	-	-	0.1	0.1	0.1	-
Hematite	-	-	-	-	-	-	-
Maghemite	-	-	-	-	-	-	-
Magnetite	0.4	-	-	-	-	0.01	0.12
Illite	12.7	10.9	10.9	9.6	7.2	14.7	6.2
Orthoclase	2.4	2.4	1.9	1.9	1.9	2.7	1.3
Quartz	2.5	1.2	1.1	1.9	1.3	1.4	1.2
Smectite	73.0	73.6	77.8	66.1	71.2	70.0	76.8
c2	2.9	2.1	3.7	2.7	3.3	5.5	2.6

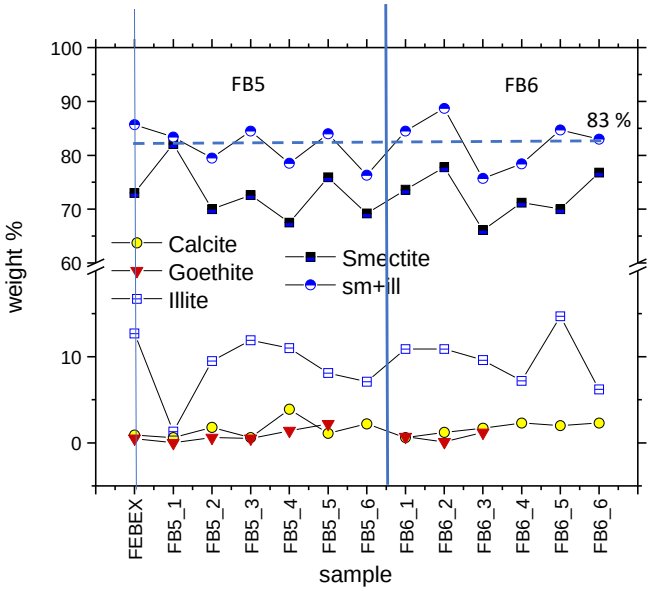

Figure 39 - Bentonite mineral contents evolution calculated by Rietveld analysis.

Elemental analysis gave very different results for FB5 and FB6 cells. One of the reasons was that the use of resin to isolate the samples after dismantling and during the sectioning work had a different impact on the two cells mainly due to the difference in water content. In this respect, FB5 contained in general more water than FB6 and the intrusion of the preserving resin to isolate the sample was very limited. This was not the case for FB6, where the resin intruded to some extent into the macropores and increased the overall carbon content from 0.3 wt.% to 3 wt.%. The main consequence is that the presence of resin has eliminated the possibility of qualitative monitoring of the carbonate dissolution-precipitation processes in the cell FB6. However, this is not the case for cell FB5 where the maximum C content (1.2 wt.%) (Figure 40) is consistent with the content determined in the saturated to non-

saturated transition zone located at 4-5 cm from the hydration source. H and S elements were rather insensitive to changes detected in salt migration and humidity.

Thermal analyses were also influenced by the presence of resin, mainly in cell FB6 (*Figure 41*), where DTG profiles showed a peak at 375 ˚C characteristic of organic polymer decomposition. The first interlaminar cation dehydration maxima were split into two with respect to the original montmorillonite in the bentonite (75 ˚C), one peak being at 50-55 ˚C and the other at 75-85 ˚C. The latter initiates the predominance of the divalent character of montmorillonite, which completes its dehydration at 145-150 ˚C. In FB 5, more visible towards the hot zone, the predominance of this effect stands out, which is compatible with the increase in magnesium with respect to sodium and, to a lesser extent, calcium according to the determination of exchangeable cations. In FB6, where this differentiation with temperature has not been observed, in splitting, the peak at lower temperature slightly predominates, a fact that is compatible with the presence of sodium in the exchange complex in both cases.

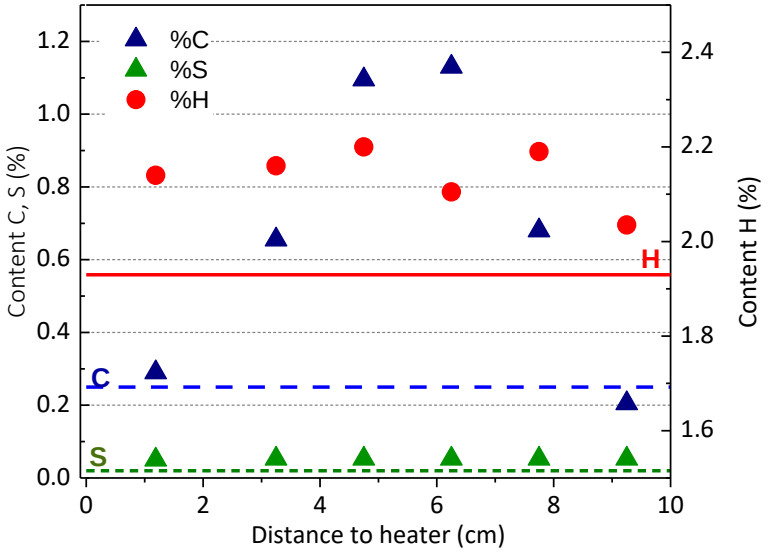

Figure 40 - Elemental analysis of FB5 bentonite sections.

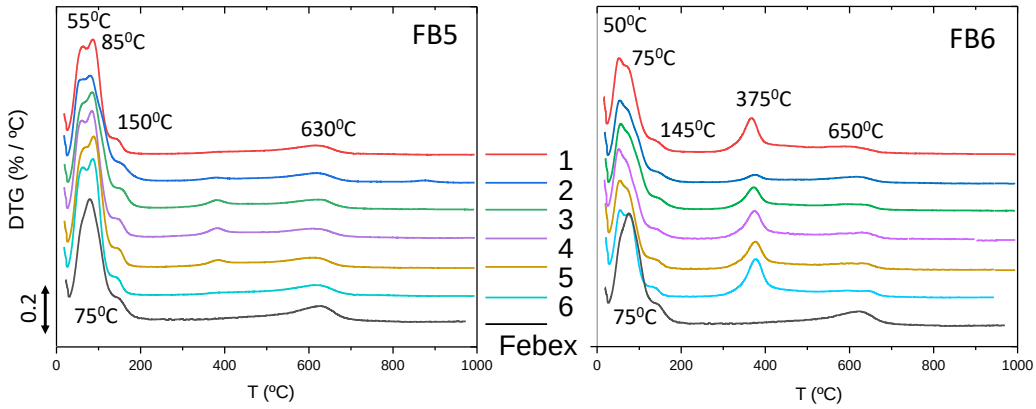

Figure 41 - Differential Thermogravimetric Analysis of long-term FB cells. Numbers refer to sampled sections in the bentonite.

The structural formulae calculated (Table 7) for a practically monomineralic fraction in montmorillonite show very little variation with respect to the original montmorillonite. A slight decrease in the total layer charge is observed towards the hydrated zone in FB5, and in general in FB6, except in the sample opposite to the heated zone. There are hardly any changes in the amount of potassium fixed in the interlayer position of smectite layers or in the tetrahedral charge (aluminium substitutions for silicon),

indicating in general a great stability of the montmorillonite as a whole. If there have been structural or crystal-chemical changes, they should be sought in very localized areas at the interfaces.

Table 7 - Structural formulae calculated in a $O_{10}(OH)_2$ basis for the Ca-homogenized <0.5 µm separated clay fraction

	FEBEX	FB5-1	FB5-2	FB5-3	FB5-4	FB5-5	FB5-6	FB6-1	FB6-3	FB6-6
Atomic proportions										
Tetrahedral sheet										
SiIV	3.897	3.893	3.883	3.891	3.893	3.887	3.875	3.890	3.882	3.917
AlIV	0.103	0.107	0.117	0.109	0.107	0.113	0.125	0.110	0.118	0.083
Octahedral sheet										
AlVI	1.368	1.362	1.381	1.375	1.369	1.367	1.378	1.375	1.377	1.376
FeVI	0.183	0.183	0.173	0.175	0.176	0.181	0.182	0.180	0.178	0.179
TiVI	0.008	0.009	0.008	0.008	0.008	0.009	0.009	0.010	0.008	0.012
MgVI	0.437	0.458	0.445	0.461	0.460	0.457	0.448	0.451	0.462	0.428
Interlayer cations (calcium homogenized)										
Ca	0.242	0.237	0.240	0.232	0.238	0.236	0.229	0.224	0.227	0.222
K	0.057	0.046	0.052	0.042	0.043	0.050	0.053	0.054	0.043	0.070
Layer charge										
LChT	0.541	0.520	0.533	0.507	0.520	0.522	0.511	0.502	0.498	0.514
LOct	0.438	0.413	0.416	0.397	0.413	0.409	0.386	0.392	0.380	0.431

IV: oxygen tetrahedral coordinated cations; VI: octahedral coordinated cations; LChT: total layer charge; LOct: octahedral layer charge.

2.1.3.2 FeMo tests

After the dismantling of the FeMo cell, data related to its microstructural characterization, effects on the cation exchange capacity and mineralogy have been obtained and are shown here for one of the sections (referred to as section 3).

2.1.3.2.1 X-ray microtomography (qualitative)

X-ray microtomography was performed on one of the six sections (referred to as section 3) into which the cell FeMo was divided during dismantling for analysis (Figure 42). At the time of writing, it has not been possible to have the analyses obtained with microtomography interpreted and quantified, so this section is purely descriptive.

The images are presented in Figure 42. Images A and B correspond to a transverse and apical view, respectively, of section 3 after analysis by microCT. Image C corresponds to a slightly rotated 3D reconstruction of the block. Image D is a part of the apical view (B) and images E and F are different slices of the cross section. From the observation of stacks D to F it can be estimated that the bentonite is apparently saturated, if we compare for example with the images of the saturated and unsaturated zones of cell FB5. It appears that the iron-bentonite interface is sharp and there is no clear penetration of iron into the bentonite. Some microcracks are observed radial to the insertion hole of the sintered tube and also perpendicular to it.

2.1.3.2.2 Chemical gradients

Cation Exchange Capacity and Exchangeable cations

The cation exchange capacity (Figure 43-A) of the bentonite is unaltered except in the area where the clay is affected by the presence of corrosion products, an area in which it decreases slightly by means of the existence of iron oxide mixture with bentonite.

Figure 43-B shows the results of the analysis of the exchangeable cations at 5 mm and 10 mm from the iron interface. Slight variations are seen when compared to the data for the original FEBEX bentonite; there is a slight decrease in Ca and Na in the exchange complex and a slight increase in Mg.

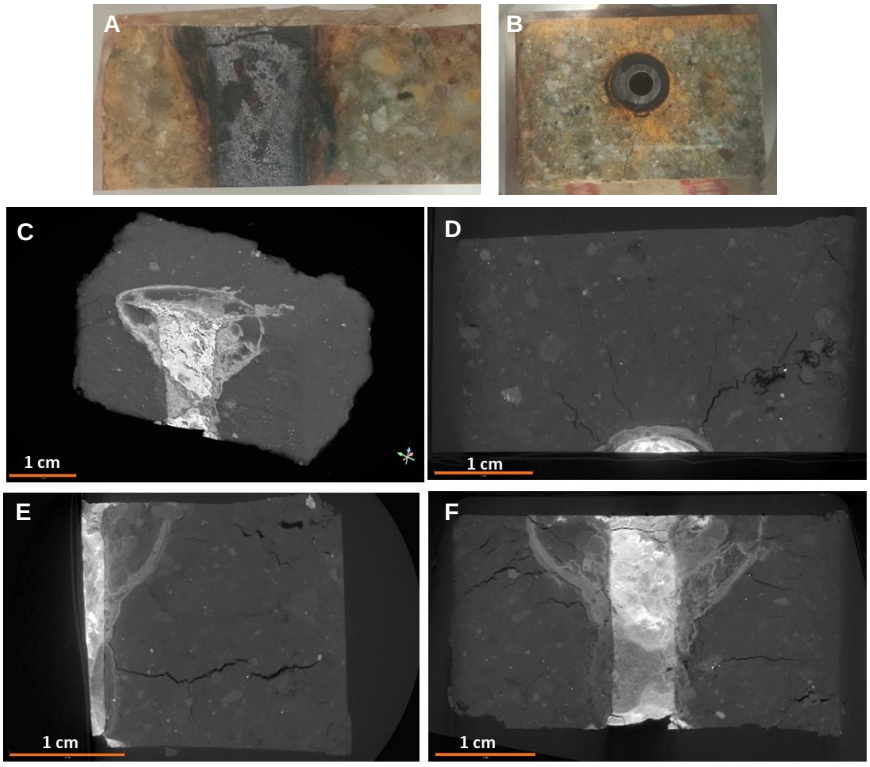

Figure 42 - Different images of section 3 of cell FeMo (Figure 10 and Figure 11). A. Transverse view. B. Apical view. C. 3D X-ray microtomography reconstruction. D. Stack showing a part of the apical view (B). E and F. Stacks showing a cross-section.

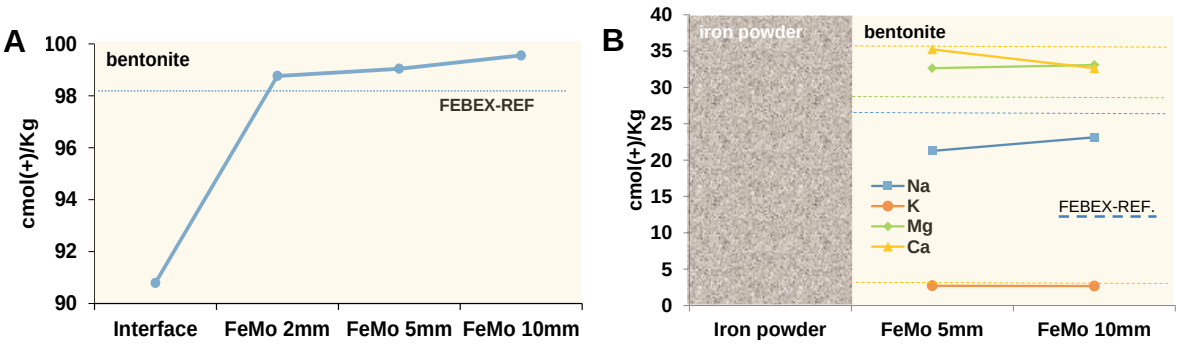

Figure 43 - A. Cation Exchange Capacity profile along the bentonite of section 3 of cell FeMo (Figure 10 and Figure 11). B. Distribution of exchangeable cations (expressed in cmol(+)/kg of bentonite) along the bentonite column of section 3 of cell FeMo.

2.1.3.2.3 Mineralogy

The environment of the cylindrical section containing steel inside and compacted iron powder in contact with the compacted bentonite is characterized by a black stripe (iron powder) followed by a brown zone of variable thickness (2-5 mm), which stains the bentonite yellowish green. The black stripe corresponding to the iron powder in contact with the FEBEX bentonite in section 3 of the FeMo experiment (Figure 11) has been analysed by XRD under hermetic conditions and always preserved from exposure to atmospheric oxygen. Figure 44 shows the location of the samples studied to obtain the mineralogical composition of the altered iron powder and the contact with the bentonite. The

mineralogical composition of the iron powder shows the predominance of magnetite (Fe_3O_4 = 50 wt.%) accompanied by goethite (FeOOH = 25 wt.%) and siderite ($FeCO_3$ = 5 wt.%), with metallic iron remaining in a proportion of around 20% by weight. These semiquantitative data were obtained by the reference intensity ratio (RIR) method, implemented in the XPERT highscore software (2005, Panalytical). The brown-stained bentonite contact contained, in addition to bentonite minerals (montmorillonite, cristobalite, feldspars and quartz), magnetite, and oxyhydroxides goethite and lepidocrocite, with minor siderite. The bentonite near this contact has the same composition as the original mineralogy described in Table 6.

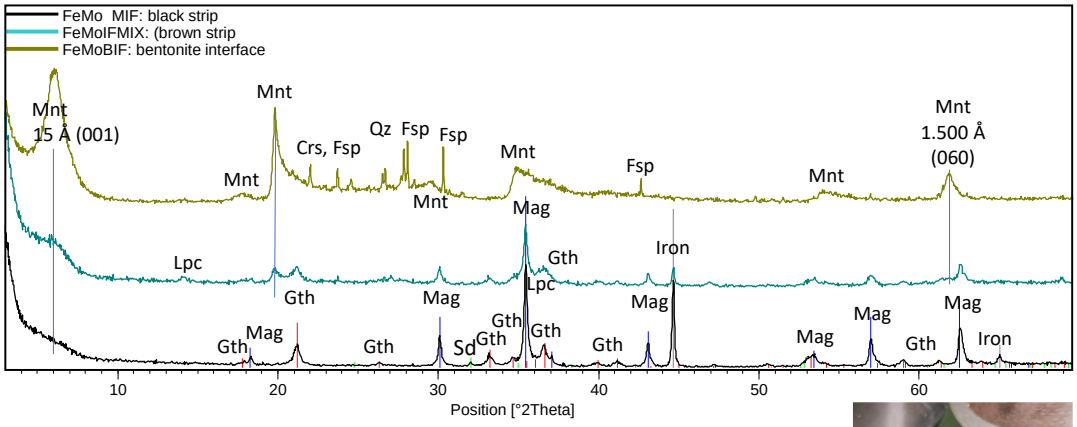

Mineralogy (%) Sample	Mnt	Qz,Crs,Fsp	Lpc	Gth	Mag	Sd	Iron
Iron powder (MIF)	<5	-	-	25	50	5	20
Iron interface (IFMIX)	40	<5	5	10	40	<5	<5
Bentonite interface (BIF)	90	10	-	-	<5	-	-

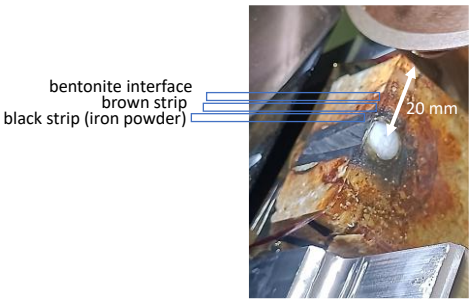

Figure 44 - FeMo experiment section 3. XDR powder patterns. Semiquantitative (wt.%) mineralogy of altered iron powder cylinder and bentonite interface. Mnt: montmorillonite; Qz: quartz, Fsp (Feldspar group minerals); Crs: cristobalite; Lpc: lepidocrocite; Gth: Goethite; Mag: Magnetite; Sd: siderite; Iron: unaltered iron powder.

Microstructure (SEM-EDX analysis, corrosion, altered thickness)

The strip of powdered iron arranged around the sintered steel cylinder is clearly visible in the longitudinal section photograph and in the backscattered electron image (BSE). In the BSE image, they can be distinguished as a compact white strip corresponding to the steel cylinder and a more porous light grey strip corresponding to the altered iron powder in contact with the bentonite (Figure 45). The elemental maps show that there are preferential zones of Fe, Mg and Ca concentration. The diffusion of the iron halo reaches up to 1 mm in the bentonite. This halo is segmented by a Mg concentration zone between 0.1 and 0.3 mm and a Ca concentration zone between 0.2 and 0.3 mm measured from the interface with the iron powder. There is a 0.1 mm band in the bentonite at the iron/bentonite contact, where Ca and Fe are preferentially concentrated. These anomalies are very restricted to the 0.5 mm zone closest to the interface, except for iron, which penetrates up to 2-3 mm into the bentonite. An anomaly of K, Al and Si is also observed in the first mm (Figure 46).

Elemental maps have also been performed on inner cross sections, perpendicular to the previous one, to assess the extent of iron diffusion and oxide precipitation in different (radial) orientations. The image in Figure 47 shows the combination of the backscattered electron images and the elemental maps (SEM-BSE + EDX) measured from that radial configuration. The result confirms a diffusion extent of Fe oxides in bentonite that does not clearly exceed the first mm of interface, although there are diffuse fringes of lower intensity with a very limited range.

These results seem to contradict the several millimetre thicknesses of brown-orange staining observed visually in the bentonite, as the results above indicate that the alteration is limited to distances of less than one millimetre. A possible explanation for this discrepancy is that the dark brown sample taken from the iron-bentonite interface may contain part of the iron layer, so we consider the SEM-EDX elemental mapping results to be more accurate.

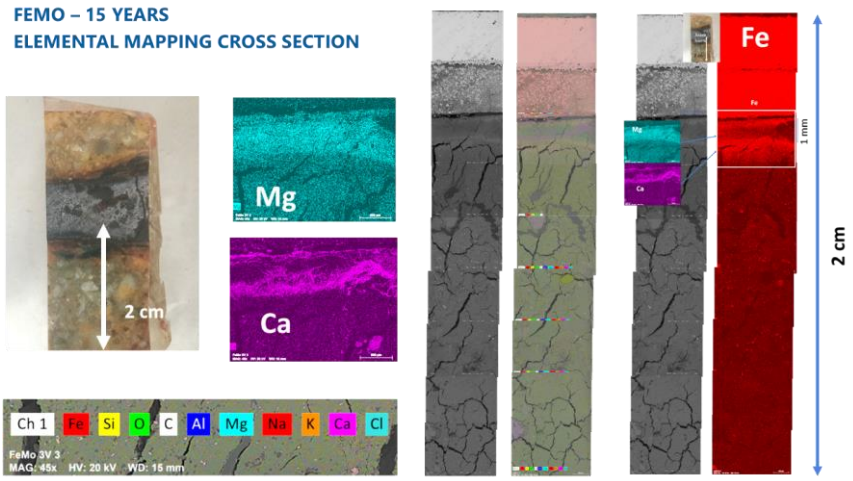

Figure 45 - FeMo experiment section 3. Cross section of iron powder bentonite contact and associated Fe, Ca and Mg chemical gradients.

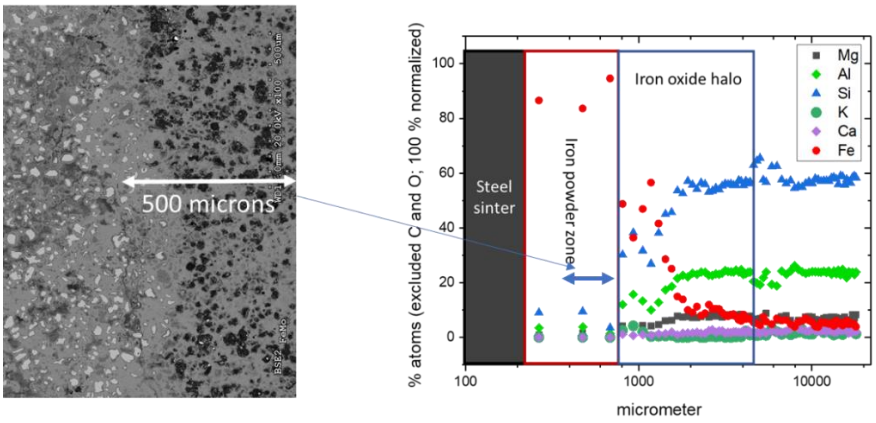

Figure 46 - FeMo. EDX chemical profiles at the iron powder-bentonite interface. Detail of iron powder.

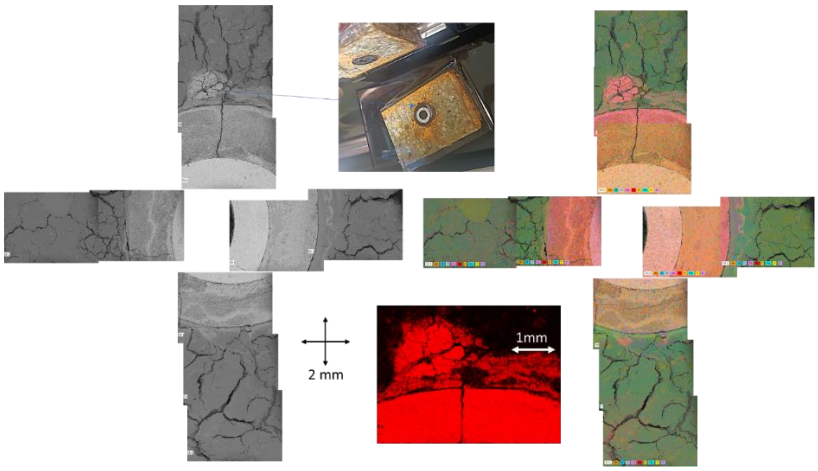

Figure 47 - Backscattered electron microscopy images and combined virtual colour image using EDX elemental maps of a transverse section made to capture the iron oxide halo around the iron powder ring disposed in FeMo experiment.

2.1.3.3 Short-term tests (PhD)

The most relevant results observed in 1- and 6-months tests, extracted from the PhD activities mentioned previously, are presented below. Some of them were published in Mota-Heredia et al. (2023).

EDX observations showed a relative enrichment in Fe from the steel hot interface to a thickness of 0.8 mm after 1 month and up to 4 mm after 6 months. This enrichment is highly asymmetric and is characterised by a 200-100 µm corrosion products crust followed by the compacted bentonite material (Figure 48). The concentration of Fe reached values superior to 40 wt.% in the first 100 µm in 1 month. Then, the concentration sharply decreased to values in the order of 10 wt.%, as in the reference MX-80 bentonite. After 6 months there were determined higher values (>80 wt.%) in a narrow zone of 200 µm from the interface, and the extension of the Fe enrichment (>15 wt.% in average) reached up to 4 mm and then smoothly decreased to the reference material composition. Mg concentrations (wt.%) increased from averaged 3 to 7 wt.% after 6 months of reaction within the zone of 200 µm from the interface.

The precipitation of newly formed pyrite in the proximity to the C-steel/bentonite interface was observed during the MX-80 test, which has been related to the presence of gypsum as accessory mineral in the bentonite. Additionally, after a period of six months, the MX-80 Montmorillonite was a Ca-clay phase rather than maintaining its original Na-clay phase nature. This is consistent with the reduction of the sulfate contained in the gypsum and the displacement of sodium in montmorillonite interlayer positions by the calcium dissolved in the process. The layer of corrosion products was observed by SEM (Figure 48) and identified by XRD. This layer was heterogeneous in composition and thickness for the different bentonites tested (Table 8).

The corrosion products detected were magnetite, maghemite (and hematite) and goethite. Close to the interface, dissolution of cristobalite and precipitation-formation of illite and saponite-like clay minerals were observed. This reaction points to the existence of an alkaline interface in the corrosion processes favouring the dissolution of poorly ordered silica minerals and the precipitation of Mg smectites. After the first 3 mm from the interface, the bentonites show minor alterations in their mineralogy. FEBEX bentonite did not show pyrite precipitation.

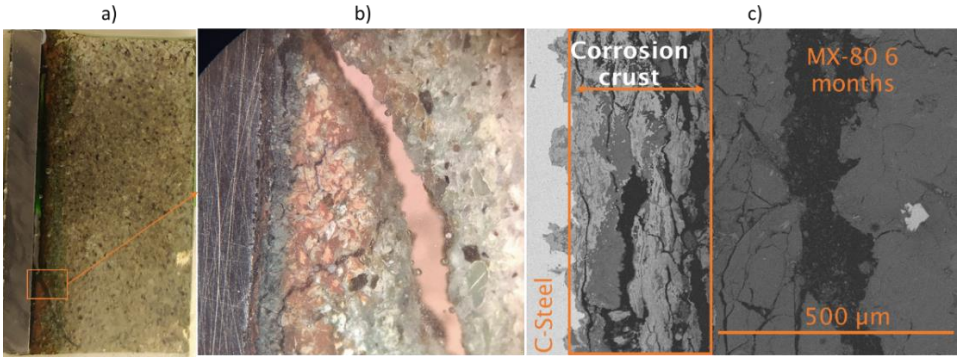

Figure 48 - Thin section of MX-80 after 6 months: a) aspect after cutting, resin embedding and polishing; b) aspect observed with the optical microscope; c) SEM image of the steel/bentonite interface.

Table 8 - Corrosion crust thickness measured at different experimental time and bentonite.

Sample	Maximum corrosion crust thickness (µm)	Fe-Minerals identified
MX-80 1 month	50	Maghemite
MX-80 6 months	250	Magnetite; Goethite
FEBEX 1 month	50	Goethite
FEBEX 6 months	150	Magnetite; Maghemite
FEBEX-Mg 6 months	140	Magnetite

2.1.4 Contribution to up-scaling/conclusion

In this section, we present the results that we consider relevant to the modelling and evaluation of the long-term performance of the disposal cell.

FB5 and FB6 cells

- Iron oxides, (simplistically: hematite and magnetite (and maghemite) phases, in order of abundance) completely fill the intergranular pores of the iron powder iron layer in a zone 2 mm thick from the interface and partially up to 3 mm. Aerobic conditions have initially prevailed at the hot dry interface, and then anhydrous Fe(III) oxides have formed.
- The bentonite has been enriched in iron in a zone 100-150 µm thick from the contact with iron. This region also shows a relative increase in Mg and Ca (less than double, in any case, with respect to the original value; qualitatively < 1% formation of new phases). Non-destructive µ-CT analyses have shown a heterogeneous increase of Fe (enhanced X-ray absorption) affecting at most a 5 mm zone starting from the contact with iron.
- Apparently, the average corrosion rate in the iron grains is low, less than 0.5 µm/y, and reflects the unsaturated and oxidizing environmental conditions at the iron-bentonite interface. The relatively dry (unsaturated) hot interface is dominated by Fe(III) oxides (hematite). This hematite has formed in the initial aerobic environment. Evaporation close to the heater led to the accumulation of salts, mainly chloride, which is concentrated towards this iron-bentonite interface and is part of the chemical composition of the iron oxides that fill the intergranular iron grain space. It is not present in the compact grain corrosion rim, presumably composed of iron and magnetite. The role of chloride as a corrosion catalyst, through the formation of Cl-replacing O-OH Fe(II) iron oxide (i.e., akaganeite), should be noted.
- The cation exchange capacity of the bentonite remains almost similar to the FEBEX original in all the sections analysed, although a slight decrease occurs at the interface. That indicates no alteration of the bentonite after 15 years of interaction, which is further supported by the mineralogical analyses. Exchangeable cations show an increase in Mg and a decrease in Na toward the heater.

The mineralogical-geochemical changes observed experimentally are consistent with redox conditions corresponding to Eh values ranging from 0 to -500 mV and pH values above 10. The existence of moderately reducing conditions and the formation of Fe(III) oxides, very insoluble products, greatly limited Fe migration into bentonite, considering also the relatively high temperature that promoted a constant condition of water unsaturation.

Experiment FB6 highlights the drastic decrease in iron reactivity under the generalized dry-hot unsaturated conditions that characterized this cell. Although a redistribution of water content within the cell is produced and ion transport occurs, with a relative enrichment of chloride toward the iron interface, no significant diffusion of chloride into the iron interface was detected in FB6. If water vapour or water evaporation and condensation processes did not occur significantly at the interface, ion transport was not efficient.

FeMo cell

The study of internal sections of one of the iron powder cylinders (not affected by surface transport processes in the contacts of the device with the cell joints) shows that, after 15 years of interaction, a diffusion halo of less than 1 mm thickness has developed in a practically preserved radial symmetry. It is composed of iron oxides (mainly magnetite and goethite). The iron powder has altered to magnetite and there is evidence of carbonation (siderite formation), with very localized deposits (µm) of Mg- and Ca-rich phases. This implies the existence of an alkaline contact produced by the oxidation of iron, and the associated OH^- production, whose propagation has been very limited in space (< 1mm). This experiment is unique in terms of its temporal dimension since there are no similar experiments of such long duration. Post-mortem characterization of future long-term experiments performed with the same bentonite and including temperature effect (i.e., mock-up FEBEX > 25 years) should provide a large set of relevant information..

The long-term FB and FeMo experiments were designed to investigate the geochemical processes occurring at the iron-bentonite interface under simultaneous hydration and heating processes providing a realistic approximation of the expected geochemical conditions during the unsaturated state of a HLW repository (although use of iron powder enhances the Fe reactivity and then introduces a conservative approach). The results show that water content gradients are related to the thermal gradient and the hydration front. We also observed that advective movement of salts towards the heater occurs and that salts precipitate right at the Fe/bentonite interface. Chloride was found on the surface of the Fe powder and may play a relevant role in the initiation of corrosion. Near the heater, the Fe particles retained their metallic luster and showed no signs of corrosion. Corrosion is limited to areas close to the interface (≈ 2 mm) and the calculated corrosion rate is less than 0.5 µm/y. Corrosion products consist of iron oxides, mainly hematite (predominant), and magnetite – maghemite (FB) and goethite (FeMo). The Fe(III) oxides also prevail under non-saturated conditions close to the heater in the in situ FEBEX test (Wersin and Kober, 2017).

After 15 years of interaction, the maximum thickness of corrosion products formed around the iron grains is about 10 µm (absolute values), and the maximum thickness of bentonite interface material affected by iron mineral formation is about 200 µm. There was no evidence of expansion or pressure increase potentially produced by increased molar volumes of oxides compared to elemental iron. Unsaturated conditions appear to locally favour a potentially oxidizing environment. On the other hand, dry conditions greatly limited the extent of the global reaction that produces the newly formed minerals. The maximum temperatures in the repositories will progressively decrease during the first 100 years. If we consider a linear increase of the corrosion thickness measured in our experiments and multiply those data by 100, we will have as a result that there will be no more than 2 mm of newly formed iron minerals or 5 cm of some iron minerals in certain places (µ-CT). After this unsaturated period, saturated conditions will prevail and corrosion oxide layers will evolve in a more reducing environment (more magnetite and siderite as in FeMo or *in situ*). It is suggested to consider these scenarios in the sensitivity analysis for modelling, even though there are important experimental uncertainties (e.g., the impact of pervasive hot conditions on the properties of the bentonite itself (agglomeration, cementation) or the mobility of Fe(II) in more reducing conditions affecting the subsequent reactivity). As emphasized so far, the study of existing experiments of longer duration seems very important to assess the significance of the extent of these coupled processes on the safety of the whole system.

2.2 Numerical modelling of FB experiment (by UDC)

2.2.1 Introduction

The first calculated thermo-hydro-mechanical and chemical results of the reactive transport model of the FB corrosion tests were presented by UDC in chapter 4 of the ACED Deliverable 2.6 (Havlova et al., 2020). It was based on the reactive transport model for the FB3 corrosion test (Mon, 2017) and was extended to the timeframe of the FB4 corrosion test (7 years). However, data from the FB4 corrosion test were not available for model calibration. Corrosion relevant processes considered include the steel corrosion at a kinetically controlled constant corrosion rate and precipitation of secondary Fe minerals (magnetite, goethite, siderite and $Fe(OH)_2$). Sensitivity runs with respect to steel corrosion rate and kinetic versus equilibrium magnetite precipitation were also presented.

This section presents the updated version of the thermo-hydro-mechanical and chemical results of the reactive transport model of the FB4 and FB5 corrosion tests. The chapter starts with a short description of the tests. Then, the conceptual and numerical reactive transport models are presented. Afterwards, model results are presented together with a comparison of model results with experimental data. The chapter ends with a discussion and the main conclusions.

Six corrosion tests (FB1 to FB6) were performed under anoxic conditions. They started in 2006 and were finished sequentially. Cell FB1 was dismantled after 6 months while FB2 was dismantled after 15 months. The durations of the tests for cells FB3, FB4 and FB5 were 4.3, 7 and 15 years, respectively (see section 2.1).

The relative humidity and the temperature were measured online with two sensors located at 18 mm and 74 mm from the heater. Bentonite samples were taken at the end of the tests after cooling to measure water content, dry density and the concentrations of soluble salts and exchangeable cations.

Goethite was detected after dismantling the FB1 cell. Goethite and hematite precipitates were found in the FB2 cell (after 15 months). The corrosion sequence found at the bentonite-iron contact in the FB3 and FB4 cells includes lepidocrocite, goethite, akaganeite, Cl-green rust, hematite/maghemite and magnetite (traces).

The available data for modelling the FB3, FB4 and FB5 laboratory corrosion tests were provided by CIEMAT (see section 2.1).

2.2.2 Model description (conceptual-numerical model/computer code)

2.2.2.1 Conceptual THCM reactive model

The thermo-hydro-mechanical model of the bentonite in FB tests is based on the model reported by Zheng et al. (2010), Samper et al. (2018) and Samper et al. (2020) for other similar heating and hydration bentonite column tests.

The conceptual geochemical model of the FB corrosion tests includes: 1) Fe powder corrosion, 2) aqueous complexation, 3) acid/base reactions, 4) redox, 5) mineral dissolution/precipitation 6) cation exchange of Ca^{2+}, Mg^{2+}, Na^{+}, K^{+} and Fe^{2+} and 7) surface complexation of H^{+} and Fe^{2+} on strong, $S^{s}OH$, weak #1, $S^{w1}OH$, and weak #2, $S^{w2}OH$, sorption sites.

The geochemical system is defined in terms of the following 12 primary species: H_2O, $O_2(aq)$, H^{+}, Na^{+}, K^{+}, Ca^{2+}, Mg^{2+}, Fe^{2+}, HCO_3^{-}, Cl^{-}, SO_4^{2-} and $SiO_2(aq)$. The chemical system includes 39 secondary aqueous species, 9 mineral phases, 5 exchanged cations, and 13 surface complexes (see Table A1 in Appendix A). Cation exchange reactions take place only in the bentonite and are modelled with the Gaines-Thomas convention (Appelo and Postma, 1993). Surface complexation reactions are assumed to take place in the bentonite and are modelled with the triple-site sorption model of Bradbury and Baeyens (1997; 1998; 2003). For the sake of convergence, sorption was also assumed in the Fe-powder zone with the same parameters as in the bentonite. The thermodynamic data of the aqueous species and minerals were taken from the EQ3/6 database (Wolery, 1992). The model accounts for the temperature dependence of the equilibrium constants, log K, of aqueous and mineral species by using the following equation (Wolery, 1992):

$$logK(T) = b_1 / T^2 + b_2 / T + b_3 lnT + b_4 + b_5 T \quad (1)$$

where b_1 to b_5 are coefficients which are computed in the UDC reactive transport code INVERSE-FADES-CORE V2 by fitting Eq. (1) to the log K values reported in the thermodynamic database at 0, 25, 60, 100, 150, 200, 250 and 300ºC.

The mineral reactions are assumed at chemical equilibrium, except for Fe powder corrosion which is kinetically-controlled according to:

$$r_m = k_m e^{-\frac{E_A}{RT}} \left| (\Omega_m^{\theta} - 1)^{\eta} \right| \quad (2)$$

where r_m is the dissolution/precipitation rate (mol/m²/s), k_m is the kinetic rate constant (mol/m²/s) at 25ºC, E_a is the activation energy, R is the gas constant (J/K·mol), T is the absolute temperature (K), Ω_m is the saturation index which is equal to the ratio of the ion activity product to the equilibrium constant (dimensionless) and Θ and η are empirical kinetic parameters.

Fe powder is treated as a porous material made of metallic iron, Fe(s). H_2O is assumed to be the oxidizing agent of Fe(s) under anaerobic conditions (Mon et al., 2017). The Fe(s) corrosion rate, k_m, is assumed to be constant. The model considers the diffusion of dissolved $H_2(aq)$ and disregards $H_2(g)$ transport through the gaseous phase.

2.2.2.2 Numerical THCM reactive model

The numerical model of the FB corrosion tests was performed with a uniform 1-D finite element mesh of grid size of 1 mm (Figure 49). The mesh considers 2 materials: bentonite (86.8 mm length) and Fe powder (13 mm). The numerical model simulates the heating and hydration during 1593 days (4.3 years) for the FB3 test, 7 years for the FB4 test and 14 years for the FB5 test. A 2-days cooling phase was considered at the end of the tests during which hydration was stopped and the temperature was decreased linearly to ambient temperature.

A liquid pressure of 600 kPa was prescribed at the top of the FB cells in the hydration system with a prescribed temperature of 25ºC. The temperature of the heater at the bottom of the column was equal to 100ºC for the FB cells. The vertical displacement was disabled at the top of the cell. The total stress was fixed to 250 kPa.

Bentonite parameters were taken from previous bentonite heating and hydration models (Zheng et al., 2010; Samper et al., 2018). Bentonite has an initial porosity of 40% and a gravimetric water content of 14 wt.%, which corresponds to a saturation of 57%. The initial temperature of the FB corrosion tests is equal to 22ºC. The initial gas pressure is equal to the atmospheric pressure. Water flow, thermal, solute transport and mechanical parameters used in the THCM model of the FB corrosion tests are shown in Table A2 to Table A5 in Appendix A.

Fe powder parameters were taken from the numerical models of the corrosion cells reported by Mon (2017). As an educated guess, the retention curve, the gas and liquid relative permeabilities and the solute diffusion coefficients of the Fe powder were assumed equal to those of the bentonite. The intrinsic permeability of the liquid in the Fe powder was assumed to be 100 times larger than that of the bentonite. The Fe powder was assumed to have an initial porosity of 0.38 for the FB corrosion tests. No deformation was assumed in the Fe powder.

The FB tests were performed under unsaturated and anoxic conditions. It was assumed that the initial oxygen in the bentonite samples was consumed in the early stages of the tests.

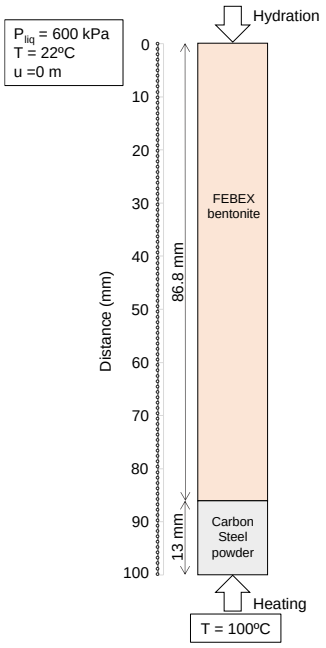

Figure 49 - Sketch of the FB corrosion cells, finite element mesh and boundary conditions of temperature, T, liquid pressure, P_{liq}, and displacement, u, of the THCM numerical model.

A Neumann boundary condition was used for solute transport according to which solute flux is equal to the product of water flux times the solute concentration of the inflow water. The pore diffusion coefficients

are equal to $2 \cdot 10^{-10}$ m^2/s for all chemical species, except for Cl^- which has a value of $9 \cdot 10^{-11}$ m^2/s (Zheng et al., 2010). The initial effective diffusion coefficient in the bentonite is equal to $9.45 \cdot 10^{-12}$ m^2/s for dissolved Cl^- and $4.2 \cdot 10^{-11}$ m^2/s for the rest of the dissolved species.

The initial chemical composition of the bentonite pore water at a water content of 14 wt.% at 25 ºC was derived from Fernández et al. (2001). The chemical composition of the granitic Grimsel hydration water was taken from Turrero et al. (2011). The initial water chemical composition of the Fe powder was assumed equal to that of the bentonite. Chemical compositions of the initial pore waters in the bentonite and Fe powder, and in the Grimsel hydration water used in the THCM model of FB corrosion tests (Mon et al., 2023) are shown in Table A6 in Appendix A.

The bentonite contains initially 1 vol.% of calcite, 1 vol.% of quartz, 0.08 vol.% of gypsum and 57.92 vol.% of non-reactive smectite (Mon et al., 2023). The initial volume fraction of the Fe powder is assumed to be 62% of iron (Samper et al., 2016; Mon et al., 2023). The following secondary minerals were allowed to precipitate: anhydrite, magnetite, goethite, siderite and $Fe(OH)_2$(s). Magnetite was assumed to be the main corrosion product in the FB tests because it is the most thermodynamic stable iron corrosion product, although only traces were detected experimentally. Table 9 shows the corrosion kinetic parameters.

The cation exchange capacity (CEC) of the bentonite is 102.75 cmol(+)/kg (Fernández et al., 2004). By using the initial bentonite pore water concentrations of dissolved Ca^{2+}, Mg^{2+}, Na^+ and K^+, the selectivity coefficients for exchanged Ca^{2+}, Mg^{2+} and K^+ were adjusted to match the concentrations of exchanged cations of the FEBEX bentonite reported by Fernández et al. (2004) (see Table A7 in Appendix A). The total concentration of the sorption sites in the bentonite is 0.629 mol/L (Bradbury and Baeyens, 1997). Strong sites have a strong binding affinity, but a small concentration of 0.015 mol/L. Weak #1 and #2 sites have binding constants weaker than those of the strong sites although their concentrations (0.307 mol/L) are larger than those of the strong sites (see Table A8 in Appendix A).

Magnetite precipitation was considered at equilibrium in the model of the FB tests. The corrosion rates in FB tests were assumed constant and equal to 0.047 µm/year in FB3, FB4 and FB5 tests. The specific surface of the Fe powder was estimated by assuming spherical grains of 30 µm radius. The resulting specific surface is equal to $9.41 \cdot 10^4$ dm^2/L (Mon et al., 2023).

Table 9 – Activation energies, Ea, kinetic rate constants, k at 25ºC and 100ºC, kinetic parameters, θ and η, and specific surfaces, σ, of Fe(s) corrosion used in the THCM models of the FB corrosion tests (De Windt and Torres, 2009; Mon et al., 2023).

Mineral	E_a (kJ/mol)	k at 25ºC (mol/m^2/s)	$K_m \cdot e^{-Ea/RT}$ at 100ºC (mol/m^2/s)	θ	η	σ (dm^2/L)
Fe (s)	11	$4.0 \cdot 10^{-10}$	$9.8 \cdot 10^{-10}$	1	0	$9.41 \cdot 10^4$

2.2.2.3 Computer code

The models were performed with INVERSE-FADES-CORE V2, a finite element code for non-isothermal multiphase flow, heat transport and multicomponent reactive transport in deformable media (Zheng et al., 2010; Mon, 2017). The code accounts for mass balance of water, air, solid and enthalpy. It is based on the reactive transport formulation of CORE2D (Xu et al., 1999; Molinero et al., 2004; Zhang et al., 2008; Samper el al., 2011; Águila et al, 2020). The state variables are liquid and gas pressures, temperature, and concentrations of chemical species. A sequential iteration method is used to solve reactive transport equations. INVERSE-FADES-CORE V2 uses the EQ3/6 thermodynamic database (Wolery, 1992). The forward routines of INVERSE-FADES-CORE have been widely verified with analytical solutions and benchmarked with other codes (Poonoosamy et al., 2018; Samper et al., 2020).

2.2.3 Model results

2.2.3.1 Thermal / hydrodynamic results

The volumetric water content (vol.%) in the bentonite and the Fe powder increases with time, being larger in the bentonite near the hydration boundary (Figure 50). The volumetric water content near the hydration boundary is larger than that near the heater because the porosity increases near the hydration zone (Figure 51). Water evaporates near the heater. The vapour diffuses and condenses in colder places. The computed volumetric water content is slightly smaller than the measured data at 1593 days (FB3 test) and 7 years (FB4 test) near the hydration boundary, while near the Fe powder the computed volumetric water content is larger than the measured values. The total amount of water intake in FB tests is equal to 0.084 L in 14 years (see Figure A1 in Appendix A). Most of the water (97%) enters during the first year.

The computed bentonite porosity increases from 0.4 to 0.488 near the hydration boundary while is like the initial value at the bentonite-Fe powder interface (Figure 52). The computed bentonite porosity is smaller than the measured data at 1593 days (FB3 test) and is similar to those measured at 7 years (FB4 test).

The computed temperature in the bentonite at the hydration boundary is equal to 25ºC while it remains equal to 100ºC at the Fe powder. The computed temperatures reach steady values after a day and then remain constant. The computed temperature is slightly larger than the measured data in the sensors (Figure 52 and Figure A2 in Appendix A). The computed relative humidity increases from 37% to 100% in the bentonite near the hydration boundary and to 80% near the Fe powder (Figure A3 in Appendix A). The computed relative humidity in the sensors located near the hydration boundary are slightly larger than the measured relative humidity data (Figure 53). The evolution of the computed relative humidity in the sensor near the heater does not reproduce the measured relative humidity data. This discrepancy could be due to problems in the water injection system during the tests or to vapour leakage through the sensors.

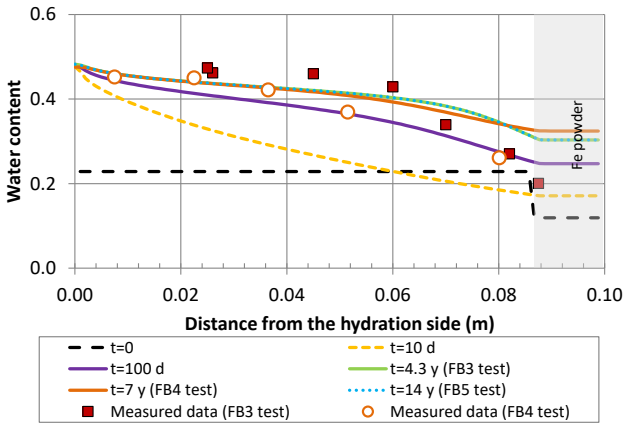

Figure 50 – Spatial distribution of the computed volumetric water contents at selected times (lines) and measured values (symbols) after the cooling phase in the FB3, FB4 and FB5 corrosion tests.

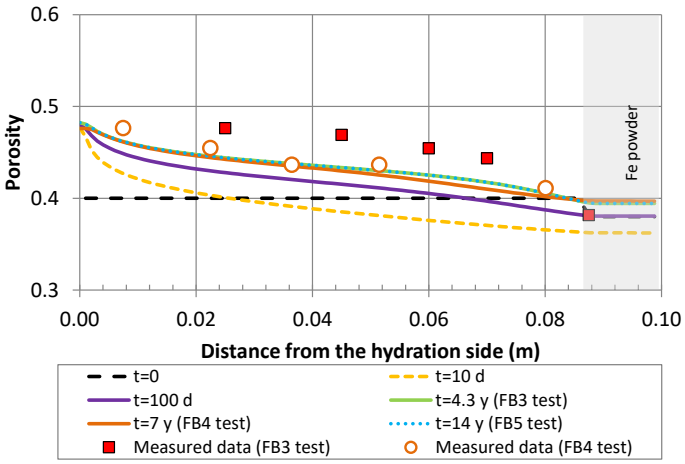

Figure 51 – Spatial distribution of the computed porosity at selected times (lines) and measured values (symbols) after the cooling phase in the FB3, FB4 and FB5 corrosion tests.

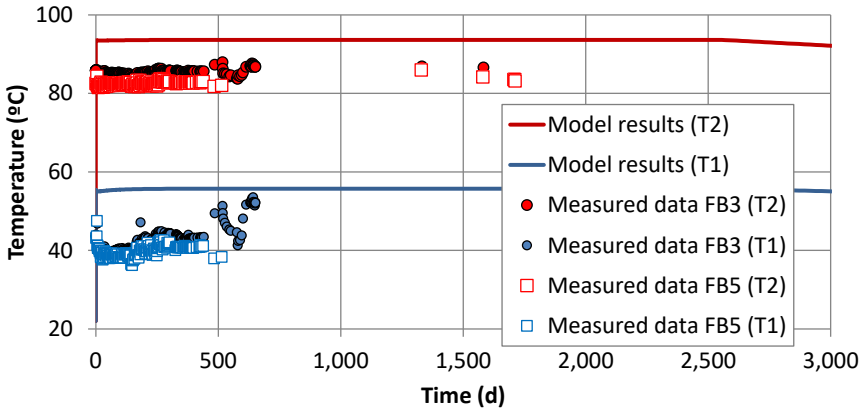

Figure 52 – Time evolution of the computed (lines) and the measured (Turrero et al., 2011) (symbols) temperature in the sensors T2 (18 mm from the heater) and T1 (74 mm from the heater) of the FB3 and FB5 corrosion tests.

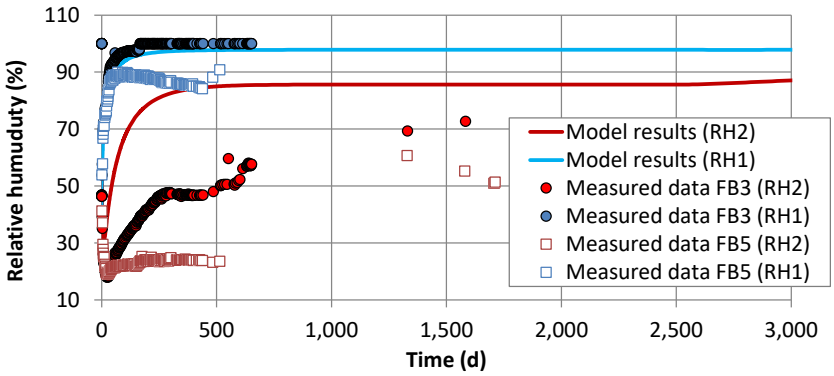

Figure 53 – Time evolution of the computed (lines) and the measured (Turrero et al., 2011) (symbols) relative humidity in the sensors RH2 (18 mm from the heater) and RH1 (74 mm from the heater) of the medium-size corrosion test on FB3 and FB5 corrosion tests.

2.2.3.2 Geochemical results

The computed pH is equal to 7.5 after the initial chemical equilibration. It decreases in the bentonite during the first 10 days, especially near the bentonite-Fe powder interface. Then, pH increases to become at the end of the test like the initial pH (7.72), except in the Fe powder where the pH increases to 9.2 (Figure 54).

The computed concentration of dissolved Cl^- in the bentonite decreases initially. This decrease is especially noticeable near the hydration boundary because the concentration of dissolved Cl^- in the hydration water is smaller than that of the bentonite pore water (Figure 55). The concentration of dissolved Cl^- near the heater, however, increases due to water evaporation. The computed concentration of dissolved Cl^- in the bentonite at later times increases slightly due to solute diffusion. These results are consistent with those of FB3, FB4 and FB5 tests which lasted 4.3, 7 and 14 years. Dissolved Cl^- shows a front which progresses with time. The computed dissolved concentrations of Na^+, Mg^{2+}, Ca^{2+} and K^+ (Figure 56 to Figure 59) show similar patterns to those of Cl^-, but they are also affected by mineral dissolution/precipitation and cation exchange reactions. Computed dissolved concentrations of Na^+, Ca^{2+} and Mg^{2+} show similar trend to measured data, except computed K^+, which is smaller than those measured.

The computed total dissolved concentration of iron decreases initially in the bentonite due to the inflow of water, and in the Fe powder due to magnetite precipitation (Figure 60). The computed concentration of dissolved iron at the end of FB3, FB4 and FB5 tests increases due to the combined effect of Fe powder corrosion, the magnetite re-dissolution and the total exchanged Fe^{2+} mass and total sorbed Fe^{2+} mass decreasing during the cooling phase.

Computed gypsum (not shown) dissolves initially in the bentonite and remains constant while computed anhydrite precipitates in the bentonite near the bentonite-Fe powder interface (75 mm < x < 86.8 mm). At 1953 days (FB3 test), 7 years (FB4 test) and 14 years (FB5 years) anhydrite re-dissolves. Computed calcite dissolved with time in the bentonite and especially near the interface with Fe powder (80 mm < x < 86.8 mm), but precipitates in the Fe powder (86.8 mm < x < 90 mm) (Figure 61).

Magnetite precipitates in the Fe powder while a small amount of magnetite precipitates in a 2 mm thick band in the bentonite near the Fe powder interface (Figure 62). The experimental observations show that magnetite does not penetrate into the bentonite. Model results show no precipitation of siderite, goethite and $Fe(OH)_2(s)$.

Fe^{2+} sorption is most important in the strong and weak #1 sites. The computed sorbed species on the strong and weak #2 sites do not show relevant changes, except for S^sOFe^+. The concentration of S^sOFe^+ decreases from its initial value in the bentonite near the Fe powder while the computed concentration of $S^{w1}OFe^+$ increases in the bentonite from its initial concentration in the FB corrosion tests. Computed sorbed iron is larger than the measured data (Figure 63).

The concentration of exchanged Fe^{2+} decreases from its initial value in the FB3, FB4 and FB5 corrosion tests (Figure 64). The computed concentrations of exchanged Ca^{2+} and Mg^{2+} in the FB corrosion test increase slightly from their initial values near the hydration boundary and decrease near the Fe powder interface (Figure 65). On the contrary, the computed concentration of exchanged Na^+ decreases from its initial value near the hydration boundary and increases near the Fe powder. The computed concentration of exchanged K^+ shows minor changes. The computed concentrations of exchanged Na^+ and Mg^{2+} do not reproduce the trend of the measured data.

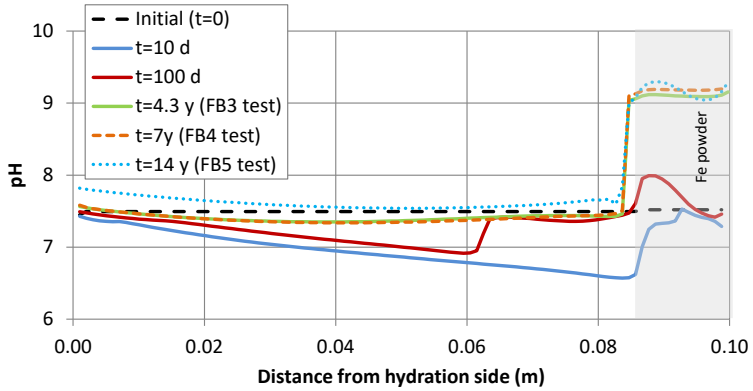

Figure 54 – Spatial distribution of the computed pH at selected times in the FB corrosion tests.

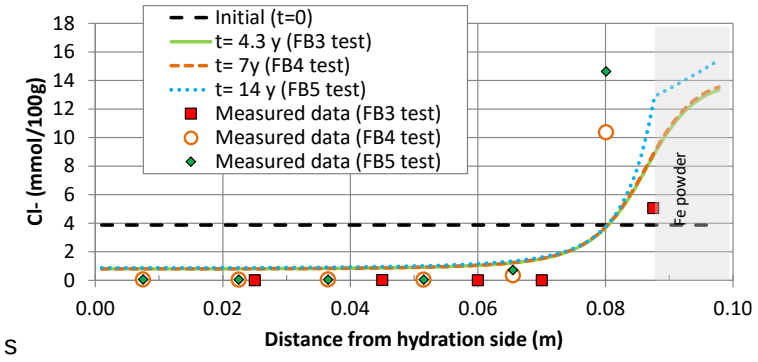

s

Figure 55 – Spatial distribution of the computed concentration of dissolved Cl^- and measured data (symbols) at selected times in the FB3, FB4 and FB5 corrosion tests.

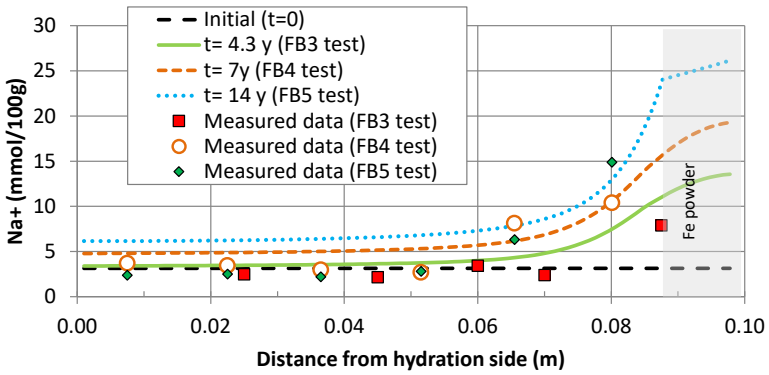

Figure 56 – Spatial distribution of the computed concentration of dissolved Na^+ and measured data (symbols) at selected times in the FB3, FB4 and FB5 corrosion tests.

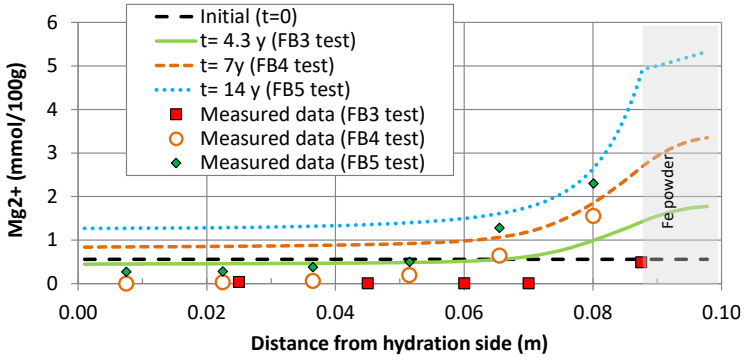

Figure 57 – Spatial distribution of the computed concentration of dissolved Mg^{2+} and measured data (symbols) at selected times in the FB3, FB4 and FB5 corrosion tests.

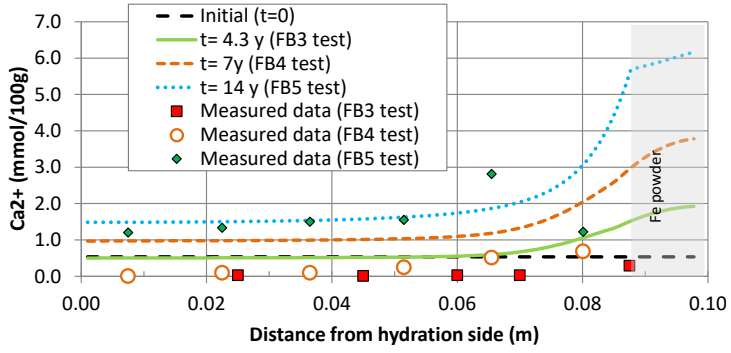

Figure 58 – Spatial distribution of the computed concentration of dissolved Ca^{2+} and measured data (symbols) at selected times in the FB3, FB4 and FB5 corrosion tests.

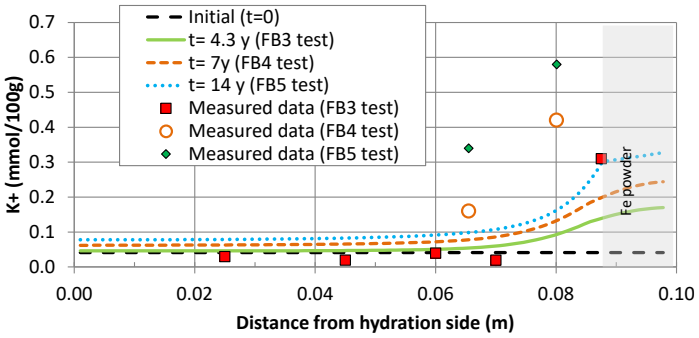

Figure 59 – Spatial distribution of the computed concentration of dissolved K^+ and measured data (symbols) at selected times in the FB3, FB4 and FB5 corrosion tests.

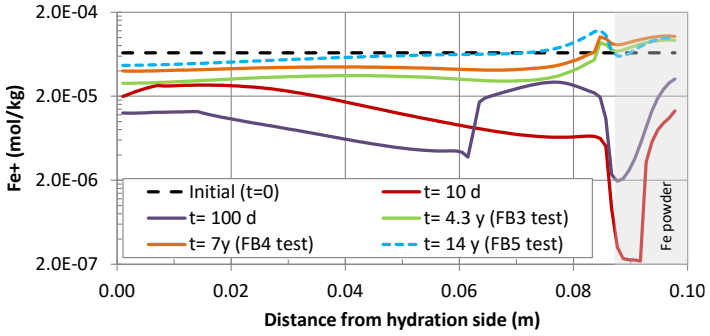

Figure 60 – Spatial distribution of the computed dissolved iron at selected times in the FB3, FB4 and FB5 corrosion tests.

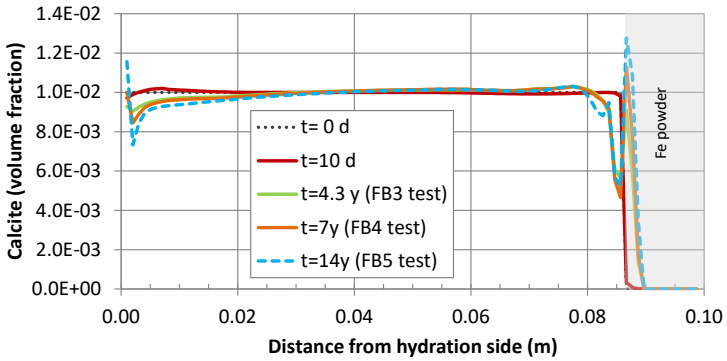

Figure 61 – Spatial distribution of the computed calcite volume fraction at selected times in the FB3, FB4 and FB5 corrosion tests.

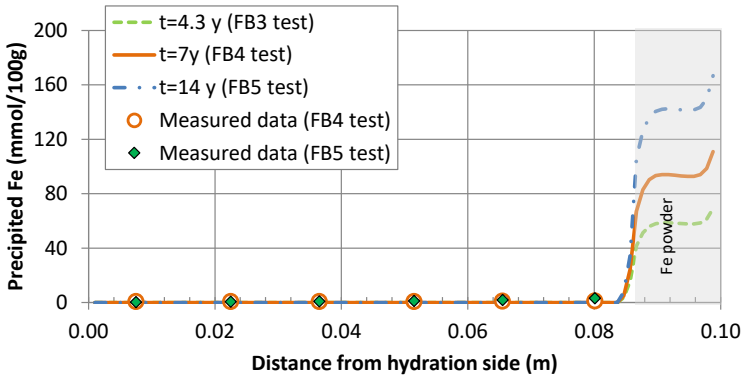

Figure 62 – Spatial distribution of the computed magnetite volume fraction and measured data at selected times in the FB3, FB4 and FB5 corrosion tests.

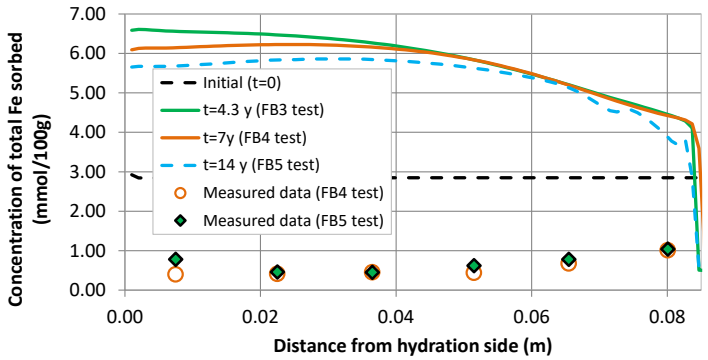

Figure 63 – Spatial distribution of the computed concentration of sorbed iron and measured data at the end of the FB3, FB4 and FB5 corrosion test.

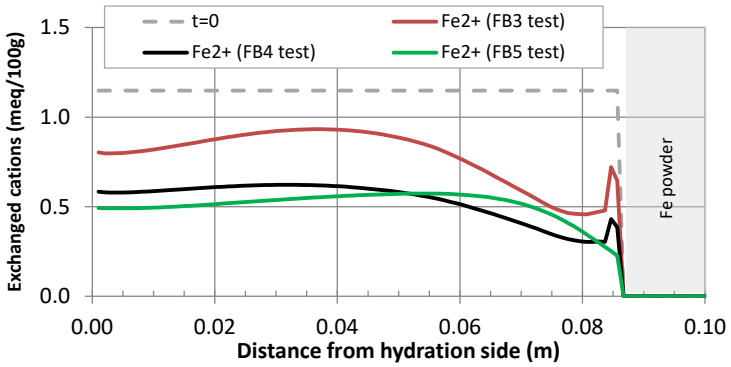

Figure 64 – Spatial distribution of the computed exchanged Fe^{2+} in the FB3, FB4 and FB5 tests.

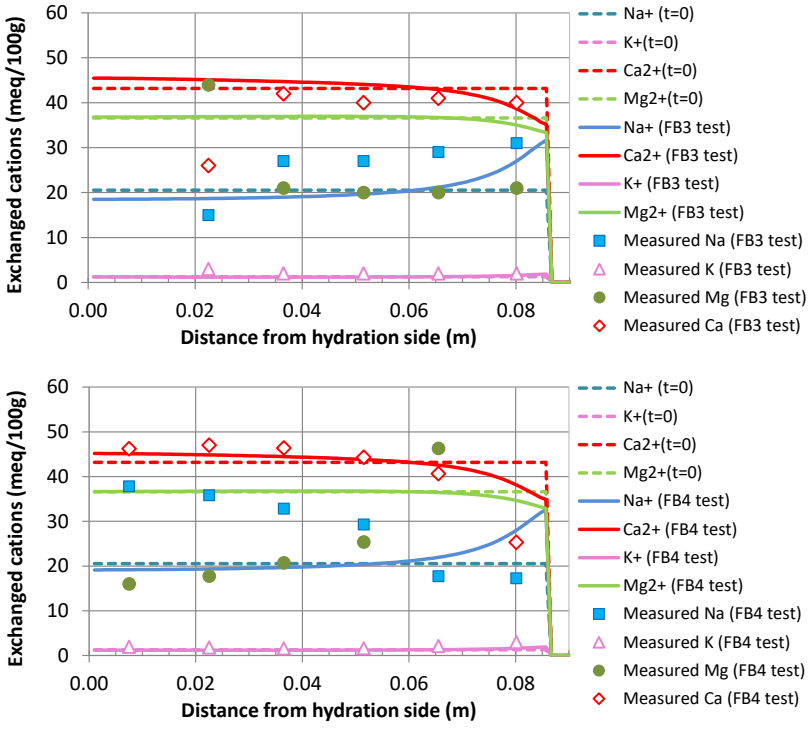

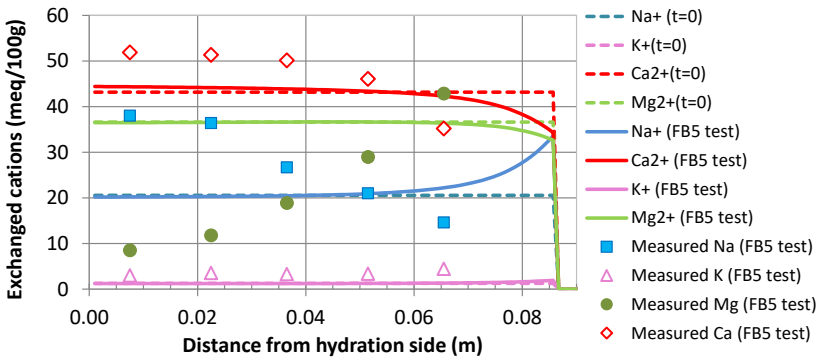

Figure 65 – Spatial distribution of the computed and the measured (symbols) exchanged Ca^{2+}, Mg^{2+}, K^{+} and Na^{+} at the end of the FB3 (up), FB4 (intermediate) and FB5 (down) corrosion tests.

2.2.4 Sensitivity runs

The sensitivity runs performed are shown in Appendix A.2. The following sensitivity runs have been performed:

- Sensitivity to the vapour tortuosity
- Sensitivity to the Fe powder thermal conductivity
- Sensitivity to the initial sorption site concentrations
- Sensitivity to the initial mineral volume fraction composition

Computed volumetric water content in the sensitivity run to the vapour tortuosity fits the measured data, however, the computed dissolved Cl^- concentrations do not reproduce the measured Cl^- trend. On the other hand, the computed temperature performed with smaller Fe powder thermal permeability fits the temperature measured data but, the computed volumetric water content and Cl^- concentration do not reproduce the data. The computed sorbed iron reproduces the measured data better than that of the base run. Considering the initial volume fraction of Fe(s), maghemite and hematite in the Fe powder shows magnetite precipitation while maghemite dissolves instantaneously and hematite dissolves slowly.

2.2.5 Conclusion

A THCM reactive transport model of the geochemical interactions of compacted bentonite and Fe powder in the heating and hydration corrosion tests performed by CIEMAT on medium-size cells (FB tests) has been presented. The model presented here extends other previous model by considering bentonite swelling, evaporation and initial unsaturated conditions in the bentonite, and by improving the assumed geochemical conceptual model.

The main conclusions of the model of the FB test include: 1) Magnetite precipitates in the whole Fe powder, but only in a small amount in the first 2 mm of the bentonite near the bentonite-Fe powder interface, 2) Although the experimental observations show that there is no magnetite penetration in the bentonite, some magnetite precipitation was observed at the interface, which is consistent with the small amount of magnetite precipitation computed at the bentonite-Fe powder interface, 3) There is no precipitation of other iron corrosion products, 4) Model results do not reproduce the precipitation of hematite and maghemite observed in the Fe powder near the bentonite interface and 5) Model results do not reproduce the patterns of exchanged Na^+ and Mg^{2+} concentrations.

The following sensitivity runs have been performed: 1) Sensitivity to the vapour tortuosity, 2) sensitivity to the Fe powder thermal permeability, 3) sensitivity to the initial sorption site concentrations and 4) sensitivity to the initial mineral volume fraction composition. Computed volumetric water content in the sensitivity run to the vapour tortuosity fits the measured data, however, the computed dissolved Cl^- concentrations do not reproduce the measured Cl^- trend. On the other hand, the computed temperature performed with smaller Fe powder thermal permeability fits the temperature measured data but, the computed volumetric water content and Cl^- concentration do not reproduce the data. The computed

sorbed iron reproduce the measured data better than that of the base run. Considering the initial volume fraction of Fe(s), maghemite and hematite in the Fe powder shows magnetite precipitation while maghemite dissolves instantaneously and hematite dissolves slowly.

The reactive transport model of the FB tests has uncertainties which could be overcome by accounting for: 1) an initial aerobic corrosion stage with a source of oxygen and the precipitation of Fe(III) oxides, hydroxides and oxyhydroxides, 2) a time-varying corrosion rate depending on pH and Fe(s) saturation index, 3) other corrosion products such as hematite, maghemite, lepidocrocite, akaganeite and Fe-phyllosilicates, 4) kinetic magnetite precipitation, 5) kinetic smectite dissolution and 6) changes in porosity, permeability and diffusion coefficients caused by mineral dissolution/precipitation. Other relevant studies could include the evaluation of model sensitivity to mechanical processes.

The use of Fe powder in steel/bentonite corrosion tests enhances Fe(s) corrosion due to its higher reactive surface but introduces other sources of uncertainty. The heterogeneity of Fe powder favours the formation of preferential pathways for vapour migration with some particles being more exposed to the oxidizing agent than others (Torres et al., 2013).

2.3 Numerical modelling of FeMo tests (by UDC)

2.3.1 Introduction

This section presents the final calculated results of the reactive transport model of the FeMo corrosion test performed by UDC. The section starts with a very short description of the test. Then, the conceptual and numerical reactive transport model is presented. Next, the main model results are presented. This section ends with a discussion and the main conclusions.

The FeMo corrosion test consists of 6 stainless-steel sinters surrounded by Fe powder emplaced in holes drilled in a FEBEX bentonite block (section 2.1.2.1.2). The bentonite block was hydrated with a granitic water through the sinters by using 6 syringes. The test was performed at room temperature by CIEMAT for 15 years. The bentonite block had a height and a width of 120 mm with a dry density of 1.65 g/cm^3. It is important to point out that the Fe powder used in the FeMo corrosion tests has two different particle sizes: 64 and 450 µm.

The available information and data for modelling the FeMo laboratory corrosion test were provided by CIEMAT.

2.3.2 Model description (data/conceptual-numerical model/computer code)

2.3.2.1 Conceptual model

It is important to point out the following features of the FeMo test: (1) the bentonite is saturated, (2) there is no water flow, (3) it is an isothermal experiment and (4) mechanical effects are not considered.

The conceptual geochemical model of the FeMo corrosion test, which is also similar to the one used in the FB tests (see chapter 2.2), includes: 1) Fe powder corrosion, 2) aqueous complexation, 3) acid/base reactions, 4) redox, 5) mineral dissolution/precipitation 6) cation exchange of Ca^{2+}, Mg^{2+}, Na^{+}, K^{+} and Fe^{2+} and 7) surface complexation of H^{+} and Fe^{2+} on strong, $S^{s}OH$, weak #1, $S^{w1}OH$, and weak #2 , $S^{w2}OH$, sorption sites.

The geochemical system is defined in terms of the following 13 primary species: H_2O, $O_2(aq)$, H^{+}, Na^{+}, K^{+}, Ca^{2+}, Mg^{2+}, Fe^{2+}, HCO_3^{-}, Cl^{-}, SO_4^{2-}, $Al(OH)_4^{-}$ and $H_4(SiO_4)$. The chemical system includes 43 secondary aqueous species, 11 mineral phases, 5 exchanged cations, and 13 surface complexes (see Table B1 in Appendix B). Cation exchange reactions take place only in the bentonite and are modelled with the Gaines-Thomas convention (Appelo and Postma, 1993). Surface complexation reactions are assumed to take place in the bentonite and are modelled with the triple-site sorption model of Bradbury and Baeyens (1997; 1998; 2003). Table B1 shows the values of the equilibrium constants at 22ºC for aqueous complexes and minerals taken from the ThermoChimie thermodynamic database (Giffaut et

al., 2014) considered in the model of the FeMo corrosion test. The protolysis constants for surface complexation reactions (Bradbury and Baeyens, 1997) and selectivity coefficients for cation exchange reactions (ENRESA, 2006b) are show in Table A1 in Appendix A.

The mineral reactions are assumed at chemical equilibrium, except for Fe powder corrosion which is kinetically-controlled (see Eq. (2) in section 2.2). Fe powder and the sinter are treated as a porous material made of metallic iron, Fe(s). H_2O is assumed to be the oxidizing agent of Fe(s) under anaerobic conditions (Mon, 2017). The corrosion rate of the Fe(s) is assumed to be constant. The corrosion rate of the sinter is assumed to be much smaller than that for the Fe powder. The model considers the diffusion of dissolved H_2(aq) and disregards H_2(g) transport through the gaseous phase.

2.3.2.2 Numerical model

The numerical model of the FeMo corrosion tests was performed with a 1-D finite element grid (*Figure* 66). The mesh considers 3 materials by using 193 nodes: the sinter (5 mm length), the Fe powder (2 mm) and the bentonite (23 mm). The numerical model simulates 15 years. The temperature of the FeMo corrosion test is equal to 22 ºC.

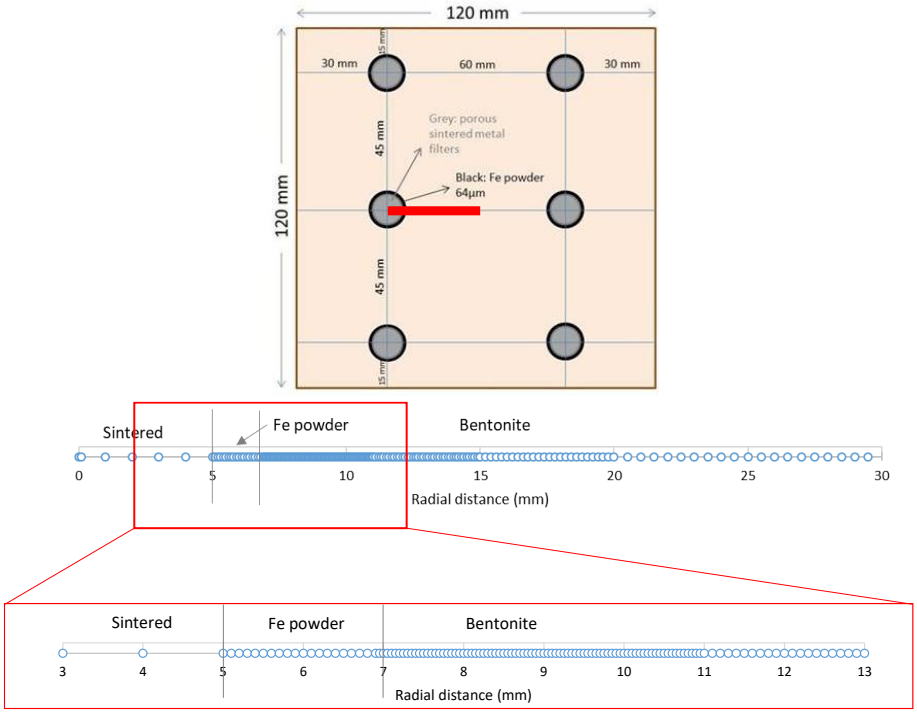

Figure 66 - *Sketch of the FeMo corrosion test and the finite element mesh used in the reactive transport model.*

The main parameters of the sinter, the Fe powder and the bentonite considered in the reactive transport model of the FeMo test are show in Table 10. Bentonite has an initial porosity of 0.407, the Fe powder has 0.38 and the sinter 0.45. The dispersivity is greater in the sinter than in the bentonite and the Fe powder. The effective diffusion coefficient is the same in the three materials. There is no flow considered in the model.

The bentonite of the FeMo tests was initially saturated with granitic water through the sinter. The FeMo test model was performed under saturated and anoxic conditions. It was assumed that the initial oxygen in the bentonite was consumed before the test starts. The initial water chemical composition at the sinter and the Fe powder is granitic water (Turrero et al., 2011). The initial chemical composition of the bentonite saturated pore water was taken from Samper et al. (2016). These two types of water are shown in Table B2 in Appendix B.

The bentonite contains initially 1 vol.% of calcite, 1 vol.% of quartz and 57.92 vol.% of non-reactive smectite. The initial volume fraction of the Fe powder is assumed to be 62% of iron (Samper et al., 2016) while in the sinter the value is 45%. The following secondary minerals were allowed to precipitate: gypsum, magnetite, goethite, siderite, greenalite, cronstedtite and saponite-Mg. Magnetite was assumed to be the main corrosion product in the FeMo test because it is the most thermodynamic stable iron corrosion product.

The cation exchange capacity (CEC) of the bentonite is 102.75 cmol(+)/kg (Fernández et al., 2004). By using the initial bentonite pore water concentrations of dissolved Ca^{2+}, Mg^{2+}, Na^{+} and K^{+}, the selectivity coefficients for exchanged Ca^{2+}, Mg^{2+} and K^{+} were adjusted to match the concentrations of exchanged cations of the FEBEX bentonite reported by Fernández et al. (2004) (see Table A7). The total concentration of the sorption sites in the bentonite is 0.629 mol/L (Bradbury and Baeyens, 1997). Strong sites have a strong binding affinity, but a small concentration of 0.015 mol/L. Weak #1 and #2 sites have binding constants weaker than those of the strong sites although their concentrations (0.307 mol/L) are larger than those of the strong sites (see Table A8).

Table 11 shows all the information for the calculation of the corrosion rates, specific surfaces and kinetic constants at the sinter and the Fe powder considered in the reactive transport of the FeMo test. The corrosion rates in the FeMo test were assumed constant and equal to 0.0006 µm/year in the sinter and 0.05 µm/year in the Fe powder for both grain sizes (i.e., 64 µm and 450 µm). The specific surface of the sinter was estimated by assuming spherical grains of 32 µm radius. The resulting specific surface is equal to 153 dm^2/L. In the case of the Fe powder at a grain size of 64 µm a specific surface of 15,300 dm^2/L was estimated by assuming spherical grains of 32 µm radius. The Fe powder at a grain size of 450 µm has a resulting specific surface equal to 2,180 dm^2/L by assuming spherical grains of 225 µm radius.

Table 10 – Main parameters (permeability, porosity, grain size, dispersivity and effective diffusion coefficient) of the sinter, the Fe powder and the bentonite considered in the reactive transport model of the FeMo test.

	Sinter	**Fe powder**	**Bentonite**
K (dm/y)	$1.8 \cdot 10^{-3}$	$1.8 \cdot 10^{-3}$	$1.8 \cdot 10^{-3}$
Porosity	0.45	0.38	0.407
Fe grain size (µm)	-	64 and 450	-
α (dm)	0.1	0.01	0.01
De (m^2/s)	$4 \cdot 10^{-11}$	$4 \cdot 10^{-11}$	$4 \cdot 10^{-11}$

Table 11 – Corrosion rates of the sinter and the Fe powder at the two grain sizes of 64 and 450 µm considered in the reactive transport model of the FeMo test.

	Sinter	**Fe powder (64 µm)**	**Fe powder (450 µm)**
Time (y)	15	15	15
Initial volume fraction (%)	0.550	0.620	0.620
Final volume fraction (%)	0.549	0.545	0.609
Total volume fraction variation (%)	0.0009	0.0746	0.0106
Total corrosion (µm)	0.0096	0.7957	0.7950
Corrosion rate (µm/y)	0.0006	0.0530	0.0530
Particle radius (µm)	32	32	225
Specific reactive surface area (dm^2/L)	153	15300	2180
Kinetic constant ($mol/m^2/y$)	0.0126	0.0126	0.0126

2.3.2.3 Computer code

The reactive transport models of the FeMo corrosion test were performed with CORE2D v5 (Zhang et al., 2008; Samper et al., 2009; Fernández, 2017; Águila et al., 2020). This finite element reactive transport code relies on several thermodynamic databases. ThermoChimie v10.a (Giffaut et al, 2014) was used for the model presented here. CORE2D V5 is based on the sequential iteration approach, considers the changes in porosity due to mineral dissolution/precipitation reactions and their feedback

effect on the flow and transport parameters (Samper et al., 2009; Águila et al., 2020). The code has been benchmarked against other reactive transport codes (Poonoosamy et al., 2018; Águila et al., 2021).

2.3.3 Model results (particle diameter of 64 µm and 450 µm)

This section contains the prediction of the geochemical evolution of the FeMo test by considering a particle size of 64 and 450 µm at the Fe powder.

Figure 67 shows the spatial distribution of the computed pH at selected times at the sinter, the Fe powder and bentonite for both 64 and 450 µm particle size tests. Computed pH increases with time in the sinter, Fe powder (9.5) and in the bentonite near the Fe powder, 7 mm and 5.5 mm into bentonite for 64 and 450 µm tests, respectively due to corrosion. Computed Eh decreases in the sinter, the Fe powder and in the bentonite near the Fe powder to -0.62 V (see Figure B1 and Figure B2 in Appendix B).

Dissolved aqueous chloride concentration diffuse from the bentonite into the Fe powder and sinter because the concentration in the bentonite is much larger than that in the sinter and in the Fe powder (Figure 68). Computed dissolved Fe increases in the sinter and in the Fe powder due to corrosion and decreases in the bentonite near the Fe powder, 8 mm and 6 mm into bentonite for 64 and 450 µm tests, respectively, (Figure 69) due to magnetite precipitation.

Quartz does not precipitate or dissolve in the model (Figure 70 Figure 1and Figure B3 in Appendix B). Figure 71 shows a minor calcite precipitation at the Fe powder/bentonite interface and slight dissolution in the bentonite (2 mm).

Figure 72 shows the spatial distribution of the computed Fe(s) at different times. The corrosion in the sinter is much smaller than that of the Fe powder. The corrosion for the 450 µm test in the Fe powder is much smaller than that for the 64 µm test. A small amount of magnetite precipitates in the sinter and in the Fe powder (Figure 73). Computed siderite and greenalite precipitates in the Fe powder at the interface with the bentonite (Figure 74 and Figure 75 and Figure B4 and Figure B5 in Appendix B). Corrosion products precipitation is similar for 64 and 450 µm at the Fe powder, however, the amounts precipitated for 64 µm are larger than those for 450 µm.

Computed smectite dissolution is inappreciable (Figure 76 and Figure B6 in Appendix B) and computed saponite-Mg precipitates in the bentonite at the interface with the Fe powder (Figure 77 and Figure B7 in Appendix B).

Figure 78 shows the spatial distribution of the computed exchanged cation concentrations at 15 years. Computed exchanged Ca^{+2} and Mg^{+2} increases slightly near the Fe interface, Na^{+} decreases slightly in the bentonite near the interface, K^{+} does not show changes. Computed exchanged Fe^{+2} is very small in the bentonite and decreases near the Fe powder interface. The computed exchanged cations concentrations results are similar for 450 µm (see Figure B8 in Appendix B).

Figure 79 shows the spatial distribution of the computed sorption concentration at 15 years for 64 µm. The main sorbed species is $S^{s}OFe^{+}$ in the strong site, $S^{w1}O^{-}$ and $S^{w1}OH$ in the weak#1 site and $S^{w2}OH$ in the weak#2 site at 15 years. The computed sorption concentration results are similar for 450 µm (see Figure B9 in Appendix B).

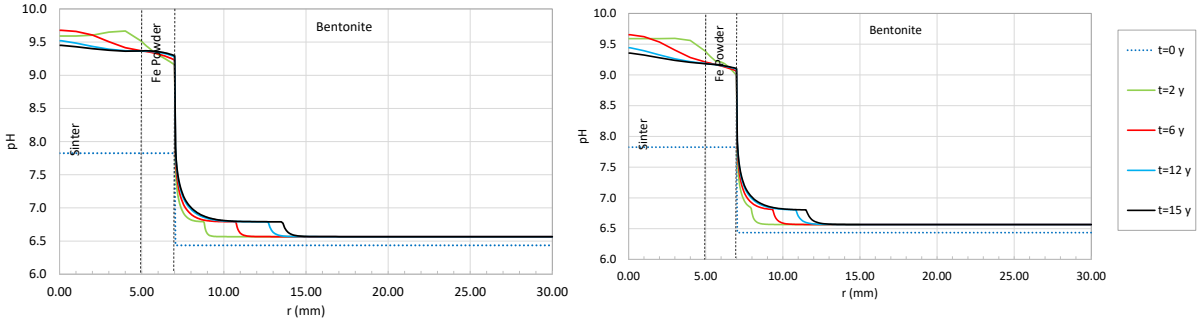

Figure 67 – Spatial distribution of the computed pH at selected times in the FeMo corrosion tests for a particle size of 64 µm (left) and 450 µm (right).

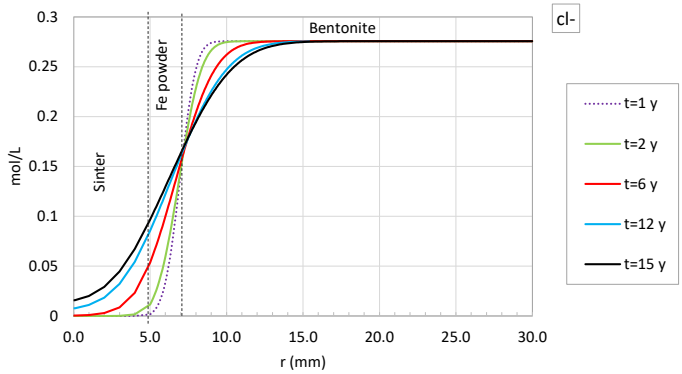

Figure 68 – Spatial distribution of the computed dissolved Cl^- at selected times in the FeMo corrosion tests for a particle size of 64 µm.

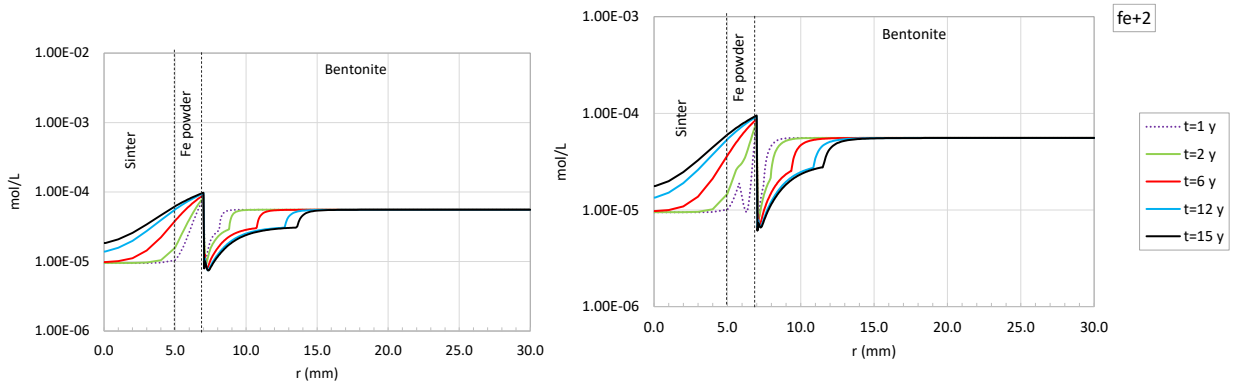

Figure 69 – Spatial distribution of the computed dissolved Fe^{2+} at selected times in the FeMo corrosion tests for a particle size of 64 µm (left) and 450 µm (right).

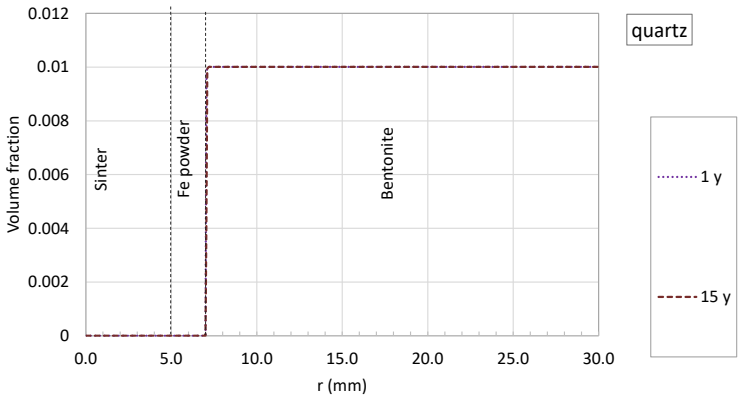

Figure 70 – Spatial distribution of the computed quartz at selected times in the FeMo corrosion tests for a particle size of 64 µm.

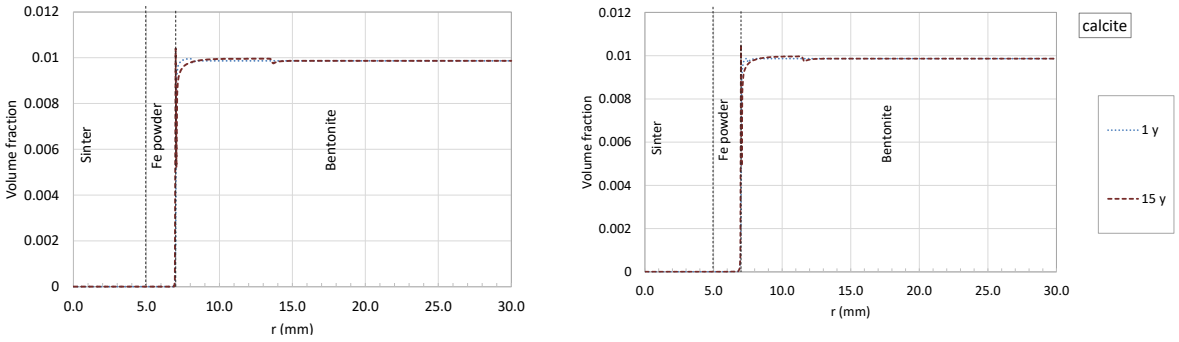

Figure 71 – Spatial distribution of the computed calcite at selected times in the FeMo corrosion tests for a particle size of 64 µm (left) and 450 µm (right).

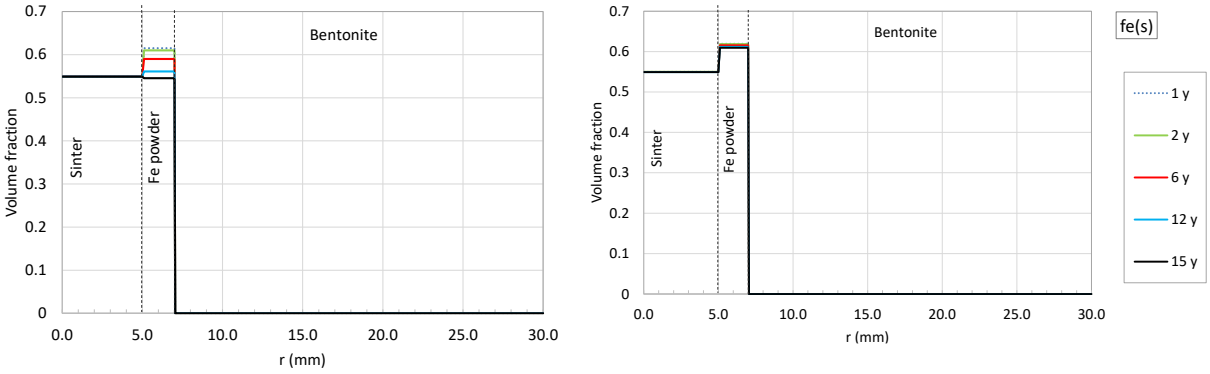

Figure 72 – Spatial distribution of the computed Fe(s) at selected times in the FeMo corrosion tests for a particle size of 64 µm (left) and 450 µm (right).

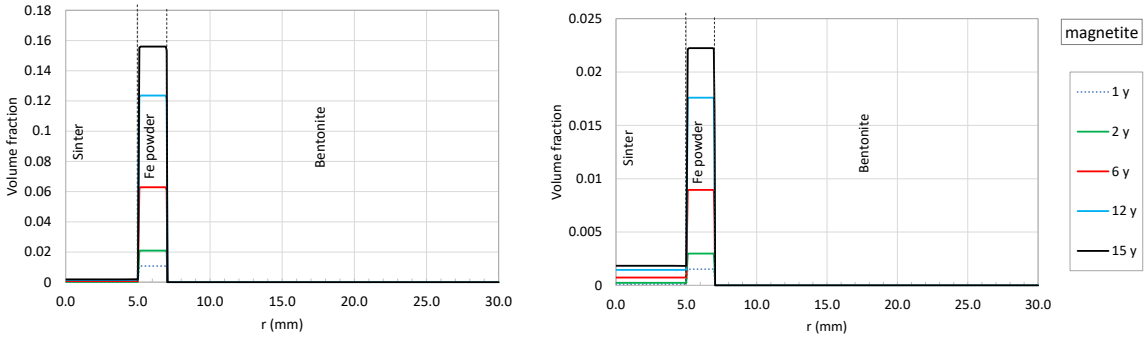

Figure 73 – Spatial distribution of the computed magnetite at selected times in the FeMo corrosion tests for a particle size of 64 µm (left) and 450 µm (right).

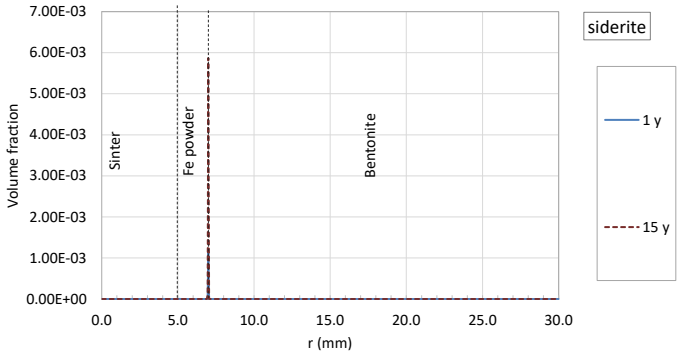

Figure 74 – Spatial distribution of the computed siderite at selected times in the FeMo corrosion tests for a particle size of 64 µm.

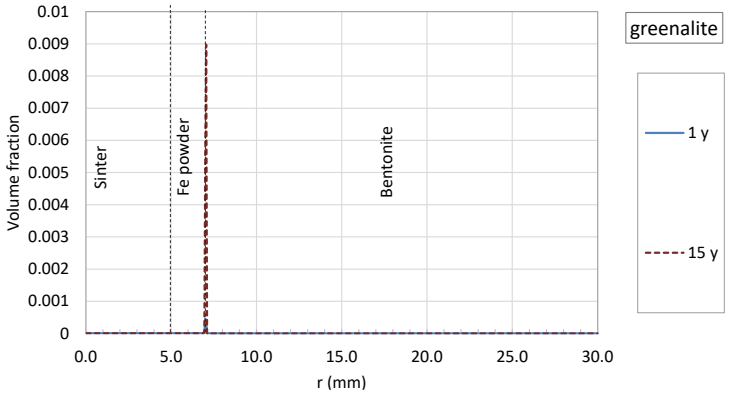

Figure 75 – Spatial distribution of the computed greenalite at selected times in the FeMo corrosion tests for a particle size of 64 µm.

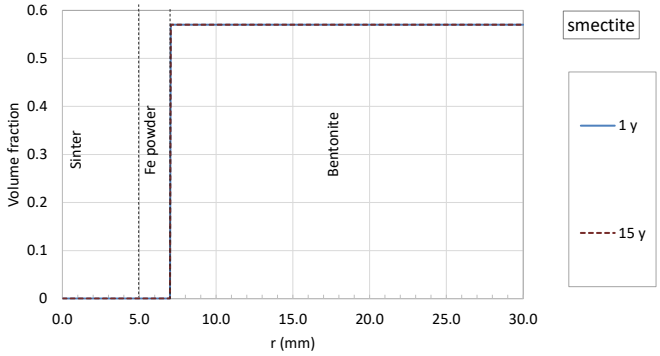

Figure 76 – Spatial distribution of the computed smectite at selected times in the FeMo corrosion tests for a particle size of 64 µm.

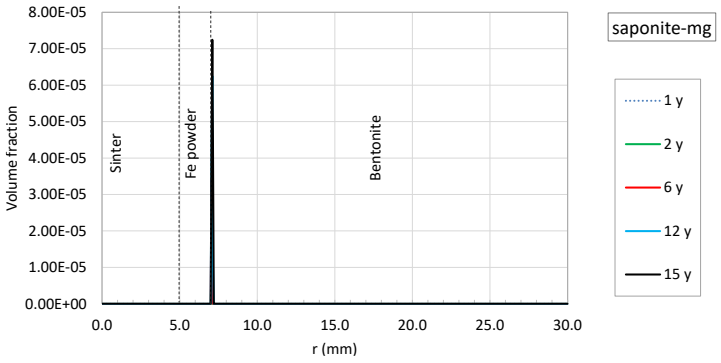

Figure 77 – Spatial distribution of the computed saponite-Mg at selected times in the FeMo corrosion tests for a particle size of 64 µm.

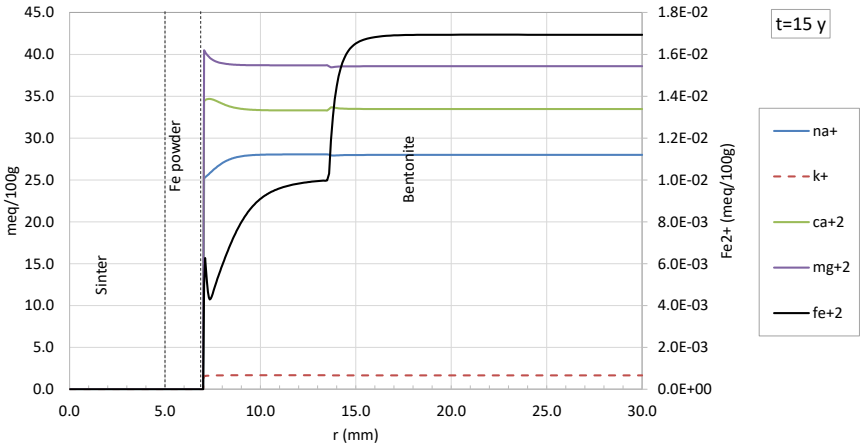

Figure 78 – Spatial distribution of the computed exchanged cations at 15 years in the FeMo corrosion tests for a particle size of 64 µm.

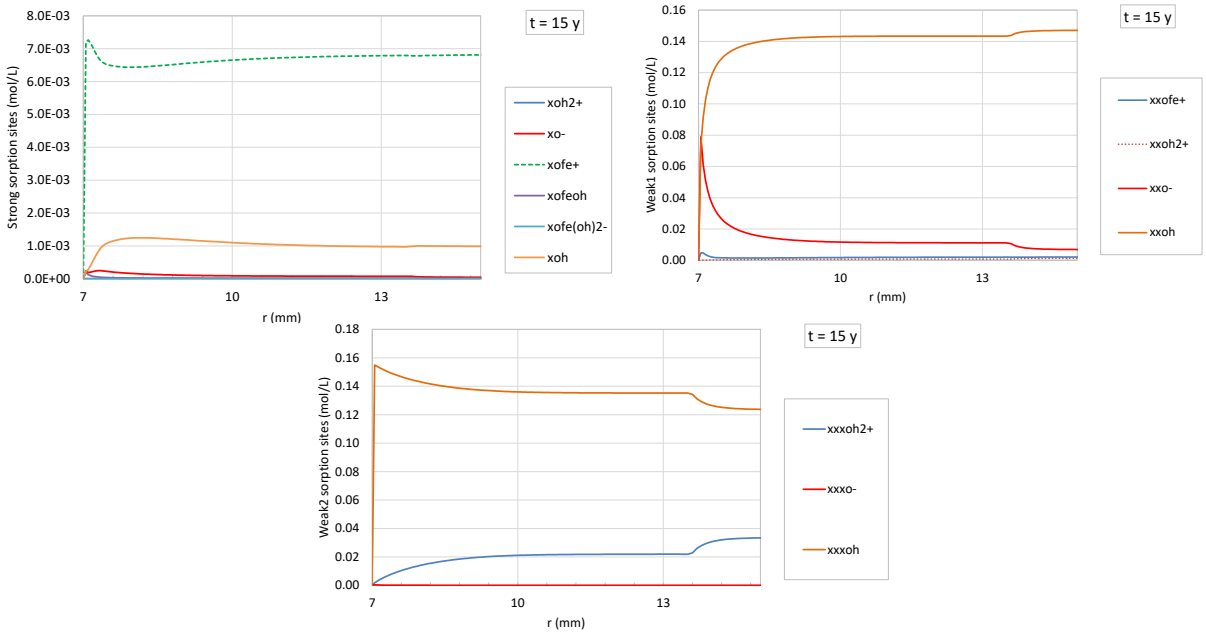

Figure 79 – Spatial distribution of the computed sorbed concentrations at 15 years in the FeMo corrosion tests for a particle size of 64 µm.

2.3.4 Conclusion

A reactive transport model of the geochemical interactions of compacted bentonite and Fe powder in the FeMo test has been presented. The model considers the geochemical evolution of the FeMo test by considering a Fe powder particle size of 64 and 450 µm.

The main conclusions of the model of the FeMo test include: 1) pH increases to 9.5 in the sinter and Fe powder; 2) Computed magnetite is the main corrosion product; 3) Computed siderite, greenalite and saponite-Mg precipitate at the Fe powder/bentonite interface; 4) Smectite, quartz and calcite show small changes; and 5) Results for particle size of 64 and 450 µm are similar, the largest difference is the larger magnetite precipitation for particle size of 64 µm.

The reactive transport model of the FeMo test has uncertainties which could be overcome by accounting for: 1) More complex 2D vertical model which considers the extension of the corrosion products along the vertical; 2) Other corrosion products such as hematite, maghemite, lepidocrocite and akaganeite.

2.4 Corrosion model steel/bentonite of FEBEX (by UDC)

2.4.1 Introduction

The first calculated thermo-hydro-mechanical and chemical results of the reactive transport model of the FEBEX in situ test were presented by UDC in chapter 5 of the ACED Deliverable 2.6 (Havlova et al., 2020). This corrosion model for the steel/bentonite interaction in the FEBEX experiment was based on the well-developed revisited THCM model of the FEBEX in-situ test presented by Samper et al. (2018).

This section presents the final thermo-hydro-mechanical and chemical results of the reactive transport corrosion model of the FEBEX in situ experiment performed by UDC. The section starts with a short description of the test. Then, the conceptual and numerical reactive transport models are presented. Next, the used reactive transport code and the main model results are presented together with a comparison of model results with experimental data. The section ends with a discussion and the main conclusions.

FEBEX was a demonstration and research project dealing with the engineered barrier system designed for sealing and containment of a radioactive waste repository (ENRESA, 2000). FEBEX was based on the Spanish Reference Concept for the disposal of radioactive waste in crystalline rocks. Besides the laboratory experiments, FEBEX included the following two main large-scale experiments, which started in February 1997: (1) The in situ full-scale test performed at the Grimsel underground research laboratory in Switzerland (Alonso and Ledesma, 2005; ENRESA, 2000; 2006a); and (2) The mock-up test operated at the CIEMAT facilities in Spain (ENRESA, 2000; 2006a; Martín and Barcala, 2005).

The FEBEX in situ test was performed in a gallery excavated in granite in the underground research laboratory (URL) of Grimsel operated by NAGRA in Switzerland. The test began in February 1997. The 1st operation period lasted from 1997 to 2002 when heater 1 was switched off and the surrounding area was dismantled. The 2nd operation period started after the emplacement of a shotcrete plug in 2002 and ended in June 2015 when the entire bentonite barrier was fully dismantled after 18 years of heating and hydration.

The FEBEX in situ test included the heating system, the clay barrier and the instrumentation, monitoring and control system. The drift was 70.4 m long and 2.27 m in diameter (ENRESA, 2000). The test zone was located in the last 17.4 m of the drift where heaters, bentonite and instrumentation were installed. The main elements of the heating system were two heaters, separated horizontally by 1 m, which simulated full-sized canisters. The heaters were placed inside a cylindrical carbon-steel liner having a diameter of 0.93 m, which had been installed concentrically with the drift. Each heater was made of carbon steel, measured 4.54 m in length and 0.90 m in diameter, had a wall thickness of 0.10 m and weighed 11 tons. The heaters were designed to maintain a maximum temperature of 100ºC at the liner/bentonite interface. The bentonite barrier was made of blocks of highly compacted bentonite. The layout of the FEBEX in situ test for the 1st operation period is shown in Figure 80. The layout of the 2nd period is shown in Figure 81.

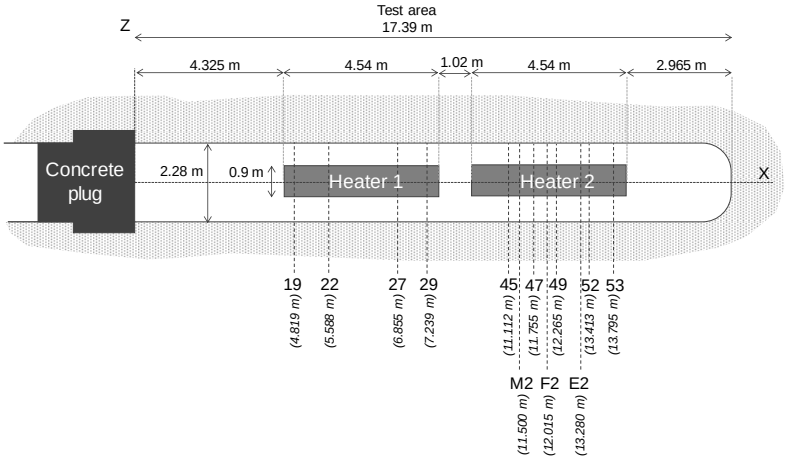

Figure 80 – General layout of the FEBEX in situ test for the 1st operation period, indicating the instrumented and sampled sections used by Samper et al. (2018). The x coordinates of the sections are referenced to the concrete plug on the left.

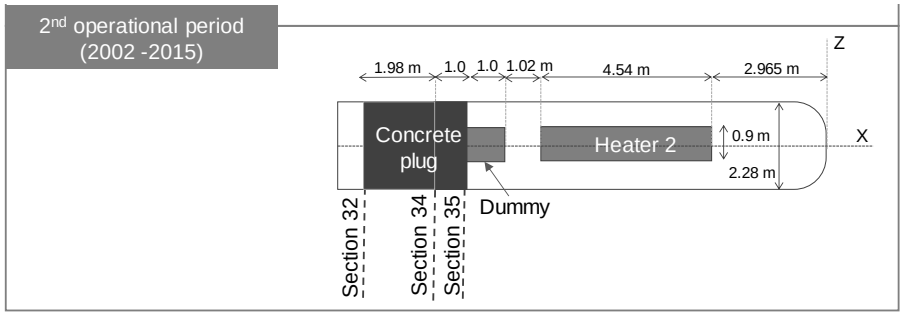

Figure 81 – General layout of the FEBEX in situ test for the 2nd operation period.

The clay barrier of the FEBEX in situ test was made of blocks of highly compacted bentonite, which were situated in vertical sections normal to the axis of the tunnel, with a diameter of 2.28 m (Figure 81). Weighted average values of initial dry density and gravimetric water content of bentonite blocks were 1.7 g/cm^3 and 14.4 wt.%, respectively (ENRESA, 2000).

The heaters, which were made of carbon steel, were placed inside a cylindrical carbon steel liner having a diameter of 0.93 m. The liner was surrounded by the clay barrier (ENRESA, 2000). The carbon steel used for the liner had the following composition: 99.04 wt.% Fe, 0.16 wt.% C, 0.30 wt.% Si, and 0.60 wt.% Mo.

Once the entire bentonite barrier of the FEBEX in situ test was fully dismantled, a comprehensive post-mortem bentonite sampling and analysis program was performed to characterize the solid and liquid phases, analyse the physical and chemical changes induced by the combined effect of heating and hydration and test THM and THC model predictions (Lanyon and Gaus, 2017; Fernández et al., 2018).

The available data used to compare the calculated results of the FEBEX in situ test were taken from Hadi et al. (2019). These authors studied experimentally the steel-iron interactions in the FEBEX in situ test and focused on the contact area between the corroding Fe source and compacted bentonite. Although the FEBEX in situ test was not specifically designed to study the steel corrosion and iron-bentonite interactions, post-mortem analyses at the end of the 1st period (2002) and especially after the 2nd period (2015) focused on this topic. According to Hadi et al. (2019) several steel components of the FEBEX in situ test retrieved after the 2nd operation period such as the liner, the heater, the dummy, the extensometers, the fissure meters, the drilling rods and the cable ducts showed clear corrosion features. The impact of corrosion and the Fe migration inside the bentonite could also be observed in some zones of the bentonite surrounding the corroded objects, appearing as concentric and coloured (red, orange, blue) halos (Figure C1 in Appendix C). Hadi et al. (2019) characterized the coloured interaction zones observed in two bentonite blocks, the newly formed Fe phases and the effect of corrosion on the

bentonite chemistry. These two blocks of the same section 41 were located between the two heaters during the first operation period of the experiment and after the dismantling of the heater 1 between the dummy and the heater 2.

According to Hadi et al. (2019), a coloured corrosion halo was observed in the bentonite buffer between the dummy and the second heater. This halo was asymmetric, and preferentially located on the upper left part of the liner, while the opposite side of the liner appeared almost unaffected by corrosion.

Goethite was the main newly formed Fe-bearing phase present in the red-orange zone observed in the bentonite (distance inferior to 50 mm from the steel-bentonite interface – thus only additional Fe^{3+}), while additional Fe^{2+} was found at a wider and Fe poorer blue zone in the bentonite (distance comprised between 50 to 120 mm from the steel-bentonite interface – without additional Fe^{3+}).

Hadi et al. (2019) proposed a conceptual model of Fe diffusion at the steel/bentonite interface where diffusion of Fe^{2+} occurs only when anaerobic corrosion starts occurring once O_2 is depleted at the surface of the steel and sufficient water saturation conditions are met. Diffusion thus proceeds in two stages. During the first stage, Fe^{2+} diffusion inside the bentonite competes with O_2 diffusion toward the interface and Fe is accumulated as Fe^{3+} oxi-hydroxides (mainly goethite) near the interface. As soon as O_2 is depleted inside the bentonite, Fe^{2+} diffuses into the bentonite. The understanding of the processes controlling Fe accumulation in the bentonite requires knowing the pre-existing Fe-bearing phases.

Measured data presented in Hadi et al. (2019) will be used to compare with the computed total Fe, goethite and hematite performed with the reactive transport model of the FEBEX in situ test. It is important to point out that there is an initial amount of Fe in the bentonite of approximately 0.49-0.50 mmol/g (see Figure C1 in in Appendix C).

2.4.2 Model description (data/conceptual-numerical model/computer code)

2.4.2.1 Reactive transport conceptual model

The stage 2 of the conceptual model of Fe diffusion at the steel/bentonite interface proposed by Hadi et al. (2019) was the starting point for the UDC reactive transport modelling of the interactions of corrosion products and bentonite in the FEBEX in situ test.

The main objectives of the reactive transport model of the FEBEX in situ test proposed by ENRESA(UDC) were: (1) the extension of the previous THCM model of the FEBEX in situ test of Samper et al. (2018) to account for redox processes, steel corrosion and the interactions of corrosion products and compacted FEBEX bentonite, (2) the testing of the conceptual geochemical model of steel corrosion in the FEBEX in situ test proposed by Hadi et al. (2019) and (3) the improvement of the numerical model of the interactions of steel/bentonite for the FEBEX in situ test and the identification of the remaining uncertainties.

The main thermo-hydrodynamic processes in the bentonite buffer of the FEBEX in situ model include: (1) advective and diffusive liquid flow and (2) heat transport (conduction).

The geochemical model accounts for aqueous complexation and acid-base reactions, mineral dissolution/precipitation, cation exchange of Ca^{2+}, Mg^{2+}, Na^{+} and K^{+} and surface complexation of H^{+} and Fe^{2+}, on three types of sorption sites (strong sites, $S^{s}OH$, weak #1 sites, $S^{w1}OH$ and weak #2 sites, $S^{w2}OH$) according to the triple-site sorption model of Bradbury and Baeyens (1997). The geochemical system was defined in terms of 12 primary species (H_2O, $O_2(aq)$, H^{+}, Cl^{-}, Ca^{2+}, Mg^{2+}, Na^{+}, K^{+}, SO_4^{2-}, HCO_3^{-}, $H_4SiO_4(aq)$ and Fe^{2+}), 34 secondary aqueous species identified from speciation runs performed with the thermodynamic database ThermoChimie (Giffaut et al., 2014) and 4 minerals (calcite, gypsum, quartz and goethite). The Gaines-Thomas convention will be used for cation exchange reactions (Appelo and Postma, 1993). The chemical reactions and their equilibrium constants at 25 ºC for secondary species and mineral dissolution/precipitation as well as the selectivity coefficients for exchanged cations and the protolysis constants for the triple-site model are listed in Table C1 in Appendix C

2.4.2.2 Reactive transport numerical model

The numerical model of the FEBEX in situ test was performed with a 1D row of triangular elements (Figure 82 and Figure 83) at the section 41, between the two heaters. The model domain only includes the bentonite barrier, which extends from r = 0.45 m to r = 1.14 m. The spatial discretization of the model has 272 nodes and 270 elements. The grid size is non uniform: Δx = 2 mm from 0.45 m < r < 0.5 m; Δx = 2.5 mm from 0.5 m < r < 0.6 m; Δx = 5 mm from 0.5 m < r < 0.75 m and Δx = 10 mm from 0.75 m < r < 1.14 m.

The simulation time horizon covers the entire duration of the in situ test from February 1997 to 2015 (18 years). The numerical model accounts for the heating stages and the cooling phases after switching off the heaters at the end of the two operation periods (heater 1 after 5 years of operation, 1st operational phase, and heater 2 after 18 years of operation, 2nd operational phase).

Bentonite has an initial porosity of 41%, a volumetric water content of 24.5 vol.%, which corresponds to a gravimetric water content of around 14.5 wt.%, a liquid saturation degree of 59% and a suction of $1.1 \cdot 10^5$ kPa. This gravimetric water content is very similar to the mean value reported by Fuentes-Cantillana and García-Siñeriz (1998). The initial temperature is uniform and equal to 12ºC. The thermal, hydrodynamic and transport parameters of the bentonite are listed in Table 12.

The water content and the temperature evolutions at the boundaries (r = 0.45 m and r =1.14 m) were taken from the previous model of Samper et al. (2018). Figure 84 and Figure 85 show the time function of the temperature and volumetric water content imposed at the boundaries, respectively. Temperature increases to 70 ºC and 40ºC at r = 0.45 m and r = 1.14 m, respectively; and then decreases when the heater 2 was switched off. The volumetric water content increases to become full saturated at r = 1.14 m and it increases slowly at r = 0.45 m.

The initial concentration of the FEBEX bentonite pore water at a gravimetric water content of 14 wt.% is taken from Fernández et al. (2001) while the composition of the granite groundwater is derived from experimental data (ENRESA, 2006a) as reported by Samper et al. (2008b) (see Table C2 in Appendix C). The concentration of the boundary water at r = 0.45 m is equal to the bentonite water and the granite groundwater was adopted as the boundary water at r = 1.14 m.

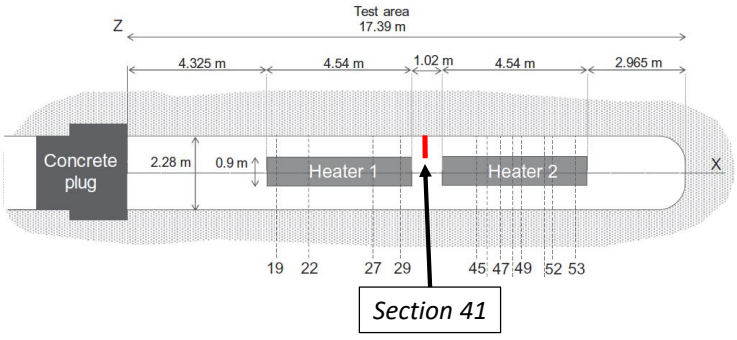

Figure 82 – General layout of the FEBEX in situ test for the 1st operation period, indicating the location in section 41 of the mesh used in the reactive transport model.

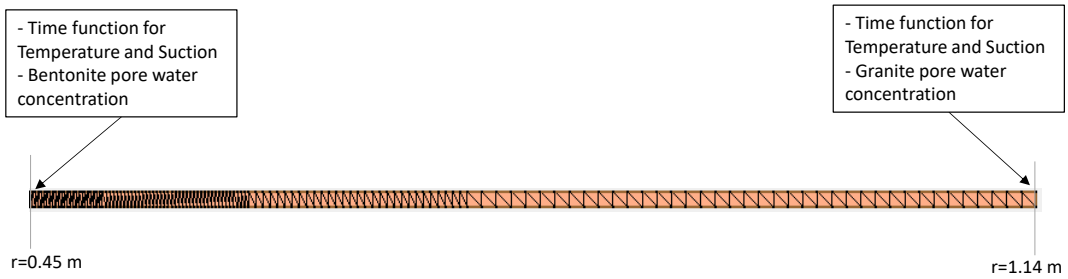

Figure 83 – Scheme of the mesh used in the reactive transport model and boundary conditions.

Table 12 – Thermal, hydrodynamic and transport parameters of the bentonite (Samper et al., 2018).

Parameter	Bentonite
Hydraulic conductivity (m/d)	$4.4 \cdot 10^{-9}$
Porosity	0.407
Retention curve relating water saturation degree, Sw, to suction, φ (kPa)	$S_w = \frac{1}{[1+(-510^{-5}\varphi)^{1.26}]^{0.21}}$
Solid density (kg/m^3)	2700
Specific heat of the solid (J/kg°K)	845.7
Thermal conductivity of the solid (W/m ºC)	1.15
Diffusion coefficient (m^2/s)	10^{-10}

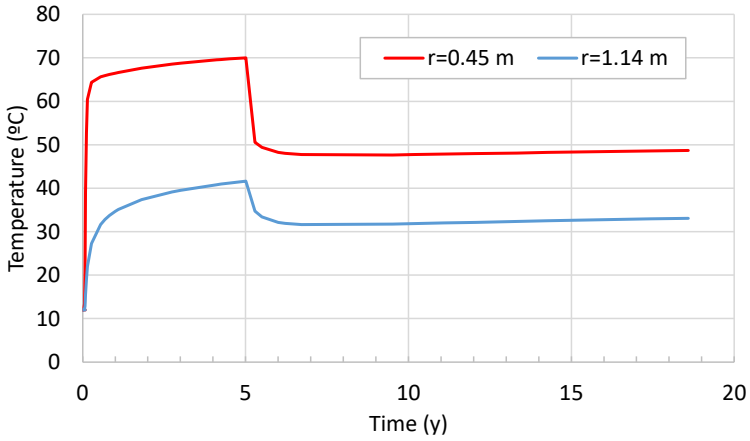

Figure 84 – Time function of the boundary temperature at r = 0.45 m and r = 1.14 m. (Samper et al., 2018).

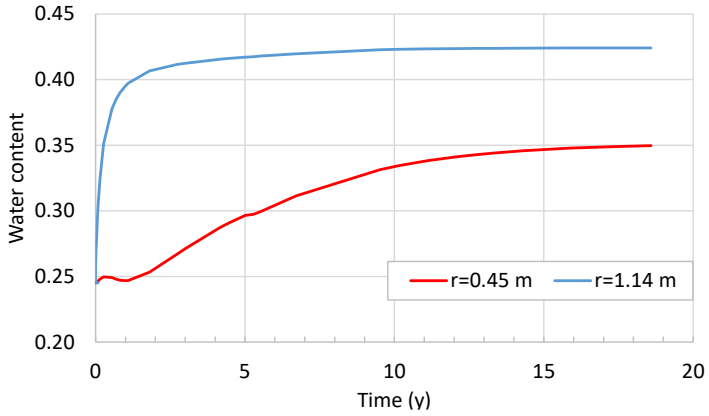

Figure 85 – Time function of the boundary volumetric water content at r = 0.45 m and r = 1.14 m. (Samper et al., 2018).

Due to the complexity of the aerobic corrosion and the lack of data of the aerobic phase, the first corrosion stage has been simplified. The corrosion has been simulated as a time function of an iron source, which increases until 2 years and then the dissolved iron decreases and remains uniform until 18 years (Figure 86). This iron source is equivalent to a large initial corrosion rate (2 µm/y) until 2 years and then, the corrosion rate decreases (Figure 87). The numerical model starts when the oxygen was depleted in the liner, and it was decreasing in the bentonite. The oxygen supply at the liner/bentonite interface was simulated with a time function shown in Figure 86.

As an educated guess, goethite is the only Fe mineral allowed to precipitate. Goethite precipitation is considered under kinetic conditions. The kinetic parameters were taken from Palandri and Kharaka (2004). The specific surface area of the goethite was calibrated (10^{-11} dm^2/L) to reproduce the measured goethite precipitation.

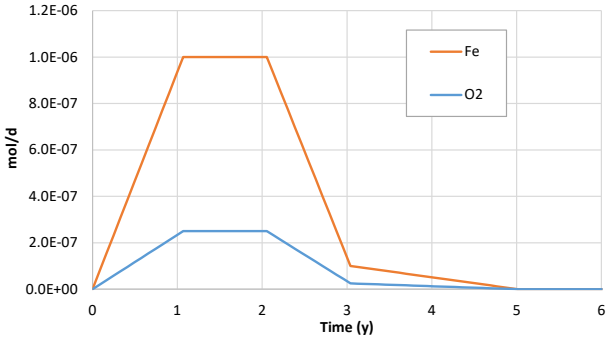

Figure 86 – Time function of the iron and oxygen source.

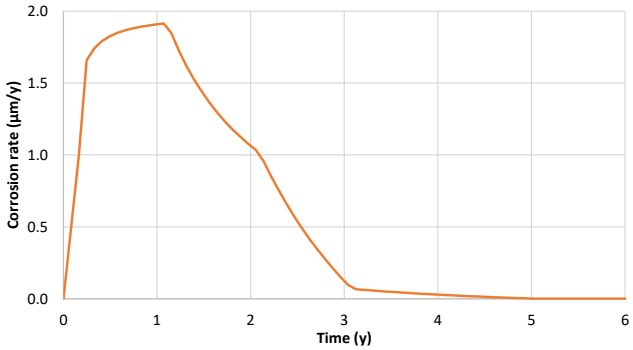

Figure 87 – Time function of the corrosion rate equivalent.

2.4.2.3 Computer code

The reactive transport model of the FEBEX in situ test were performed with the finite element reactive transport code CORE2D v5 (Zhang et al., 2008; Samper et al., 2009; Fernández, 2017; Águila et al., 2020) which relies on the thermodynamic database ThermoChimie v10.a (Giffaut et al, 2014). A short description of this code is presented in section 2.3.2.3.

2.4.3 Model results

2.4.3.1 Thermal and hydrodynamic results

The computed saturation degree and the temperature was compared with the measured data of the closed instrumented section H. The saturation increases with time, faster closer to the granite interface. The computed results reproduce the measured saturation evolution (see Figure C2 in Appendix C). The temperature increases while the heater 1 is working and it decreases when the heater 1 is switched off. The computed temperature fit the measured data (see Figure C3 in Appendix C).

2.4.3.2 Geochemical results

The computed dissolved Cl^- concentrations decrease in the bentonite near the granite boundary due to the hydration from the granite and the low Cl^- concentration of the granite water boundary (Figure 88). Oxygen concentration decreases while goethite precipitates (Figure 90).

Calcite precipitates in the bentonite near the liner (Figure C5 in Appendix C). Computed goethite precipitates 1 dm into the bentonite, especially in the first 0.25 dm near the liner (Figure 89). Computed goethite precipitation reproduces the trend of the measured data. The computed goethite is slightly larger than the measured data at the interface and slightly smaller than the measured data in the interval $20 < d < 50$ mm, where d is the distance from the interface.

The computed dissolved iron penetrates into the bentonite and it decreases slightly near the liner due to goethite precipitation (Figure 91). The computed pH decreases near the liner due to the goethite

precipitation (Figure 92). The computed Eh becomes reducing with time as the oxygen is being consumed and the anaerobic corrosion phase begins (see Figure C4 in Appendix C).

Figure 93 shows the time evolution of the dissolved iron and oxygen and goethite precipitation at *r* = 0.45 m and *r* = 0.5 m. The computed iron and oxygen follow the trend of the considered iron and oxygen source at the bentonite/liner interface. The computed goethite starts to precipitate when the iron and oxygen arrived, and goethite precipitation stops when the iron and oxygen sources decrease.

The computed exchanged concentrations and sorbed concentrations show alteration in the bentonite from *r* = 0.45 m to r = 0.7 m (Figure C7 and Figure C8 in Appendix C).The computed total iron (dissolved, exchanged, sorbed and dissolved/precipitated) reproduces well the measured data, although the computed iron is slightly smaller than the measured data in the interval 20 < *d* < 50 mm (Figure 94). The computed concentrations of exchanged and sorbed concentrations show changes in the bentonite in the interval 45 < *d* < 70 mm. The computed concentration of dissolved iron is smaller than the concentrations of exchanged and sorbed iron (Figure 95).

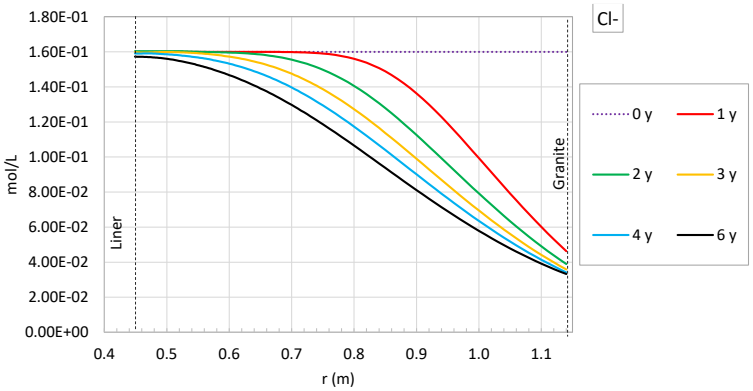

Figure 88 – Spatial evolution of the computed dissolved Cl^- at several times.

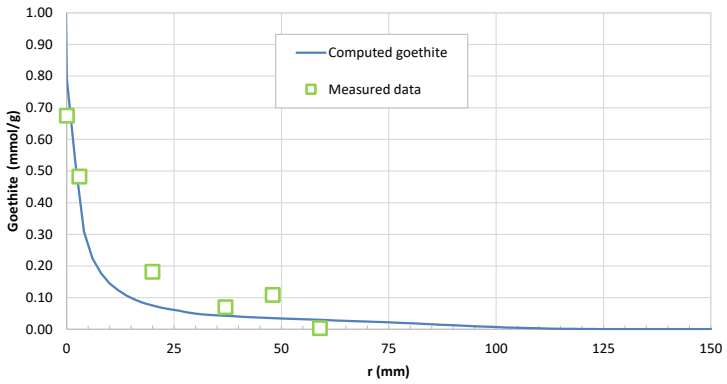

Figure 89 – Spatial distribution of the computed goethite at 6 years and measured data (symbols). Distance from the liner/bentonite interface.

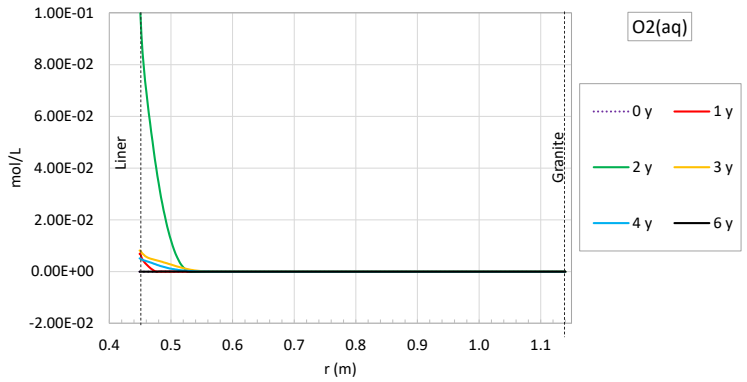

Figure 90 – Spatial evolution of the computed dissolved O_2(aq) at several times.

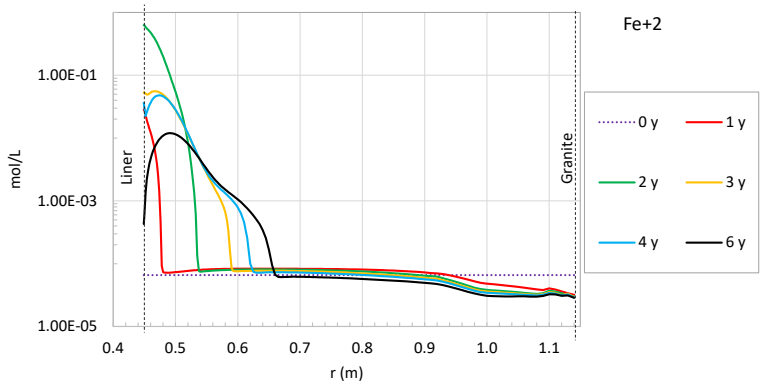

Figure 91 – Spatial evolution of the computed dissolved Fe^{2+} at several times.

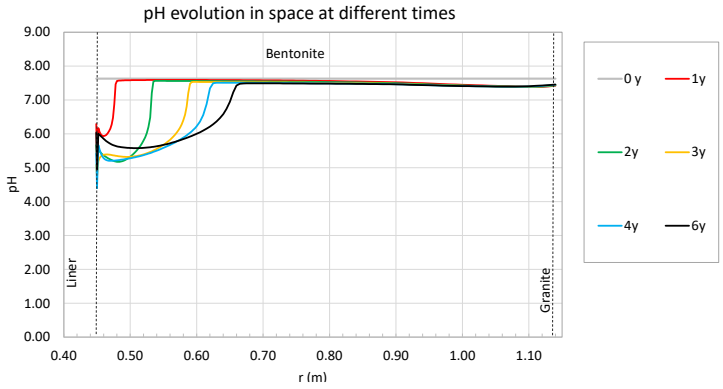

Figure 92 – Spatial evolution of the computed pH at several times.

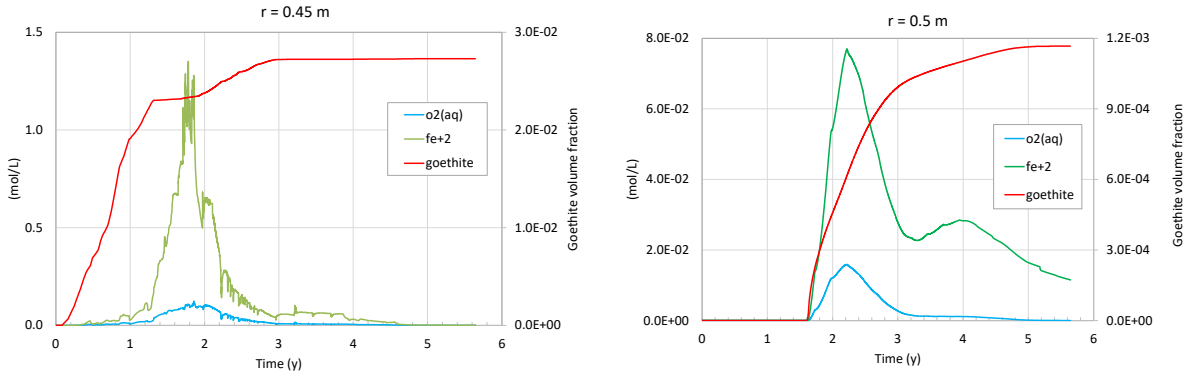

Figure 93 – Time evolution of the computed dissolved iron and oxygen (left axis) and goethite volume fraction (right axis) at r = 0.45 m and r = 0.5 m.

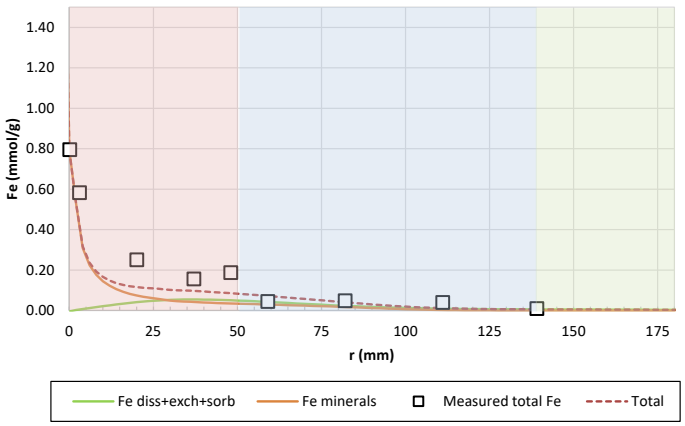

Figure 94 – Spatial distribution of the computed dissolved, exchanged and sorbed iron, iron minerals and total iron at 6 years and measured data (symbols). Distance from the liner/bentonite interface.

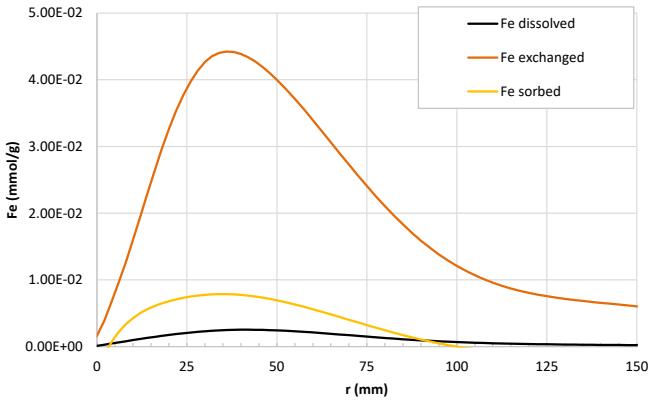

Figure 95 – Spatial distribution of the computed dissolved, exchanged and sorbed iron at 6 years. Distance from the liner/bentonite interface.

2.4.4 Conclusion

A reactive transport model of the geochemical interactions of compacted bentonite and Fe liner in the FEBEX in situ test has been presented. The model simplified the corrosion stage by considering a source of iron and oxygen to trigger goethite precipitation.

The main conclusions of the model of the FEBEX in situ test include: 1) goethite precipitates in the bentonite, mostly near the iron source (d < 50 mm), 2) the fronts of dissolved, exchanged and sorbed iron penetrate 150 mm into the bentonite, 3) pH and Eh decrease due to goethite precipitation and 4) model results reproduce goethite and total iron measured data.

The reactive transport model of the FEBEX in situ tests has uncertainties which could be overcome by accounting for: 1) more realistic corrosion model accounting an initial aerobic corrosion stage with a source of oxygen and the precipitation of Fe(III) oxides, hydroxides and oxyhydroxides and 2) other corrosion products such as magnetite, siderite, hematite, maghemite, lepidocrocite, akaganeite and Fe-phyllosilicates.

2.5 Corrosion model for FEBEX (by Uni.Bern)

2.5.1 Introduction

This section presents the steel-bentonite interaction model developed by University of Bern. The overall goal of this model development is to improve the modelling capabilities of complex coupled Fe corrosion and Fe-clay interactions within the numerical codes used already for reactive transport models within the context of safety assessment. Thus, it should contribute to the current efforts to develop

comprehensive reactive transport models (RTM) for clay barriers in the near field of HLW repository settings. In this respect, the FEBEX-in-situ test serves as an example setting. The experiment is described briefly in section 2.4.1. More details are provided in ENRESA (2000, 2006a).

The RTM provides a tool to decipher the major processes and controlling factors of Fe-bentonite interactions in the early transient phase from aerobic to anaerobic corrosion. An integral part of the model is the evaluation of the interaction of Fe(II) produced by the corrosion process with the bentonite during the transition from the initial oxic to anoxic conditions. This should improve the general understanding of steel/bentonite interactions observed within in situ experiments and support the conceptual process model proposed by Hadi et al. (2019a). The model builds on previous and current efforts in the development of a reactive transport model for clay barriers and their interaction with other material components. The powerful simulator PFLOTRAN (www.pflotran.org), an open source, massively parallelised subsurface flow and reactive transport code, is used for numerical implementation.

2.5.2 Conceptual model and simplification

The conceptual model accounts for the thermal, hydrological and chemical evolution in a cylindrical 1D axi-symmetric cross section of the FEBEX in situ test over a period of 18 years. It focusses on the zone between the two heaters, to assess the amount of corroded steel and Fe-bentonite interaction under a given temperature gradient. The simulated processes include the corrosion of the steel liner, the formation of corrosion products and Fe-bentonite interaction during the transition from aerobic to anaerobic conditions. It follows the phenomenological process model presented by Hadi et al. (2019a). The main processes and required simplifications can be summarized as follows.

- The rate of aerobic steel corrosion depends on the concentration of dissolved O_2 at the steel surface. The total O_2 inventory includes i) the O_2 initially entrapped in the porosity of the partly saturated bentonite and ii) O_2 entering the system along the steel liner over a certain time period at the start of the experiment. The latter is inferred from mass balance calculations (Wersin and Kober, 2017) and sensor measurements (Fernandez and Giraud, 2016), which indicate that a gas pathway, presumably between the heaters and the liner or along the sensor tubing, existed for some period of time. Other processes than corrosion, which may contribute to the oxygen consumption in an EBS are neglected.
- Once the O_2 concentration at the steel liner surface approaches zero, anaerobic corrosion sets in with an assumed constant rate.
- Corrosion products precipitate according to solubility constraints. In the presence of oxygen, goethite is considered as the main corrosion product. In the anaerobic corrosion phase, the evolution of dissolved Fe^{2+} concentrations in the corrosion layer is thought to be controlled by the rapid precipitation of the meta-stable precursor phase $Fe(OH)_2$ or of siderite, whereas magnetite is assumed to form only slowly as a transformation product.
- Hydrogen released during anaerobic corrosion is considered to be non-reactive.
- Neo-formation of hydrous Fe-rich secondary silicates are neglected.
- Transport of O_2(g) and other gases occurs by diffusion and advection of the bulk gas phase in the unsaturated bentonite. Solutes and dissolved gases can migrate in the pore water by diffusion or advection, with the latter induced by the saturation of the bentonite with the granitic groundwater from the outer side. The coupled hydration - transport behaviour in the gas and liquid phase requires a simplification of the inherent complexity of the bentonite porosity in the simulations. A constant, single total porosity assumption is made for the compacted bentonite and the same diffusion coefficient for all dissolved species is assumed.
- Fe(II) migrating in the bentonite can react with residual O_2 and precipitate as goethite. In the absence of O_2, Fe^{2+} may sorb via cation exchange or surface complexation on montmorillonite of the FEBEX bentonite.
- The process model of Hadi et al. (2019a) considers a potential e-transfer of Fe(II) sorbing on montmorillonite to structural Fe(III) in the montmorillonite. As shown in Chapter 3 this process

seems to be restricted to dispersed systems or direct interfaces. Thus, it is not included in the Base Case (BC) scenario but assessed separately in specific sensitivity cases (Appendix D).

- All aqueous reactions, exchange reactions, surface protonation/de-protonation and surface complexation reactions assume chemical equilibrium.

2.5.3 Numerical model

2.5.3.1 Spatial and temporal discretization

The model domain is a cylindrical 1D radial axi-symmetric grid, with 1 cell in the yz dimension and cells of variable size in the x dimension. Smaller cell sizes (0.5-10 mm) are selected for the interface regions, while cells of up to 1 m are selected for the granite. The corroding steel is implemented as a 1 mm thick porous boundary layer. The grid extends 20 m into the rock (Figure 96).

The standard simulation time covered the 18 years of the FEBEX in situ test. For some variant cases however, the simulation time was adjusted in order to simulate an equal period of the anaerobic corrosion phase.

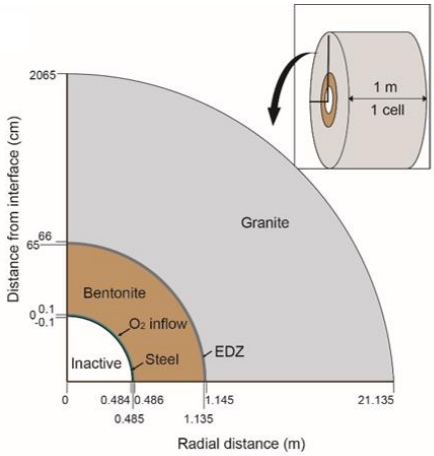

Figure 96 – Model domain of the FEBEX-in-situ model of UniBern.

2.5.3.2 Boundary Conditions

The left boundary of the 1-D system is placed 1 mm into the steel from the steel-bentonite interface (IF) and renders the remaining steel and inner part of the system inactive. It is defined as a no-flow and zero-gradient boundary. In the BC a constant temperature of 40°C was prescribed for the entire calculation time.

The right boundary is set 20 m into the rock. It is defined as Dirichlet type boundary with a granite pore water composition, a constant temperature of 12°C and a liquid pressure of 500 kPa.

2.5.3.3 Parameterization

The hydrodynamic and thermal parameterization of the bentonite and granite is listed in Table 13**.** The hydrodynamic and transport properties of the thin steel boundary layer are the same as those of the bentonite, whereas the thermal properties were set to those of steel (specific heat capacity of 502 J/(kg·°C), the thermal conductivity of 45 W/(°C·m) and the steel density of 7860 kg/m^3). The Excavation Damaged Zone (EDZ) is parameterized in an identical way as the granitic rock, with the exception of a maximum allowed desaturation of 10% instead of 1% in the host rock.

The effective diffusion coefficients in the water D_e^l and gas phase D_e^g are coupled to the saturation via a linear relationship (i.e., by multiplying the pore diffusion coefficients D_p^l and D_p^g with the volumetric content of the water and gas phase, respectively). A reduced ratio of D_p^g / D_p^l of 100 compared to the ratio of the self-diffusion coefficients was selected for the BC. This enables the D_e^g at high liquid

saturation to be more in line with values indicated by non-linear relationships such as of Millington (1959) or of Aachib et al. (2004) applied by De Windt et al. (2014).

Table 13 – *Hydrodynamic and thermal parameters of bentonite (B) and granite (G), based on (1) Enresa (2000); (2) Alonso et al. (2005); (3) Samper et al. (2018); (4) Kant et al. (2017)*

Parameter	**Bentonite**	**Granite**	**Ref.** (B / G)
Retention curve	$S_{el} = \left[1 + \left(\frac{s}{30.3MPa}\right)^{\frac{1}{1-0.32}}\right]^{-0.32}$ with $S_{el} = \frac{s_l - 0.1}{1-0.1}$	$S_{el} = \left[1 + \left(\frac{s}{0.01MPa}\right)^{\frac{1}{1-0.5}}\right]^{-0.5}$ with $S_{el} = \frac{s_l - 0.99}{1-0.99}$	1 / 2
Relative permeability functions	$k_{rl} = \sqrt{S_{el}}\left\{1 - \left(1 - {S_{el}}^{0.32}\right)^{3.125}\right\}^2$ $k_{rg} = \sqrt{1 - S_{eg}}\left\{1 - {S_{eg}}^{3.125}\right\}^{0.64}$ with $S_{eg} = 1 - \frac{s_l - 0.1}{1-0.1}$	$k_{rl} = \sqrt{S_{el}}\left\{1 - \left(1 - {S_{el}}^{0.5}\right)^2\right\}^2$ $k_{rg} = \sqrt{1 - S_{eg}}\left\{1 - {S_{eg}}^{2}\right\}^{1}$ with $S_{eg} = 1 - \frac{s_l - 0.99}{1-0.99}$	
Intrinsic permeability [m^2]	$1.0 \cdot 10^{-20}$	$8.0 \cdot 10^{-18}$	3
Porosity [-]	0.41	0.01	1 / 2
Thermal conductivity k_{dry} // k_{wet} [W/°C·m]	$\kappa = \kappa_{dry} + \sqrt{s_l}(\kappa_{sat} - \kappa_{dry})$		
	0.57 // 1.3	3.095 // 3.193	1 / 4
Specific heat capacity [J/kg·°C]	835	769	2 / 4
D_p^l [m^2/s]	$4.88 \cdot 10^{-11}$	$5.0 \cdot 10^{-10}$	3
D_p^g [m^2/s]	$4.88 \cdot 10^{-9}$	$5.0 \cdot 10^{-8}$	

The geochemical model accounts for 12 primary species (O_2(aq), H^+, Na^+, Ca^{2+}, Mg^{2+}, K^+, Cl^-, CO_3^{2-}, Fe^{2+}, SO_4^{2-}, H_4SiO_4, Al^{3+}), 60 secondary aqueous species and 4 gas species (O_2(g), CO_2(g), H_2(g) and $H_{2\_non\text{-}reactive}$(g)). $H_{2\_non\text{-}reactive}$(g) denotes the H_2 released during corrosion. The Andra/Thermochimie v.9b database was applied for all thermodynamic calculations (Giffaut et al., 2014; Grivé et al., 2015) utilizing the Lawrence Livermore National Laboratory (LLNL) parameterization of the extended Debye-Hückel aqueous activity model. All thermodynamic calculations take into account the temperature dependence of the equilibrium state, with the exception of some Fe-carbonate and chloride complexes, for which no enthalpy data are available. The geochemical model includes precipitation and dissolution reactions of 12 mineral phases as summarized in Table 14. Mineral reactions are formulated as kinetic reactions with the parameterization given in Table 15.

The O_2 entering the system adjacent to the steel boundary layer is implemented as a mineral reaction, in which a dissolving generic oxygen source fixes the O_2 concentrations in the liquid and gas phase in equilibrium with atmospheric pO_2. The time over which O_2 enters the system is thus controlled by the amount of the O_2 source mineral.

The aerobic corrosion of steel is represented as

$$Fe^0 + 0.5O_2(aq) + 2H^+ \rightarrow Fe^{2+} + H_2O \quad (3)$$

with a 1st order kinetic rate with respect to O_2(aq) and a rate constant of $2.75 \cdot 10^{-4}$ mol/m^2/s. This corresponds at an atmospheric partial pressure of O_2(g) and a temperature of 40°C to a corrosion rate of 13 µm/year. The Fe^{2+} released is subsequently oxidized and precipitated as goethite.

The anaerobic corrosion of steel is implemented as

$$Fe^0 + 2H^+ \rightarrow Fe^{2+} + H_2(aq)_{(non\text{-}reactive)} \quad (4)$$

with a constant corrosion rate of 2 µm/year. Fe^{2+} released by this process may react further and precipitate as a corrosion product or migrate into the bentonite. The overall corrosion rate is the sum of both corrosion reactions, but it should be noted that the Fe^{2+} released in the aerobic phase is immediately oxidized and precipitates as a ferric corrosion product.

Parameterization of cation exchange and surface complexation reactions are listed in Table 16. Note, that for the BC, the site capacity of edge sites accessible for Fe^{2+} is reduced to 20%, whereas all sites are available for protonation/deprotonation reactions. This is further discussed and assessed with sensitivity cases in section 2.5.5.3. Description and parametrization of the e-transfer reactions assessed in sensitivity cases are provided in the respective section.

*Table 14 – Equilibrium constants and reaction enthalpies applied in the reactive transport calculations, based on (1) Andra/Thermochimie v. 9.0b db, * increased following approach of Appelo et al. (1999), (2) Lee and Wilkin (2010).*

Mineral	Reaction	log K 25°C	ΔH (kJ/mol)	Ref.
Montmorillonite-HCCa	$Ca_{0.3}Mg_{0.6}Al_{1.4}Si_4O_{10}(OH)_2 : 4.45H_2O + 6H^+ + 4H_2O \leftrightarrow 0.3Ca^{2+} + 0.6Mg^{2+} + 1.4Al^{3+} + 4H_4SiO_4$	6.89	-163.896	1
Calcite	$CaCO_3 \leftrightarrow Ca^{2+} + CO_3^{2-}$	-8.48	-10.62	1
Gypsum	$CaSO_4 : 2H_2O \leftrightarrow Ca^{2+} + SO_4^{2-} + 2H_2O$	-4.61	-1.05	1
Anhydrite	$CaSO_4 \leftrightarrow Ca^{2+} + SO_4^{2-}$	-4.4	-17.94	1
Cristobalite	$SiO_2 + 2H_2O \leftrightarrow H_4SiO_4$	-3.16	16.5	1
Kaolinite	$Al_2(Si_2O_5)(OH)_4 + 6H^+ \leftrightarrow 2Al^{3+} + 4H_4SiO_4 + H_2O$	6.51	-169.718	1
Goethite	$FeOOH + 3H^+ \leftrightarrow Fe^{3+} + 2H_2O$	3.39	-61.522	1*
Hematite	$Fe_2O_3 + 6H^+ \leftrightarrow 2Fe^{3+} + 3H_2O$	1.02	-123.679	1
Magnetite	$Fe_3O_4 + 8H^+ \leftrightarrow 2Fe^{3+} + Fe^{2+} + 4H_2O$	10.41	-215.92	1
$Fe(OH)_2$(cr)	$Fe(OH)_2 + 2H^+ \leftrightarrow Fe^{2+} + 2H_2O$	12.76	-99.056	1
Siderite	$FeCO_3 \leftrightarrow Fe^{2+} + CO_3^{2-}$	-10.8	-12.012	1
Chukanovite	$Fe_2(OH)_2(CO_3) + 2H^+ \leftrightarrow 2Fe^{2+} + CO_3^{2-} + 2H_2O$	1.549	-	2

Table 15 – Mineral dissolution (d) and precipitation (p) kinetic data. If not indicated the same parameterization is used for both processes. Surfaces areas are indicated for steel (s), bentonite (b) and rock (r). Rates are based on (1) Marty et al. (2015), (2) Palandri and Kharaka (2004). LE: Local equilibrium approach for corrosion products considered to control dissolved Fe concentrations.

Mineral	surface area m^2/m^3 unless otherwise noted	Log*k* 25°C ($mol/m^2/s$)	Ea (kJ/mol)	Reaction order n^{H+} or n^{OH-}	Ref.
Montmorillonite-HCCa	8.5 m^2/g	-14.03	63		1
		-10.28	54	$n^{H+} = 0.69$	
		-11.54	61	$n^{OH-} = 0.34$	
Calcite	100 (s, b, r)	-0.30	14.4	$n^{H+} = 1.0$	2
		-5.81	23.5		
Gypsum	100 (s, b) / 1 (r)	-2.79	-		2
Anhydrite	100 (s, b) / 1 (r)	-3.19	14.3		2
Cristobalite	100 (s, b) / 1 (r)	-12.31 (d) -9.42 (p)	65 (d) 49.8 (p)		2
Kaolinite	1 (s, b, r)	-12.26 (p)	66 (p)		1 for (p)

Goethite	1000 (s) 100 (b) /1 (r)	-5 (d) -5 (p)	- (d) - (p)		(d) LE (p)
Magnetite	100 (s) / 1(r)	-17	18.6		Arbitrarily slow
$Fe(OH)_2(cr)$	100 (s, b) / 1 (r)	-5			LE
Siderite	100 (s, b) / 1 (r)	-8.68 (d) -5 (p)	56 (d) 108 (p)		1 (d) LE (p)
Chukanovite	100 (s, b) / 1 (r)	-8.68 (d) - 5 (p)	56 (d) 108 (p)		Same as siderite

Table 16 – Parameterization of site types, site capacities, protolysis constants and sorption parameters as considered in the Base Case.

Surface complexation reaction	**Log K**	**Reference**
$\equiv S^{s/w1}OH \leftrightarrow S^{s/w1}O^- + H^+(aq)$	-7.9	Bradbury and Baeyens (1997a)
$\equiv S^{s/w1}OH + H^+(aq) \leftrightarrow S^{s/w1}OH_2^+$	4.5	
$\equiv S^{w2}OH \leftrightarrow S^{w2}O^- + H^+(aq)$	-10.5	
$\equiv S^{w2}OH + H^+(aq) \leftrightarrow S^{w2}OH_2^+$	6.0	
$\equiv S^{s}OH + Fe^{2+} \leftrightarrow \equiv S^{s}OFe^+ + H^+$	1.9	Soltermann et al. (2014b) for Fe rich montmorillonite (SWy-2)
$\equiv S^{w1}OH + Fe^{2+} \leftrightarrow \equiv S^{w1}OFe^+ + H^+$	-1.7	
Cation exchange reaction	**Log $K_{sel\text{-}GT}$**	
$K^+ + NaX \leftrightarrow KX + 2\ Na^+$	0.86	Samper et al. (2018)
$Ca^{2+} + 2\ NaX \leftrightarrow CaX_2 + 2\ Na^+$	0.53	
$Mg^{2+} + 2\ NaX \leftrightarrow MgX_2 + 2\ Na^+$	0.64	
$Fe^{2+} + 2\ NaX \leftrightarrow FeX_2 + 2\ Na^+$	0.80	Soltermann et al. (2014b)
Site capacities	[mol/kg] / [eq/kg]	
$\equiv S^{s}OH$	1.84E-03 (for Fe: 3.68E-04)	Based on Bradbury and Baeyens (1997a) for montmorillonite; 20% accessibility for Fe^{2+} assumed in BC
$\equiv S^{w1}OH$	3.68E-02 (for Fe: 7.36E-04)	
$\equiv S^{w2}OH$	3.68E-02	
CEC	9.59E-01	Fernández et al. (2004)

2.5.3.4 Initial conditions

The initial composition of the FEBEX bentonite and granite pore waters, the considered mineral phases and the initial composition of the cation exchange are listed in Table 17. The initial composition of the pore water in the reactive steel is set identical to the FEBEX bentonite pore water. The initial temperature in both, the bentonite and granite, is uniform and set to 12°C. For the FEBEX bentonite, a dry density of 1600 kg/m³ is used, which corresponds to a total porosity of 0.41. The initial liquid saturation degree is set to 0.59, which equals a volumetric and gravimetric water content of 24.2 vol.% and 15.1 wt.%, respectively (Enresa, 2000).

Table 17 – Initial conditions of FEBEX and granite pore waters, mineralogy and sorption.

Parameter	**Unit**	**FEBEX**	**Granite**	**Reference**
Initial pore water composition				
pH		7.77	9.34	(Samper et al., 2018; Zheng et al., 2011); based on (Fernandez et al., 2001)) adjusted for
Na^+	[mol/kg_w]	1.3E-01	3.8E-04	
K^+	[mol/kg_w]	1.7E-03	7.8E-06	
Ca^{2+}	[mol/kg_w]	2.3E-02	1.8E-04	

Parameter	Unit	FEBEX	Granite	Reference
Mg^{2+}	[mol/kg$_w$]	2.3E-02	1.3E-06	equilibrium with calcite and gypsum at 12°C
Cl^-	[mol/kg$_w$]	1.6E-01	1.3E-05	
CO_3^{2-}	[mol/kg$_w$]	6.0E-04	3.9E-04	
SO_4^{2-}	[mol/kg$_w$]	3.02E-03	7.9E-05	
$Fe^{2+/3+}$	[mol/kg$_w$]	8.0E-11	1E-11	
Si^{4+}	[mol/kg$_w$]	5.1E-4	6.1E-4	Eq. with cristobalite
Al^{3+}	[mol/kg$_w$]	2.3E-10	1.9E-8	Eq. with montmorillonite (HHCa) (FEBEX) / kaolinite (Granite)
log pO_2	[bar]	-0.68	-56.3	
log pCO_2	[bar]	-3.5	-5.08	
Initial mineralogy				
Smectite	[wt.%]	92	0	Enresa (2000), Small amount of goethite to account for limited accessibility/surface area in FEBEX bentonite (Hadi et al., 2019a)
Calcite	[wt.%]	1	1	
Gypsum	[wt.%]	0.14	0	
Goethite	[wt.%]	0.003	0	
Cristobalite	[wt.%]	4	29	
Ion exchanger composition				
Total CEC	[meq/kg]	959		(Fernández et al., 2004)
Na^+	[meq/kg]	327		Calculated for modified pore water with selectivity coefficients of
Ca^{2+}	[meq/kg]	267		
Mg^{2+}	[meq/kg]	335		
K^+	[meq/kg]	31		
Surface site capacities				
$\equiv S^sOH$	[mol/kg]	1.84E-03 (for Fe: 3.68E-04)		Based on (Bradbury and Baeyens, 1997a) for montmorillonite; BC: 20% accessibility for Fe^{2+}
$\equiv S^{w1}OH$	[mol/kg]	3.68E-02 (for Fe: 7.36E-04)		
$\equiv S^{w2}OH$	[mol/kg]	3.68E-02		

2.5.3.5 Model calibration

The majority of the thermo-hydrological and transport parameters were adopted from previous modelling studies focussing on the thermo-hydro-mechanical evolution of the FEBEX in situ experiment. A comparison of various modelled and experimental data sets (e.g., saturation, temperature and solute concentrations) was already presented in the progress report of this project (Havlova et al., 2020).

The corrosion model for the BC was calibrated with the observed corrosion depth at the unheated liner areas of the experiment at the end of FEBEX I (5 years) and FEBEX II (18 years). Calibrated parameters include the aerobic corrosion rate and the required amount of O_2 entering the system that controls the duration of the aerobic corrosion phase.

2.5.3.6 Sensitivity analyses

Sensitivity analyses were performed with different sets of calculation cases targeting at the effect of experimental variability such as hydration and temperature (the latter shown in Appendix D), parameterization (i.e., the transport in the gas and liquid phase) and conceptualization (Fe^{2+} sorption models and Fe-montmorillonite redox interaction) (Table 18).

Table 18 – Summary of the sensitivity cases. The Base Case (BC) parameterization is included in each set for direct comparison.

Case	Sensitivity cases with respect to:	Parameter	Values
1A	**Effect of bentonite hydration** Vary the amount of the generic O_2 source: This changes the point in time when the O_2(g) inflow into the system stops and the system transforms into a closed system. This alters the hydration of the bentonite domain during the transition phase	Amount of O_2 added (M) // Time when O_2 source is depleted (y)	0 // 0
BC			7 // 5.6
1B			11 // 8.4
1C			15 // 11.1
BC	**Transport parameterization** Assessment of the influence of an increased pore diffusion coefficient in the gas phase (D_p^g and/or in the liquid phase (D_p^l))	D_p^g // D_p^l (m²/s)	5E-9 // 5E-11
2A			5E-8 // 5E-11
2B			5E-9 // 5E-10
2C			5E-8 // 5E-10
2D			5E-7 // 5E-10
BC	**Sorption and e-transfer**	Edge site capacity accessible for Fe^{2+}// e^- transfer reaction	20% // -
3A	Sorption capacity for Fe(II) of edge sites		80% // -
3B	Uptake of Fe(II) due to the interaction with structural Fe(III): Implementation as an additional sorption complex according to results from section III: $\equiv S^{Str\_Fe(III)}OH + Fe^{2+} \leftrightarrow \equiv S^{str\_Fe(II)}OFe^{+} + H^{+}$ with logK -3.1	$\equiv S^{Str\_Fe(III)}OH$ (mol/$kg_{bentonite}$)	0.37 in entire bentonite domain
3C			0.37 in 1st bentonite cell only (1mm)
3D	Redox dependent e^- transfer according to concept of Muurinen et al. (2014a): pH dependent sorption of Fe(II) at edge sites, transfer of e^- from sorbed Fe(II) to structural Fe(III) depending on redox conditions according to Fe_str(III) +e- ↔ Fe_str(II)	$\equiv S^{Str\_Fe(III)} + e^- \leftrightarrow \equiv S^{str\_Fe(II)}$	LogK=-2
4	Temperature: presented in Appendix D		

2.5.4 Results for Base Case

2.5.4.1 Corrosion rates / corrosion products

Figure 97 visualizes the computed evolution of the corrosion rate and cumulative corrosion depth in the BC. The BC considers an O_2 influx during FEBEX I that allows for an average aerobic corrosion rate of 15 µm/year, by this approximating the cumulative corrosion depth of 50-100 µm reported by Wersin and Kober (2017) for FEBEX I. Upon the stop of the O_2 influx, the aerobic corrosion rates are calculated to slow down over a time period of around 2 years, until the corrosion takes place under completely anaerobic conditions at t=7.3 years. With the anaerobic corrosion rate of 2 µm/year a final corrosion depth of ~100 µm is calculated, which is at the lower end of the corrosion depth observed at the liner position after dismantling FEBEX II (Wersin and Kober, 2017). Note that without any additional O_2 inflow, the aerobic corrosion rate would slow down over ~5 years. The final maximum corrosion depth after 18 years would be ~50 µm only, half of which is attributed to the anaerobic corrosion phase (not shown).

In the aerobic corrosion phase, all Fe corroded is calculated to precipitate as goethite within the corrosion boundary layer (Figure 97b). The subsequent anaerobic corrosion phase is dominated by the precipitation of $Fe(OH)_2$ and the formation of magnetite involving the gradual re-dissolution of goethite. In the first year, the precipitation of siderite consumes ~10% of the Fe(II) released by corrosion. After that, siderite re-dissolves and is replaced by calcite, rendering it negligible in the final calculated corrosion product assemblage (Figure 97c). Chukanovite remained undersaturated, but calculations indicate that the pore water in the corrosion layer is oversaturated with respect to the Fe-rich silicate minerals (Fe(III)-bertherine, chamosite, cronstedite, greenalite) and green rust phases, which were not considered as potential corrosion products in the BC. The final corrosion product assemblage in the

boundary layer after ~7 years of aerobic and 11 years of anaerobic corrosion, is dominated by goethite, in line with the experimental observations (Hadi et al., 2019a; Wersin and Kober, 2017), whereas the anaerobic corrosion products account for ~1/4 of the corroded Fe (Figure 97c*).*

2.5.4.2 Iron – bentonite interaction

The migration of Fe(II) from the corrosion boundary layer into the bentonite is limited to the anaerobic corrosion phase. In the early anaerobic phase up to 30% of the Fe(II) released from anaerobic corrosion migrates into the bentonite. After 2.5 years however, this fraction decreases to less than 10% (Figure 97b). This evolution reflects the different phases of the Fe-bentonite interaction, which are visualized in Figure 97d-f for three distances to the steel boundary layer, in the 1st bentonite interface cell (1 mm), in 5 mm distance and in 9 mm distance. The initial Fe front evolving into the bentonite meets remaining O_2, which leads to the rapid precipitation of this Fe as goethite. By this a high gradient of Fe(II) concentrations from steel to bentonite is maintained initially, which triggers the diffusive flux of Fe(II) in the bentonite. In a second stage, the precipitation of goethite becomes limited by the O_2 flux towards the Fe(II) front and Fe(II) starts to sorb in notable amounts. These two stages, the precipitation of Fe as goethite and the saturation of the sorption sites, occur in principle in each cell reached by the Fe front. With ongoing time and distance to the interface however, the O_2 encountered by the Fe front becomes less, due to the continuous diffusion of O_2 towards the Fe front. In the BC, this leads to the situation that at 9 mm distance, the O_2 concentrations just ahead of the Fe front are depleted to a degree that renders the precipitation of goethite negligible. Note that the calculations indicate that O_2 concentrations decrease with time in the entire bentonite, but reach post-oxic conditions (< 1.10^{-6} mol/L) only in a limited area close to the steel interface (Figure 97e). This is broadly in line with measurements in the water and gas phase of the pipes during the FEBEX test (Fernandez and Giraud, 2016), although uncertainties remained, to which degree the observed O_2 levels were affected by artefacts during sampling. With distance to the interface, not only the precipitation of goethite decreases, but also the accumulation rate of Fe(II) by sorption changes. It occurs at a lower rate and over longer times, due to the dilution of Fe concentrations by the diffusive gradients, the radial geometry and the advective flux of the saturation front.

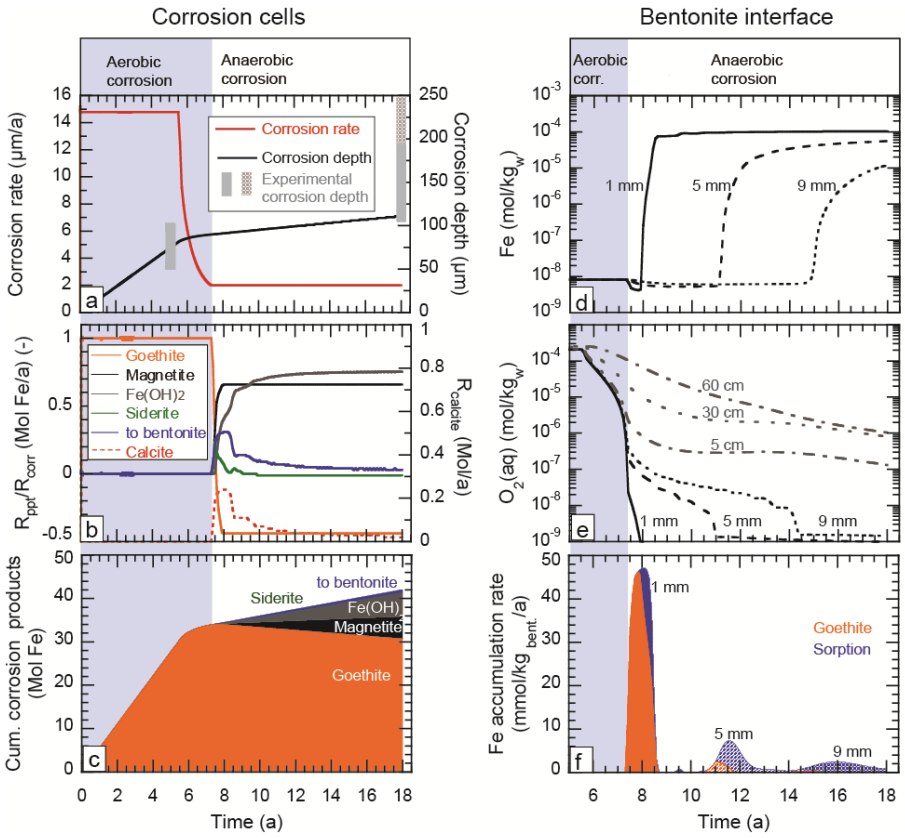

Figure 97 - Evolution in the corrosion layer (left panel) and in the bentonite (right panel) as calculated in the Base Case of (a) corrosion rates and cumulated corrosion depth, (b) the formation of corrosion products normalized to the corroded Fe and (c) as cumulated amount in the model domain. The right panel follows the evolution of (d) the Fe concentrations, (e) O_2 concentrations and (f) the evolution of the Fe accumulation rate at three different distances to the steel boundary layer over time. Note that in the right panel, the early aerobic corrosion phase is truncated for a better resolution of the anaerobic phase.

Figure 98 depicts the Fe front in the bentonite as calculated for the final time of 18 years, thus representing 10.7 years of anaerobic corrosion. It shows a concave shape of the Fe accumulation front, in line with the characteristic profile shape observed in the FEBEX in-situ experiment (Hadi et al., 2019a; Wersin and Kober, 2017)) and in the Alternative Buffer Experiments (ABM) in Aspö (Wersin et al., 2021). In both, model and experimental observations, the high accumulation of Fe at the interface is dominated by goethite, whereas sorbed Fe dominates further in the bentonite. These different interaction processes were suggested to be responsible for the characteristic-coloured halo formation observed in the FEBEX in situ experiment (Figure 98, top photograph).

In the BC calculations, sorbed Fe(II) (~8 mmol/kg bentonite) is clearly dominated by surface complexes at edge sites, despite the assumption of a reduced accessibility of these sites for Fe. Cation exchange accounts for <1 mmol Fe/kg of bentonite accumulation, which corresponds to a share of <0.2% of the CEC by Fe(II). This can be explained by the high concentrations of other divalent cations (Ca^{2+}, Mg^{2+}) in the FEBEX pore water supressing the retention of Fe(II) on the exchanger. Note that in the BC Fe sorption and e- transfer due to the presence of structural Fe(III) in montmorillonite are not taken into account given the results of the Fe(II) diffusion experiment (Chapter 3), but are assessed in a set of sensitivity cases in section 2.5.5.3.

The above evaluation of the BC results demonstrates that the model qualitatively reproduces the two most characteristic features of the Fe-bentonite interaction observed in in situ experiments: the concave shape of the Fe accumulation front and the distinct zonation. It reveals however a deviation to the profile reported by Hadi et al. (2019a) for a zone of extreme interaction with respect to i) the size of the Fe interaction zone, which was almost 10 times larger than calculated in the BC and ii) the extent of sorption within the zone of goethite precipitation (only detected in direct vicinity to the steel).

The following sensitivity analyses aim at an increased understanding of the underlying processes and factors controlling the zonation described above for the Base Case both from the perspective of the experimental conditions and of the model parameterization.

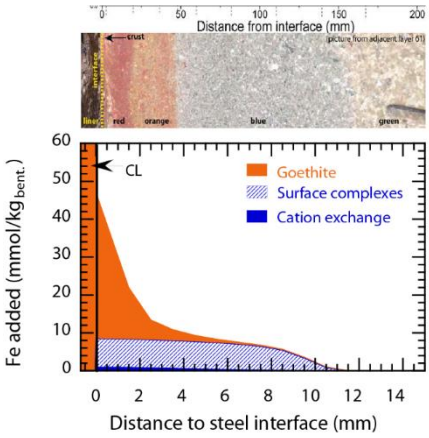

Figure 98 - Final profile of Fe accumulation in the bentonite as calculated for the Base Case. Top photograph with scale from Hadi et al. (2019) showing the visual colour zonation in the sample with extreme Fe-bentonite interaction.

2.5.5 Sensitivity cases

2.5.5.1 Bentonite hydration

A major uncertainty in the interpretation of corrosion features and Fe-bentonite interaction zones in the FEBEX in situ experiment is associated with the unknown history of O_2 availability as well as the heterogeneity in the saturation history of the experiment (Villar et al., 2016). The investigation of the final saturation state of the FEBEX in situ experiment revealed a significant variation of the hydration in the area between the two heaters. While some parts were rather dry (forgotten plastic sheet, Villar et al. (2016)), others gave indication of a rapid saturation due to some elevated water inflow. In this set of sensitivity cases, the effect of the bentonite hydration is evaluated. This is realized by shifting the onset of the closed system behaviour to different points in time, namely to year 0, 8.4 and 11.1 in Sensitivity Cases 1A, 1B and 1C, respectively (BC: year 5.6) (Table 18). The transition to the anaerobic corrosion phase is then calculated for year 4.8, 9.5 and 11.6 in 1A, 1B and 1C respectively (BC: year 7.3). Figure 99a presents the hydration stage of the FEBEX bentonite buffer calculated for these latter times. While in case 1A the hydration front just reached the centre of the bentonite domain, a saturation of more than 90% over the entire bentonite thickness is calculated for case 1C. For an evaluation of the effect of hydration on the evolution of the Fe-bentonite interaction, for each case the situation after an equal time of anaerobic corrosion is compared in Figure 99b-e. The following main observations are made:

- With a higher degree of saturation at the time when the O_2 inflow stops, the transition time towards an anaerobic corrosion becomes shorter.
- The O_2(aq) concentrations in the bentonite pore water well ahead of the Fe front differ by four orders of magnitude, with higher remaining O_2 concentrations calculated for the cases characterized by a higher hydration in the transition phase (Figure 99b).
- A higher saturation increases the amount of goethite precipitation in the bentonite, both in terms of the maximum accumulation as well as in terms of the extent of the precipitation front (Figure 99c).

  The Fe sorption front becomes shorter with higher hydration at the time of redox transition (Figure 99d). If we divide the profile in terms of the dominating Fe accumulation mechanism, the calculation cases indicate that a low hydration at the transition to anaerobic corrosion increases the total interaction zone and promotes the formation of a sorption dominated zone (blue halo) ahead of the precipitation front (orange halo) (Figure 99e). Vice versa, a high

saturation at the transition phase supresses the formation of the sorption-dominated zone, favouring precipitation of goethite throughout the interaction zone.

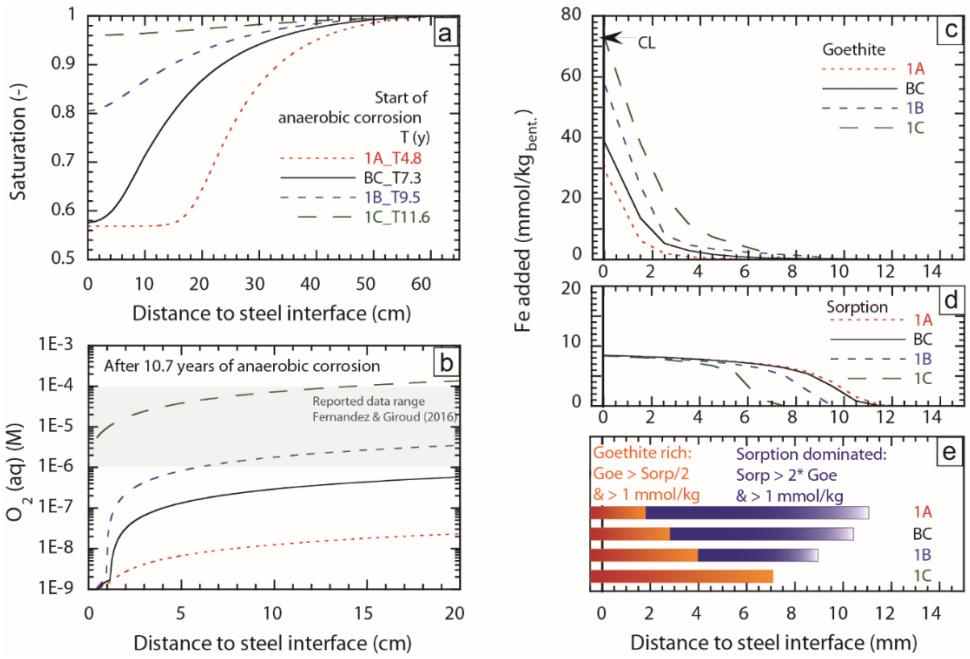

Figure 99 - Results for the Sensitivity Cases with respect to hydration: (a) hydration front at the transition to anaerobic corrosion, (b) aqueous O_2 concentration profile (c) goethite accumulation front and (d) Fe sorption front calculated for the bentonite after equal time of anaerobic corrosion, (e) visualization of the different zones of Fe accumulation based on a generic definition.

These observations point to the importance of the unsaturated porosity fraction in the entire bentonite on the Fe-bentonite interaction. The gas phase provides a fast pathway for O_2(g) towards the point of O_2 consumption, namely the steel layer itself in the aerobic corrosion phase and the zone next to the Fe migration front in the anaerobic corrosion phase. In these conditions, the pore water in contact with the gas phase becomes rapidly depleted in O_2(aq), which limits the precipitation of Fe(III) minerals in the later phases. If a high saturation suppresses the fast transport of O_2 in the gas phase, O_2 remains entrapped in the pore water and its transport to the interface is controlled by the comparably slower diffusion in the aqueous phase. In this scenario, the progressing Fe front is retarded by the ongoing precipitation by the in-diffusion of O_2.

2.5.5.2 Transport parametrization

The sensitivity calculations with respect to the hydration state already highlighted the importance of transport in the gas phase for the extent and pattern of the Fe-bentonite interaction. In this set of sensitivity calculations, the effect of transport in the gas and liquid phase is examined from the perspective of the model uncertainty. A focus is set on the effect of an increased diffusivity. Figure 100a illustrates the D_e in the liquid and gas phase as a function of the saturation as applied in the Base Case and the different sensitivity cases. For the sensitivity cases either the $D_e(g)$ (2A), $D_e(l)$ (2B) or both (2C, 2D) were increased by one order of magnitude (exception: 2D: D_e (g) x 100). Based on the O_2(aq) and Fe profiles calculated for the final time of 18 years (11 +-0.3 years of anaerobic corrosion) (Figure 100b-e) the effect of transport parameterization on the Fe-bentonite interaction can be summarized as follows.

An increased diffusivity in the gas phase, in combination with a large fraction of unsaturated porosity in the transition phase leads to:

- an effective removal of O_2 from the bentonite pore water far beyond the interface region.
- inhibition of the precipitation of goethite in the bentonite, as the O_2 is rapidly transported to the steel interface, where it prolongs the aerobic corrosion phase. Thus, the total amount of aerobic corrosion products is increased, but spatially restricted to the corrosion layer itself.

- sorption being the dominant Fe accumulation process in the bentonite. The effect on the extent of the sorption front is however small.

An increased diffusivity for solutes by a factor of 10 leads to

- a reduction of the final O_2 concentrations in the pore water, but to a lesser extent than observed for the cases with increased gas diffusion coefficients.
- a slightly larger goethite accumulation zone, while flattening the concave shape of the precipitation profile (only, if $D_e(g)$ is not increased simultaneously).
- an increase of the Fe bentonite interaction zone to 35 mm, thus by a factor of ~3.

Thus, the variation of the $D_e(g)$ mainly affects the accumulation of goethite in the bentonite. The effect on the overall interaction zone is less than ±5 mm, even when taking the results of the sensitivity cases with respect to the hydration into account. Higher $D_e(l)$ values of around 1-2×10 $^{-10}$ m^2/s, which is rather at the upper end of $D_e(l)$ reported for dry densities of 1600 kg/m^3 (Kiczka et al., 2022b), increase the overall interaction zone, mainly due to the progression of the sorption front. The calculated extent of 35 mm is however still far below the extreme profile reported by Hadi et al. (2019a). This suggests that an additional Fe transport process may have been present in the experiment, which is not captured by the model applied here. One hypothesis is that an additional advective flow from the steel into the bentonite might have been present over a certain time, due to vapour convection cells induced by the heating blocks. Note that the inclusion of surface diffusion of Fe(II) associated with cation exchange reactions would not alter the calculated profiles significantly, given the negligible fraction of Fe(II) calculated to be associated with cation exchange.

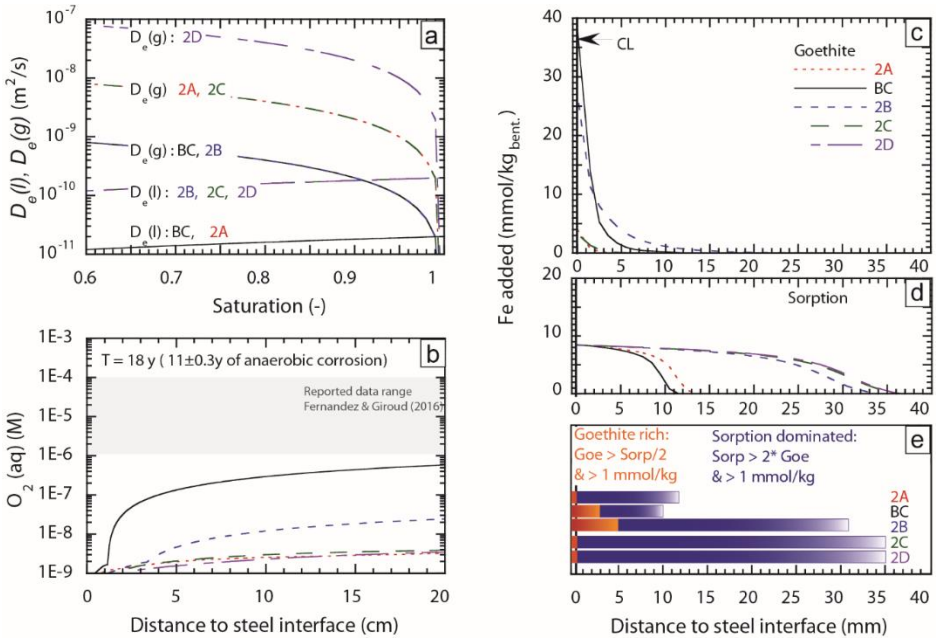

Figure 100 - Sensitivity cases regarding transport parameterization. (a): D_e in gas ($D_e(g)$) and water ($D_e(l)$ as a function of the bentonite saturation as applied in the Base Case and sensitivity cases 2A to 2D. (b) aqueous O_2 concentration profile (c) goethite accumulation front and (d) Fe sorption front calculated for the bentonite after 18 years, covering ~11 years of anaerobic corrosion, (e) visualization of the different zones of Fe accumulation based on a generic definition.

2.5.5.3 Sorption capacity / electron transfer

In the BC, the sorption and interaction of Fe with the montmorillonite fraction of the bentonite is constrained by cation exchange and by the formation of Fe surface complexes at S^s and S^{w1} edge sites. While the full cation exchange capacity is included, the accessibility of the edge sites for Fe is limited to 20% of the full site capacity. The latter limitation accounts for sorption competition with trace metals,

presumably present in the FEBEX pore water, which are however not included in the model. Though, the quantification of the effect of sorption competition is however a rather arbitrary choice. In Sensitivity Case 3A we therefore tested the effect of an increased accessibility of 80% of the edge sites.

In the second group of sensitivity cases the effect of electron transfer to structural Fe(III) is investigated. As outlined in detail in Chapter 3, batch experiments indicated that the transfer of an e^- of Fe(II) to the structural Fe(III) in montmorillonite provides an additional sorption/precipitation process for Fe(II). For the batch experiments, this additional sequestration process could be described for a large range of pH conditions and Fe concentrations by the inclusion of an additional pH dependent sorption reaction according to

$$\equiv S^{Str\_Fe(III)}OH + Fe^{2+} \leftrightarrow \equiv S^{str\_Fe(II)}OFe^{+} + H^{+} \quad (5)$$

with a logK of -3.1.

The Fe(II) diffusion experiment on the other hand indicated that in compacted systems, this process only occurs at the direct interface regions (~0.8 mm), although the reason for this is not yet fully understood. Thus, two sensitivity cases are evaluated: the inclusion of the additional Fe(II)-$S^{Str\_Fe(III)}$ interaction in the entire bentonite domain (Sensitivity Case 3B) and the restriction of this interaction to the first mm of the bentonite only (Sensitivity Case 3C).

Muurinen et al. (2014a) proposed an alternative model for the redox interaction of Fe(II) and structural Fe(III) in smectites based on the modelling of a large set of experiments performed at lower Fe concentrations than the experiments reported in Chapter 3. Their process involves 1) the specific pH dependent sorption of Fe(II) at the edge sites, 2) the redox dependent e-transfer from the sorbed Fe(II) to the structural reactive Fe(III), 3) specific pH dependent desorption of Fe(III) and 4) Fe-hydroxide precipitation. In Sensitivity Case 3D, we evaluated how this surface oxidation may affect the sorption front and how much of the sorbing Fe would be predicted to transfer an electron to the structural Fe(III). To this end, a sorption reaction at the S^s and the S^{w1} was included, which accounts for both the pH dependent complex formation and the redox-dependent electron transfer reaction according to

$$\equiv S^{Str\_Fe(III)} + e^- \leftrightarrow \equiv S^{strFe(II)} \quad (6)$$

with logK = -2 , as proposed by Muurinen et al. (2014a). Note that the Fe sorption model proposed by Soltermann et al. (2014b) also includes redox-dependent sorption complexes of Fe^{2+} on the S^s and S^{w1} sites. These describe an increased sorption of Fe^{2+} with increasing Eh, accounting for sorption of Fe^{3+}. With this model, an almost complete saturation of the edge sorption sites is calculated for aerobic conditions and neutral pH despite low total dissolved Fe concentrations. This renders the model inappropriate for reactive transport calculations dealing with aerobic conditions at the first hand and treating sorption as an equilibrium process.

Figure 101 shows how the alternative sorption models affect the calculated Fe-bentonite interaction pattern. Generally, the effect is rather limited to the direct Fe-bentonite interaction zone. Parameters such as the O_2 evolution in greater distance are not sensitive to these processes (not shown). Some common observations are made for those calculation cases, which include an increased retention sorption capacity, either by the increased accessibility of the $S^{s/w}$ sites (Case 3A) or by an additional retention process (Cases 3B, 3C).

- The fraction of Fe migrating from the corrosion layer into the bentonite increases. This is due to the prolonged time characterized by high gradient at the interface, during the saturation of the sorption sites (Figure 101a). When the Fe front evolves further into the bentonite, this effect diminishes.
- The Fe concentrations in the pore water within the evolving sorption front decrease by up to one order of magnitude (Figure 101b).
- The goethite accumulation profile steepens and shortens, due to the retarded migration of Fe into the bentonite. This allows for a larger fraction of the O_2 to diffuse closer to the steel surface (Figure 101c).

- The total amount of Fe accumulation close to the interface increases significantly due to the increased Fe sorption, whereas the overall Fe accumulation zone shortens significantly. Depending on the sorption capacity and mechanism, Fe sorption/Fe-redox interaction may even become dominant over Fe(III) precipitation within the entire bentonite interaction zone (Figure 101d,e*).*

The maximum amount of Fe sorption in Sensitivity Case 3A, reaches 30 mmol/kg$_{bentonite}$, 4 times more than the 7-8 mmol in the BC as expected for the increased site accessibility from 20 to 80%. With the inclusion of additional sorption/retention process linked to the structural Fe(III) (3B, 3C), the amount of sorbed Fe would increase to 150 mmol/kg$_{bentonite}$, of which the interaction with the structural Fe would account for 140 mmol/kg. Note, that this high value is due to the rather high pH of ~8.5 calculated for the interface region. Given the structural Fe(III) content of the FEBEX bentonite of 370 mmol/kg, and considering a 100% redox-transfer this would translate to a reduction of 38% of the structural Fe. However, the comparison with the experimentally determined Fe sorption within the FEBEX in- situ experiment clearly indicates that this process - which was calibrated to batch experiments - cannot be simply applied to the compacted in situ situation. The maximum amount of Fe(II) accumulation determined by Hadi et al. (2019a) for the direct interface (<0.1mm) was less than 80 mmol/kg and 50 to 60 mmol/kg in a localized zone of increased sorption further into the bentonite. In between they detected only negligible Fe(II) accumulation of 0-10 mmol/kg, similar to the observations reported in Wersin and Kober (2017) for citric acid extracts which indicate <4 mmol sorbed Fe/kg$_{bentonite}$. It should be pointed out that these measurements only indicate a net accumulation of Fe(II) but did not allow for a distinction between Fe(II) sorption with and without electron transfer. Hence, an increased uptake due to the interaction with the structural Fe(III) in montmorillonite may locally occur. But the comparison of model results and experimental data rather point to a limited accessibility of sorption sites and a suppression of the additional Fe retention by the redox-interaction, in line with the results presented in Chapter 3 for the compacted system.

Sensitivity Case 3D does not involve a change in the overall retention capacity, which is reflected in the almost identical Fe accumulation front calculated for the Sensitivity and Base Case. 10-20% of the sorbing Fe are calculated to transfer an electron to the structural Fe(III), based on the underlying redox dependency of Muurinen et al. (2014a), this would correspond to only a minor fraction of less than 1% of the overall structural Fe in the FEBEX bentonite.

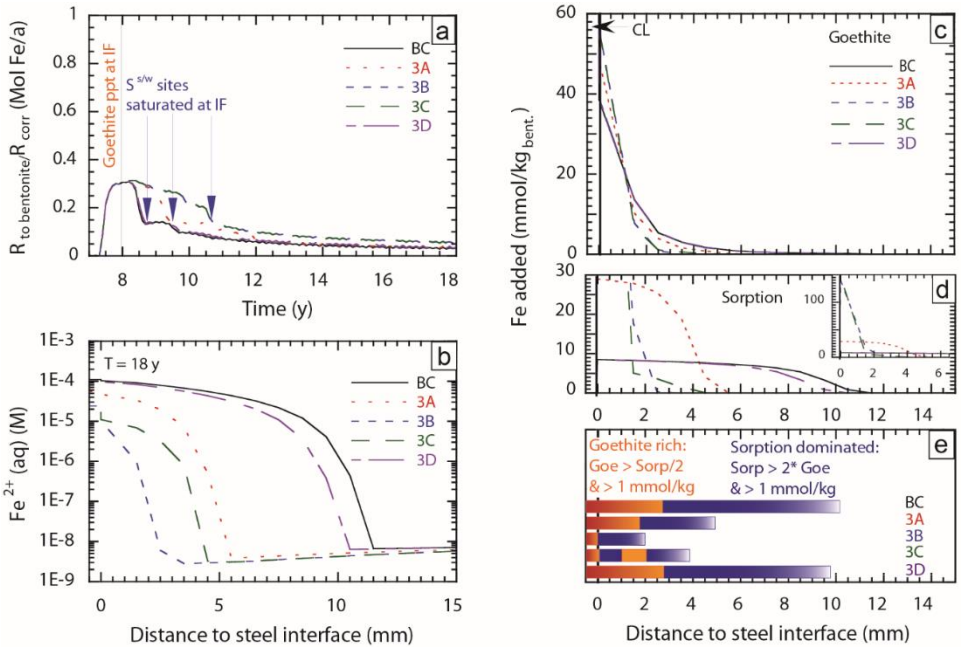

Figure 101 - Sensitivity cases with respect to sorption and e- transfer as described in the text and summarized in Table 18. (a) Fraction of Fe migrating into the bentonite relative to the corroded Fe over time, the initial phase is characterized by goethite precipitation (ppt) in the first bentonite cell, (b) dissolved

Fe concentration profiles (c) goethite and (d) sorption accumulation profile after 18 years (10.7 years of anaerobic corrosion, (e) visualization of the different zones of Fe accumulation based on a generic definition.

2.5.6 Conclusion

The model for the FEBEX in situ experiment newly developed and implemented in PFLOTRAN by the University of Bern describes the transient evolution of the steel/bentonite interface in the evolution from the early aerobic corrosion to the anaerobic corrosion phase taking into account the hydration of the bentonite and the evolving temperature gradients.

The model successfully reproduced the major processes of the conceptual model of Hadi et al. (2019a): an aerobic corrosion phase with Fe accumulation as goethite within the corrosion layer, a transition to the anaerobic corrosion phase with the accumulation of anaerobic corrosion products in the corrosion layer and the migration of Fe^{2+} into the bentonite. During the progression of the Fe front into the bentonite, two stages are observed: first, the interaction with O_2 diffusing towards the steel and second, after the local consumption of O_2, Fe sorption on the clay minerals. The calculations indicate that these two processes successively take place with progression of the Fe front. With time and increasing distance to the corroding steel, precipitation becomes however less important due to the gradual depletion of the O_2 ahead of the Fe front. Thus, the counter-diffusion of Fe and O_2 can explain the classical concave shape of the Fe accumulation front observed not only in the FEBEX in situ experiment but also in other similar settings. Moreover, sensitivity cases with respect to transport in gas and liquid phases and to bentonite hydration identifies the diffusion of gaseous O_2 as an important driving force for the depletion of the pore water in O_2 over larger distances and the formation of the characteristic zonation of Fe accumulation: a corrosion product dominated zone close to the steel and a sorption dominated zone without notable amounts of precipitation products further in the bentonite. Sensitivity cases with respect to different temperature gradients (presented in Appendix D) highlighted the high degree of coupling between geochemical process and physical processes, which strongly affect the evolution of the Fe-bentonite interaction zone. Generally, higher temperatures reduce the extent of the Fe-bentonite interaction zone, in line with experimental observations.

Despite the general compliance with the underlying phenomenological model, the calculations could not reproduce the extremely large interaction zones observed by Hadi et al. (2019a). This indicates an additional transport process, which is not resolved with the present model. Two hypotheses can be made, either the fast transport of e- across the oxide layer as postulated by Hadi et al. (2019a), or an additional advective flow path from the steel into the bentonite due to the water vapour convection around the heaters, which is not captured with the simple 1 D-axis symmetric model geometry. Further dedicated experiments to support the first hypothesis or extension of the model to the full 3-D geometry might help to decipher this additional localized process.

One objective of the project was the implementation and calibration of the interaction of corrosion derived Fe^{2+} with the structural Fe(III) in montmorillonites. Two different approaches were tested, one based on the results of the dedicated batch and diffusion experiments performed at UniBern within this Task 2 and one based on an earlier model developed by Muurinen et al. (2014a). The calculations indicate that the high Fe sequestration and redox transfer observed in batch experiments are not directly transferable to the compacted system, thus supporting the observation made for the Fe(II) diffusion experiment (Chapter 3). A clear understanding of this process is however lacking so far and complicated by the non-quantified e^--transfer in the FEBEX-experiment. Nevertheless, the model supported the experimental findings that Fe sorption via cation exchange was largely suppressed in the FEBEX-in-situ test due to the high concentrations of competing cations (Na^+, Ca^{2+}, Mg^{2+}). The Fe-redox interaction model considering e- transfer at the edge sites suggest an only limited reduction of the structural Fe in montmorillonite.

3. FE II Working Group

3.1 Fe II WG introduction/context

Following several repository concepts (e.g., Switzerland, Czech Republic), high level radioactive waste will be contained in carbon steel canisters surrounded by a compacted bentonite buffer and placed into tunnels dug inside a claystone formation or crystalline rock. After repository closure, anaerobic corrosion will eventually occur on canister surfaces in contact with the bentonite, releasing Fe^{2+} into the bentonite.

The global mechanism of Fe^{2+} diffusion into compacted bentonite, and how it may alter the sealing properties (e.g., swelling pressure, redox properties), is not fully understood. Most proposed models are based on results of steel-bentonite interaction experiments either in small scale short term batch or mock-up set-ups, or in fewer cases of full scale long-term *in situ* tests (Hadi et al., 2017; Hadi et al., 2019b; Kaufhold et al., 2015; Kaufhold et al., 2020; Leupin et al., 2021; Wersin et al.; Xia et al., 2005). These models are in general sequential, due to the evolving interaction between steel and bentonite as a function of bentonite water saturation and oxygen content (sequences generally include at least water saturation, aerobic corrosion, and anaerobic corrosion). On the one hand, small scale batch experiments are in general accelerated by heat and pressure and result in mixtures of steel, bentonite, and corrosion products, exposing small interfaces, and making characterisation of possible bentonite alteration more difficult. Such experiments are rather focused on interaction occurring at the close vicinity of the steel-bentonite interface (i.e., steel surface and a few mm into clay/bentonite at most). On the other hand, larger scale and longer termed *in situ* experiments (e.g., ABMs, LOT, FEBEX) generally indicate larger interaction zones (cm to dm), but often lack control or information on the *in situ* conditions as a function of time. Use of natural bentonite containing many accessory minerals (including Fe bearing ones) also makes the characterisation of possible smectite alteration more difficult.

Steel-bentonite interaction models often differ regarding the possible bentonite alteration occurring at the close vicinity of the steel-bentonite interface (e.g. crack formation, nature of main corrosion products, or possible clay neoformation of Fe rich saponite, odinite, cronstedtite or else) but generally agree that the longer and main sequence will consist of anaerobic steel corrosion and diffusion of Fe^{2+} further away from the interface into the bentonite (Hadi et al., 2019b). The way Fe^{2+} interacts with the clay during this sequence remains unclear. The number of studies on controlled experiments and modelling of Fe^{2+} diffusion in compacted clay is more limited. Models for the interaction of Fe^{2+} with clay are in fact mainly derived from batch experiments at low clay and Fe concentrations (Gehin et al., 2007; Muurinen et al., 2014b; Soltermann et al., 2014a; Soltermann et al., 2014c; Soltermann et al., 2013) and consider cation exchange (CE) and surface complexation (SC) at the edge sites as the main interaction mechanisms, but also include possible redox interactions (further referred to Redox Sorption or RS) between sorbed Fe (Fe_{sorb}) and clay structural Fe (Fe_{str}). Parameters for the redox interactions were so far derived from batch experiment conducted at higher Fe concentrations, mainly using Fe rich nontronites (Neumann et al., 2013; Neumann et al., 2015; Schaefer et al., 2011). More recently, similar experiments using montmorillonites (Latta et al., 2017; Tsarev et al., 2016), the main component of bentonite, have shown that the Fe poor smectites behave to some extent similar as the Fe rich ones, with high Fe uptake (above CEC) and extended Fe_{str} reduction (up to 70%) above pH 6.0.

The present study investigates the interaction of Fe^{2+} with purified SWy-3 montmorillonite in anaerobic batch and diffusion experiments. The objective of these experiments is to understand the effects of Fe corrosion on bentonite stability for the long-term anaerobic phase. The focus is on the interaction of Fe(II) with smectite without complicating factors from the transient phase (e.g. variable saturation, variable redox conditions such as encountered in the FEBEX experiment). Main objectives are the understanding and quantification of the electron transfer of sorbed Fe(II) to structural Fe(III) in the octahedral montmorillonite structure and an increased understanding of the Fe migration (retention and diffusion) in compacted bentonite. The batch experiments focus on the Fe – bentonite interaction at variable conditions and aim at quantifying the redox-sorption process. The reactive transport model aims at coupling and quantifying Fe retention and diffusion processes. It should provide insights into (i) the main sorption mechanisms, (ii) the importance of the e-transfer process, and (iii) the transferability of

information obtained in batch experiments to compacted systems. The implementation of these processes in a reactive transport model should further enhance the capabilities of reactive transport codes to model the migration of Fe(II) in bentonite in the context of the long-term evolution of a deep geological repository.

Analyses carried out include Fe concentrations and redox speciation in solution and in the solid (following total acid digestion) by UV-Vis spectrometry (phenanthroline method) and Fe redox speciation in the solid by ^{57}Fe Mössbauer spectrometry. Fe_{str} and Fe_{sorb} are usually difficult to discern using Mössbauer spectrometry, especially at low Fe loading ($Fe_{sorb} < Fe_{str}$). For the diffusion experiments and a part of the batch experiments, isotopically purified $^{56}Fe^{2+}$ (transparent to Mössbauer spectrometry) is used in order to better assess the extent of possible electron transfer between Fe_{sorb} and Fe_{str}, since only Fe_{str} should be visible. Swelling pressure was also recorded during the diffusion experiments.

3.2 Materials and methods

3.2.1 Studied materials and chemicals

All experiments were conducted with SWy-3 montmorillonite (CMS, Chantilly, USA). The material was purified by an elutriation technique (Yamamoto, 2000), and was sodium saturated (further detailed in following section). Another similar smectite (PGN, from Nanocor, USA) was also used in some batch pre-tests. A complete list of chemicals and corresponding use(s) is displayed in Table 19.

Table 19 – Complete list of chemicals and use(s).

Chemical	Purity	Supplier	Use
$FeCl_2 \cdot 4H_2O$	99.9%	Sigma-Aldrich	UV-vis calibration Batch experiments
Fe(0)	99.9%	Sigma-Aldrich	Method validation Batch experiments
^{56}Fe(0)	99.5%	Neonest AB	Batch and diffusion experiments
Fe(III) IC standard		Fluka	UV-vis method validation
$NH_4Fe(SO_4)_2 \cdot 12H_2O$	99.9%	Sigma-Aldrich	UV-vis method validation
1-10 Phenanthroline hydrochloride monohydrate	99.9%	Sigma-Aldrich	UV-vis Fe analysis
Tris-Na-citrate dehydrate	99.9%	Sigma-Aldrich	pH buffer for Fe analysis following acidic digestion
Hydroxylamine hydrochloride	99.9%	Sigma-Aldrich	Reducer for total Fe analysis
MOPS	99.9%	Sigma-Aldrich	pH buffer in batch and diffusion experiments
MOPS-Na	99.9%	Sigma-Aldrich	pH buffer in batch and diffusion experiments
NaOH	99.9%	Sigma-Aldrich	Neutralisation of acidic Fe dissolutions
NaCl	99.9%	Sigma-Aldrich	Clay saturation Background electrolyte in batch and diffusion experiment
NaBr	99.9%	Sigma-Aldrich	Anionic tracer in diffusion experiment
D_2O	>99.8% D	Roth	Neutral tracer in diffusion experiments
HCl	30%	Sigma-Aldrich	Acidic Fe(0) dissolution
H_2SO_4	96%	Sigma-Aldrich	Acidic clay dissolution
HF	40%	Sigma-Aldrich	Acidic clay dissolution

H_3BO_4	99.9%	Sigma-Aldrich	Neutralization of HF following acidic clay dissolution

The ferrous solutions were prepared from various Fe^{2+} sources: commercial $FeCl_2 \cdot 4H_2O$ salt (99.9%, Sigma-Aldrich, USA), or $FeCl_2$ concentrated solutions derived from commercial pure natural Fe powder (Sigma-Aldrich, USA), or from commercial isotopically purified (99.5% ^{56}Fe, 0.2% ^{57}Fe) elemental ^{56}Fe powder, (Buy Isotopes, Neonest AB, Sweden), using hot HCl dissolution (further detailed in experimental section).

Ferric solutions were employed for the validation of the spectrophotometric methods for analysing Fe(II) in solutions (using Fe(III) IC standard, Sigma-Aldrich, USA) and solids (using Ferric alum, $NH_4Fe(SO_4)_2 \cdot 12H_2O$ (99.9%, Sigma-Aldrich, USA).

3.2.1.1 Clay purification

The SWy-3 montmorillonite was received as a finely ground powder. It was purified by extracting the clay rich fraction (< 2 µm), using an elutriation (Yamamoto, 2000) apparatus (further detailed in Appendix E.1). Clay purity was assessed by XRF, ^{57}Fe Mössbauer spectrometry, CEC measurements (using the hexaamminecobalt method, (Hadi et al., 2016)) and interlayer water content by gravimetric measurements (before and after drying small aliquots overnight at 110°C).

3.2.1.2 Anaerobic conditions

Unless stated otherwise, all experiments (besides clay purification) were prepared and sampled in a glovebag with a 95:5 N_2:H_2 atmosphere equipped with two palladium catalyst scrubbers (Coy Laboratory Products Inc., Grass Lake, Michigan, USA). The ultrapure Milli-Q® water was degassed by bubbling with N_2 for a few hours and then exposed to the atmosphere of the anaerobic chamber for a few more days. The materials studied were also exposed to the atmosphere of the anaerobic chamber for a few weeks prior to use.

3.2.2 Experimental series

Experimental work was divided into three main sequences. In a first sequence, clay material was purified and acidic Fe digestions tests were conducted with natural Fe in order to optimise the conversion of the isotopically purified $^{56}Fe(0)$ solid powder into a concentrated $Fe(II)Cl_2$ solution. Second sequence consisted of various series of batch experiments, using purified clay and Fe(II) solutions, in order to better dimension the conditions (e.g. Fe concentration, pH buffering) of the diffusion experiments. In parallel, the diffusion experiments were set up and saturation (with Fe-free solutions, 180 mM NaCl, pH 7.2) was initiated. In the last sequence, following a given saturation time, $^{56}Fe(II)$ diffusion experiments were initiated, monitored for several months, and finally dismantled and analysed.

3.2.2.1 Elemental Fe dissolution and production of $FeCl_2$ stock solutions

All Fe dissolution experiments were carried out at 105°C in HCl (30%), using a heater block (DigiPREP MS from SCP Science, France) and PE tubes (DigiTUBEs, SCP Science). A controlled volume of 5 mM NaOH was rapidly added to the acidic Fe dissolutions, in order to raise the pH to ~7 and precipitate Fe(III) hydroxides. Those hydroxides were filtered out (1 µm), resulting in a concentrated (0.5 M) $Fe(II)Cl_2$ solution with pH ranging between 1.5 and 3.5.

3.2.2.2 Batch experiments

Batch experiments were led in 35 ml PSF centrifuge tubes (Nalgene™ Oak Ridge centrifuge tube, Thermo Fischer Scientific). All experiments were prepared gravimetrically. Solid sample was first introduced into a tared tube. The reacting solution (section 3.3.2) was then added and the solution mass was adjusted by a pipette in order to set the desired L:S ratio. The tube was stirred using a rotating shaker. After a given reaction time, solutions were centrifuged (8-15 min at 28 408 g). The supernatants

were collected. The solid was kept in the reaction tubes until the freeze-drying step (further detailed below).

3.2.2.3 Diffusion experiments

Diffusion experiments were conducted in cylindrical Ti chambers (25 mm radius) equipped with a piston and a force transducer to monitor the swelling pressure (Figure 102), inside the anaerobic chamber. A peristaltic pump individually flushed Ti filters at top and bottom of the clay core. The clay core was made from 56 g clay (50 g dry mass), pressed to approximatively 20 mm thickness in order to get a dry density of ~1300 kg·m^{-3}. Actual thickness of the pressed pellets core was 20.55 mm in experiment #1, and 24.38 mm in experiment #2, thus the dry densities were estimated at 1239 and 1044 kg·m^{-3} respectively in exp. #1 and #2.

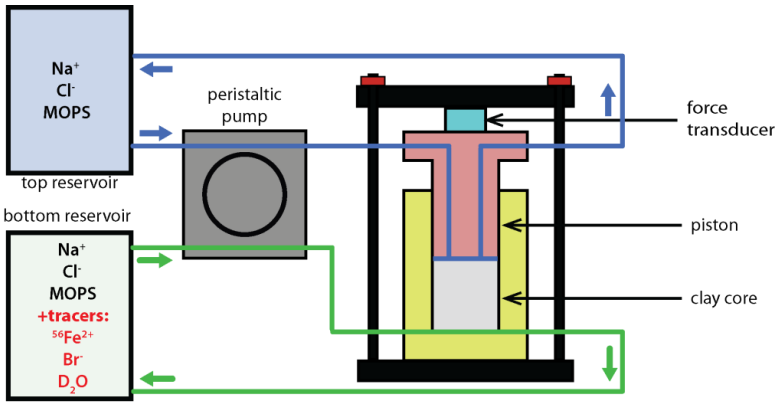

Figure 102 - Scheme of the diffusion experiment cell.

During the initial clay pre-saturation phase, the same solution was circulated on both sides of the clay cores in both experiments (one 200 ml reservoir per experiment, Table 20). The solution was first circulated only at the bottom of the core for a month, and then circulated at the top as well for few more months. This equilibrated solution became the output (top) solution during the Fe diffusion sequence. Anionic (Br^-) and neutral (D_2O) tracers were diffused along with Fe. Small solution samples (1.0-1.5 ml) were periodically collected (for analysis of Fe and other tracers' concentrations, and pH).

Table 20 – Experimental plan of the diffusion experiments.

Italicized values are planned values, other values were measured. n.d.= not determined. b.d. = below detection

Phase	Volume	[Fe]	[Na]	[Cl]	[Br]	MOPS acid	MOPS base	[D_2O]	pH
	(l)	(mM)						%VSMOW	
Pre-equilibration[a]	0.2	*0*	*180*	*155*	*0*	*25*	*25*	*Low*	*> 7.0*
		b.d.	175	148	b.d.	n.d.	n.d.	-80.12	7.23
Diffusion experiments[b]	1.0	*10*	*160*	*142*	*10*	*0*	*50*	*1000*	*> 7.0*
		11	160	148	10	n.d.	n.d.	989	7.27

a. Same reservoir for input (bottom) and output (top) solutions.
b. Solution for input reservoir, the output solution is the pre-equilibration solution.
n.d. = not determined

The maximum amount of Fe(II) accumulated in the "blue zone" of the FEBEX experiment (developing during the anaerobic period, see section 2.5) was equivalent to ~10% of the Fe_{str} content. In the present diffusion experiment, the initial ^{56}Fe concentration and solution volume was arranged so that the total amount of added ^{56}Fe in the experiment (in reservoirs and clay core) would represent a fraction of clay Fe_{str}. It was about 40% (25 mmol of Fe in clay core, 10 mmol of Fe in solution).

Two diffusion experiments were conducted in parallel (hereafter referred to as exp. #1 and exp. #2 respectively). Exp. #2 was delayed by ~6 month regarding exp. #1 and was initially intended at part as a back-up experiment, and at part for a "out diffusion" experiment aiming at reversing the diffusion experiment and removing mobile Fe from the core (for a potential reversibility study). In fact, exp. #2 was eventually stopped and dismantled before exp. #1, a few weeks following Fe breakthrough in the top reservoir of exp. #2. Exp. #1 was continued for a longer time, until an unanticipated event (leak in bottom reservoir circulation system and loss of most of the ferrous inlet solution) occurred. At that moment, both bottom and top solutions were replaced by Fe-free solution in order to remove mobile Fe from the core. During this last sequence, the volume of the top reservoir was increased to 1 L, and both solutions were renewed two times in order to accelerate Fe out-diffusion. Exp. #1 was finally stopped and dismantled after a substantial portion of Fe had been extracted.

Dismantling was conducted inside the anaerobic chamber. First, both top piston and bottom base were removed. The clay core was then progressively pushed out of the bottom of the Ti cylinder and sliced (2-3 mm) using a ceramic knife. Each slice was rapidly weighed, then subsampled for analysis (wet Fe analysis by digestion, and Mössbauer spectroscopy), weighed again and freeze-dried. Once dried, the final dry weigh was measured (in order to determine total gravimetric water content). Exp. #2 was dismantled before exp. #1. The sampling was improved for the second dismantling (exp. #1); especially at the vicinity of the input interface where finer sampling was achieved.

3.2.3 Sample drying and solution analyses

3.2.3.1 Sample Drying

Prior to freeze drying, the samples were placed in Weck canning glass jars (Weck, Germany). These jars were first placed in the airlock of the chamber, then the airlock was evacuated and refilled quickly in order to vacuum collapse the jars. Once vac sealed, these jars were placed in a freezer (-30°C) overnight. The still sealed jars were then placed in the freeze drier, and the freeze-drying process was started. The jar was only reopened when sufficient vacuum was reached in the freeze drier's chamber (due to pressure difference). Freeze drying was continued for two days. At the end, the chamber was refilled rapidly with air, in order to vacuum collapse the jars again, and keep them sealed until being re-introduced into the glovebag. Solid samples were then crushed by hand in an agate mortar and were stored in closed glass tubes.

3.2.3.2 UV-Vis

UV-Vis spectroscopy was employed to determine the Fe(II) and total Fe concentrations in solutions, using the o-phenanthroline (phen) method. For Fe(II) analysis, a small sample aliquot (60 to 200 µl) was weighed in a tube, and 7-15 ml of a 0.6 mM phen solution was added. For total Fe analysis, the same procedure was repeated, but also adding hydroxylamine to the solution (with a 5-10 fold excess regarding expected total Fe concentrations). Analyses were carried out at 510 nm on a Cary 50 UV-Vis spectrophotometer (Varian, USA), using PS cuvettes. Samples were in general analysed in duplicate. Reported error bars account for 2 times the standard deviation on replicate analyses.

3.2.3.3 Ion Chromatography

IC was employed to determined Na (DIN EN ISO 14911 (E34): 1999-12), Cl, and Br (DIN EN ISO 10304 (E20): 2009-07) concentrations in solutions. Reported error bars account for 2% of the analysed values.

3.2.3.4 Isotope

Deuterium

Deuterium concentrations were determined by using a L2130-i Isotope and Gas Concentration Analyzer (Picarro, USA). Method's (QMA 504-2/23: 2012-02) standard deviation is ±1.5 ‰. Samples were diluted (25 times) before analysis. The same diluting water was used for all the samples. Error bars were derived following Gaussian error propagation.

Fe isotopes

Iron isotope ratios of the samples coming from bottom and top reservoirs of both experiments were measured in order to control if isotopic exchange occurred between solution and solid samples. Analyses were carried out with a single-collector high-resolution ICP-MS instrument (ELEMENT XR, Thermo Scientific, Bremen, Germany). Preliminary quantitative Fe analyses of the samples were carried out in order to adjust the Fe concentration to 150 ppb or 25 ppb (depending on the initial Fe concentration) in 2% HNO_3 (v/v) for Fe isotopic measurements.

The instrument was tuned for highest sensitivity on 1 ppb Fe containing solutions (SCP Sciences ®) while keeping a $^{238}U/^{232}Th$ ratio close to 1 and a $^{232}Th^{16}O/^{232}Th$ ratio below 0.1%. A low concentration was selected to limit Fe contamination.

Measurements were performed using the operating and data acquisition parameters detailed in Table H5 (Appendix H). The analysis sequence consisted of 5 replicate analyses of the sample solution bracketed by 0.06% HCL / 2% HNO_3 (v/v) and 2% HNO_3 (v/v) washing followed by a 2% HNO_3 (v/v) blank measurement. Every 3 samples, Fe standard measurements were collected. A first measurement was collected on a 150 ppb solution prepared from 1000 ppm SCP Science® Fe standard solution diluted in 2% HNO3 (v/v). A second measurement was collected and a similar standard solution diluted in the same matrix as the sample (see Table 20 for sample composition). The isobaric interference from ^{54}Cr on ^{54}Fe was corrected using the measured signal intensity of ^{53}Cr and the abundance ratio $^{53}Cr/^{54}Cr$ equalling 4.017.

The Fe isotope ratios ($^{56}Fe/^{54}Fe$, $^{56}Fe/^{57}Fe$, and $^{57}Fe/^{54}Fe$) were corrected for instrumental mass fractionation using the following exponential law:

$$R_c = R_m e^{\Delta m \times \delta} \quad (7)$$

with R_c, the corrected isotopic ratio, R_m the measured isotopic ratio, Δm the difference between the mass of the considered isotope for each ratio and δ :

$$\delta = \ln\left(R_n / R_{m\text{-}std}\right)\Delta m \quad (8)$$

with R_n, the natural isotopic ratio and $R_{m\text{-}std}$ the measured isotopic ratio in the standard.

The mass bias factor applied to the sample analyses is the average of such factors calculated from analyses of the matrix containing Fe standard both before and after the sample analyses. The errors calculated on Fe isotope ratios in samples correspond to two standard deviations from the mean (1σ) based on five replicates analyses of the same sample. The relative abundancy of ^{54}Fe, ^{56}Fe and ^{57}Fe were calculated from $^{54}Fe/^{57}Fe$, $^{56}Fe/^{54}Fe$ and $^{57}Fe/^{56}Fe$ ratios. The ^{58}Fe abundancy (≈ 0,2%) was neglected in the calculation due to the use of a Ni skimmer cone and sampler leading to large overestimation on ^{58}Fe measurements.

3.2.4 Solid analyses

3.2.4.1 Fe II / Fe tot

Fe reduction level and total content in the raw material and the samples from the diffusion experiment were determined by the HF digestion method developed by Stucki and Anderson (1981a; b) and modified by Amonette and Templeton (1998), using the same set-up as for the hot acidic Fe dissolutions (section 3.2.4.1). Raw material was analysed as a dry powder, and samples from the diffusion experiments were analysed as compacted saturated samples. During dissolution, hot tubes were periodically transferred to an ultrasonic bath for a few seconds, in order to enhance sample dissolution, especially dealing with the compacted and saturated samples from diffusion experiments. The Fe concentration was determined by UV-Vis spectrophotometry, using the phenanthroline method (section 3.2.3.2).

3.2.4.2 ^{57}Fe / Mössbauer Spectrometry

Sample preparation was performed in the anaerobic chamber and progressively adapted to minimise newly observed artefacts (further detailed in Appendix E.4). In the initial preparations, an aliquot of dry powdered sample (~400 mg depending on the iron content to have ~5 mg/cm^2 of Fe per sample to avoid the presence of thickness and polarisation effects) was sealed in a small PMMA cup, by directly covering it with degassed araldite resin (further referred to as “embedded samples”). In a second preparation approach, the sample was first protected by a PMMA disc in order to avoid direct contact with the sealing resins (further referred to as “dry samples”). In the case of the diffusion experiments, water saturated compact samples taken directly from the experiments were pressed into the sample cup, before being covered with a PMMA disc and sealed with degassed resin (further referred to as “compacted and saturated samples”).

The Mössbauer spectra were recorded at room temperature (RT, 300 K) and in many cases also at 77 K using a bath cryostat, with a constant acceleration spectrometer (driving unit supplied by WissEl GmbH, Germany) and a ^{57}Co source diffused in a rhodium matrix. Velocity calibrations were carried out using an α-Fe foil at RT. The values of the hyperfine parameters were refined using a least-squares fitting procedure (Varret F., Teillet J. unpublished MOSFIT program, Le Mans Université, France) with a discrete number of independent quadrupolar doublets and magnetic sextets composed of Lorentzian lines. The values of isomer shift (I.S.) are quoted relative to that of the α-Fe spectrum obtained at RT. The proportions of each Fe species are proportional to the relative spectral area. This is because the f-Lamb-Mössbauer factors, which correspond to the fraction of gamma rays emitted and absorbed without recoil, are assumed to be the same for the different phases present in the samples and for the different Fe species present in the same phase (Gütlich et al., 2011; Mössbauer, 1958; Tzara, 1961).

Finally, it is important to note that the addition of ^{56}Fe in the samples in certain experiments does not affect the hyperfine structure of the Mössbauer spectra because the Mössbauer effect can be only observed with the ^{57}Fe isotope.

All observed quadrupolar doublets correspond to high-spin state octahedral Fe paramagnetic species (further referred to as “para-Fe”) which are in most cases interpreted as clay structural Fe (Fe_{str}) in the present study. All magnetic sextets represent magnetically ordered species (in octahedral coordination as well) interpreted as non-clay structural Fe (rather Fe in impurities such as (oxyhydr)oxides). All spectra and hyperfine parameters are presented in Appendix F.

3.2.4.3 LA-ICP-MS

Pellet preparation

The chemical evolution and Fe isotopic variations in the SWy-3 montmorillonite cylinders coming from exp. #1 and #2 were assessed by LA-ICP-MS measurements collected on pellets. Pellets were prepared from a fraction of the homogenised powder coming from the slicing, drying and crushing of the clay cores. Pellets of 5 mm diameter were pressed at 0.5 tons using a Speccac© mold composed of 440C stainless steel body die and tungsten carbide pressing pellets. With such preparation, each sample pellet was considered as representative of the corresponding slice of the clay core.

Elementary analyses

LA-ICP-MS analyses of 58 elements were collected on each SWY-3 pellet in order to assess the chemical evolution of the SWY-3 along the whole cylinders after dismantling of experiment 1 and 2. The instrument was tuned for highest sensitivity on NIST SRM612 glass reference material while keeping a ^{238}U/^{232}Th ratio close to 1 and a ^{232}Th^{16}O/^{232}Th ratio below 0.1%. Usually, a major element from the material (e.g. Al, Si) is employed as internal standard to correct the signal derivation with time. As the concentration of major elements were susceptible to vary (e.g. due to dissolution processes), the sum normalisation process was used to calculate the concentrations of the 58 elements measured (Gagnon et al., 2008; van Elteren et al., 2009). The detailed sample acquisition parameters are reported in

Table I5. Both NIST 1881b and NIST 610 were used as external standards to check the consistency between the results obtained with two standards presenting different concentrations and different behaviour under the laser beam. The NIST 1881b was prepared in an Ar filled glovebox by mixing Milli-Q water with NIST 1881b cement powder with a water to cement ratio of 0.42. The hydrated cement paste cylinder was let to harden for 28 days and dried in a glove box prior to its embedding in resin and polishing down to 1 µm with diamond paste. Values obtained on the five main elements (Si, Al, Fe, Mg, and Na) in the pristine SWy-3 with the two different calibrations were compared to those obtained with XRF (Figure I1). Results for Si, Al, and Fe were more consistent between methods using the standard NIST 610 rather than NIST 1881b (within a ±5% and ±10% error respectively). Still, results were less consistent for Na and Mg, which were notably overestimated or underestimated respectively. Slightly better results were obtained with standard NIST 1881b for these two latter elements. For this reason, results for these two elements were calibrated with the standard NIST 1881b, while results for the other elements (also including minor ones) were calibrated with standard NIST 610.

Isotopic analyses

Fe isotopic analyses were also conducted on the montmorillonite pellets. The instrument was tuned for highest sensitivity on NIST SRM612 glass reference material while keeping a $^{238}U/^{232}Th$ ratio close to 1 and a $^{232}Th^{16}O/^{232}Th$ ratio below 0.1%. The detailed Fe isotopic analyse parameter conditions are given in

Table I5. As for the isotopic analyses in solution, the ^{54}Fe measurements were corrected from the ^{54}Cr signal by measuring ^{53}Cr. Blank corrections were applied by bracketing sample measurements with independent gas blank measurements in pulse counting detection mode. Sample measurements were also corrected from mass fractionation by bracketing sample measurements with 3 measurements on pristine SWy-3 montmorillonite considering a natural isotopic abundancy (Meija et al., 2016) in this sample and using the exponential law. As for solution isotopic analyses, the relative abundancy of ^{54}Fe,^{56}Fe and ^{57}Fe were calculated from $^{54}Fe/^{57}Fe$, $^{56}Fe/^{54}Fe$ and $^{57}Fe/^{56}Fe$ ratios neglecting the ^{58}Fe contribution.

3.2.5 Modelling

3.2.5.1 Batch experiments

Modelling of batch experiments was performed with PhreeqC (v. 3.7) and the ANDRA/Thermochimie Database v9.b (Giffaut et al., 2014; Grivé et al., 2015). The Fe sorption model is based on the 2-site protolysis non-electrostatic surface complexation and cation exchange model of Soltermann et al. (2014a), which was extended by an additional surface complexation reaction accounting for the interaction of Fe(II) with structural Fe (RS) (Table 21). The latter process was calibrated to the pH and Fe/Na batch series such that it describes the Fe sorption/precipitation that is not explained by the original (Soltermann et al., 2014a) model. The model was applied to predict sorbed Fe on the solid phase in equilibrium with the final experimental solution. Input parameters included the S/L, the final [Fe], [Na], [Cl] concentrations and pH. For some experiments, final [Na] and [Cl] were not available and the initial concentrations were used instead. Calculations were performed for two cation exchange selectivity coefficients, i.e., a $\log K_{sel}$ of 0.8 and 0.5, thus the best estimate and lower limit proposed by Soltermann et al. (2014a).

Table 21 – Sorption model of Soltermann et al. (2014a) and extension of the present study

Site types	**Site capacity**	**Reference**
$\equiv S^{s}OH$	$2*10^{-3}$ mol/kg	Bradbury and Baeyens (1997b)
$\equiv S^{w1}OH$	$4*10^{-2}$ mol/kg	
$\equiv S^{w2}OH$	$4*10^{-2}$ mol/kg	
CEC	0.87 eq/kg	
$\equiv S^{Str}OH$	0.51 mol/kg	This study
Surface complexation reaction	**log K**	**Reference**

$\equiv S^{s/w1}OH \leftrightarrow S^{s/w1}O^- + H^+(aq)$	-7.9	Bradbury and Baeyens (1997b)
$\equiv S^{s/w1}OH + H^+(aq) \leftrightarrow S^{s/w1}OH_2^+$	4.5	
$\equiv S^{w2}OH \leftrightarrow S^{w2}O^- + H^+(aq)$	-10.5	
$\equiv S^{w2}OH + H^+(aq) \leftrightarrow S^{w2}OH_2^+$	6.0	
$\equiv S^{s}OH + Fe^{2+} \leftrightarrow \equiv S^{s}OFe^+ + H^+$	1.9	Soltermann et al. (2014a) for Fe rich montmorillonite (SWy-2)
$\equiv S^{w1}OH + Fe^{2+} \leftrightarrow \equiv S^{w1}OFe^+ + H^+$	-1.7	
$\equiv S^{s}OH + Fe^{2+} \leftrightarrow \equiv S^{s}OFe^{2+} + H^+ + e^-$	-1.4	
$\equiv S^{w1}OH + Fe^{2+} \leftrightarrow \equiv S^{w1}OFe^{2+} + H^+ + e^-$	-3.8	
$\equiv S^{Str}OH + Fe^{2+} \leftrightarrow \equiv S^{str}OFe^+ + H^+$	-3.1	This study
Cation exchange reaction	**log K_{sel-GT}**	
$Fe^{2+} + 2\ NaX \leftrightarrow FeX_2 + 2\ Na^+$	0.8 //0.5	Soltermann et al. (2014a)

3.2.5.2 Diffusion test

A reactive transport model which was developed includes chemical processes, in particularly the sorption of Fe on montmorillonite and diffusion processes. The powerful simulator PFLOTRAN (www.pflotran.org), an open source, massively parallelised subsurface flow and reactive transport code, is used for numerical implementation. The ANDRA/Thermochimie Database v9.b (Giffaut et al., 2014; Grivé et al., 2015) is used for the calculation of aqueous reactions. The reactive transport calculations are supported by static calculations for individual pore water/solid phase couples with PhreeqC, applying the same database and sorption model.

Conceptual Model

The Fe(II) experiments represent a simplified experimental system. The main processes to be considered include:

- Diffusion of solutes, including water tracers (D_2O as water tracer), anions (Br^- as anion tracer) and Fe.
- Sorption of Fe on montmorillonite, including i) the formation of surface complexes at the edge sites, ii) cation exchange reactions with Na and iii) retention due to interaction with structural Fe(III) (redox-sorption).

Important assumptions, simplifications, limitations

- The montmorillonite is fully water-saturated initially and throughout the experiment. The initial state assumes the absence of residual atmospheric oxygen in neither the montmorillonite nor the reservoir solutions.
- All aqueous reactions, exchange reactions, surface protonation/de-protonation and surface complexation reactions assume chemical equilibrium. No mineral dissolution and precipitation reactions are considered.
- Isothermal conditions of 25°C (lab temperature) are considered throughout the experiment.
- The implemented interaction of Fe^{2+} with structural Fe(III) is reversible and is similar to the formation of a surface complex. The interaction is limited to a small < 1mm thick zone adjacent to the filters, based on experimental observation.
- Transport in the clay is by diffusion only. The full porosity is considered in the models for the diffusion of neutral tracers and Fe. For the modelling of anion tracer diffusion (Br^-), a reduced effective diffusion coefficient due to an only partly accessible porosity fraction is assumed. Diffusion coefficients are constant during the entire experimental duration. Sorbed Fe and Na exhibit a certain mobility, which leads to an increased effective diffusion coefficient compared to a neutral water tracer.

- The filter exerts a small diffusive resistance, despite the continuous flushing. The reservoirs are well mixed throughout the experiment.
- Changes of the reservoir volumes due to sampling are neglected.

Numerical model

Spatial and temporal discretization

The experimental system is modelled as a 1-D structured cylindrical grid with a single cell in radial direction having a diameter of 5 cm. Top and bottom reservoir are described as single cells, with the length according to the volume of the reservoirs (990 ml inlet reservoir; 200 ml outlet reservoir), the filters as single cells of 0.1 cm each (Table 22). The clay discs are divided according to the *post-mortem* characterization, with the clay cells adjacent to the filter split in two cells to account for the interaction of Fe^{2+} with structural Fe at the surface of the clay discs, only.

Total calculation time is set to 2 years with a maximum time stepping of 0.1 days.

Boundary Conditions and transport

The experimental system is a closed system. The outer boundaries of the reservoirs are no-flux boundaries.

Transport is by diffusion only. Different D_e values were fit in separate calculation runs to best describe the evolutions of Br, water tracer, and Fe(II)/Na in the top and bottom reservoirs.

Geochemical model

The geochemical model is constrained to the following processes:

- Aqueous chemistry of Na, Cl, Br^- and Fe including the following species: Fe^{2+}, Fe^{3+}, $Fe(OH)_2$, $Fe(OH)_2^+$, $Fe(OH)_3$, $Fe(OH)_3^-$, $Fe(OH)_4^-$, $Fe(OH)_4^{2-}$, $FeOH^+$, $FeOH^{2+}$, $FeCl^+$, $FeCl^{2+}$, $FeCl_2$, $FeCl_2^+$, $FeCl_4^-$, $FeCl_3^-$, $FeCl_3$, Na^+, NaCl(aq), H_2(aq), O_2(aq), OH^-, H^+, Br^-.
- ^2H is included as an unreactive tracer.

Protonation and de-protonation reactions of the montmorillonite edge sites contributing to pH buffering. pH buffering by MOPS-/MOPSH.

- Cation exchange involving Na and Fe(II).
- Fe(II) surface complexation reactions (non-electrostatic) on strong and weak sites of montmorillonite without electron transfer.
- Sorption process of Fe(II) on montmorillonite linked to the structural Fe(III) of the montmorillonite, considered as an additional surface complexation reaction.

The implemented reaction equations and their parameterization as taken from literature and/or calibrated to the experimental data are summarized in Table 21.

Initial conditions

Based on the *post-mortem* experimental results (section 3.3.3.3), individual models for exp. #1 and exp. #2 were developed, accounting for the different size, measured final dry density and porosity distribution in the montmorillonite discs. Table 22 provides the average parameters of each cell. The initial conditions considered for the reservoirs and montmorillonite pore water are provided in Table 23.

Table 22 – Geometry and solid phase characteristics of the model domains.

	Experiment #1 Clay		**Experiment #2 Clay**		**Reservoirs**	**Filter**
	Average	Range	Average	Range		
Total length of domain [cm]	2.055		2.48		50.4 (inlet) 10.2 (outlet)	0.1
Subdivision of model domain (# of cells)	19		21		1	1

Dry density [kg/m^3]	1215	1093 - 1249	1043	995 - 1109	-	-
Porosity [-]	0.55	0.54 – 0.59	0.61	0.59 – 0.63	1	0.27

Table 23 – Initial composition of reservoir solutions and montmorillonite pore water in the models of exp. #1 and exp. #2

Parameter		Inlet reservoir		Outlet Reservoir		Pore water	
		Exp. #1	Exp. #2	Exp. #1	Exp. #2	Exp. #1	Exp. #2
pH		7.27	7.27	7.13	7.13	7.13	7.13
Pe			-4.2		-4.0		
Na	[mol/L]	$1.60*10^{-1}$	$1.60*10^{-1}$	$1.76*10^{-1}$	$1.81*10^{-1}$	$1.80*10^{-1}$	$1.80*10^{-1}$
Cl	[mol/L]	$1.48*10^{-1}$	$1.52*10^{-1}$	$1.65*10^{-1}$	$1.50*10^{-1}$	$1.50*10^{-1}$	$1.50*10^{-1}$
Fe	[mol/L]	$1.05*10^{-2}$	$1.05*10^{-2}$	0	0	0	0
Br	[mol/L]	$1.00*10^{-2}$	$1.00*10^{-2}$	0	0	0	0
^{2}H	[‰VSMOW]	989.75	989.75	-80.17	-80.17	-80.17	-80.17

Model calibration

The calibration of the reactive transport model comprised two main sets of parameters: i) the effective diffusion coefficients (D_e) and ii) the Fe sorption model.

The D_e values for the conservative tracers were calibrated based on the evolution of the tracers in the inlet and outlet reservoirs. For each tracer and experiment, the D_e best describing the breakthrough in the outlet reservoir was selected as the "best fit" (Table 24). Bounding D_e values were determined, such that the data in both reservoirs is well constrained, representing the uncertainty envelope with respect to the model parameterization. Details on uncertainties for the various solution data are given in the analytical method section (section 3.2.3). Note that PFLOTRAN is a forward modelling code and does not allow for an inverse numerical fitting of the parameters.

For reactive species, in particular Fe, the evolution in the reservoirs is determined by both diffusion and retention properties. Thus, in a first step, the sorption model was calibrated and in a second step, the "best fit" and uncertainty envelope for the D_e value determined in analogy for the conservative tracers.

The sorption model applied here is based on Soltermann et al. (2014a) and calibrated based on both the batch sorption data (described in section 3.3.2) and the Fe profiles obtained *post-mortem* from the diffusion experiments #1 and #2 (section 3.3.3) performed with the corresponding Fe concentrations in the pore water. Two main adjustments were required for a successful description of the experimental observations i) the inclusion of an additional sorption complex accounting for the interaction of Fe^{2+} with structural Fe(III) and ii) the reduction of the accessible sorption sites in the compacted system. The interaction of Fe^{2+} with structural Fe(III) was first calibrated based on the batch experimental data. A large range of the batch experiments could be well described by including an additional pH dependent sorption complex as given in Table 21. Note, that the sorption model of Soltermann et al. (2014a) accounts for a redox-dependent sorption at the S^s and S^{w1} sites. Due to the limitation by the edge site capacity it failed however to describe the full amount of Fe sorbed/precipitated in the batch experiments at high Fe concentrations and pH (section 3.3.2.2). Based on the Fe profiles it was concluded, that the interaction of Fe(II) with the structural Fe(III) was limited to the surface of the clay samples. The extent of this zone was set equal for all four surfaces of experiments #1 and #2. It was calibrated such that the final amount of Fe in the surface samples could be described by mixing of a zone including full reactivity of structural Fe(III) and a zone without any interaction.

Reactive transport calculations as well as static PhreeqC calculations for the final conditions failed to describe the experimental observations if a full site capacity and simultaneously the best estimate Fe/Na exchange coefficients according to Soltermann et al. (2014a) were applied. Thus, based on the *post-mortem* Fe-profiles and the interpolated/modelled Fe-pore water concentrations, the sorption model was

adapted to fit the experimental data. A choice was made to reduce equally the accessible edge sites and cation exchange capacity to 80%, while applying the best-estimate selectivity coefficient and surface complex formation constants as proposed by Soltermann et al. (2014a). Note, that different combinations of a reduced K_{sel} for the Fe/Na exchange and higher capacity would have allowed for a similar result.

Table 24 – Calibrated effective diffusion coefficients (D_e) with Best fit and uncertainty envelope.

u.e. = uncertainty envelope; w.m. = well mixed assumption

	Experiment #1		**Experiment #2**		**Reservoirs**	**Filter**
	Best fit	Model u.e.	Best fit	Model u.e.		
D_e ^2H [m^2/s]	5×10^{-11}	$2 - 6\times10^{-11}$	6×10^{-11}	$2 - 7\times10^{-11}$	3×10^{-7} (w.m.)	4×10^{-11}
D_e Br^- [m^2/s]	5×10^{-12}	$4 - 6\times10^{-12}$	9×10^{-12}	$7 - 11\times10^{-12}$	3×10^{-8} (w.m.)	5×10^{-12}
D_e Fe^{2+} [m^2/s]	2×10^{-10}	$1 - 3\times10^{-10}$	6×10^{-11}	$2 - 7\times10^{-11}$	2×10^{-6} (w.m.)	2×10^{-10}

3.3 Results and discussion

3.3.1 Purification of montmorillonite

Chemical analysis of the purified SWy-3 by XRF (Table 25) showed the absence of calcium, accounting for the absence of exchangeable Ca (and calcite) and was consistent with sodium saturation of the purified material. Small amounts of potassium were present, presumably as fixed interlayer cations in either collapsed layers or illitic sheets. Titanium was considered as an impurity (presumably in anatase). In ambient conditions, a water content of 10.91 wt.% was gravimetrically determined (after drying for 24h at 105°C).

Table 25 – Total chemical composition of purified material by XRF: major elements (in wt.%) (b.d. below detection limit).

SiO_2	Al_2O_3	Fe_2O_3	TiO_2	MgO	CaO	Na_2O	K_2O	P_2O_5	LOI	SUM
58.00	19.40	3.84	0.13	2.19	b.d.	2.42	0.12	b.d.	12.9	98.99

Both raw and purified material were analysed by ^{57}Fe Mössbauer spectrometry (spectra in Figure F1) and parameters in Table F in Appendix F). Analysis of the raw material revealed the presence of 25% of total Fe present as Fe(III) in small (submicron) sized (oxyhydr)oxides (20% goethite and 4% hematite). Analysis of the purified material showed that 9% of total Fe still remained present as Fe(III) in small sized (oxyhydr)oxides (harder to identify but likely similar as in raw material, only smaller), and also that total reduction level was lower than in the raw material (25% and 4% respectively for raw and purified material). The paramagnetic Fe(II) (=total Fe(II) measured in all samples hereafter) was assumed to be present on octahedral sites either in collapsed layers, or illitic sheets (consistent with the presence of small amounts of K).

The structural formula determined for the purified clay (Scheme 3-1) accounts for small presence of Fe^{2+} and K, presumably in either collapsed layers or illitic sheets. This structural formula was consistent with Wyoming montmorillonites (according to the classification of Grim and Kulbicki, 1961; Schultz, 1969). The calculated CEC (897 meq·kg^{-1}) was consistent with that determined by the CoHex (Hadi et al., 2016) method (886.6 ±0.6 meq·kg^{-1}).

Scheme 3-1 – Structural formula of the purified SWy-3 montmorillonite

$$Na_{0.64}K_{0.02}(Al_{3.10}Fe^{3+}_{0.38}Fe^{2+}_{0.02}Mg_{0.45})[Si_{7.96}Al_{0.04}]O_{20}OH_4$$

3.3.2 Batch experiments

Several series of batch experiments were conducted in order to investigate how the main solution parameters ([Fe], [Na], pH, and L/S) influence the Fe-clay interaction (Table 26). All results are detailed in Analytical results

Table G1 and Table G2 (Appendix G) and summarized in the diagrams below. In most series, one parameter was varied whereas the others were initially fixed.

Table 26 – Initial experimental plan of the batch experiments (n.a. = not applicable).

Exp. Number	Exp. Series	[Fe] (mM)	L/S ($L \cdot kg^{-1}$)	pH	[Na] (mM)
T1 to T12	vary pH&Na	10	50	3.75-8.40	0-25
T13 to T16	vary Na	10	50	~8.20	250-2000
T17 to T20	vary Fe (high)	20-50	50	~8.00	25
T21 to T24	vary L/S	10	64-223	8.27	25
T25 to T30	vary pH	10	50	3.75-8.40	25
T31 to T35	vary Fe (low)	1-8	50	~8.20	25
T1B to T12B	blanks (vary pH&Na)	10	n.a.	3.75-8.40	0-25
T25B to T30B	blanks (vary pH)	10	n.a.	3.75-8.40	25
T31 to T35	vary Fe (low)	1-8	n.a.	~8.20	25
^{56}T1-^{56}T6	^{56}Fe	2-20	50	1.8-8.1	~200

3.3.2.1 Setting solution pH

Final solution pH was strongly influenced by Fe and clay concentration. Pure SWy-3 clay suspensions have a rather neutral pH (pH 7.5 at L/S of 50 $L \cdot kg^{-1}$). Ferrous chloride solutions have a slightly acidic pH (pH 3.4 at 10 mM Fe). In absence of a buffer, mixing such solutions resulted in an acidic pH (about pH 4.0). In a first series of pre-test experiments (data not shown), the initial pH of the ferrous chloride solution was tentatively raised above pH 7.0 by addition of NaOH, which induced slight precipitation of (oxyhydr)oxides (about 5-10% of total Fe). Filtering such solution (0.1 µm) would result in a pH drop from pH 7.2 to pH 5.2. Mixing either such filtered (pH 5.20) or unfiltered solution (pH 7.2) with clay (L/S of 50 $L \cdot kg^{-1}$) would result in a pH drop to the same value (pH 4.5). Adding a pH buffer to the solution was thus deemed necessary in order to better constrain the pH variations and investigate Fe-clay interactions in circumneutral pH region (as the *in situ* pH initially envisioned in the clay core of the diffusion experiments).

The pH was at part set by mixing various proportions of MOPS acid and MOPS base buffers in order to keep a fixed MOPS buffer concentration at any pH (25 mM in most experiments, except in ^{56}Fe series where the MOPS concentration was doubled to 50 mM du the more acidic ^{56}Fe stock solution). Addition of 10 mM $FeCl_2$ to 25 mM MOPS solution induced a small pH drop, especially above pH 8.0 and below pH 6.0 (Figure 103, also see initial pH blank experiments series in Table G2 in Appendix G). In solutions with initial pH above 7.0, the pH significantly dropped further with time (Figure 103), due to the precipitation of a portion of solution Fe (up to 10%, Table G2 in Appendix G) to (oxyhydr)oxides (green rust). Addition of clay to the 10 mM Fe(II) solutions had a much stronger influence on the final pH, inducing a notable drop of 0.5-1.5 pH units in any case, with the exception of the lowest pH experiments (T1, T25 ^{56}T2, ^{56}T3, ^{56}T6) where the pH increased (Figure 103). At the highest initial pH (100% MOPS base), increasing the initial Fe concentration (from 10 to 50 mM, as in vary Fe experiments series; Table 26) induced a higher apparent Fe uptake (per mass of solid) and a more important pH drop down to pH 5.9. These results showed how the Fe-clay interaction had a strong effect on pH.

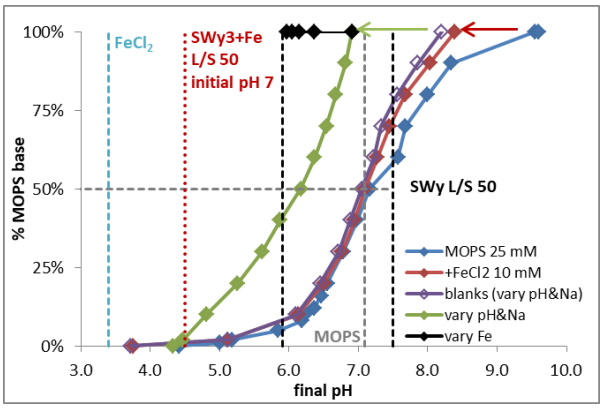

Figure 103 - pH of solutions versus proportions of MOPS base buffer in various series of experiments (blanks, vary pH&Na, and vary Fe).

3.3.2.2 Measured and modelled Fe uptake

Addition of clay to buffered Fe(II) solutions had an important impact on both final pH and final Fe concentration (Figure 104 left). At fixed initial Fe concentrations (10 mM), Fe uptake was limited in the absence of clay (< 2% below pH 7, up to 11% above pH 8,), whereas it was almost total in presence of clay (>97% at pH 6.9). Highest final pH in all experiments at 10 mM Fe was pH 6.95. Below pH 6.9, Fe uptake was proportional to the pH. Higher final pH (up to 8.1) could be reached with lower starting Fe concentration (vary Fe (low) series), and with virtually complete (98% to 100%) relative Fe uptake.

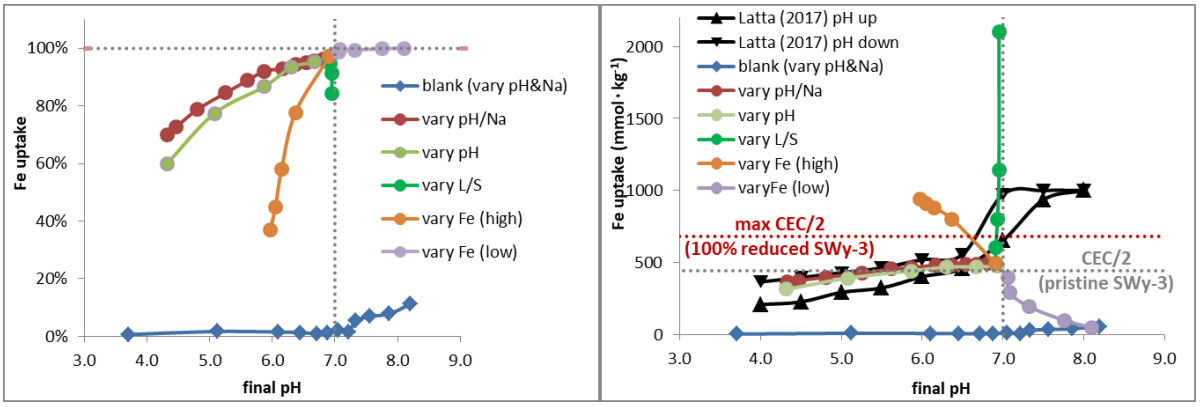

Figure 104 - Fe uptake as a function of pH, expressed either in (left) in % of aqueous Fe or (right) mmol·kg^{-1} of sample.

The amount of Fe consumed per mass of clay sample (Figure 104 right) was in many cases higher than the cation exchange capacity of the pristine clay. One must note that above pH 6.5, clay Fe_{str} is expected to be highly reduced (as shown by Latta et al., 2017, and further below with ^{56}Fe experiments series), which would lead to an increase of the CEC (Hadi et al., 2013; Stucki et al., 1984). One can derive a maximum CEC value for the reduced clay (at 100% Fe_{str} reduction) by assuming a direct compensation of the layer charge increase due to Fe_{str} reduction by an increase of the CEC, which is actually an overestimation due to the compensation mechanism of dehydroxylation (Hadi et al., 2013). The Fe uptake was in some cases even several times higher than this maximum CEC (Figure 104 right). In the present study, a maximum of ~2100 mmol·kg^{-1} was measured at particularly high L/S and pH 6.95. A previously published study (Tsarev et al., 2016) reported even higher Fe uptake of up to ~3800 mmol·kg^{-1} by a similar montmorillonite (Australian MAu-1), above pH 8. Such high Fe uptakes indicate the occurrence of other processes along with cation exchange and edge sorption.

At fixed initial Fe concentrations and above pH 6.9, the Fe uptake was linearly proportional to the L/S ratio and the initial Fe concentration (Figure 105), with a nearly (>97%) complete Fe removal from solution. The slope of the linear regression is therefore close to the value of the initial Fe concentration.

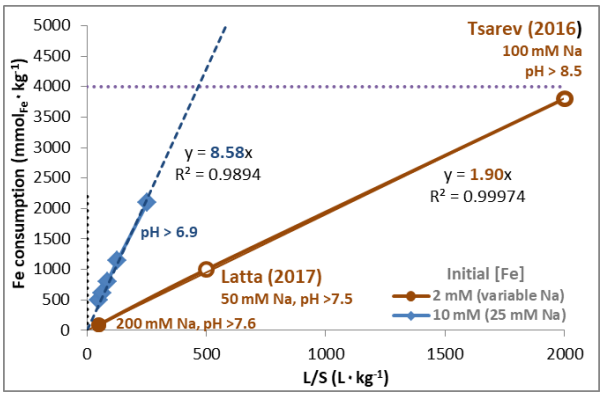

Figure 105 - Fe uptake as a function of the L/S ratio.

Open symbols: data from Tsarev et al. (2016) and Latta et al. (2017)

The same linear relationship can be seen when representing the Fe uptake as a function of the initial Fe concentration (at fixed L/S ratio, above pH 6.9, Figure 106 left), in this case the slope of the linear regression being relatively close to the value of the L/S. This trend notably changed as the Fe concentration was increased, but it must be emphasized that the final pH in these latter experiments was also notably affected (lowered by ~1 unit). One may expect notably higher Fe uptake if the pH would have been maintained above pH 6.9 (e.g. using higher MOPS buffer concentrations), as reported by Tsarev et al. (2016). At such lower pH (6.0-6.2), the Fe uptake (Figure 106 left), and, therefore, the final Fe concentration (Figure 106 right), were proportional to the initial Fe concentration.

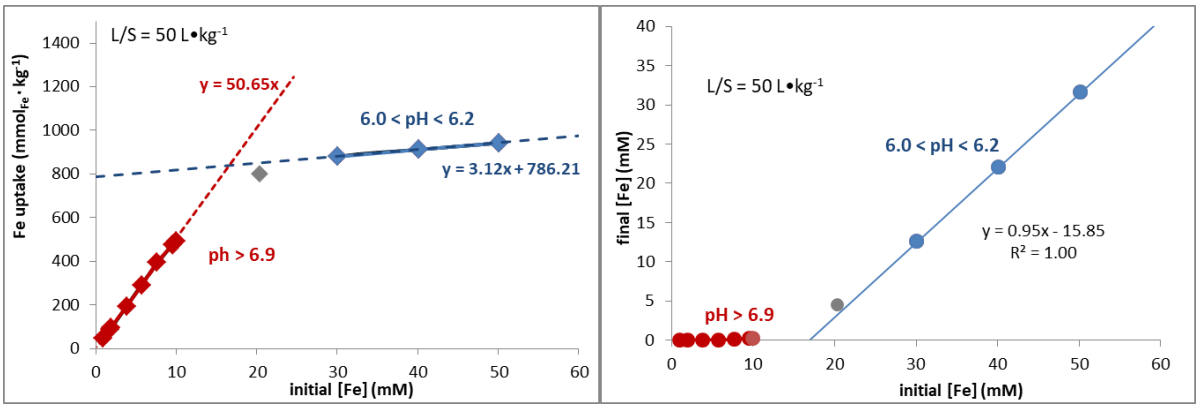

Figure 106 - (right) final Fe concentration and (left) Fe uptake as a function of the initial Fe concentration.

The effect of cation exchange was tested by increasing the Na concentration up to 2 M (vary Na experiments series, Figure 107 and Analytical results

Table G1 in Appendix G). At fixed initial Fe concentrations of 10 mM, Fe uptake decreased with increasing Na concentration from ~500 mmol·kg^{-1} down to a fixed value of ~340 mmol·kg^{-1} above 1 M Na (Figure 107 left). The [Na] threshold, where the minimum Fe uptake is achieved, may actually be lower (between 250 and 1000 mM, Figure 107 right). About 70% of the Fe uptake process observed at pH 6.2-6.5 appeared to be independent of the Na concentration. It can be hypothesized that the underlying process may involve surface sorption and/or precipitation, which are in fact not competing with the cation exchange process. Edge sorption (Bradbury and Baeyens, 1997b) is one of such additional Fe uptake mechanisms, but would account for at most 8% of Fe uptake at pH 6.5. Thus, ~60% of the Fe uptake can be attributed to another process than cation exchange or edge sorption, which is further explored below by the sorption model.

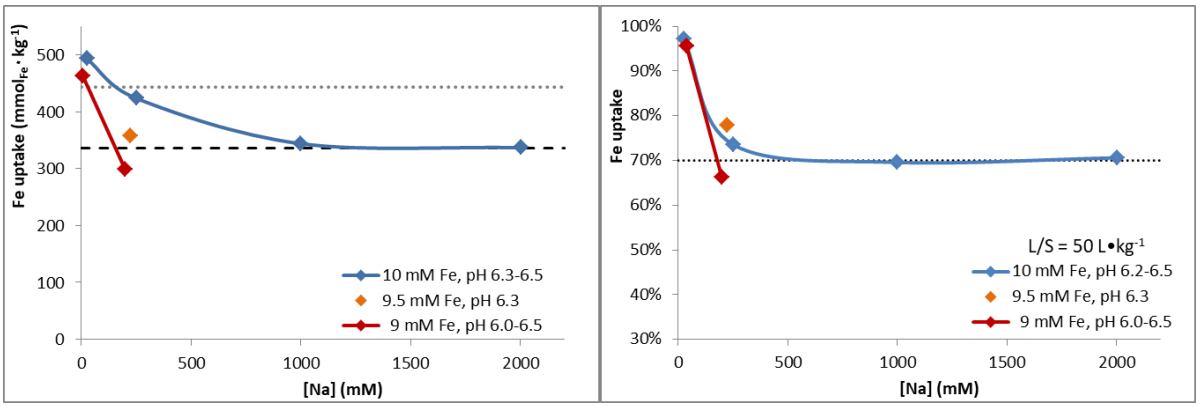

Figure 107 - Fe uptake as a function of sodium concentration, expressed either in (left) mmol of Fe per mass of sample or in (right) percent of initial aqueous Fe.

The final Na concentration was assayed in a few series of experiments (vary pH & Na and vary pH). Fe uptake increased linearly with the pH between pH 4.3 and pH 6.2 and reached a pseudo-plateau between pH 6.2 and pH 6.9 (Figure 108 left). In parallel, the amount of extracted Na decreased linearly with increasing pH on the entire explored pH domain (pH 4.3 to 6.9), which indicated that cation exchange decreased with increasing pH. At pH 4.3, the amount of extracted Na was actually equal to the Fe uptake (in terms of equivalents, Figure 108 right), which is consistent with cation exchange being the main Fe uptake process at low pH. Contribution of cation exchange to the Fe uptake markedly decreased with increasing pH, down to only 20%, due to the increasing importance of pH dependent sorption processes and reduced cation exchange. At pH 6.5 the apparent contribution of cation exchange is 40%. This is consistent with the above observation that other major Fe consuming processes accounting for up of 70% of the Fe uptake occur in addition to the cation exchange process.

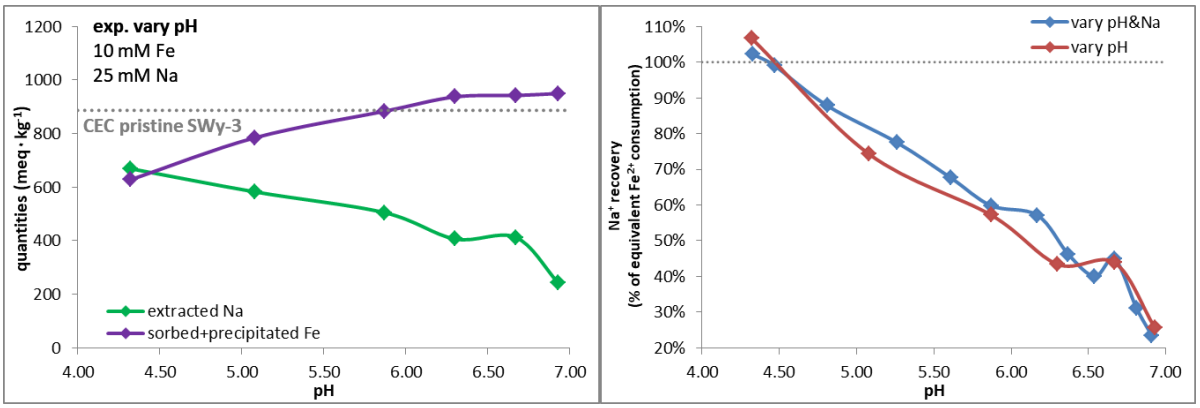

Figure 108 - (left) quantities of extracted Na and consumed Fe as function of pH and (right) corresponding Na^+/Fe^{2+} equivalent ratio as a function of pH.

Figure 109 depicts the contribution of the three Fe sorption processes 1) the cation exchange with Na, 2) the formation of surface complexes at the montmorillonite edge sites and 3) the newly introduced redox-sorption process linked to the Fe_{str} sites as calculated for the experimental series at a S/L ratio of 20 g/L with the sorption model presented in section 3.2.5. An example PhreeqC input file is given in Appendix G.2. In comparison with the experimental results, the following observations are made:

- The Fe/Na cation exchange is well characterized by a $logK_{sel\text{-}GT}$ between 0.5 and 0.8, as already shown by earlier investigations by Soltermann et al. (2014a) (*Figure 109*, top panel). With increasing pH, the absolute amount of exchanged Fe decreases. This is due to the increasing impact of surface complexation to edge sites and reaction with structural Fe(III) with increasing pH, which decreases the dissolved Fe(II) concentration controlling the cation exchange. This is

manifested in final Fe equilibrium concentrations decreasing by one order of magnitude from ~3 mmol·L^{-1} to 0.3 mmol·L^{-1} in the pH series T1-12 (Figure 109 top left, Table G1 in Appendix G).

- Surface complexation at the clay edge sites contributes to a minor degree to the total sequestrated Fe due to the limited site capacity. At the final equilibrium Fe(II) concentrations of >0.1 mmol/L, sites are basically saturated at pH values of ≥5.5.
- The redox sorption process successfully describes the increasing additional Fe sorption/sequestration over a pH range from 4.3 to 7.
- The redox sorption process successfully describes the increasing Fe sorption with increasing Fe concentrations until it accounts for approximately 75% of the structural Fe. At higher Fe concentrations, the model starts to underpredict the actually observed Fe uptake, pointing either to some additional process or to underestimation of the dependency on the Fe concentration. At the experimental pH of ~6 to 6.4 redox sorption approaches a fraction of ~80% of the structural Fe sites with Fe concentrations in the final solution of up to 35 mmol/L.
- At Na and Cl concentrations > 0.25 M, cation exchange of Fe(II) is largely suppressed. At these high Cl concentrations, Fe-Cl complexes constitute an important and increasing fraction to the Fe(II) speciation, reducing (together with the overall increased salinity) the activity of Fe^{2+}. This decreases the redox sorption in the model calculations. The comparison with the experimental data indicates, however, that the redox sorption process seems to be less dependent on salinity effects than suggested by the calculations.

The here applied simple redox sorption process may account for a maximum Fe uptake equivalent to the structural Fe content. Given the parallel contribution of cation exchange and surface complexation at the edge sites, Fe uptake exceeding either the cation/edge site capacity or redox sorption capacity may be observed. Fe uptakes exceeding both capacities were however observed in the experiment with extremely low S/L ratio, indicating, that additional precipitation reactions occur when the capacity of the structural Fe reaction exceeds a certain threshold.

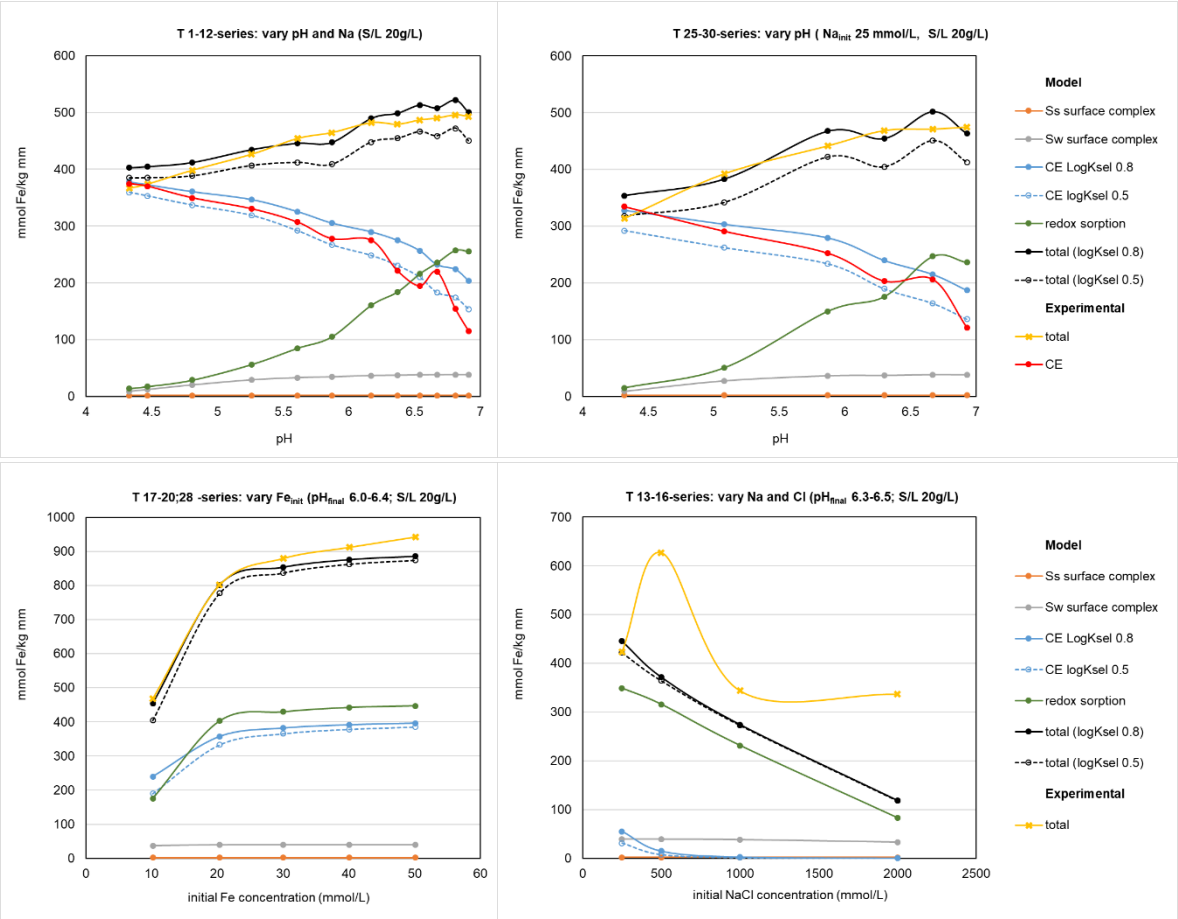

Figure 109 - Comparison of modelled Fe sorption in different batch experimental series with measured Fe sorption. Modelling was performed with the final solution composition. For the experiments in the bottom panel, no final Na measurements were available and initial values were used instead. CE was modelled with two different selectivity coefficients (log$K_{sel\text{-}GT}$ = 0.8 and 0.5). The experimental CE is calculated from the measured difference between initial and final Na in solution.

3.3.2.3 Experiments with isotopically purified ^{56}Fe

A part of the experiments employing high Fe concentrations (above 9 mM Fe, exp. ^{56}T2, ^{56}T3 and ^{56}T6, Table 27) resulted in lower pH than anticipated (below pH 3) due to the higher acidity of the ^{56}Fe stock solution (Appendix E.2) and despite the use of doubled MOPS buffer concentrations with regard to the other batch experiments (50 mM, section 3.3.2.1).

Table 27 - Results of batch experiments using ^{56}Fe.

xp.	L/S	[^{56}Fe]		Fe^{2+} uptake			pH		$[Na^+]_{aq}$	Fe$_{str}$ reduction[c]	oxidation of Fe$_{sorb}$
		initial[a]	final[b]				initial[a]	final[b]	initial[a]		
	(L·kg^{-1})	(mM)	(mM)	(%Fe$_{aq}$)	(mmol·kg^{-1})	(%Fe$_{str}$)			(mM)	(%Fe$_{str}$)	(%Fe$_{sorb}$)
^{56}T1	50.6	1.8	0.1	96.6%	85.9	17%	6.69	5.81	187.1	20%	100%
^{56}T2	49.8	9.1	7.5	18.2%	82.8	16%	2.28	2.49	198.5	5%	6%
^{56}T3	49.9	18.3	15.9	13.3%	121.8	24%	1.79	1.88	212.8	9%	22%
^{56}T4	50.2	1.9	0.0	99.7%	93.4	18%	8.06	7.61	187.2	21%	100%
^{56}T5	50.0	9.0	3.1	66.2%	299.2	59%	7.09	6.01	198.4	36%	57%
^{56}T6	49.9	18.3	15.6	14.7%	134.3	26%	2.53	2.87	212.8	10%	24%

a. In stock solution a few minutes after preparation

b. In supernatant after 48 hours
c. Determined by Mössbauer spectrometry (4% in pristine clay)

All experiments resulted in a substantial decrease in Fe(II) concentrations and a more or less significant pH shift (Table 27). The pH increased in experiments initiated at low pH (pH <3) and decreased in experiments initiated at higher pH (pH >6). Various levels of Fe uptake were obtained depending on pH and Fe concentration, representing in any case only a portion of the amount of Fe_{str} (20% to 60%, Table 27). With low initial Fe(II) concentrations in solution (exp. ^{56}T1 and ^{56}T4), almost all Fe (>99%) was sorbed onto the clay. Conversely, at higher Fe(II) concentrations (^{56}T2, ^{56}T3, ^{56}T5, and ^{56}T6), only a minor portion of Fe(II) was sorbed onto the clay, and equivalent or even higher quantities of Fe(II) (from the reacted solution remaining with the sample following centrifugation) were precipitated with the clay during freeze drying (Fe_{add}, Appendix E.1).

Mössbauer spectroscopy revealed substantial reduction of Fe_{str} in most samples (excluding ^{56}T2), accounting for reduction by Fe_{sorb} at any pH (Table 27). At low Fe concentrations and initial pH >6 (exp. ^{56}T1 and ^{56}T4), Fe_{str} reduction extent corresponded to the Fe uptake (*i.e.,* complete electron transfer between Fe_{str} and sorbed Fe). But notably lower reduction extents were reached in experiments with higher Fe concentrations. Reduction extents were strongly influenced by solution pH (limited below pH 5, and higher above pH 5).

Calculations of the contributions of the different sorption processes for the Fe uptake in experiment ^{56}T5 (final pH of 6, final Fe and Na concentrations of 3.1 mM/L and ~200 mM/L, respectively) indicate that 207 $mmol_{Fe}·kg^{-1}$ are associated with the redox sorption process. If each Fe sorbing by this process is considered to transfer an e^- to the structural Fe in the montmorillonite, this corresponds to a final calculated Fe_{str} reduction level of 38%. This is well in line with the Fe_{str} reduction level of 36% determined experimentally by Mössbauer spectroscopy for the dried samples (Table 27). For the experiments at a pH < 3, the model calculations predict negligible redox interaction. Taking into account the model and measurement uncertainties, this is broadly in line with the observations for the dried samples. At very low final Fe concentrations, the model fails to predict the extent of sorbed Fe (strong underestimation), which may give an indication that the redox sorption process is less reversible than classical surface complexation reactions.

Fe_{str} reduction extent primarily depends on the quantity of Fe_{sorb}. Both parameters depend on pH and on the ratio between dissolved Fe_{aq} and Fe_{str} (Figure 110). At fixed Fe_{aq}:Fe_{str} ratio, Fe_{str} reduction increased linearly with pH (cf. data from Latta et al. (2017), Figure 110 left), logically as observed for Fe_{sorb} (*Figure 104*). But pH dependency was also seen at fixed Fe_{sorb} content (cf. exp ^{56}T1 and ^{56}T2, Table 27). As discussed in the previous section, at low pH (^{56}T2), Fe sorption is dominated by cation exchange, whereas at higher pH and simultaneously lower final Fe concentrations (^{56}T1), the sorption process is dominated by the pH dependent surface complexation reactions. The different observed reduction extent in both experiments thus supports the assumption that structural Fe reduction is primarily associated with an additional interaction process and does not occur in notable amounts for Fe involved in cation exchange. At low to moderate Fe_{aq} concentrations regarding Fe_{str} (below 1:1) and above pH 6, most Fe_{aq} (above 94%, Table 27) got sorbed to the clay, and a notable quantity of the resulting Fe_{sorb} (above 60%) transferred electrons to Fe_{str} (Figure 110 right). Such levels were consistent with the above observation that around pH 6.3 and a ratio of 1:1, up to ~70% of the Fe uptake was due to other process(es) than cation exchange.

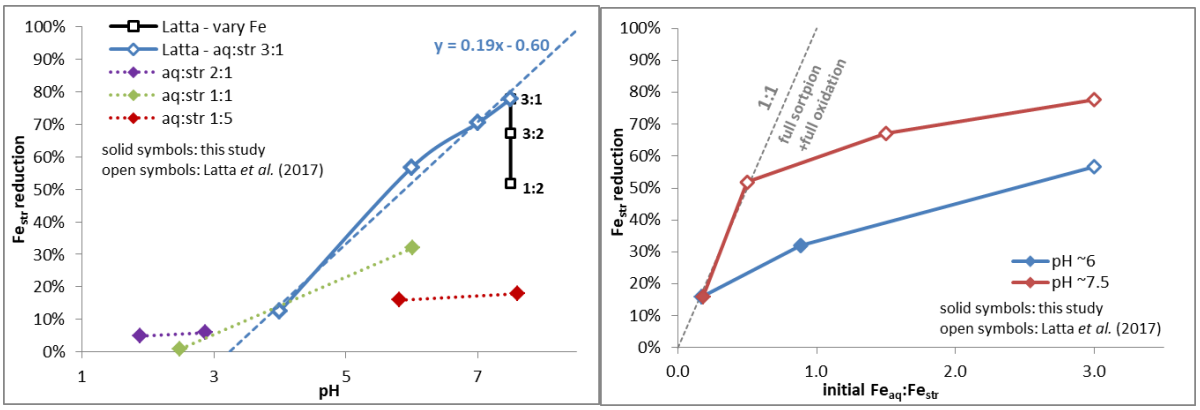

Figure 110 - Fe_{str} reduction achieved (left) as function of pH and (right) as a function of the initial ratio between aqueous Fe and structural Fe.

3.3.2.4 Reaction mechanism

Different reactions can occur between Fe^{2+} and Na-SWy-3. Below pH 4.5, cation exchange involving Na and Fe(II) is the dominant Fe uptake process (Bergaya et al., 2013):

$$Fe^{2+} + 2\,NaX \leftrightarrow FeX_2 + 2Na^+ \qquad (9)$$

Fe(II) can also undergo surface complexation reactions on edges sites of clay sheets (Bradbury and Baeyens, 1997b):

$$\equiv OH + Fe^{2+} + OH^- \leftrightarrow \equiv OFe^+ + H_2O \qquad (10)$$

This reaction depends on pH, but remains, in the experimental conditions, minor regarding cation exchange at the Fe concentrations applied here in the batch experiments (at most about 40 mmol·kg^{-1} of Fe uptake at pH 6.9). Earlier studies have hypothesized that edge sorption at the vicinity of Fe_{str} sites could be accompanied by electron transfers to certain "reactive clay edge functional groups" (Gehin et al., 2007) or more specifically to neighbouring Fe_{str} edge sites (Soltermann et al., 2014a; Soltermann et al., 2014c):

$$Fe^{3+}_{str\,s} \equiv OH + Fe^{2+} + OH^- \leftrightarrow Fe^{2+}_{str\,s} \equiv OFe^{2+} + H_2O \qquad (11)$$

Fe_{str} is located as isolated sites within the octahedral sheet of montmorillonites (Gates, 2005; Vantelon et al., 2001). The amount of edge Fe_{str} sites is too limited to account for the extended reduction reported recently (Latta et al., 2017), and in the present study (Table 27 and *Figure 110* right). The probability of neighbouring Fe_{str} sites, allowing electron transfer from one Fe_{str} site to another, is also rather low. Extended $Fe(III)_{str}$ reduction in montmorillonite by $Fe(II)_{aq}$ (above 70% reduction, (Latta et al., 2017)) indicates that electron transfer occurs at the basal surface on almost any Fe_{str} site. Reduction of Fe_{str} induces an increase of the negative layer charge (Stucki et al., 1984) which is compensated at part by an increase of CEC and at part by dehydroxylation (Hadi et al., 2013; Lear and Stucki, 1985). Dehydroxylation occurs because Fe_{str} reduction induces layer distortions as well and cannot only be compensated by a CEC increase. Dehydroxylation acts therefore both as a charge compensation and as a distortion lowering process. For the experimental conditions met in most experiments of the present study (Fe_{aq}:Fe_{str} <2:1), this could be well quantified by a simple surface complexation reaction comparable to equation (10). In a more general view, the complex interaction of Fe_{str} reduction by Fe_{aq}, can be envisioned as a mechanism where the reduction of Fe_{str} is coupled to the precipitation of a Fe(III) hydroxide at the surface following:

$$\left\{Fe^{3+}OH\right\}_{str} + Fe^{2+} + 2OH^- \leftrightarrow \left\{Fe^{2+}OH_{(1-n)}\right\}^{(1-n)-}_{str} [Fe^{3+}OH_{(2+n)}]^{(1-n)+}_{sorb} \qquad 0 \le n \le 1 \qquad (12)$$

The Fe(III) hydroxide would be "anchored" to the clay surface, at part due to its positive electrostatic charge compensating the negative charge induced by Fe_{str} reduction, and at part by sharing *n* OH_{str} groups with the clay structure. Following this clay reduction mechanism, the negative layer charge is partly compensated by a non-exchangeable immobile sorbate (i.e. not a CEC increase *sensu stricto*) and by a partial dehydroxylation of the reduced Fe_{str} site (the OH_{str} groups would not leave the clay structure, but would be instead shared between the two structures). In case where *n* = 0, the two structures would be only linked by electrostatic forces. This means the clay structure would be more and more distorted as Fe_{str} sites reduction progresses. In case where *n*= 1, $Fe(OH)_3$ would precipitate at the surface, and the clay would get reduced without layer charge increase. The value of *n* may either be at a fixed value between 0 and 1, or may vary in this range as a function of Fe_{str} reduction extent (similarly to the ratio between CEC increase and dehydroxylation (Hadi et al., 2013), or to the variation of the reduction potential of Fe_{str} (Gorski et al., 2012)).

If all Fe_{str} was reactive toward Fe_{aq}, the mechanism in Eq. (12) could account for a maximum uptake of ~500 mmol·kg^{-1} and result in 100% reduction of Fe_{str}. Supplementary mechanism(s) must therefore be invoked to account for the notably higher Fe uptake observed for instance in the vary-L/S experiments (~2000 mmol·kg^{-1} at pH 7.0, Figure 103 right). The Fe(III) hydroxide could further act as a seed for precipitation of more Fe^{2+}, following a similar mechanism as for green rust (GR, Génin et al. (2005)):

$$\left\{Fe^{2+}OH_{(1-n)}\right\}^{(1-n)-}_{str}\left[Fe^{3+}OH_{(2+n)}\right]^{(1-n)+}_{sorb} + \frac{n}{1-n}Fe^{2+} + \frac{n+n^2}{1-n}OH^- \leftrightarrow \left\{Fe^{2+}OH_{(1-n)}\right\}^{(1-n)-}_{str}\left[\left(Fe^{2+}_{\frac{n}{1-n}}Fe^{3+}\right)OH_{\frac{2}{1-n}}\right]^{(1-n)+}_{sorb} \qquad 0.5 \le n \prec 1 \tag{13}$$

This would result in an association between a cationic clay (the smectite) and a group of anionic clay particles (the surface Fe sorbate/precipitate, Figure 111). GR adopts the structure of Layered Double Hydroxides (LDH), for which the value of *n* is often reported to vary between 0.66 and 0.80 (Génin et al., 2005; Hadi et al., 2014; Sideris et al., 2012). In the present case, this range of *n* values may be extended to 0.5, to account for the precipitation of only one supplementary Fe^{2+} atom. The highest reported Fe(II) uptake by a montmorillonite (Mau-1, slightly poorer than SWy-2 in Fe, Tsarev et al., 2016) was ~3800 mmol·kg^{-1} above pH 8.6, which corresponds to about 10 times the Fe_{str} content in the montmorillonite. It can be argued that, given the high pH, such a high Fe uptake may have been caused by the side precipitation of separate Fe(II) hydroxides. Such separate precipitation does however not happen below pH 7 (see blanks in *Figure 104*). The highest Fe uptakes measured in the present experiments (~2000 mmole·kg^{-1} at pH 7.0, *Figure 104* right) can be deemed to be predominantly due to the surface precipitation of tiny GR domains (as proposed in equation (13) and on Figure 111). Such uptake corresponds to 4 times the content in Fe_{str} of SWy-3, or an n value of 0.80, consistent with the maximum generally reported for the LDH structure (Hadi et al., 2014; Ma et al., 2011).

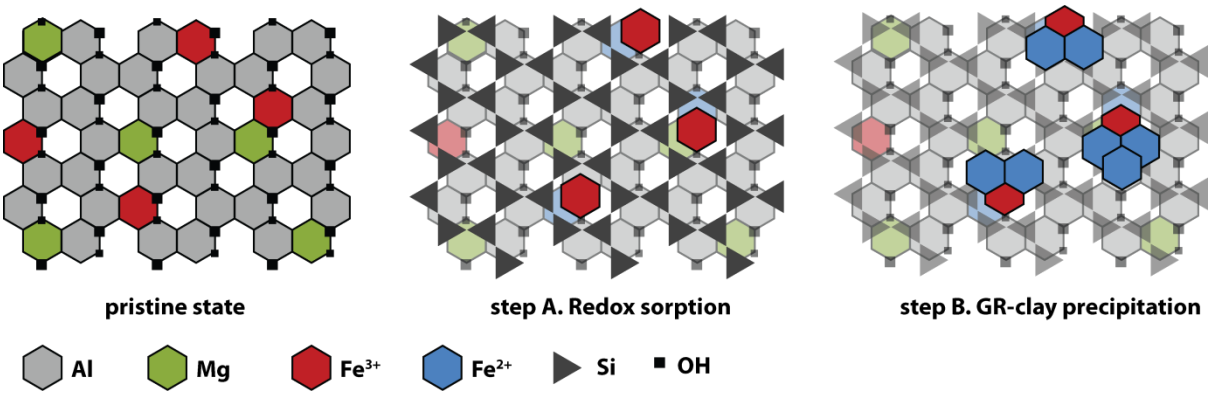

Figure 111 - Scheme of the SWy-3 octahedral and upper tetrahedral layer in its pristine state, and as external Fe progressively undergo RS and GR-clay precipitation (note that similar process can occur on the other side of the clay sheet as well).

3.3.2.5 Conclusion of batch experiments

The results of the batch experiments in which aqueous Fe^{2+} reacted with montmorillonite are in line with previously published similar studies (Latta et al., 2017; Tsarev et al., 2016). Fe^{2+} uptake by clay depends on multiple factors, especially on the pH and on the relative Fe_{aq} and Fe_{str} concentrations and the Fe/Na ratio (or of other competing cations). At low pH (below pH 4.5), cation exchange largely dominates the Fe_{aq}-clay interaction. As the pH increases above 6, other Fe uptake reactions become successively more important relative to cation exchange. Surface complexation at edge sites accounts only for a minor portion of the Fe uptake, due to the limited site capacity. A major part of the Fe uptake observed at pH values between 6 and 7 is due to other reactions, involving electron transfers toward Fe_{str} and at higher Fe loadings presumably the stepwise surface precipitation of tiny GR-like Fe hydroxide domains at the vicinity of the reduced Fe_{str} sites scattered on clay surfaces. This can lead to high Fe uptake by the clay, up to four times its CEC.

The Fe uptake process could be adequately modelled for the largest range of experimental conditions in the present study. It included a rather simple pH dependent surface complexation reaction linked to Fe_{str} sites as analogue for the proposed reduction-sorption process and accounted for the additional Fe uptake by the montmorillonite, which exceeded cation exchange and edge site surface complexation. Deviations between model and experimental conditions at high salinities indicated that this process is less affected by Fe speciation than suggested by the calculations. At high L/S ratios, the underestimation of the Fe uptake by the model may be linked to the clay-GR precipitation reaction, not included in the sorption model.

Conditions explored in the batch experiments (high Fe concentrations and high L/S) were in general quite different from the envisioned *in situ* repository conditions (lower Fe fluxes, higher salinity, compacted clay). However, substantial Fe_{sorb}:Fe_{str} ratios can be expected in repository conditions (1:10 in the blue zones of the FEBEX *in situ* test, Hadi et al., 2019b) which is close to the range explored in various batch experiments (*e.g.* 1:5 in ^{56}T1 and ^{56}T4). The aim of the diffusion experiments is to reach Fe_{sorb}:Fe_{str} ratios varying in such range (1:10 to 1:5), with clear Fe diffusion fronts and sufficient contrast between the input interface, the output interface and the original material.

3.3.3 Diffusion experiments

3.3.3.1 Experiments main events

The main events in both experiments are listed in Table 28. In the early stage of exp. #1, sampling of the output reservoir was not as frequent as in the input reservoir (cf. times in Table H1 and Table H2 in Appendix H). Fe breakthrough in exp. #1 was detected only 2-3 months after Fe would have started to be detectable in solution (above 0.005 mM). It was thus decided to first dismantle exp. #2 a few weeks following Fe breakthrough, when the maximum Fe gradient within the core would be expected.

Exp. #1 was conducted further until the input tube eventually broke and most of the remaining Fe input solution was lost. The experiment was then isolated for a few weeks (disconnected from reservoirs and closed). Solution circulation was started again a few weeks after, using Fe-free solutions (same solution as pre-equilibration ones, with larger volume of 1 L to back-exchange the Fe from the clay core). The extracting solution was renewed twice, in order to accelerate Fe out-diffusion.

Table 28 - Main events in the two diffusion experiments

Date (dd.mm.aaaa)	Days from start of Fe diffusion (month)	Event
Experiment #1		
07.01.2021	-4.2	Start of circulation of the Fe-free pre-equilibrium solution at bottom of the core.
12.03.2021	-2.1	Circulation of the Fe-free pre-equilibrium solution at top of the core.
13.05.2021	0.0	Start of ^{56}Fe diffusion from the bottom of the core
23.08.2021 -23.09.2021	*3.4-4.4*	Projected time of the Fe breakthrough
09.06.2022	13.1	Loss of 70% of the Fe input solution due to tube leaks, Fe diffusion experiment stopped, clay core disconnected from reservoir and isolated.
24.06.2022	13.6	Change of top and bottom reservoir for 1L Fe free solutions.
02.09.2022	15.9	Renewal of Fe free solutions
08.12.2022	19.1	Renewal of Fe free solutions
30.01.2023	20.9	Dismantling of experiment #1
Experiment #2-		
30.12.2020	-9.6	Start of circulation of Fe-free pre-equilibrium solution
12.03.2021	-7.5	Circulation of the Fe-free pre-equilibrium solution from top of the core.
08.06.2021	-4.5	Beginning of progressive pressing of the clay core
08.07.2021	-3.5	End of progressive pressing of the clay core
22.10.2021	0.0	Start of ^{56}Fe diffusion from the bottom of the core
26.04.2022	6.2	Dismantling of experiment #2

3.3.3.2 Solution data

Reservoirs pH

During the pre-equilibration phase, the solution was buffered by 50 mM MOPS acid:base 1:1 buffer to a pH of 7.25. This solution became the output reservoir solution during the in-diffusion phase. The solution in the input reservoir in the in-diffusion experiment was buffered by 50mM MOPS base, which together with the added 10 mM $^{56}FeCl_2$ resulted in a pH of 7.27, thus similar to the pre-equilibration and output reservoir solution. The same results were observed in both experiments (Figure 112). The pH in the input reservoirs remained stable throughout the whole course of the experiment, although the Fe concentration decreased (by up to 70% in experiment #1). The pH in output reservoirs slightly increased (by 0.1 units) in the first 100 days, but eventually decreased slightly below 7.0. This decrease coincides with the Fe^{2+} breakthrough in the output reservoirs and can be attributed to the acidic properties of Fe^{2+} and to deprotonation of the edge sites within the core.

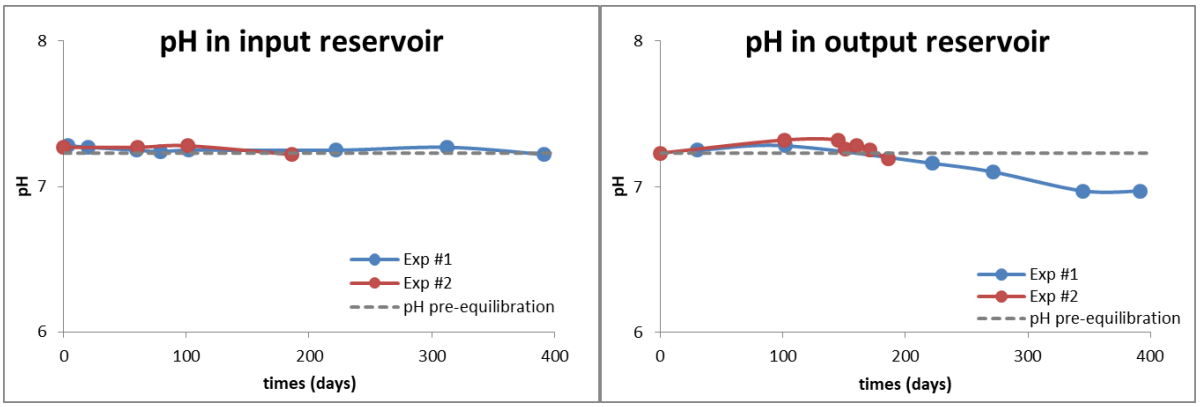

Figure *112 - Evolution of pH in (left) input reservoirs and in (right) output reservoirs.*

Data in Table H6 and Table H7 in Appendix H.

Fe concentration in reservoirs

Very similar trends were observed in both experiments during the Fe diffusion phase (Figure 113 left). Exp. #1 was slightly in advance (by only 11 days difference after 160 days of experiment) regarding exp. #2, with slightly faster decrease in input Fe concentration and increase in output Fe concentration, despite the differences in core length and density/porosity. Exp.#2 was interrupted and dismantled first, after 6 month of Fe circulation and about two months following Fe breakthrough. About 55% of Fe^{2+} in the input reservoir diffused in the core, and 1.4% reached the output reservoir.

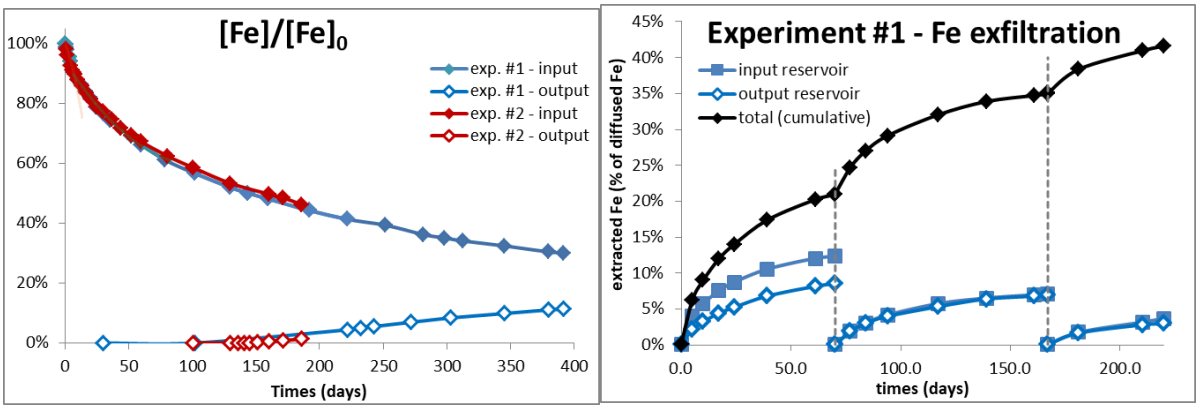

Figure 113 - Evolution of the Fe concentration for both experiments #1 and #2 in and out diffusion phases (left) and out-diffusion phase for experiment #1 (right). Data in Table H1, Table H2, and Table H3 (right) in Appendix H. Dashed grey lines indicate the time where reservoirs contents were renewed with Fe free solutions.

During the Fe infiltration phase in exp. #1, 65% of input Fe diffused into the core, and 27% diffused out in the output reservoir. 38% of input Fe was thus retained in the core. About 40% of this in-diffused Fe was recovered over a period of 7 months, before the experiment was stopped (Figure 113 right). This indicated that the diffusion process is largely reversible. After two months of back-diffusion, the evolution in the two reservoirs was the same.

Fe isotopic distribution in reservoirs

A progressive change of the isotopic composition of Fe was observed in all solutions (Figure 114). In the input reservoirs, the proportion of ^{56}Fe decreased to the benefit of ^{54}Fe and ^{57}Fe. In the output reservoir (only analysed for exp. # 1), the changes in the Fe isotopic composition were more pronounced and the trend reversed. These observations can be attributed to the enrichment of the porewater solution in ^{54}Fe and ^{57}Fe due to isotopic exchange with the Fe (oxyhydr)oxides impurities (Handler et al., 2014; Rosso et al., 2010) in the solid sample (9% of total Fe in solid, section 3.3.1 and Table F2 in Appendix F). All Fe in the output reservoir diffused through the clay core, which altered its isotopic composition,

whereas the isotopic modified Fe back-diffusing from the core into the input reservoir became diluted in the initial pure ^{56}Fe solution.

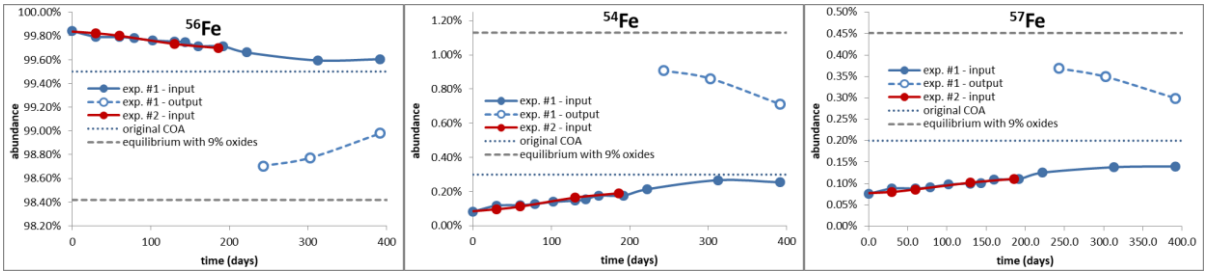

Figure 114 - Evolution of the isotopic abundances of Fe in the input reservoirs of the two experiments, and in the output reservoir of exp. #1. Blue dotted lines indicate the values displayed on the COA from supplier. Grey dashed lines indicate the equilibrium values reached in case of full isotopic exchange with the 9% Fe (oxyhydr)oxides (regarding total Fe in solid) present in the clay core (assuming natural isotopic distribution in the (oxyhydr)oxides).

Assuming natural isotopic proportions in the Fe (oxyhydr)oxides impurities in the solid sample (Meija et al., 2016), the observed changes in isotopic composition accounted for exchange with 15% of the Fe in (oxyhydr)oxides (*i.e.,* 1.5% of total Fe in solid). These results indicated limited isotopic exchange, and that $^{57}Fe_{aq}$ remained very low throughout the whole experiments, remaining even lower than what was indicated on the supplier COA (Certificate Of Analysis). The contribution from solution and the sorbed fraction could therefore be neglected in the Mössbauer analysis.

Water tracer (D_2O) and anionic tracer (Br^-) concentration in reservoirs

Very similar trends were observed in both exp. #1 and exp. #2 (Figure 115). Contrary to the case of Fe, exp. #2 appears slightly in advance regarding exp. #1 (but within the error), with a faster increase in output concentration despite the slightly longer distance. For D_2O a depletion in the input reservoir of 8% was reached after 185 days in exp. #2, and 11% after 400 days in exp. #1. Clearly less through diffusion of the anionic tracer was observed. Data in input reservoirs are scattered, but a slight increase of 2-3% was observed in the output reservoirs.

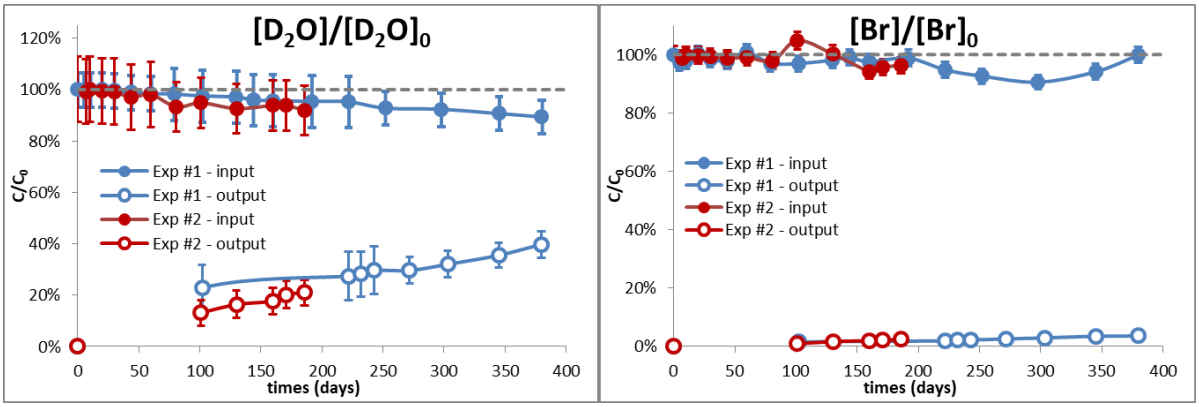

Figure 115 - Evolution of the concentration of (left) D_2O and (right) Br^-. Data in Table H6 and Table H7 in Appendix H.

Na and Cl concentrations in reservoirs

Very similar trends were observed in both experiments (Figure 116). In input reservoirs, Na concentrations rapidly increased. Na concentrations in output reservoirs remained constant within error. These changes could be ascribed to out-diffusion from the clay core, following cation exchange with Fe(II), and the concentration gradient (reverse to that of Fe). Cl concentrations in input reservoirs seemed to eventually decrease after 200 days. Instead, in output reservoirs, it progressively increased.

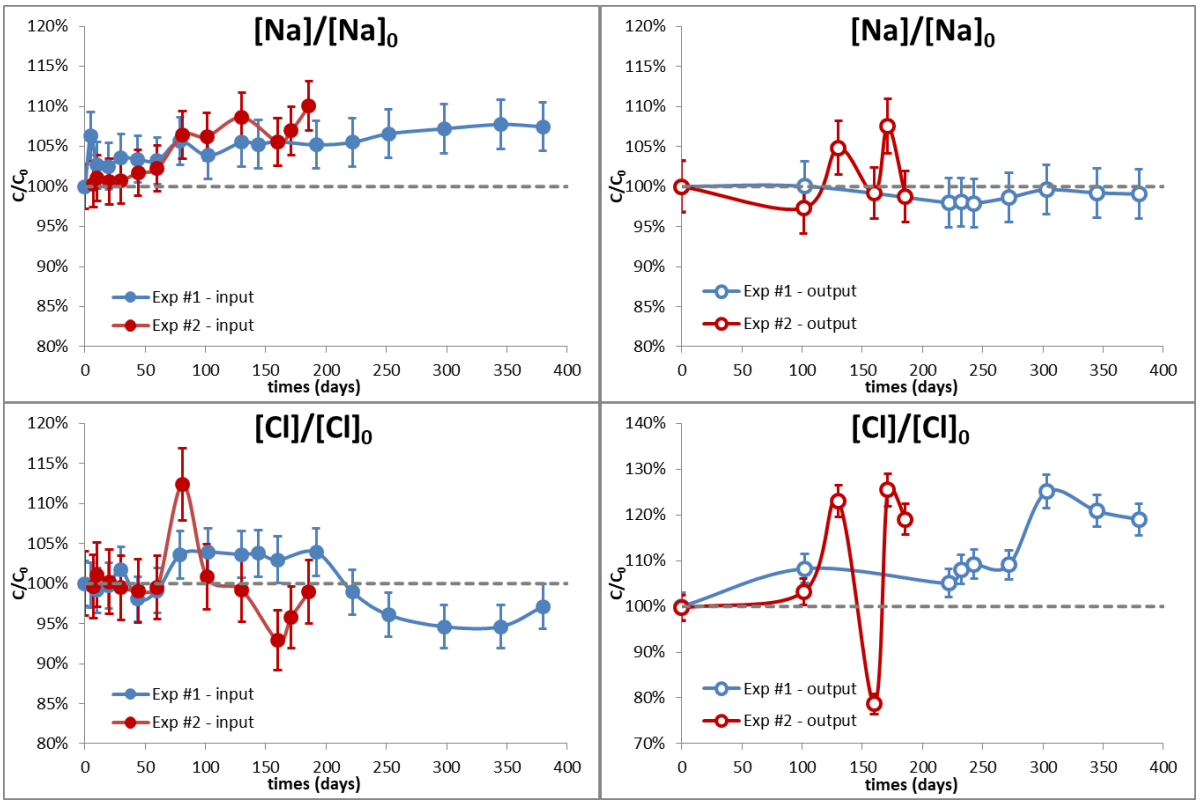

Figure 116 - Evolution of Na and Cl concentration in (left) input reservoirs and in (right) output reservoirs. Data in Table H6 and Table H7 in Appendix H.

3.3.3.3 Clay core data

Swelling pressure (P_S)

After saturation and equilibration with the reservoirs, P_s in experiment #1 was 2190 kPa (dry density 1273 kg·m^{-3}), and 1980 kPa in exp #2 (dry density 1061 kg·m^{-3}). Extrapolation of data from Karnland et al. (2006) resulted in 2170 kPa and 660 kPa for experiments #1 and #2, respectively. Although literature data and extrapolation especially at low densities are prone to large errors, the exceptionally high measured P_s of experiment #2 might be due to the applied volume reduction during saturation and still ongoing density homogenisation afterwards, supported by a still decreasing P_s and a large gradient in the water content profile (*Figure 117*). In addition, a several mm large pore was detected during *post-mortem* slicing of the core, also indicating incomplete homogenisation. Before Fe in-diffusion was started, P_s in both experiments were not stable, but changed at a much slower rate than during early saturation. As expected, exchange of Na in the core with Fe decreased P_s in both experiments by 4 to 9%. P_s is lower with divalent than with monovalent cations on the exchanger (at experimental density and ionic strength (Karnland et al., 2006)). This might be simply due to the fact that 50% less interlayer cations are needed to compensate the same charge, and the interlayer distance can, thus, decrease compared with monovalent cations.

During Fe out-diffusion in experiment #1, P_s increased strongly and above the value before Fe in-diffusion. This, as well as the pressure increase by 10% during the second half of the Fe in-diffusion interval, might indicate a still ongoing saturation, or might be due to a higher pumping pressure (see below). Saturation, homogenisation, and equilibration of such thick cores are very time consuming, which is why cores in the mm range are preferred for pressure measurements.

The increase of P_s during Fe out-diffusion, to unexpected high values, suggests no substantial irreversible decrease of the swelling properties of the clay.

The pressure induced by the pump circulating the solutions seemed also to have an influence on the measured P_S. In exp. #1, input tube failure was followed by a significant drop (-10%) of the swelling pressure. Following tube change and pump restart, a higher pressure was obtained (+5%).

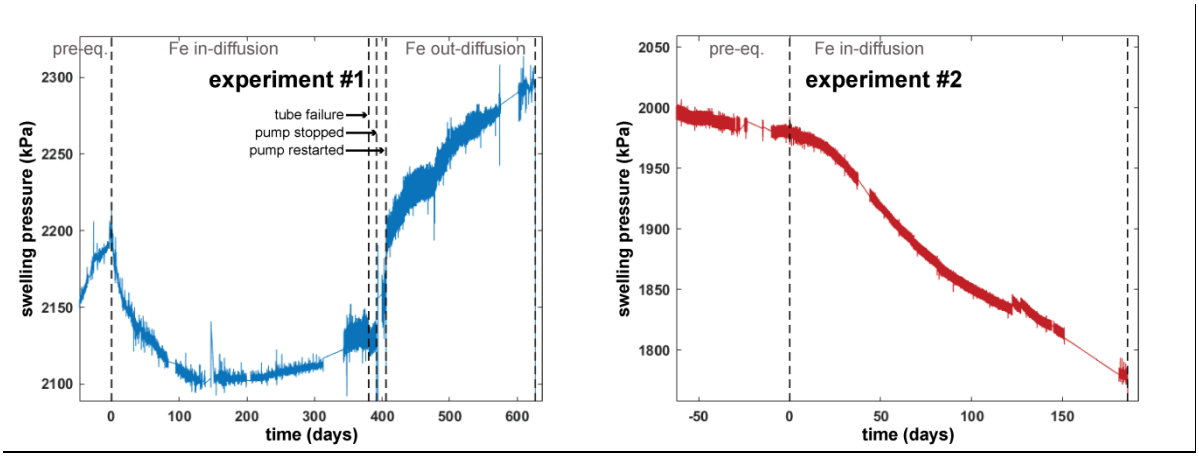

Figure 117 - Evolution of swelling pressure in the two diffusion experiments.

Pictures from dismantling of the two diffusion experiments

Similar observation could be made regarding both clay cores. There were visual indications with notable colour contrast between vicinities (<2 mm) of the filters (especially at the inlet) and the bulk of the core (Table 29, Figure 118, Figure 119).

In exp. #2, a thin (few tens of µm at most) green layer could be seen at the direct contact with the filter (Figure 118), followed by a slightly thicker (only few hundreds of µm) layer of orange colour. The interface between input filter and first slice was damaged during sampling. A portion of the green layer remained stuck on the filter and was collected separately from the first 2.6 mm slice (limited amounts of sample, for Mössbauer analysis only). Beyond the thin orange layer, the sample colour was between dark green and brown. This same colour was observed throughout the entire sample, until the last slice. A thin (few tens of µm at most) orange/brown layer was also observed at the direct contact with the output filter.

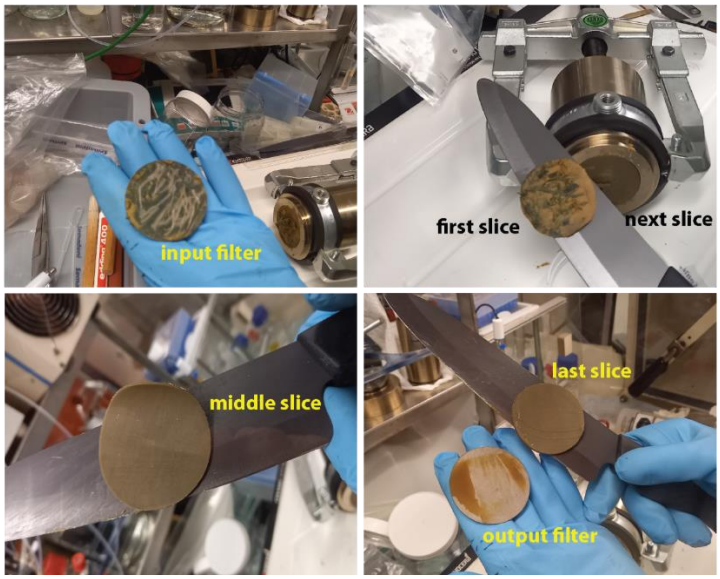

Figure 118 - Pictures from dismantling of experiment #2.

In exp. #1, a thin (few tens of µm at most) dark blue/black layer could be seen at the direct contact with the filter (Figure 119), followed by a slightly thicker (only few hundred µm at most) layer of orange colour. The first slice was ~0.5 mm thick. The orange colour persisted up to a portion of the second slice

(~1.2 mm thick). The interface between input filter and first slice was less damaged compared to exp. #2 and a smaller portion of the dark layer remained stuck on the filter and was again collected separately from the first slice (for Mössbauer analysis only). The colour transition was observed up to the third slice (1.5 mm thick). The same colour was then observed throughout the entire sample, until the last slice. This colour appears similar as in exp. #2, between dark green and brown, but lighter. A thin (few tens of µm at most) orange/brown layer was also observed at the vicinity of the output filter. The surface at the direct contact with the output filter appeared red.

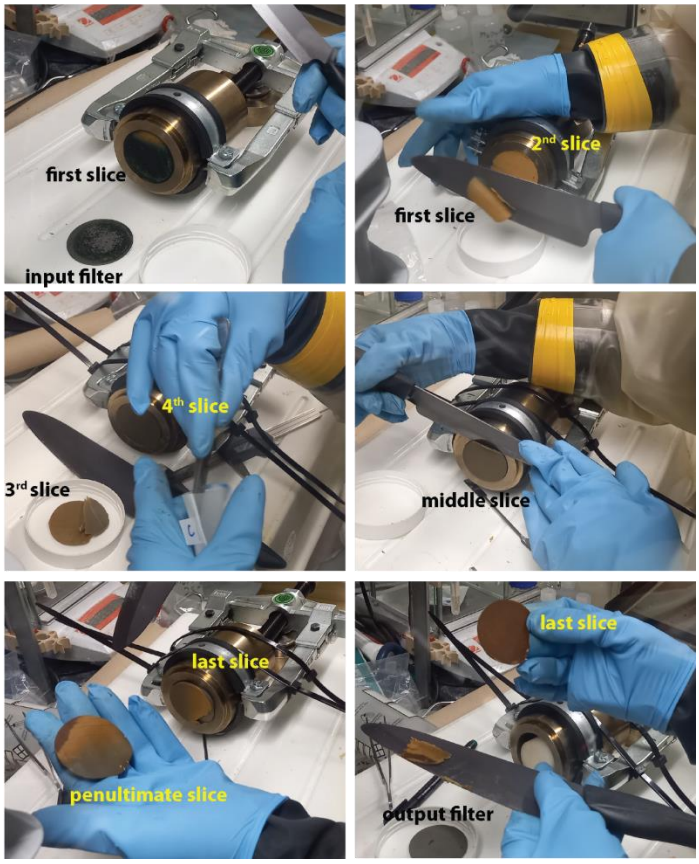

Figure 119 - Pictures from dismantling of experiment #1.

Table 29 - Notable zones contrasting with the bulk of the cores.

	Exp. #1	**Exp. #2**
Input green/black layer	few 10s of µm	few 10s of µm
Input orange layer	~1 mm	few 100s µm
Output orange/red layer	Few 10s of µm	few 10s µm

Water content in clay cores

Notable contrasts could be observed between and also in each of the two experiments (Figure 120). Water content was globally higher in exp. #2 than in exp. #1, which is consistent with the difference in dry density (lower in exp. #2). In exp. #1, the two outermost layers had a higher water content (+5-10%) than the bulk of the sample, where the gravimetric water content was very homogeneous (44.4 wt.% in average). In exp. #2, the water content increased linearly from input to output side (53 wt.% to 63 wt.%). This indicates that dry density was not homogeneous in this clay core. It was calculated at 1044 $kg \cdot m^{-3}$ based on cell geometry and sample mass, but it varied between 1000 and 1150 $kg \cdot m^{-3}$ from input to output side of the core. Two reasons could explain such gradient. On the one hand, it could be due to the fact that this core was progressively compressed during the water saturation sequence (with a piston on the top, section 3.3.3.1). On the other hand, it could be related to chemical gradients between the input (high Fe, lower Na) and the output (low Fe, higher Na) as further shown by the chemical analysis of this clay core.

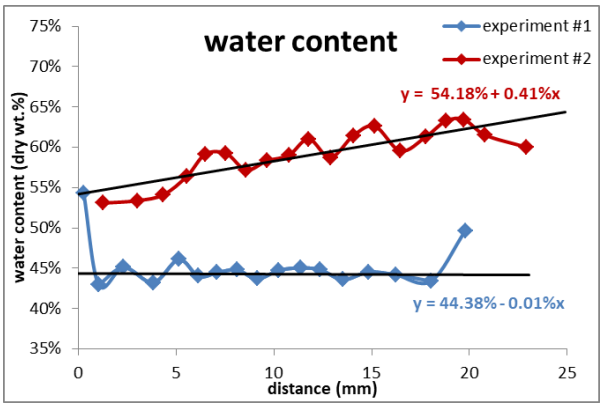

Figure 120 – Gravimetric water content in the clay cores of the two diffusion experiments. Data in Table I1 and

Table I2 in Appendix I.

Fe concentration in clay cores

Fe uptake (Figure 121) was calculated from acidic digestion data (Table I1 and

Table *I2* in Appendix I), by subtracting the Fe contents (Fe^{2+} or total Fe) in the pristine sample from the measured values (which includes Fe uptake and structural Fe).

The pristine SWy-3 was analysed at two instances (at each dismantling sessions, as a control sample), and yielded a total Fe content of 0.50±0.02 mmol·g^{-1}. This was in the same range, but 9% lower than obtained from XRF. A reduction level of 4.0±0.7% was determined, which was consistent with Mössbauer data (section 3.3.1). Small black residues could be observed (only with pristine material) during digestion. The reasons for the difference in total Fe content are unclear (method uncertainties and/or oxides embedded in an insoluble silica matrix).

A notable contrast between interfaces and bulk of the core was observed in both experiments. Fe contents at the very vicinity of the interfaces (first few hundred µm) are higher than what the trends inferred from bulk samples indicate, given that the Fe content was averaged over the entire slice. The concentration contrasts were consistent with the colour zonation (Figure 118 and Figure 119).

There were overall no indications of oxidation by an external oxidant (e.g. O_2). No Fe^{3+} was detected, besides a few traces at the input of experiment #1. This was maybe due to temporary exposure to glovebag atmosphere following input tube failure (section 3.3.3.1). Fe recoveries were overall consistent. In exp. #2, 94.5±17.3% of the in-diffused Fe(II) was recovered in the clay core (following total digestion). In exp. #1, 39.5±0.5% of the Fe taken up by the clay core at the end of the diffusion phase were recovered in the reservoirs in the out-diffusion phase, while 53.2±6.4% remained in the clay core (accounting together for 92.7±6.9% total). Given the methods' uncertainties this indicates no or only limited (<8%) oxidation of Fe_{aq}^{2+} (e.g. by external O_2) during the course of the experiments. The Fe_{sorb} content was globally below the Fe_{str} content (representing 5% to 30% of Fe_{str}), except perhaps at the vicinities of the interfaces where it could be higher than Fe_{str}.

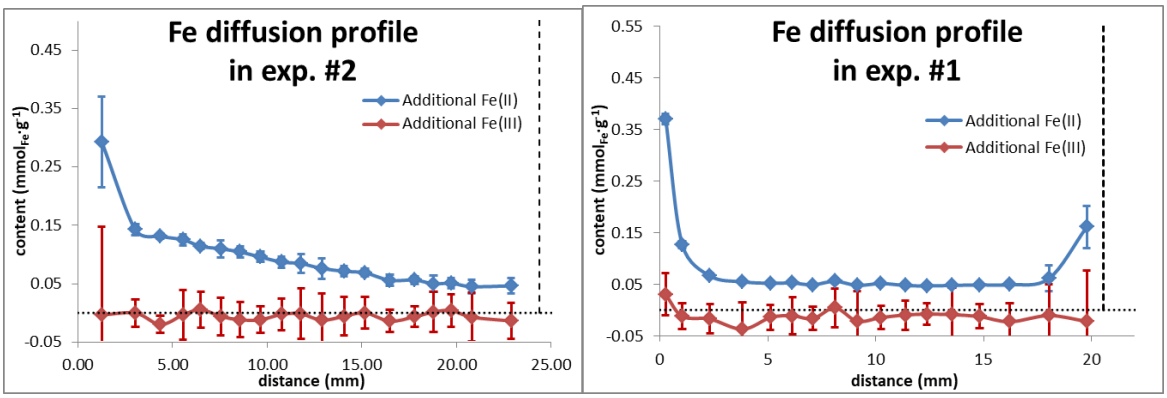

Figure 121 - Profile of additional Fe(II) and Fe(III) in the clay cores of two experiments.

In exp. #1, excluding the outermost samples, the Fe content was homogeneous throughout the entire profile. In contrast with the bulk, additional Fe accumulation processes occurred at the vicinities of the interfaces, and these processes appear rather irreversible.

Elemental concentration in clay core of experiment #2

"Al-normalized" profiles (Figure 122 and Figure 123) were calculated from LA-ICP-MS elemental profiles (

Table I4 in Appendix I). In the experimental conditions, amongst the structural elements, Al is assumed to be the least likely to be dissolved and transported elsewhere. This makes this element a good proxy to track relative changes in content of other more soluble elements.

Results showed no notable changes in contents of Si and Mg throughout the entire profile, which indicated that no notable clay dissolution occurred. The profile of Fe enrichment was consistent with data from HF digestion (here normalized by Al from XRF data). The decrease of sodium content mirrored the increase of Fe content, which was consistent with cation exchange occurring throughout the entire profile. Comparison between extent of Na depletion regarding the pristine material (which varied linearly between 60 and 98% throughout the core, Figure 124 left) and quantities of additional Fe (determined by HF method, cf. previous section) outlines that cation exchange can account for most of the Na and Fe variations within the whole profile excluding the first slice (Figure 124 right).

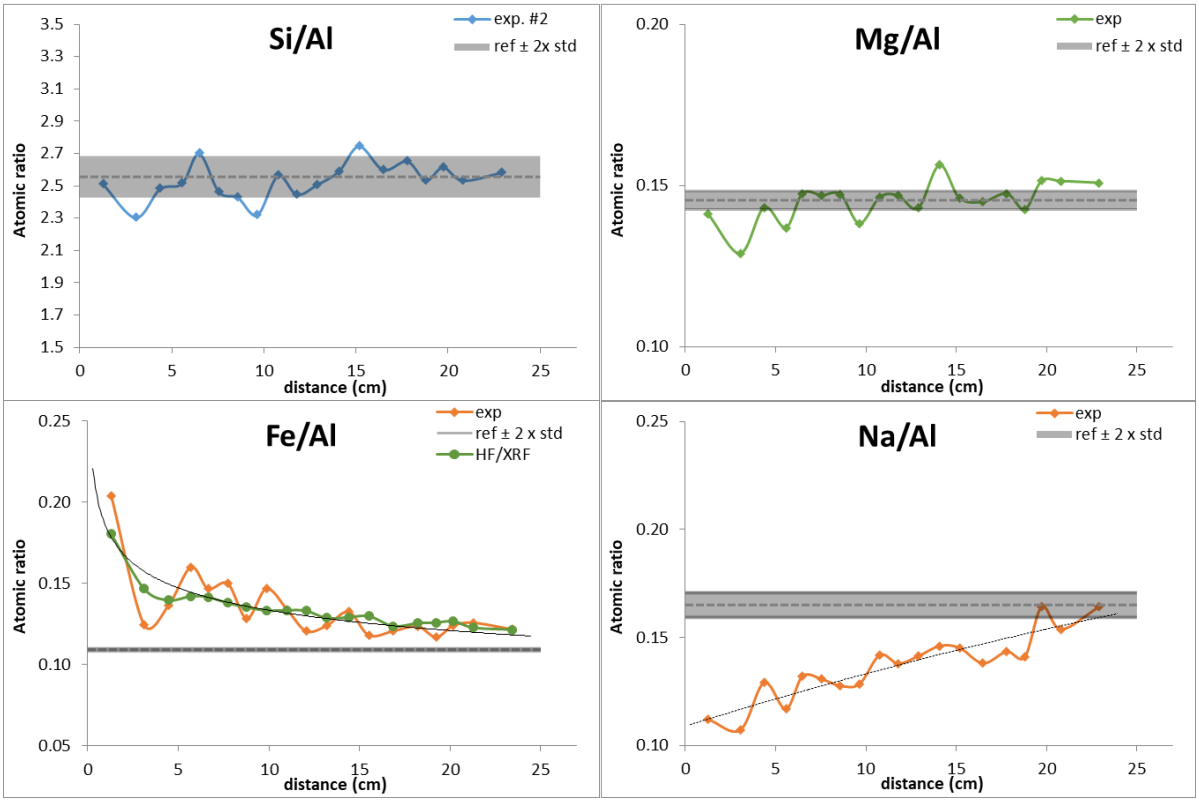

Figure 122 - Al-normalized elemental profiles of major elements (Si, Mg, Fe, and Na) determined by LA-ICP-MS. Calculated from data in
Table I4. For Fe, data obtained by total digestion (

Table I2) and normalized by Al XRF data (Table 25) is also displayed. Ref values are averages obtained on two samples of unreacted purified SWy-3. Black lines are polynomial fits.

The pristine material was devoid of S. Small amounts of S are now present throughout the entire profile, accounting for the diffusion of MOPS buffer (the sole S-bearing chemical employed in the preparation of solutions) in the clay core. No notable changes were detected for other minor elements (Ca, K, Ti, P), besides Zn (and Cr, data not shown), which showed a small depletion, similarly to Na. This is consistent with some exchange with Fe(II) (presumably on edge sorption sites, since the clay was initially Na saturated).

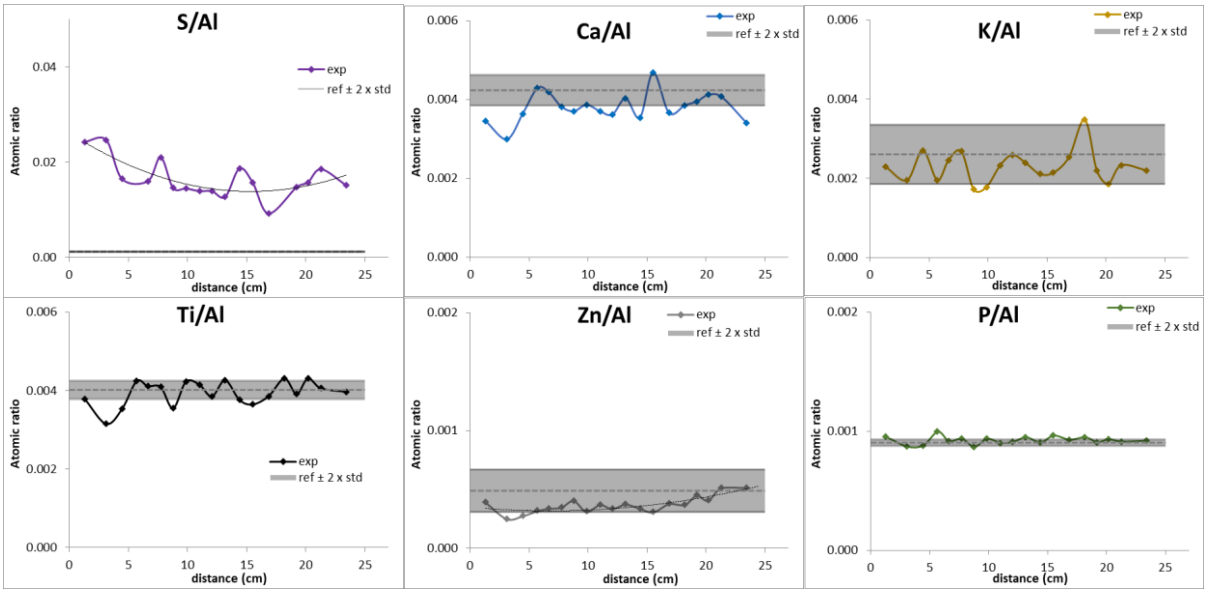

Figure 123 - Al-normalized elemental profile of minor elements (S, Ca, K, Ti, Zn, and P) determined by LA-ICP-MS. Ref values are averaged on two samples of unreacted purified SWy-3. Black lines are polynomial fits. Calculated from data in Table I4.

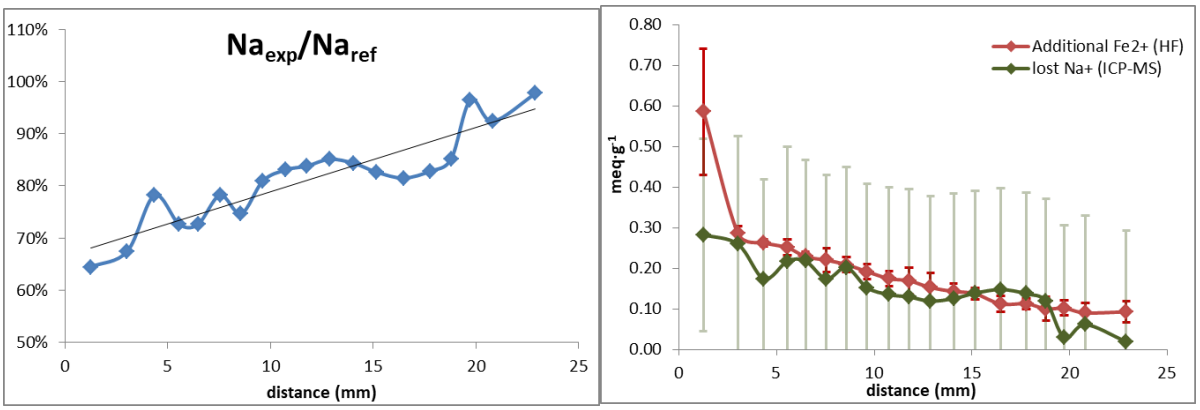

Figure 124 - (left) ratio between Na content in the clay core (Na_{exp}) and Na content in the pristine SWy-3 (Na_{ref}) (right) Comparison between equivalent quantities of additional Fe^{2+} (determined by HF method, Table I1 in Appendix I) and of lost Na^{+} (regarding the pristine material).

Fe Isotopic distribution in clay core of experiment #2

Measurements performed without correction indicated that the $^{54/56/57}$Fe isotopic distribution in unreacted purified SWy-3 was consistent with natural relative abundances (5.5±1.5%/92.4±23.9%/2.1±0.7%, (Meija et al., 2016)). The isotopic profiles in the clay core from exp. #2 showed enrichment in ^{56}Fe only. There was no notable isotopic exchange between solution and solid material. These results confirmed that the main and only Fe diffusing Fe species was $^{56}Fe^{2+}$.

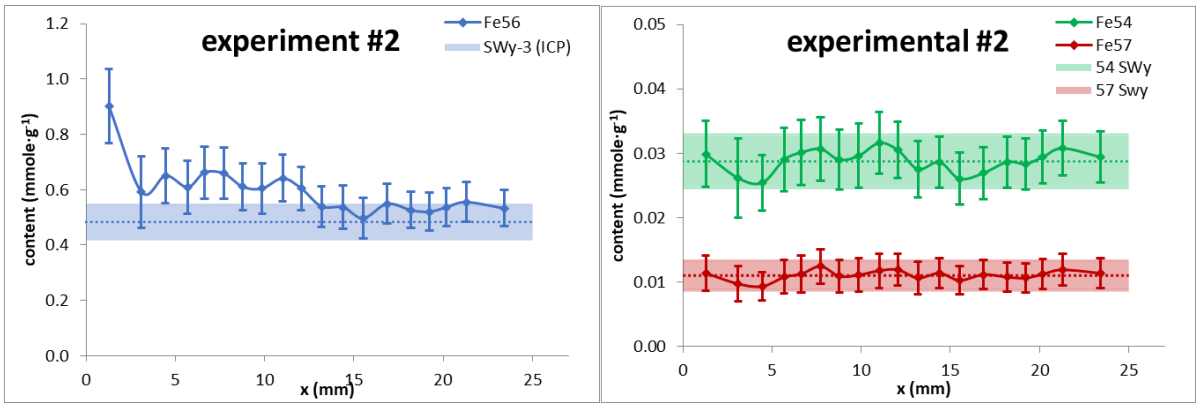

Figure *125 - Fe isotopic profiles in the clay core of experiment #2.*

Fe_{str} redox speciation in clay core of experiment #2

Mössbauer data collected on the samples from diffusion exp. #2 (Table F4 and Table F5 in Appendix F) are summarized in Table 30 below, along with data for pristine samples and batch experiments. A notable difference was observed between bulk samples and the outermost ones, especially dealing with those scraped from the two filters, and the first slice (first 2.5 mm). Important Fe_{str} reduction levels were detected at the vicinity of the interfaces, which was consistent with colour zonation (cf. pictures from dismantling in Figure 118 and Figure 119), and also with a higher Fe content at the vicinity of the filter/core interface associated to more irreversible processes.

These Mössbauer data showed a systematic difference between the data at 300 K and those at 77 K data over the entire profile, with the former showing smaller reduction than the latter (cf. $\Delta_{77K\text{-}300K}$ in Table 30). This was not the case for the pristine materials and for the samples from the batch experiment, for which the data at the two temperatures were consistent within the method error (±2%). The data at 300 K actually showed no electron transfer at all in the bulk of the sample. Data for the same samples at 77 K showed a slight reduction level of Fe_{str} (+5% compared to the pristine material). This temperature contrast is even more pronounced for the outermost samples.

The Mössbauer spectra were dependent on the conditions of the sample preparation (dry, embedded, saturated compacted) and by the addition of ^{56}Fe. For some reacted samples, spectrum fitting required the use of a large Fe(III) singlet (Table 30) to account for the poorly defined baseline. This was often the case for dried batch reacted samples and became systematic for the bulk samples from the diffusion experiment. Using such a large singlet increases the baseline and may tend to underestimate the Fe^{2+} contribution. This could be said to be the difference for the systematic discrepancy in reduction levels observed between 300 K and 77 K. However, this discrepancy is even larger for the outermost sample of both diffusion experiments, for which no singlet is used for the fitting. In the present report, 300 K data are considered to be representative of the experiment (which was conducted at room temperature).

Another notable change in the Mössbauer data of the reacted samples is the increase of the contribution from the Fe (oxyhydr)oxides impurities (almost doubled in some cases). The opposite would be expected after the addition of ^{56}Fe, which, by isotopic exchange with ^{57}Fe in the oxides, should reduce their contribution. The isotopic data from solutions (section 3.3.3.2) and solids (section 3.3.3.3) have shown that the exchange was however slow and limited. The reason for this increase remains unclear. It can be due to a peculiar network of the oxides in the compacted samples, which may be expanded by the presence of ^{56}Fe in the surrounding solution. It could be also partially attributed to the contribution of a large Fe(III) singlet.

Finally, a “texture effect” was observed for the large Fe(II) contribution in the outermost sample from the contact with the input filter (in both experiments). This is figured by a highly asymmetric doublet probably due to the morphology of the samples.

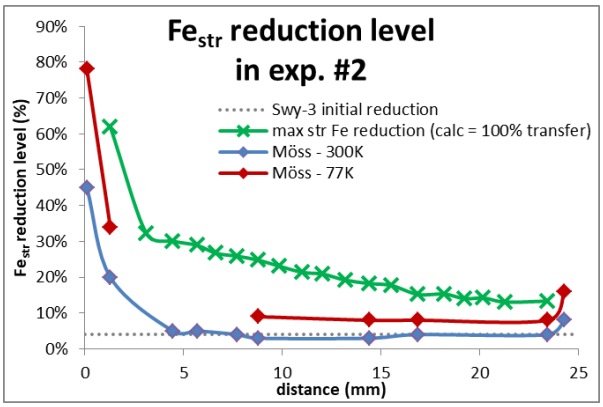

Figure 126 - Fe_{str} reduction level in the clay core of experiment #2 and in unreacted pristine SWy-3. Blue and red data are Fe_{str} reduction levels measured by Mössbauer spectrometry at two different temperatures. Green data are calculated assuming 100% of the $^{56}Fe(II)$ diffusing in transfers electrons toward clay Fe_{str}. Grey dotted line indicates the initial reduction level in SWy-3.

Absence of electron transfers between Fe_{sorb} and Fe_{str} in the bulk of the clay core is in clear contrast to the batch experiments done in similar conditions (e.g. exp. $^{56}T1$ and $^{56}T4$, Table 30), where complete electron transfer was observed. Thus, clay compaction seems to impede the processes associated to e-transfer, except at the vicinity of the filter (over a few hundred µm at most). Different reasons can be hypothesised. The batch experiments indicated that the redox interaction is pH dependent and becomes mitigated with decreasing pH and even supressed at pH below pH 5 (section 3.3.2).

It can be thus hypothesized that the pH in the interlayer of the clay sheets in the compacted clay core may be notably lower than in the reservoirs, because of anion exclusion. Indeed, the acidic Fe_{aq}^{2+} (a 10 mM solution has a pH ~3.4) and the MOPS acid (pH~4.4 at 25 mM) has in theory more access to the clay surfaces than the OH^- and anionic MOPS base. This should result in a strong pH gradient between interlayer water and free pore water. Batch experiments also showed that the reaction of clay and Fe(II) induces a pH shift toward relatively acidic pH (down to pH 4.5 in absence of buffer, section 3.3.2.1). Given the more limited Fe accumulation in the clay and even more limited e-transfers in the clay, a pH below 5.0 should be envisioned in the compacted clay core. The notably higher Fe-accumulation and e-transfers observed at the vicinity of the filters would account for an abrupt gradient in clay compaction (and pH) between the contacts with the filters and the bulk of the core.

Although no e-transfers were detected in the bulk of the clay core at RT, the different specific spectral features of the Mössbauer data (temperature contrast, large Fe(III) singlet and texture effect) account for a relatively distorted Fe_{str} environment, compared to the pristine material, as if some e-transfers were on the verge to occur, but were somehow prevented. Lowering the temperature down to 77 K revealed that a small portion of Fe_{sorb} could reduce Fe_{str}. Although it is not clear how temperature impacts Fe_{str} redox potential (increasing or decreasing the reducibility), this confirmed at least that this portion of Fe_{sorb} (~25%) was present at the vicinity of Fe_{str} sites and would have a potential to reduce Fe_{str}.

Table 30 - Sum-up of the Mössbauer analysis of the samples from batch and diffusion experiments.

Sample.	Condition	H_2O content (wt.%)	pH	$^{56}Fe_{sorb}$ % of Fe_{str}	$Fe(II)_{str}$ 300K (%)	$Fe(II)_{str}$ 77K (%)	Δ_{77-300} (%)	Oxides 77K	Fe(III) singlet 300K	Fe(III) singlet 77K	e-transfers 300K	e-transfers 77K
											% of Fe_{sorb}	
Raw	dry	10.91%	~7.00	0%	17%	16%	-1%	24%				
pur.	Dry	10.91%	~7.00	0%	4%	n.d.	n.d.	n.d.				
pur. 2	Dry	10.91%	~7.00	0%	2%	4%	2%	9%	40%			
^{56}T1	emb.	n.d.	>7.00	16.4%	23%	24%	1%	20%	14%		116%	122%
^{56}T2	emb.	n.d.	>7.00	30.4%	38%	34%	-4%	13%			112%	99%
^{56}T3	emb.	n.d.	>6.00	43.4%	41%	38%	-3%	10%			85%	78%
^{56}T4	emb.	n.d.	>7.00	17.7%	21%	25%	4%	19%	41%		96%	119%
^{56}T5	emb.	n.d.	>7.00	60.3%	52%	52%	0%	9%			80%	80%
^{56}T6	emb.	n.d.	>6.00	53.4%	41%	42%	1%	6%			69%	71%
^{56}T1	Dry	n.d.	5.81	16.3%	22%	20%	-2%	10%	25%	17%	110%	98%
^{56}T2	Dry	n.d.	2.49	15.6%	5%	n.d.	n.d.	n.d.	38%		6%	n.d.
^{56}T3	Dry	n.d.	1.88	22.9%	n.d.	9%	n.d.	10%		16%	n.d.	22%
^{56}T4	Dry	n.d.	7.61	17.6%	n.d.	22%	n.d.	11%		16%	n.d.	102%
^{56}T5	Dry	n.d.	6.01	56.3%	36%	n.d.	n.d.	n.d.	36%		57%	n.d.
^{56}T6	Dry	n.d.	2.87	25.3%	n.d.	10%	n.d.	12%		18%	n.d.	24%
input. filter	sat. comp.	n.d.	n.d.	>59.7%	45%	78%	33%	b.d.			68%	123%
1.26 mm	sat. comp.	34.67%	n.d.	59.7% ±16.5%	27%	34%	7%	12%	25%		27%	50%
4.35 mm	sat. comp.	35.11%	n.d.	27.2% ±1.3%	7%	5%	-2%	18%	34%	32%	4%	59%
7.55 mm	sat. comp.	37.20%	n.d.	22.1% ±3.3%	4%	n.d.	n.d.	n.d.	42%	n.d.	0%	n.d.
8.57 mm	sat. comp.	36.38%	n.d.	21.2% ±2.2%	3%	9%	6%	17%	37%	25%	-5%	24%
14.06 mm	sat. comp.	38.06%	n.d.	14.3% ±2.1%	3%	8%	5%	10%	42%	33%	-7%	28%
16.48 mm	sat. comp.	37.32%	n.d.	11.3% ±2.1%	4%	8%	4%	12%	44%	27%	0%	35%
22.90 mm	sat. comp.	37.51%	n.d.	9.4% ±2.7%	4%	-3%	-1%	11%	30%	26%	0%	43%
out. filter	sat. comp.	n.d.	n.d.	>9%	12%	17%	5%	15%	29%		44%	144%

pur. = purified; emb. = embedded (in epoxy); sat. comp. = compacted and water saturated; input. filt. = input filter; out. filt. = output filter
n.d. = not determined;

3.3.3.4 Modelling

Tracer concentration in reservoirs

Figure 127 compares the modelled evolution of the non-reactive tracers (^{2}H, Br^-) in the inlet and outlet reservoirs with the experimental data. Based on the evolution in the outlet reservoirs, the D_e values can be well constrained as summarized in Table 30. The evolution in the inlet reservoir alone suggests somewhat lower D_e values compared to the outlet reservoir, in particularly for ^{2}H. This may be attributed to some analytical uncertainty (section 3.2.3 and Figure 115). A locally reduced porosity in the filter or at the clay disc surface, as indicated by the visual observation of small amounts of precipitates at the inlet side cannot be ruled out either. The D_e values derived for exp. # 2 are slightly higher than those determined for exp. #1, despite the similar evolution in the reservoirs. The higher diffusion coefficients in exp. #2 are in line with a lower dry density and higher porosity compared to exp. #1. Due to the longer diffusive distance in exp. #2, the breakthrough of the tracers in both experiments occurs almost simultaneously. The D_e values of 4-7 x10^{-11} m^2/s obtained here are slightly lower than the values reported by Bestel et al. (2018) for HTO diffusion in Milos montmorillonite of 7 x10^{-11} to 3 x10^{-10} m^2/s at comparable dry densities. However, it is still within the range of D_e values span by a larger set of experiments as compiled in Kiczka et al. (2022a).

The evolution of the anionic tracer Br^- in the reservoirs of exp. #1 and exp. #2 indicates D_e values, respectively, 10 and 7 times lower than the values for the water tracer. This demonstrates significantly reduced anion accessible porosities in these experiments, in line with porosity distributions constrained by theoretical models, such as *e.g.* a triple porosity model of Wersin et al. (2016). Based on their model, taking the experimental conditions into account and considering a stacking number of 5, the interlayer porosity would account for ~50% and the diffuse double layer (outer mineral surface area with limited accessibility for anions) for 20-30% and the free, fully anion accessible porosity for <30% of the total porosity.

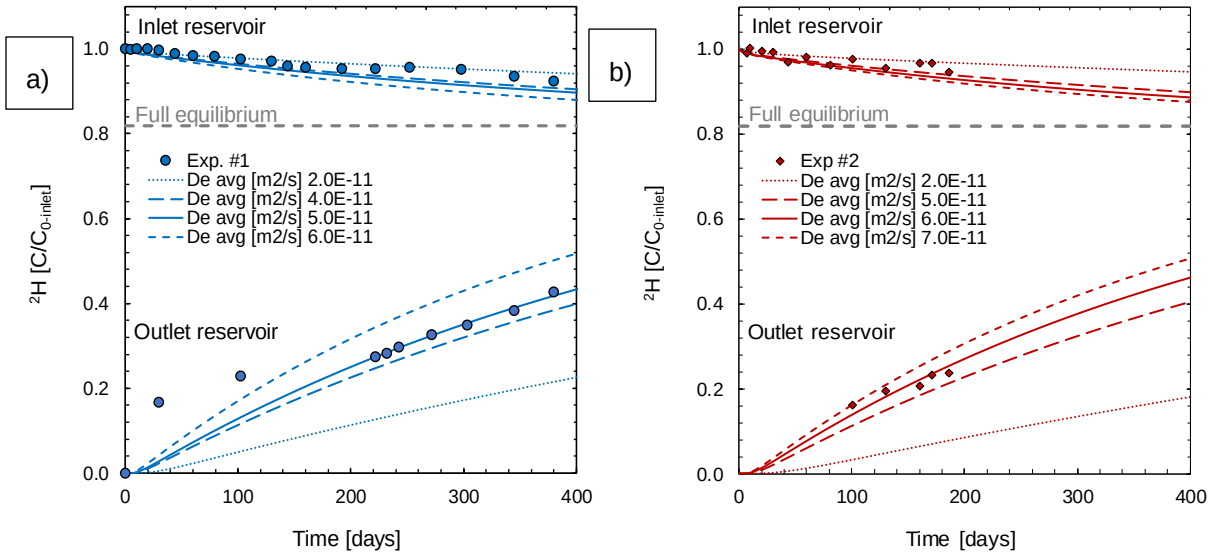

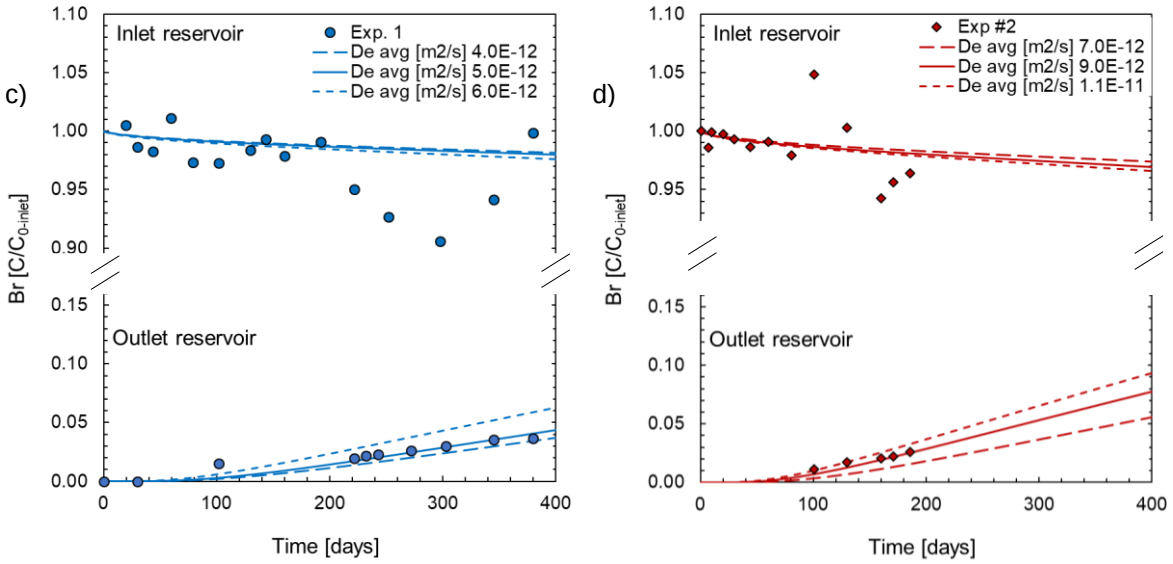

Figure 127 - Out and in-diffusion of the conservative tracers ^2H (a, b) and Br^- (c, d) in the inlet and outlet reservoirs of (left) experiment #1 and (right) experiment #2 as determined experimentally (symbols) and modelled with D_e values as indicated (lines). Note the axis break in the Br figures.

Fe concentration in reservoirs

Figure 128 compares the evolution of the Fe concentrations in the reservoirs as calculated with the transport parameterization given in Table 24 and the sorption model of Table 21 with the experimental data. The diffusion of Fe from the inlet reservoirs into the clay and from the clay into the outlet reservoir can be constrained by D_e values of 1 – 3 x10^{-10} m^2/s and 2 – 4 x10^{-10} m^2/s for exp. #1 and exp. #2, respectively. As for both water and anionic tracers, the shift towards higher diffusion coefficients for exp. #2 is in line with the lower dry density in this experiment. Three main features are observed in both experiments:

- The D_e values presenting the lower boundary for the experimental data are still significantly higher than the D_e values constrained for the conservative water tracer.
- The depletion of Fe in the inlet reservoir indicates a constant to slightly increasing D_e within the first ~50 days. After a transition phase, the out-diffusion can be described by a constant D_e, slightly higher than for the initial phase.
- The measured breakthrough time of Fe in the outlet reservoir is closely matched (±10 days) by the models with the D_e value best describing the late evolution in the inlet reservoir.
- The subsequent increase of Fe concentrations in the outlet reservoir however exhibits a flatter slope than predicted by the model that best describes the breakthrough point. The slope indicates a slightly lower D_e value as visualized by the grey curves for exp. #1 (Figure 128c). Exp. #2 was terminated shortly after the breakthrough, and thus does not allow a detailed evaluation of the long-term evolution of the Fe diffusion out of the clay disc.

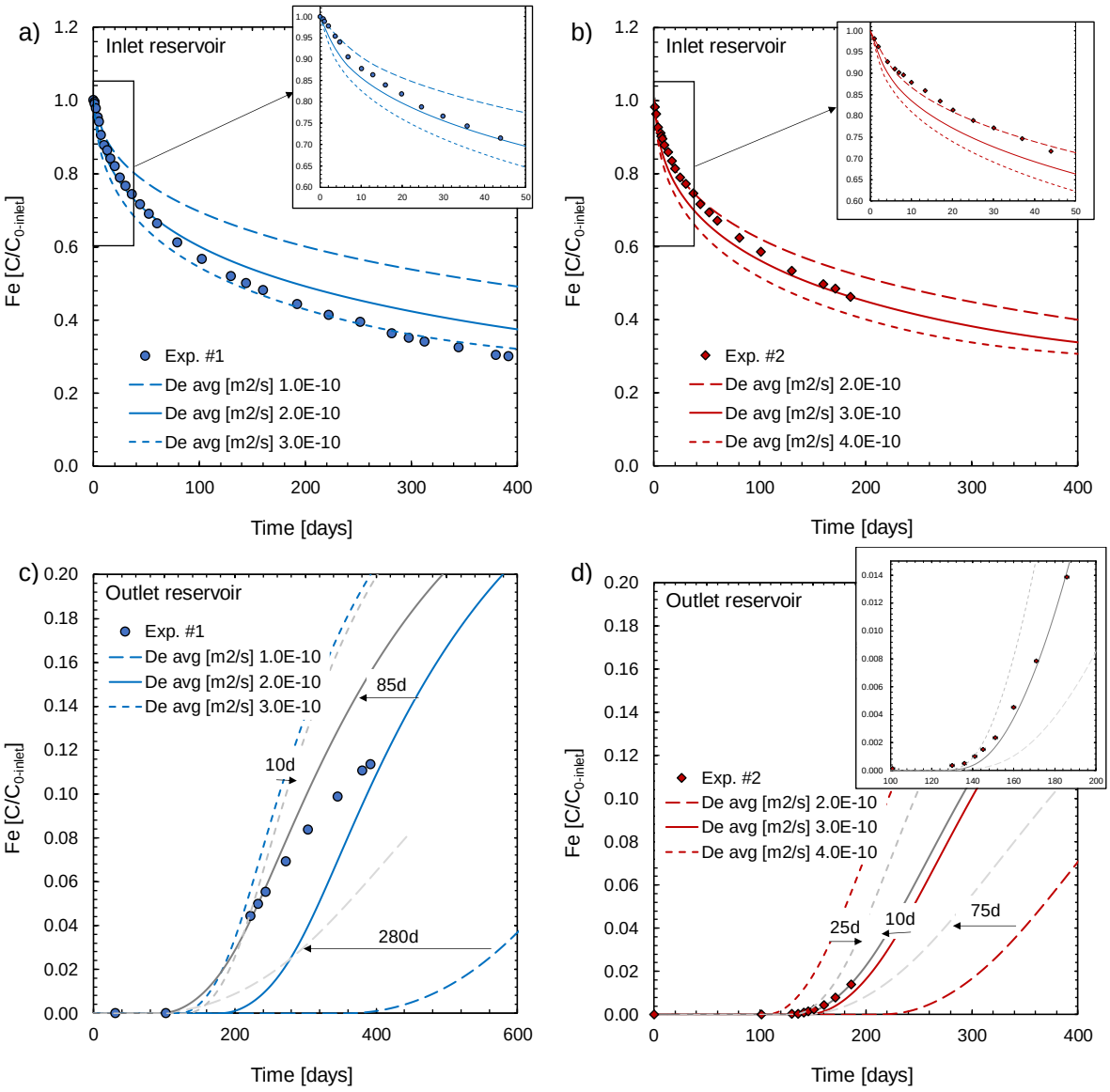

Figure 128 – Evolution of Fe in the in the inlet (a, b) and outlet (c, d) reservoirs of experiment #1 (left) and experiment #2 (right) as determined experimentally (symbols) and modelled (lines). Modelled with the sorption model as given in Table 21 and the D_e values as indicated in the legend. Grey lines in © and (d) represent the modelled breakthrough curves shifted by the indicated time period for a better comparison of the modelled slope with the slope of the experimental data. Insets provide a blow-up of the area indicated by the box in the main figure, for exp. #2 only the time-shifted model lines are given for clarity.

Fe profiles in clay cores

The simultaneous description of both in-and out-diffusion phases by the reactive transport model already provides evidence for the appropriate quantification of the Fe retention in the clay by the model. This is further supported by the comparison of the Fe profile calculated by the reactive transport model for the final stage of exp. #2 with the *post-mortem* Fe profile (Figure 129b). For exp. #1, the in-diffusion phase of ~390 days was followed by a closed system (some weeks) and an out-diffusion period of 237 days. After the out-diffusion phase, solute concentrations in the two connected reservoirs were almost identical (Figure 113 right).Thus, it was deemed more accurate to use an extrapolation between the reservoirs for final pore water composition in each cell rather than concentration profiles resulting after simulating the out-diffusion over several reservoir changes. The Fe profile (Figure 129a), as well as the reservoir Fe concentrations shown above, were calculated with the identical database and sorption model (Table 21) with CEC and $S^{W/W1}$ reduced to 80%, RS limited to interface region) implemented in the reactive transport code using PhreeqC. In both cases, the calculated Fe accumulation profile reflects the

experimental data. The model further indicates the contribution of the different sorption mechanisms to the overall Fe accumulation. At low Fe concentrations present at the Fe sorption front (exp. #2) or after the out-diffusion phase (exp. #1), sorption complexes at the edge sites dominate and Fe at the cation exchange sites represents a minor contribution. Note, that the redox-dependent surface complexes proposed by Soltermann et al. (2014a), are negligible in this model given the high Fe concentrations and low redox prevailing at the experiment. At the interfaces, the high sorption capacity of the structural Fe implemented in the model allows for a successful description of the Fe accumulation at different Fe concentrations (Table 31). Some minor underestimation at the Fe inflow site is observed, which might give an indication that the sequestration of Fe by structural Fe(III) is not fully reversible or that some precipitation of Fe might have occurred. The reduction level of structural Fe calculated from the modelled redox sorption process and the reduction determined by Mössbauer spectrometry fairly well match, in particular when taking into account the overall uncertainty associated with the Mössbauer data, the model uncertainties with remaining discrepancies between calculated and measured total Fe uptake and the simplification of a sharp discretised interface region (Table 31). Hence, the results for the interface region of the diffusion experiment support the interpretation that the new sorption process developed for the batch experiments indeed reflects the additional uptake mechanism associated with the reduction of the structural Fe in montmorillonite.

Table 31 - Comparison of modelled and measured Fe accumulation and reduction of structural Fe(III) at the interfaces in the Fe(II) diffusion experiment. Measured data re-calculated to account for initial Fe(II) content of 0.02 mol/kg and 4% reduction level of pristine purified montmorillonite.

	Additional Fe(II) (mol·kg$_{mm}^{-1}$)		**Additional reduction of Fe$_{str}$ (%)**	
	modelled	measured	Modelled	Measured (300 K)
Experiment #1				
Inlet: 0-0.53 mm	$3.0*10^{-1}$	$3.7*10^{-1}$	50	
Inlet: 0.53-1.54 mm	$1.2*10^{-1}$	$1.3*10^{-1}$	15	
Outlet: 19.01-20.55 mm	$1.6*10^{-1}$	$1.6*10^{-1}$	23	
Outlet: 0.8 / filter	$2.7*10^{-1}$		45	
Experiment #2				
Inlet: 0.8 / filter	$5.2*10^{-1}$		76	41
Inlet: 0-2.51 mm	$2.6*10^{-1}$	$2.9*10^{-1}$	24	16
Outlet: 21.42-24.38 mm	$5.3*10^{-2}$	$4.7*10^{-2}$	3	1
Outlet: 0.8 / filter	$1.5*10^{-1}$		23	4

The increasing (and in the later stages rather constant) fraction of Fe associated with cation exchange reactions provides an explanation for the observed evolution in the Fe diffusivity. Cations involved in cation exchange are known to exert a specific mobility, generally termed surface mobility (*e.g.* Gimmi and Kosakowski (2011)), whereas Fe sorbed by surface complexation reactions may be considered rather immobile. Thus, with increasing retention of Fe by cation exchange, a higher D_e is required and using a constant D_e of a conservative neutral tracer (^{2}H) would progressively underestimate the apparent diffusion of Fe. It should be emphasized that this is only one approach to describe cation diffusion through clay and clay rocks. The RS site successfully implemented in the present model is planned to be implemented in a dual porosity model approach accounting for electrostatic effects, together with edge sites and surface diffusion.

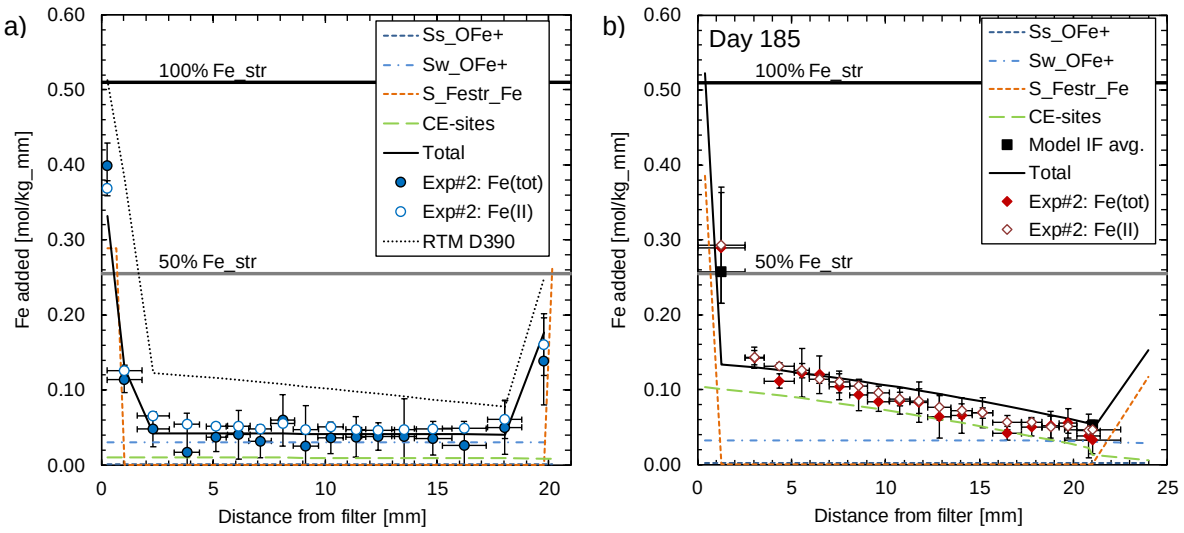

Figure 129 - Measured and modelled Fe accumulation at the end of Exp. #1 (a) and Exp. #2 (b). Dotted black line in (a) indicates the calculated Fe accumulated profile at the end of the in-diffusion phase (calculation case with D_e = 2x10^{-10} m^2·s^{-1}); model calculations for exp. # 2 with D_e = 3 x10^{-10} m^2·s^{-1})

3.3.3.5 Conclusion of diffusion experiments

Two successful through-diffusion experiments were conducted, which showed no signs of Fe oxidation by an external oxidant (e.g. O_2), and very limited isotopic exchange between the ^{56}Fe rich solution and the sample core, indicating the stability of the solid phase.

Diffusion and uptake of Fe^{2+} had a limited effect on the swelling pressure (small drop, <10%), which was apparently reversible. This drop is roughly in the range expected when exchanging a fraction of the monovalent cations on the CE sites with a bivalent cation. The main chemical changes in the core where the accumulation of Fe and a mirroring depletion of Na consistent with Fe-Na cation exchange.

Notable contrasts were seen between the vicinity (<2 mm) of the filters and the bulk of the clay cores. At the vicinity of the filter, results were consistent with those of batch experiments above pH 6 with notable Fe accumulation associated with electron transfer to Fe_{str}, and vivid colour changes. In the bulk of the clay core, Fe accumulation was much more limited and there was virtually no electron transfer to Fe_{str}. Clay compaction seemed to impede the processes associated to e-transfers. In dilute conditions of the batch experiments, the Fe redox sorption was supressed below pH 5 (Section 3.3). One can envision that the pH at the surface of the clay sheets (on outer clay surfaces and in interlayers) in the compacted clay core had a lower pH than in the reservoir solutions, and likely than in larger pores, such that the RS process was mitigated. Models accounting for electrostatic effects on the pore water composition suggest lower OH^- /higher H^+ concentrations close to the charged clay sheet surface, but corresponding activities are still under debate.

The Fe out-diffusion experiment was conducted for a too short period to fully assess the reversibility of the global Fe uptake process. The Fe uptake process occurring at the vicinity of the filters appears to be not fully reversible compared to cation exchange processes. The measurements provide no information about the reversibility of Fe sorption on edge sites.

The Fe diffusion process in the anaerobic bulk of the core could be adequately modelled by CE and surface complexation at the edge sites only. Fe sorption on the RS site successfully used for modelling the batch experiments had only to be invoked at the vicinity of the filters according to experimental observations. It must however be emphasized that the current model considers the same pH (initial pH 7.2) in reservoir and in the entire clay core porosity. Multi porosity modelling with dedicated modelling of the pH at the clay grain surfaces/interlayers may supersede the arbitrary choice of the distance where RS can occur. A lower surface pH would not only affect the RS process but also the ES process, as both are pH dependent.

3.4 Conclusion

Fe^{2+} uptake by clay depends on multiple factors, especially on the pH and on the relative Fe_{aq} and Fe_{str} concentrations. At low pH cation exchange largely dominates the Fe_{aq}-clay interaction whereas at higher pH sorption to edge sites and interaction with Fe_{str} becomes more important.

In batch experiments at high Fe(II) equilibrium concentrations (>0.1 mmol/L), edge sorption accounts only for a minor portion of the Fe uptake. A major part of the Fe uptake observed at pH between 6 and 7 could be described by a pH dependent complexation reaction linked to Fe_{str} sites. Mössbauer spectroscopy of selected experiments performed with ^{56}Fe (transparent to Mössbauer spectroscopy) have demonstrated that this process involves an electron transfer to Fe_{str}. At higher Fe uptake, this process presumably extends to the stepwise surface precipitation of tiny GR-like Fe hydroxide domains at the vicinity of the reduced Fe_{str} sites scattered on clay surfaces. By this, very high Fe uptake by the clay can be reached that exceeds the initial CEC and Fe_{str} capacity by up to a factor of two (if not more). It should however be taken into account that such high Fe uptake was only observed in case of extremely high Fe concentrations in solution (>25 mmol/L) or very high L/S ratios. These reactions are clearly pH dependant and are mitigated at low pH.

In compacted conditions, as in the Fe(II) diffusion experiments (dry density above 1000 $kg \cdot m^{-3}$), the processes involving electron-transfers were limited to the close vicinity of the filters (< 1 mm) and suppressed within the core bulk material.

The Fe diffusion and retention in the anaerobic bulk of the core could be therefore modelled by a classical 2-site non-electrostatic surface complexation and cation exchange model only. A supplementary Fe uptake process (analogous to RS in the batch experiments) had only to be invoked at the vicinity of the filter based on experimental observations. Within the single porosity model of the reactive transport calculations, the D_e for Fe was increased compared with the neutral tracer deuterium, to account for surface mobility of Fe(II) associated with cation exchange.

So far, the reason for this significant difference between observations from batch and diffusion experiments with respect to the redox interaction of Fe^{2+} and Fe_{str} is not yet entirely understood. The batch experiments indicate that the pH has a major control on this process and low pH (below 5) could largely supress the redox interaction. It can thus be hypothesized that, due to ion exclusion and interaction with Fe^{2+}, the pH at clays surfaces and in the interlayer may have been notably lower in the compacted clay core than in the reservoirs (pH 7.2). Such local processes at the surface/interlayer of the clay were not included in the applied reactive transport model, due to lack of process understanding.

4. High Concentration Working Group

4.1 Iron-Steel-Bentonite modelling (UJV)

The main aim of the modeling of the experiments from Havlova et al. (2020), carried out at UJV, is to allow for a further description, assessment and understanding of the chemical evolution in the iron–bentonite–water systems of interest. In addition, the modeling includes the consideration of the simulation of the development and transfer of the corrosion products that evolved under the experimental conditions described previously.

4.1.1 Conceptual model

The objectives are to provide a description of the conceptual context, identify the geochemical disturbances that occur during the long-term evolution of disposal cells, prepare the relevant input datasets, create a set of geochemical models and process the 1D reactive-transport modeling calculations for the laboratory experiments considered. All these aspects are described in the following sections. By assessing the obtained results, the main goal is the identification of the most important processes that occur within the iron–bentonite–water systems.

4.1.1.1 Modeling concept

The geochemical modeling approach applied is based on a three-step procedure. Firstly, the construction of a simple equilibrium model of the iron–bentonite–water systems for the identification of the main chemical driving processes that occur within these systems over a hypothetical long term period (Section 4.1.2.2). Secondly, the development of a model that considers kinetic effects and thus the time-dependence of the various geochemical processes (Section 4.1.2.3). Thirdly, the development and application of a one-dimensional (1D) reactive-transport model that includes not only kinetic effects but also transport phenomena (Section 4.1.2.4). Such a model allows for a more realistic understanding of the temporal and spatial development of steel corrosion and the formation of corrosion products within iron–bentonite–water systems. This three-stage modeling workflow is similar to that applied in the previously conducted UJV Corrosion Products project (Gondolli et al., 2018a; Gondolli et al., 2018b; Gondolli et al., 2018c).

Prior to commencing the three-stage modeling research, it was also necessary to perform a number of preliminary geochemical calculations in connection particularly with the modeling of the bentonite pore waters (BPWs) that are assumed to be in equilibrium with the bentonite materials before the addition of the iron material to the system. Results of such calculations are presented in section 4.1.2.1.

It should also be noted that the results of the equilibrium and kinetic models presented in this report are different from those presented earlier within the SURAO technical report No. 557/2021 (Klajmon et al., 2021), since some of the input parameters and aspects regarding the modeling approach have been re-considered and improved.

4.1.1.2 Processes to be modeled

The geochemical processes studied comprise:

- the dissolution (and re-precipitation) of the primary minerals of the bentonite,
- the dissolution of solid iron,
- changes in the composition of the aqueous solution,
- cation exchange and surface complexation within the bentonite materials,
- the precipitation of secondary solid phases including corrosion and bentonite alteration products.

The final (third) stage of our modeling effort, that is, the reactive transport model, will include the computational investigation of both the temporal and spatial evolution of these processes.

4.1.1.3 Initial conditions and input parameters

This section provides a summary of the characterization and properties of the initial aqueous solutions and bentonite materials used in the three previous UJV projects considered in this WP. This data was used as the input data for the geochemical modeling calculations performed in this study (see further) and were carefully considered and discussed.

4.1.1.3.1 Initial aqueous solutions

The chemical composition and other parameters of the initial aqueous solutions (groundwaters) considered for the saturation of the bentonite materials, i.e., synthetic groundwater (SGW) and Grimsel groundwater (GGW), are shown in Table 32.

4.1.1.3.2 Bentonite materials

The mineralogical composition and other parameters of the bentonite materials, i.e., the BaM and MX-80 bentonites, are shown in Table 33. The contents of the well-soluble salts were determined as follows (in mol kg^{-1}): $5.1 \cdot 10^{-4}$ of halite, $8.7 \cdot 10^{-4}$ of gypsum, $4.1 \cdot 10^{-4}$ of $Mg(NO_3)_2$ and $4.0 \cdot 10^{-4}$ of nahcolite for the BaM material (Červinka and Gondolli, 2015), and $1.35 \cdot 10^{-4}$ of halite for the MX-80 bentonite (Bradbury and Baeyens, 2002).

4.1.1.3.3 Cation exchange

The cation exchange reactions on the montmorillonite interlayer sites were considered for the cations Na^+, K^+, Ca^{2+}, Mg^{2+} and Fe^{2+} applying the Gaines–Thomas convention (Gaines and Thomas, 1953). The equilibrium constants (log *K*) of the exchange reactions were taken from the PHREEQC.DAT database distributed with PHREEQC (Parkhurst and Appelo, 2013) and are shown in Table 34. These log *K* values correspond very well with those reported for the MX-80 bentonite (Bradbury and Baeyens, 2002) and were also used in our previous modeling studies on bentonite and iron–bentonite systems (Červinka et al., 2018; Gondolli et al., 2018b). Table 34 also includes the cation exchange capacity (CEC) characteristics and the initial composition of the respective exchangeable sites for the BaM and MX-80 bentonites.

Table 32. Chemical composition and other parameters of the initial aqueous solutions.

Aqueous solution	SGW[a]		GGW[b]	
Project(s)	CoPr, UOS		MaCoTe	
Ion/Concentration	mg kgw^{-1}	mol kgw^{-1}	mg kgw^{-1}	mol kgw^{-1}
Na^+	10.4	4.46E-04[c]	8.30	3.11E-04[c]
K^+	1.8	4.60E-05	0.20	5.12E-06
Ca^{2+}	19.0	4.74E-04	7.50	1.87E-04
Mg^{2+}	7.0	2.88E-04	0.01	4.11E-07
Cl^-	33.6	9.48E-04	0.90	2.54E-05
SO_4^{2-}	27.7	2.88E-04	5.64	5.87E-05
HCO_3^-	30.4	4.98E-04	18.10	2.97E-04
Al^{3+}	0.1	3.71E-06	0	0
Si	10.1	1.68E-04	0	0
Fe^{2+}	0.1	1.79E-06	0.1	1.79E-06
F^-	0	0	3.90	2.05E-04
pH	7.90		9.25	
E_h (V)	0.181		0.203	
pe[d]	3.06		3.43	
I [mol kgw^{-1}] [e]	2.97E-03		9.38E-04	
log P_{CO2} [atm][f]	−3.43		−5.02	

[a] The composition was taken from (Gondolli et al., 2018a; Gondolli et al., 2018c).
[b] The composition was taken from (Dobrev et al., 2022).
[c] Adjusted to attain the charge balance of the solution.
[d] pe = E_h/0.05917.
[e] Ionic strength.
[f] Calculated from the solution composition.

Table 33. Mineralogical composition and other parameters of the BaM and MX-80 bentonites.

Parameter	*M* [g mol^{-1}]	*ρ* [g cm^{-3}][a]	BaM		MX-80	
			w	*n* [mol dm^{-3}][a]	*w*	*n* [mol dm^{-3}][a]
Mineral						
Montmorillonite[b]	366.21/376.72[c]	2.69/2.63[c]	0.877	9.2492	0.850	7.8919
Quartz (SiO_2)	60.08	2.62	0.053	3.4071	0.037	2.1541
Anatase (TiO_2)	79.88	3.90	0.039	1.8856	-	-
CaMg-Siderite ($Ca_{0.1}Mg_{0.33}Fe_{0.57}CO_3$)	103.86	3.55	0.031	1.1528	-	-
Calcite ($CaCO_3$)	100.09	2.71	-	-	0.013	0.4543
Muscovite ($KAl_2AlSi_3O_{10}(OH)_2$)	398.31	2.82	-	-	0.048	0.4215
Feldspar (Albite; $NaAlSi_3O_8$)	262.22	2.62	-	-	0.052	0.6936
Porosity			0.415		0.430	
V_{water} [dm^{-3}]			1		1	
$m_{bentonite}$ [kg]			3.86		3.50	
S/L ratio [kg dm^{-3}]			3.86		3.50	
$\rho_{mineralogical}$ [g cm^{-3}]			2.74		2.64	
ρ_{dry} [g cm^{-3}]			1.60		1.50	
$\rho_{saturated}$ [g cm^{-3}]			2.02		1.93	

[a] The mineral density values (*ρ*) were taken from http://webmineral.com. The mole numbers of the minerals (*n*) are per dm^3 of the aqueous solution (pore water) assuming the given S/L ratio.
[b] Different montmorillonites occur in BaM and MX-80. The mean chemical compositions are $Ca_{0.17}Mg_{0.34}Al_{1.66}Si_4O_{10}(OH)_2$ and $Na_{0.409}K_{0.024}Ca_{0.009}(Si_{3.738}Al_{0.262})(Al_{1.598}Mg_{0.214}Fe_{0.208})O_{10}(OH)_2$ for the montmorillonites in the BaM and MX-80, respectively. The chemical formula for the MX-80 montmorillonite was taken from the Thermoddem database (Blanc et al., 2012).
[c] Values for BaM montmorillonite/MX-80 montmorillonite.

Table 34. Cation exchange characteristics of the studied bentonites.

Cation exchange reaction[a]	log K^b	Initial composition [eq kg^{-1}][c]	
		BaM	MX-80
$Na^+ + X^- =$ **NaX**	0	0.039	0.524
$K^+ + X^- =$ **KX**	0.700	0.034	0.014
$Ca^{2+} + 2\ X^- =$ **CaX_2**	0.800	0.117	0
$Mg^{2+} + 2\ X^- =$ **MgX_2**	0.602	0.357	0.132
$Fe^{2+} + 2\ X^- =$ **FeX_2**	0.444	0	0
CEC_{sum}		0.547	0.670

[a] The symbol X denotes montmorillonite exchangeable sites.
[b] From the PHREEQC.DAT database (Parkhurst and Appelo, 2013).
[c] The data was taken from (Červinka and Gondolli, 2015) and (Klajmon et al., 2021) for the BaM and MX-80, respectively

4.1.1.3.4 Surface complexation

The surface complexation reactions included the protonation and deprotonation reactions of the specific surface edge sites (i.e., the surface hydroxyl groups ≡SOH) of the montmorillonite minerals.

Concerning the MX-80 bentonite, the surface complexation site types, their equilibrium constants and capacity were all taken from Bradbury and Baeyens (2002) and are shown in Table 35.

The surface complexation characteristics of the BaM were unknown. However, an earlier study by Červinka and Hanuláková (2013) determined these characteristics for B-75 bentonite, which is considered to be analogous to the BaM material. We therefore assumed that BaM has identical surface complexation characteristics to B-75 (shown in Table 35). It should be noted that Červinka and Hanuláková (2013) applied a relatively large surface site capacity value of 0.151 mol kg^{-1}, which corresponds to approx. 28% of the total CEC of BaM (this value is usually only around 10–15% of the CEC (e.g. Bradbury and Baeyens (2002))). Therefore, we applied a lower value of 0.082 mol kg^{-1}, corresponding to 15% of the CEC of BaM, in the respective Bentonite Pore Water (BPW) models. It was estimated that a surface area value of 30 $m^2\ g^{-1}$ was available for the surface complexation reactions for both bentonites (Bradbury and Baeyens, 2002). The initial compositions of the surface edge sites were calculated in PHREEQC according to a simple protocol proposed by Bradbury and Baeyens (2002), which is based on the equilibration of the surface sites with a 0.001 mol kgw^{-1} NaCl solution at pH = 8, and atmospheric O_2 (log P_{O2}/atm = −0.68) and CO_2 (log P_{CO2}/atm = −3.40). The results are shown in Table 35. Finally, it should be noted that the electrical diffuse layer was not considered in the PHREEQC modeling of the surface complexations, which corresponds to the approach applied by Červinka and Hanuláková (2013).

Table 35. Surface complexation characteristics of the studied bentonites.

BaM			MX-80		
Surface complexation reaction[a]	log K^a	Number of moles per 3.86 kg of BaM	Surface complexation reaction[b]	log K^b	Number of moles per 3.50 kg of MX-80
≡SOH + H^+ = **≡SOH$_2^+$**	4.15	4.462E-05	≡S^{A}OH + H^+ = **≡S^{A}OH$_2^+$**	4.50	1.960E-05
≡SOH = **≡SOH**	0	3.159E-01	≡S^{A}OH = **≡S^{A}OH**	0	6.197E-02
≡SOH = **≡SO$^-$** + H^+	-10.48	1.046E-03	≡S^{A}OH = **≡S^{A}O$^-$** + H^+	-7.90	7.801E-02
			≡S^{B}OH + H^+ = **≡S^{B}OH$_2^+$**	6.00	1.382E-03
			≡S^{B}OH = **≡S^{B}OH**	0	1.382E-01
			≡S^{B}OH = **≡S^{B}O$^-$** + H^+	-10.50	4.370E-04

[a] Taken from Červinka et al. (2018). Only one weak complexation type was considered for the BaM.
[b] Taken from Bradbury and Baeyens (2002). Two types of weak complexation sites (A and B) were considered for the MX-80.

4.1.1.3.5 Modeling tools applied

The PHREEQC hydrochemical modeling code, version 3.6.3 (Parkhurst and Appelo, 2013) was used for all the geochemical calculations performed in the study together with the Thermoddem thermodynamic database, version V1.10 (Blanc et al. (2012); https://thermoddem.brgm.fr/). PHREEQC is a freeware modeling tool developed by the USGS that is suitable for the modeling of aqueous solutions, equilibrium and kinetic reactions and 1D reactive transport. In order to capture the non-ideality of the aqueous phase, the activity coefficients of the ionic species were modeled in PHREEQC using the Lawrence Livermore National Laboratory (LLNL) aqueous model (Parkhurst and Appelo, 2013), given by:

$$log\gamma_i = \frac{A_\gamma z_i^2 \sqrt{I}}{1 + \mathring{a}_i B_\gamma \sqrt{I}} + \dot{B} I \qquad (14)$$

where γ_i, z_i and $\mathring{a}_i$ are the activity coefficient, charge number and diameter of the ionic species i, respectively, I is the ionic strength and A_γ, B_γ and $\dot{B}$ are the temperature-dependent Debye-Hückel parameters. The LLNL model is considered to provide a reasonable estimation of the activity coefficients up to an ionic strength value of 1 mol kg^{-1}. This range covers all the aqueous solutions considered in this study. In accordance with our previous modeling approaches regarding iron–bentonite–water interactions (Gondolli et al., 2018a; Gondolli et al., 2018b; Gondolli et al., 2018c), we suppressed S(VI), C(IV), and N(V) reductions in the aqueous solution (see the PHREEQC code fragment entitled "include_SOLUTION_SPECIES.phr" in Klajmon (2024)).

4.1.2 Modeling results

4.1.2.1 Modeling of bentonite pore water (BPW) compositions

Prior to the modeling of the bentonite-iron-water systems, calculations of the initial pore water composition of the bentonite materials were required to be able to determine the input solutions for the subsequent equilibrium, kinetic and reactive-transport modeling calculations.

The modeling of bentonite pore water is a complex geochemical modeling task, which includes a number of phenomena that need to be adequately described. More information on this topic can be found, for example, in Bradbury and Baeyens (2002), Wersin (2003), Wersin et al. (2004) and Curti (2011).

In principle, the estimation of the composition of BPW is based on the thermodynamic equilibration of an initial solution containing bentonite minerals and well-soluble salts, the cation exchange and surface edge sites of montmorillonite minerals, and selected gases (Bradbury and Baeyens, 2002; Červinka et al., 2018). The BPW composition is then influenced primarily by the mineralogical composition of the bentonite, the initial solution composition, the gas phase composition, the degree of bentonite compaction, and the diffusion of dissolved species through the bentonite (Červinka and Gondolli, 2015; Červinka et al., 2018).

This section describes the considerations, parameters and other details concerning the equilibrium bentonite pore water (BPW) models developed in this study; this is followed by the presentation and discussion of the calculated compositions of the BPW.

The BPW models discussed in this report were constructed in accordance with earlier equilibrium BPW models developed at UJV over the last decade (Červinka and Gondolli, 2015; Červinka and Hanuláková, 2013; Červinka et al., 2018; Gondolli et al., 2018a; Gondolli et al., 2018b; Gondolli et al., 2018c). In principle, all these models can be seen as modifications of the conventional approach proposed by Bradbury and Baeyens (2002). The BPW models developed were successfully validated against data calculated for other BPW models that is available in the literature (Bradbury and Baeyens, 2002; Červinka and Hanuláková, 2013); for details, see Červinka et al. (2017).

A total of 6 different BPW compositions were studied in order to reflect (i) the different combinations of bentonite materials and initial aqueous solutions used in the earlier UJV experiments, and (ii) the different temperatures considered (i.e., 25 and 70°C). These 6 BPWs are, for the sake of clarity, listed in Table 36. Henceforth, the BPW model identifiers shown in Table 36 will be used to refer to the respective BPWs.

The BPW models considered the following features aimed at capturing the real chemical processes that occur between the bentonite material and the aqueous solution:

- thermodynamic equilibrium between the aqueous solution, bentonite primary minerals (except montmorillonite and anatase, see Table 33), bentonite well-soluble salts and the following secondary minerals: calcite ($CaCO_3$), dolomite ($CaMg(CO_3)_2$), goethite ($FeO(OH)$), and kaolinite ($Al_2Si_2O_5(OH)_4$),
- reactions between the species in the aqueous phase (e.g., the acid-base and complexation reactions),
- cation exchange reactions on the interlayer sites of the montmorillonite minerals (this included the exchange reactions for the cations Na^+, K^+, Ca^{2+}, Mg^{2+} and Fe^{2+}),
- surface complexation reactions (i.e., protonation/deprotonation) on the surface edge sites of the montmorillonite minerals.
- For completeness, anoxic conditions with a constant CO_2 partial pressure of $3.98 \cdot 10^{-4}$ atm (i.e., $\log P_{CO2}/\text{atm} = -3.40$) were considered in all BPW calculations.

Table 36. Overview of the BPW models developed.

#	Bentonite	Initial solution	Project(s)	*t* [°C]	BPW model identifier
1	BaM	SGW	CoPr, UOS	25	BPW-BAM-SGW-25
2				70	BPW-BAM-SGW-70
3	BaM	GGW	MaCoTe	25	BPW-BAM-GGW-25
4				70	BPW-BAM-GGW-70
5	MX-80	GGW	MaCoTe	25	BPW-MX80-GGW-25
6				70	BPW-MX80-GGW-70

The presented modeling approach considered the equilibration of the aqueous solution with the bentonite materials, including all the relevant processes listed above, to comprise a rapid equilibrium process, with the consideration of neither temporal nor spatial effects. This is a common simplification that has been applied in previous studies on the modeling of BPW (Bradbury and Baeyens, 2002; Gondolli et al., 2018b).

The BPW model developed and applied in this study, including all the necessary PHREEQC scripts, is attached to this report as an electronic annex (Klajmon, 2024).

The chemical compositions for the BPW models listed in Table 36 were calculated using the developed BPW model. The resulting BPW compositions and other related data are shown in Table 37 and illustrated graphically by means of a bar chart and Piper diagram in Figure 130 and Figure 131, respectively (also in comparison to the initial SGW and GGW).

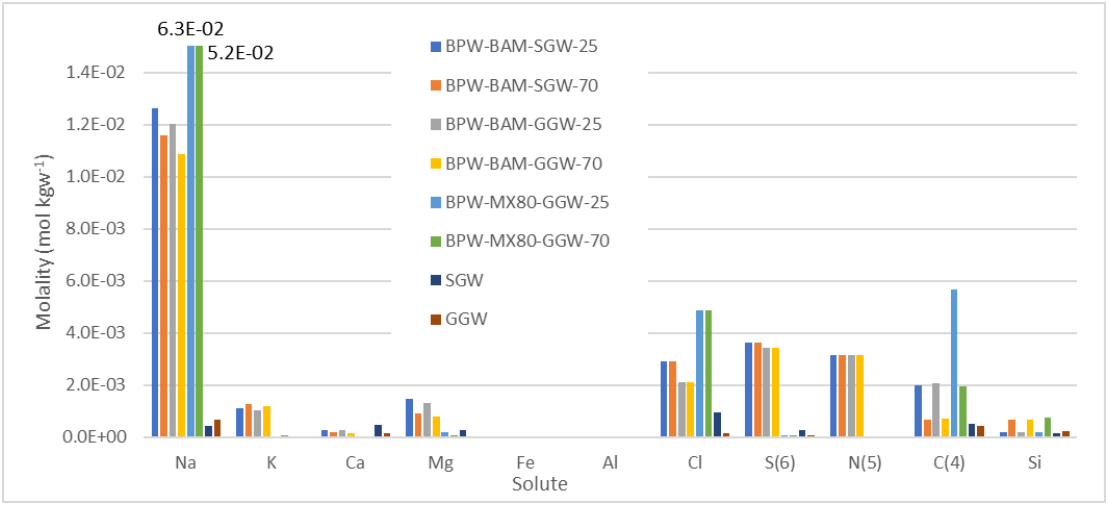

Figure 130. Calculated chemical compositions of the BPWs considered.

It can be seen from Table 37 that the resulting calculated pH values were between 8.3 and 8.9; the MX-80-based BPWs can be seen to evince slightly higher pH values than those of the BaM material. With regard to the differences between the calculated BPWs and the initial solutions (SGW and GGW), Table 37 and Figure 131 show that all the calculated BPWs contained more Na^+, Mg^{2+}, chlorides and carbonates than the respective initial solutions. The calculated BaM-based BPWs all had very similar compositions; furthermore, it can be seen from the Piper diagram in Figure 131 that, in general, the initial solution composition and the temperature exerted relatively minor effects, whereas the bentonite composition exerted the dominant effect on the resulting chemical compositions of the BPWs. This explains the differences between the BaM- and MX-80-based BPWs.

The apparent charge imbalance of the calculated BPWs reported in Table 37 was due to the presence of charged surface complexation sites, not included in the charge balance of the solutions; the whole of the bentonite–water systems including the surface sites were, however, charge balanced and electroneutral, as required.

Table 37. Calculated chemical compositions of the BPWs considered and the resulting bentonite mineralogical compositions, exchanger compositions and surface edge site compositions.

Parameter/BPW	BPW-BAM-SGW-25	BPW-BAM-SGW-70	BPW-BAM-GGW-25	BPW-BAM-GGW-70	BPW-MX80-GGW-25	BPW-MX80-GGW-70
pH	8.44	8.27	8.46	8.29	8.85	8.68
pe	-4.04	-6.22	-4.06	-5.97	-2.65	-4.30
T [°C]	25	70	25	70	25	70
log P_{CO2} (atm)	-3.40	-3.40	-3.40	-3.40	-3.40	-3.40
I [mol kgw^{-1}]	0.020	0.018	0.019	0.017	0.037	0.030
Charge imbalance [%]	5.9	3.3	6.8	4.0	70.5	75.6
Concentration [mol kgw^{-1}]						
Na	1.264E-02	1.161E-02	1.203E-02	1.089E-02	6.227E-02	5.193E-02
K	1.110E-03	1.280E-03	1.053E-03	1.196E-03	7.082E-07	8.788E-05
Ca	2.822E-04	1.736E-04	2.537E-04	1.513E-04	5.239E-05	5.116E-05
Mg	1.464E-03	9.087E-04	1.317E-03	7.918E-04	1.988E-04	6.113E-05
Fe	6.929E-08	8.556E-08	6.640E-08	7.884E-08	6.430E-11	3.346E-11
Al	4.043E-08	1.305E-06	4.211E-08	1.378E-06	5.074E-08	3.281E-07
Cl	2.914E-03	2.914E-03	2.127E-03	2.127E-03	4.882E-03	4.881E-03
S(6)	3.642E-03	3.643E-03	3.416E-03	3.416E-03	6.103E-05	6.102E-05
N(5)	3.155E-03	3.155E-03	3.155E-03	3.155E-03	0.000E+00	0.000E+00
C(4)	1.999E-03	6.607E-04	2.081E-03	6.971E-04	5.664E-03	1.945E-03
Si	1.918E-04	6.563E-04	1.922E-04	6.601E-04	2.062E-04	7.698E-04
Minerals [mol]						
Quartz	3.407	3.407	3.407	3.407	2.447	2.370
CaMg-siderite	1.153	1.153	1.153	1.153	-	-
Muscovite	-	-	-	-	0.471	0.458
Albite	-	-	-	-	0.547	0.586
Calcite	0	0	0	0	3.14E-01	1.98E-01
Dolomite	0.038	0.038	0.038	0.038	0.080	0.134
Kaolinite	0	0	0	0	0	0

Parameter/BPW	BPW-BAM-SGW-25	BPW-BAM-SGW-70	BPW-BAM-GGW-25	BPW-BAM-GGW-70	BPW-MX80-GGW-25	BPW-MX80-GGW-70
Goethite	2.47E-12	0	1.48E-12	3.46E-08	0	0
Exchanger [mol]						
NaX	2.948E-01	2.958E-01	2.955E-01	2.970E-01	1.923E+00	1.895E+00
KX	1.299E-01	1.298E-01	1.300E-01	1.298E-01	1.100E-04	1.282E-02
CaX_2	1.919E-01	1.914E-01	1.916E-01	1.911E-01	6.012E-02	1.215E-01
MgX_2	6.517E-01	6.517E-01	6.516E-01	6.515E-01	1.505E-01	9.659E-02
FeX_2	7.772E-06	1.168E-05	7.766E-06	1.166E-05	2.936E-09	2.967E-09
Surface sites [mol]						
$\equiv SOH_2^+$	1.620E-05	2.397E-05	1.547E-05	2.258E-05	-	-
$\equiv SOH$	3.141E-01	3.150E-01	3.140E-01	3.149E-01	-	-
$\equiv SO^-$	2.850E-03	1.936E-03	2.980E-03	2.054E-03	-	-
$\equiv S^AOH_2^+$	-	-	-	-	6.380E-07	1.321E-06
$\equiv S^AOH$	-	-	-	-	1.420E-02	1.996E-02
$\equiv S^AO$-	-	-	-	-	1.258E-01	1.200E-01
$\equiv S^BOH_2^+$	-	-	-	-	1.943E-04	2.881E-04
$\equiv S^BOH$	-	-	-	-	1.368E-01	1.376E-01
$\equiv S^BO^-$	-	-	-	-	3.044E-03	2.079E-03

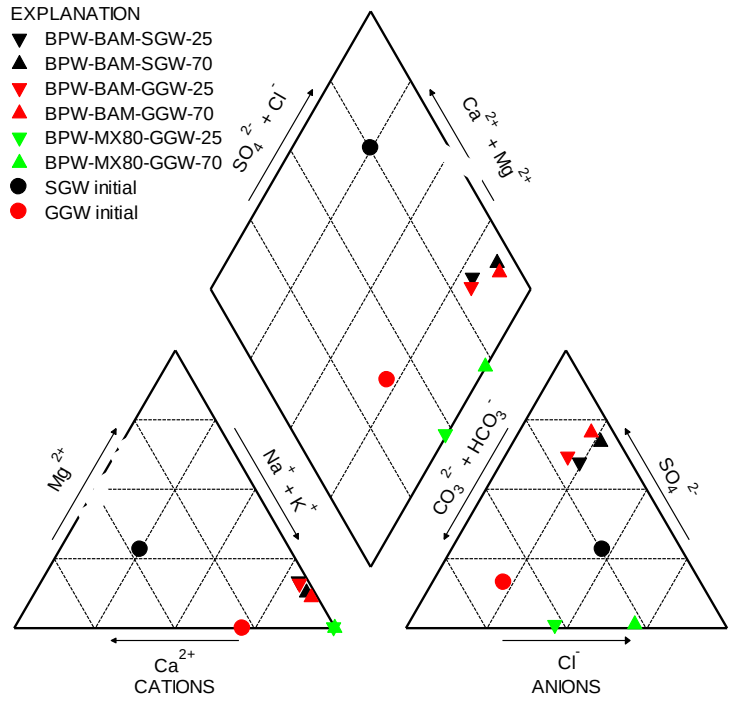

Figure 131. Comparison of the initial solutions and the calculated BPWs via a Piper diagram.

It should be noted that with respect to all the calculations of the BPWs shown in Table 37, the pH of the resulting BPWs appeared to be controlled by the fixed CO_2 partial pressure and the equilibrium with calcite rather than by the surface complexation reactions involved (Bradbury and Baeyens, 2002). In a closed system without a fixed CO_2 partial pressure, however, the pH would likely be determined by the surface reactions. Since the laboratory experiments conducted in the UOS and Corrosion Products projects were carried out under a pressure of 5 MPa in a closed cell emplaced in a glove box, we also performed a test BPW calculation without the assumption of a fixed CO_2 pressure to examine the effect of such an approach on the modeling results. The BPW-BAM-SGW-25 material was chosen for this purpose. It was determined that the calculations without a constant CO_2 pressure resulted in an unrealistic BPW composition with a pH = 6.3 and a total C^{IV} molality of around 0.1 mol kgw^{-1}, which corresponded to a very high CO_2 partial pressure value of 1.4 atm. A possible explanation of such non-standard behavior comprised the presence of the mineral nahcolite ($NaHCO_3$) in the ensemble of well-soluble salts of the BaM material, which acted as an enormous donor of inorganic carbon to the system. The dissolved carbon had no mineral carbonate to precipitate (the Ca and Mg concentrations were not high enough for calcite or dolomite to precipitate, as indicated by their negative saturation index values) and, thus, it remained in the solution. The only way to avoid this problem would be to suppress the dissolution of nahcolite, which would result in a reasonable pH value of 8.1 (controlled by the surface edge sites) and a C^{IV} molality value of 6.8E-04 mol kgw^{-1}. However, such an approach would not correspond to reality since the presence of nahcolite in BaM has been verified beyond doubt (Červinka and Gondolli, 2015). Therefore, for the purposes of the subsequent UJV modeling calculations, only BPWs whose pHs were controlled by a fixed CO_2 pressure (Table 37) were considered. It should be noted that the issue described above was observed with respect only to the BaM-based BPWs since MX-80 contains no other well-soluble salt than NaCl.

4.1.2.2 Equilibrium modeling of interactions in iron–bentonite–water systems

The equilibrium modeling performed in this project was based on the equilibration of the considered iron–bentonite–water systems and included neither kinetic nor transport effects. Thus, the equilibrium modeling followed a significantly simplified approach, the sole purpose of which was to predict (i) the qualitative “direction” of the chemical processes from the initial to the final (equilibrium) state; and (ii) the equilibrium state itself, as provided by the hypothetical assumption that the systems have infinite time to equilibrate. The results of the equilibrium model should, therefore, be considered with a sufficient degree of caution; a more representative modeling investigation into iron-bentonite-water interaction over a realistic time scale is conducted in the context of the kinetic and, in particular, the reactive transport modeling in Sections 4.1.2.3 and 4.1.2.4, respectively.

In principle, the assemblage of the bentonite primary minerals in the equilibrium model was equilibrated with solid iron, a bentonite exchanger, bentonite surface complexation sites, bentonite pore water, and gaseous CO_2. The compositions of these materials can be found in Sections 4.1.1.3 and 4.1.2.1. In addition to the primary minerals, selected secondary minerals (i.e., those minerals that were not initially present in the system) were allowed to precipitate if thermodynamically possible. The secondary minerals considered were selected on the basis of a detailed literature investigation performed previously (Gondolli et al., 2018a; Gondolli et al., 2018c). More than 20 secondary minerals were considered in the model, including corrosion products (e.g., magnetite, siderite, chukanovite, hematite, goethite, etc.), bentonite alteration products (e.g., Fe-rich phyllosilicate minerals such as chamosite, greenalite, cronstedtite, berthierine, saponite, etc.), and other potential secondary minerals (e.g. calcite, dolomite, gypsum, kaolinite and others). The list of the secondary minerals considered in the model can be found in the respective PHREEQC script attached to this report (Klajmon, 2024). The primary bentonite minerals only were allowed to dissolve, as applied in previous UJV iron–bentonite–water models (Gondolli et al., 2018a; Gondolli et al., 2018c). Anoxic conditions were assumed in all cases, with fixed log P_{CO2}/atm = −3.40 (corresponding to atmospheric CO_2 partial pressure) for the experiments carried out in laboratory (UOS and CoPr) and log P_{CO2}/atm = −1.50 (approximating CO_2 partial pressure in the soil) for the *in situ* experiments (MaCoTe). The calculations were performed at two different temperatures, 25 and 70°C. For the sake of simplicity, 5 mol (corresponding to 0.28 kg) of solid iron

were assumed to be initially present in the iron–bentonite–water systems in all cases, together with approx. 3.5 kg of bentonite, depending on the type of bentonite (BaM or MX-80).

More details on the equilibrium model can be found in the respective PHREEQC code which accompanies this report as an electronic annex. With concern to the tests described in the following text, the presentation and discussion of the results obtained are organized with respect to the time sequence of the UJV projects: UOS, CoPr, and MaCoTe.

4.1.2.2.1 UOS and CoPr experiments

This section comprises the presentation and discussion of the equilibrium modeling results for iron–bentonite–water systems consisting of solid iron, BaM bentonite and BPWs based on a combination of BaM and SGW (i.e. BPW-BAM-SGW-25 and BPW-BAM-SGW-70). These systems were studied in two previous UJV projects, i.e., UOS and CoPr. The results presented in this section thus apply to both these projects since the equilibrium model was unable to distinguish between the different forms of solid iron used in the respective projects, i.e., iron plates (UOS) and powdered iron (CoPr).

The equilibrium modeling results of the UOS and CoPr projects at the two temperatures are shown graphically in Figure 132 (solid and dashed blue lines) in terms of the absolute change in the molar number of the minerals (i.e., change between initial and equilibrium state). The moles of the minerals not displayed in Figure 132 remained unchanged following equilibration, i.e., these minerals did not react. This applied, e.g., to quartz, goethite, berthierine and others.

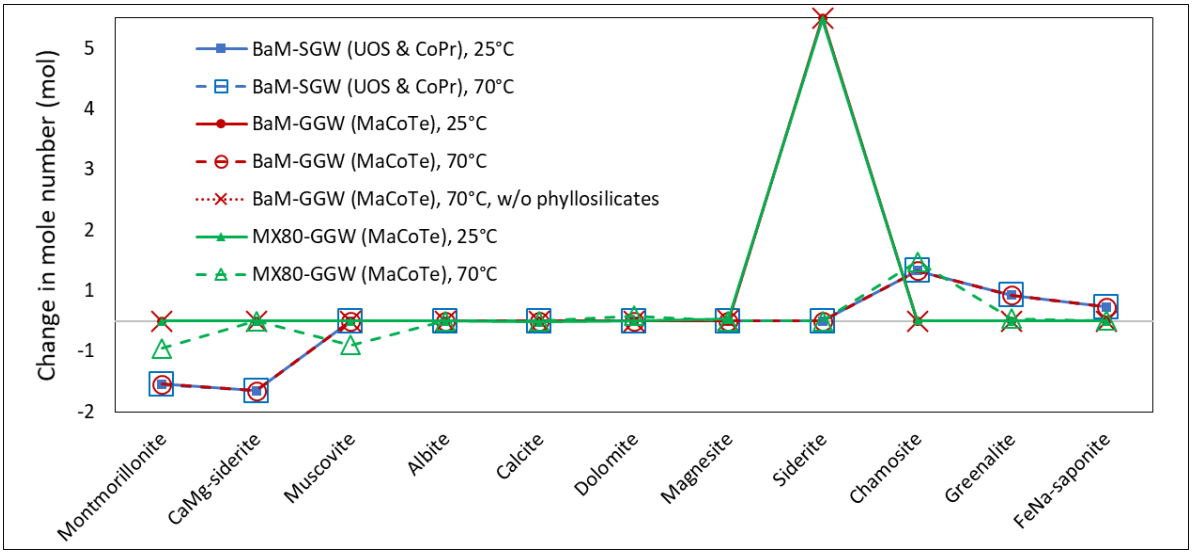

Figure 132. Results of the equilibrium model for the iron–bentonite–water systems in terms of the absolute change in the molar number of the minerals at two different temperatures. Fixed CO_2 partial pressures: log P_{CO2}/atm = −3.40 for UOS & CoPr and log P_{CO2}/atm = −1.50 for MaCoTe.

First, the temperature appeared to exert almost negligible influence on the results in the case of UOS and CoPr both quantitatively and qualitatively (this might be explained by means of stoichiometric aspects; the equilibrium state of some specific systems and the corresponding equilibrium amounts of minerals may be controlled via stoichiometric, i.e., material balance restrictions rather than temperature effects). At both 25 and 70°C, around 1 mol of the primary BaM minerals montmorillonite and CaMg-siderite dissolved. The only corrosion/bentonite alteration products comprised the secondary phyllosilicate minerals chamosite, greenalite, and FeNa-saponite, each of them forming in the amount of 0.8, 0.4, and 0.2 mol, respectively. Neither magnetite nor chukanovite were predicted to occur in the equilibrium state (but this does not necessarily exclude them to act as temporary metastable phases; see the kinetic and transport modeling in Sections 4.1.2.3 and 4.1.2.4, respectively). At both temperatures, the solid iron completely dissolved, as expected. The pH of the equilibrium aqueous

solution was calculated to be around 7 and slightly decreased with increasing temperature of the simulation.

4.1.2.2.2 MaCoTe experiments

The MaCoTe project involved the experimental study of two iron–bentonite–water systems that differed in terms of the bentonite material used, i.e., BaM and MX-80. In both cases, the GGW initial solution was used. We remind the reader that, since the MaCoTe experiments were performed under *in situ* conditions, the calculations were performed with an elevated CO_2 partial pressure of log P_{CO2}/atm = −1.50 (which corresponds to $P_{CO2} = 3.16 \cdot 10^{-2}$ atm). The equilibrium modeling results for the systems with both BaM and MX-80 are shown in Figure 132.

In contrast to the results obtained for UOS and CoPr, the temperature did have a significant effect in the case of MaCoTe. Regardless of the specific bentonite (BaM or MX-80), it can be seen that the mineralogical changes at 25°C are dominated by the precipitation of a relatively large amount of siderite. In addition to the siderite precipitation, a very small amount of chamosite precipitated as a minor corrosion product. However, at an elevated temperature of 70°C, siderite did not precipitate at all, and the Fe-bearing phyllosilicates chamosite, greenalite, and FeNa-saponite were predicted as the main corrosion/bentonite alteration products. Regarding the dissolution of primary bentonite components montmorillonite, CaMg-siderite (BaM), muscovite (MX-80), albite (MX-80) showed the general tendency to dissolve at both temperatures; however, from quantitative perspective, the dissolved amounts were higher at 70°C than 25°C The only difference between BaM- and MX-80-based systems within MaCoTe was that a very small amount of secondary carbonates (magnesite at 25°C and dolomite at 70°C) precipitated in the latter. This suggested that the type of bentonite (BaM or MX-80) had rather a slight to negligible effect on the equilibrium modeling results.

Comparison of the results for BaM-based systems from UOS/CoPr and MaCoTe experiments (blue and red lines in Figure 132) allows for investigating the effects of CO_2 partial pressure on the equilibrium modeling results (assuming that the different initial ground waters, i.e., SGW and GGW have negligible effect on the results). At 70°C, the equilibrium results appear to be more or less the same, suggesting that P_{CO2} has no significant effect at elevated temperatures (at least in the considered log P_{CO2}/atm range of −3.40 to −1.50). However, at 25°C, more significant differences can be seen: in UOS & CoPr (log P_{CO2}/atm = −3.40), Fe-phyllosilicates are the main corrosion products, while siderite is the dominant corrosion product in the case of MaCoTe (log P_{CO2}/atm = −1.50). This would indicate that, at lower temperatures, an increased P_{CO2} shifts the formation of corrosion products towards Fe-carbonates. This is also supported by the fact that CaMg-siderite did not dissolve at all at 25°C in the calculation with the BaM-based system within MaCoTe. For completeness, the equilibrium pH was predicted to be 7 and 8 for BaM- and MX-80-based systems.

As discussed above, the secondary Fe-phyllosilicates chamosite, greenalite, and saponite were predicted as the dominant corrosion products in many systems and conditions. However. it is a question whether such complex minerals really can form (in their crystalline form) and in which timescale. Specifically, it appears that these minerals (and particularly chlorites such as chamosite) do not form in significant amounts in Fe–bentonite systems (at least within the first thousand years of the system evolution), as discussed, e.g., in Stoulil et al. (2022), Forman et al. (2021); Gondolli et al. (2018c); Savage et al. (2010); Stoulil et al. (2022) . Therefore, we performed one more equilibrium modeling run for the BaM-based MaCoTe system at 70°C in which these Fe-phyllosilicates were suppressed to precipitate (in other words, they were not considered at all). The results are shown in Figure 132 (red dotted line). Without the phyllosilicates, the results were qualitatively very similar to those obtained at 25°C, which was mainly manifested by the fact that the main corrosion product was siderite (again around 5 mol). This very well corresponds to our experimental results, since siderite was identified as a corrosion product in all UOS, CoPr, and MaCoTe experiments. Therefore, in the subsequent modeling stages (kinetic and reactive transport), we suppressed the Fe-phyllosilicates in all cases in order to rationalize the modeling approach applied (see Section 4.1.2.3).

4.1.2.2.3 Summary of the equilibrium modeling

To summarize the equilibrium modeling results obtained, it was predicted that:

- the bentonite primary minerals (montmorillonite, CaMg-siderite) had a general tendency to dissolve,
- the main corrosion products comprised siderite (at 25 °C) and the Fe-phyllosilicates chamosite, greenalite, and FeNa-saponite (at 70 °C),
- the increased CO_2 partial pressure level has a notable effect particularly at lower temperatures and supports the formation of Fe-carbonates (siderite) over Fe-phyllosilicates as corrosion products,
- an artificial suppression of Fe-phyllosilicates allows siderite to act as the dominant corrosion product,
- neither magnetite nor chukanovite were calculated as equilibrium corrosion products.

More detailed information on the geochemical processes that occurred in the iron–bentonite–water systems were obtained from the kinetic and reactive transport modeling results which are presented and discussed in the following sections.

4.1.2.3 Kinetic modeling of interactions in iron–bentonite–water systems

Unlike the equilibrium modeling, the kinetic approach allows for the study of the timescales of both the hydrochemical and mineralogical evolution of iron–bentonite–water systems. This approach allows for the more detailed study of the evolution of corrosion and bentonite-alteration products as well as for the identification of potential metastable mineral phases. However, unlike coupled reactive transport modeling, it involves neither diffusion nor the spatial characteristics of the investigated system.

The kinetic model developed as part of this study was based on an extension of the PHREEQC equilibrium model (discussed in Section 4.1.2.2) via the addition of reaction rate equations for irreversible iron corrosion and the dissolution of primary bentonite minerals. In principle, the developed model is similar to those proposed earlier in the literature by other research groups (e.g. De Combarieu et al. (2007), Torres (2011), and Ngo et al. (2015)) and was previously successfully tested against the modeling data published by De Combarieu et al. (2007) (for details, see Gondolli et al. (2018c)).

The reaction rate equations for the minerals were expressed in the following form based on the transition state theory (Palandri and Kharaka, 2004):

$$r = kA_{sp}Mn[1-(Q/K)^{\theta}]^{\eta} \tag{15}$$

where r is the reaction rate (in mol s^{-1}), k is the rate constant (mol m^{-2} s^{-1}), A_{sp} is the specific reactive surface area (m^2 g^{-1}), M is the molar mass (g mol^{-1}), n is the molar number (mol), Q is the reaction quotient (sometimes termed the activity product), and K is the equilibrium constant. The symbols θ and η are empirical parameters. Positive and negative r values correspond to dissolution and precipitation, respectively. The rate constant k is in fact the sum of the various terms that reflect the various reaction mechanisms, e.g., the acid, neutral and base mechanisms:

$$k = k_{acid}a_{H^+}^{n_{acid}} + k_{neut} + k_{base}a_{H^+}^{n_{base}} \tag{16}$$

where a denotes the thermodynamic activity of H^+ in the aqueous solution and n is the reaction order (an empirical parameter). The temperature dependence of k is described via the Arrhenius equation:

$$k_{mech}^{T} = k_{mech}^{T_{ref}} exp\left[\frac{-E_{a,mech}}{R}\left(\frac{1}{T}-\frac{1}{T_{ref}}\right)\right] \tag{17}$$

where the subscript "mech" denotes one of the above mechanisms (acid, neutral or base), E_a is the activation energy (J mol^{-1}), R is the gas constant (R = 8.314 J K^{-1} mol^{-1}), and T_{ref} is the reference temperature (typically 25 °C).

The dissolution rate parameters (k, E_a, θ, and η) for the primary bentonite minerals considered in this study were taken from Marty et al. (2015) or from the classical compilation by Palandri and Kharaka (2004). Their values can be found in the PHREEQC code fragment entitled "include_RATES.phr" attached to this report. The kinetic phases, i.e., the iron and bentonite primary minerals were not allowed to precipitate. The secondary minerals were considered equilibrium phases, i.e., they were not addressed by the kinetic equations but allowed to precipitate/dissolve immediately without any kinetic constraints[5]. The formation of iron (II) hydroxide, $Fe(OH)_2$(s), and particularly the Fe-phyllosilicates (chamosite, greenalite, FeNa-saponite) were suppressed in all cases.

In order to model the corrosion of the iron plates in the UOS and MaCoTe projects, the rate constant k (used in Eq. 15) was based on experimental data obtained by Dobrev et al. (2022) (specifically, k_{Fe} = 6.7·10^{-8} mol m^{-2} s^{-1}, which corresponds to a measured average iron corrosion rate of 15 µm y^{-1}). The parameters θ and η in Eq. 15 for iron were determined in this study by adjusting them to known experimental data on the amount of corroded iron at 70 °C measured at UJV too (Dobrev et al., 2022), with the resulting values being θ = 0.05 and η = 10 for MaCoTe and θ = 0.08 and η = 10 for UOS. Regarding the CoPr project, for which the kinetic data on the corrosion of the iron powder were unknown, the parameters θ and η were conventionally set to unity (i.e., the common default value), and the rate constant k was calculated based on the standard iron corrosion rate estimate of 1 µm y^{-1} (Gondolli et al., 2018a; Gondolli et al., 2018c).

One of the essential input parameters in terms of kinetic modeling concerns the specific surface areas of minerals available for reactions (A_{sp} in equation 15). Ideally, they should be determined experimentally for each material studied; however, due to the lack of such data, it is often necessary to rely on expert estimates. The specific surface areas thus represent a considerable uncertainty concerning the kinetic modeling results. The A_{sp} values for primary minerals used in this study were either carefully selected from data available in the literature or estimated using the geometric approach (Gondolli et al., 2018c; Gondolli et al., 2018b), whereas those for the solid iron were adopted from experimental measurements (Gondolli et al., 2018c; Lhotka, 2021). All the A_{sp} values applied in this study are shown in Table 38.

The systems considered in the kinetic modeling phase contained solid iron, bentonite minerals, bentonite pore water (always 1 dm^3), a bentonite exchanger and surface complexation sites for protonation/deprotonation. The compositions of these materials can be found in Sections 4.1.1.3 and 4.1.2.1. The initial molar amount of iron was again set to 5 mol in all cases. As in the equilibrium modeling, anoxic conditions were assumed in all the kinetic calculations, with log P_{CO2}/atm = −3.40 for UOS and CoPr and log P_{CO2}/atm = −1.50 for MaCoTe experiments. More details on the kinetic model can be found in the respective PHREEQC code which accompanies this report as an electronic annex.

Table 38. The mineral specific surface areas used in this study and their sources.

Mineral	A_{sp} [m^2 g^{-1}]	Source
Montmorillonite	8.50	Marty et al. (2015)

[5] Although the precipitation of secondary minerals is, in principle, influenced by kinetic effects, reliable data on the precipitation kinetics of minerals are (unlike those on dissolution) typically very scarce or unknown. It is possible to use the same data as for dissolution for the precipitation kinetics, however such an approach introduces substantial uncertainty to the results obtained. Nevertheless, our earlier modelling studies Gondolli, J., Klajmon, M. and Kouril, M. 2018c Chování UOS pro VJP a RAO/Korozní produkty. Závěrečná zpráva [in Czech]. MS SURAO TZ 329/2018, SÚRAO, Prague, Czech Republic. showed that the precipitation of some secondary phases may be governed by slow dissolution of the primary minerals (e.g., montmorillonite), which was taken into account in this study.

Quartz	0.23	Geometric approach assuming spherical particles with a diameter of 10 µm
CaMg-siderite	0.17	Geometric approach assuming spherical particles with a diameter of 10 µm
Muscovite	0.21	Geometric approach assuming spherical particles with a diameter of 10 µm
Albite	0.08	Marty et al. (2015)
Calcite	0.22	Geometric approach assuming spherical particles with a diameter of 10 µm
Iron	0.12	MaCoTe; Fe plate; (Lhotka, 2021)
	0.25	UOS; Fe plate; (Lhotka, 2021)
	10	CoPr; Fe powder; (Gondolli et al., 2018a; Gondolli et al., 2018c)

4.1.2.3.1 MaCoTe experiments

The MaCoTe experiments are considered first in this connection since they allow for the comparison of the iron corrosion rates modeled using conventional corrosion rate parameters with their experiment-based counterparts. This is because of the existence of unique data on the amounts of corroded iron (at 70 °C) at different times from the beginning of the experiments measured as part of the MaCoTe project (Dobrev et al., 2022).

Figure 133 illustrates the evolution of Fe(s) and the mineral phases with (a) the parameters θ and η in equation (15) conventionally set to unity and (b) with θ = 0.05 and η = 10 adapted to known experimental data on the amount of corroded iron (Dobrev et al., 2022). It can be seen from Figure 133a that the extent of the iron corrosion was largely overestimated with the conventional $\theta = \eta = 1$ (roughly by two orders of magnitude concerning the weight of the corroded iron), whereas excellent agreement with the experiment-based data was achieved with the adapted θ and η parameters (Figure 133b). As a result, mineral changes and their extent associated with the iron corrosion depicted in Figure 133b should be more realistic compared to those in Figure 133a (at least quantitatively). Specifically, the case with $\theta = \eta = 1$ predicted siderite to be the only corrosion product (~ 5 mol) for the studied ten years of evolution. The modeling case with the adapted parameters θ and η, which corresponded to the experimental observation, predicted again siderite to be the main corrosion product, but with ca. 10^{-2} mol only. In addition to siderite, an extremely small amount of Fe^{II}-illite precipitated as the minor corrosion/bentonite alteration product.

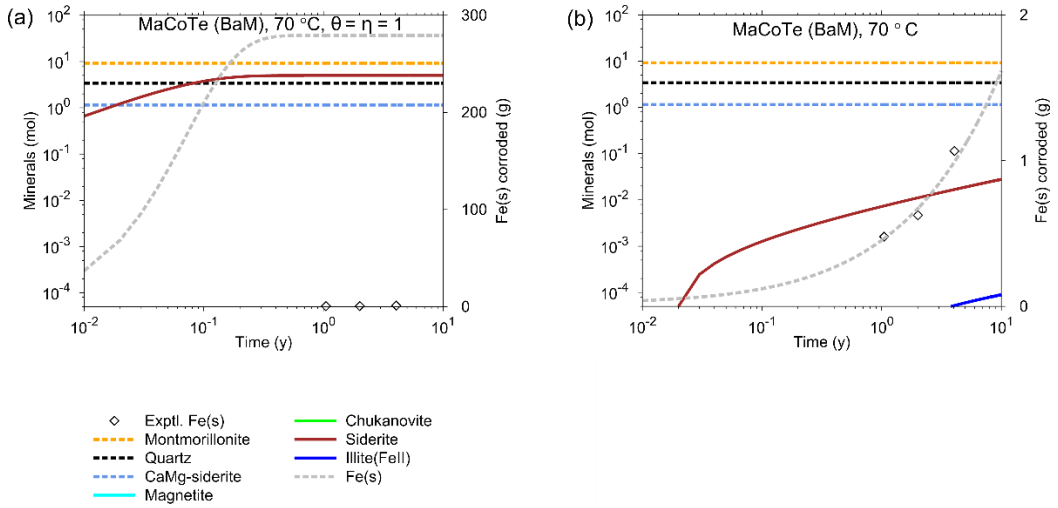

Figure 133. Evolution of Fe(s) and the mineral phases for the iron–BaM–water system considered in the MaCoTe project at 70 °C with (a) the parameters θ and η in equation (15) conventionally set to unity and (b) with θ = 0.05 and η = 10 adapted to known experimental data on the amount of corroded iron. Note the differing ranges of the second y-axes.

The MaCoTe project investigated two different iron–bentonite–water systems that differed in terms of the type of bentonite studied, i.e., BaM and MX-80. The results for the former are depicted in Figure 134 and Figure 135 for two different temperatures 25 and 70 °C, respectively. The results for the system with MX-80 are depicted in Figure 136 and Figure 137 for 25 and 70°C, respectively. The parameters in equation (15) were $\theta = 0.05$ and $\eta = 10$ in all cases. We considered not only the evolution of the solid phases but also those of selected aqueous species and both surface and exchanger sites.

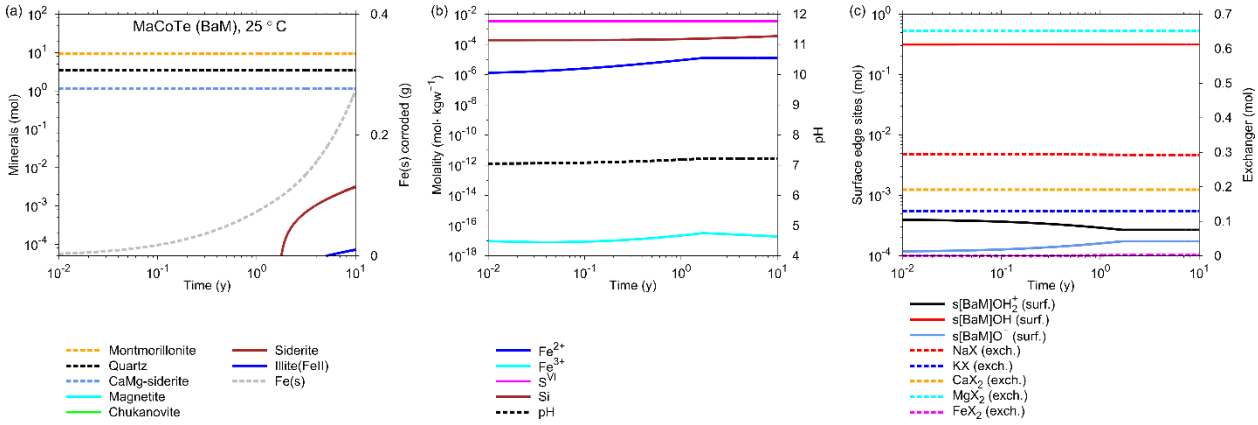

Figure 134. Evolution of (a) Fe(s) and the other mineral phases, (b) selected aqueous species, and (c) surface/exchanger sites for the iron–BaM–water system considered in the MaCoTe project at 25°C.

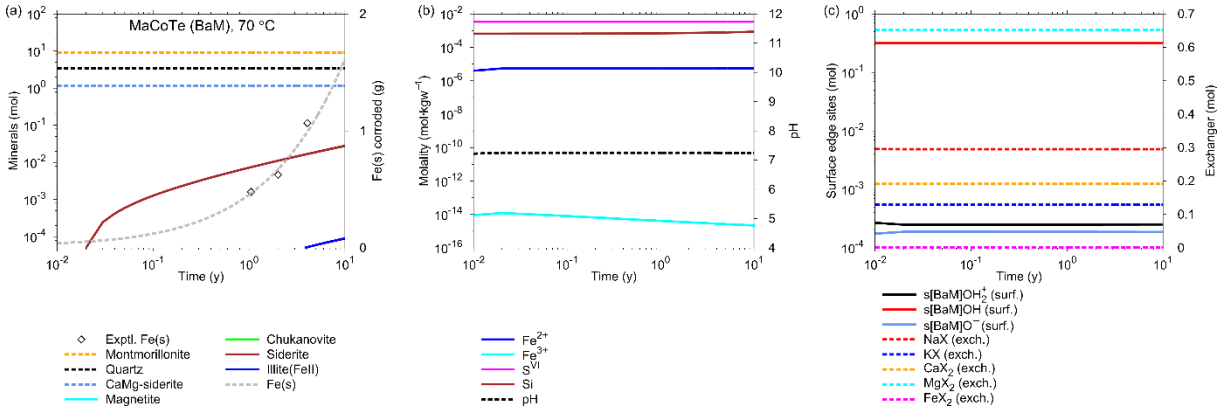

Figure 135. Evolution of (a) Fe(s) and the other mineral phases, (b) selected aqueous species, and (c) surface/exchanger sites for the iron–BaM–water system considered in the MaCoTe project at 70°C.

It can be seen in both Figure 135 and Figure 137 that at 70 °C, the iron corrosion rate corresponded very well with the available experimental data. The dominant corrosion product was siderite in all cases, which is in agreement with the results from the corresponding experiments. However, the MaCoTe experiments on the systems with BaM also reported chukanovite to be among the corrosion products, which was not the case in the respective kinetic model. Instead, Fe^{II}-illite was predicted in a very small amount as a minor corrosion/alteration product (this type of illite in iron–bentonite systems was qualitatively detected within CoPr but not MaCoTe experiments, see further discussion in Section 4.1.2.3.3). The amount of iron corroded and the corresponding siderite precipitated is more pronounced at the elevated temperature, as expected. Regarding the differences in the results for systems with BaM and MX-80, it can be concluded that the systems behaved qualitatively similar regardless of the bentonite type considered with siderite being the dominant corrosion product, which corresponds with the equilibrium results. The systems with BaM tended to slightly lower pH values of the aqueous solution (pH ≈ 7.3) than those with MX-80 (pH ≈ 8.0). The systems with BaM also contain a higher aqueous concentration of S^{VI} compared to their MX-80 counterparts.

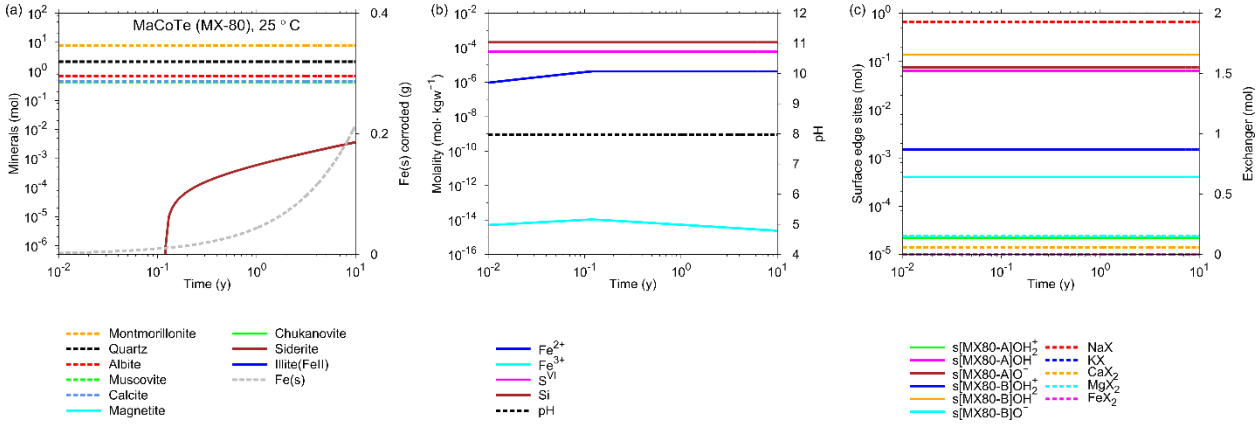

Figure 136. Evolution of (a) Fe(s) and the other mineral phases, (b) selected aqueous species, and (c) surface/exchanger sites for the iron–MX-80–water system considered in the MaCoTe project at 25°C.

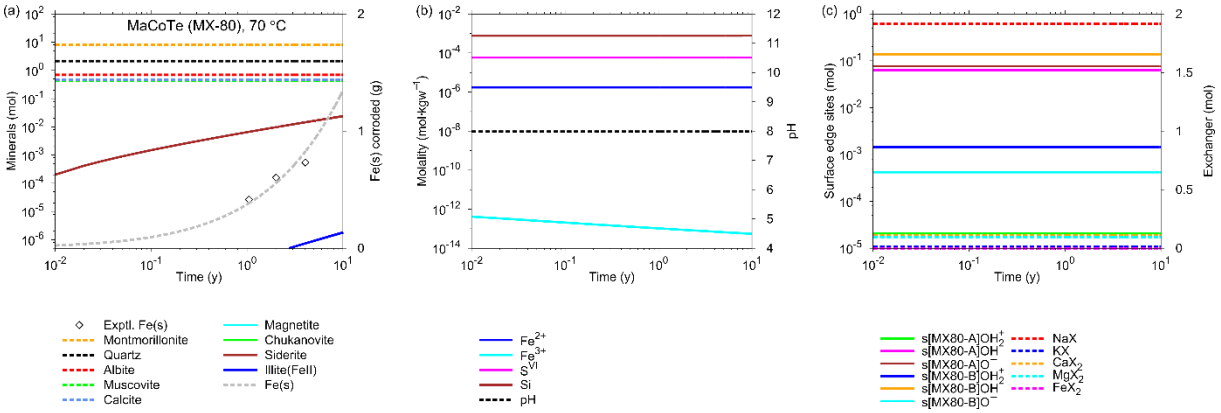

Figure 137. Evolution of (a) Fe(s) and the other mineral phases, (b) selected aqueous species, and (c) surface/exchanger sites for the iron–MX-80–water system considered in the MaCoTe project at 70°C.

4.1.2.3.2 UOS experiments

In order to model the UOS experiments, we again used non-unit values of the iron corrosion rate parameters (specifically, θ = 0.08 and η = 10), adapted to known experimental data on the amount of corroded iron from the MaCoTe project (Dobrev et al., 2022)(due to the similarity of the iron materials used in UOS and MaCoTe (i.e., iron plates)). The results for the iron–BaM–water system considered in the UOS project are shown in Figure 138 and Figure 139 for 25 °C and 70 °C, respectively.

It can be seen that, overall, the results are similar to those obtained for the iron–BaM–water system considered in the MaCoTe project, with siderite and Fe^{II}-illite being the main and minor corrosion products, respectively. The presence of siderite is in agreement with experimental observations made within the UOS project. One of the slight differences is that, at 25 °C, calcite is predicted to precipitate to a small extent as the reactions begin, but it further starts to slowly dissolve in favor of siderite, revealing its role in the system as a metastable product. Another difference is that the aqueous solutions of the UOS project tend to higher pH values (pH ≈ 7.2 for MaCoTe; pH ≈ 8.3 for UOS), which may be a result of the lower P_{CO2} level considered in UOS.

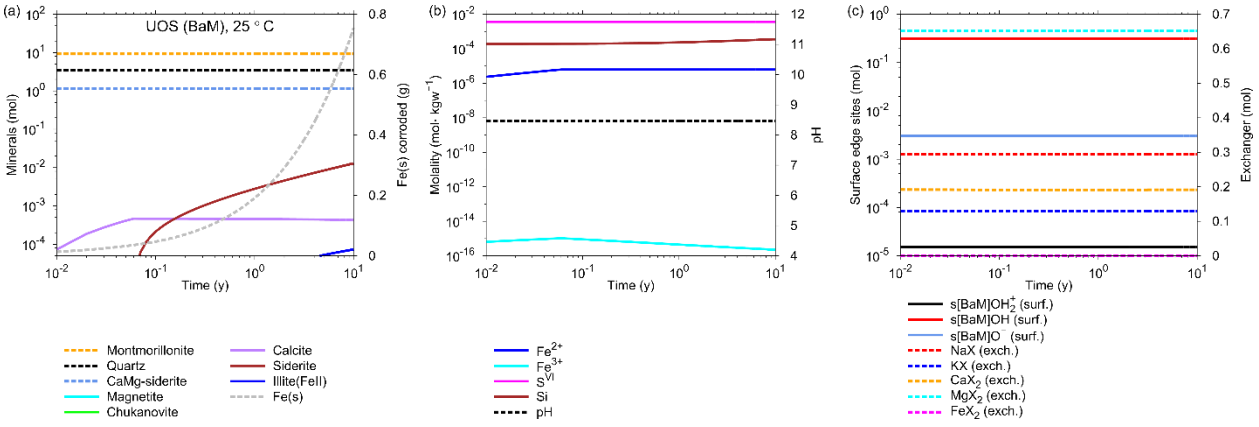

Figure 138. Evolution of (a) Fe(s) and the other mineral phases, (b) selected aqueous species, and (c) surface/exchanger sites for the iron–BaM–water system considered in the UOS project at 25°C.

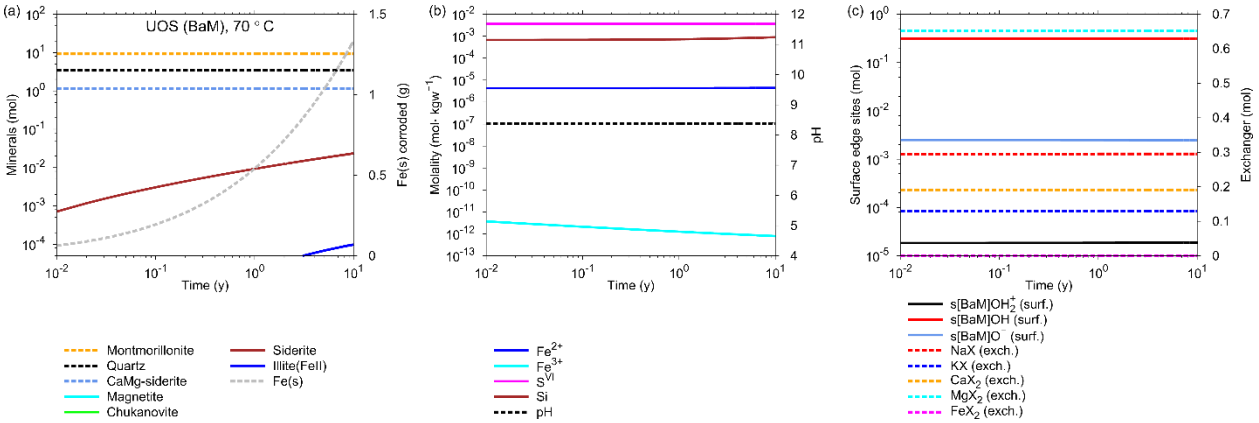

Figure 139. Evolution of (a) Fe(s) and the other mineral phases, (b) selected aqueous species, and (c) surface/exchanger sites for the iron–BaM–water system considered in the UOS project at 70°C.

4.1.2.3.3 CoPr experiments

Unlike in the MaCoTe and UOS projects, an iron powder was considered in the iron–bentonite–water systems of the CoPr project. Moreover, no experimental data on the iron corrosion rate was available from this project to which the parameters θ and η in Equation (15) could be adapted. As a result of the lack of such information, we used $\theta = \eta = 1$ for the kinetics of the iron powder, and a rate constant value (k_{Fe}) that corresponded to the most commonly applied corrosion rate value quoted in the literature, i.e., 1 μm y^{-1} (Gondolli et al., 2018a; Gondolli et al., 2018c).

The estimated evolution of the iron powder–BaM–water systems considered in CoPr are shown in Figure 140, Figure 141, and Figure 142 for 25, 40, and 70°C, respectively. At all temperatures, the main corrosion product is again siderite, later accompanied by a very small amount of Fe^{II}-illite.

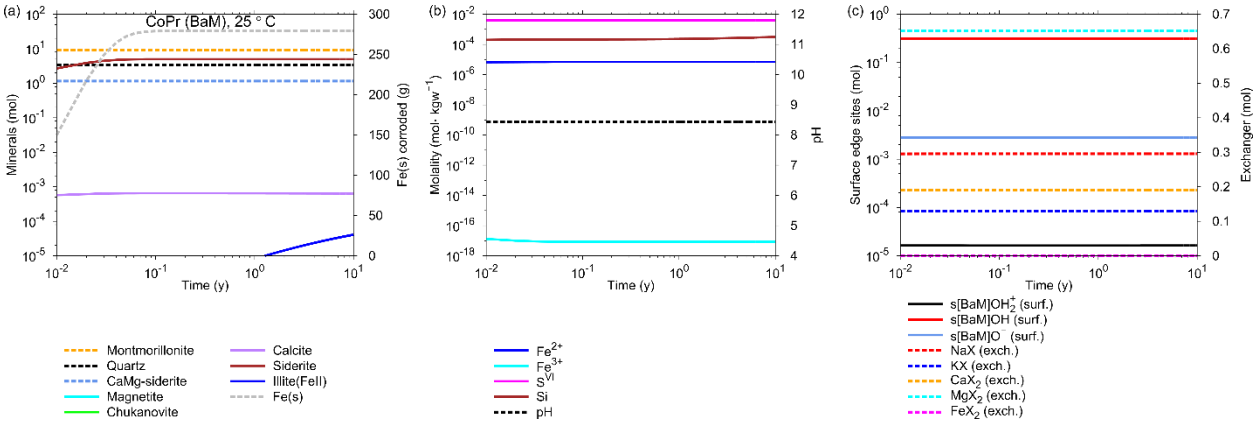

Figure 140. Evolution of (a) Fe(s) and the other mineral phases, (b) selected aqueous species, and (c) surface/exchanger sites for the iron powder–BaM–water system considered in the CoPr project at 25°C. The parameters θ and η in equation (15) were conventionally set to unity due to the lack of experimental data on the iron powder corrosion rate.

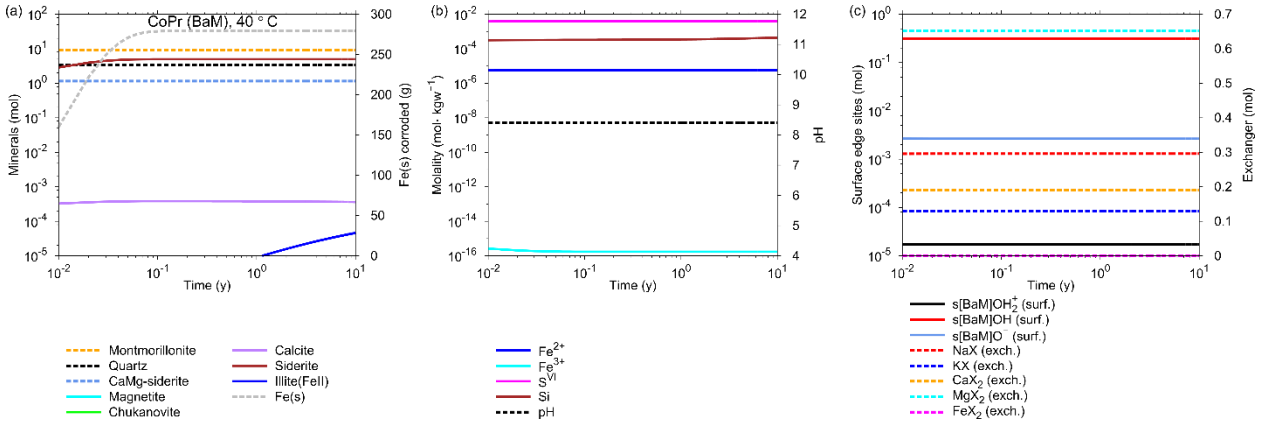

Figure 141. Evolution of (a) Fe(s) and the other mineral phases, (b) selected aqueous species, and (c) surface/exchanger sites for the iron powder–BaM–water system considered in the CoPr project at 40°C. The parameters θ and η in equation (15) were conventionally set to unity due to the lack of experimental data on the iron powder corrosion rate.

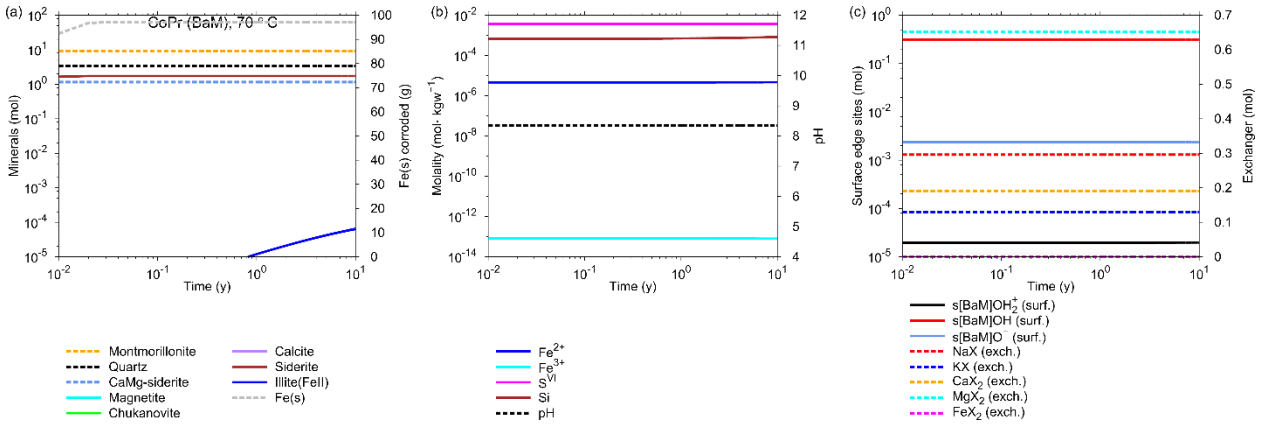

Figure 142. Evolution of (a) Fe(s) and the other mineral phases, (b) selected aqueous species, and (c) surface/exchanger sites for the iron powder–BaM–water system considered in the CoPr project at 70°C. The parameters θ and η in equation (15) were conventionally set to unity due to the lack of experimental data on the iron powder corrosion rate.

The extent of the iron corrosion, as modeled by the considered rate parameters of the iron powder, and the associated amount of siderite precipitated, is somewhat unrealistically overestimated. This was quantitatively in contradiction with the experimental findings from the CoPr experiments that a large amount of the iron in the samples was present in the form of unreacted iron (Gondolli et al., 2018a; Gondolli et al., 2018c) even after 1.5 years of the corrosion process. The corrosion rate should likely be damped artificially; however, no experimental data on the corrosion rate, against which the iron powder corrosion parameters could be optimized, is available for the CoPr project.

The presence of siderite, other Ca/Mg/Fe carbonates, and illite was experimentally confirmed in the CoPr experiments (with siderite being detected within in Fe-powder and carbonates and illite in the bentonite). Therefore, the kinetic results obtained for CoPr are in qualitative agreement with the experiment in this regard. In addition to these minerals, chukanovite was detected in the considered Fe-powder samples after the experiment, which is not the case in the model. Therefore, we performed an additional run of the kinetic model; however, the formation of secondary siderite was artificially suppressed this time. The results are shown in Figure 143. It can be seen that, in the absence of siderite, chukanovite is really formed instead of siderite as the main corrosion product. This means that, in the model, chukanovite is the second most thermodynamically stable Fe-carbonate phase, which, however, does not form when siderite is allowed to precipitate. In reality, one would likely detect both these phases, with chukanovite being a metastable product. It should be noted that the formation of chukanovite, after the suppression of siderite, was only predicted in the case of CoPr.

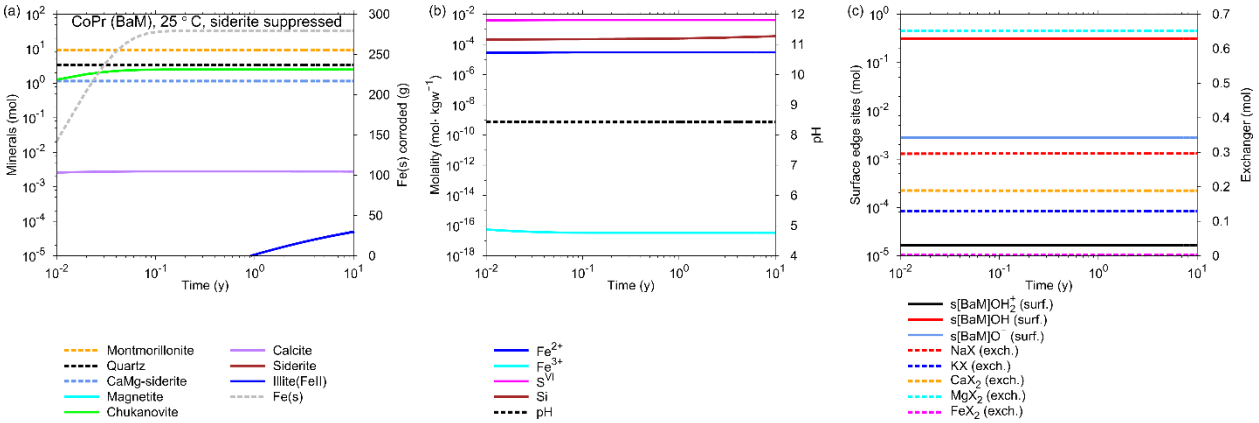

Figure 143. Evolution of (a) Fe(s) and the other mineral phases, (b) selected aqueous species, and (c) surface/exchanger sites for the iron powder–BaM–water system considered in the CoPr project at 25°C. The formation of siderite was suppressed this time.

The CoPr project was the only project of UJV in which magnetite was detected experimentally (specifically, in Fe-powder at 70°C). However, magnetite was not predicted to precipitate in the respective kinetic models. This can be explained by means of a molality-versus-pH diagram of Fe shown in Figure 144 and calculated using the Hydra/Medusa package (https://github.com/ignasi-p/eq-diagr). The diagram shows the most stable species and selected solid phases of Fe at a temperature of 25 °C (because this is the only possible temperature possible with respect to the Hydra database). The red solid circle in Figure 144 represents the aqueous solution composition obtained from the kinetic model of CoPr at a time of 5 years of system evolution. The diagram corresponds to and explains what we see in the kinetic model results: the most thermodynamically stable Fe-bearing mineral with respect to the solution at the given conditions (temperature, Fe concentration, log P_{CO2}, pH = 8.4) is siderite. For chukanovite or magnetite to be stable, it would be needed to increase the pH to almost 10, as suggested by the diagram in Figure 144.

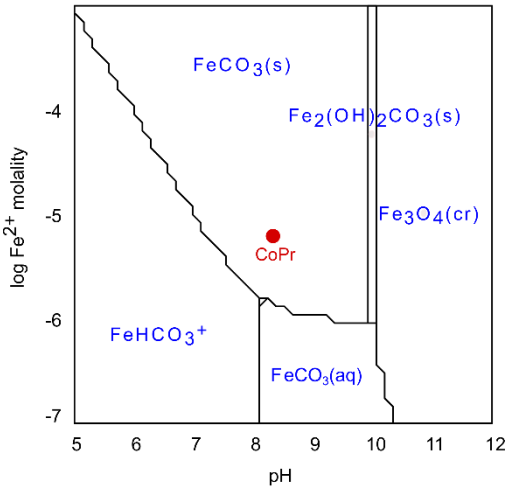

Figure 144. Molality versus pH diagram of Fe showing the most stable species and selected solid phases of Fe [namely, $FeCO_3$(s) – siderite; $Fe_2(OH)_2CO_3$(s) – chukanovite; Fe_3O_4(cr)– magnetite] at 25 °C and log P_{CO2}/atm = -3.40. The red solid circle represents the solution composition obtained from the kinetic model of CoPr at a time of 5 years of system evolution.

4.1.2.3.4 Summary of the kinetic modeling

To summarize the results of the kinetic modeling study, it was found that:

- the adaptation of the iron corrosion parameters θ and η allowed for the successful reproduction of the generally slow corrosion rate observed experimentally in MaCoTe,
- the major corrosion product was siderite in all cases, regardless of the specific bentonite material and log P_{CO2} considered, which corresponds with experimental findings. The minor corrosion product and, at the same time, a bentonite alteration product, was Fe^{II}-illite. Chukanovite was predicted only for CoPr when the formation of siderite was suppressed. Magnetite was not predicted to form at all,
- the bentonite primary minerals (particularly montmorillonite and quartz) underwent relatively minor and slow changes throughout the considered timescale of 10 years. In particular, the slow dissolution of montmorillonite predetermined that Fe^{II}-illite formed only in extremely small amounts, which corresponded to our earlier experimental observations,
- there are differences between the kinetic results presented in this study and those presented by us in previous works (Gondolli et al., 2018b; Gondolli et al., 2018c; Klajmon et al., 2021). The main reasons for these differences are the following: (i) the adapted iron corrosion parameters; (ii) the higher levels of P_{CO2}; (iii) the suppression of the secondary phyllosilicate minerals (e.g., chamosite and greenalite) applied in this work,
- the kinetic modeling also demonstrated that different considerations regarding the model parameters, in particular the corrosion rate parameters, provided quantitatively different results. We took advantage of having the experimental data on the iron corrosion rate to which the iron corrosion parameters were fitted for its application in the modeling of the MaCoTe and UOS experiments.

4.1.2.4 Reactive transport modeling of interactions in iron–bentonite–water systems

The 1D reactive transport model was developed in this project in PHREEQC with the aim of studying not only kinetic but also diffusive transport processes in the iron–bentonite–water system. The reactive transport model allows for a more detailed and realistic description of the reactive system with respect to the timescale of the processes and spatial character of the occurring reactions such as dissolution/precipitation of solid phases.

The model applied in this work was developed on the basis of our previous PHREEQC model described in Gondolli et al., (2018a,c) . In the model, all the thermodynamic and kinetic parameters and consideration used in the kinetic model remained unchanged; only the TRANSPORT datablock (Parkhurst and Appelo, 2013) was added to the script to describe the diffusive transport of aqueous solution species. The current PHREEQC script for the reactive transport model is attached to this report in the electronic annex.

The geometry used in our 1D reactive transport model was based on the parameters of the iron powder/assemblage used in the considered experiments. The geometry is illustrated in Figure 145 for the CoPr experiment as an example. A corrosion cell (Cell 1 in Figure 145, thickness 1 mm) containing only iron and the respective BPW was attached to the bentonite, which was divided into 10 cells, each with a thickness of 1 mm. Such a model, called the “corrosion cell model”, is often used in literature studies (e.g., Hunter et al. (2007), Wilson et al. (2015)). In each of the 10 bentonite cells, 1 dm^3 of a given BPW (as the initial liquid phase) was considered, together with the bentonite material (3.86 kg of bentonite for BaM and 3.50 kg for MX-80, corresponding to the porosities of 0.415 and 0.430, respectively; see Table 33). The mole number of Fe(s) in the corrosion cell was adapted so that it corresponded to the bentonite/iron ratio used in the real experiments. For CoPr as an example, assuming the total weight of bentonite of 38.6 kg (10 x 3.86 kg) and the bentonite/iron ratio of 3.5:1, the mole number of Fe(s) was 198 mol (i.e., 11 kg).

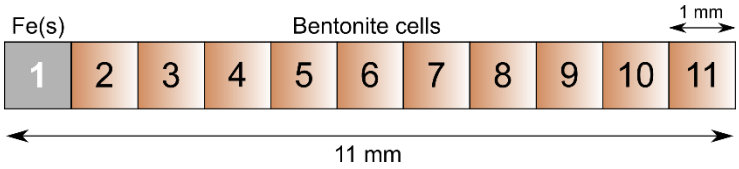

Figure 145. Geometry of the iron–bentonite assemblage considered in the 1D reactive transport model of the CoPr experiment. Cell 1 is the iron corrosion cell, whereas cells 2–11 represent the bentonite.

For each aqueous solution species, the effective diffusion coefficient (D_e) at 25°C was set to 1.3×10^{-10} $m^2\,s^{-1}$, as used previously in Červinka et al. (2018). In order to recalculate this value so that it corresponds to the elevated temperatures of 40 and 70°C, we used the following relation (Bildstein et al., 2006):

$$D_e(T) = D_e(298.15)\exp\left[-\frac{E_a}{R}\left(\frac{1}{T}-\frac{1}{298.15}\right)\right] \quad (18)$$

where E_a is the activation energy (E_a = 13.8 kJ mol^{-1} (Li and Gregory, 1974)). The values at 40°C and 70°C were calculated to be $D_e = 1.7\times10^{-10}$ $m^2\,s^{-1}$ and $D_e = 2.7\times10^{-10}$ $m^2\,s^{-1}$, respectively (see Gondolli et al. (2018c) for further details). The reaction system was considered closed on both sides with respect to the diffusion.

The time scale of the performed reactive transport calculation was not 10 years as for the kinetic model but was extended to 30 years in order to include also the long-term evolution of the systems beyond the experimental scales; however, the states of the system roughly corresponding to the duration of the experiments are reported in the figures below. The calculations were again performed at 25 and 70°C (and 40°C in the case of CoPr).

4.1.2.4.1 MaCoTe experiments

The results of the reactive transport model for the MaCoTe experiment are shown in Figure 146 to Figure 149 in the form of the geochemical evolution of solid phases (in mole numbers) and molality of Fe in the transport cells of the system at four different times (1, 5, 15 and 30 years) from the beginning of the simulation. The simulated system contained one corrosion and 11 bentonite cells (each having 1 mm), to capture the experimental geometry (the bentonite layer considered in MaCoTe had around 11 mm).

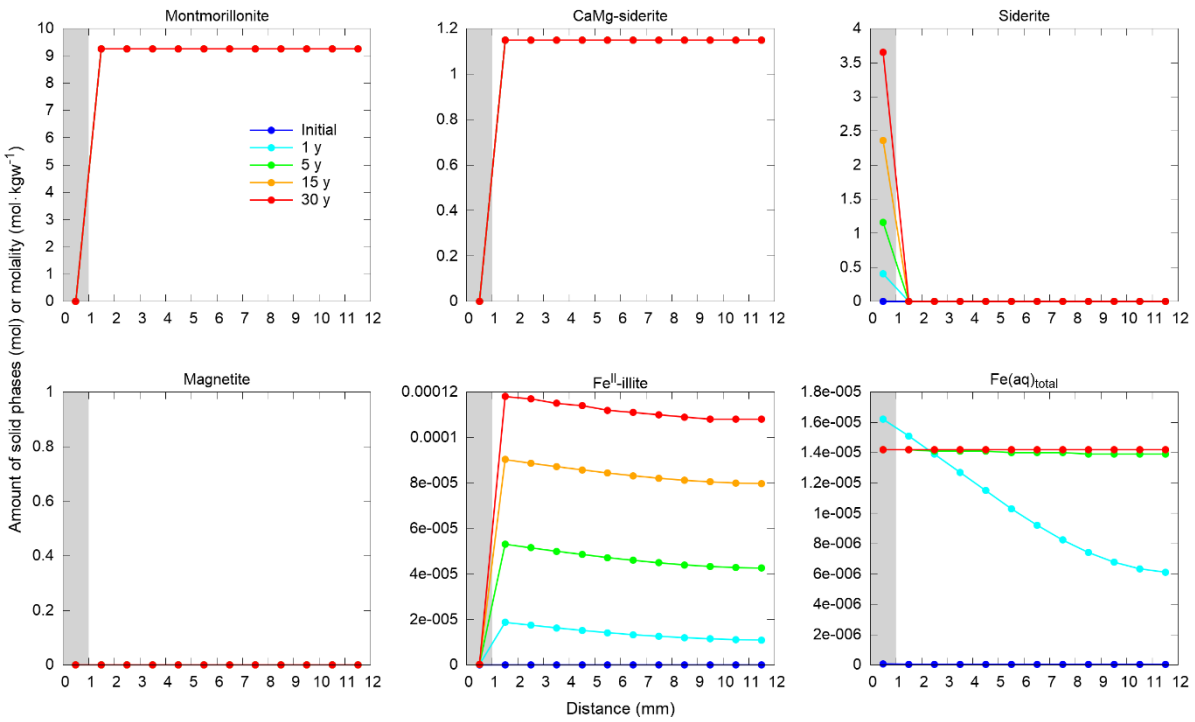

Figure 146. Evolution of the bentonite primary minerals, secondary minerals, and aqueous molality of Fe in the iron–BaM–water system considered in the MaCoTe project at 25°C after 1, 5, 15, and 30 years after the start of the simulation. The grey zone represents the corrosion cell.

The results for the system with BaM as the bentonite at 25°C are shown in Figure 146. As can be seen, the amounts of montmorillonite and CaMg-siderite did not change significantly throughout the entire simulation period of 30 years. This would mean that montmorillonite dissolution does not represent a significant geochemical process in the studied experimentally-relevant timescale. The only corrosion products were siderite and Fe^{II}-illite. Siderite, the dominant corrosion product, precipitated directly and only in the iron corrosion cell (i.e., siderite was not formed in the bentonite cells). This can be explained by the fact that only the solution in the corrosion cell was sufficiently concentrated with Fe(aq) and supersaturated with respect to siderite (the saturation index of siderite exceeded the value of 0, i.e., the saturation state) (Savage et al., 2010). In terms of the transport modelling in PHREEQC, the water from the corrosion cell was then "sent" to the bentonite cells (cells 2–12 in Figure 146) where siderite precipitation did not occur since the water was no longer supersaturated with respect to this mineral. The precipitation of siderite in the iron corrosion cell indicates the possibility of filling this space by newly formed crystals, thus decreasing its porosity and possibly inhibiting the Fe corrosion rate. Neither magnetite nor chukanovite were predicted to precipitate. Fe^{II}-illite precipitated only in the bentonite cells. However, it appears that the iron corrosion and the subsequent transport of Fe(aq) to the bentonite material has an effect on the amount of Fe^{II}-illite precipitated, as the first bentonite cells always contain slightly more Fe^{II}-illite than the other cells.

Regarding the evolution of the Fe concentration, 1 year from the beginning of the simulation, the values in the corrosion cell and also in the first bentonite cells were significantly increased, which was the result of the corrosion reaction. In the following time period (5 years), Fe gradually reached constant levels across all bentonite cells until they finally reached approximately the same values between 5 to 15 years of the simulation.

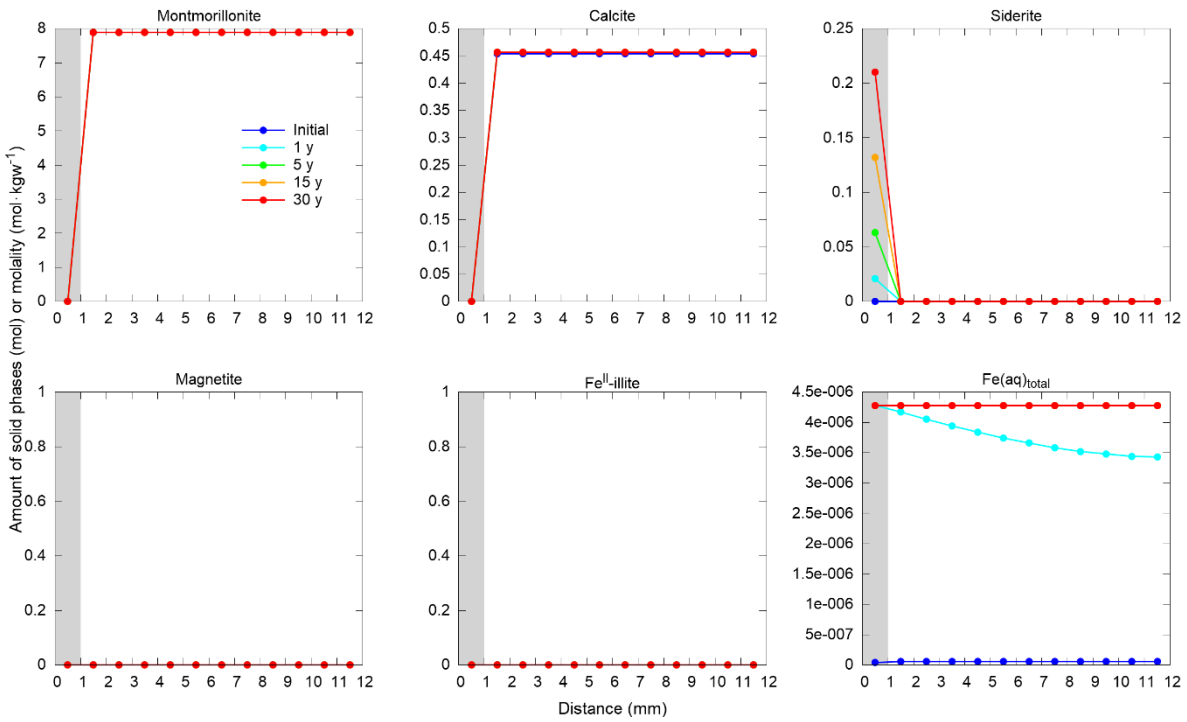

Figure 147. Evolution of the bentonite primary minerals, secondary minerals, and aqueous molality of Fe in the iron–MX-80–water system considered in the MaCoTe project at 25°C after 1, 5, 15, and 30 years after the start of the simulation. The grey zone represents the corrosion cell.

The results for the system with MX-80 as the bentonite at 25°C are depicted in Figure 147. The dissolution of the primary minerals of MX-80 (montmorillonite, muscovite, albite, and calcite) again represented a quantitatively insignificant process in the considered time scale. The dominant corrosion product was siderite (forming again only in the corrosion cell). Fe^{II}-illite did not precipitate this time, which was already predicted by the kinetic model (see Section 4.1.2.3.1 or Figure 136). This may qualitatively indicate a lesser propensity of this system to illitization compared to the system with BaM.

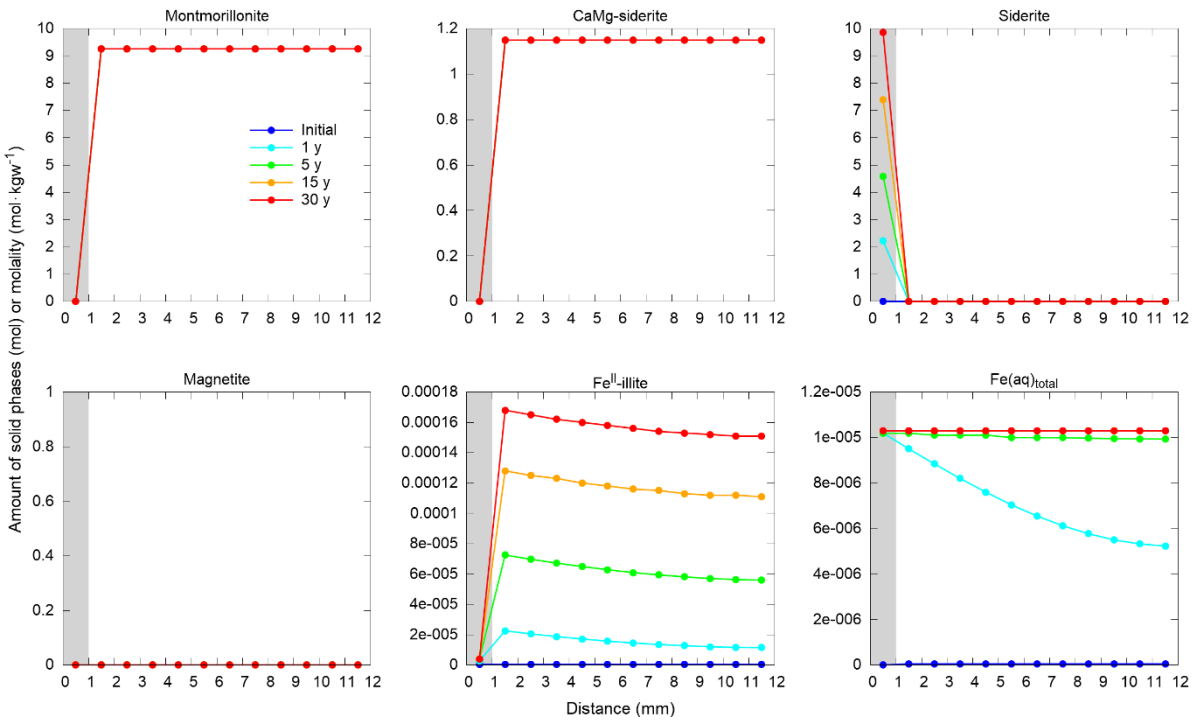

Figure 148. Evolution of the bentonite primary minerals, secondary minerals, and aqueous molality of Fe in the iron–BaM–water system considered in the MaCoTe project at 70°C after 1, 5, 15, and 30 years after the start of the simulation. The grey zone represents the corrosion cell.

The results for both systems at 70°C are shown in Figure 148 and Figure 149. It can be seen that the on-going geochemical processes are faster at 70°C compared to the situation at 25°C. However, the amount of the primary minerals remained almost unchanged even after 30 years of the evolution. The main corrosion product was again siderite in both BaM- and MX-80 based systems. Fe^{II}-illite did precipitate at 70°C even in the MX-80 based system. Furthermore, Fe^{II}-illite precipitated not only in the bentonite cells but also in the iron corrosion cell (but relatively only slightly; see Figure 148 and Figure 149). Searching for an explanation, we found that the initial BPW has already been supersaturated with respect to Fe^{II}-illite at the elevated temperature of 70°C, with Si and Al molalities high enough for Fe^{II}-illite to precipitate. Note that Fe^{II}-illite was not considered as an equilibrium phase in the BPW calculation (Section 4.1.2.1). This enabled the precipitation of the illite even in the corrosion cell.

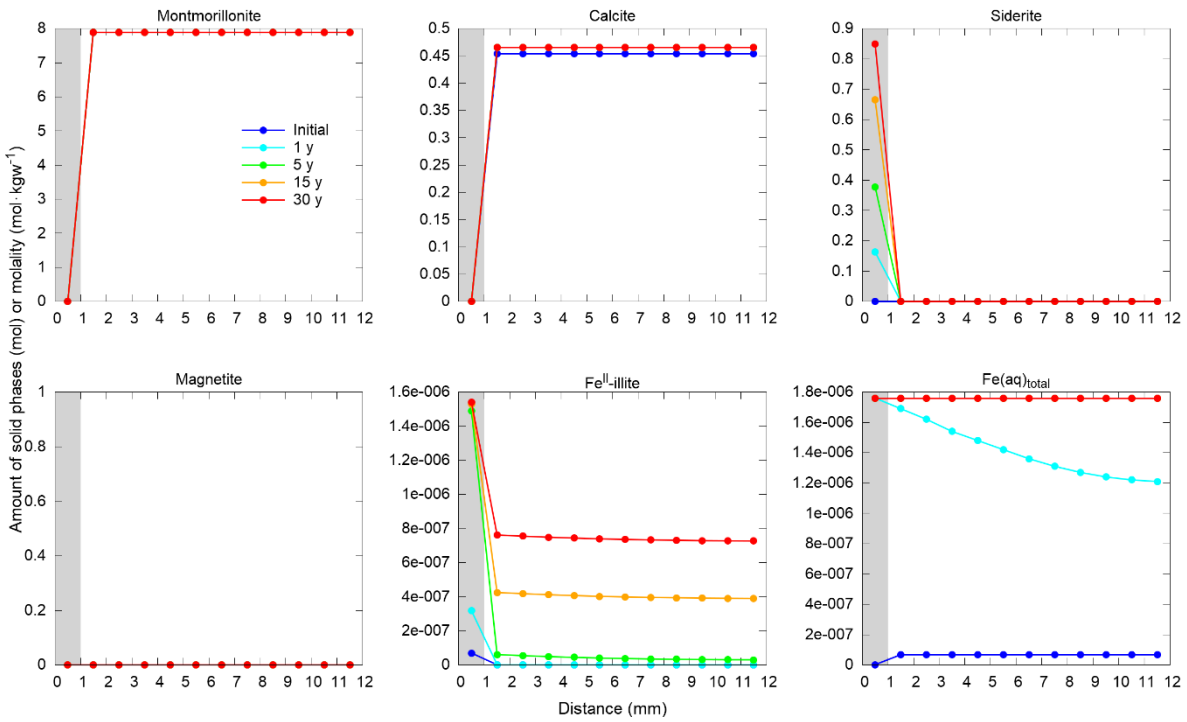

Figure 149. Evolution of the bentonite primary minerals, secondary minerals, and aqueous molality of Fe in the iron–MX-80–water system considered in the MaCoTe project at 70°C after 1, 5, 15, and 30 years after the start of the simulation. The grey zone represents the corrosion cell.

4.1.2.4.2 UOS experiments

The results of the reactive transport model for the UOS experiment at 25 and 70°C are shown in Figure 150 and Figure 151, respectively. The simulated system contained one corrosion and 11 bentonite cells (each having 1 mm), to capture the experimental geometry (the bentonite layer considered in UOS had 11 mm).

At 25°C, the main character of the evolution of the system is similar to that of the iron–BaM–water system considered in the MaCoTe project at the same temperature (i.e., siderite is the main and Fe^{II}-illite the minor corrosion product). However, at 70°C, magnetite is surprisingly formed as the main corrosion product instead of siderite. This is in contrast to both the kinetic results obtained for this system at 70°C (see Figure 139) and the results obtained for the (similar) BaM-based system considered in the MaCoTe project (see Figure 148), where magnetite did not precipitate at all. One possible explanation for that is the lower P_{CO2} value considered in UOS, which may result in sufficiently high pH for magnetite to precipitate. However, the possibility of magnetite to be a corrosion product is not completely irrelevant, as magnetite (in the vicinity of corroding iron) was detected experimentally at 70°C in the CoPr project (Gondolli et al., 2018a; Gondolli et al., 2018c).

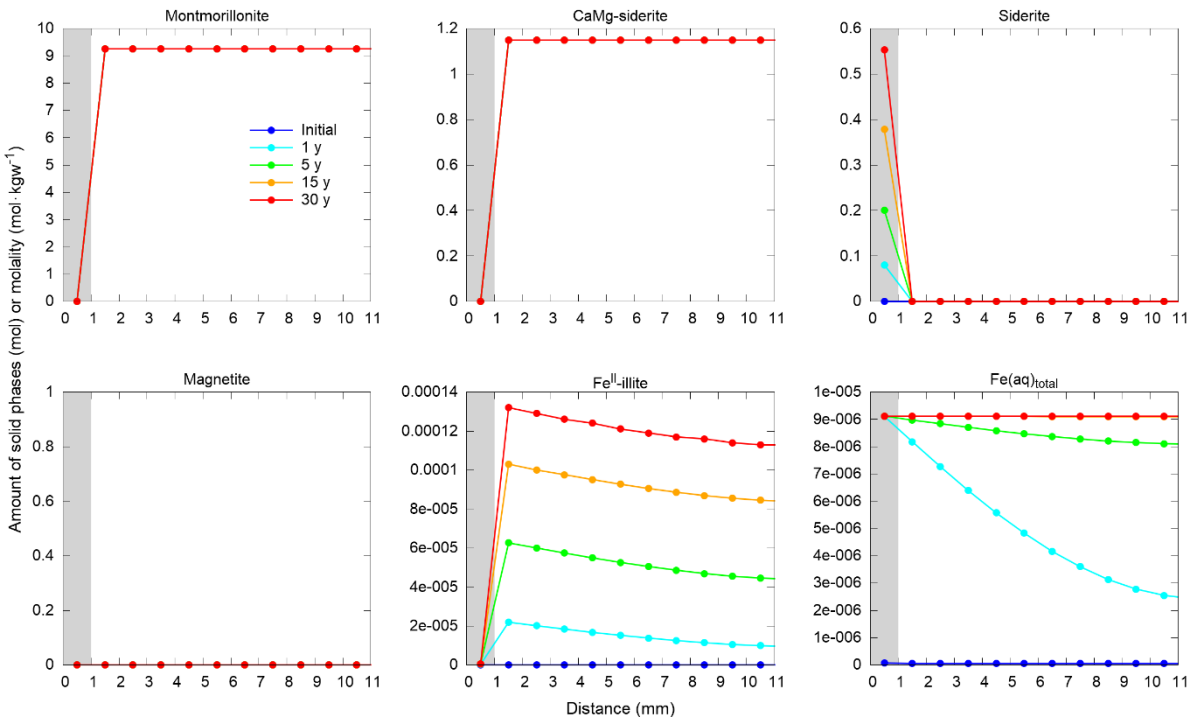

Figure 150. Evolution of the bentonite primary minerals, secondary minerals, and aqueous molality of Fe in the iron–BaM–water system considered in the UOS project at 25°C after 1, 5, 15, and 30 years after the start of the simulation. The grey zone represents the corrosion cell.

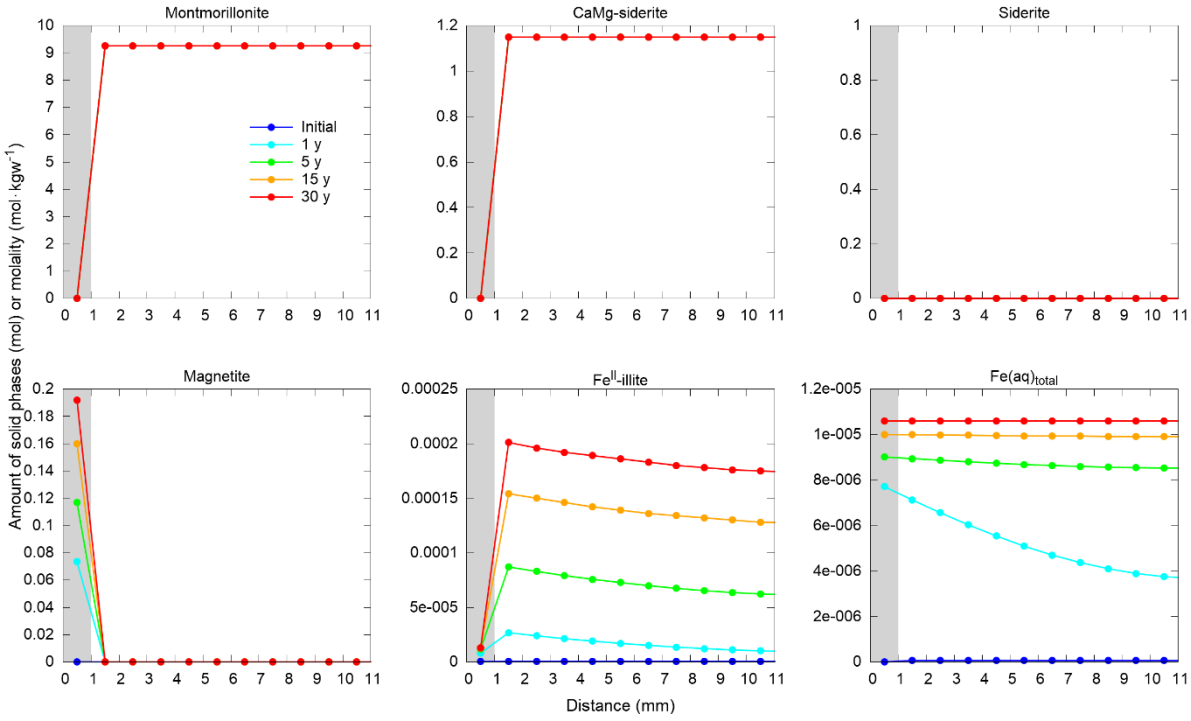

Figure 151. Evolution of the bentonite primary minerals, secondary minerals, and aqueous molality of Fe in the iron–BaM–water system considered in the UOS project at 70°C after 1, 5, 15, and 30 years after the start of the simulation. The grey zone represents the corrosion cell.

4.1.2.4.3 CoPr experiments

The results of the reactive transport model for CoPr are shown in Figure 152, Figure 153, and Figure 154 for 25, 40, and 70°C, respectively. The simulated system contained one corrosion and 10 bentonite cells (each having 1 mm), to capture the experimental geometry (see Figure 145).

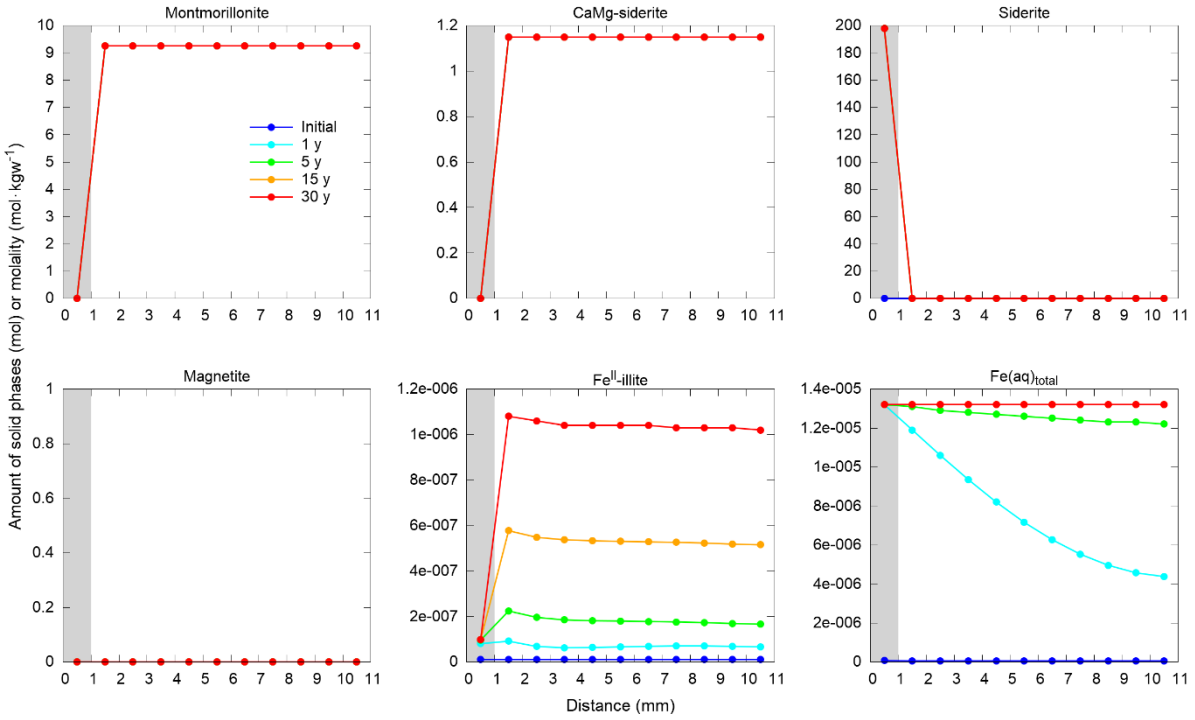

Figure 152. Evolution of the bentonite primary minerals, secondary minerals, and aqueous molality of Fe in the iron powder–BaM–water system considered in the CoPr project at 25°C after 1, 5, 15, and 30 years after the start of the simulation. The grey zone represents the corrosion cell.

Regarding the results of the reactive transport model for CoPr, the main corrosion product was siderite, with Fe^{II}-illite being again the minor corrosion/alteration product. However, the on-going reactions are significantly faster and, thus, quantitatively more extensive than those in both UOS and MaCoTe due to the overestimated iron corrosion rate, as discussed in Section 4.1.2.3. Most of the geochemical reactions (e.g., iron corrosion, siderite precipitation) are "finished" within first years from the beginning of the simulation. On the other hand, other processes such as Fe^{II}-illite precipitation appeared to be more continuous, with its amount gradually increasing over the simulated period of 30 years. The same is true also for the aqueous Fe concentration. In the future model for CoPr, the corrosion rate of the iron powder used in CoPr will need an artificially reduction to obtain more realistic modeling data; at the moment, however, there is no experiment-based data to adjust the corrosion rate (see Section 4.1.2.3). The amount of Fe^{II}-illite precipitated seemed to increase with increasing temperature.

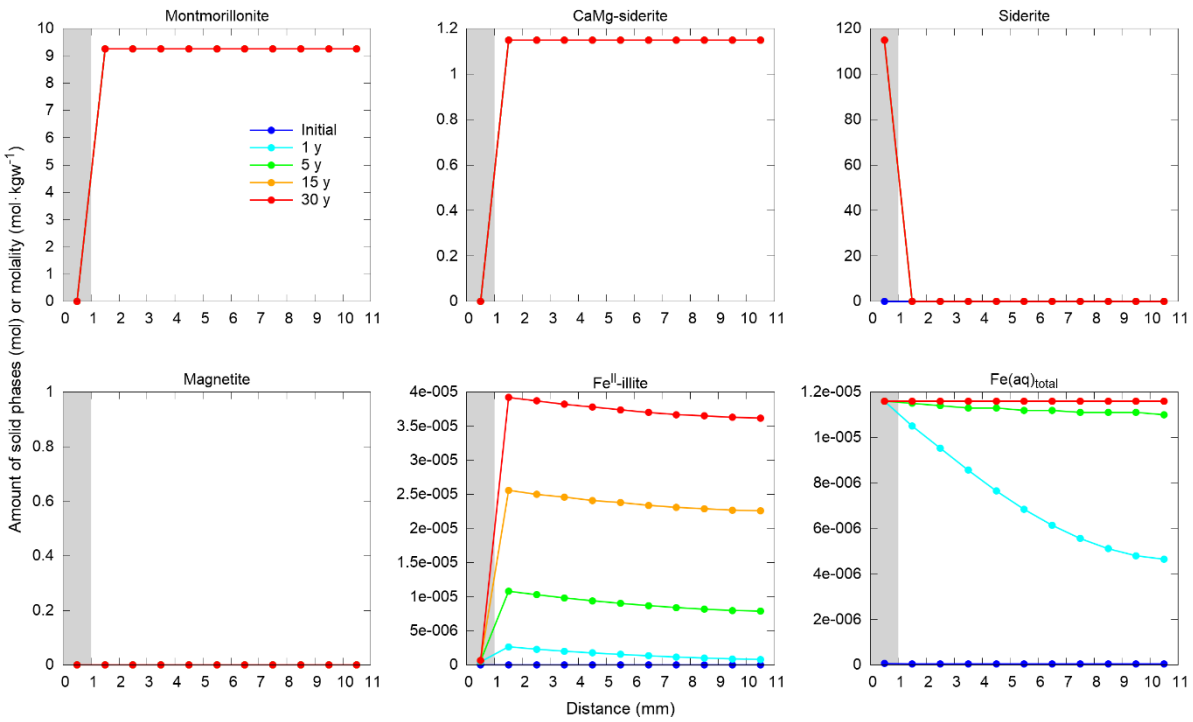

Figure 153. Evolution of the bentonite primary minerals, secondary minerals, and aqueous molality of Fe in the iron powder–BaM–water system considered in the CoPr project at 40°C after 1, 5, 15, and 30 years after the start of the simulation. The grey zone represents the corrosion cell.

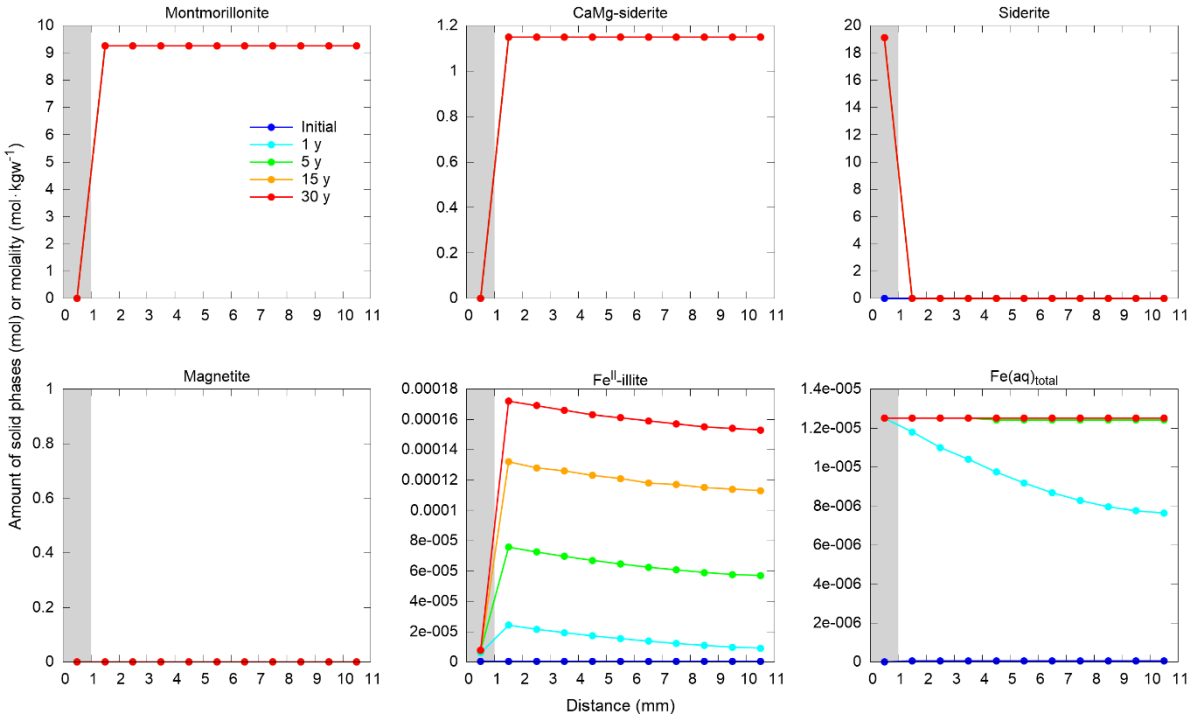

Figure 154. Evolution of the bentonite primary minerals, secondary minerals, and aqueous molality of Fe in the iron powder–BaM–water system considered in the CoPr project at 70°C after 1, 5, 15, and 30 years after the start of the simulation. The grey zone represents the corrosion cell.

4.1.2.4.4 Summary of the reactive transport modeling

To summarize the results of the reactive transport modeling, it was found that:

- the results were generally consistent with those of the kinetic model in most cases, but allowed for a more detailed insight into the spatial location of the geochemical changes,
- in most cases, the main corrosion product was siderite and was formed exclusively in the iron corrosion zone (the corrosion cell) and not inside the bentonite cells,
- Fe^{II}-illite was formed (but in very small amounts) in the bentonite, with its amount i) decreasing with increasing distance from the iron corrosion zone and ii) increasing with increasing temperature,
- quantitatively, the dissolution of the bentonite primary minerals was an insignificant process.

4.1.2.5 Limitations and uncertainties of the model

Modeling of iron–bentonite–water interactions represents a very complex and challenging task. This is particularly because the high number of system components and physicochemical processes included. All these processes need to be adequately described and parametrized. However, the parameters are not always available for the systems of interest. Therefore, it is necessary to apply adequate simplifications and estimates. These are, however, inevitably associated with lesser or greater uncertainties that may influence the modeling results (e.g., Samper et al. (2008), Itälä (2009)). The goal of the modeling activities was to develop and apply reasonably simplified geochemical models for the considered iron–bentonite–water systems that would still be complex enough to capture the character of the main geochemical processes at least qualitatively. Therefore, the presented results have to be interpreted with a sufficient degree of caution. The fundamental limitations of the simple equilibrium and kinetic models were already discussed in sections 4.1.2.2 and 4.1.2.3, respectively (e.g., no time or spatial characteristics of the reactions accounted for). Even the reactive transport model exerts the following important limitations and uncertainties:

- diffusive transport in only one dimension was considered, although it is, in reality, a 3D process (therefore, the modeled diffusion and geochemical evolution can be overestimated (Červinka et al., 2018; Gondolli et al., 2018c)),
- not considering changes in porosity and subsequent modification in diffusivity due to mineral dissolution/precipitation reactions,
- uncertainties in kinetic parameters (rate constants, corrosion rate, reactive surface areas, etc.),
- precipitation/dissolution of secondary phases was considered to be an equilibrium (immediate) and not a kinetic process,
- selection of appropriate secondary phases,
- CO_2 partial pressure may achieve different values in real systems,
- the same effective diffusion coefficient value is considered for all ions and neutral species (Itälä, 2009),
- bentonite swelling is not considered in the PHREEQC model,
- the model does not account for the three different water types in bentonite (i.e., interlayer, double layer, and free waters) (Itälä, 2009),
- as mentioned by (Itälä, 2009), the thermodynamic data itself may have uncertainties, particularly at elevated temperatures (e.g., 70°C considered in this study).

4.2 Experiments and modelling of interaction between steel and Boda clay (MTA EK, SCK CEN)

4.2.1 Introduction

The aim of the present experiments is to gain information on corrosion processes that can impact carbon-steel/clay interfaces for different applied conditions (chemical environement, temperature,

saturated conditions). The present work is an attempt to implement the values of corrosion intensity which we measured in laboratory tests.

We worked to do comprehensive characterization of the systems, with special focus on the proper understanding of the processes occurring on the surface of the steel/clay interface.

All states that engage in any kind of nuclear application must consider the management of radioactive waste and make sure it is handled in a safe manner regarding the level of radioactivity and complying with national/international regulations. There is a broad consensus that the preferred method of ensuring long term safety for high level radioactive waste (HLW) is isolation in a deep geological repository (DGR), which will provide passive multibarrier isolation of radioactive materials. The vitrified HLW form in a steel canister is specifically designed for long term durability in storage and disposal (Hill Shannon, 2016, Gras, 2002). The requirements for container lifetime and integrity depend on the DGR concept and the chosen geological medium (Crusset et al., 2017). The focus is on two contacting materials to obtain information on the geochemical evolution close to an interface in terms of chemical variables and alteration in solid phase composition at a detailed small scale.

The interface between carbon steel and clay is a key issue in the design of a disposal cell for vitrified HLW in argillaceous rock formations for the Hungarian national waste disposal program. The design relies on steel-containers (S235JR carbon steel) containing the HLW encased in a prefabricated cylindrical clay buffer material. The clay is originated from the Boda Claystone Formation (BCF), the host rock considered for the final disposal program in Hungary (Lazar & Mathe, 2012, Breitner et al., 2014). The pH must be kept at high values during the thermal phase, and for a much longer period after, to keep the carbon steel container passivated for limiting corrosion and ultimately to prevent radionuclide release. The aim of the present study is to gain information on chemical-physical alterations of the steel/clay interface, for different environmental conditions (temperature, groundwater). Lab scale experiments were performed during 12 months under water-saturated and anaerobic conditions. A set of complementary characterization methods were applied to the liquid and solid phases with the support of geochemical modelling.

4.2.2 Experimental details

4.2.2.1 Boda Clay and carbon steel composition

The Boda Block of BCF forms an anticline structure. In this block the maximum thickness of the BCF varies between 700-1000 meters in the central region. During the sedimentation catagenetic stage was finally reached under high temperature (200-250 °C) and pressure (120-150 MPa). Six main rock types of BCF can be defined based on mineralogical, geochemical, and textural considerations: albitic claystone, albitolite, „true" siltstone, dolomite interbeddings, sandstone and conglomerate. The BCF has the following parameters: porosity (%): 0.6-1.4; hydraulic conductivity (m/s): 10^{-11}-10^{-13}; solid density (kg/m^3): 2300-2700, cation exchange capacity (m_{eq}/100 g): min: 11.2, best estimate: 12, max: 16.2. Since albitic claystone is the most dominant rock type of the formation, a representative section of the BAF-2 drilling core was selected for the present study.

The mineralogical composition of the claystone section of the BAF-2 drilling core of BCF: analcime (13 wt.%), calcite (12 wt.%), dolomite (2 wt.%), quartz (9 wt.%), Na-plagioclase (11 wt.%), K-feldspar (4 wt.%), hematite (6 wt.%), chlorite (5 wt.%), muscovite/illite (29 wt.%), illite/smectite (7 wt.%).

The initial water phase considered in the experiment is a synthetic BCF pore water (SBPW) with the following composition (mol/L): Na^+: 1.7×10^{-2}, Ca^{2+}: 3.1×10^{-3}, Mg^{2+}: 2.3×10^{-3}, K^+: 1.8×10^{-4}, Sr^{2+}: 1.5×10^{-5}, Cl^-: 2.3×10^{-2}, HCO^{3-}: 6.1×10^{-4}, SO_4^{2-}: 1.9×10^{-3} pH: 8.1, Eh= -300 ± 10 mV (measured at RT) (Breitner et al., 2014).

The steel container was made of untreated S235JR carbon steel. The chemical purity of the C-steel corresponded to ≤0.17 C, ≤0.3 Si, ≤1.4 Mn, 0.035 P, 0.035 S, ≤0.55 Cu, ≤0.012 N in wt.%.

4.2.2.2 Design of the experiment

The design of the experiment and the selected parameters (BCF and synthetic pore water) are based on the following considerations.

Transport processes are anticipated to remain diffusion-dominated over geologic time frames (hundreds of thousands to millions of years): BCF has a self-healing capacity potential, a weak sensitivity of hydraulic conductivity to changes in loading, there are thick topset beds over the potential disposal zone and the uplift of W-Mecsek is low, so that no major changes in hydraulic gradient are expected, porosity and hydraulic conductivity of the intact rock matrix is very low, a very small amount of swelling clays is fundamentally influencing rock behavior. The flow of free water is limited as well by the size of capillaries. Mostly diffusion processes take place inside the rock even on the level of fractures (Lazar & Mathe, 2012). Geochemical stability of the groundwater-pore water system over geologic time frames: the lack of organic material and pyrite helps to maintain the long-term geochemical stability of the formation, intensive oxidation processes influencing the rock's mechanical status considerably are not expected to occur within the lifetime of the repository, due to the burial (thermal) history of BCF, the possible impact of heat production of HLW's (e.g. alteration of clay minerals, thermal softening) will be rather limited. Geomechanical stability of the formations to natural perturbations: the potential disposal zone is protected from the natural perturbations by the thick topset beds.

The experimental set-up was prepared in triplicate as shown in Figure 155. For each system two Teflon containers were built, to ensure saturation during the experiments: an external Teflon container: height: 160 mm, diameter: 90 mm and an internal Teflon container: h: 100 mm, d: 50 mm.

The inside is composed by a steel container.

During the experiments the crushed BCF claystone was steeped with synthetic pore water resulting in a saturation of 100%. The initial BCF pore water considered in the experiment was a modelled synthetic pore water. The conditioning of Boda claystone with the applied SBPW was carried out at room temperature. The calculations of the Boda pore water chemistry were performed with the geochemical speciation code MINSORB and the Nagra/PSI 01/01 thermodynamic database (Bradbury and Baeyens 2017a and Bradbury and Baeyens 2017b). The chemical composition of the Boda pore water was calculated at fixed p_{CO2} ($10^{-3.5}$ bar)/pH (=8.0) i.e., in equilibrium with atmospheric p_{CO2}, and under the constraint of calcite, dolomite and quartz saturation. Na^+ or Cl^- concentration was adjusted to maintain charge neutrality, while Ca, Mg, Si and C(IV) concentrations were defined over the above boundary conditions.

After being filled with synthetic pore water, all three systems were closed. The clay was kept fully saturated. During the experiment, a constant temperature of 80±2 °C was imposed. The corrosion potential was monitored using a platinum wire that was embedded within the clay and C-steel wire (also S235JR) spot welded on the container. Measurements were taken at 20-second intervals. Initially, the potential between the platinum wire and a calomel electrode was checked using a Metrohm Autolab PGStat204 potentiostat. The measurements were conducted in the soaking water under specific conditions, namely at pH 8.1 and for a temperature of 22.8 °C. To ensure accurate interpretation and comparison of the results, the obtained corrosion potential was then adjusted using an offset correction. This correction was applied to align the results with the standard hydrogen electrode (SHE) scale. By making this adjustment, the corrosion potential values can be properly referenced and analyzed in relation to other electrochemical systems or experiments conducted using the SHE scale.

After 3, 7 and 12 months one experimental setup was opened for post-mortem characterization (hereafter referred as CSC-3M, CSC-7M, CSC-12M respectively (CSC as C-steel-clay).

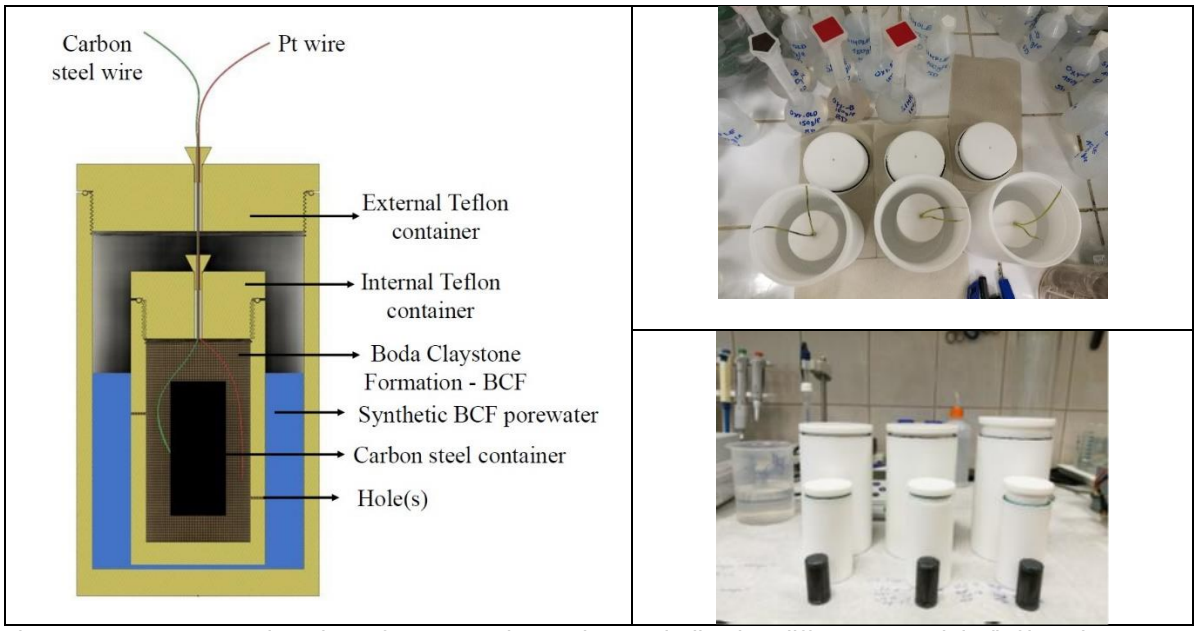

Figure 155 - Cross-section view of one experimental setup indicating different materials (left) and a photograph showing the parts of the experimental setup in triplicate (right).

When retrieved, after 3, 7 and 12 months, the C-steel containers were covered with adhering clay making direct characterization of steel surface difficult. The corrosion interfaces were thus investigated on cross-sections.

4.2.3 Experimental results

The corrosion products formed at the C-steel/clay interfaces (for anoxic environment and constant 80°C temperature), were characterized using different techniques such as SEM/EDX analysis and micro-Raman (µRaman). Changes of cation/anion concentrations in the surrounding synthetic pore water were measured by ICP-OES and IC.

4.2.3.1 Corrosion potential

Figure 156 gives the relationship of corrosion potential with months of exposure. The evolutions of the corrosion potential measured on the two first steel/clay setups (3M, 7M) show a random fluctuation throughout the first and last stage of experiments. It is assumed that an increase in corrosion potential indicates the formation of a passive layer, with a sudden drop indicating the loss of this film layer. This fluctuation indicates local corrosion processes.

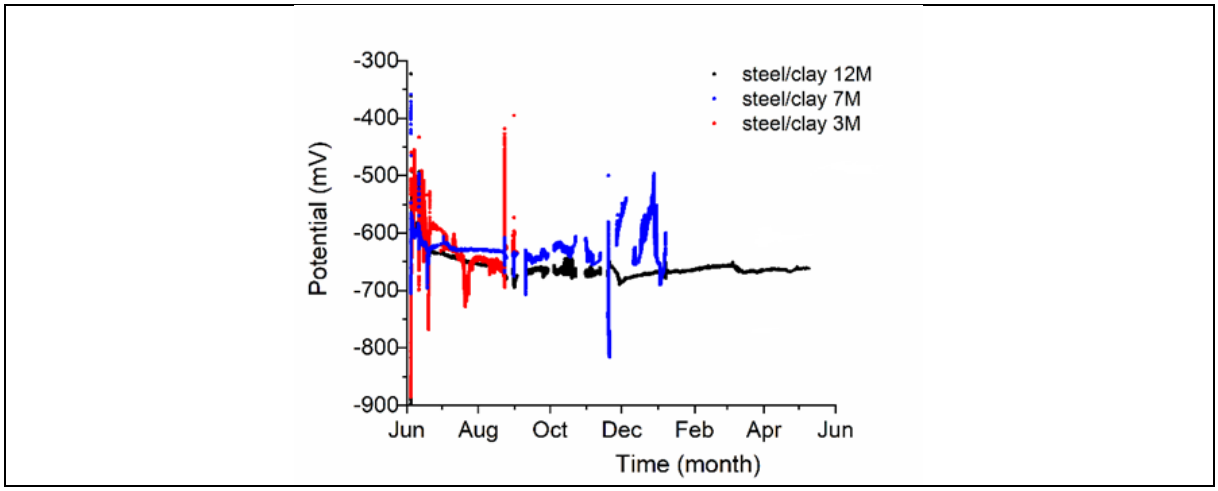

Figure 156 - Evolution with time of the measured corrosion potentials on the standard hydrogen scale for the three cells at 80 °C.

A decreasing corrosion potential with the time on the CSC-12M sample can be observed after the corrosion is initiated. After that equilibrium was reached, the potential assumed a constant value with a small rise indicating film repassivation. Negative potential has been detected throughout the experiments, which is generally considered to be consistent with a higher probability of C-steel corrosion.

4.2.3.2 SEM/EDX

The composition and nature of alteration products formed on the steel and within the clay were investigated by scanning electron microscopy/energy dispersive X-ray spectroscopy (SEM/EDX). The measurements were performed at 20 kV, 1.6 nA, using a Thermo Scientific Scios2 dual beam microscope, Oxford X-maxn 20 SDD EDX.

Figure 157 presents SEM-EDX images of the steel/clay interfaces after 3 months experimental time. There is no indication of void or free space in between the clay and the steel. The pouring of the clay had let to tight interfaces since the beginning of the experiments. On each of the three samples the formation of 30-40 µm long Fe-oxide ingrowths were detected. These SEM results show that micro-cracks appeared even in a short term (3 months) and could have initiated changes of the carbon steel surface (Figure 157). However, these ingrowths remained relatively short and did not exceed 100 µm in length after 7 and 12 months (*Figure 158* and *Figure 159*).

Table 39 gives SEM-EDX analyses for minerals at the corrosion interfaces after 3 months (SC-3M) based on the points marked in Figure 157. Corrosion products consisted of Fe – O (spectra 1-3). Table 40 gives the EDX analyses after 7 months with again a Fe – O signature typical of iron oxide corrosion products. But there is also a mixed signal composed of Ca – Al – Si – S and Fe oxide.

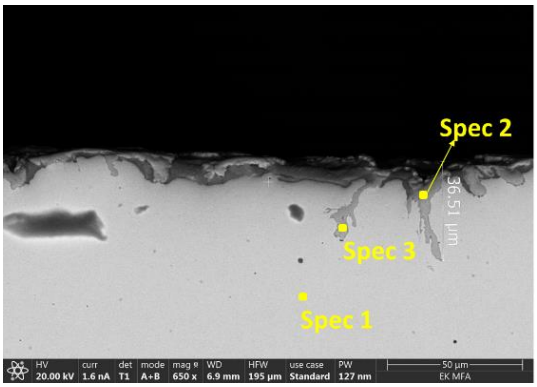

Figure 157 - SEM micrograph showing micro-cracks initiated on steel exposed for 3 months in a saturated clay.

Table 39 - SEM-EDX analyses for minerals at the corrosion interface of CSC-3M sample (based on the Figure 157).

Spectrum Label	Spec 1 (steel)	Spec 2 (corr. prod)	Spec 3 (corr. prod)
O		48.00	52.64
Si	0.44		
Mn	0.66	0.39	0.26
Fe	98.91	51.61	47.10
Total (at %)	100.00	100.00	100.00

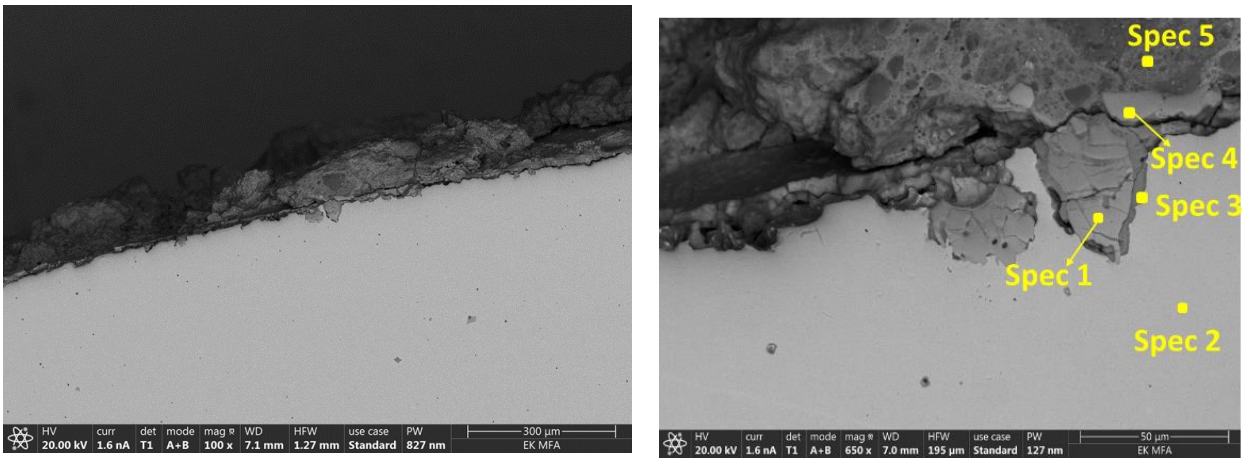

Figure 158 - SEM micrograph on the C-steel-clay interface after 7 months.

Table 40 - SEM-EDX analyses for minerals at the corrosion interface of CSC-7M sample (based on the Figure 158).

Spec. Label	Spec 1 (corr. prod)	Spec 2 (C-steel)	Spec 3 (corr. prod)	Spec 4 (corr. prod)	Spec 5 (clay)
O	48.04		64.90	61.42	67.07
Na					0.64
Mg					2.47
Al					4.11
Si		0.36	0.38	1.49	9.82
K					0.64
Ca					0.78
Cr	0.13			0.52	
Mn	1.08	0.65	0.53	0.88	
Fe	50.74	98.99	34.18	35.68	14.47
Total (at %)	100.00	100.00	100.00	100.00	100.00

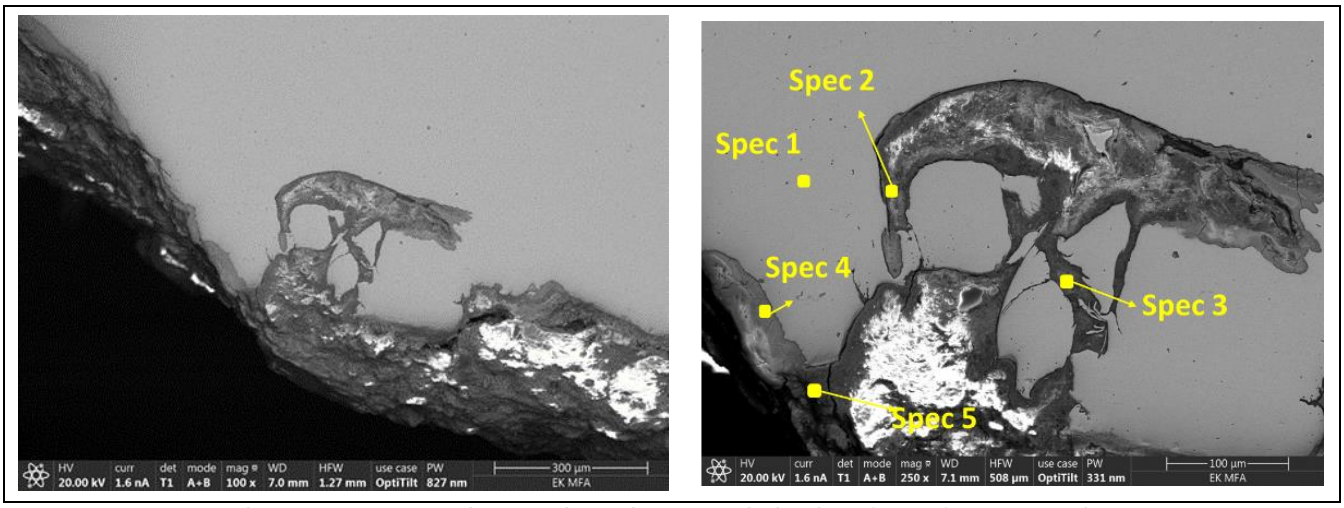

Figure 159 - SEM micrograph on the C-steel-clay interface after 12 months.

Table 41 - SEM-EDX analyses for minerals at the corrosion interface of CSC-12M sample (based on the Figure 159).

Spec. Label	Spec 1 (C-steel)	Spec 2 (clay)	Spec 3 (clay)	Spec 4 (corr. prod)	Spec 5 (clay)
C	6.51	6.11	4.38	5.76	8.79
O		59.35	58.90	47.08	56.87
Na		1.12	1.35		1.45
Mg		1.76	1.82		1.45
Al		5.46	6.63		4.24
Si	0.38	11.50	15.35	0.32	11.23
K		1.56	1.55		
Ca		1.40	0.78		6.50
Ti		0.09	0.15		0.07
Cl				1.05	0.04
Mn		0.64	0.98	0.32	
Fe	93.11	11.67	9.09	44.27	8.03
Total (at %)	100.00	100.00	100.00	100.00	100.00

4.2.3.3 µRaman

According to the results of the SEM/EDX, the corrosion process has an impact on the steel-clay interfaces. To identify the corrosion products micro-Raman investigations were performed.

The analyses were carried out using a HORIBA JobinYvon LabRAM HR 800 Raman microspectrometer. A frequency doubled Nd-YAG green laser with a 532 nm excitation wavelength was used to illuminate the samples, displaying ~0.2 mW on the sample surface. An OLYMPUS 50× (Numerical Aperture = 0.6) and 100× (Numerical Aperture = 0.9) objective was used to focus the laser. For Raman mapping 100 µm confocal hole, 600 grooves/mm optical grating, 4-10 s cumulated exposition time were used. The spectral resolution of measurements was 3.0 cm^{-1}. The step size of the Raman maps varied between 1

and 0.5 µm for magnifications 50× and 100×, respectively. Representative Raman maps and their spectra are shown in *Figure 160*.

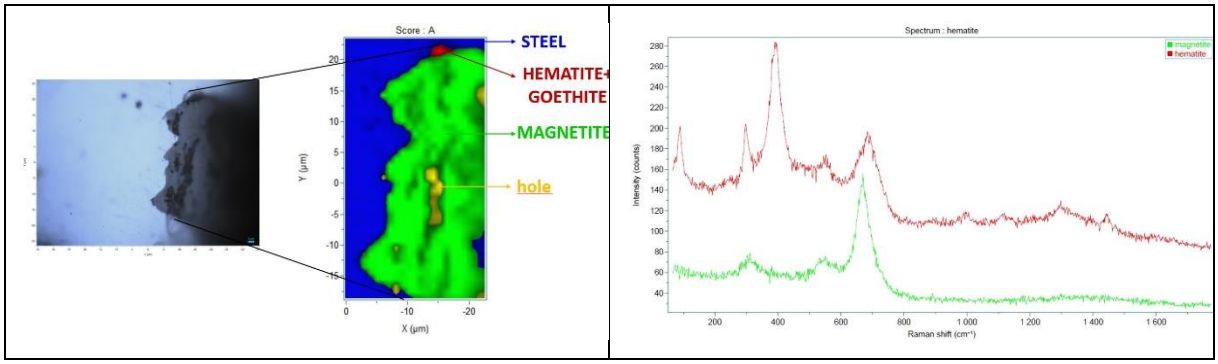

Figure 160 - µRaman map and characteristic spectra obtained for the C-steel-clay system after 3 months.

Mainly magnetite (Fe_3O_4) and hematite (α-Fe_2O_3)-goethite (α-FeO(OH)) can be identified on the SC-3M sample (Figure 160). Formation of Fe_3O_4 confirms the anoxic corrosion of the carbon steel under anaerobic conditions (Hill Shannon, 2016). All iron-oxides present a main peak in the region of 600-700 cm^{-1}, except in the case of hematite and goethite (Schlegel et al., 2010).

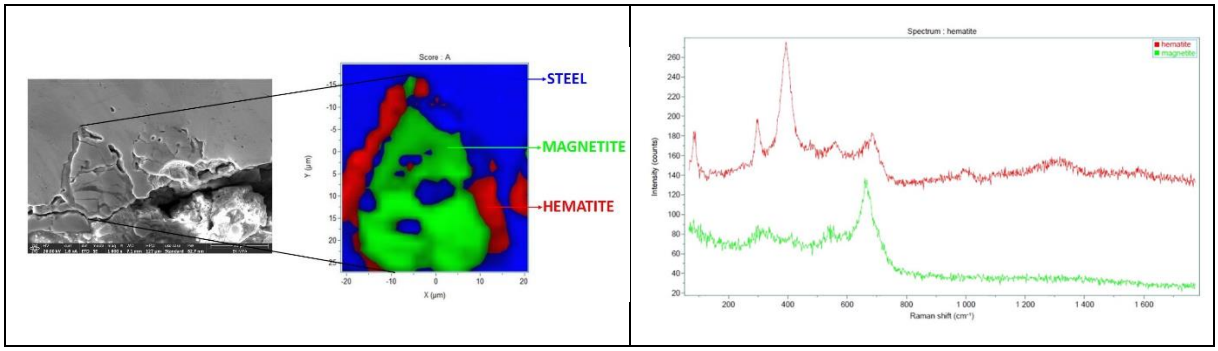

Figure 161 - µRaman map and characteristic spectra obtained for the C-steel-clay system after 7 months.

Hematite (α-Fe_2O_3) and magnetite (Fe_3O_4) can be identified as corrosion products after 7 months (Figure 161). Corrosion protrusion is formed by magnetite, which is surrounded by hematite. No other corrosion products could be identified by the methods used. In clay environments, the carbon steel surface is likely to be passive due to the formation of a stable Fe_3O_4 film, and will persist under anaerobic conditions, ensuring passivity until degradation of the clay barrier.

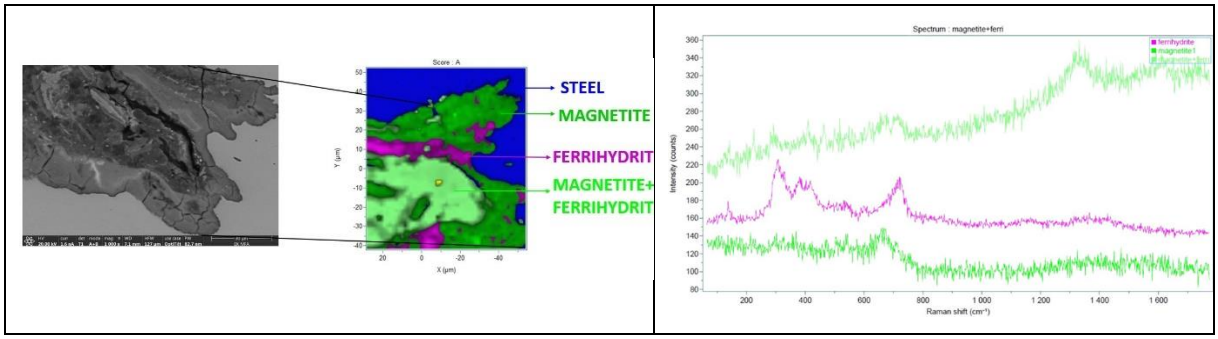

Figure 162 - µRaman map and characteristic spectra obtained for the C-steel-clay system after 12 months.

After 12 months of experiments substantial changes in the Raman spectra were observed (Figure 162). Magnetite (Fe_3O_4) and ferrihydrite ($Fe_{10}O_4(OH)_2$) were detected. Ferrihydrite has been shown to form in

atmospheric corrosion conditions (Hill Shannon, 2016), which suggests that at the last stage of the experiments (i.e., 12 months) the initial anaerobic conditions became partly aerobic. The anaerobic conditions may coexist with aerobic ones: oxygen in gaseous form could be present in the macro-environment (water). The occurrence of an aerobic SBPW and anaerobic clay systems can be defined as anaerobic, saturated aqueous phase. The chemistry of the SBPW could evolve over time. The primary corrosion product of anaerobic C-steel corrosion is widely accepted to be $Fe(OH)_2$, however, is not considered to be thermodynamically stable and under anaerobic conditions generally transforms to Fe_3O_4. The high temperature also favours the formation of Fe_3O_4, which was detected after 3M, 7M and found after 12M. In presence of O_2 (a slightly oxidizing condition could appear, thanks to the dissolution of O_2 from SBPW) (Arriba-Rodriguez et al., 2018), Fe^{III} oxides/oxyhydroxides become the corrosion product species. FeOOH corrosion products formed on the steel container due to the presence of trace levels of O_2 (after 12M the ferrihydrite was detected). The conditions could become progressively more aerobic with time. Carbon steel corrosion in simulated geological conditions (clay, SBPW) results in a variety of corrosion products of varying proportions with exposure time. During the exposure time magnetite was identified as the main corrosion product while at longer times (12M) ferrihydrite is formed. These structural modifications are due to changes of conditions with time exposure. No iron-carbonates or iron-sulfides were identified.

4.2.3.4 Chemical analyses of aqueous solution

We were able to collect samples from the liquid phase surrounding the inner Teflon container of which inductively coupled plasma - optical emission spectrometry (ICP-OES) and ion chromatography (IC) investigations were performed after 3, 7 and 12 months.

ICP-OES measurements were carried out on a Perkin Elmer Avio 200 sequential instrument. All elements were tested in radial view using Y as internal standard. The leachates were filtered through a cellulose acetate membrane (dp > 220 nm) and then acidified with 2 m/m% nitric acid. The power of the generator was set to 1200 W during the measurements and the flow of plasma argon was 12 L/min. IC analyses were performed on Thermo Scientific Dionex Aquion equipment. B, Ca, K, Mg, Na and Si concentrations were determined using ICP-OES (Table 42), while IC was used for Cl^- and SO_4^{2-} (Table 43).

Higher K, B and Na concentrations were found in the final pore water of the CSC-7M and CSC-12M systems compared to the initial conditioned pore water. Elevated K and B concentrations from baseline can be traced back to the clay content, having initially 4.7 wt.% K_2O and 200-300 mg/kg B (Toth et al., 2020). The concentration of K increased by one order of magnitude. Concentration of bivalent cations (Ca and Mg) did not change significantly. A higher Si concentration was measured after 7 months but showed a decrease afterwards. The dissolution of K and Na increased after 7 months.

Table 42 - ICP-OES results, comparing the 7-12 months sampling.

	B	**Ca**	**K**	**Mg**	**Na**	**Si**
[mg/l]						
SBPW recipe	-	125	7	57	380	-
SBPW conditioned	0.12	108	22	49	492	5.9
CSC-7M	1.7	100	48.3	55.1	454	34.9
CSC-12M	4.6	106	134	50.2	534	31.4

IC analysis of the liquid phase shows that chloride concentrations remained near the concentration of the pore water. In contrast, the dissolved concentration of sulphate increased up to month 7, after that, to month 12 became constant. The increase was less than 10% for chloride but higher for sulphate.

Table 43 - IC results, comparing the 3-7-12 months sampling.

	Cl^-	SO_4^{2-}
[mg/l]		
SBPW recipe	817	182
SBPW conditioned	823	183
CSC-3M	819.1	193.7
CSC-7M	819.6	221.7
CSC-12M	831.1	221

4.2.4 Modelling approach and results

4.2.4.1 Model description

The scoping calculations done here restrict the geometry of the set-up to a one-dimensional radial problem. The solute and heat transport conditions are assumed for fully saturated and isothermal water and temperature (at 80°C) conditions, and concern only diffusive transport. From a geochemical point, apart from aqueous equilibrium speciation reactions, we consider:

- Kinetic dissolution of primary Boda Clay minerals, except those that react fast enough for which equilibrium is assumed (see below)
- Equilibrium precipitation of secondary minerals (see below)
- Kinetic steel dissolution
- Ion exchange and Fe(II) surface complexation on illite in Boda Clay

Note that:

- Temperature dependence is taken into account for the thermodynamic constants of the aqueous species and the minerals and the rate constants of the rate models for the minerals
- Temperature dependence is not taken into account for the thermodynamic constants for the 2 SPNE SC/CE model (no data available)

The generic coupled reactive transport model HPx (Jacques et al., 2018) as embedded in HYDRUS 5 (Simunek et al., 2023) is used for the numerical simulations. HPx couples the HYDRUS software for flow, solute transport and heat transport in saturated-variable porous media (Simunek et al., 2022a; Simunek et al., 2022b) with the geochemical solvers PHREEQC (Parkhurst and Appelo, 2013) and ORCHESTRA (Meeussen, 2003) via a non-iterative sequential approach (Jacques et al., 2006). For the geochemical calculations, PHREEQC-3.17 as embedded in HPx is used.

The ThermoChimie database v11 is used for the thermodynamic constants. The extended Debye-Hückel model for calculating aqueous activity correction factors is used.

4.2.4.1.1 Mineralogy of Boda Clay

The reference composition and the corresponding minerals from the database are listed in Table 44.

Table 44 – Mineral composition Boda Clay assuming a bulk density of 2.5 kg/dm³

Mineral	Weight percentage	Database Name Formula	Gram/dm³ of Boda Clay	Mole/dm³ of Boda Clay
Quartz	9	Quartz	225	3.74

		SiO_2		
Na Plagioclase	11	Albite-low $NaAlSi_3O_8$	275	1.05
K Feldspar	4	Microcline $KAlSi_3O_8$	100	0.36
Analcime	13	Analcime $Na_{0.99}Al_{0.99}Si2.0106{:}H_2O$	325	1.48
Calcite	12	Calcite $CaCO_3$	300	3.00
Dolomite	2	Dolomite $CaMg(CO_3)_2$	50	0.271
Chlorite	5	Clinochlore $Mg_5Al_2Si_3O_{10}(OH)_2$	125	0.27
Muscovite/Illite	29	Illite-Al $K_{0.85}Al_{2.85}Si_{3.15}O_{10}(OH)_2$	900	2.29
Illite/Smectite	7			

4.2.4.1.2 Kinetic dissolution/precipitation of (primary) minerals

Mineral kinetics are described with rate equations based on the transition state theory (Aagaard and Helgeson, 1982) and following the formalism of Palandri and Kharaka (2004) and Zhang et al. (2019):

$$r = A\left(\sum_{j}^{n} r_j\right) f\left(\Delta G_{\mathrm{r}}\right) \tag{19}$$

where r is the rate (mol/dm³/s), A is the reactive surface area (m²/dm³), r_j are partial rates depending on the solution chemistry (in this study limited to pH dependence), and $f(\Delta G_r)$ is the rate dependency as a function of Gibbs free energy of the dissolution reaction. The reactive surface area is obtained as:

$$A = A_0\left(\frac{m}{m_0}\right)^n \tag{20}$$

where A_0 is the initial surface area (m²/dm³), m_0 and m are the initial and the current amounts of the mineral (mole/dm³) and n is a parameter. A_0 is obtained by:

$$A_0 = A_s m_0 M_{\mathrm{w}} \tag{21}$$

where A_s is the specific surface area (m²/g) and M_w is the molar mass. pH dependence is described by three piecewise equations as:

$$r_{\mathrm{H}} = A_H \exp\left[-\frac{E_{\mathrm{A,H}}}{R}\left(\frac{1}{T}-\frac{1}{T_{\mathrm{r}}}\right)\right] a_{H^+}^{n_1} \tag{22}$$

$$r_{\mathrm{n}} = A_{\mathrm{n}} \exp\left[-\frac{E_{\mathrm{A,n}}}{R}\left(\frac{1}{T}-\frac{1}{T_{\mathrm{r}}}\right)\right] \tag{23}$$

$$r_{OH} = A_{OH} \exp\left[-\frac{E_{A,OH}}{R}\left(\frac{1}{T}-\frac{1}{T_r}\right)\right] a_{OH^-}^{n_2} \quad (24)$$

where A_H, A_n and A_{OH} are pre-exponential factors, R is the universal gas constant, T is temperature (K), T_r is the reference temperature (298.15 K), $E_{A,H}$, $E_{A,n}$, and $E_{A,OH}$ are apparent activation energy (kJ/mol), a_x denotes the activity of species x, and n_1 and n_2 are the reaction order for the acid (n_1) and alkaline (n_2) mechanism. The affinity term $f(\Delta G_r)$ is expressed as:

$$f\left(\Delta G_r\right) = \left(1-\Omega^{\theta}\right)^{\eta} \quad (25)$$

where Ω is the saturation index, and η and θ are empirical parameters. Parameters are summarized in Table 45.

Table 45 – Rate parameters for primary minerals – n, η and θ are 1 for all minerals, except θ equals 0.49 for analcime (Heřmanská et al., 2023). Pre-exponential factors are at 298.15 K.

Mineral	A_s m²/g	A_H 1/m²/s	$E_{A,H}$ J/mol	n_1	A_n 1/m²/s	$E_{A,n}$ kJ	A_{OH} 1/m²/s	$E_{A,OH}$	n_2	Reference
Quartz	0.05	-	-	-	6.14E-14	77	1.9E-10	80	0.34	Marty et al. (2015)
Albite-low	0.08	8.5E-11	58.4	0.335	5.1E-20	57	1.4E-10	55.5	0.317	Marty et al. (2015)
Microcline	0.11	1.7E-11	31	0.27	1.0E-14	31	1.4E-10	31	0.35	Marty et al. (2015)
Analcime	25	5.0E7	63	1.0	1E-1	58.5	7.5^{E}-5	58	-0.4[&]	[*]Sakizci (2016), Heřmanská et al. (2023)
Calcite	0.7	5.0E-1	14	1	1.6E-6	24	-	-	-	Marty et al. (2015)
Dolomite	0.06	2.8E-4	46	0.41	1.1E-8	31	-	-	-	Marty et al. (2015)
Clinochlore	0.0027	8.2E-9	17	0.28	6.4E-17	16	6.9E-9	16	0.34	Marty et al. (2015)
Illite-Al	30	9.8E-12	36	0.52	3.3E-17	35	3.1E-12	48	0.38	Marty et al. (2015)

4.2.4.1.3 2 SPNE SC / CE model for illite

Similar to the models for Fe(II) fate on montmorillonite as discussed in several sections above in this report, Chen et al. (2022) made a model for Fe(II) sorption on illite according to the two site protolysis non-electrostatic surface complexation and cation exchange model (2 SPNE SC/CE) of Bradbury and Baeyens (2009). Reactions, thermodynamic constants, and site capacities are listed in Table 46.

Table 46 – Reactions equations, thermodynamic constants and site capacities of the 2 SPNE SC/CE model for Fe(II) fate on illite, after Chen et al. (2022)

Cation exchange model				
Capacity	12	meq/100g		

Half reaction	log K			
$X^- + Na^+ \Leftrightarrow NaX$	0			
$X^- + K^+ \Leftrightarrow KX$	0.7			
$2X^- + Ca^{2+} \Leftrightarrow CaX_2$	0.8			
$2X^- + Mg^{2+} \Leftrightarrow MgX_2$	0.6			
$2X^- + Fe^{2+} \Leftrightarrow FeX_2$	0.44			
Two site protolysis - non-electrostatic surface complexation model				
Site densities (eq/kg) (Bradbury and Baeyens, 2009)				
$\equiv S^SOH$	2.0×10^{-3}			
$\equiv S^{w1}OH$	4.0×10^{-2}			
$\equiv S^{w2}OH$	4.0×10^{-2}			
Protolysis reaction constants (Bradbury and Baeyens, 2009)				
Reaction		log K		
$\equiv S^SOH \Leftrightarrow \equiv S^SO^- + H^+$		-6.2		
$\equiv S^SOH + H^+ \Leftrightarrow \equiv S^SOH_2^+$		4.0		
$\equiv S^{w1}OH \Leftrightarrow \equiv S^{w}O^- + H^+$		-6.2		
$\equiv S^{w1}OH + H^+ \Leftrightarrow \equiv S^{w1}OH_2^+$		4.0		
$\equiv S^{w2}OH \Leftrightarrow \equiv S^{w2}O^- + H^+$		-10.5		
$\equiv S^{w2}OH + H^+ \Leftrightarrow \equiv S^{w2}OH_2^+$		8.5		
Model 1: Fe(2) – Illite interaction (Chen et al., 2022)				
$\equiv S^SOH + Fe^{2+} \Leftrightarrow \equiv S^SOFe^+ + H^+$		3.5		
$\equiv S^{w1}OH + Fe^{2+} \Leftrightarrow \equiv S^{w}OFe^+ + H^+$		1.4		
Model 2 : Fe(2)/Fe(3)- Illite interaction (Chen et al., 2022)				
$\equiv S^SOH + Fe^{2+} \Leftrightarrow \equiv S^SOFe^+ + H^+$		1.9		
$\equiv S^SOH + Fe^{2+} \Leftrightarrow \equiv S^SOFe^{2+} + H^+ + e^-$		-2.2		
$\equiv S^SOH + Fe^{2+} + 3H_2O \Leftrightarrow \equiv S^SOFe(OH)_3^- + 4H^+ + e^-$		-22.0		
$\equiv S^SOH + Fe^{2+} + 5H_2O \Leftrightarrow \equiv S^SOFe(OH)_4^{2-} + 5H^+ + e^-$		-31.5		
$\equiv S^{w1}OH + Fe^{2+} \Leftrightarrow \equiv S^{w}OFe^+ + H^+$		-1.7		

$\equiv S^{w1}OH + Fe^{2+} \Leftrightarrow \equiv S^{w}OFe^{2+} + H^{+} + e^{-}$	-4.0	

4.2.4.1.4 Steel Corrosion

The reaction for steel corrosion is:

$$Fe(s)+2H^{+} \rightarrow Fe^{2+}+H_2 \quad (26)$$

Kinetics of steel corrosion is modelled with a simple zero-order rate equation:

$$\frac{dFe(s)}{dt} = A_{Fe(s)}k \quad (27)$$

where $A_{Fe(s)}$ is the reactive area of Fe(s), and k is the zero-order coefficient (m/s) calculated as:

$$k = \frac{r_c \rho}{M_{Fe} t_{conv}} \quad (28)$$

where r_c is the steel corrosion rate (µm/year), ρ is the steel density (g/cm³), M_{Fe} is the molecular weight of Fe (55.85 g/mol) and t_{conv} is a constant to convert from year to second (86400*365). In the simulations, r_c and ρ are, respectively, 2 µm/year and 7.8 g/cm³.

4.2.4.1.5 Model geometry, initial conditions and transport properties

In this set of calculations, we consider a simplified one-dimensional radial simulation domain with the inner boundary at 10 mm (steel) and the outer boundary at the outer radius of the water reservoir (Figure 164). For this simulation, the area of the steel over the volume of Boda Clay is 66.67 m^{-1}.

The selected transport domain is a 2D vertical axisymmetric domain (Figure 163). For the simplified 1D radial model, the domain is a simple 2D domain (left figure in Figure 163) consisting of only 2 rows of nodes in the vertical direction. During the geochemical calculations, only one row of nodes is calculated and results are then copied to the second row. For the 2D axisymmetric model, the general 2D domain (right figure in Figure 163) could be selected.

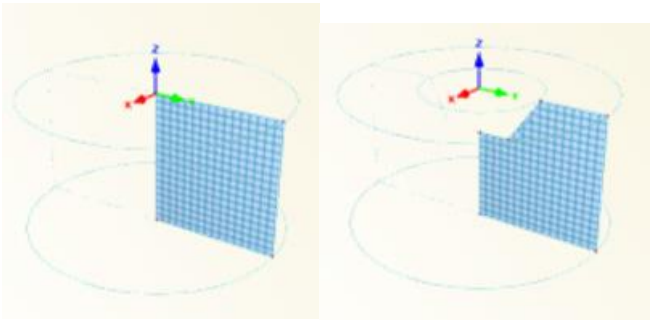

Figure 163 – Axisymmetric models used in Hydrus 5: Simple 2D domain for 1D radial model (left), and General 2D domain for a 2D axisymmetric model (right)

Figure 165 shows the discretization – in the Boda Clay, discretization is 0.25 mm; in the Teflon tube and the water reservoir, grid sizes are gradually increasing (in total 60 nodes are defined).

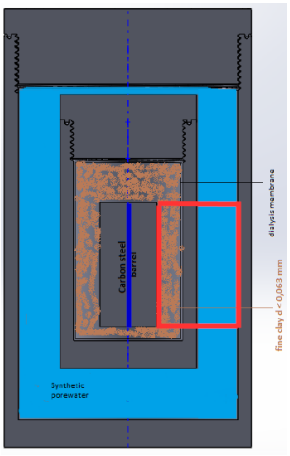

Figure 164 - Simulated domain - Red rectangle shows the domain considered in the model; the thick blue line shows the symmetry axis. All boundaries (red lines) are considered as closed boundaries, thus, a simplified one-dimensional radial model is used.

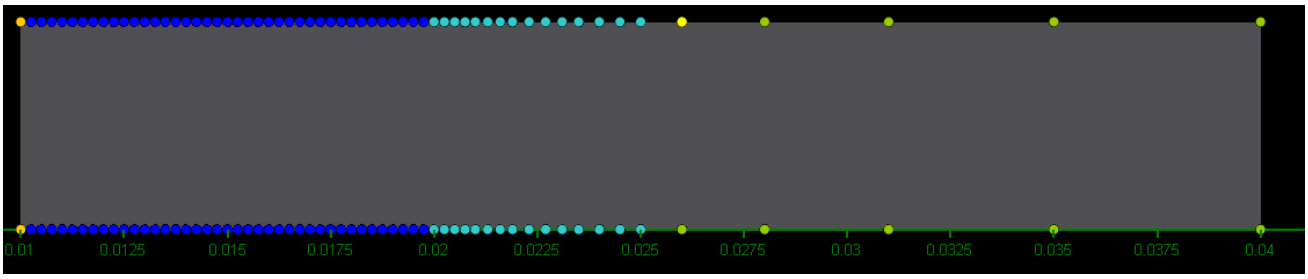

Figure 165 – The one-dimensional radial transport domain (in meters). The yellow node is the steel & Boda clay domain, the dark blue nodes are Boda Clay, the light blue nodes is the Teflon and the green nodes are the water reservoir.

Transport properties of the four materials are listed in Table 47. Tortuosity, τ [-] is defined as:

$$D_e = \eta D_p = \eta \tau D_0 \quad (29)$$

where D_e, D_p and D_0 are the effective, the pore and the aqueous diffusion coefficient (m^2/s) an η is the porosity (-). D_0 is 10^{-9} m^2/s for all species.

Table 47 – Transport properties for the different materials in the experimental set-up for the steel-Boda clay interaction experiments.

Material	Porosity	Tortuosity
Steel	0.014[&]	$\eta^{1/3}$
Boda Clay	0.014	$\eta^{1/3}$
Teflon	0.0003	1[$]
Water Reservoir	1	1

[&] The steel cell is also filled with Boda Clay, but with a Fe source (kinetic steel corrosion)

[$] calculated to have a D_e of 3.0×10^{-13} m/s, value calibrated from similar steel/cement interaction experiments (Fabian et al., 2023)

As explained in the experimental details (section 4.2.2), synthetic Boda pore water is used in the experiments; it is assumed that the Boda clay compartment and the water reservoir have the synthetic Boda pore water composition (see section 4.2.2.1).

4.2.4.2 Model results

4.2.4.2.1 Temperature effect on saturation indices of primary minerals of Boda Clay

The aqueous geochemistry was calculated for three cases: the SBPW at 25 °C, the SBPW at 25 °C after equilibration with calcite, dolomite and analcime, and the SBPW at 80°C starting from the previous solution (i.e., equilibrated with calcite, dolomite and analcime). The rationale for equilibration with calcite, dolomite and analcime is that the kinetics for these minerals are so fast that equilibrium conditions are reached very fast, even at 25°C.

Saturation indices are shown in Table 48. pH values are, respectively, 8.1, 7.98, and 7.36 for SBPW at 25°C, SBPW value at 25°C after equilibration with calcite, dolomite and analcime, and SBPW value at 80°C after equilibration with calcite, dolomite and analcime. pe values are, respectively, -5.08, -4.9, and -5.1.

Table 48 – Saturation indices for SBPW at 25 °C and 80°C.

Mineral	SBPW 25°C	SBPW 25°C Equilibrium calcite, dolomite, analcime	Increase to 80°C
Quartz	-4.27	-0.86	-1.44
Albite-low	-15.83	-0.49	-3.19
Microcline	-15.11	0.22	-3.19
Analcime	-11.91	0.00	-2.10
Calcite	0.13	0.00	0.02
Dolomite	0.30	0.00	0.44
Clinochlore	-9.99	9.41	10.76
Illite-Al	-21.25	4.26	-1.32

4.2.4.2.2 Kinetic dissolution of primary minerals at 25°c and 80 °C

The first set of simulations are the kinetic dissolution of Boda clay at 25°C or 80 °C starting from an initial pore water composition equal to the synthetic Boda pore water (1 dm^3 bulk solid material in contact with 1 kg of water). pH, concentrations and saturation indices of the primary minerals are shown in Figure 166. The pH is relatively stable (at 80°C, the increase from 7.36 without equilibrium with analcime, calcite and dolomite to about 8 is due to equilibration with these three minerals). The most striking result is the very fast kinetics at 80°C (an E_a of 50 and 70 kJmol results in an increase in rate of 20 to 80 times, respectively). Most primary minerals reach conditions very close to equilibrium, except chlinochlore that remains oversaturated as precipitation was not allowed. When chlinochlore is allowed to precipitate, pH values at 80°C are below 6.5, K concentrations drop significantly (to values as low as 10^{-8} M), and K-feldspar becomes strongly undersaturated (beside other changes in both concentrations and saturation indices, results not shown). Therefore, in the current study, chlinochlore is only allowed to dissolve.

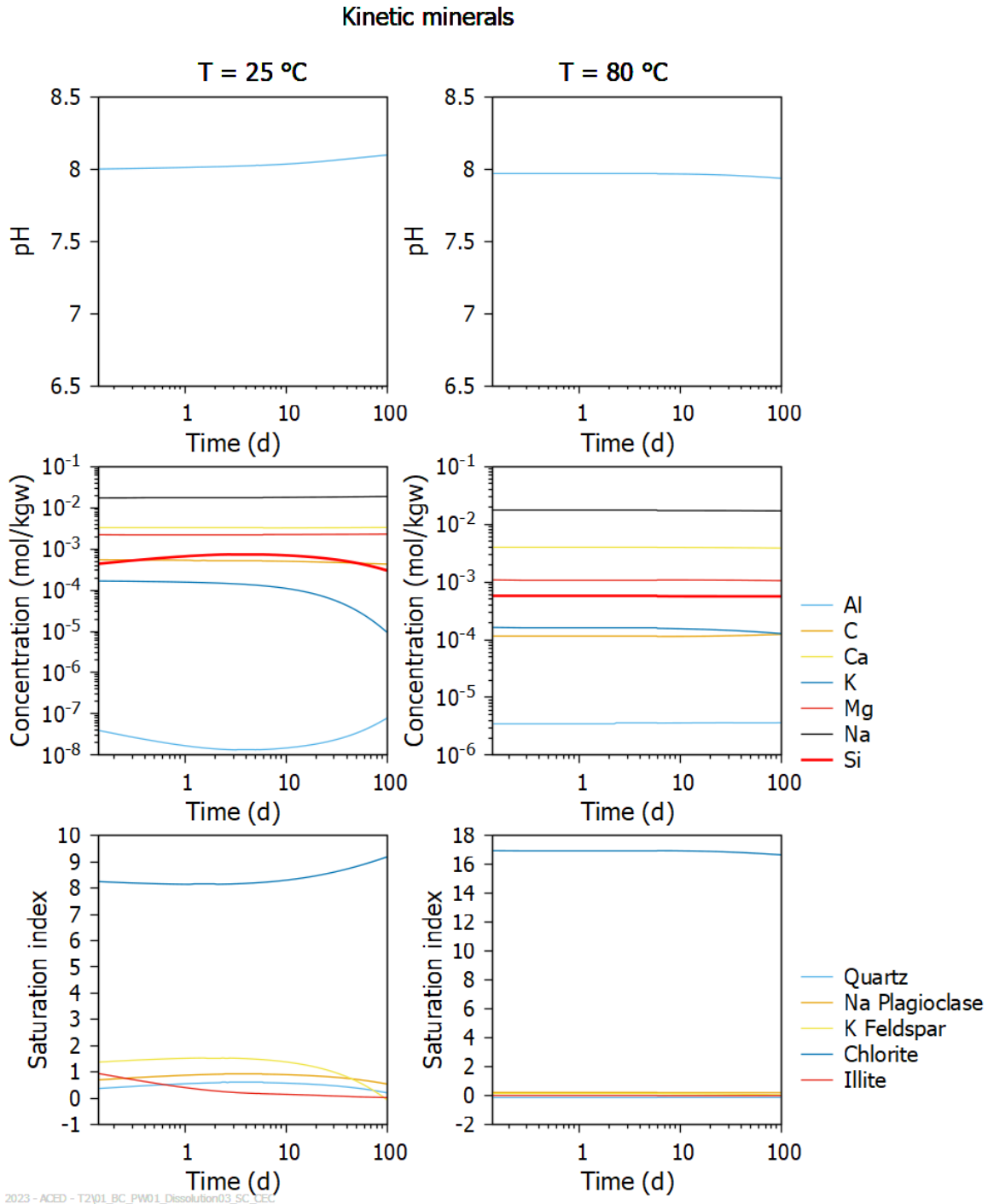

Figure 166 – pH, elemental concentrations and saturation index evolution of SBPW at 25°C (left) and 80°C (right). Saturation indices of calcite, dolomite and analcime are always zero and are not shown.

4.2.4.2.3 Steel Corrosion – Fe Sorption Model 1

Figure 167 and Figure 168 show aqueous concentrations at selected times in the simulation domain or the node interfacing the steel surface, respectively. The pore water chemistry in the Boda Clay is relatively insensitive to the distance to the steel interface indicating that for many elements the dissolution/precipitation reactions with the primary are probable the controlling factors. Beside for Fe which steadily increases with time (Figure 168) and have decreasing concentrations further from the steel interface, C and K shows the largest variation with distance to the interface.

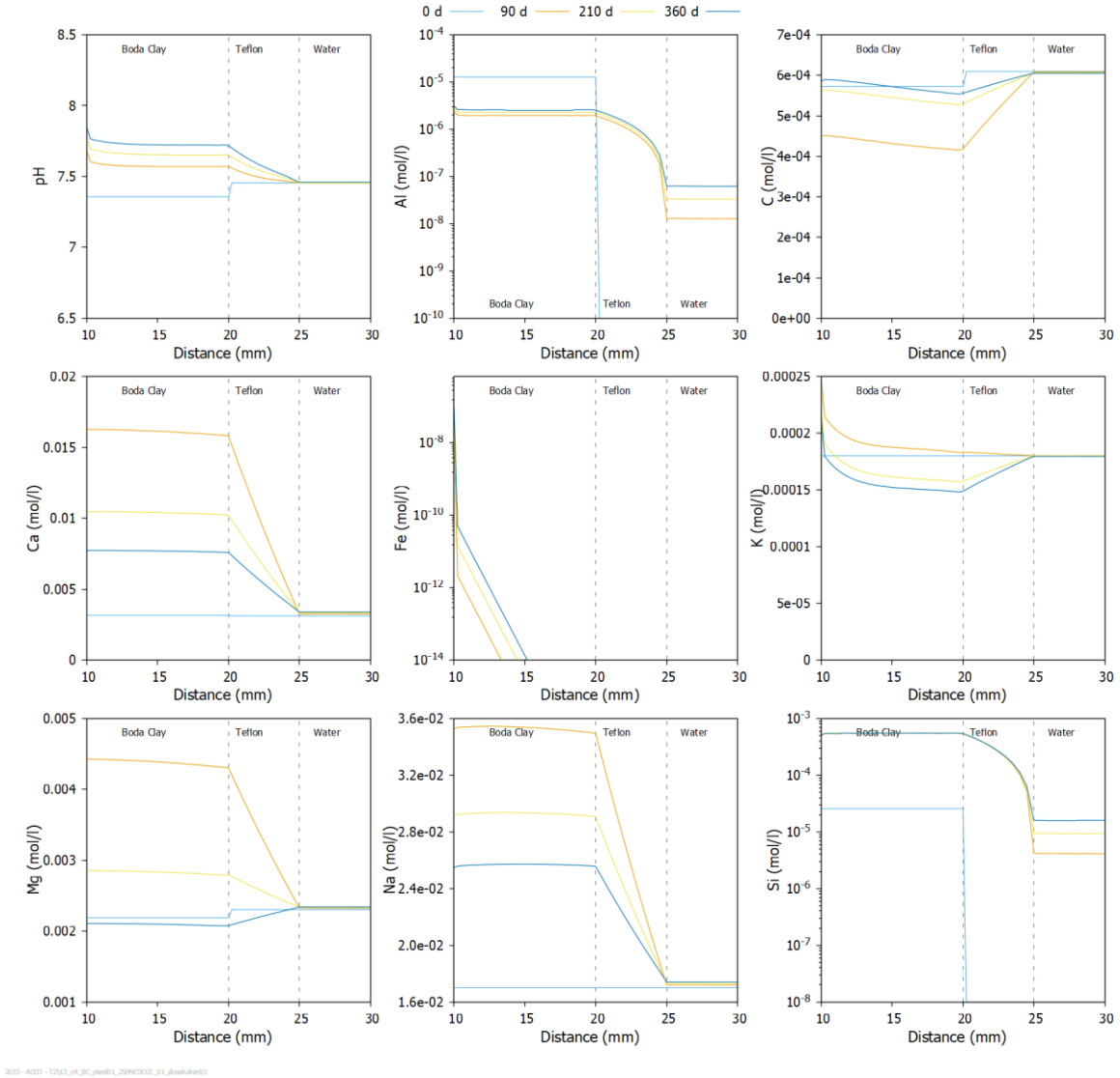

Figure 167 – Aqueous concentration profiles at selected times (Fe sorption model 1).

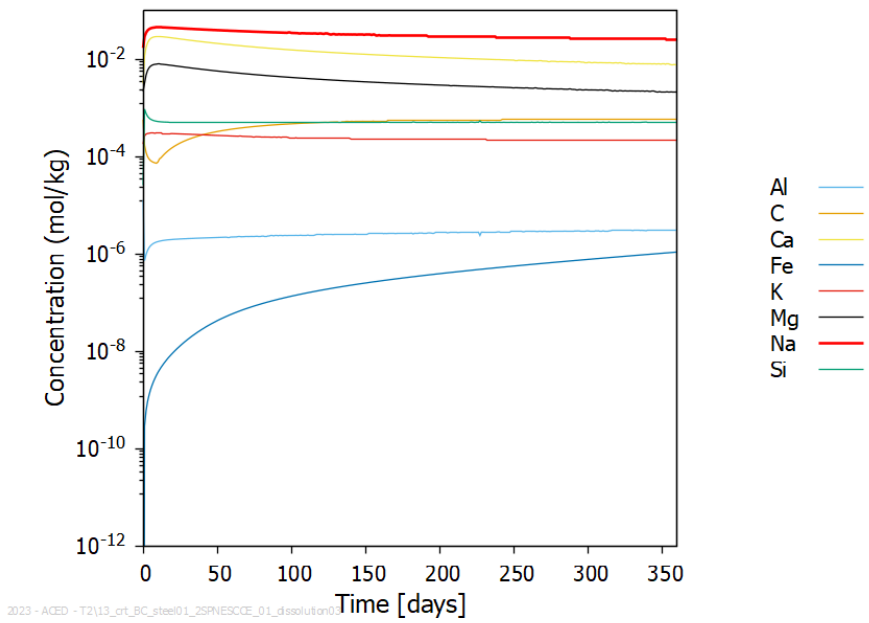

Figure 168 – Time evolution of aqueous concentrations in the first cell with Boda Clay next to the steel interface (Fe sorption model 1)

The model did not predict any Fe-precipitate at the interface or in the Boda clay. On the one hand, the two minerals for which thermodynamic equilibrium was assumed remain undersaturated during the complete simulation period; a few other ones (greenalite, Illite-Fe(II)) have positive saturation indices at the end of the simulation (but were not included in the model for mineral dynamics).

The speciation of the sorbed Fe is shown in Figure 169 along the radial distance in the Boda clay and Figure 170 as a function of time in the first Boda Clay node at the interface with steel. The amount of sorbed Fe increases with time. The fraction of Fe sorbed on the cation exchange complex is only a very small fraction compared to the fraction on the surface complex. Further from the steel – Boda Clay interface, the strong sorption sites contribute the most to the sorption. For the node at the interface (Figure 170), the Fe sorbed to the weak sites is the most dominant type.

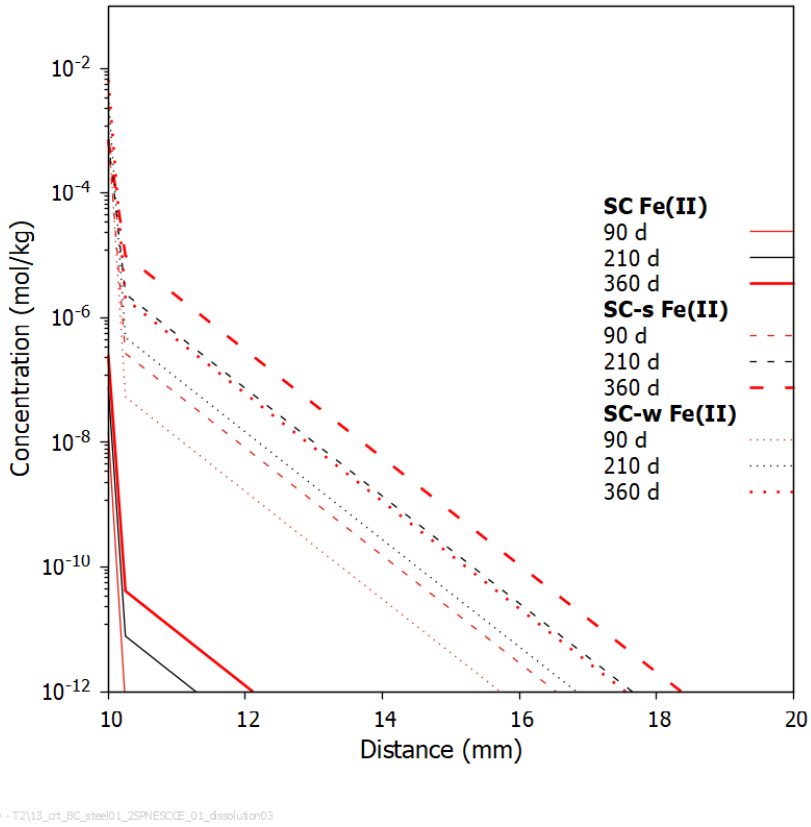

Figure 169 – Profiles of sorbed Fe speciation in the Boda Clay at selected times (Fe sorption model 1).

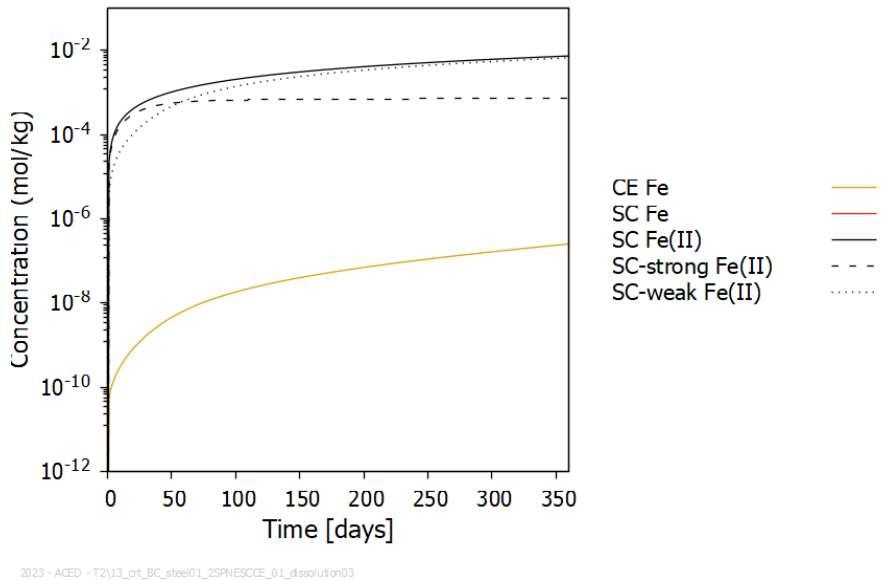

Figure 170 – Time series of sorbed Fe speciation in the first cell in Boda Clay at the steel interface (Fe sorption model 1)

4.2.4.2.4 Steel Corrosion – Fe sorption model 2

Concentration profiles for the Fe sorption model 2 (Figure 171) are quite similar to model 1. However, aqueous concentrations of Fe are significantly higher throughout the profile (and have a smaller difference between the first cell and the other cells). Fe concentrations in the first cell at the steel

interface increase fast up to 50 days and then flatten (Figure 172). This corresponds with precipitation of magnetite (note that greenalite and Illite-Fe(II) are over saturated at that point, thus should precipitate if thermodynamic equilibrium with those phases was allowed in the model). The complexation parameters in model 2 are indeed lower than in model 1 for the sites without electron transfer.

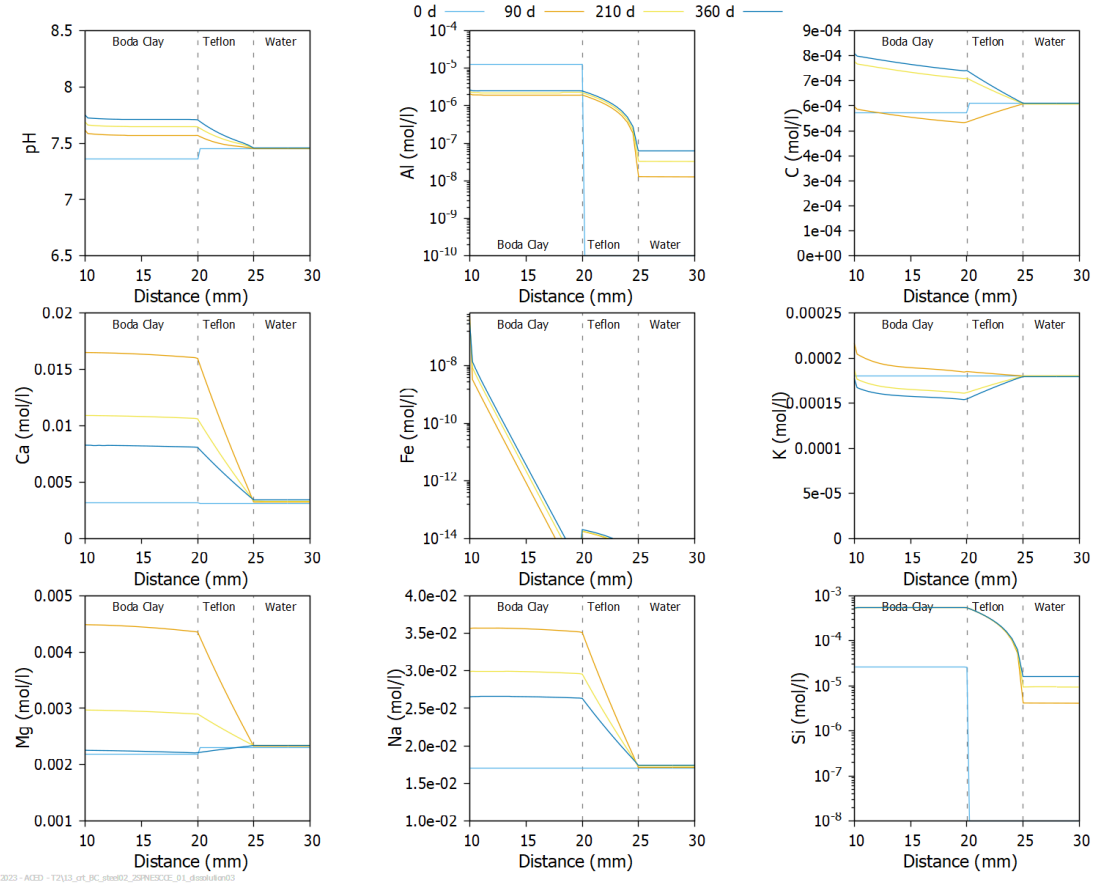

Figure 171 – Aqueous concentration profiles at selected times (Fe sorption model 2).

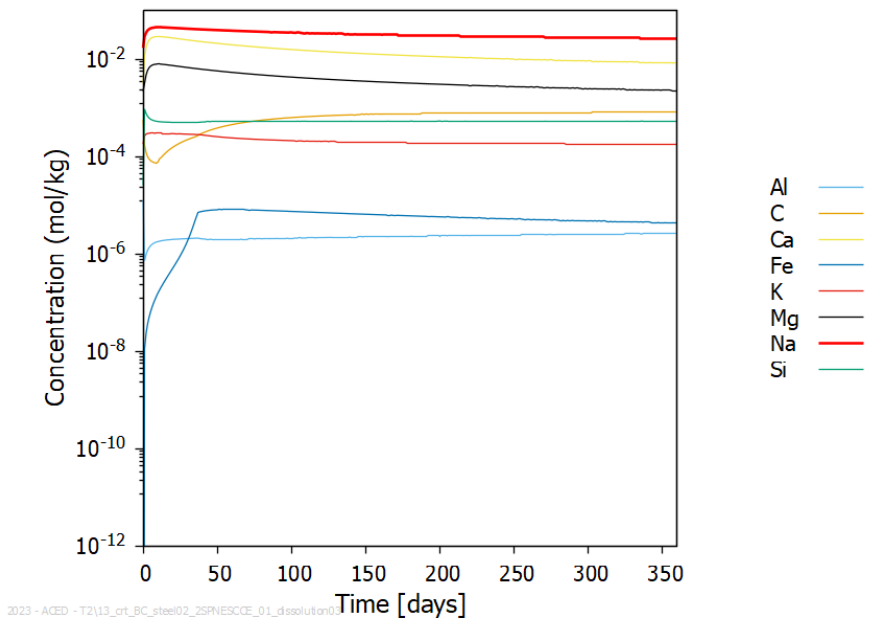

Figure 172 – Time evolution of aqueous concentrations in the first cell with Boda Clay next to the steel interface (Fe sorption model 2).

Figure 173 and Figure 174 show again the sorbed Fe speciation. The sites of electron transfer to structural Fe do not play a role in sorbed Fe speciation. Also the Fe sorbed via cation exchange reaction is much smaller than via surface complexation. The dynamics in the first cell is smaller than in model 1: Fe sorbed on the strong sites is increasing until magnetite is formed. Then, sorbed iron (and aqueous iron) remains quite constant, although magnetite is continuously precipitating (not shown). Note also that only mainly the strong sites are now involved.

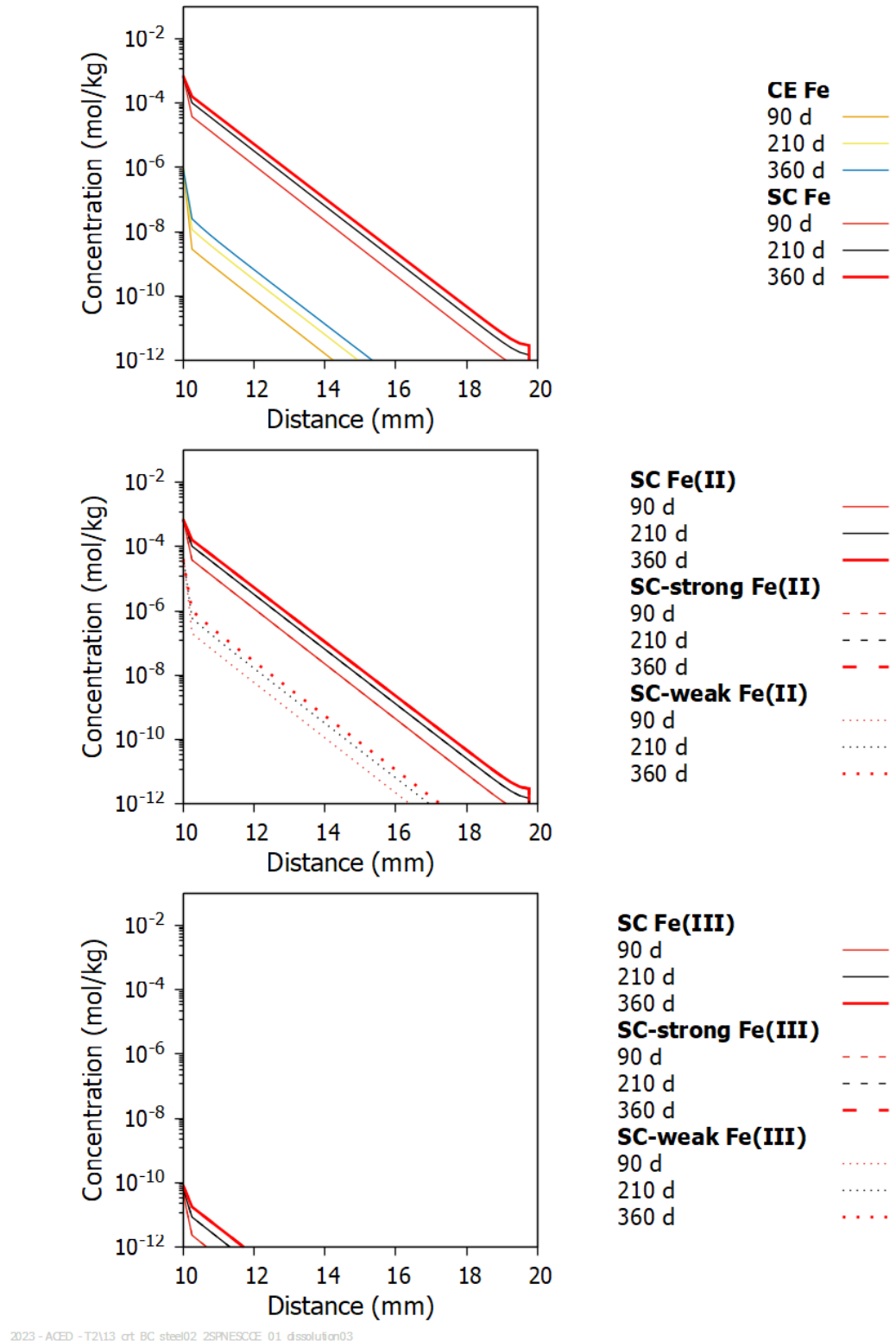

Figure 173 – Profiles of sorbed Fe speciation in the Boda Clay at selected times (Fe sorption model 2).

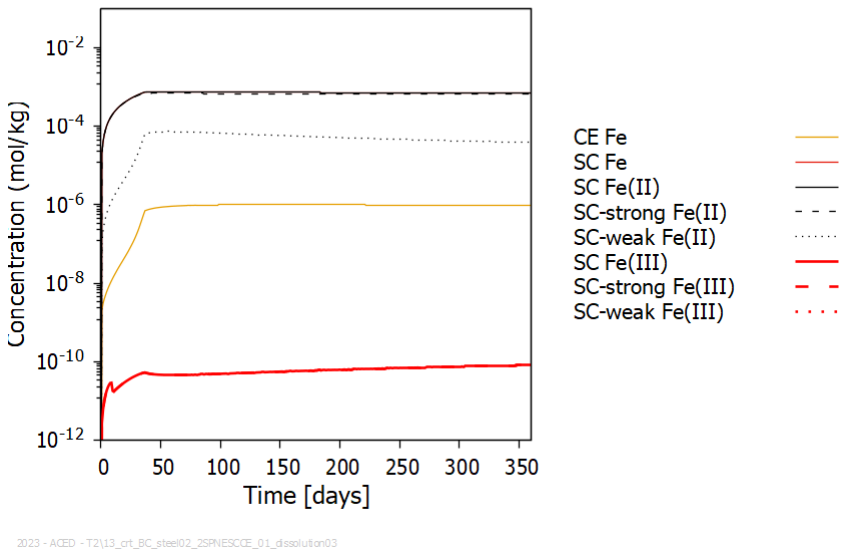

Figure 174 – Time series of sorbed Fe speciation in the first cell in Boda Clay at the steel interface (Fe sorption model 2)

4.2.5 Discussion

Several studies focus on understanding of corrosion activity in clay-rich formations under DGR conditions or predicted conditions (Toth et al., 2020, Behrends & Bruggeman, 2016, El Mendili et al., 2014, Schlegel et al., 2021, Necib et al., 2017, Smart et al., 2017). The Hungarian radioactive waste management company (PURAM) is designing a DGR in Boda Claystone Formation (BCF) in West-Mecsek (SW-Hungary). To date there has been no corrosion investigations for the BCF, therefore the present investigations were conducted to optimize and finalize this repository concept with the aim to ensure its long-term safety.

The corrosion experiment lasted for one year. During the experiment the temperature was controlled, the corrosion potential was monitored. Corrosion potential fluctuation can be detected for the samples during the experiment, except for the CSC-M12 sample where the corrosion potential reached a nearly constant value after six months. To exclude leakage and ensure saturation, the mass of each experimental setup was inspected monthly.

Microstructural characterization shows that all three C-steel containers corroded in BCF. The corrosion interfaces bear some similarities in the behavior of 3-, 7- and 12-months samples. The 3- and 7-months samples contain magnetite and hematite, with low Cl activity, but significant sulphate movement that is notable in the pore water composition. The amount of Fe(III)- and Fe(II)-oxide phases are remarkable, but other Fe-based phases (e.g. Fe-silicate, Fe-sulphide) are absent. The presence of significant amounts of Fe-hydroxide for CSC-M12, clearly indicates oxic conditions, however, the exact timing of this interaction remains uncertain, predicted between 7M and 12M. Higher amounts of Cl can be found in the CSC-12M solution, indicating a higher dissolution than for 3M and 7M samples. Sulphate dissolution remains at the same level as in 7M sample.

Based on the SEM/µRaman results for the CSC-3M and CSC-7M samples the presence of a corrosion layer can be identified, the main corrosion product containing magnetite and hematite. These results are strongly analogous with similar experiments conducted under anaerobic conditions (Schlegel et al., 2008, El Hajj et al., 2013).

The model limited changes near the clay – steel interface with the formation of Fe-precipitates, interaction of with the clay resulting in a small Fe front in the clay. The dynamics in the water buffer are very limited by the limited diffusion across the Teflon. In this study, the diffusion coefficient of the Teflon was put equal to that calibrated in the steel-cement experiments (Fabian et al., 2023).

4.2.6 Conclusion

Carbon steel corrosion in simulated geological conditions (BCF, pore water, 80°C) results in a variety of corrosion products of varying proportions with exposure time. At short time (3M and 7M) exposure magnetite and hematite were identified as the main corrosion products, while at longer time (12M) magnetite and ferrihydrite are formed. These mineralogical modifications are due to changes of conditions from anoxic to oxic with time including chloride and sulfate activity. As expected from the literature, non-uniform general corrosion has been identified and the different corrosion products as well as their chronological order of formation have been highlighted.

A reactive transport model (1D radial geometry) included the main expected processes: diffusion, kinetic steel corrosion, kinetic dissolution of primary minerals, formation of corrosion products and interaction of Fe with the Boda Clay – in addition, the high temperature was accounted for although not all thermodynamic constants were adapted for temperature (e.g., those related to sorption). The model predicted the formation of corrosion products near the steel – Boda Clay interface and an interesting behavior of Fe in the clay; no experimental data were available to validate the latter. Nevertheless, it illustrates that such type of models should be used together with experiments for a better understanding.

The present work shows that it is important to consider all the components of a disposal site to explain the corrosion mechanism and need to conclude that the present timeframe was not sufficient to understand all corrosion mechanisms which could take place in the investigated systems.

5. General conclusion and perspectives

The combined modeling-experimental approach developed within Subtask 2.1 of the ACED work package of EURAD allowed to study the carbon steel/clay material interfaces interactions that would occur for Deep Geological Repository barrier systems.

First, geochemical processes occurring at the iron/FEBEX compacted bentonite interface under simultaneous hydration and heating were investigated thanks to long-term laboratory experiments. Results showed the impact of temperature on both water distribution inside the bentonite (existence of water gradient) and salts precipitation (Cl^- precipitation at iron/bentonite interface) that can play a relevant role in corrosion processes initialization. Non saturated conditions seem to favour the potential oxidizing conditions but on the other hand, dry conditions limited a lot the extent of the overall reactions producing newly formed minerals. Near the heater, Fe particles preserved their metallic luster and did not show any sign of corrosion. Corrosion is restricted to zones close to the interface (≈ 2 mm) and the calculated corrosion rate is inferior to 0.5 µm/year. Corrosion products consist of iron oxides, mainly hematite (prevailing), and magnetite – maghemite and/or goethite. After 15 years of interaction, the maximum thickness of corrosion products formed around iron grains is about 10 µm (absolute values), and the maximum thickness of bentonite interface material affected by iron mineral formation is about 200 µm.

Geochemical interactions occurring at iron powder/FEBEX compacted bentonite interface for such experiments have been modelled with a THCM reactive transport model that considers bentonite swelling, evaporation and initial unsaturated conditions in the bentonite, and assume a geochemical conceptual model. The main conclusion arising from FB tests simulations showed that in contrast to experimental observation, magnetite is the only corrosion product observed and it precipitated in the whole iron powder, but only in a small amount in the first 2 mm into the bentonite (magnetite precipitation observed at iron powder/bentonite interface). Model results also showed difficulties to reproduce the evolution patterns of exchanged Na^+ and Mg^{2+} concentrations. To improve results, sensitivity runs were performed to change values of either the vapor tortuosity or the Fe powder thermal conductivity or the initial sorption site concentrations or the initial mineral volume fraction composition. Even if the computed sorbed iron reproduce the measured data better than that of the base run, there are still some discrepancies between the numerical representation and experimental data especially regarding water content/dissolved Cl^- concentration/temperature evolution. The reactive transport model of FB tests has uncertainties which could be overcome by accounting for several parameters as (i) an initial aerobic corrosion stage and the associated Fe(III) oxides, hydroxides and oxyhydroxides precipitation, (ii) a time-varying corrosion rate depending on pH and saturation index, (iii) some kinetic aspects (magnetite precipitation or smectite dissolution) and (iv) some changes in porosity, permeability and diffusion coefficients caused by mineral dissolution/precipitation. Other relevant studies could include the evaluation of model sensitivity to mechanical processes. The use of Fe powder in steel/bentonite corrosion tests enhances Fe(s) corrosion due to its higher reactive surface but introduces other sources of uncertainty. The heterogeneity of Fe powder favors the formation of preferential pathways for vapor migration with some particles being more exposed to the oxidizing agent than others.

The main observations associated to FeMo tests simulations showed firstly that results obtained for different iron particle sizes are similar. Then, computed magnetite is the main corrosion product and it precipitated with siderite, greenalite and saponite-Mg at the Fe powder/bentonite interface. Parallelly, pH values increased in the metallic sinter and the iron powder (up to pH 9.5) and also in the bentonite (more slightly) with small changes in smectite, quartz and calcite contents. Such model includes uncertainties which could be overcome by accounting for a more complex 2D vertical model considering non uniform conditions along the vertical direction, and also by taking into account the precipitation of other corrosion products (hematite, maghemite, lepidocrocite and akageneite).

The FEBEX *in situ* experiment has also been modelled parallelly thanks to two different models (UDC and UniBern models). The reactive transport model presented by UDC uses a simplified corrosion approach by considering a source of iron and oxygen to trigger goethite precipitation. The main

conclusions associated to this model showed that both goethite precipitation in the bentonite (mostly near the iron source, d < 50 mm) and total iron measured data are well reproduced. The modelled fronts of dissolved, exchanged and sorbed iron penetrate 150 mm into the bentonite. The model also showed that goethite precipitation induced a decrease in pH and Eh. This model includes uncertainties which could be overcome by accounting for a more realistic corrosion model considering an initial aerobic corrosion stage and the associated Fe(III) oxides, hydroxides and oxyhydroxides precipitation, and also by taking into account the precipitation of other corrosion products (magnetite, siderite, hematite, maghemite, lepidocrocite, akaganeite and Fe-phyllosilicates).

The model developed and implemented in PFLOTRAN by UniBern describes the transient evolution of the steel/bentonite interface in the evolution from the early aerobic corrosion to the anaerobic corrosion phase taking into account the hydration of the bentonite and the evolving temperature gradients. The model successfully reproduced the aerobic corrosion phase (Fe accumulation as goethite within the corrosion layer), the transition to the anaerobic corrosion phase (accumulation of anaerobic corrosion products in the corrosion layer) and the migration of Fe^{2+} into the bentonite. During the progression of the Fe front into the bentonite, two stages successively take place: first, the interaction with O_2 diffusing towards the steel and second, after the local consumption of O_2, Fe sorption on the clay minerals. With time and increasing distance to the corroding steel, precipitation becomes however less important due to the gradual depletion of the O_2 ahead of the Fe front. Moreover, sensitivity cases with respect to transport in gas and liquid phases and to bentonite hydration identifies the diffusion of gaseous O_2 as an important driving force for the depletion of the porewater in O_2 over larger distances and the formation of the characteristic zonation of Fe accumulation: a corrosion product dominated zone close to the steel and a sorption dominated zone without notable amounts of precipitation products further in the bentonite. Sensitivity cases with respect to different temperature gradients highlighted the high degree of coupling between geochemical process and physical processes, which strongly affect the evolution of the Fe-bentonite interaction zone (higher temperatures reduce the extent of the Fe-bentonite interaction zone). Despite the general compliance with the underlying phenomenological model, it appears that an additional transport process is not considered within the present model: either the fast transport of e^- across the oxide layer or an additional advective flow path from the steel into the bentonite (due to water vapour convection around the heaters) which is not captured with the simple 1 D-axis symmetric model geometry. Further dedicated experiments to support the first^t hypothesis or extension of the model to the full 3-D geometry might help to decipher this additional localized process.

Secondly, investigation on the anaerobic Fe(II)/montmorillonite interactions, with a focus on the possible redox processes (electron transfers between dissolved Fe and structural Fe) have been presented. Various sets of batch experiments on dispersions were conducted, as well as diffusion experiments on compacted clay cores. Analytical methods included colorimetry, ion chromatography, ^{57}Fe Mössbauer spectrometry and isotopic analysis were used to distinguish between the different Fe(II) uptake processes. Fe(II) uptake by clay depends on multiple factors, especially the pH and the relative Fe_{aq} and Fe_{str} concentrations. Cation exchange dominates at low pH (below pH 5.0) but other processes (involving electron transfer and presumably Fe precipitation) are more prominent at higher pH (above pH 6.0). Such processes can lead to high Fe uptake by the clay, and two new mechanisms are proposed to explain the Fe uptake processes. Results of the diffusion experiments (pH 7.3) clearly show that the redox process between in-diffusing Fe(II) and structural Fe(III) in the compacted clay core does not occur, except at the vicinity of the filter (interfaces between the compacted core and the ferrous solutions). The interaction of dissolved Fe with compacted clay seems to be limited to cation exchange (planar sites) and surface complexation on edge sites, in contrast to dispersed clay.

Thirdly, Chemical evolution of several iron–bentonite–water systems was studied thanks to modelling of existing experiments (PHREEQC and Thermoddem V1.10). The geochemical modelling approach applied is based on a three-step procedure: (i) construction of a simple equilibrium model for iron/bentonite/water systems to identify the main chemical driving processes occurring at long term, (ii) development of a kinetic model considering kinetic effects and time-dependence of geochemical processes and (iii) development and application of a one-dimensional (1D) reactive-transport model

including kinetic effects and transport phenomena. Such modelling includes the consideration of the simulation of the development and transfer of the corrosion products that evolved under the experimental conditions. The main conclusions associated to equilibrium modelling showed that the main corrosion product identify at 25°C is siderite and that temperature increase (70°C) favor the formation of Fe- phyllosilicates (neither magnetite nor chukanovite calculated as equilibrium corrosion products). The impact of CO_2 partial pressure level has been observed (support siderite formation instead of Fe-phyllosilicates), particularly at lower temperatures. Parallelly, a partial dissolution of bentonite primary minerals (montmorillonite) has been noticed. The main observations associated to kinetic modelling suggested that siderite is the only corrosion product to be form (regardless of bentonite material and pCO_2 considered, no magnetite formation prediction). Some FeII-illite phases induced by bentonite alteration caused by FeII dissolved ions from corrosion processes are also very locally observed. It has been noticed that bentonite underwent relatively minor and slow changes throughout the considered timescale of 10 years. Overall, kinetic modeling demonstrated that different considerations regarding the model parameters (adapted corrosion rate, higher pCO_2 and suppression of the secondary phyllosilicate minerals) provided quantitatively different results. The main conclusions associated to reactive transport modelling showed that results were generally consistent with those of the kinetic model in most cases but allowed for a more detailed insight into the spatial location of the geochemical changes. Once again, we observed that siderite was the main corrosion product (precipitation on metallic surface, not in bentonite) and that very small amounts of FeII-illite was formed in the bentonite at the interface iron/bentonite, especially when temperature increases. Finally, it appears that the dissolution of bentonite primary minerals was an insignificant process.

Fourthly, the interaction between Boda clay and steel at high temperature (80°C) has been studied. Carbon steel corrosion experiments in such simulated geological conditions result in a variety of corrosion products of varying proportions with exposure time. At short time (3 months and 7 months) exposure magnetite and hematite were identified as the main corrosion products, while at longer time (12 months) magnetite and ferrihydrite are formed. These microstructural modifications are due to changes of conditions from anoxic to oxic with time including chloride and sulfate activity. It was demonstrated that it is important to consider all the components of a disposal site to explain the corrosion mechanism and longer timeframe experiments are needed to understand all corrosion mechanisms which could take place in the investigated systems. For the first time, the interaction between Boda clay and steel at high temperature was modelled using a coupled reactive transport model. Although the iron corrosion was presented with a simple model (zero-order steel corrosion), advanced models were used to (i) simulate the behaviour of Boda clay at high temperature using kinetic dissolution models for the primary minerals, and (ii) Fe fate in Boda clay based on a state-of-the-art model including (no-electrostatic) surface complexation and ion exchange. It was demonstrated that different model assumptions affect to a given degree the simulated Fe fate. These types of models can be used to, at one side, design future experiments to discriminate between model formulations, and on the other site, make long term assessment of potential evolutions of Boda Clay under high temperature (and in contact with steel).

References

Aachib, M., Mbonimpa, M. and Aubertin, M. 2004. Measurement and Prediction of the Oxygen Diffusion Coefficient in Unsaturated Media, with Applications to Soil Covers. Water, Air, and Soil Pollution 156(1), 163-193.

Aagaard, P. and Helgeson, H.C. 1982. Thermodynamic and kinetic constraints on reaction rates among minerals and aqueous solutions, 1. Theoretical considerations. American Journal of Science 282, 237-285.

Águila, J.F., Samper, J., Mon, A., Montenegro, L., (2020). Dynamic update of flow and transport parameters in reactive transport simulations of radioactive waste repositories. Applied Geochemistry, https://doi.org/10.1016/j.apgeochem.2020.104585.

Águila J.F., V. Montoya, J. Samper, G. Kosakowski, P. Krejci, W. Pfingsten, L. Montenegro, 2021. Modelling Cs migration through Opalinus clay: A benchmark for single- and multi-species sorption-diffusion models, Comp. Geos, doi.org10.1007/s10596-021-10050-5.

Agullo, J., Bataillon, C., Michau, N., 2017. Preliminary electrochemical corrosion monitoring of iron in mixture cement paste–bentonite, Corros. Eng. Sci. Technol. 52, 155–161. doi:10.1080/1478422X.2017.1305675.

Alonso, E.E., Alcoverro, J., Coste, F., Malinsky, L., Merrien-Soukatchoff, V., Kadiri, I., Nowak, T., Shao, H., Nguyen, T.S., Selvadurai, A.P.S., Armand, G., Sobolik, S.R., Itamura, M., Stone, C.M., Webb, S.W., Rejeb, A., Tijani, M., Maouche, Z., Kobayashi, A., Kurikami, H., Ito, A., Sugita, Y., Chijimatsu, M., Börgesson, L., Hernelind, J., Rutqvist, J., Tsang, C.F. and Jussila, P. 2005. The FEBEX benchmark test: case definition and comparison of modelling approaches. International Journal of Rock Mechanics and Mining Sciences 42(5), 611-638.

Amonette, J.E. and Templeton, J.C. 1998. Improvements to the quantitative assay of non-refractory minerals for Fe(II) and total Fe using 1,10-phenanthroline. Clays & Clay Minerals 46(1), 51-62.

Angst U M et al., The steel–concrete interface, Materials and Structures 50, 1-24 (2017).

Angst, U., Elsener, B., Larsen, C.K., Vennesland, Ø. 2009. Critical chloride content in reinforced concrete - A review. Cement and Concrete Research 39, 1122–1138. https://doi.org/10.1016/j.cemconres.2009.08.006.

Appelo, C.A.J., Postma, D., 1993. Geochemistry, Groundwater and Pollution. A. A. Balkema, Brookfield, VT.

Appelo, C.A.J., Drijver, B., Hekkenberg, R. and de Jonge, M. 1999. Modeling In Situ Iron Removal from Ground Water. Groundwater 37(6), 811-817.

ASTM. 2011. Standard Practice for Preparing, Cleaning, and Evaluating Corrosion Test Specimens., 19428–2959.

Barbarulo, R., Peycelon, H., Leclercq, S., 2007. Chemical equilibria between C–S–H and ettringite, at 20 and 85 C. Cement and Concrete Research, 37 1176–1181.

Barzgar, S., Tarik, M., Ludwig, C. & Lothenbach, B. (2021): The effect of equilibration time on Al uptake in C-S-H. Cement and Concrete Research 144, 106438.

Benning, L.G., Wilkin, R.T., Barnes, H.L. 2000. Reaction pathways in the Fe-S system below 100°C. Chemical Geology 167, 25–51. https://doi.org/10.1016/S0009-2541(99)00198-9.

Bergaya, F., Lagaly, G. and Vayer, M. (2013) Developments in Clay Science. Bergaya, F. and Lagaly, G. (eds), pp. 333-359, Elsevier.

Bestel, M., Glaus, M.A., Frick, S., Gimmi, T., Juranyi, F., Van Loon, L.R. and Diamond, L.W. 2018. Combined tracer through-diffusion of HTO and ^{22}Na through Na-montmorillonite with different bulk dry densities. Applied Geochemistry 93, 158-166.

Bildstein, O., Trotignon, L., Perronnet, M. and Jullien, M. 2006. Modelling iron-clay interactions in deep geological disposal conditions. Physics and Chemistry of the Earth 31(10-14), 618-625.

Bildstein, O., Claret, F., Frugier, P., 2019. RTM for Waste Repositories. Reviews in Mineralogy and Geochemistry 85, 419–457.

Blanc, P., Lassin, A., Piantone, P., Azaroual, M., Jacquemet, N., Fabbri, A. and Gaucher, E.C. 2012. Thermoddem: A geochemical database focused on low temperature water/rock interactions and waste materials. Applied Geochemistry 27(10), 2107-2116.

Bonnet, J., Mosser-Ruck, R., Sterpenich, J., Bourdelle, F., Verron, H., Michau, N., Bourbon, X., Linard, Y. 2022. Chemical and mineralogical characterizations of a low-pH cementitious material designed for the disposal cell of the high-level radioactive waste (HLW). Cement and Concrete Research 162, 107013.

Bouakkaz, R., Abdelouas, A., El Mendili, Y., David, K., Grambow, B. 2019. Alteration of 29Si-doped SON68 borosilicate nuclear waste glass in the presence of near field materials. Applied Geochemistry 111, 104436.

Bouikni, A., Swamy, R.N., Bali, A. 2009. Durability properties of concrete containing 50% and 65% slag. Construction and Building Materials 23, 2836–2845. https://doi.org/ 10.1016/j.conbuildmat.2009.02.040.

Bourdoiseau, J.A., Jeannin, M., Rémazeilles, C., Sabot, R., Refait, P. 2011. The transformation of mackinawite into greigite studied by Raman spectroscopy. Journal of Raman Spectroscopy 42, 496–504. https://doi.org/10.1002/jrs.2729.

Bradbury, M.H. and Baeyens, B. 1997. A mechanistic description of Ni and Zn sorption on Na-montmorillonite Part II: modelling. Journal of Contaminant Hydrology 27(3), 223-248.

Bradbury, M.H., Baeyens, B., 1998. A physicochemical characterisation and geochemical modelling approach for determining pore water chemistries in argillaceous rocks. Geochem. Cosmochim. Acta 62, 783-795.

Bradbury, M.H. and Baeyens, B. 2002 Porewater chemismy in compacted re-saturated MX-80 bentonite: Physicochemical characterisation and geochemical modeling. PSI report 02-10. – Paul Scherrer Institut (PSI). Switzerland.

Bradbury, M.H., Baeyens, B., 2002. Sorption of Eu on Na- and Ca-montmorillonites: Experimental investigations and modelling with cation exchange and surface complexation. Geochimica et Cosmochimica Acta 66, 2325–2334.

Bradbury, B., Baeyens, B., 2003. Pore water chemistry in compacted resaturated MX-80 bentonite. J. Contam. Hydrol. 61, 329-338.

Bradbury, M.H. and Baeyens, B. 2009. Sorption modelling on illite Part I: Titration measurements and the sorption of Ni, Co, Eu and Sn. Geochimica et Cosmochimica Acta 73(4), 990-1003.

Brand, R.A. (1987). Improving the validity of hyperfine field distributions from magnetic alloys. Part I: Unpolarized source. In Nuclear Instruments and Methods in Physic Research Section B Beam Interaction with Materials and Atoms; Elsevier: Amsterdam, The Netherlands, 1987; Volume 28, pp. 398–416.

Carriere, C., Neff, D., Martin, C., Tocino, F., Delanoë, A., Gin, S., Michau, N., Linard, Y., Dillmann, P. 2020. AVM nuclear glass / steel / claystone system altered by Callovo – Oxfordian poral water with and without cement – bentonite grout at 70°C. Materials Corrosion 72, 474–482. https://doi.org/10.1002/maco.202011766.

Červinka, R. and Gondolli, J. 2015 Projekt UOS č. 14E1054 – Modelování pórové vody kompaktovaného bentonitu BaM. Revize 1 [in Czech]. ÚJV Řež, a. s., Czech Republic.

Červinka, R. and Hanuláková, D. 2013 Laboratorní výzkum tlumících, výplňových a konstrukčních materiálů. Geochemické modelování – bentonitová pórová voda (Závěrečná zpráva řešení podetapy 4.2 projektu TIP FR-TI1/362) [in Czech]. ÚJV Řež, a. s., TU Liberec, Czech Republic.

Červinka, R., J., G., M., K., Tomasova, Z., Rukavickova, L., Rihosek, J., Pacheroa, P., Zeman, J. and Vencelides, Z. 2017 Chování horninového prostředí/Příprava geochemického modelu úložiště – Definice vstupních dat a příprava modelů [in Czech]. MS SURAO TZ 271/2017, SÚRAO, Prague, Czech Republic.

Červinka, R., Klajmon, M., Zeman, J. and Vencelides, Z. 2018 The Geochemical Evolution of DGR: Preparation of Geochemical Model. Geochemical Calculations and Reactive Transport Modeling. MS SURAO, TZ 271/2018/ENG; SÚRAO, Prague, Czech Republic.

Charles, C. J., Rout, S. P., Garratt, E. J., Patel, K., Laws, A. P., Humphreys, P. N. 2017. Floc Formation Reduces the pH Stress Experienced by Microorganisms Living in Alkaline Environments. Applied and Environmental Microbiology 83:6.

Charlet L., Tournassat C. (2005): Fe(II)-Na(I)-Ca(II) cation exchange on montmorillonite in chloride medium: evidence for preferential clay adsorption of chloride - metal ion pairs in seawater, Aqua. Geochem. 11: 115-137.

Chautard, C., 2013. Intéractions fer/argile en conditions de stockage géologique profond - Impacts d'activités bactériennes et d'hétérogénéités, Ecole nationale supérieure des mines de Paris.

Chen, P., Van Loon, L.R., Fernandes, M.M. and Churakov, S. 2022. Sorption mechanism of Fe(II) on illite: Sorption and modelling. Applied Geochemistry 143, 105389.

Chernyshova et al (2007): Size-dependent structural transformations of hematite nanoparticles. 1. Phase transition. Phys. Chem. Chem. Phys., 2007, 9, 1736–1750

Chomat L, Amblard E, Varlet J, Blanc C, Bourbon X, Passive corrosion of steel reinforcement in blended cement-based material in the context of nuclear waste disposal. Corrosion Engineering, Science and Technology 52, 148-154 (2017).

Collier, N.C., Milestone, N.B., Hill, J., Godfrey, I.H. 2009. Immobilisation of Fe floc: Part 2, encapsulation of floc in composite cement. Journal of Nuclear Materials 393, 92-101.

Cudennec, Y., Lecerf, A. 2006. The transformation of ferrihydrite into goethite or hematite, revisited. Journal of Solid State Chemistry 179, 716–722. https://doi.org/10.1016/j.jssc.2005.11.030.

Cuevas, J., Villar, M.V., Fernández, A.M., Gómez, P., Martín, P.L. (1997): Pore waters extracted from compacted bentonite subjected to simultaneous heating and hydration. Applied Geochemistry. 12, 473-481.

Cuevas, J., Villar, M.V., Martín, M., Cobeña, J.C., Leguey S. (2002): Thermo-hydraulic gradients on bentonite: distribution of soluble salts, microstructure and modification of the hydraulic and mechanical behaviour. Applied Clay Science 22: 25-38.

Cuevas, J.; Cabrera, M.Á.; Fernández, C.; Mota-Heredia, C.; Fernández, R.; Torres, E.; Turrero, M.J.; Ruiz, A.I. (2022): Bentonite Powder XRD Quantitative Analysis Using Rietveld Refinement: Revisiting and Updating Bulk Semiquantitative Mineralogical Compositions. Minerals, 12, 772. https://doi.org/10.3390/min12060772.

Curti, E. 2011 Comparison of Bentonite Pore Water calculations carried out with conventional and novel models. AN-44-11-18, Paul Scherrer Institut (PSI). Switzerland.

Dauzères, A. 2010. Etude expérimentale et modélisation des mécanismes physico-chimiques des interactions béton-argile dans le contexte du stockage géologique des déchets radioactifs. PhD thesis, Université de Poitiers (France).

De Combarieu, G., Barboux, P. and Minet, Y. 2007. Iron corrosion in Callovo-Oxfordian argilite: From experiments to thermodynamic/kinetic modeling. Physics and Chemistry of the Earth 32, 346-358.

De Combarieu, G., Schlegel, M.L., Neff, D., Foy, E., Vantelon, D., Barboux, P., Gin, S. 2011. Glass-iron-clay interactions in a radioactive waste geological disposal: An integrated laboratory-scale experiment, Applied Geochemistry 26, 65–79. https://doi.org/10.1016/j.apgeochem.2010.11.004.

De Faria, D. L. A.; Venancio Silva, S.; de Oliveira, M. T. Raman Microspectroscopy of some Iron Oxides and Oxyhydroxides. J. Raman Spectrosc. 1997, 28, 873–878.

De Windt, L., Torres, E., 2009. Modélisation d'expériences en cellule reproduisant les conditions THC d'une alvéole de déchets HAVL. Rapport Technique R201009LDEWI, Ecole des Mines de Paris (France).

De Windt, L., Marsal, F., Corvisier, J. and Pellegrini, D. 2014. Modeling of oxygen gas diffusion and consumption during the oxic transient in a disposal cell of radioactive waste. Applied Geochemistry 41, 115-127.

De Windt, L., Spycher, N., 2019. Reactive transport models for long-term safety assessment of nuclear waste disposal. Elements 15, 99–102.

De Windt L., Miron G. D., Fabian M., Goethals, J., Wittebroodt C. (2020). First results on the thermodynamic databases and reactive transport models for steel-cement interfaces at high temperature. Deliverable D2.8 of the HORIZON 2020 project EURAD. EC Grant agreement no: 847593.

De Windt L., Samper J., Cochepin B., Garcia E., Mon A., Montenegro L., Samper A., Raimbault L., Veilly E. (2023). Integrated reactive transport models for assessing the chemical evolution at the disposal cell scale. Deliverable D2.17 of the HORIZON 2020 project EURAD. EC Grant agreement no: 847593.

Deissmann G., Ait Mouheb N., Martin C., Name N., Jacques, D., Weetjens E., Kursten B., Leivo M., Somervuori, M., Carpen, L., 2020. Experiments and numerical model studies on interfaces. Deliverable D2.5 of the HORIZON 2020 project EURAD. EC Grant agreement no: 847593.

Diler, E., Leblanc, V., Gueuné, H., Larché, N., Deydier, V., Linard, Y., Crusset, D., Thierry, D. 2021. Potential influence of microorganisms on the corrosion of carbon steel in the French high- and intermediate-level long-lived radioactive waste disposal context. Materials Corrosion 72, 218–234. https://doi.org/https://doi.org/10.1002/maco.202011779.

Diler, E., Leblanc, V., Gueuné, H., Maillot, V., Linard, Y., Charrier, G., Crusset, D. 2023. Potential influence of microorganisms on the corrosion of the carbon steel in the French high-level long-lived nuclear waste disposal context at 50°C. Materials and Corrosion, 1-18.

Dillmann, P., Gin, S., Neff, D., Gentaz, L., Rebiscoul, D. 2016. Effect of natural and synthetic iron corrosion products on silicate glass alteration processes. Geochimica and Cosmochimica Acta 172, 287–305. https://doi.org/10.1016/j.gca.2015.09.033.

Dilnesa, B.Z. (2012): Fe-containing Hydrates and their Fate during Cement Hydration. https://doi.org/10.5075/EPFL-THESIS-5262

Dilnesa, B.Z., Lothenbach, B., Le Saout, G., Renaudin, G., Mesbah, A., Filinchuk, Y., Wichser, A. & Wieland, E. (2011): Iron in carbonate containing AFm phases. Cement and Concrete Research 41, 311–323.

Dilnesa, B.Z., Lothenbach, B., Renaudin, G., Wichser, A. & Wieland, E. (2012): Stability of monosulfate in the presence of iron. Journal of the American Ceramic Society 95, 3305–3316.

Dilnesa, B.Z., Lothenbach, B., Renaudin, G., Wichser, A., Kulik, D., 2014a. Synthesis and characterization of hydrogarnet Ca3(AlxFe1-X)2(SiO4)y(OH)4(3-y). Cem. Concr. Res. 59, 96–111.

Dilnesa, B.Z., Wieland, E., Lothenbach, B., Dähn, R. & Scrivener, K.L. (2014b): Fe-containing phases in hydrated cements. Cement and Concrete Research 58, 45–55.

Diomidis N, Scientific Basis for the Production of Gas due to Corrosion in a Deep Geological Repository, Nagra Working Report NAB, 14-21 (2014).

Dobrev, D., Jankvosky, F., Mendoza Miranda, A.N., Steinova, J. and Zuna, M. 2022 Korozní zkouška v přírodním granitoidním prostředí - zapojení v projektu Material Corrosion Test (MaCoTe), část zakázky č. 2 realizace a vyhodnocení MaCoTe experimentu v Grimsel Test Site [in Czech]. MS SURAO TZ 194/2017 (revision 5); SÚRAO, Prague, Czech Republic.

Drever J.I. (1988): The Geochemistry of Natural Waters. Prentice Hall, New Jersey.

El Mendili, Y., Abdelouas, A., Ait Chaou, A., Bardeau, J.F., Schlegel, M.L. 2014. Carbon steel corrosion in clay-rich environment. Corrosion Science 88, 56–65. https://doi.org/10.1016/j.corsci.2014.07.020.

El Mendili, Y., Abdelouas, A., Bardeau, J.-F. 2013. Insight into the mechanism of carbon steel corrosion under aerobic and anaerobic conditions. Physical Chemistry Chemical Physics 15, 9197–9204.

El Mendili, Y., Bardeau, J.F., Randrianantoandro, N., Greneche, J.M., Grasset, F. 2016. Structural behavior of laser-irradiated γ-Fe2O3 nanocrystals dispersed in porous silica matrix : γ-Fe2O3 to α-Fe2O3 phase transition and formation of ε-Fe2O3. Science and Technology of Advanced Materials 17, 597-609.

ENRESA,1997. Evaluación del comportamiento y de la seguridad de un almacenamiento geológico profundo en granito, ENRESA, Madrid.

ENRESA (1998). FEBEX. Bentonite: Origin, Properties and Fabrication of Blocks. Technical Publication ENRESA 4/98, Madrid.

ENRESA 2000 FEBEX project - full-scale engineered barriers experiment for a deep geological repository for high level radioactive waste in crystalline host rock - FINAL REPORT.

ENRESA, 2006a. Full-Scale Engineered Barriers Experiment: Updated Final Report. ENRESA Tech. Publ. PT 05-02/2006, 589 pp.

ENRESA, 2006b. FEBEX: Final THG modelling report. ENRESA Techn. Publ. PT 05-3/2006, 155 pp.

ENRESA (2008): Chemical (thermo-hydromechanical) evolution of the EBS: evolution of porewater chemistry; effects of canister corrosion and concrete degradation; and radionuclide retention. NF-PRO project. Enresa, Documentos internos de referencia 03/2008.

Fabian, M., Czompoly, O., Tolnai, I. and De Windt, L. 2023. Interactions between C-steel and blended cement in concrete under radwaste repository conditions at 80 °C. Scientific Reports 13(1), 15372.

Faria and Lopes (2007): Heated goethite and natural hematite: Can Raman spectroscopy be used to differentiate them? Vibrational Spectroscopy, 45(2): 117-121

Feil F, Elter E, Otterbein J, Nenyei A, Reducing the volume of liquid radioactive waste at the MVM Paks Nuclear Power Plant (in Hungarian), Nukleon VII. 167-169 (2014).

Fernandez, A.M., Cuevas, J. and Rivas, P. 2001. Pore water chemistry of the febex bentonite. Material Research Society Symposium Proceedings 603, 573-588.

Fernández, A., Baeyens, B. and Bradbury, M. 2004. Analysis of the Porewater Chemical Composition of a Spanish Compacted Bentonite Used in an Engineered Barrier. Physics and Chemistry of the Earth, Parts A/B/C 29, 105-118.

Fernández, A.M., Villar, M.V. (2010): Geochemical behaviour of a bentonite barrier in the laboratory after up to 8 years of heating and hydration. Applied Geochemistry, 25, 809-824.

Fernández, R., Ruiz, A.I., Cuevas, J. (2014). The role of smectite composition on the hyperalkaline alteration of bentonite, Applied Clay Science, 95, 83-94, https://doi.org/10.1016/j.clay.2014.03.015.

Fernandez, A.M. and Giraud, N. 2016 Gas and Water Sampling in different pipes from the FEBEX in situ test at the Grimsel Test Site. Nagra, Wettingen, Switzerland.

Fernández, J., 2017. Reactive Transport Models of low Permeability Structured Porous and Fractured Media. Ph.D. Dissertation. Universidad de A Coruña, Spain.

Forman, L., Picek, M., D., D., Gondolli, J., Mendoza Miranda, A.N., Straka, M., Kouřil, M., Stoulil, J., Matal, O., Čermák, J., Král, L., Žaloudek, J., Vávra, M. and Čupr, M. 2021 Závěrečná technická zpráva výzkumná část projektu Výzkum a vývoj ukládacího obalového souboru pro hlubinné ukládání vyhořelého jaderného paliva do stadia realizace vzorku [in Czech]. MS SÚRAO TZ 544/2021, SÚRAO, Prague, Czech Republic.

Gaines, G.I. and Thomas, H.C. 1953. Adsorption studies on clay minerals II. A formulation of the thermodynamics of exchange adsorption. J Chem Phys 21, 714–718.

Gam, Z., Daumas, S., Casalot, L., Bartoli-Joseph, M., Necib, S., Linard, Y., Labat, M., 2016. Thermanaeromonas burensis sp. nov., a thermophilic anaerobe isolated from a subterranean clay environment, Int. J. Syst. Evol. Microbiol. 66, 445–449. doi:10.1099/ijsem.0.000739.

Garralón, A., Gómez, P., Turrero, M.J., Torres, E., Buil, B., Sánchez, L., Peña, J. (2017). Hydrogeochemical characterisation of the groundwater in the FEBEX gallery. Arbeitsbericht. NAB 16-14. 125pp.

Gates, W.P. (2005) The Application of Vibrational Spectroscopy to Clay Minerals and Layered Double Hydroxides. Kloprogge, J.T. (ed), pp. 126-168, The Clay Mineral Society, Aurora, Colorado, USA.

Gehin, A., Greneche, J.M., Tournassat, C., Brendle, J., Rancourt, D.G. and Charlet, L. 2007. Reversible surface-sorption-induced electron-transfer oxidation of Fe(II) at reactive sites on a synthetic clay mineral. Geochimica et Cosmochimica Acta 71(4), 863-876.

Genchev, G. and Erbe, A. 2016. Raman Spectroscopy of Mackinawite FeS in Anodic Iron Sulfide Corrosion Products. Journal of The Electrochemical Society 163, C333–C338. https://doi.org/10.1149/2.1151606jes.

Génin, J.-M.R., Aïssa, R., Géhin, A., Abdelmoula, M., Benali, O., Ernstsen, V., Ona-Nguema, G., Upadhyay, C. and Ruby, C. 2005. Fougerite and FeII–III hydroxycarbonate green rust; ordering, deprotonation and/or cation substitution; structure of hydrotalcite-like compounds and mythic ferrosic hydroxide. Solid State Sciences 7(5), 545-572.

Ghazizadeh, S., Hanein, T., Provis, J.L. & Matschei, T. (2020): Estimation of standard molar entropy of cement hydrates and clinker minerals. Cement and Concrete Research 136, 106188.

Giffaut, E., Grivé, M., Blanc, P., Vieillard, P., Colàs, E., Gailhanou, H., Gaboreau, S., Marty, N., Madé, B. and Duro, L. 2014. Andra thermodynamic database for performance assessment: ThermoChimie. Applied Geochemistry 49, 225-236.

Giffaut, E., Grivé, M., Blanc, P., Vieillard, P., Colàs, E., Gailhanou, H., Gaboreau, S., Marty, N., Madé, B., Duro, L., 2019. Andra thermodynamic database for performance assessment: ThermoChimie, Appl. Geochem. 49, 225–236.

Gimmi, T. and Kosakowski, G. 2011. How Mobile Are Sorbed Cations in Clays and Clay Rocks? Environmental Science & Technology 45(4), 1443-1449.

Glasser, L. & Jenkins, H.D.B. (2016): Predictive thermodynamics for ionic solids and liquids. Physical Chemistry Chemical Physics 18, 21226–21240.

Glasser, L. (2021): The effective volumes of waters of crystallization & the thermodynamics of cementitious materials. Cement 3, 100004.

Goethals, J., de Windt, L., Wittebroodt, C., Abdelouas, A., de la Bernardie, X., Morizet, Y., Zajec, B., Detilleux, V. 2023. Interaction between carbon steel and low-pH bentonitic cement grout in anoxic, high temperature (80 °C) and spatially heterogeneous conditions. Corrosion Science 211, p. 110852.

Gondolli, J., Dobrev, D., Klajmon, D., Mendoza, A., Černousek, T., Kouril, M. and Stoulil, J. 2018a Behaviour of Waste Package for Spent Nuclear Fuel and High-Level Waste: Corrosion Products (final report). MS SURAO TZ 329/2018/ENG; SÚRAO, Prague, Czech Republic.

Gondolli, J., Dobrev, D., Klajmon, M., Černousek, T. and Kouril, M. 2018b Chování UOS pro VJP a RAO/Korozní produkty. 3. Průběžná zpráva [in Czech. MS SURAO TZ 217/2018, SÚRAO, Prague, Czech Republic.

Gondolli, J., Klajmon, M. and Kouril, M. 2018c Chování UOS pro VJP a RAO/Korozní produkty. Závěrečná zpráva [in Czech]. MS SURAO TZ 329/2018, SÚRAO, Prague, Czech Republic.

Gorski, C.A., Klüpfel, L., Voegelin, A., Sander, M. and Hofstetter, T.B. 2012. Redox properties of structural Fe in clay minerals: 2. Electrochemical and spectroscopic characterization of electron transfer irreversibility in ferruginous smectite, SWa-1. Environmental Science & Technology 46(17), 9369-9377.

Grim, R.E. and Kulbicki, G. 1961. Montmorillonite: high temperature reactions and classification. The American Mineralogist 46, 1329-1369.

Grivé, M., Duro, L., Colàs, E. and Giffaut, E. 2015. Thermodynamic data selection applied to radionuclides and chemotoxic elements: An overview of the ThermoChimie-TDB. Applied Geochemistry 55, 85-94.

Grousset, S., Urios, L., Mostefaoui, S., Dauzeres, A., Crusset, D., Deydier, V., Linard, Y., Dillmann P., Mercier-Bion, F., Neff, D. 2020. Biocorrosion detection by sulphur isotopic fractionation measurements. Corrosion Science 165. https://doi.org/10.1016/j.corsci.2019.108386.

Guillaume D., Neaman A., Cathelineau M., Mosser-Ruck R., Peiffert C., Abdelmoula M., Dubessy J., Villiéras F., Michau N. (2004): Experimental study of the transformation of smectite at 80 and 300 °C in the presence of Fe oxides. Clay Minerals 39: 17–34.

Gütlich, P., Bill, E. and Trautwein, A.X. (2011) Mössbauer Spectroscopy and Transition Metal Chemistry, Springer-Verlag, Berlin Heidelberg, Germany.

Hadi, J., Grangeon, S., Warmont, F., Seron, A. and Greneche, J.M. 2014. A novel and easy chemical-clock synthesis of nanocrystalline iron-cobalt bearing layered double hydroxides. Journal of colloid and interface science 433, 130-140.

Hadi, J., Tournassat, C., Ignatiadis, I., Greneche, J.M. and Charlet, L. 2013. Modelling CEC variations versus structural iron reduction levels in dioctahedral smectites. Existing approaches, new data and model refinements. Journal of colloid and interface science 407, 397-409.

Hadi, J., Tournassat, C. and Lerouge, C. 2016. Pitfalls in using the hexaamminecobalt method for cation exchange capacity measurements on clay minerals and clay-rocks: Redox interferences between the cationic dye and the sample. Applied Clay Science 119(2), 393-400.

Hadi, J., Wersin, P., Jenni, A. and Greneche, J.M. 2017 Redox evolution and Fe-bentonite interaction in the ABM2 experiment, Äspö Hard Rock Laboratory. NTB 17-10. p. 304, Nagra, Wettingen, Switzerland.

Hadi, J., Wersin, P., Serneels, V. and Greneche, J.-M. 2019a. Eighteen years of steel–bentonite interaction in the FEBEX in situ test at the Grimsel Test Site in Switzerland. Clays and Clay Minerals 67.

Hadi, J., Wersin, P., Serneels, V. and Greneche, J.M. 2019b. Eighteen years of steel-bentonite interaction in the FEBEX “in situ” test at the Grimsel Test Site in Switzerland. Clays & Clay Minerals 67, 111-131.

Hallet, V., Pedersen, M.T., Lothenbach, B., Winnefeld, F., Eykens, L., De Belie, N. & Pontikes, Y. (2023): The hydration of ternary blended cements with Fe-rich slag from non-ferrous metallurgy and limestone. Cement and Concrete Research 169, 107155.

Hanesch, M. 2009. Raman spectroscopy of iron oxides and (oxy)hydroxides at low laser power and possible applications in environmental magnetic studies. Geophysical Journal International 177, 941–948. https://doi.org/10.1111/j.1365-246X.2009.04122.x.

Handler, R.M., Frierdich, A.J., Johnson, C.M., Rosso, K.M., Beard, B.L., Wang, C., Latta, D.E., Neumann, A., Pasakarnis, T. and Premaratne, W.A.P.J. 2014. Fe(II)-Catalyzed recrystallization of goethite revisited. Environmental Science & Technology 48, 11302-11311.

Havlova, V., Kiczka, M., Mendoza Miranda, A., Klajmon, M., Wersin, P., Pekala, M., Jenni, A., Hadi, J., Samper, J., Montenegro, L., Mon, A., Fabian, M., Osan, J., Dauzeres, A. and Jacques, D. 2020 Modelling of the steel-clay interface – approaches, first results and model refinements.

Helgeson, H.C., Delany, J.M., Nesbitt, H.W. & Bird, D.K. (1978): Summary and critique of the thermodynamic properties of rock-forming minerals. American Journal of Science 278A, 1–229.

Heřmanská, M., Voigt, M.J., Marieni, C., Declercq, J. and Oelkers, E.H. 2023. A comprehensive and consistent mineral dissolution rate database: Part II: Secondary silicate minerals. Chemical Geology 636, 121632.

Honti G, NRWR-National Radioactive Waste Repository, Ed. Gabriella Honti, https://rhk.hu/storage/338/NRHT_nagy-_angol_kicsi.pdf (2019).

Hummel, W. & Thoenen, T. (2021): The PSI Chemical Thermodynamic Database 2020. Nagra Technical Report, NTB 21-03. Villigen, Switzerland.

Hunger, S., Benning, L.G. 2007. Greigite: A true intermediate on the polysulfide pathway to pyrite. Geochemical Transactions 8, 1–20. https://doi.org/10.1186/1467-4866-8-1.

Hunter, F., Bate, F. and Heath, T. 2007 Geochemical investigation of iron transport into bentonite as steel corrodes. SKB Technical Report TR-07-09. Svensk Kärnbränslehantering AB, Stockholm, Sweden.

IAEA-NS-ARTEMIS Integrated review service for radioactive waste and spent fuel management, decommissioning and remediation (ARTEMIS), 2022 Ed. Department of Nuclear Safety and

Security (https://www.iaea.org/sites/default/files/documents/review-missions/final_artemis_report_-_hungary.pdf) Accessed 26 June 2023

Itälä, A. 2009 Chemical evolution of bentonite buffer in a final repository of spent nuclear fuel during the thermal phase. VTT Publications 721, Espoo, Finland.

Jacques, D., Simunek, J., Mallants, D. and van Genuchten, M.T. 2018. The HPx software for multicomponent reactive transport during variably-saturated flow: Recent developments and applications. JOURNAL OF HYDROLOGY AND HYDROMECHANICS 66(2), 211-226.

Jacques, D., Šimůnek, J., Mallants, D. and van Genuchten, M.T. 2006. Operator-splitting errors in coupled reactive transport codes for transient variably saturated flow and contaminant transport in layered soil profiles. Journal of Contaminant Hydrology 88, 197-218.

Jubb, A. M.; Allen, H. C. Vibrational Spectroscopic Characterization of Hematite, Maghemite, and Magnetite Thin Films Produced by Vapor Deposition. ACS Appl. Mater. Interfaces 2010, 2, 2804–2812.

Kant, M.A., Ammann, J., Rossi, E., Madonna, C., Höser, D. and Rudolf von Rohr, P. 2017. Thermal properties of Central Aare granite for temperatures up to 500°C: Irreversible changes due to thermal crack formation. Geophysical Research Letters 44(2), 771-776.

Karnland, O., Olsson, S. and Nilsson, U. 2006 Mineralogy and sealing properties of various bentonites and smectite-rich clay material. SKB Technical Report, TR-06-30. SKB, Stockholm.

Kaufhold, S., Hassel, A.W., Sanders, D. and Dohrmann, R. 2015. Corrosion of high-level radioactive waste iron-canisters in contact with bentonite. Journal of Hazardous Materials 285, 464-473.

Kaufhold, S., Klimke, S., Schloemer, S., Alpermann, T., Renz, F. and Dohrmann, R. 2020. About the Corrosion Mechanism of Metal Iron in Contact with Bentonite. ACS Earth and Space Chemistry 4(5), 711-721.

Kiczka, M., Pekala, M. and Wersin, P. (2022a) Radionuclide Solubility Limits and Migration Parameters for the Backfill for the Safety Case SC-OLA.

Kiczka, M., Pękala, M. and Wersin, P. 2022b Radionuclide solubility limits and migration parameters for the canister, buffer and buffer-rock interface for the safety case SC-OLA. Posiva Oy, Olkiluoto, Finnland.

Klajmon, M., Havlová, V., Mendoza, A.M. and Dobrev, D. 2021 WP 2 ACED: Summary of the outputs of the Czech contribution to the EURAD project. MS SURAO TZ 557/2021/EN, SURAO, Prague, Czech Republic.

Klajmon, M. (2024). PHREEQC Scripts for Modeling the Geochemical Evolution of Iron-Bentonite-Water Systems (UJV Contribution to EURAD ACED Project) (Version 1.0, as of 2024-04-19). Zenodo. https://doi.org/10.5281/zenodo.10992837

Kulik, D.A., Miron, G.D. & Lothenbach, B. (2022): A structurally-consistent CASH+ sublattice solid solution model for fully hydrated C-S-H phases: Thermodynamic basis, methods, and Ca-Si-H2O core sub-model. Cement and Concrete Research 151, 106585.

Kulik, D.A., Wagner, T., Dmytrieva, S. V., Kosakowski, G., Hingerl, F.F., Chudnenko, K. V. & Berner, U.R. (2013): GEM-Selektor geochemical modeling package: Revised algorithm and GEMS3K numerical kernel for coupled simulation codes. Computational Geosciences 17, 1–24.

Kyritsis, K., Meller, N., Hall, C. 2009. Chemistry and Morphology of Hydrogarnets Formed in Cement-Based CASH Hydroceramics Cured at 200°C to 350°C. Journal of the American Ceramic Society 92, 1105-1111.

Lafuente, B., Downs, R. T., Yang, H., Stone, N. 2015. The power of databases: the RRUFF project., in: Highlights in Mineralogical Crystallography. T Armbruster R M Danisi, Eds. Berlin, Ger. W. Gruyter, 2015: pp. 1–30.

Lalan, P., Dauzères, A., De Windt, L., Bartier, D., Sammaljärvi, J., Barnichon, J.D., Techer, I., Detilleux, V., 2016. Impact of a 70 °C temperature on an ordinary Portland cement paste/claystone interface: An in situ experiment, Cement and Concrete Research 83, 164-178.

Lalan, P., Dauzères, A., De Windt, L., Sammaljärvi, J., Bartier, D., Techer, I., Detilleux, V., Siitari-Kauppi, M., 2019. Mineralogical and microstructural evolution of Portland cement paste/argillite

interfaces at 70 °C – Considerations for diffusion and porosity properties. Cement and Concrete Research 115, 414–425.

Lanson, B., Lantenois, S., Van Aken, P.A., Bauer, A., Plançon, A. 2012. Experimental investigation of smectite interaction with metal iron at 80 °c: Structural characterization of newly formed Fe-rich phyllosilicates. American Mineralogist 97, 864–871. https://doi.org/10.2138/am.2012.4062.

Latta, D.E., Neumann, A., Premaratne, W.A.P.J. and Scherer, M.M. 2017. Fe(II)–Fe(III) Electron Transfer in a Clay Mineral with Low Fe Content. ACS Earth and Space Chemistry 1(4), 197-208.

Lear, P.R. and Stucki, J.W. 1985. Role of structural hydrogen in the reduction and reoxidation of iron in nontronite. Clays and Clay Minerals 33, 539-545.

Lee, T.R. and Wilkin, R.T. 2010. Iron hydroxy carbonate formation in zerovalent iron permeable reactive barriers: Characterization and evaluation of phase stability. Journal of Contaminant Hydrology 116(1), 47-57.

Leupin, O.X., Smart, N.R., Zhang, Z., Stefanoni, M., Angst, U., Papafotiou, A. and Diomidis, N. 2021. Anaerobic corrosion of carbon steel in bentonite: An evolving interface. Corrosion Science 187, 109523.

Lhotka, M. (2021) Stanovení specifického povrchu ocelí [in Czech], University of Chemistry and Technology, Prague, Czech Republic.

Li, Y.H. and Gregory, S. 1974. Diffusion of ions in sea water and in deep-sea sediments. Geochimica et Cosmochimica Acta 38, 703-714.

Litvan, G.G. and Meyer, A. Carbonation of granulated blast furnace slag cement concrete during twenty years of field exposure. 1986. ICA Special Publication, in: 91, Fly, Ash, Silica Fume, Slag, and Natural Pozzolans in Concrete: Proceeding of the 2nd International Conference: 1986, Madrid, Spain, 1986, pp. 1445–1462. Collection: NRC Publications Archive.

Lothenbach B, Scrivener K, Hooton R D, Supplementary cementitious materials, Cement and Concrete Research 41, 1244-1256 (2011).

Lothenbach L, Le Saout G, Ben Haha M, Figi R, Wieland E, Hydration of a low-alkali CEM III/B–SiO2 cement (LAC), Cement and Concrete Research 42, 410–423 (2012).

Lothenbach, B., Kulik, D.A., Matschei, T., Balonis, M., Baquerizo, L., Dilnesa, B., Miron, G.D. & Myers, R.J. (2019): Cemdata18: A chemical thermodynamic database for hydrated Portland cements and alkali-activated materials. Cement and Concrete Research 115, 472–506.

Lothenbach, B., Matschei, T., Möschner, G., Glasser, F.P., 2008. Thermodynamic modelling of the effect of temperature on the hydration and porosity of Portland cement. Cem. Concr. Res. 38, 1–18.

Lublóy E, Kopecsko K, Balazs G L, Szilagyi I M, Madarasz J, Improved fire resistance by using slag cements, J Therm Anal Calorim 125, 271-279 (2016).

Ma, R.Z., Liang, J.B., Takada, K. and Sasaki, T. 2011. Topochemical Synthesis of Co-Fe Layered Double Hydroxides at Varied Fe/Co Ratios: Unique Intercalation of Triiodide and Its Profound Effect. J. Am. Chem. Soc. 133(3), 613-620.

Mancini, A., Wieland, E., Geng, G., Dähn, R., Skibsted, J., Wehrli, B. & Lothenbach, B. (2020): Fe(III) uptake by calcium silicate hydrates. Applied Geochemistry 113.

Mancini, A., Wieland, E., Geng, G., Lothenbach, B., Wehrli, B. & Dähn, R. (2021): Fe(II) interaction with cement phases: Method development, wet chemical studies and X-ray absorption spectroscopy. Journal of Colloid and Interface Science 588, 692–704.

Marty, N.C.M., Claret, F., Lassin, A., Tremosa, J., Blanc, P., Madé, B., Giffaut, E., Cochepin, B. and Tournassat, C. 2015. A database of dissolution and precipitation rates for clay-rocks minerals. Applied Geochemistry 55, 108-118.

Matray, J.-M., Savoye, S., Cabrera, J., 2007. Desaturation and structure relationships around drifts excavated in the well-compacted Tournemire's argillite (Aveyron, France). Engineering Geology 90, 1–16.

Meeussen, J.C.L. 2003. ORCHESTRA: An object-oriented framework for implementing chemical equilibrium models. Environmental Science & Technology 37(6), 1175-1182.

Mehra, O.P., Jackson, M.L. (1960): Iron oxide removal from soils and clays by a dithionite-citrate system buffered with sodium bicarbonate, Seventh National Conference on Clays and Clay Minerals, 1960.

Meija, J., Coplen, T.B., Berglund, M., Brand, W.A., De Bièvre, P., Gröning, M., Holden, N.E., Irrgeher, J., Loss, R.D., Walczyk, T. and Prohaska, T. 2016. Isotopic compositions of the elements 2013 (IUPAC Technical Report). 88(3), 293-306.

Millington, R.J. 1959. Gas Diffusion in Porous Media. Science 130(3367), 100-102.

Miron, G.D., Kulik, D.A. & Lothenbach, B. (2022a): Pore water compositions of Portland cement with and without silica fume calculated using the fine-tuned CASH+NK solid solution model. Materials and Structures 2022 55:8 55, 1–13.

Miron, G.D., Kulik, D.A., Yan, Y., Tits, J. & Lothenbach, B. (2022b): Extensions of CASH+ thermodynamic solid solution model for the uptake of alkali metals and alkaline earth metals in C-S-H. Cement and Concrete Research 152, 106667.

Miron, G.D., Leal, A.M.M., Dmytrieva, S. V. & Kulik, D.A. (2023): ThermoFun: A C++/Python library for computing standard thermodynamic properties of substances and reactions across wide ranges of temperatures and pressures. Journal of Open Source Software 8, 4624.

Molinero, J.J., Samper, G. Zhang, Yang, C., 2004. Biogeochemical reactive transport model of the redox zone experiment of the Aspo hard rock laboratory in Sweden. Nucl. Technol. 148, 151–165.

Mon, A. 2017. Coupled thermo-hydro-chemical-mechanical models for the bentonite barrier in a radioactive waste repository. Ph. D. Dissertation. University of A Coruña, Spain.

Mon, A., Samper, J., Montenegro, L., Naves, A., Fernández, J., 2017. Long-term non-isothermal reactive transport model of compacted bentonite, concrete and corrosion products in a HLW repository in clay. Journal of Contaminant Hydrology 197, 1-16. http://dx.doi.org/10.1016/j.jconhyd.2016.12.006.

Mon, A., Samper, J., Montenegro, L., Turrero, M.J., Torres, E., Cuevas, J., Fernández, R., De Windt, L., (2023). Reactive transport models of the geochemical interactions at the iron/bentonite interface in laboratory corrosion tests. Applied Clay Science 240, 106981. https://doi.org/10.1016/j.clay.2023.106981.

Montes-H, G., Marty, N., Fritz, B., Clement, A., Michau, N., 2005. Modelling of long-term diffusion–reaction in a bentonite barrier for radioactive waste confinement. Appl. Clay Sci. 30, 181–198

Möschner, G., Lothenbach, B., Rose, J., Ulrich, A., Figi, R. & Kretzschmar, R. (2008): Solubility of Fe-ettringite (Ca6[Fe(OH)6]2(SO4)3 · 26H2O). Geochimica et Cosmochimica Acta 72, 1–18.

Möschner, G., Lothenbach, B., Winnefeld, F., Ulrich, A., Figi, R. & Kretzschmar, R. (2009): Solid solution between Al-ettringite and Fe-ettringite (Ca6[Al1 - xFex(OH)6]2(SO4)3·26H2O). Cement and Concrete Research 39, 482–489.

Mössbauer, R.L. 1958. Kernresonanzabsorption von Gammastrahlung in Ir^{191}. Naturwissenschaften 45(22), 538-539.

Mota-Heredia C., Cuevas J., Ruiz A.I., Ortega A., Torres E., Turrero M.J., Fernández R. 2023. Geochemical interactions at the steel-bentonite interface caused by a hydrothermal gradient. Applied Clay Science 240, 106984. https://doi.org/10.1016/j.clay.2023.106984.

Muurinen, A., Tournassat, C., Hadi, J. and Greneche, J.M. 2014a Sorption and diffusion of FE(II) in bentonite. p. 92, Finland.

Muurinen, A., Tournassat, C., Hadi, J. and Greneche, J.M. 2014b Sorption and diffusion of Fe(II) in bentonite. WR 2014-04. Posiva (ed), p. 84, Posiva, Olkiluoto, Finland.

Necib, S., Linard, Y., Crusset, D., Michau, N., Daumas, S., Burger, E., Romaine, A., Schlegel, M.L., 2016. Corrosion at the carbon steel–clay borehole water and gas interfaces at 85 °C under anoxic and transient acidic conditions, Corrosion Science 111, 242–258. doi:10.1016/j.corsci.2016.04.039.

Neumann, A., Olson, T.L. and Scherer, M.M. 2013. Spectroscopic Evidence for Fe(II)-Fe(III) Electron Transfer at Clay Mineral Edge and Basal Sites. Environmental Science & Technology 47(13), 6969-6977.

Neumann, A., Wu, L., Li, W., Beard, B.L., Johnson, C.M., Rosso, K.M., Frierdich, A.J. and Scherer, M.M. 2015. Atom Exchange between Aqueous Fe(II) and Structural Fe in Clay Minerals. Environmental Science & Technology 49(5), 2786-2795.

Ngo, V.V., Clément, A., Michau, N. and Fritz, B. 2015. Kinetic modeling of interactions between iron, clay and water: Comparison with data from batch experiments. Applied Geochemistry 53, 13-26.

Ni, C., Wu, Q., Yu, Z., Shen, X. 2021. Hydration of Portland cement paste mixed with densified silica fume: From the point of view of fineness. Construction Building Materials 272. https://doi.org/10.1016/j.conbuildmat.2020.121906.

Nos B, Needs of countries with longer timescale for deep geological repository implementation, EPJ Nuclear Sci. Technol. 6, 22 (2020).

Osborne, G.J. 1986. Carbonation of blast furnace slag cement concretes. Durability of Building Materials 4, 81–96.

Page, C., Short, N., El Tarras, A., 1981. Diffusion of chloride ions in hardened cement pastes. Cement and Concrete Research 11, 395–406.

Palandri, J.L. and Kharaka, Y.K. 2004 A Compilation of Rate Parameters of Water-Mineral Interaction Kinetics for Application to Geochemical Modeling. Open File Report 2004-1068. p. 64.

Pally, D., Le Bescop, P., Schlegel, M.L., Miserque, F., Chomat, L., Neff, D., L'Hostis, V. 2020. Corrosion behavior of iron plates in cementitious solution at 80 °C in anaerobic conditions, Corrosion Science 170, 108650. https://doi.org/10.1016/j.corsci.2020.108650.

Parkhurst, D.L. & Appelo, C. a. J. (2013): Description of Input and Examples for PHREEQC Version 3 — A Computer Program for Speciation , Batch-Reaction , One-Dimensional Transport , and Inverse Geochemical Calculations. U.S. Geological Survey Techniques and Methods, book 6, chapter A43, 497 p., Techniques and Methods, book 6, chapter A43. U.S. Geological Survey.

Pignatelli, I., Bourdelle, F., Bartier, D., Mosser-Ruck, R., Truche, L., Mugnaioli, E., Michau, N. 2014. Iron-clay interactions: Detailed study of the mineralogical transformation of claystone with emphasis on the formation of iron-rich T-O phyllosilicates in a step-by-step cooling experiment from 90 degrees Celsius to 40 degrees Celsius. Chemical Geology 387, 1–11. https://doi.org/10.1016/j.chemgeo.2014.08.010.

Pignatelli, I., Mosser-Ruck, R., Mugnaioli, E., Sterpenich, J., Gemmi, M. 2020. The Effect of the Starting Mineralogical Mixture on the Nature of Fe-Serpentines Obtained during Hydrothermal Synthesis AT 90 degrees Celsius. Clays and Clay Minererals 68, 394–412.

Pignatelli, I., Mugnaioli, E., Marrocchi, Y. 2018. Cronstedtite polytypes in the Paris meteorite. European Journal of Mineralogy 30, 349–354. https://doi.org/10.1127/ejm/2018/0030- 2713.

Pitty, A., Alexander, R. 2011. (Eds.), Maqarin Phase IV Report, NDA RWMD516 2011. https://nora.nerc.ac.uk/id/eprint/20953/

Poonoosamy J., C Wanner, P Alt Epping P., J Águila, J Samper, L Montenegro, M Xie, D Su, U Mayer, U Mäder, LR Van Loon & G Kosakowski, 2018, Benchmarking of reactive transport codes for a 2D setup with mineral dissolution/precipitation reactions and feedback on transport parameters, Comp. Geos. 25, 1337-1358.

Qin, Z., Demko, B., Noël, J., Shoesmith, D., King, F., Worthingham, R., Keith, K. 2004. Localized dissolution of millscale-covered pipeline steel surfaces. Corrosion 60, 906–914. https://doi.org/10.5006/1.3287824.

Rémazeilles, C., Saheb, M., Neff, D., Guilminot, E., Tran, K., Bourdoiseau, J.A., Sabot, R., Jeannin, M., Matthiesen, H., Dillmann, P., Refait, P. 2010. Microbiologically influenced corrosion of archaeological artefacts: Characterisation of iron(II) sulfides by Raman spectroscopy, Journal of Raman Spectroscopy 41, 1425–1433. https://doi.org/10.1002/jrs.2717.

Rizoulis, A., Steele, H. M., Morris, K., Lloyd, J. R. 2012. The potential impact of anaerobic microbial metabolism during the geological disposal of intermediate-level waste. Mineralogical Magazine 76, 3261.

Robie, R. & Hemingway, B.S. (1995): Thermodynamic Properties of Minerals and Related Substances at 298.15K and 1 Bar, U.S. Geological Survey Bulletin.

Robineau, M., Deydier, V., Crusset, D., Bellefleur, A., Neff, D., Vega, E., Sabot, R., Jeannin, M., Refait, P. 2021. Formation of iron sulfides on carbon steel in a specific cement grout designed for radioactive waste repository and associated corrosion mechanisms. Materials (Basel). 14. https://doi.org/10.3390/ma14133563.

Robineau, M., Romaine, A., Sabot, R., Jeannin, M., Deydier, V., Necib, S., Refait, P. 2017. Galvanic corrosion of carbon steel in anoxic conditions at 80 °C associated with a heterogeneous magnetite (Fe3O4)/mackinawite (FeS) layer, Electrochimica Acta 255, 274–285. https://doi.org/10.1016/j.electacta.2017.09.183.

Robineau, M., Sabot, R., Jeannin, M., Deydier, V., Crusset, D., Refait, P. 2020. Mechanisms of localized corrosion of carbon steel associated with magnetite/mackinawite layers in a cement grout. Materials Corrosion 72, 194–210. https://doi.org/10.1002/maco.202011696.

Rosso, K.M., Yanina, S.V., Gorski, C.A., Larese-Casanova, P. and Scherer, M.M. 2010. Connecting observations of hematite (alpha-Fe_2O_3) growth catalyzed by Fe(II). Environmental Science & Technology 44, 61-67.

Roy, A. 2009. Sulfur speciation in granulated blast furnace slag: An X-ray absorption spectroscopic investigation. Cement and Concrete Research 39, 659–663. https://doi.org/10.1016/j.cemconres.2009.05.007.

Ruiz-Gómez, S.; Serrano, A.; Carabias, I.; García, M. A.; Hernando, A.; Mascaraque, A.; Pérez, L.; González-Barrio, M. A.; Rodriguez de la Fuente, O. Formation of a Magnetite/Hematite Epitaxial Bilayer Generated with Low Energy Ion Bombardment. Appl. Phys. Lett. 2017, 110, 093103)

Sakizci, M. 2016. INVESTIGATION OF THERMAL AND STRUCTURAL PROPERTIES OF NATURAL AND ION-EXCHANGED ANALCIME. Anadolu University Journal of Science and Technology A - Applied Sciences and Engineering 17(4), 724 - 734.

Samper, J., Lu, C.H. and Montenegro, L. 2008. Reactive transport model of interactions of corrosion products and bentonite. Physics and Chemistry of the Earth 33, S306-S316.

Samper, J., Xu, T., Yang, C., 2009. A sequential partly iterative approach for multicomponent reactive transport CORE2D. Comput. Geosci. 13, 301-316.

Samper, J, C Yang, L. Zheng, L. Montenegro, T Xu, Z Dai, G Zhang, C Lu & S Moreira, 2011, CORE2D V4: A code for water flow, heat and solute transport, geochemical reactions, and microbial processes, Chapter 7 of the Electronic book Groundwater Reactive Transport Models, F Zhang, G-T Yeh, C Parker & X Shi (Ed), Bentham Science Publishers, pp 161-186.

Samper, J., Naves, A., Montenegro, L., Mon, A., 2016. Reactive transport modelling of the long-term interactions of corrosion products and compacted bentonite in a HLW repository in granite: Uncertainties and relevance for performance assessment. Appl. Geochem., 67, 42-51. https://doi.org/10.1016/j.apgeochem.2016.02.001.

Samper, J., Mon, A. and Montenegro, L. 2018. A revisited thermal, hydrodynamic, chemical and mechanical model of compacted bentonite for the entire duration of the FEBEX in situ test. Applied Clay Science 160, 58-70.

Samper, J., Mon, A., Montenegro, L., Cuevas, J., Turrero, M.J., Naves, A., Fernández, R., Torres, E., 2018. Coupled THCM model of a heating and hydration concrete-bentonite column test. Appl. Geochem. 94, 67–81.

Samper J., A. Mon, L. Montenegro & A Naves, 2020, THCM numerical simulations of the engineered barrier system for radioactive waste disposal. Environmental Geotechnics. https://doi.org/10.1680/jenge.19.00104.

Savage, D., Watson, C., Benbow, S. and Wilson, J. 2010. Modelling iron-bentonite interactions. Applied Clay Science 47(1), 91-98.

Sawhney, B.L., 1970. Potassium and cesium ion selectivity in relation to clay mineral structure. Clay Clay Miner. 18, 47–52.

Schaefer, M.V., Gorski, C.A. and Scherer, M.M. 2011. Spectroscopic evidence for interfacial Fe(II)-Fe(III) electron transfer in a clay mineral. Environmental Science & Technology 45, 540-545.

Schlegel, M.L., Bataillon, C., Brucker, F., Blanc, C., Prêt, D., Foy, E., Chorro, M. 2014. Corrosion of metal iron in contact with anoxic clay at 90°C: Characterization of the corrosion products after two years of interaction. Applied Geochemistry. 51, 1–14. https://doi.org/10.1016/j.apgeochem.2014.09.002.

Schlegel, M.L., Martin, F., Fenart, M., Blanc, C., Varlet, J., Foy, E., Prêt, D., Trcera, N. 2019. Corrosion at the carbon steel-clay compact interface at 90°C: Insight into short- and long-term corrosion aspects. Corrosion Science 152, 31–44. https://doi.org/10.1016/j.corsci.2019.01.027.

Schultz, L.G. 1969. Lithium and potassium adsorption, dehydroxylation temperature, and structural water content of aluminous smectites. Clays and Clay Minerals 17, 115-149.

Schwaminger, Sebastian P., Christopher Syhr, and Sonja Berensmeier. 2020. "Controlled Synthesis of Magnetic Iron Oxide Nanoparticles: Magnetite or Maghemite?" Crystals 10, no. 3: 214. https://doi.org/10.3390/cryst10030214

Scott, P.W., Critchley, S.R., Wilkinson, F.C.F. 1986. The chemistry and mineralogy of some granulated and pelletized blast furnace slags. Mineralogical Magazine 50, 141–147. https://doi.org/10.1180/minmag.1986.050.355.19.

Shannon L W H, Electronic Thesis and Dissertation Rep. The University of Western Ontario, Graduate program in Chemistry (2016).

Sherar, B.W.A., Keech, P.G., Shoesmith, D.W. 2011. Carbon steel corrosion under anaerobic-aerobic cycling conditions in near-neutral pH saline solutions - Part 1: Long term corrosion behaviour. Corrosion Science 53, 3636–3642. https://doi.org/10.1016/j.corsci.2011.07.015.

Sherar, B.W.A., Keech, P.G., Shoesmith, D.W. 2011. Carbon steel corrosion under anaerobic-aerobic cycling conditions in near-neutral pH saline solutions. Part 2: Corrosion mechanism. Corrosion Science 53, 3643–3650. https://doi.org/10.1016/j.corsci.2011.07.008.

Sherar, B.W.A., Keech, P.G., Shoesmith, D.W. 2013. The effect of sulfide on the aerobic corrosion of carbon steel in near-neutral pH saline solutions. Corrosion Science 66, 256–262. https://doi.org/10.1016/j.corsci.2012.09.027.

Sherar, B.W.A., Power, I.M., Keech, P.G., Mitlin, S., Southam, G., Shoesmith, D.W. 2011. Characterizing the effect of carbon steel exposure in sulfide containing solutions to microbially induced corrosion. Corrosion Science 53, 955–960. https://doi.org/10.1016/j.corsci.2010.11.027.

Sideris, P.J., Blanc, F., Gan, Z.H. and Grey, C.P. 2012. Identification of cation clustering in Mg-Al layered double hydroxides using multinuclear solid state nuclear magnetic resonance spectroscopy. Chem. Mat. 24(13), 2449-2461.

SikaFume HR/TU, Product Data Sheet, 2009 https://hun.sika.com/content/dam/dms/hucon/6/sikafume_hrtu_hu0910ta.pdf Accessed 26 June 2023

Simunek, J., Brunetti, G., Jacques, D., van Genuchten, M.T. and sejna, M. 2023. Developments and Applications of the HYDRUS Computer Software Packages since 2016. Vadose Zone J.

Simunek, J., Sejna, M., Brunetti, G. and van Genuchten, M.T. 2022a The HYDRUS Software Package for Simulating One-, Two-, and Three-Dimensional Movement of Water, Heat, and Multiple Solutes in Variably-Saturated Porous Media, Technical Manual I, Hydrus 1D, Version 5.x. p. 334, PC Progress, Prage, Czech Republic.

Simunek, J., van Genuchten, M.T. and Sejna, M. 2022b The HYDRUS Software Package for Simulating One-, Two-, and Three-Dimensional Movement of Water, Heat, and Multiple Solutes in Variably-Saturated Porous Media, Technical Manual II, Hydrus 2D/3D, Version 5.x. p. 283, PC Progress, Prague, Czech Republic.

Siramanont, J., Walder, B.J., Emsley, L. & Bowen, P. (2021): Iron incorporation in synthetic precipitated calcium silicate hydrates. Cement and Concrete Research 142, 106365.

Sisomphon, K. and Franke, L. 2007. Carbonation rates of concretes containing high volume of pozzolanic materials. Cement and Concrete Research 37, 1647–1653. https://doi.org/10.1016/j.cemconres.2007.08.014.

Smart N R, Corrosion behavior of carbon steel radioactive waste packages: A summary review of Swedish and U.K. Research, Corrosion 65(3), 195-212 (2009), https://doi.org/10.5006/1.3319128

Smart, N.R., Rance, A.P., Nixon, D.J., Fennell, P.A.H., Reddy, B., Kursten, B. 2017. Summary of studies on the anaerobic corrosion of carbon steel in alkaline media in support of the Belgian supercontainer concept. Corrosion Engineering Science and Technology 52, 217–226. https://doi.org/10.1080/1478422X.2017.1356981.

Soltermann, D., Baeyens, B., Bradbury, M.H. and Fernandes, M.M. 2014a. Fe(II) uptake on natural montmorillonites. II. Surface complexation modeling. Environmental Science & Technology 48(15), 8698-8705.

Soltermann, D., Baeyens, B., Bradbury, M.H. and Marques Fernandes, M. 2014b. Fe(II) Uptake on Natural Montmorillonites. II. Surface Complexation Modeling. Environmental Science & Technology 48(15), 8698-8705.

Soltermann, D., Fernandes, M.M., Baeyens, B., Dahn, R., Joshi, P.A., Scheinost, A.C. and Gorski, C.A. 2014c. Fe(II) uptake on natural montmorillonites. I. Macroscopic and spectroscopic characterization. Environmental Science & Technology 48(15), 8688-8697.

Soltermann, D., Fernandes, M.M., Baeyens, B., Miehe-Brendle, J. and Daehn, R. 2013. Competitive Fe(II)-Zn(II) uptake on a synthetic montmorillonite. Environmental Science & Technology 48(1), 190-198.

Stefanoni, M., Angst, U. & Elsener, B. (2020): The mechanism controlling corrosion of steel in carbonated cementitious materials in wetting and drying exposure. Cement and Concrete Composites 113, 103717.

Stoulil, J., Mukhtar, S., Lhotka, M., Bureš, R., Kašpar, V., Šachlová, Š., Pecková, A., Havlová, V., Danielisová, A., Malyková, D., Barčáková, L., Machová, B., Březinová, H., Ottenwelte, r.E., Němeček, J. and Němeček, J. 2022 Archeologické analogy pro verifikaci modelů životnosti kontejneru pro hlubinná úložiště radioaktivního odpadu [in Czech]. MS SÚRAO TZ 623/2022, SÚRAO, Prague, Czech Republic.

Stucki, J.W. and Anderson, W.L. 1981a. The quantitative assay of minerals for Fe^{2+} and Fe^{3+} using 1,10-Phenanthroline: I. Sources of variability. Soil Science Society of America Journal 45, 633-637.

Stucki, J.W. and Anderson, W.L. 1981b. The quantitative assay of minerals for Fe^{2+} and Fe^{3+} using 1,10-Phenanthroline: II. A photochemical method. Soil Science Society of America Journal 45, 638-641.

Stucki, J.W., Golden, D.C. and Roth, C.B. 1984. Effects of reduction and reoxidation of structural iron on the surface charge and dissolution of dioctahedral smectites. Clays and Clay Minerals 32, 350-356.

Sudheer Kumar, R.; Podlech, C.; Grathoff, G.;Warr, L.N.; Svensson, D. Thermally Induced Bentonite lterations in the SKB ABM5 Hot Bentonite Experiment. Minerals 2021, 11, 1017. https://doi.org/10.3390/min11091017

Takai, K., Moser, D. P., Onstott, T. C., Spoelstra, N., Pfiffner, S. M., Dohnalkova, A., Fredrickson, J. K. 2001. Alkaliphilus transvaalensis gen. nov., sp. nov., an extremely alkaliphilic bacterium isolated from a deep South African gold mine. International Journal of Systematic and Evolutionary microbiology 51:4, 1245.

Tinseau, E., Bartier, D., Hassouta, L., Devol-Brown, I., Stammose, D., 2006. Mineralogical characterization of the Tournemire argillite after in situ interaction with concrete. Waste Management 26, 789-800.

Torres E., Escribano A., Baldonedo J.L., Turrero M.J., Martin P.L., Peña J., Villar M.V. (2009): Evolution of the Geochemical Conditions in the Bentonite Barrier and Its Influence on the Corrosion of the Carbon Steel Canister. Mater. Res. Soc. Symp. Proc., 1124: 301-306.

Torres, E. (2011) Geochemical processes at the C-steel/bentonite interface in a deep geological repository: Experimental approach and modeling, Universidad Complutense de Madrid.

Torres, E., Turrero, M.J. and Escribano, A., 2013. Synthesis of corrosion phenomena at the iron/bentonite interface under unsaturated conditions. Technical Note CIEMAT/DMA/2G210/02/2013. PEBS Project. 2016

Torres, E., Turrero, M.J., Escribano, A., Fernández, R., Ruíz, A.I., Cuevas, J. (2014). Temporal evolution of the Fe/FEBEX bentonite system under simultaneous hydration and heating – Results up to seven years. A. Schäfers & S. Fahland (Eds.): Proceedings International Conference on the Performance of Engineered Barriers: Physical and Chemical Properties, Behavior and Evolution. BGR. Hannover. Germany. 153-160.

Toth, E., Hrabovszki, E., Toth, T.M., Schubert, F. 2020. Shear strain and volume change associated with sigmoidal vein arrays in the Boda Claystone. Journal of Structural Geology 138, 104105.

Turrero, M. J., Villar, M. V., Torres, E., Escribano, A., Cuevas, J., Fernández, R., Ruiz, A.I., Vigil de la Villa, R., del Soto, I., 2011. Deliverable 2.3-3-1 of PEBS Project. Laboratory tests at the interfaces, Final results of the dismantling of the tests FB3 and HB4, 2011. CIEMAT.

Tsarev, S., Waite, T.D. and Collins, R.N. 2016. Uranium Reduction by Fe(II) in the Presence of Montmorillonite and Nontronite. Environmental Science & Technology 50(15), 8223-8230.

Tzara, C. 1961. Diffusion des photons sur les atomes et les noyaux dans les cristaux. Journal de Physique et Le Radium 22(5), 303-307.

Van der Lee, J., De Windt, L., Lagneau, Goblet, P., 2003. Module-oriented modeling of reactive transport with HYTEC. Computers and Geosciences 29, 265–275.

Vantelon, D., Pelletier, M., Michot, L., Barrès, O. and Thomas, F. 2001. Fe, Mg and Al distribution in the octahedral sheet of montmorillonites. An infrared study in the OH-bending region. Clay Miner 36, 369-379.

Villar, M.V., Iglesias, R.J., Abos, H., Martinez, V., de la Rosa, C. and Manchon, M.A. 2016 FEBEX-DP on-site analyses report.

Wersin, P. 2003. Goechemical modeling of bentonite porewater in high-level waste repositories. journal of Contaminant Hydrology 61, 405-422.

Wersin, P., Curti, E. and Appelo, C.A.J. 2004. Modeling bentonite–water interactions at high solid/liquid ratios: swelling and diffuse double layer effects. Applied Clay Science 2004, 249-257.

Wersin, P., Hadi, J., Jenni, A., Svensson, D., Grenèche, J.-M., Sellin, P. and Leupin, O.X. 2021 Interaction of Corroding Iron with Eight Bentonites in the Alternative Buffer Materials Field Experiment (ABM2).

Wersin, P., Hadi, J., Kiczka, M., Jenni, A., Grenèche, J.-M., Diomidis, N., Leupin, O.X., Svensson, D., Sellin, P., Reddy, B., Smart, N. and Zhang, Z. Unravelling the corrosion processes at steel/bentonite interfaces in in situ tests. Materials and Corrosion n/a(n/a).

Wersin, P., Kiczka, M. and Koskinen, K. 2016. Porewater chemistry in compacted bentonite: Application to the engineered buffer barrier at the Olkiluoto site. Applied Geochemistry 74, 165-175.

Wersin, P. and Kober, F.e. 2017 FEBEX-DP. Metal corrosion and iron-bentonite interaction studies. Wersin, P. and Kober, F. (eds), Nagra, Wettingen, Switzerland.

Wieland, E., Miron, G.D., Ma, B., Geng, G., Lothenbach, B. 2023. Speciation of iron(II/III) at the iron-cement interface: a review. Materials and Structure 56:31.

Wilkin, R.T., Barnes, H.L. 1996. Pyrite formation by reactions of iron monosulfides with dissolved inorganic and organic sulfur species. Geochimica and Cosmochimica Acta 60, 4167–4179. https://doi.org/10.1016/S0016-7037(97)81466-4.

Wilson, J.C., Benbow, S., Sasamoto, H., Savage, D. and Watson, C. 2015. Thermodynamic and fully-coupled reactive transport models of a steel–bentonite interface. Applied Geochemistry 61, 10-28.

Wittebroodt, C., Savoye, S., Frasca, B., Gouze, P., Michelot, J.-L., 2012. Diffusion of HTO, 36Cl- and 125I- in Upper Toarcian argillite samples from Tournemire: Effect of initial iodide concentration and ionic strength. Applied Geochemistry 27, issue 7, 1432-1441.

Wolery, T.J., 1992. EQ3/3. A software package for geochemical modeling of aqueous system: package overview and installation guide version 7.0. UCRL-MA-110662-PT-I, Lawrence Livermore National Laboratory, Livermore, California.

Xia, X., Idemitsu, K., Arima, T., Inagaki, Y., Ishidera, T., Kurosawa, S., Iijima, K. and Sato, H. 2005. Corrosion of carbon steel in compacted bentonite and its effect on neptunium diffusion under reducing condition. Applied Clay Science 28(1-4), 89-100.

Xu, T., Samper, J., Ayora, C., Manzano, M., Custodio, E., 1999. Modeling of non-isothermal multi-component reactive transport in field scale porous media flow system. J. Hydrol. 214 (1-4), 144–164. https://doi.org/10.1016/S0022-1694(98) 00283-2.

Yamamoto, J.K. 2000. A simple and practical device for wet elutriation of sediments. Journal of Sedimentary Research 70(2), 423-426.

Yan, Y. (2022): Effect of alkali, aluminium and equilibration time on calcium-silicate-hydrates. https://doi.org/10.5075/EPFL-THESIS-9572

Yan, Y., Bernard, E., Miron, G.D., Rentsch, D., Ma, B., Scrivener, K. & Lothenbach, B. (2023): Kinetics of Al uptake in synthetic calcium silicate hydrate (C-S-H). Cement and Concrete Research 172, 107250.

Zhang, Y., Hu, B., Teng, Y., Tu, K. and Zhu, C. 2019. A library of BASIC scripts of reaction rates for geochemical modeling using phreeqc. Computers & Geosciences 133, 104316.

Zhang G, J. Samper & L. Montenegro, 2008, Coupled thermo-hydro-bio-geochemical reactive transport model of the CERBERUS heating and radiation experiment in Boom clay, Appl Geochem, Vol 23/4: 932-949.

Zheng, L., Samper, J., Montenegro, L. and Fernández, A.M., 2010. A coupled model of heating and hydration laboratory experiment in unsaturated compacted FEBEX bentonite. Journal of hydrology 386, 80-94.

Zheng, L.G., Samper, J. and Montenegro, L. 2011. A coupled THC model of the FEBEX in situ test with bentonite swelling and chemical and thermal osmosis. Journal of Contaminant Hydrology 126(1-2), 45-60.

Appendix A Numerical modelling of the FB lab corrosion tests performed by CIEMAT/UAM on the interactions of FEBEX bentonite and steel corrosion products (UDC)

A.1. Tables

Table A1– Chemical reactions and equilibrium constants for aqueous complexes and minerals (Wolery, 1992), protolysis constants for surface complexation reactions (Bradbury and Baeyens, 1997) and selectivity coefficients for cation exchange reactions (ENRESA, 2006b) at 25ºC considered in the THCM models of the FB corrosion tests.

Aqueous complexes	Log K
$CaCO_3(aq) + H^+ \Leftrightarrow Ca^{2+} + HCO_3^-$	7.0017
$CaHCO_3^+ \Leftrightarrow Ca^{2+} + HCO_3^-$	-1.0467
$CaSO_4(aq) \Leftrightarrow Ca^{2+} + SO_4^{2-}$	-2.1111
$CaOH^+ + H^+ \Leftrightarrow Ca^{2+} + H_2O$	12.850
$CO_2(aq) + H_2O \Leftrightarrow H^+ + HCO_3^-$	-6.3447
$CO_3^{2-} + H^+ \Leftrightarrow HCO_3^-$	10.3288
$KSO_4^- \Leftrightarrow K^+ + SO_4^{2-}$	-0.8796
$MgCO_3(aq) + H^+ \Leftrightarrow Mg^{2+} + HCO_3^-$	7.356
$MgHCO_3^+ \Leftrightarrow Mg^{2+} + HCO_3^-$	-1.0357
$MgSO_4(aq) \Leftrightarrow Mg^{2+} + SO_4^{2-}$	-2.4117
$MgOH^+ + H^+ \Leftrightarrow Mg^{2+} + H_2O$	11.785
$NaHCO_3(aq) \Leftrightarrow Na^+ + HCO_3^-$	-0.1541
$NaSO_4^- \Leftrightarrow Na^+ + SO_4^{2-}$	-0.8200
$NaCO_3^- + H^+ \Leftrightarrow Na^+ + HCO_3^-$	9.8156
$NaOH(aq) + H^+ \Leftrightarrow Na^+ + H_2O$	14.180
$OH^- + H^+ \Leftrightarrow H_2O$	13.9951
$H_3SiO_4^- + H^+ \Leftrightarrow 2H_2O + SiO_2(aq)$	9.8120
$HSO_4^- \Leftrightarrow H^+ + SO_4^{2-}$	1.9791
$HS^- + 2O_2(aq) \Leftrightarrow H^+ + SO_4^{2-}$	138.31
$Fe^{3+} + 0.5H_2O \Leftrightarrow H^+ + 0.25O_2 + Fe^{2+}$	-8.490
$FeHCO_3^+ \Leftrightarrow Fe^{2+} + HCO_3^-$	-2.050
$FeCO_3(aq) + H^+ \Leftrightarrow Fe^{2+} + HCO_3^-$	5.5682
$FeCl^+ \Leftrightarrow Fe^{2+} + Cl^-$	0.1605
$FeCl^{2+} + 0.5H_2O \Leftrightarrow Fe^{2+} + Cl^- + H^+ + 0.25O_2$	-7.675
$FeOH^+ + H^+ \Leftrightarrow Fe^{2+} + H_2O$	10.895
$FeOH^{2+} \Leftrightarrow Fe^{2+} + 0.5H_2O + 0.25O_2$	-4.1083
$Fe(OH)_2(aq) + 2H^+ \Leftrightarrow Fe^{2+} + 2H_2O$	20.60
$Fe(OH)_3(aq) + 2H^+ \Leftrightarrow Fe^{2+} + 2.5H_2O + 0.25O_2$	3.6834
$Fe(OH)_4^- + 3H^+ \Leftrightarrow Fe^{2+} + 3.5H_2O + 0.25O_2$	13.109
$Fe(OH)_2^+ + H^+ \Leftrightarrow Fe^{2+} + 1.5H_2O + 0.25O_2$	-2.8185
$Fe(SO_4)_2^- + 0.5H_2O \Leftrightarrow Fe^{2+} + 2SO_4^{2-} + H^+ + 0.25O_2$	-11.703
$FeSO_4(aq) \Leftrightarrow Fe^{2+} + SO_4^{2-}$	-2.20
$FeHSO_4^{2+} + 0.5H_2O \Leftrightarrow Fe^{2+} + 2H^+ + SO_4^{2-} + 0.25O_2$	-10.029
$Fe_2(OH)_2^{4+} \Leftrightarrow 2Fe^{3+} + H_2O + 0.5O_2$	-9.699
$KOH(aq) + H^+ \Leftrightarrow K^+ + H_2O$	14.46
$H_2(aq) + 0.5O_2 \Leftrightarrow H_2O$	46.10
$NaHSiO_3(aq) + H^+ \Leftrightarrow H_2O + Na^+ + SiO_2(aq)$	8.3040
$HSiO_3^- + H^+ \Leftrightarrow H_2O + SiO_2(aq)$	9.9525
$MgH_3SiO_4^+ + H^+ \Leftrightarrow 2H_2O + Mg^{2+} + SiO_2(aq)$	8.5416
Minerals	**LogK**
$Calcite + H^+ \Leftrightarrow Ca^{2+} + HCO_3^-$	1.8487
$Anhydrite \Leftrightarrow Ca^{2+} + SO_4^{2-}$	-4.3064
$Gypsum \Leftrightarrow Ca^{2+} + SO_4^{2-} + 2H_2O$	-4.4823
$Quartz \Leftrightarrow SiO_2(aq)$	-3.9993
$Magnetite + 6H^+ \Leftrightarrow 3Fe^{2+} + 0.5O_2(aq) + 3H_2O$	-6.5076
$Siderite + H^+ \Leftrightarrow Fe^{2+} + HCO_3^-$	-0.1920
$Goethite + 2H^+ \Leftrightarrow Fe^{2+} + 1.5H_2O + 0.25O_2(aq)$	-7.9555
$Fe(OH)_2(s) + 2H^+ \Leftrightarrow Fe^{2+} + 2H_2O$	13.9045
$Fe(s) + 2H^+ + 0.5O_2(aq) \Leftrightarrow Fe^{2+} + H_2O$	59.033

Surface complexation reactions	LogK
$_{\equiv}S^{S}OH_2^+ \Leftrightarrow {}_{\equiv}S^{S}OH + H^+$	-4.5
$_{\equiv}S^{S}O^- + H^+ \Leftrightarrow S^{S}OH$	7.9
$_{\equiv}S^{s}OFe^+ + H^+ \Leftrightarrow {}_{\equiv}S^{s}OH + Fe^{2+}$	0.6
$_{\equiv}S^{s}OFeOH + 2H^+ \Leftrightarrow {}_{\equiv}S^{s}OH + Fe^{2+} + H_2O$	10.0
$_{\equiv}S^{s}OFe(OH)_2^- + 3H^+ \Leftrightarrow {}_{\equiv}S^{s}OH + Fe^{2+} + 2H_2O$	20.0
$_{\equiv}S^{W1}OH_2^+ \Leftrightarrow {}_{\equiv}S^{W1}OH + H^+$	-4.5
$_{\equiv}S^{W1}O^- + H^+ \Leftrightarrow {}_{\equiv}S^{W1}OH$	7.9
$_{\equiv}S^{W1}OFe^+ + H^+ \Leftrightarrow {}_{\equiv}S^{W1}OH + Fe^{2+}$	3.3
$_{\equiv}S^{W2}OH_2^+ \Leftrightarrow {}_{\equiv}S^{W2}OH + H^+$	-6.0
$_{\equiv}S^{W2}O^- + H^+ \Leftrightarrow {}_{\equiv}S^{W2}OH$	-10.5
Cation Exchange reactions	**$K_{Na\text{-}cation}$**
$Na^+ + X\text{-}K \Leftrightarrow K^+ + X\text{-}Na$	0.1456
$Na^+ + 0.5\ X_2\text{-}Ca \Leftrightarrow 0.5\ Ca^{2+} + X\text{-}Na$	0.3265
$Na^+ + 0.5\ X_2\text{-}Mg \Leftrightarrow 0.5\ Mg^{2+} + X\text{-}Na$	0.3766
$Na^+ + 0.5\ X_2\text{-}Fe \Leftrightarrow 0.5\ Fe^{2+} + X\text{-}Na$	0.5

Table A2 – Water flow parameters used in the THCM model of the FB corrosion tests (ENRESA, 2006a; Zheng et al., 2010; Samper et al., 2018; Mon et al., 2023).

	Bentonite	**Fe powder**
Intrinsic permeability of the liquid, k^{il} (m^2) as a function of porosity	$k^{il} = k_0 \frac{\emptyset^3}{(1-\emptyset)^2} \frac{(1-\emptyset_0)^2}{\emptyset_0^3}$ with $\emptyset_o$=0.40 k_o= 2.75·10^{-21}	with $\emptyset_o$=0.40 for SC tes with $\emptyset_o$=0.38 for FB tes k_o= 2.75·10^{-19}
Liquid relative permeability k^{rl} as a function of liquid saturation S_l	$k_{rl} = S_l^3$	
Retention curve: liquid saturation S_l as a function of suction Ψ (Pa)	$S_l = \frac{(1 - 9.1 \cdot 10^{-7}\Psi)^{1.1}}{[(1 + 5 \cdot 10^{-5}\Psi)^{1.22}]^{0.18}}$	
Liquid viscosity (kg/m·s) as a function of temperature T (K)	$0.6612 \cdot (T - 229)^{-1.562}$	
Liquid density (kg/m^3) as a function of liquid pressure p^l and temperature	$998.2 \cdot e^{[5 \cdot 10^{-5} \cdot (p^l - 100) - 2.1 \cdot 10^{-4} \cdot (T - T_{ref})]}$	
Reference temperature, T_{ref} (ºC)	22	
Gas intrinsic permeability (m^2)	5·10^{-10}	
Gas relative permeability k^{rg}	$k_{rl} = (1 - S_l)^3$	
Vapour tortuosity	0.1	1
Gas viscosity (kg/m·s)	1.76·10^{-5}	
Solid density (kg/m^3) as a function of temperature T(ºC)	$2750 \cdot e^{[-2 \cdot 10^{-5} \cdot (T - T_{ref})]}$	$2785 \cdot e^{[-2 \cdot 10^{-6} \cdot (T - T_{ref})]}$
Thermo-osmotic permeability (m^2/K/s)	4.2·10^{-13}	

Table A3 – Thermal parameters used in the THCM models of the FB corrosion tests (ENRESA, 2006a; Zheng et al., 2010; Samper et al., 2018; Mon et al., 2023).

	Bentonite	**Fe powder**
Specific heat of the liquid (J/kg·ºC)	4202	
Specific heat of the air (J/kg·ºC)	1000	
Specific heat of the vapour (J/kg·ºC)	1620	
Specific heat of the solid (J/kg·ºC)	835.5	480
Reference temperature (ºC)	22	
Thermal conductivity of the liquid (W/m·ºC)	1.5	
Thermal conductivity of the air (W/m·ºC)	2.6·10^{-2}	
Thermal conductivity of the vapour (W/m·ºC)	4.2·10^{-2}	
Thermal conductivity of the solid (W/m·ºC)	1.23	50.16
Vaporization enthalpy (J/kg)	2.45.10^6	

Table A4 – Solute transport parameters used in the THCM models of the FB corrosion tests (ENRESA, 2006a; Zheng et al., 2010; Samper et al., 2018; Mon et al., 2023).

	Bentonite	Fe powder
Molecular diffusion coefficient in water $D_o(T)$ in m²/s as a function of T (ºC) and the molecular diffusion coefficient at the reference temperature T_{ref} (ºC), $D_o(T_{ref})$	$D_o(T) = D_o(T_{ref})\frac{T}{T_0}\frac{\mu_0^l}{\mu^l}$ $D_o(T_{ref}) = 2 \cdot 10^{-10}$ (except Cl^-, $D_o(T_{ref}) = 9 \cdot 10^{-11}$)	
Reference temperature (ºC)	22	
Longitudinal dispersivity (m)	0.001	0.01
Solute tortuosity τ as a function of volumetric water content θ and porosity $\emptyset$	$\tau = \frac{\theta^{7/3}}{\emptyset^2}$	

Table A5 – Mechanical parameters used in the THCM model of the FB corrosion tests (ENRESA, 2006a; Zheng et al., 2010; Samper et al., 2018; Mon et al., 2023).

	Bentonite	Fe powder
Water mechanical compressibility (Pa^{-1})	$5 \cdot 10^{-7}$	
Water thermal expansion (K^{-1})	$2.1 \cdot 10^{-4}$	
Solid thermal expansion (K^{-1})	$2 \cdot 10^{-5}$	$2 \cdot 10^{-6}$
State surface parameters	$e = A + B \cdot ln\sigma' + C \cdot \ln(\Psi + P^a) +$ $+ D \cdot ln\sigma' \cdot \ln(\Psi + P^a)$ A = 0.76; B = -0.052446; C= - 0.0406413; D = 0.00479977	-

Table A6 – Chemical compositions (mol/L) of the initial pore water in the bentonite and Fe powder (Fernández et al., 2001; Mon et al., 2023) and in the Grimsel hydration water (Turrero et al., 2011; Mon et al., 2023) used in the THCM model of FB corrosion tests.

	Initial bentonite pore water	Grimsel hydration water
Na^+	$1.3 \cdot 10^{-1}$	$3.7 \cdot 10^{-4}$
Ca^{2+}	$2.2 \cdot 10^{-2}$	$1.8 \cdot 10^{-4}$
Mg^{2+}	$2.3 \cdot 10^{-2}$	$1.6 \cdot 10^{-5}$
K^+	$1.7 \cdot 10^{-3}$	$2.2 \cdot 10^{-5}$
SO_4^{2-}	$3.2 \cdot 10^{-2}$	$6.1 \cdot 10^{-5}$
Cl^-	$1.6 \cdot 10^{-1}$	$2.3 \cdot 10^{-5}$
$SiO_2(aq)$	$1.0 \cdot 10^{-4}$	$1.9 \cdot 10^{-4}$
HCO_3^-	$5.8 \cdot 10^{-4}$	$3.9 \cdot 10^{-4}$
Fe^{2+}	$6.6 \cdot 10^{-5}$	$1.8 \cdot 10^{-8}$
pH	7.72	9.7
Eh (V)	-0.046	0.303

Table A7 – Initial concentrations of exchanged cations and cation exchange capacity, CEC (in cmol(+)/kg) for the FEBEX bentonite (Fernández et al., 2004; Mon et al., 2023) used in the THCM model of the FB corrosion tests.

Exchanged cation	Ca^{2+}	Mg^{2+}	Na^+	K^+	Fe^{2+}	CEC
Concentration cmol(+)/kg	42.0	33.0	25.5	2.2	0.05	102.75

Table A8 – Surface complexation reactions and site capacities (in mol/L) of strong, weak #1 and weak #2 sorption sites for the FEBEX bentonite (Bradbury and Bayens, 1997, 2003; Mon et al., 2023) used in the THCM model of the FB corrosion tests.

Types of sorption sites	Sorption primary species	Bentonite	
		Surface complexes	Site capacity (mol/L)
Strong	S^S-OH	S^S-OH_2^+ S^S-O^- S^S-OFe^+ S^S-OFeOH S^S-$OFe(OH)_2^-$	0.015
Weak #1	S^{w1}-OH	S^{w1}-OH_2^+ S^{w1}-O^- S^{w1}-OFe^+	0.307
Weak #2	S^{w2}-OH	S^{w2}-OH_2^+ S^{w2}-O^-	0.307

A.1. Figures

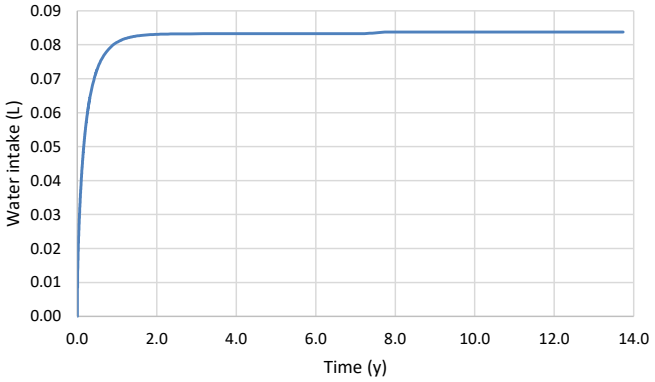

Figure A1 – Time evolution of the computed water intake of the FB corrosion tests.

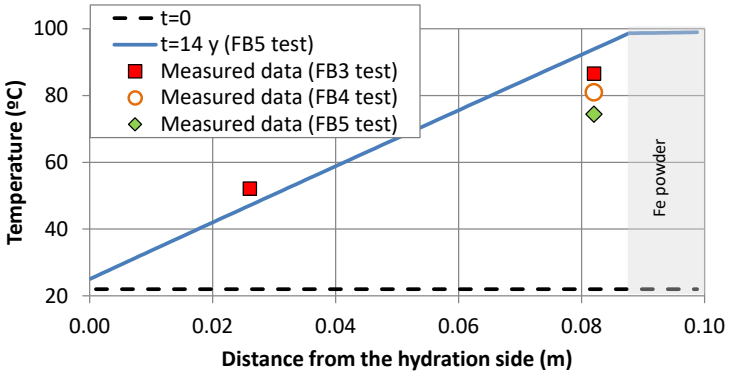

Figure A2 – Spatial distribution of the computed (lines) and measured temperatures (symbols) at the end of the FB3, FB4 and FB5 corrosion tests.

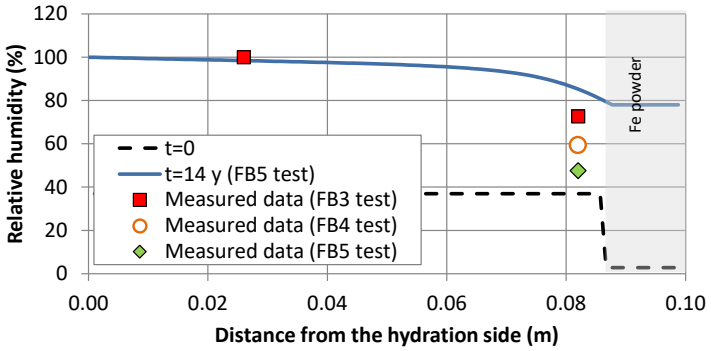

Figure A3 – Spatial distribution of the computed (lines) and measured relative humidity (symbols) at the end of the FB3, FB4 and FB5 corrosion tests.

A.2. Sensitivity runs

A.2.1. Sensitivity to the vapour tortuosity and the thermal conductivity

Computed water content and temperature are slightly larger than the measured data in the bentonite near the Fe powder in the base run. Sensitivity runs to the vapour tortuosity and to the Fe powder thermal permeability have been performed to improve the computed results. The vapour tortuosity has been increased two times in the sensitivity run and the thermal permeability of the Fe powder has been reduced equal to the bentonite thermal conductivity.

Figure A4 shows computed volumetric water content for the base run and for the sensitivity runs to the vapour tortuosity and to the thermal permeability. Computed volumetric water content is smaller in the sensitivity run to the vapour tortuosity than that of the base run and it fits the measured data better that of the base run. On the other hand, the computed water content increases in the sensitivity run to the thermal permeability. Computed temperature decreases when the Fe powder thermal permeability decreases in the bentonite near the Fe powder (Figure A5). However, the computed temperature in the sensitivity run to the vapour tortuosity is similar to that of the base run.

Figure A6 shows the dissolved Cl^- concentration in the base run and in the sensitivity runs. The concentrations decrease in the bentonite near the Fe powder and in the Fe powder which do not reproduce the trend of the measured data.

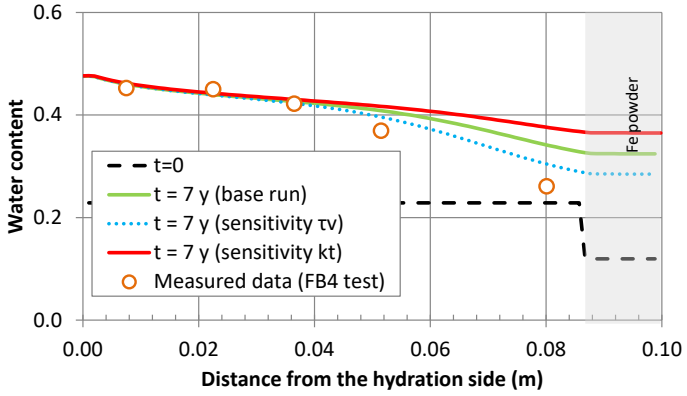

Figure A4 – Spatial distribution of the computed volumetric water content for the base run and the sensitivity runs to vapour tortuosity and thermal conductivity and measured data at 7 years.

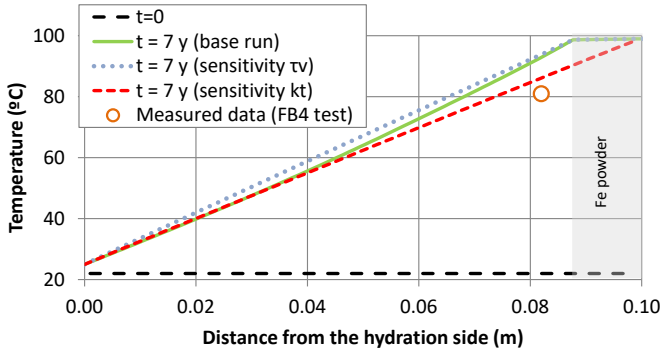

Figure A5 – Spatial distribution of the computed temperature for the base run and the sensitivity runs to vapour tortuosity and thermal conductivity and measured data at 7 years.

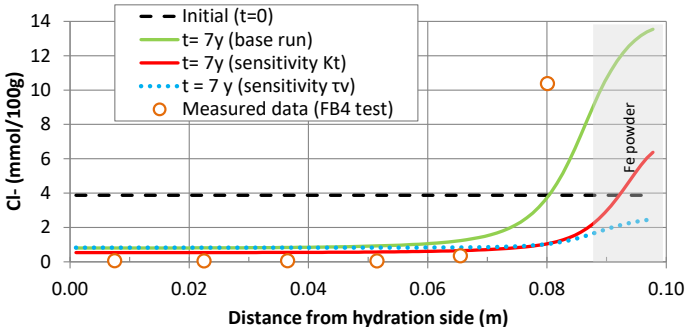

Figure A6 – Spatial distribution of the computed dissolved Cl^- concentration for the base run and the sensitivity runs to vapour tortuosity and thermal conductivity and measured data at 7 years.

A.2.2. Sensitivity to the initial sorption site concentration

A sensitivity run to the initial sorption site concentrations has been performed. The initial sorption site concentrations have been decreased 5 times in the strong, weak#1 and weak#2 sites. Figure A7 shows the total computed and measured iron sorption concentrations at the end of the FB4 test for the base run and the sensitivity run. The computed sorbed iron concentration for the sensitivity run is smaller than that of the base run and it fits the measured data.

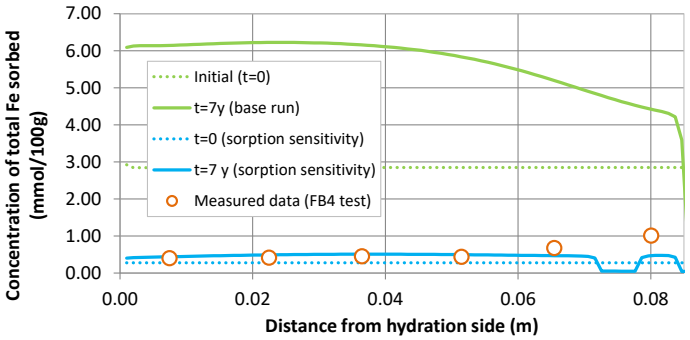

Figure A7 – Spatial distribution of the computed sorbed iron concentration for the base run and the sensitivity run to the initial sorption site concentrations and measured data at 7 years.

A.2.3. Sensitivity to the initial mineral phases composition

A sensitivity run has been performed to improve the initially considered mineral phases in the Fe powder after the initial aerobic phase. Maghemite, hematite (under kinetic control), magnetite, goethite, siderite and Fe(s) have been initially considered in the sensitivity run. The Fe powder composition is 62% iron in the base run, while iron, maghemite and hematite have been considered in the sensitivity run. The Fe powder has been divided into 3 different zones: 1) A first zone, Fe powder FB4R, with an extension of

2 mm from the bentonite-Fe powder interface; 2) a second zone, Fe powder FB4A, from 2 to 4 mm from the bentonite-Fe powder interface; and 3) the last zone, Fe powder, in the 9 mm more inside the Fe powder. Table A9 lists the initial mineral volume fractions considered in the base run and in the sensitivity cases. The hematite precipitation/dissolution has been considered with the following kinetic expression (Palandri and Kharaka, 2004):

$$r_m = e^{\frac{66.2}{RT}}(2.51 \cdot 10^{-15}(\Omega - 1) + 4.07 \cdot 10^{-10}(\Omega - 1)[H^+])$$

The specific surface area was adopted equal to 10 dm^2/L.

Computed maghemite is initially present and re-dissolves instantaneously (Figure A8). Computed hematite dissolves with time very slowly (Figure A9). Goethite precipitates at initial times and then redissolves (Figure A10). Computed magnetite precipitates in the Fe powder, especially near the bentonite where the maghemite dissolves (Figure A11).

The pH, Eh, dissolved, exchanged and sorbed concentrations are similar in the base run and in the sensitivity run (not shown here).

Table A9 – Mineral volume fractions for the base run and the sensitivity runs.

	Base run		Sensitivity run	
	Mineral	**Initial volume fraction**	**Mineral**	**Initial volume fraction**
Bentonite	Calcite	0.01	Calcite	0.01
	Quartz	0.01	Quartz	0.01
	Gypsum	0.00008	Gypsum	0.00008
Fe powder FB4R (2mm)	Fe(s)	0.63	Fe(s)	0.0042
			Maghemite	0.165
			Hematite	0.42
Fe powder FB4A (2mm)	Fe(s)	0.63	Fe(s)	0.396
			Maghemite	0.142
			Hematite	0.082
Fe powder (9 mm)	Fe(s)	0.63	Fe(s)	0.63

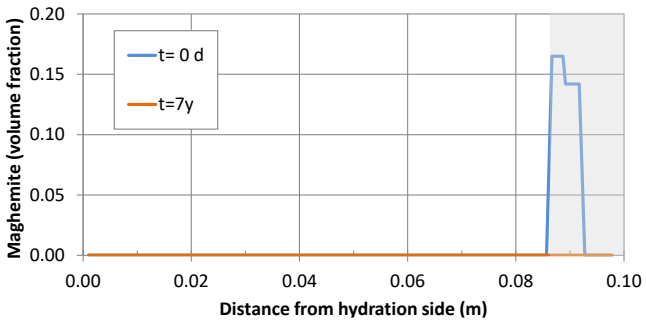

Figure A8 – Spatial distribution of the computed maghemite for the sensitivity run at selected times.

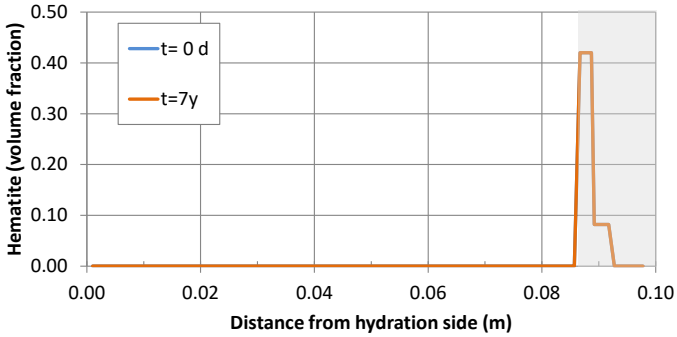

Figure A9 – Spatial distribution of the computed hematite for the sensitivity run at selected times.

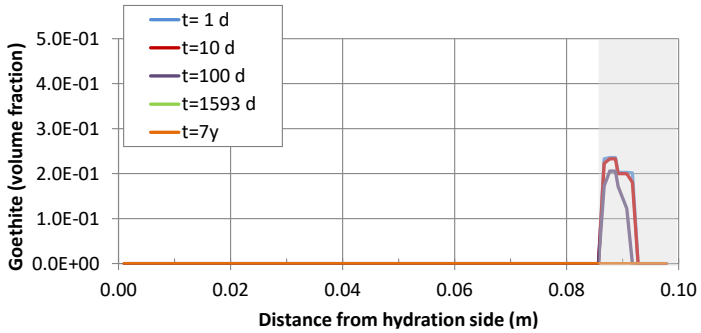

Figure A10 – Spatial distribution of the computed goethite for the sensitivity run at selected times.

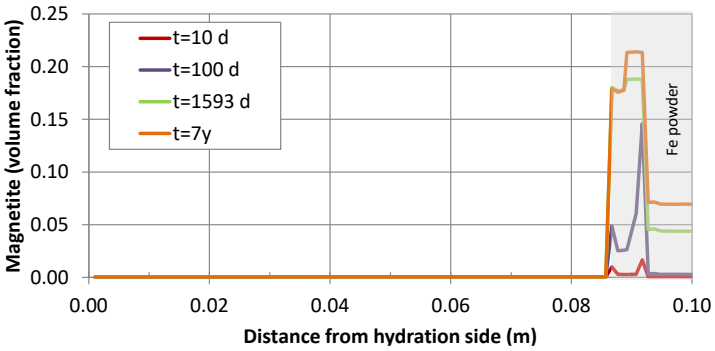

Figure A11 – Spatial distribution of the computed magnetite for the sensitivity run at selected times.

Appendix B Numerical modelling of the FeMo laboratory corrosion test performed by CIEMAT/UAM on the interactions of FEBEX bentonite and steel corrosion products (UDC)

B.1. Tables

Table B1 – Equilibrium constants at 22ºC for aqueous complexes and minerals (Giffaut et al., 2014) considered in the model of the FeMo corrosion test.

Aqueous complexes	LogK (22ºC)	Aqueous complexes	LogK (22ºC)
OH^-	14.10	$Fe(OH)_2$	20.80
CO_3^{-2}	10.40	$Fe(OH)_3$	4.08
$CaCO_3$	7.16	$Fe(OH)_4^-$	13.20
$Ca(HCO_3)^+$	-1.12	$Fe(OH)_2^+$	-2.86
$Ca(SO_4)$	-2.30	$Fe(SO_4)_2^-$	-14.00
$Ca(OH)^+$	12.90	$Fe(SO_4)$	-2.18
$Mg(CO_3)$	7.39	$FeHSO_4^{+2}$	-13.10
$Mg(HCO_3)^+$	-1.04	$Fe_2(OH)_2$+4	-14.30
$Mg(SO_4)$	-2.22	K(OH)	14.60
$Mg(OH)^+$	11.80	$K(SO_4)^-$	-0.88
Na(OH)	14.80	$Na(SO_4)^-$	-0.95
$Na(CO_3)^-$	9.15	$H(SO_4)^-$	-1.94
$Na(HCO_3)$	0.23	$H_2(aq)$	46.60
CO_2	-6.37	$Al(OH)_2^+$	-12.40
HS^-	140.00	$Al(OH)_3$	-6.51
Fe^{+3}	-8.66	Al^{+3}	-23.20
$FeHCO_3^+$	-1.41	$Al(OH)^{+2}$	-18.20
$Fe(CO_3)$	4.66	$H_3(SiO_4)^-$	9.89
$FeCl^+$	-0.14	$H_2(SiO_4)^{-2}$	23.30
$FeCl^{+2}$	-10.10	$Ca(H_3SiO_4)^+$	8.89
$Fe(OH)^+$	9.60	$Mg(H_3SiO_4)^+$	8.63
$Fe(OH)^{+2}$	-6.39		
Minerals	**LogK (22ºC)**	**Minerals**	**LogK (22ºC)**
Quartz	-3.780	Fe(s)	59.50
Calcite	1.900	Greenalite	22.10
Gypsum	-4.610	Cronstedtite	-0.76
Magnetite	-6.530	Smectite	-21.60
Goethite	-8.160	Saponite-Mg	21.40
Siderite	-0.422		

Table B2 – Initial water chemical composition of the sinter, the Fe powder (Grimsel hydration water (Turrero et al., 2011)) and the saturated bentonite pore water (Samper et al., 2016) considered in the reactive transport model of the FeMo test.

	Initial bentonite pore water	Grimsel hydration water
Na^+	$1.8\cdot10^{-1}$	$3.7\cdot10^{-4}$
Ca^{2+}	$3.2\cdot10^{-2}$	$1.8\cdot10^{-4}$
Mg^{2+}	$3.6\cdot10^{-2}$	$1.6\cdot10^{-5}$
K^+	$1.5\cdot10^{-3}$	$2.2\cdot10^{-5}$
SO_4^-	$2.0\cdot10^{-2}$	$6.1\cdot10^{-5}$
Cl^-	$2.7\cdot10^{-1}$	$2.3\cdot10^{-5}$
H4SiO4(aq)	$9.6\cdot10^{-5}$	$1.9\cdot10^{-4}$
HCO_3^-	$7.6\cdot10^{-3}$	$3.9\cdot10^{-4}$
Fe^{2+}	$6.6\cdot10^{-5}$	$1.8\cdot10^{-8}$
$Al(OH)_4^-$	$1.0\cdot10^{-8}$	$1.8\cdot10^{-6}$
pH	6.46	9.7
Eh (V)	-0.078	0.303

B.2. Figures

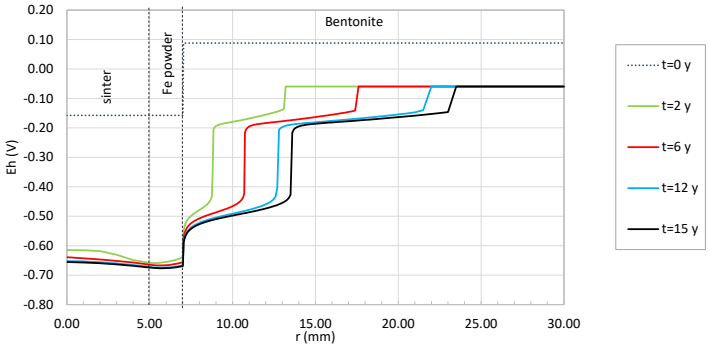

Figure B1 – Spatial distribution of the computed Eh at selected times in the FeMo corrosion tests for a particle size of 64 µm.

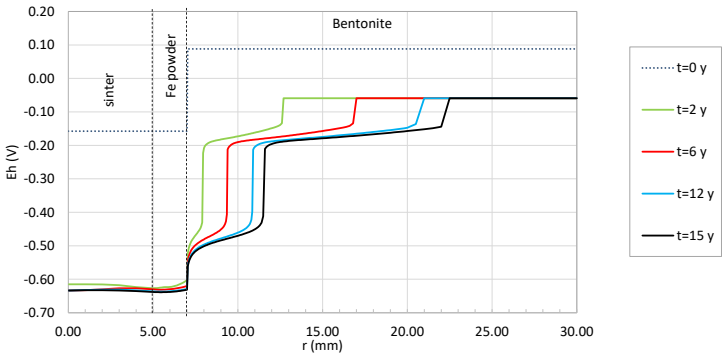

Figure B2 – Spatial distribution of the computed Eh at selected times in the FeMo corrosion tests for a particle size of 450 µm.

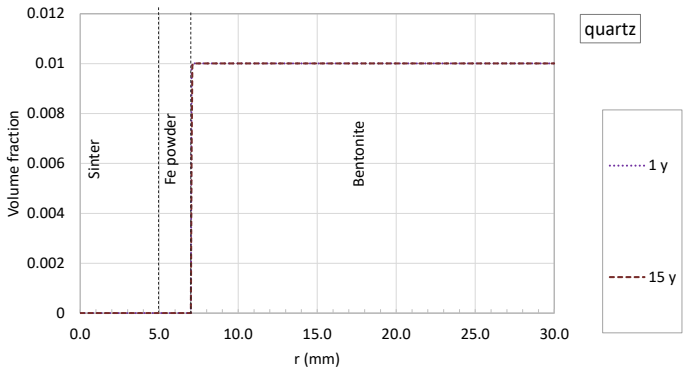

Figure B3 – Spatial distribution of the computed quartz at selected times in the FeMo corrosion tests for a particle size of 450 µm.

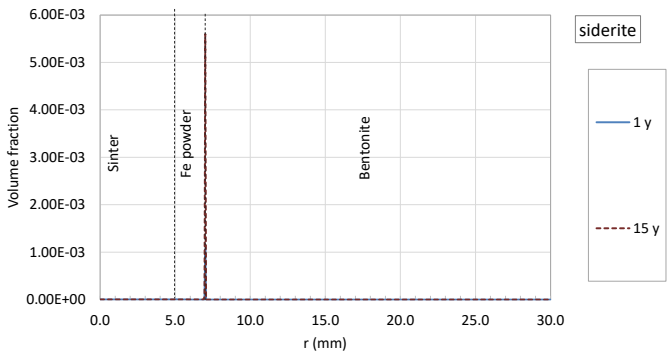

Figure B4 – Spatial distribution of the computed siderite at selected times in the FeMo corrosion tests for a particle size of 450 µm.

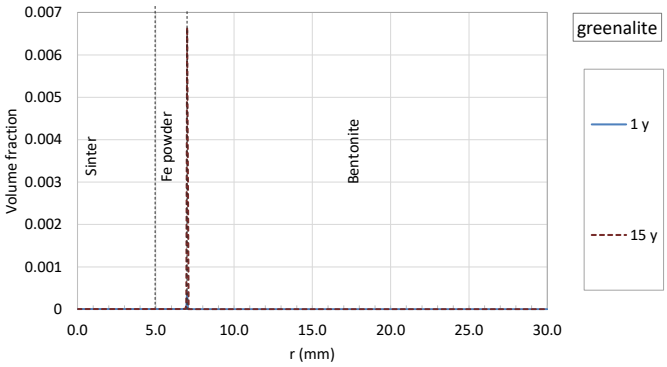

Figure B5 – Spatial distribution of the computed greenalite at selected times in the FeMo corrosion tests for a particle size of 450 µm.

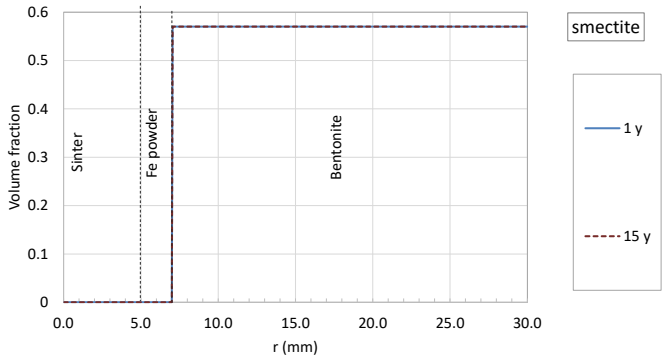

Figure B6 – Spatial distribution of the computed smectite at selected times in the FeMo corrosion tests for a particle size of 450 µm.

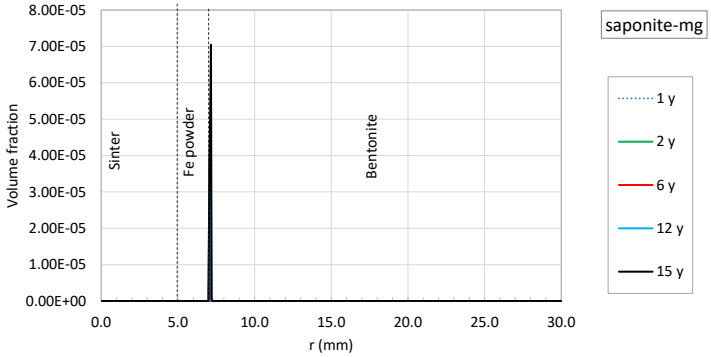

Figure B7 – Spatial distribution of the computed saponite-Mg at selected times in the FeMo corrosion tests for a particle size of 450 µm.

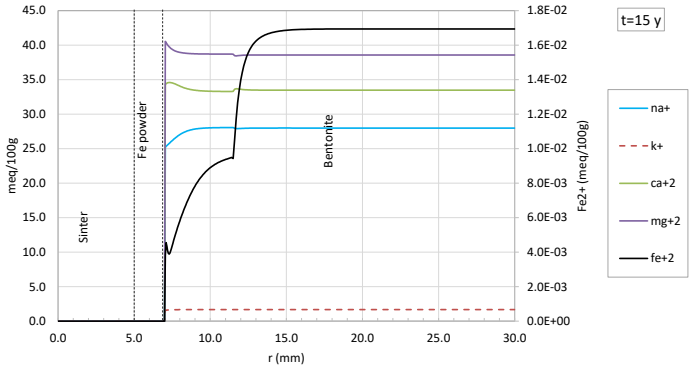

Figure B8 – Spatial distribution of the computed exchanged concentrations at 15 years in the FeMo corrosion tests for a particle size of 450 µm.

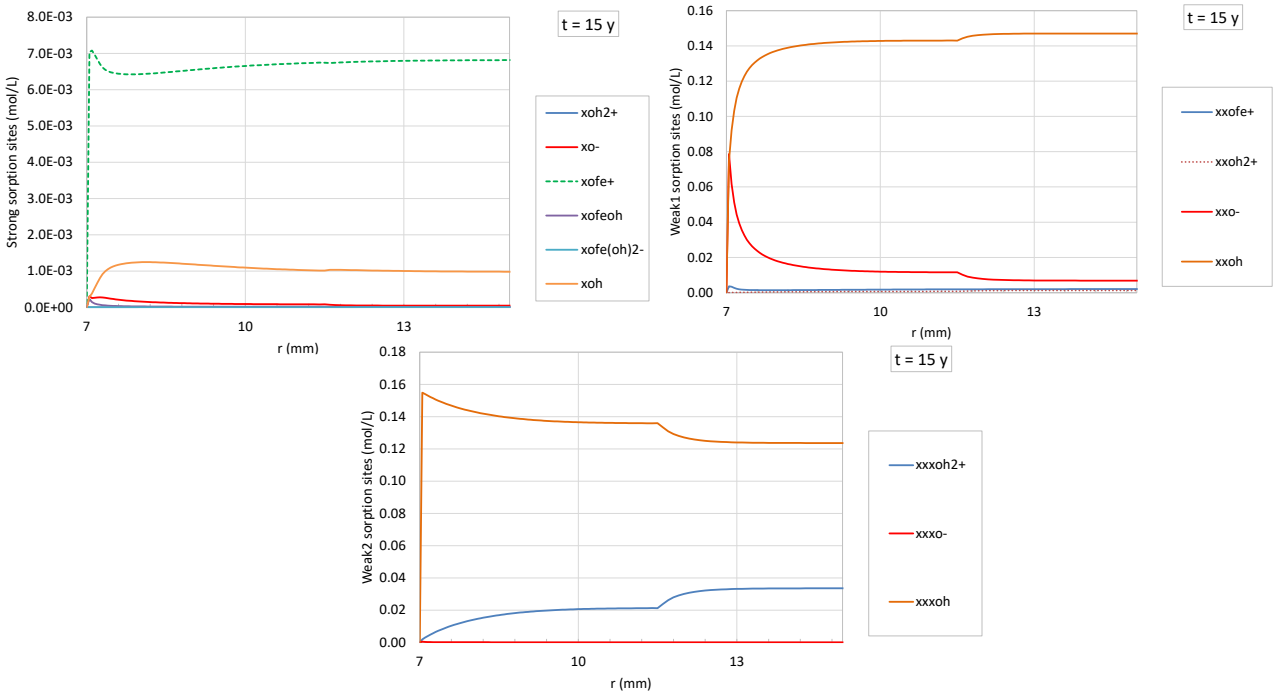

Figure B9 – Spatial distribution of the computed sorption concentrations at 15 years in the FeMo corrosion tests for a particle size of 450 µm.

Appendix C Corrosion model of the steel bentonite interactions in the FEBEX in situ experiment – UDC approach (UDC)

C.1. Tables

Table C1 – Reactions and equilibrium constants for aqueous species and mineral dissolution/precipitation at 25 °C taken from ThermoChimie v10.a (Giffaut et al., 2014); protolysis constants for surface complexation reactions for a triple-site sorption model (Bradbury and Baeyens, 2005); and selectivity constants for cation exchange reactions (ENRESA, 2006a).

Aqueous complexation	**Log K (25ºC)**
$CaCl^+ \Leftrightarrow Ca^{2+} + Cl^-$	0.290
$CaCl_2(aq) \Leftrightarrow Ca^{2+} + 2Cl^-$	0.640
$CaCO_3(aq) + H^+ \Leftrightarrow Ca^{2+} + HCO_3^-$	7.110
$CaHCO_3^+ \Leftrightarrow Ca^{2+} + HCO_3^-$	-1.100
$CaSO_4(aq) \Leftrightarrow Ca^{2+} + SO_4^{2-}$	-2.310
$Ca(H_3SiO_4)^+ + H^+ \Leftrightarrow Ca^{2+} + H_4SiO_4(aq)$	8.830
$CO_2(aq) + H_2O \Leftrightarrow H^+ + HCO_3^-$	-6.350
$CO_3^{2-} + H^+ \Leftrightarrow HCO_3^-$	10.330
$KSO_4^- \Leftrightarrow K^+ + SO_4^{2-}$	-0.880
$KCl(aq) \Leftrightarrow K^+ + Cl^-$	0.500
$K(OH)(aq) + H^+ \Leftrightarrow K^+ + H_2O$	14.460
$MgCl^+ \Leftrightarrow Mg^{2+} + Cl^-$	-0.350
$MgCO_3(aq) + H^+ \Leftrightarrow Mg^{2+} + HCO_3^-$	7.350
$MgHCO_3^+ \Leftrightarrow Mg^{2+} + HCO_3^-$	-1.040
$MgSO_4(aq) \Leftrightarrow Mg^{2+} + SO_4^{2-}$	-2.230
$Mg(H_3SiO_4)^+ H^+ \Leftrightarrow Mg^{2+} + H_4SiO_4(aq)$	8.580
$Na(CO_3)^- + H^+ \Leftrightarrow Na^+ + HCO_3^-$	9.060
$NaHCO_3(aq) \Leftrightarrow Na^+ + HCO_3^-$	0.250
$NaSO_4^- \Leftrightarrow Na^+ + SO_4^{2-}$	-0.940
$NaCl(aq) \Leftrightarrow Na^+ + Cl^-$	0.500
$OH^- + H^+ \Leftrightarrow H_2O$	14.000
$H_2(aq) + 0.5O_2 \Leftrightarrow H_2O$	46.070
$Fe^{3+} + 0.5H_2O \Leftrightarrow H^+ + 0.25O_2 + Fe^{2+}$	-8.485
$FeHCO_3^+ \Leftrightarrow Fe^{2+} + HCO_3^-$	-1.440
$FeCO_3(aq) + H^+ \Leftrightarrow Fe^{2+} + HCO_3^-$	4.640
$FeCl^+ \Leftrightarrow Fe^{2+} + Cl^-$	-0.140
$FeCl^{2+} + 0.5H_2O \Leftrightarrow Fe^{2+} + H^+ + Cl^- + 0.25O_2$	-9.885
$FeOH^+ + H^+ \Leftrightarrow Fe^{2+} + H_2O$	9.500
$Fe(OH)_3^- + 3H^+ \Leftrightarrow Fe^{2+} + 3H_2O$	31.900
$Fe(OH)_2(aq) + 2H^+ \Leftrightarrow Fe^{2+} + 2H_2O$	20.60
$Fe(OH)_2^+ \Leftrightarrow Fe^{2+} + 0.5H_2O + 0.25O_2$	-6.295
$Fe(SO_4)_2^- + 0.5H_2O \Leftrightarrow Fe^{2+} + H^+ + 0.25O_2 + 2SO_4^{2-}$	-13.885
$FeSO_4(aq) \Leftrightarrow Fe^{2+} + SO_4^{2-}$	-2.200
$FeHSO_4^{2+} + 0.5H_2O \Leftrightarrow Fe^{2+} + 2H^+ + 0.25O_2 + SO_4^{2-}$	-12.955
Minerals	**Log K (25ºC)**
$Calcite + H^+ \Leftrightarrow Ca^{2+} + HCO_3^-$	1.850
$Gypsum \Leftrightarrow Ca^{2+} + SO_4^{2-} + 2H_2O$	-4.610
$Quartz + 2H_2O \Leftrightarrow H_4SiO_4(aq)$	-3.740
$Goethite + 2H^+ \Leftrightarrow Fe^{2+} + 1.5H_2O + 0.25O_2(aq)$	-8.095
Ion exchange	**$K_{Na\text{-}cation}$**
$Na^+ + X\text{-}K \Leftrightarrow K^+ + X\text{-}Na$	0.138
$Na^+ + 0.5X_2\text{-}Ca \Leftrightarrow 0.5Ca^{2+} + X\text{-}Na$	0.294
$Na^+ + 0.5X_2\text{-}Mg \Leftrightarrow 0.5Mg^{2+} + X\text{-}Na$	0.288
$Na^+ + 0.5\ X_2\text{-}Fe \Leftrightarrow 0.5\ Fe^{2+} + X\text{-}Na$	0.5
Surface complexation	**Log K_{int}**
$\equiv S^SOH_2^+ \Leftrightarrow \equiv S^SOH + H^+$	-4.5
$\equiv S^SO^- + H^+ \Leftrightarrow S^SOH$	7.9
$\equiv S^{W1}\ OH_2^+ \Leftrightarrow \equiv S^{W1}OH + H^+$	-4.5
$\equiv S^{W1}\ O^- + H^+ \Leftrightarrow \equiv S^{W1}OH$	7.9
$\equiv S^{W2}\ OH_2^+ \Leftrightarrow \equiv S^{W2}OH + H^+$	-6.0

$\equiv S^{W2}\,O^- + H^+ \Leftrightarrow \equiv S^{W2}OH$	10.5
$\equiv S^{s}OFe^+ + H^+ \Leftrightarrow \equiv S^{s}OH + Fe^{2+}$	0.6
$\equiv S^{s}OFeOH + 2H^+ \Leftrightarrow \equiv S^{s}OH + Fe^{2+} + H_2O$	10.0
$\equiv S^{s}OFe(OH)_2^- + 3H^+ \Leftrightarrow \equiv S^{s}OH + Fe^{2+} + 2H_2O$	20.0
$\equiv S^{W1}OFe^+ + H^+ \Leftrightarrow \equiv S^{W1}OH + Fe^{2+}$	3.3

Table C2 – Initial pore water composition (Fernández et al., 2001; Samper et al., 2008a) and granitic water (Samper et al., 2008b).

	Bentonite	Granite
pH	7.72	8.35
O_2(aq) (mol/L)	$3.06\cdot10^{-14}$	$1.6\cdot10^{-75}$
Na^+ (mol/L)	$1.3\cdot10^{-2}$	$3.8\cdot10^{-4}$
K^+ (mol/L)	$1.7\cdot10^{-3}$	$7.8\cdot10^{-6}$
Ca^{2+} (mol/L)	$2.2\cdot10^{-2}$	$1.8\cdot10^{-4}$
Mg^{2+} (mol/L)	$2.3\cdot10^{-2}$	$1.3\cdot10^{-6}$
Fe^{2+} (mol/L)	$6.58\cdot10^{-5}$	$1.7\cdot10^{-8}$
HCO_3^- (mol/L)	$4.1\cdot10^{-4}$	$3.9\cdot10^{-4}$
SO_4^{2-} (mol/L)	$3.2\cdot10^{-2}$	$7.9\cdot10^{-5}$
Cl^- (mol/L)	$1.6\cdot10^{-1}$	$1.3\cdot10^{-5}$
H_4SiO_4(aq) (mol/L)	$1.1\cdot10^{-4}$	$1.4\cdot10^{-4}$

C.2. Figures

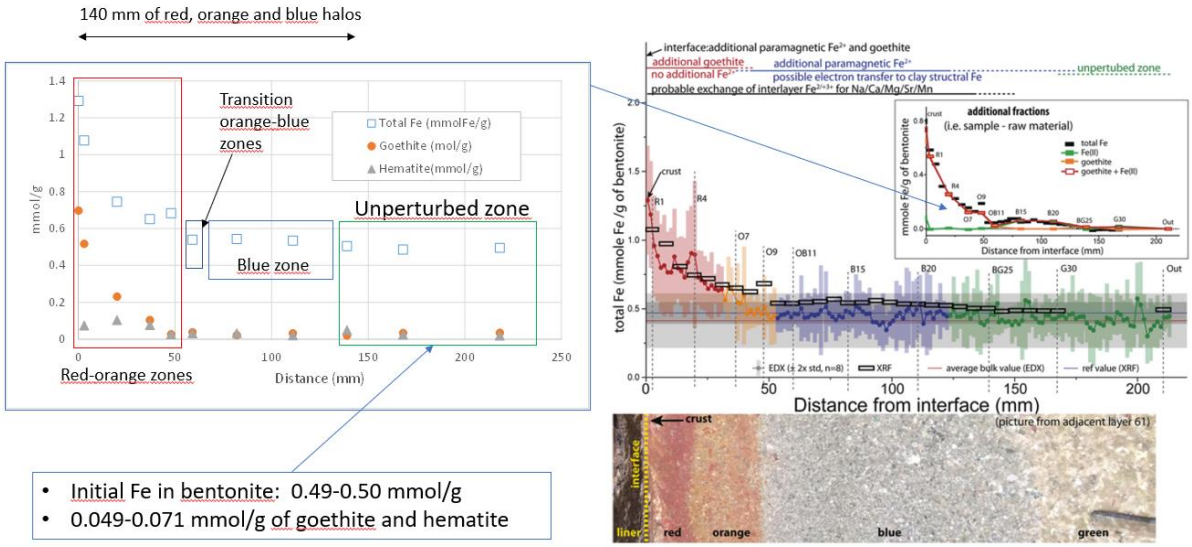

Figure C1 – Measured total Fe, goethite and hematite spatial distribution at the bentonite block BM-B-41-1 (Hadi et al., 2019).

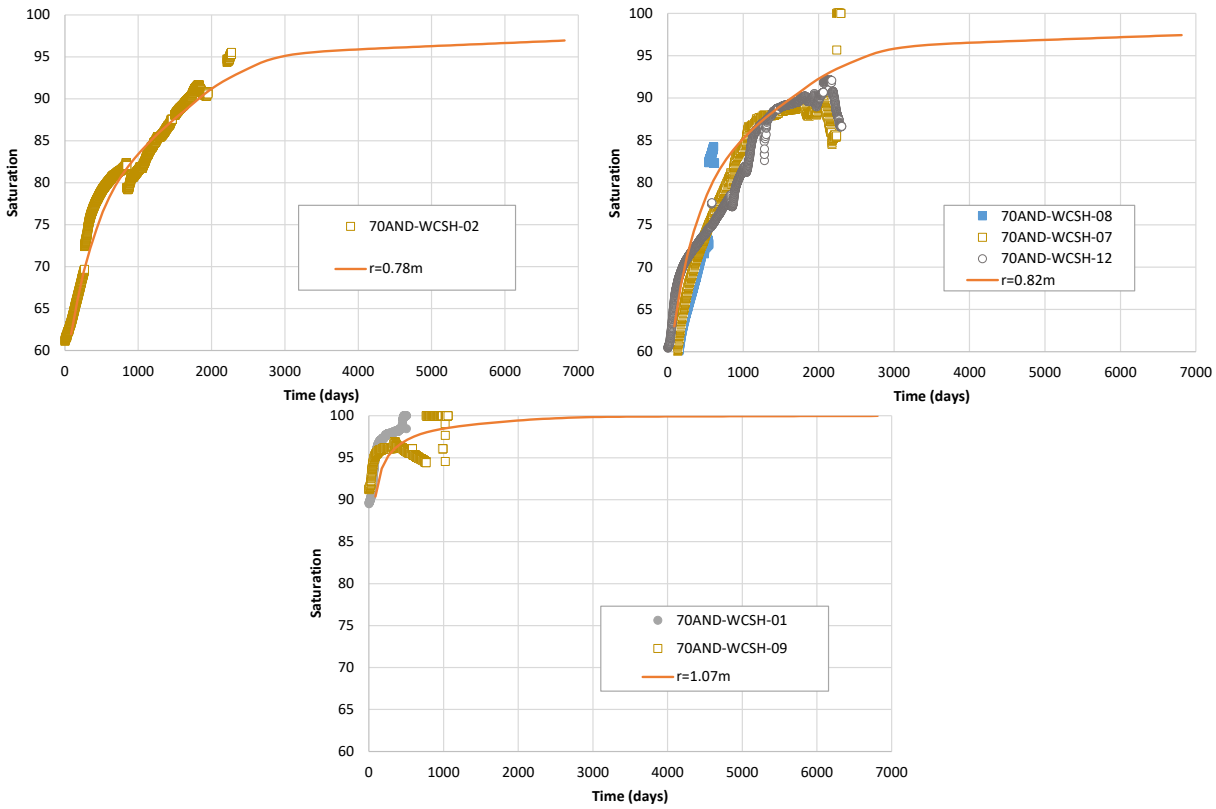

Figure C2 – Time evolution of the computed saturation degree at r = 0.78 m, r = 0.82 m and r = 1.07 m and measured data at section H.

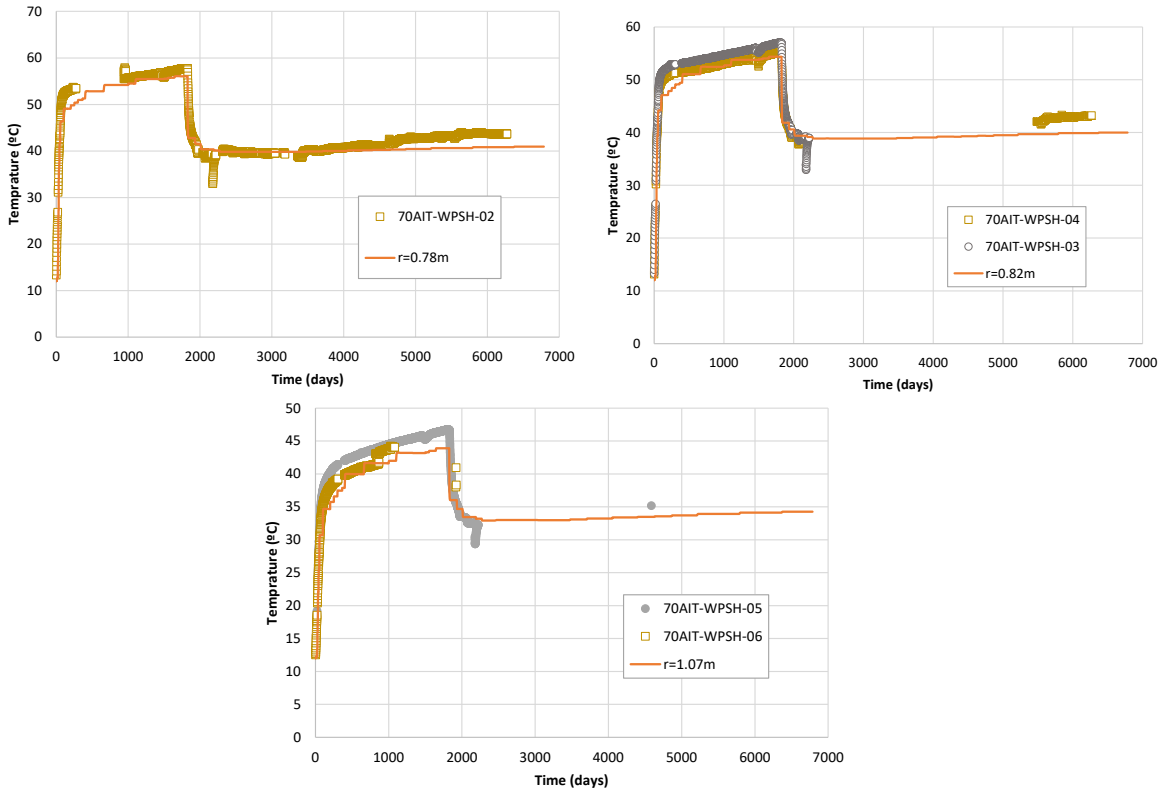

Figure C3 – Time evolution of the computed temperature at r = 0.78 m, r = 0.82 m and r = 1.07 m and measured data at section H.

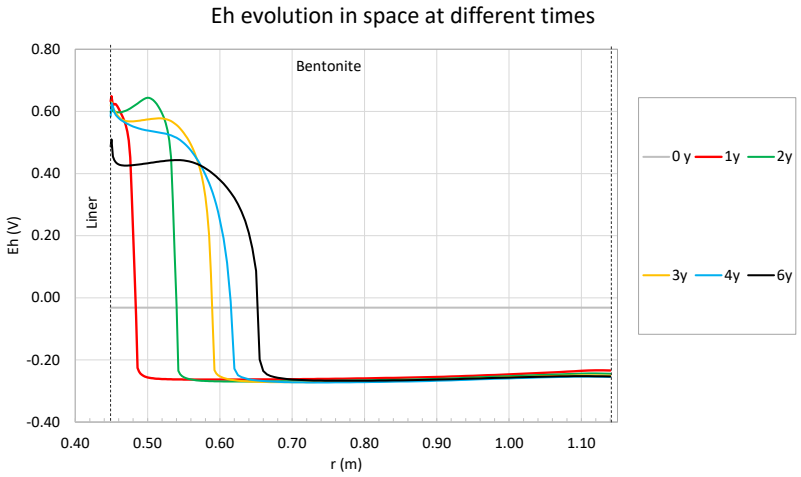

Figure C4 – Spatial evolution of the computed Eh at several times.

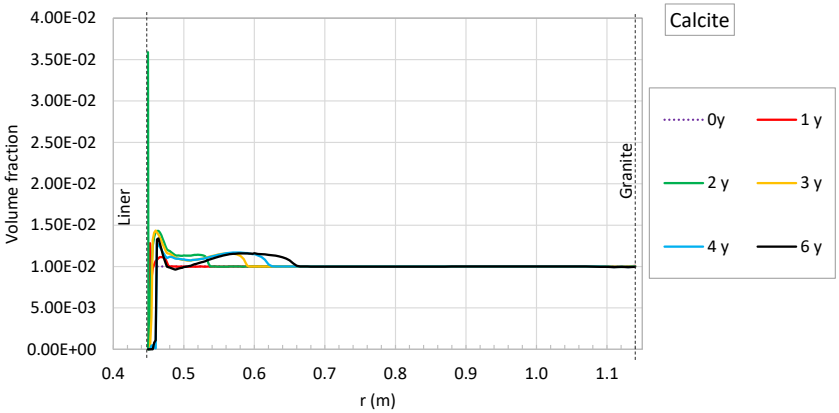

Figure C5 – Spatial evolution of the computed calcite volume fraction at several times.

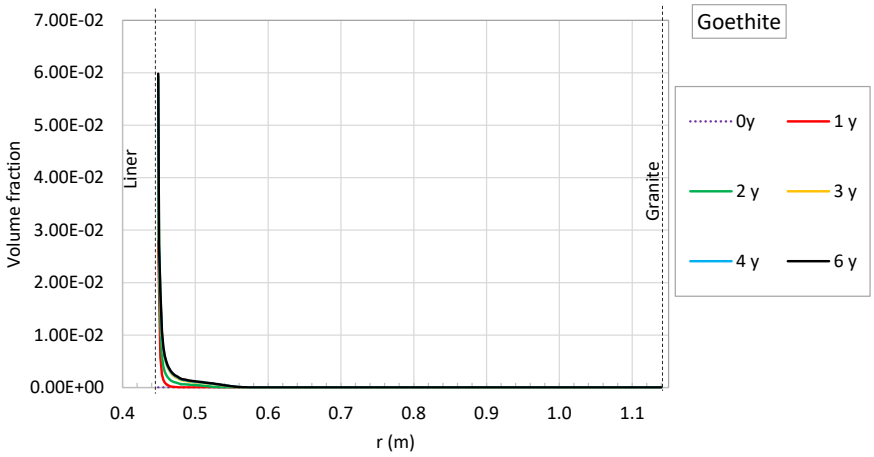

Figure C6 – Spatial evolution of the computed goethite volume fraction at several times.

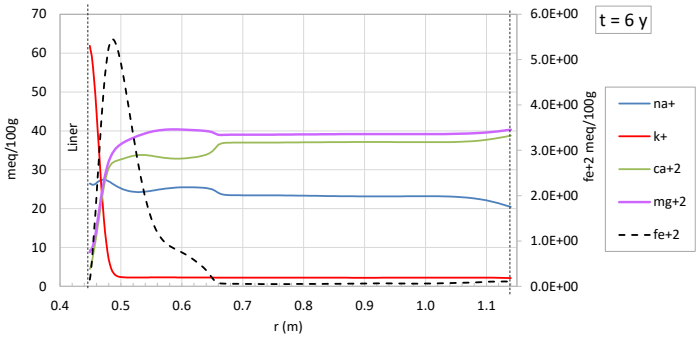

Figure C7 – Spatial evolution of the computed cation exchanger concentrations at 6 years.

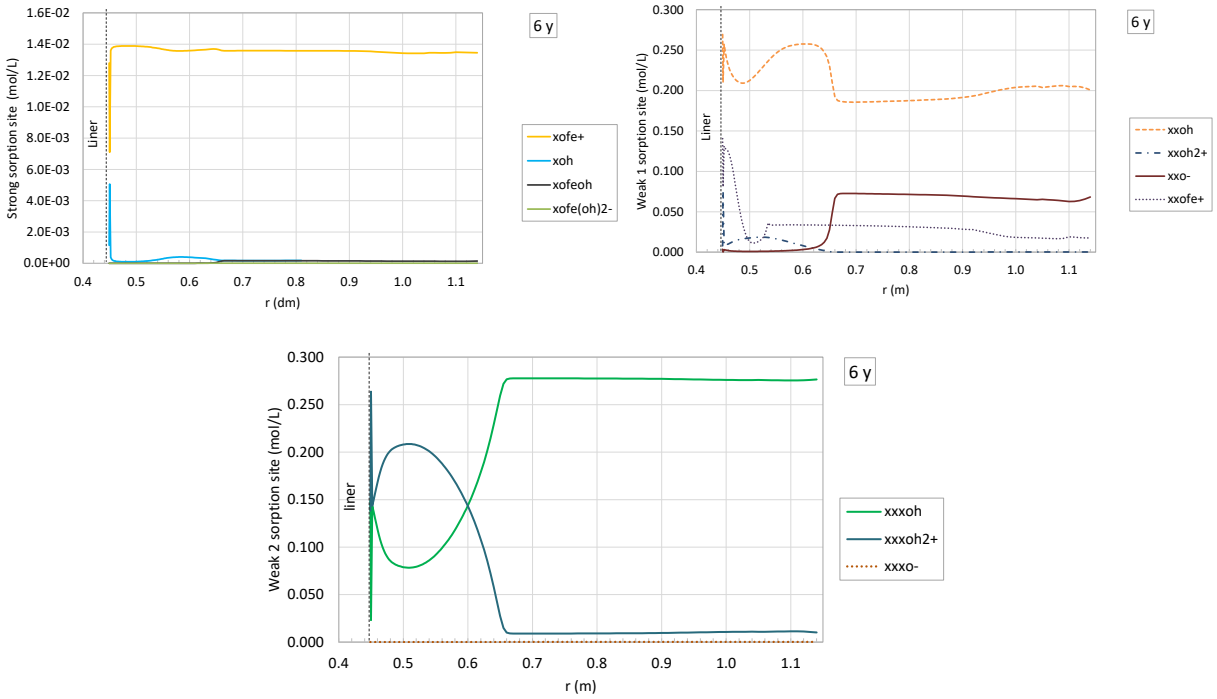

Figure C8 – Spatial evolution of the computed sorbed concentrations at 6 years.

Appendix D FEBEX in-situ model by UniBern – Sensitivity cases with respect to temperature

Case	Sensitivity cases with respect to:	Parameter	Values
4A	**Temperature** Assessment of the effect of different temperature gradient on the Fe –bentonite interaction in the transition stage The closer of the O_2 inflow is set to the same point in time as in the BC, by adjusting the generic O_2 source	T at liner (°C) – constant over entire calculation time	25
BC			40
4B			70
4C			97
4D		Additional inclusion of hematite for the high T-case	97 + hematite ppt

The FEBEX in-situ experiment was characterized by a complex temperature field induced by the two heating blocks, the non-heated zone in-between and the replacement of one heating block by a dummy after 5 years. Thus, as detailed in section 2.4.2 and Havlova et al. (2020), temperatures close to the heaters reached around 97°C, whereas the zone between the two heaters, which is the focus of the present work, experienced temperatures of around 70°C during FEBEX I and around 40°C after dismantling FEBEX II. For the sake of simplicity and better comparability of different calculation cases, the Base Case considers a constant temperature at the steel liner throughout the experiment. A temperature of 40°C was selected, as this corresponds to the temperature relevant for the evolution of the Fe-bentonite interaction zones. In the following the effect of elevated temperatures at the steel liner as representative for the FEBEX I phase (Sensitivity Case 4B: 70°C) and for the heater zone (4C: 97°C) is evaluated. Sensitivity Case 4C does not consider the precipitation of hematite, which was however included in Sensitivity Case 4D. This allowed to separately evaluating the effect of the transition from goethite to hematite precipitation. In addition, a low temperature Sensitivity Case (4A: 25°C) is included for comparison.

The effect of temperature on the interface evolution is manifold and presents a complex coupling of different processes, including e.g. chemical equilibria and mineral solubility products, but also physical processes such as transport and bentonite hydration. Their temperature dependencies are implemented in the reactive transport code or the thermodynamic database. Thus, the final evolution of the interface region under different temperature gradients as visualized in Figure D1 cannot be traced back to one specific process. In the following, some of the major effects are described. A full discussion of the complex coupling is however beyond the scope of the present report.

- One important effect of temperature in the early oxic phase is the decreasing solubility of O_2 with increasing temperatures. With the implementation of the aerobic corrosion kinetics (first order rate law with respect to the O_2(aq) concentration) in the present model, a reduced solubility of O_2 slows down the aerobic corrosion rate. For a better comparability of the different calculation cases, the duration of the O_2 inflow to the system was set equal to the Base Case, which however alters the total amount of aerobic corrosion products calculated.
- Due to a reduced viscosity of the water at higher temperature, a faster progression of the hydration front is calculated in the here applied cylindrical 1D radial axi-symmetric grid. It should however be noted that in the in-situ situation the 3 D geometry and temperature field induced a more complex hydration pattern, as water vapour could be transported laterally away from the central heated parts towards the colder outer/middle zones. The hydration fronts calculated for the transition to the anaerobic corrosion for the investigated temperatures are depicted in Figure D1a. Their range is comparable with the range discussed in detail in the sensitivity analyses for the bentonite hydration (Figure 99).
- With increasing temperature, the solubility of the major corrosion products decreases. This is reflected in the decreasing Fe concentrations at the steel boundary layer from 40°C (BC) to 70°C (4B) and 97°C (4C,D) (Figure D1b). The 25°C case (4A), however plots outside the trend, with an Fe equilibrium concentration below the Base Case. This can be explained by the

counteracting effect of increasing CO_3^{2-} solubility at lower temperatures. In calculation cases with 40°C and higher temperatures, the pore water in the corrosion boundary layer remains undersaturated with respect to the Fe(II)-hydroxide-carbonate mineral chukanovite. In the 25°C case however, 30-50% of the Fe corroded in the early anaerobic corrosion phase is predicted to precipitate as chukanovite, which therefore exerts an additional control on the Fe solubility in the corrosion layer. At higher temperatures, the lower solubility of hematite compared with goethite further decreases the Fe concentrations in the corrosion boundary layer itself.

- With the decreasing Fe concentrations in the corrosion boundary layer, the evolution of the Fe front in the bentonite changes considerably. The accumulation of Fe(III) precipitation products in the bentonite decreases, both in maximum amount and lateral extent. But not only the precipitation becomes restricted, also the Fe sorption, both, in concentration and in the extent of the sorption front. While this is on the one hand a direct function of the Fe equilibrium concentrations, this is also affected by the pH. At higher temperatures, the increase of pH induced by the corrosion reactions is more buffered by the precipitation of the anaerobic corrosion products. Thus, while in the Base Case final pH values of around 8.2 are calculated for the bentonite adjacent to the corrosion layer, this value drops to 7.8 at higher temperatures and increases to 8.8 in the 25°C case, due to the calculated precipitation of substantial amounts of Fe^{2+} as chukanovite instead of $Fe(OH)_2$.

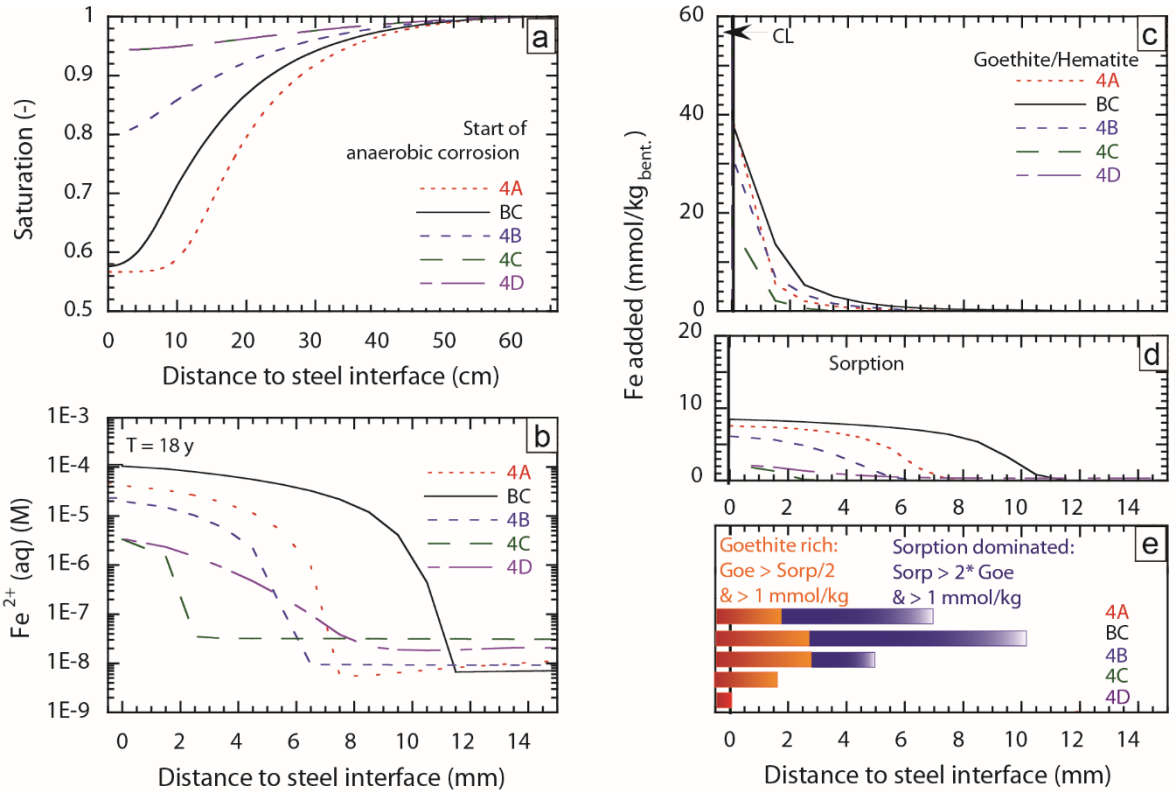

Figure D1 – Sensitivity Cases with respect to temperature. (a) hydration front at the transition to anaerobic corrosion (b) dissolved Fe concentration profiles (c) goethite and (d) sorption accumulation profile after 18 years, (e) visualization of the different zones of Fe accumulation based on a generic definition

The reduction of the Fe-bentonite interaction with increasing temperature clearly exceeds the effects observed for the sensitivity cases with respect to the hydration. Thus, despite several superimposed temperature dependent processes, the temperature sensitivity cases indicate that higher temperatures reduce the interaction of corrosion derived Fe with the bentonite, due to a retention of the Fe within the corrosion layer itself. This is in line with the experimental observations of limited interaction zones in the range of a few mm maximum with in the heated areas of the FEBEX in-situ experiment or the ABM experiments (Wersin et al., 2021). It also illustrates the plethora of coupled processes linked to changes in temperature, rendering the interpretation of non-isothermal models challenging but also stresses the importance of their consideration in reactive transport modelling.

Appendix E Details of experimental procedure and results

E.1. Clay purification

The SWy-3 montmorillonite was received as a finely ground powder. It was purified by extracting the clay rich fraction (< 2 µm), using an elutriation (Yamamoto, 2000) apparatus (Figure E1). To this end, 80 g of ground bentonite were suspended in 2 L of pure water. This slurry was then distributed between three parallel elutriation tubes with a cone shaped bottom. Using a peristaltic pump, a stream of pure water was introduced into each elutriation tube, from the bottom, generating an upstream flow toward the outlet located on the top side of the elutriation tube. The inlet flowrate of the peristaltic pump (2 $mL \cdot min^{-1}$) was set in sort that the upstream flowrate in each elutriation tube (with section of 100 cm^2) would carry along only particles smaller than 2 µm in diameter according to Stokes law (assuming spherical particles).

Figure E1– Purification of smectite by elutriation.

The outlet flow of each elutriation tube, carrying the clay particles, was driven into a 10 L bottle. Water feeding was carried on for 6 days (~8 L per day). Two 10 L collection bottles were used alternatively, by daily swapping them at the outlet of the elutriation tube. Once one collection bottle was full, a volume of concentrated 5 M NaCl solution was added, in order to reach a concentration of 0.5 M NaCl in the collection bottle, allowing rapid sedimentation of the clay particle to the bottom of the bottle in few hours, and reducing the volume of the purified clay suspension by 80% (by pumping the clear supernatant out). The volume of the suspension was further decreased by centrifugation in 600 ml pots (3096 g). The resulting gel was then collected in the same 2 L bottle. The clay gel was then re-suspended into a 2 M NaCl solution and stirred for a few days in order to fully saturate the clay exchanger with sodium. Following this, the clay was collected by centrifugation, and again suspended in 2 L of pure water as a first cleaning step. The clay was again separated by centrifugation and suspended in a small volume (1.4 L) of pure water. The resulting slurry was further cleaned by dialysis (MEMBRA-CEL® MD77, 14 kDa, Viskase Companies Inc., USA). The resulting gel was finally freeze dried, ground by hand in an agate mortar, and sieved (< 500 µm).

E.2. Acidic Fe dissolution

Isotopically purified ^{56}Fe was commercially available only as an elemental Fe powder. Acidic dissolution using HCl was, thus, necessary for producing the stock $^{56}Fe(II)Cl_2$ solution for the diffusion experiment.

Prior proceeding with the ^{56}Fe powder, series of pre-tests were performed with natural Fe powder (99.9%). The main goals were to optimize the experimental parameters (acid concentration, dissolution time, base addition) in order to maximise the recovery of solid Fe(0) as dissolved Fe(II), and minimise the possible oxidation to Fe(III), while minimising the use of acid, and thus the subsequent amount of base necessary for the final neutralization (and thus minimising the concentration of Na^+ and Cl^- in the final stock solution). Such pre-test were also necessary for exercising, since this operation had to be carried out in ambient conditions, contrary to previously reported methods in analogous studies (e.g. (Handler et al., 2014; Neumann et al., 2013; Neumann et al., 2015)).

All dissolution tests were using 1 g of Fe powder in 30 ml of concentrated acid solution (1 N to 6 N acid). Theoretically, a twofold excess of acid regarding Fe quantity should be necessary to produce $Fe(II)Cl_2$. Using an excess of acid can however accelerate Fe dissolution and minimise exposure time to ambient conditions. Moreover, a small portion of acid evaporates upon heating. In a first series of tests, acid:Fe ratios ranging from 1.7 to 10 were investigated. Sulfuric acid was used for comparison, since HCl is often reported as more oxidative.

Results obtained in this first series of experiments tended to confirm that an excess was necessary to achieve complete dissolution and that HCl is slightly more oxidative than H_2SO_4, based on coloration of the final solutions (Figure E2 left) and the corresponding Fe recovery (Figure E3 left). All the H_2SO_4 solutions displayed the same pale blue colour and high (97%) recoveries, with minimal acid excess likely below 3.4 fold. Instead, HCl solution showed more pronounced yellowish colour with a higher excess necessary for similar recoveries. Still, measured reduction levels (Figure E3 right) indicated that Fe was recovered as 99.6-100.2% Fe(II), hence with virtually no oxidation to Fe(III) in any case. HCl colour changes as a function of acid excess may rather be a result of changing Fe(II) complex colour as a function of Cl concentration.

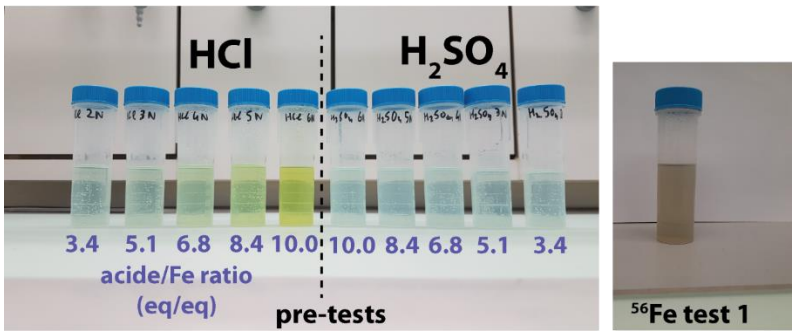

Figure E2 – Fe solutions following hot acidic dissolution by HCl or H_2SO_4.

Based on these first results, a second series of experiments using HCl excess between 3.4 and 5.6 was conducted in order to refine the acid excess necessary for maximal Fe recovery. In this second series, more attention was also paid to the dissolution time, which is a function of the acid concentration, and indicated by the H_2 bubbling produced by acidic Fe dissolution. The results of this second HCl series were actually very similar to those obtained with H_2SO_4, showing similar recovery levels and thus indicating that the minimal necessary acid excess is likely lower than 3.4 times Fe. In fact, the lower recovery obtained in the first series with the test at 3.4 time excess was likely not performed for a long enough time. No further attempt to refine the value of the ideal excess was conducted and 3.4 times was found to be satisfying as it did not involve to add too much NaOH in the subsequent neutralization step.

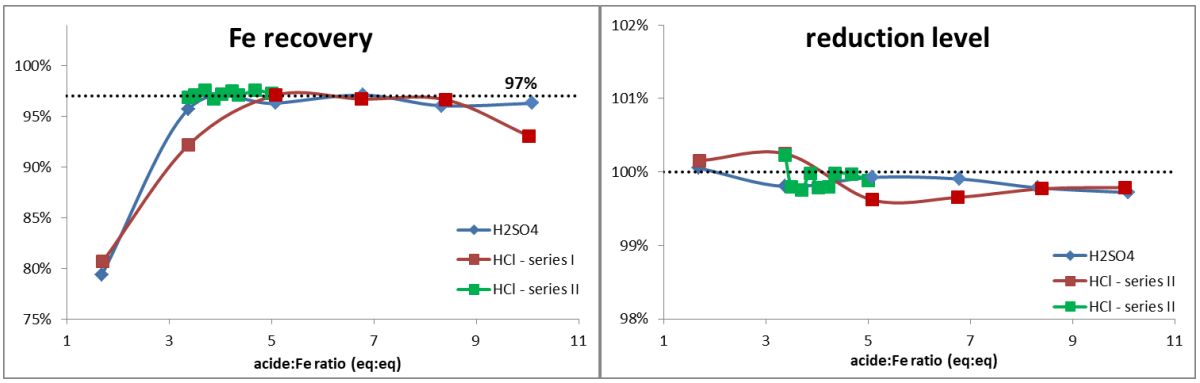

Figure E3 – (left) Fe recovery and (right) reduction level following hot acidic of natural Fe powder by HCl or H_2SO_4.

The NaOH neutralization step was also a critical step in the production of the $FeCl_2$ concentrate. The pH of the solution was raised by the means of addition of a concentrated (5 M, to minimise Fe dilution) NaOH solution, in order to neutralize the excess acid remaining after the dissolution step, and to remove the Fe(III) potentially present (by precipitation of (oxyhydr)oxide and filtration). The amount of base must not be to excessive to avoid the precipitation of $Fe(OH)_2$ and further Schikorr reaction, forming insoluble magnetite. In addition, although conducted in anaerobic conditions, the operation should be carried out rapidly to avoid loss of Fe(II) through oxidation by residual O_2 (base addition promotes heat, and increases oxidation). In this operation, the pH was rapidly raised from <1 to ~7. Eventual precipitation of hydroxides actually results in a lower pH, closer to 6. Final filtration of this solution resulted, ideally, in a pH between 3 and 3.7 for such concentrated Fe solutions.

In order to determine the correct amount of base (as a function of acid and/or Fe concentration, Figure E4), series of pre-test were performed with the digestate of natural Fe. Neutralization was deemed successful based on pH prior and after filtration, also based on visual observations of the solutions, and on the extent of final Fe(II) recovery. Ideal pH should be as close to 7 (but still lower) as possible prior to filtration, and in the 3-3.7 range after filtration. Prior to filtration, the solution should appear yellowish/orange (not green), and no white/green (hydroxides) or black (magnetite) precipitates should form. After filtration, colour can be slightly green but should be as pale as possible. In the most successful tests, recoveries ranged between 90 and 98%.

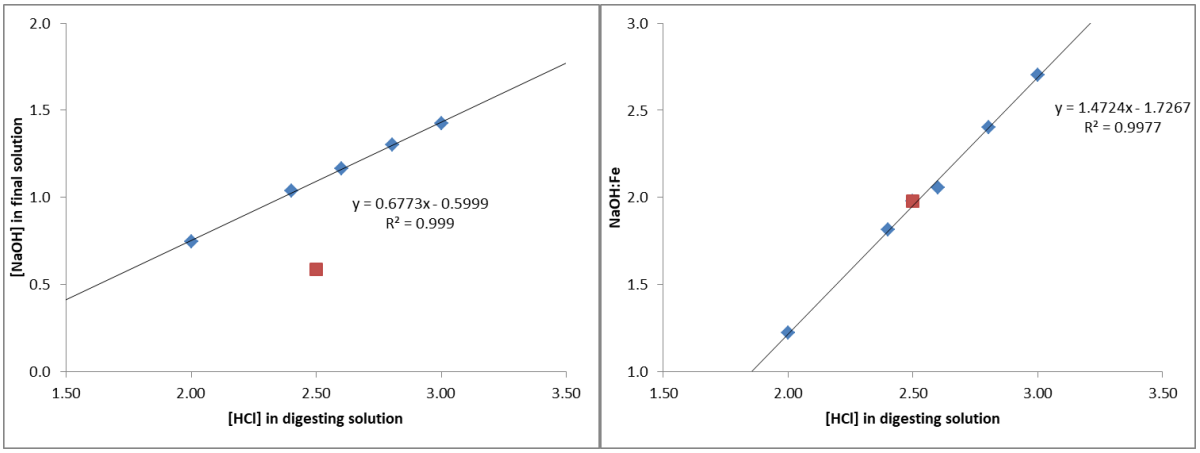

Figure E4 – Empirical relationship for determination of convenient neutralization conditions.

E.3. Suspensions colours

Thus, according to the pre-tests, using 30 ml of a 2N digesting solution for 1 g of Fe powder (i.e., 3.4 time excess acid regarding Fe) at 105°C for 40 minutes should have been sufficient, and following neutralization would have resulted in a final Na:Fe ratio of ~1.22, with a final Fe(II) concentration ~0.7-

0.8 M at a pH of ~3-3.7. Dissolution of the ^{56}Fe powder was however marred by an unanticipated issue and an operation error. After the 40 minutes of digestion, the solution remained grey and dark Fe particles were still visible, indicating that Fe dissolution was actually incomplete. To maximise Fe(II) recovery, it was decided at that point to increase the volume of acid (20 ml additional) and extend the digestion time (30 minutes additional time). The resulting solution remained grey (Figure E2 right), accounting for incomplete Fe dissolution. In the subsequent base neutralization step, only half of the ideal amount of base was employed, resulting in a final Fe solution more acidic than expected following final filtration (pH 1.5 instead of 3.4). However, final Fe(II) recovery was actually 95%, and it was decided to proceed to next steps. The issues encountered with incomplete Fe dissolution were attributed to the fact that the ^{56}Fe powder was coarser than the natural Fe powder employed in the pre-tests, either needing a higher acid excess or perhaps the use of ultrasound (as it was further figured out, dealing with the samples from diffusion experiment, section 3.3.3.3).

In the absence of clay (blank experiments), little precipitation of (oxyhydr)oxides could be observed. These precipitates were yellow below pH 7.27 (likely lepidocrocite and goethite) and were green above pH 7.27 (likely Cl-Green Rust, or Cl-GR). Addition of clay to the suspension resulted in important Fe uptake associated in most cases to notable colour changes of the slurry. The colour seemed to be primarily influenced by Fe_{sorb}:Fe_{str} ratio, and to some extent by the pH. When $Fe_{sorb} < Fe_{str}$, the colour gradually varied from beige at below pH 4.3 to brown at pH 6.9. The beige colour below pH 4.3 is the same colour as of Fe-free suspension of SWy-3. At this pH (and Fe loading), CE can be deemed to be the dominant Fe uptake process (cf. section 3.3.2.2). Thus, exchanged Fe(II) appears to display no notable colour (at least at low pH).

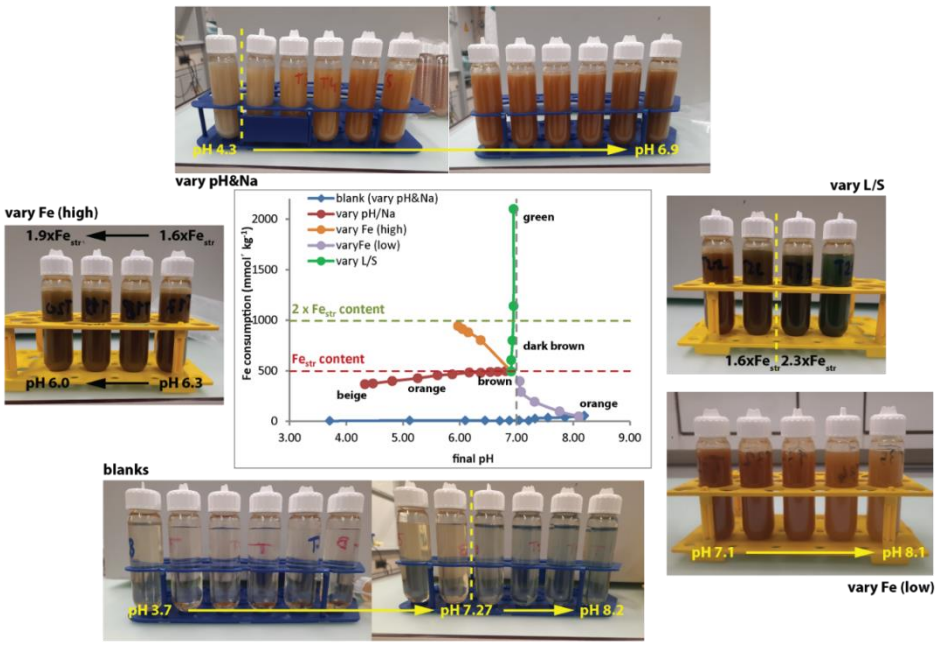

Figure E5 – Pictures of suspensions from various series of batch experiments.

Suspension's colour turned from beige to orange and then brown as pH increased toward 6.9, which can be interpreted as a sign of oxidation of Fe_{sorb} at the surface of the clay particles. In the vary Fe (low) experiments series, suspension's colour turned from brown back to orange with increasing pH but decreasing Fe_{sorb} content. This indicates that the suspension colour was primarily influenced by the quantities of Fe_{sorb} undergoing surface oxidation. When Fe_{sorb} was increased between 1 and 2 times Fe_{str} content, all suspensions exposed a similarly dark brown colour. When Fe_{sorb} was further increased above 2 times the Fe_{str} content, suspension's colour evolved from dark brown to blue and further to a green colour, similar to green rust colour. Such green colour could be interpreted as a mixed $Fe^{2+/3+}$ species sorbed at the surface of clay particles.

E.4. Mössbauer analysis of samples from batch experiments with ^{57}Fe

Mössbauer spectrometry revealed substantial reduction of Fe_{str} in most samples, accounting for the reduction by Fe_{sorb} at any pH (Table E1). In a first approach, resin embedded samples (*cf.* section 3.2.4.2) were analysed and the Fe_{str} reduction extent was notably higher than expected in many experiments. Indeed, at low Fe concentrations, Fe_{str} reduction extent corresponded to the amount of Fe_{sorb} (*i.e.* complete electron transfer). In most experiments with an initial Fe concentration of ≥10 mM, the observed reduction of structural Fe exceeded the quantity of sorbed Fe determined from the final Fe concentration in solution (e.g., in experiment $^{56}T2$ by almost a factor of two). This discrepancy reduces, if the amount of Fe^{2+} added to the embedded sample mass by the remaining solution in the solid sample after centrifugation is taken into account (Fe_{add}, Table E1). Upon drying of the sample, this previously dissolved Fe^{2+} came into contact with the montmorillonite surface, where it could act as an electron donor and reduce further structural Fe. Mössbauer analysis of "dry" samples gave very similar results for the samples obtained at low Fe concentration (exp. $^{56}T1$ and $^{56}T4$), but indicated notably lower reduction extents for experiments with higher Fe concentrations. Reduction extents were much more consistent with the amount of Fe_{sorb} (i.e. not exceeding it) and strongly influenced by solution pH (limited below pH 5 and extended above pH 5).

Table E1 – Final parameters of the products and results of Mössbauer spectrometry. Italicized values are abnormal results obtained when the additional Fe is not taken into account.

Exp.	Final pH	Final			Embedded samples			Dry samples	
		Fe_{sorb}	Fe_{add}[a]	Fe_{sorb}/Fe_{str}	Fe_{str} reduction[b]	Corresponding oxidation of Fe_{sorb}		Fe_{str} reduction[b]	Corresponding oxidation of Fe_{sorb}
		mmole·kg^{-1}	mmole·kg^{-1}	%Fe_{str}	%Fe_{str}	%Fe_{sorb}	%(Fe_{sorb} +Fe_{add})	%Fe_{str}	%Fe_{sorb}
$^{56}T1$	5.81	86	1	17%	20%	100%	99%	20%	100%
$^{56}T2$	2.49	83	149	16%	34%	*195%*	100%	5%	6%
$^{56}T3$	1.88	122	205	24%	38%	*150%*	79%	9%	22%
$^{56}T4$	7.61	93	0	18%	21%	100%	100%	21%	100%
$^{56}T5$	6.01	299	40	59%	52%	86%	81%	36%	57%
$^{56}T6$	2.87	134	283	26%	42%	*152%*	72%	10%	24%

a. Additional Fe(II) from the drying of reacted solution, determined from final Fe(II) concentration and mass loss upon freeze drying
b. Determined by Mössbauer spectrometry (4% in pristine clay)

During sample preparation, it was also observed that the samples obtained with high Fe concentrations, appearing as white dry powders, turned blue after being contacted with the resin (Figure E6). These contrasted Fe_{str} reduction between embedded and dry samples revealed that the epoxy resin employed for embedding the sample also acted as a solvent able to re-solubilise the $Fe(II)_{add}$ and allowed its sorption at the surface of the clay and subsequent reduction of Fe_{str}. The safety data sheet of the Araldite 2020 resin reports a pH of about 7 at a concentration of 500 g·L^{-1}. In house tests of the pure resin components (using pH paper strips) indicated a pH of 5, 9 and 8 for the resin, the hardener, and the cured resin, respectively. The resins thus appear to show both sufficiently high pH and strong enough buffering capacity to allow substantial electron transfer between Fe_{sorb} and Fe_{str}. These results outline the importance of avoiding contact between samples and epoxy resins, especially in the case of pH sensitive redox reactions. The rather basic pH of epoxy resin (>7.5) can indeed affect the extent of redox reaction achieved in acidic samples. This artefact was therefore avoided by covering the sample cup with a PMMA disc, before sealing with the epoxy resin.

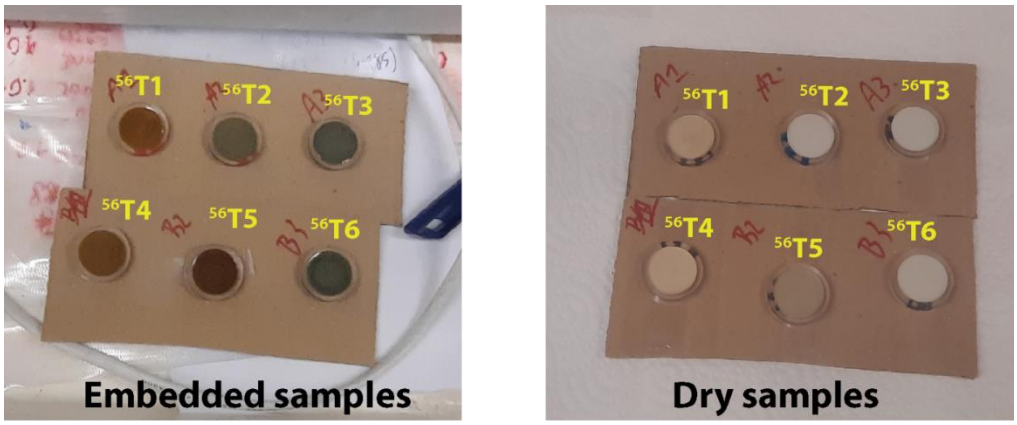

Figure E6 – Embedded and dry samples for Mössbauer spectrometry.

Appendix F Appendix G. Mössbauer spectra and hyperfine parameters

F.1. Uncertainties and nomenclature

The following nomenclature is used in description of the Mössbauer parameters:

- I.S. = Isomer shift value relative to that of the α-Fe at 300 K. (mm·s^{-1})
- F.W.H.M = Full width of line at half height. (mm·s^{-1})
- Q.S. or 2ε = Quadrupolar splitting or quadrupolar shift
- B_{hf} = Magnetic hyperfine field (T)
- Para-Fe(II/III) = paramagnetic Fe(II/III)

Uncertainties are 0.02 mm·s^{-1} for I.S., Q.S., 2ε, and F.W.H.M.; 0.5 T for Bhf, and 2% for the area.

F.2. Raw and purified SWy-3 montmorillonite

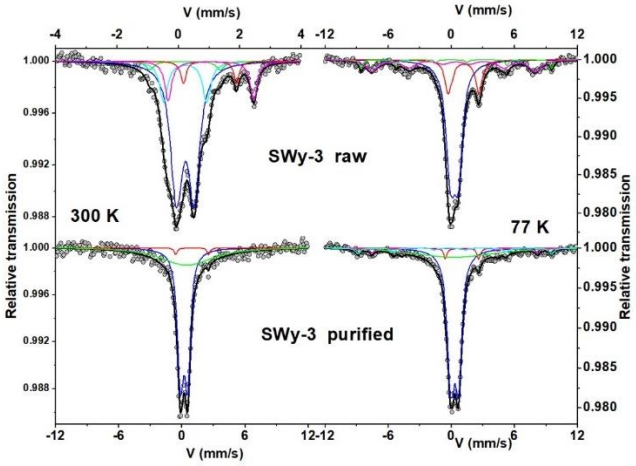

Figure F1 – Mössbauer spectra of raw and purified SWy-3 montmorillonite.

Table F1 – Refined values of Mössbauer parameters and doublet structural attributions for raw and purified SWy-3 montmorillonite. Spectra shown in Figure F1 terminology and nomenclature described in Appendix F.1.

300K – 12 mm·s^{-1}						77K – 12 mm·s-1					
Hyperfine parameters					Attribution	Hyperfine parameters					Attribution
I.S.	F.W. H.M.	Q.S. or 2ε	B_{hf}	Area (%)		I.S.	F.W. H.M.	Q.S. or 2ε	B_{hf}	Area (%)	
SWy-3 – raw											
0.35	0.44	0.55		65%	para-Fe(III)	0.44	0.95	0.67		60%	para-Fe(III)
0.35	0.32	1.36		15%	para-Fe(III)	1.32	0.72	2.82		16%	para-Fe(II)
0.31	0.22	2.29		3%	para-Fe(III)	0.41	0.32	0.46	56.0	4%	hematite
1.14	0.22	1.73		5%	para-Fe(II)	0.49	1.36	-0.26	47.9	20%	goethite
1.19	0.27	2.75		12%	para-Fe(II)						
SWy-3 – purified (sample 1)											
0.34	0.69	0.66		88%	para-Fe(III)						
1.14	0.40	2.82		4%	para-Fe(II)						
- 0.60	0.40	-0.02	25.4	8%	oxyhydr.						
SWy-3 – purified (sample 2)											

0.34	0.69	0.66		58%	para-Fe(III)	0.46	0.83	0.67		87%	para-Fe(III)
0.45	6.00	0.00		48%	para-Fe(III)	1.18	0.36	3.11		4%	para-Fe(II)
1.14	0.30	3.03		2%	para-Fe(II)	0.33	0.50	0.32	56.6	5%	Hematite
						0.33	0.50	0.33	48.2	4%	Goethite

F.3. Batch reacted SWy-3

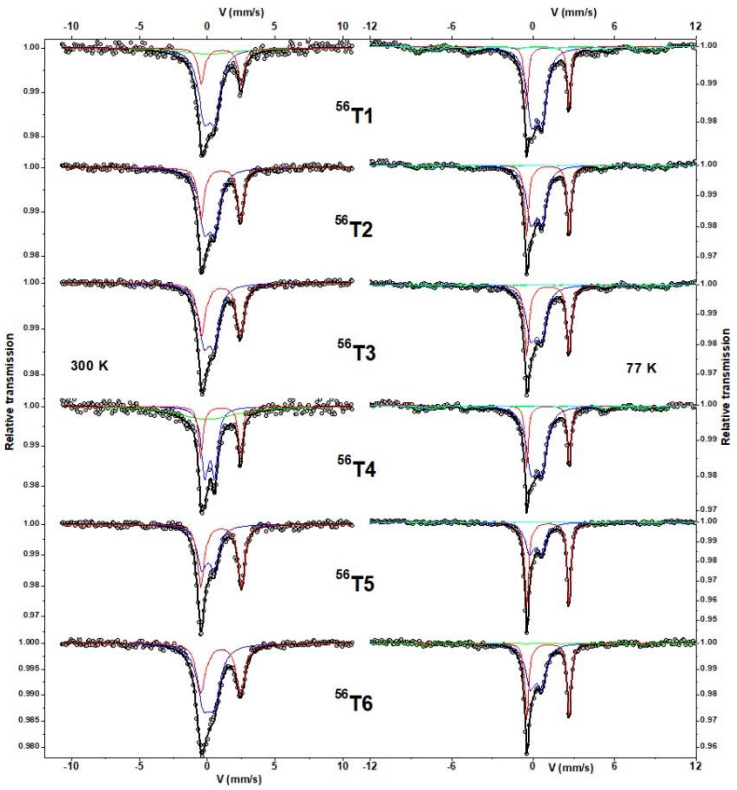

Figure F2 – Mössbauer spectra of SWy-3 montmorillonite reacted with ^{56}Fe in batch experiments. (Samples embedded in epoxy resin).

Table F2 – Refined values of Mössbauer parameters and doublet structural attributions for SWy-3 montmorillonite reacted with ^{56}Fe in batch experiments (samples embedded in epoxy resin). Spectra shown in Figure F-2, terminology and nomenclature described in section F-1.

300K – 12 mm · s^{-1}						**77K – 12 mm · s-1**					
Hyperfine parameters					**Attribution**	**Hyperfine parameters**					**Attribution**
I.S.	**F.W. H.M.**	**Q.S. or 2ε**	**B_{hf}**	**Area (%)**		**I.S.**	**F.W. H.M.**	**Q.S. or 2ε**	**B_{hf}**	**Area (%)**	
^{56}T1 – embedded											
0.30	0.95	0.73		63%	para-Fe(III)	0.42	0.79	0.70		56%	para-Fe(III)
0.30	5.00	0.00		14%	para-Fe(III)	1.24	0.37	3.05		24%	para-Fe(II)
1.18	0.60	2.86		23%	para-Fe(II)	0.46	0.64	-0.11	54.6	9%	hematite
						0.27	1.10	0.08	47.7	11%	goethite
^{56}T2 – embedded											
0.32	0.81	0.70		62%	para-Fe(III)	0.41	0.78	0.75		53%	para-Fe(III)
1.13	0.46	2.84		38%	para-Fe(II)	1.25	0.35	3.05		34%	para-Fe(II)
						0.48	0.60	0.41	56.3	6%	hematite
						0.51	0.60	0.22	49.4	7%	goethite
^{56}T3 – embedded											
0.33	0.69	0.71		59%	para-Fe(III)	0.39	0.84	0.73		51%	para-Fe(III)
1.14	0.32	2.87		41%	para-Fe(II)	1.26	0.41	3.05		38%	para-Fe(II)

					0.51	0.60	0.37	56.9	5%	hematite
					0.52	0.60	-0.23	48.8	5%	goethite
^{56}T4 – embedded										
0.32	0.56	0.66	38%	para-Fe(III)	0.42	0.83	0.71		56%	para-Fe(III)
0.18	5.39	0.00	41%	para-Fe(III)	1.26	0.37	3.05		25%	para-Fe(II)
1.14	0.37	2.86	21%	para-Fe(II)	0.47	0.64	0.28	55.6	8%	hematite
					0.54	1.10	-0.21	47.8	11%	goethite
^{56}T5 – embedded										
0.22	1.04	0.72	48%	para-Fe(III)	0.35	0.73	0.82		39%	para-Fe(III)
1.15	0.52	2.54	30%	para-Fe(II)	1.25	0.33	3.03		52%	para-Fe(II)
1.16	0.45	3.10	22%	para-Fe(II)	0.36	0.60	-0.12	55.8	4%	hematite
					0.66	0.60	-0.59	47.0	5%	goethite
^{56}T6 – embedded										
0.28	0.96	0.72	59%	para-Fe(III)	0.36	0.78	0.76		52%	para-Fe(III)
1.16	0.48	2.98	28%	para-Fe(II)	1.26	0.33	3.04		42%	para-Fe(II)
1.13	0.42	2.46	13%	para-Fe(II)	0.51	0.60	-0.15	48.0	6%	goethite

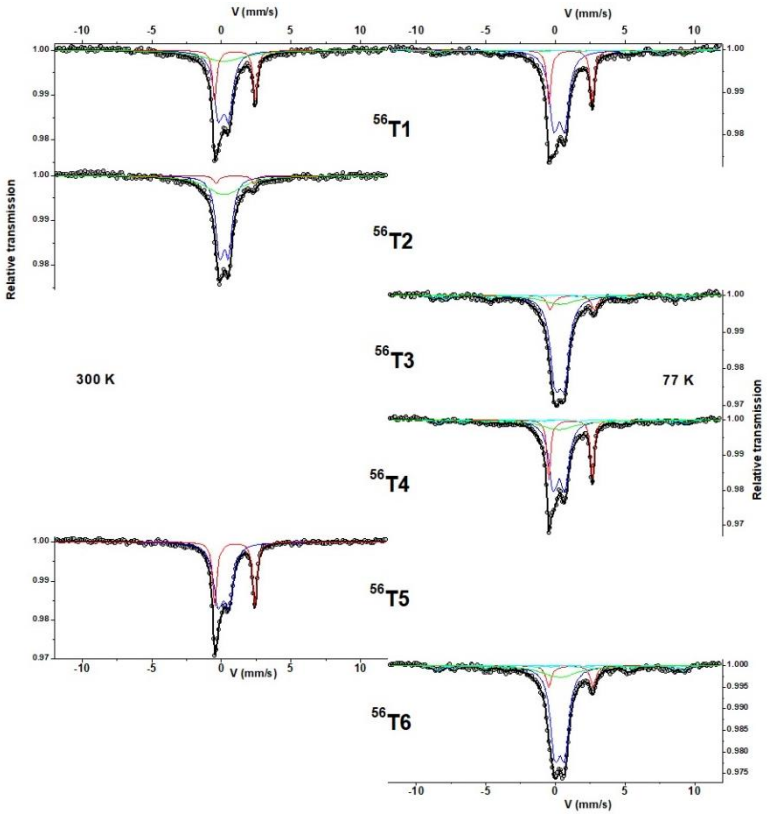

Figure F3 – Mössbauer spectra of SWy-3 montmorillonite reacted with ^{56}Fe in batch experiments (dry samples, protected from contact with epoxy resin).

Table F3 – Refined values of Mössbauer parameters and doublet structural attributions for SWy-3 montmorillonite reacted with ^{56}Fe in batch experiments (dry samples, protected from contact with epoxy resin). Spectra shown in Figure F-3, terminology and nomenclature described in section F-1.

300K – 12 mm · s^{-1}						77K – 12 mm · s-1					
Hyperfine parameters					Attribution	Hyperfine parameters					Attribution
I.S.	F.W. H.M.	Q.S. /2ε	B_{hf}	Area (%)		I.S.	F.W. H.M.	Q.S. /2ε	B_{hf}	Area (%)	
^{56}T1 – dry											
0.31	0.73	0.66		53%	para-Fe(III)	0.43	0.76	0.71		53%	para-Fe(III)
0.45	3.60	0.00		25%	para-Fe(III)	0.46	3.00	0.00		17%	para-Fe(III)
1.14	0.35	2.84		22%	para-Fe(II)	1.25	0.36	3.02		20%	para-Fe(II)
						0.45	0.60	-0.42	55.1	5%	hematite
						0.53	0.60	-0.15	46.3	5%	goethite
^{56}T2 – dry											
0.35	0.63	0.58		57%	para-Fe(III)	0.46	0.54	0.63		32%	para-Fe(III)
0.36	3.00	0.00		38%	para-Fe(III)	0.51	1.77	0.03		44%	para-Fe(III)
1.15	0.44	2.64		5%	para-Fe(II)	1.29	0.40	3.22		2%	para-Fe(II)
						0.49	1.19	0.25	54.9	13%	hematite
						0.52	0.88	-0.16	46.9	9%	goethite
^{56}T3 – dry											
0.35	0.58	0.64		67%	para-Fe(III)	0.48	0.80	0.60		65%	para-Fe(III)
0.42	1.41	0.00		29%	para-Fe(III)	0.46	3.00	0.00		16%	para-Fe(III)
1.10	0.28	2.96		4%	para-Fe(II)	1.39	0.54	3.09		9%	para-Fe(II)
						0.48	0.60	0.40	57.3	3%	hematite
						0.50	0.60	-0.23	51.7	7%	goethite
^{56}T4 – dry											
0.23	0.53	0.55		49%	para-Fe(III)	0.42	0.74	0.75		51%	para-Fe(III)
0.25	0.77	1.31		29%	para-Fe(III)	0.39	3.00	0.00		17%	para-Fe(III)
1.04	0.32	2.84		22%	para-Fe(II)	1.26	0.32	3.04		22%	para-Fe(II)
						0.53	0.60	0.34	55.0	5%	hematite
						0.82	0.60	0.45	46.0	5%	goethite
^{56}T5 – dry											
0.31	0.76	0.70		64%	para-Fe(III)						
1.14	0.37	2.79		36%	para-Fe(II)						
^{56}T6 – dry											
0.31	1.16	1.59		28%	para-Fe(III)	0.47	0.76	0.63		60%	para-Fe(III)
0.34	0.52	0.55		68%	para-Fe(III)	0.46	3.00	0.00		18%	para-Fe(III)
1.07	0.28	2.38		4%	para-Fe(II)	1.28	0.48	3.10		10%	para-Fe(II)
						0.41	0.60	0.28	54.4	7%	hematite
						0.99	0.60	-0.37	48.9	5%	goethite

F.4. Samples from diffusion experiment

F.4.1. Experiment #2

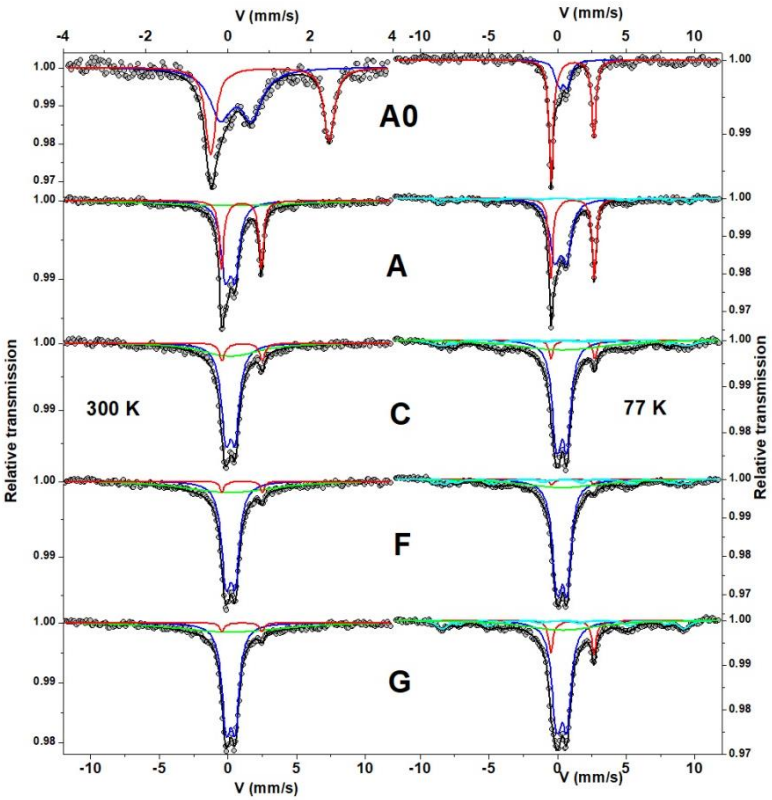

Figure F4 – Mössbauer spectra of samples from experiment #2 (part 1).

Table F4 – Refined values of Mössbauer parameters and doublet structural attributions for samples from experiment #2 (part 1). Spectra shown in Figure F-4, terminology and nomenclature described in section F-1.

300K – 12 mm · s^{-1}						77K – 12 mm · s-1					
Hyperfine parameters					Attribution	Hyperfine parameters					Attribution
I.S.	F.W. H.M.	Q.S. or 2ε	B_{hf}	Area (%)		I.S.	F.W. H.M.	Q.S. or 2ε	B_{hf}	Area (%)	
A0 –from direct contact input filter – x < 0.50 mm											
0.31	0.62	0.73		55%	para-Fe(III)	0.54	0.58	0.55		27%	para-Fe(III)
1.18	0.29	2.85		45%	para-Fe(II)	1.26	0.38	3.02		73%	para-Fe(II)
A (first slice) – x = 1.25 mm											
0.33	0.74	0.64		48%	para-Fe(III)	0.39	0.82	0.78		54%	para-Fe(III)
0.33	6.00	0.00		25%	para-Fe(III)	1.27	0.35	3.06		34%	para-Fe(II)
1.14	0.40	2.81		27%	para-Fe(II)	0.48	0.57	0.43	56.1	7%	Hematite
						0.50	0.70	-0.25	47.8	5%	Goethite
B – x = 3.03 mm											
C – x = 4.35 mm											
0.35	0.76	0.62		59%	para-Fe(III)	0.47	0.71	0.67		45%	para-Fe(III)

0.35	6.00	0.00		34%	para-Fe(III)	0.49	8.47	0.00		32%	para-Fe(III)
1.19	0.52	2.83		7%	para-Fe(II)	1.29	0.35	3.09		5%	para-Fe(II)
						0.50	0.60	0.41	55.0	15%	Hematite
						0.53	0.60	-0.20	48.2	3%	Goethite
D – x = 5.56 mm											
F – x = 7.55 mm											
0.35	0.73	0.61		54%	para-Fe(III)						
0.35	6.00	0.00		42%	para-Fe(III)						
1.20	0.34	2.88		4%	para-Fe(II)						
G – x = 8.57 mm											
0.36	0.70	0.61		41%	para-Fe(III)	0.46	0.75	0.67		49%	para-Fe(III)
0.36	6.00	0.00		54%	para-Fe(III)	0.51	6.60	0.00		25%	para-Fe(III)
1.17	0.34	2.87		5%	para-Fe(II)	1.26	0.37	3.05		9%	para-Fe(II)
						0.48	0.60	0.34	54.3	13%	Hematite
						0.52	0.60	-0.21	46.6	4%	Goethite
I – x = 10.76 mm											

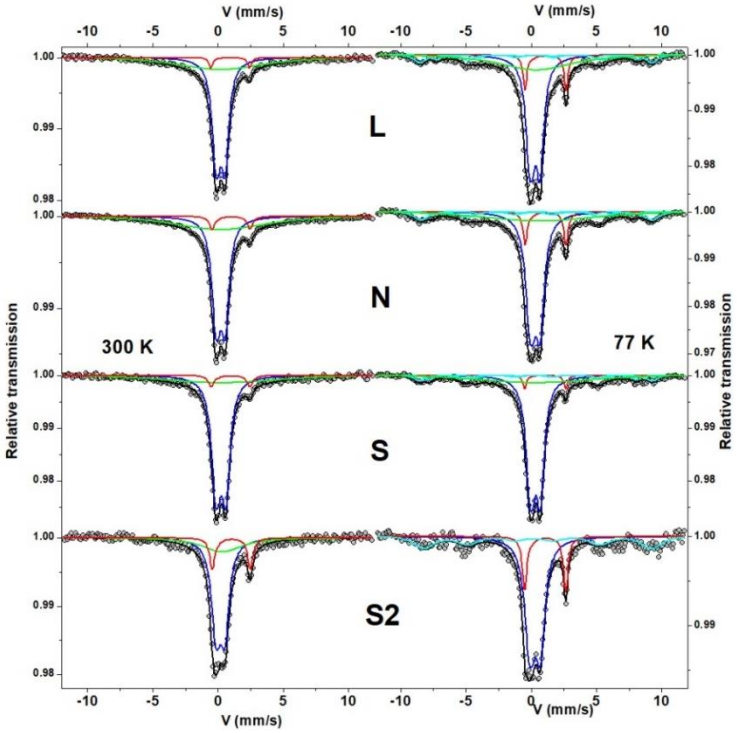

Figure F5 – Mössbauer spectra of samples from experiment #2 (part 2).

Table F5 – Refined values of Mössbauer parameters and doublet structural attributions for samples from experiment #2. Spectra shown in Figure F-5, terminology and nomenclature described in section F-1.

300K – 12 mm · s^{-1}						77K – 12 mm · s-1					
Hyperfine parameters					Attribution	Hyperfine parameters					Attribution
I.S.	F.W. H.M.	Q.S. or 2ε	B_{hf} or angle	Area (%)		I.S.	F.W. H.M.	Q.S. or 2ε	B_{hf} or angle	Area (%)	
K – x = 12.88 mm											
L – x = 14.06 mm											
0.36	0.70	0.61		55%	para-Fe(III)	0.44	0.71	0.67		46%	para-Fe(III)
0.36	6.60	0.00		42%	para-Fe(III)	0.51	6.60	0.00		33%	para-Fe(III)
1.09	0.34	2.87		3%	para-Fe(II)	1.26	0.35	3.05		8%	para-Fe(II)
						0.48	0.70	0.40	54.8	7%	Hematite
						0.50	0.70	-0.23	47.2	3%	Goethite
N – x = 16.48 mm											
0.36	0.77	0.62		52%	para-Fe(III)	0.45	0.72	0.66		53%	para-Fe(III)
0.35	7.00	0.00		44%	para-Fe(III)	0.51	6.60	0.00		27%	para-Fe(III)
1.15	0.51	2.83		4%	para-Fe(II)	1.26	0.39	3.03		8%	para-Fe(II)
						0.46	0.70	0.40	54.8	8%	Hematite
						0.50	0.70	-0.23	47.4	4%	Goethite
P – x = 18.79 mm											
0.35	0.67	0.61		93%	para-Fe(III)						
0.31	0.23	1.26		4%	para-Fe(III)						
1.04	0.24	1.90		3%	para-Fe(II)						
Q – x = 19.73 mm											
R – x = 20.81 mm											
S – x = 22.90 mm											
0.38	0.73	0.68		66%	para-Fe(III)	0.48	0.72	0.67		60%	para-Fe(III)
0.38	6.60	0.00		30%	para-Fe(III)	0.48	11.64	0.00		26%	para-Fe(III)
1.12	0.51	2.89		4%	para-Fe(II)	1.23	0.28	3.04		3%	para-Fe(II)
						0.47	0.70	0.35	55.2	6%	Hematite
						0.50	0.70	-0.21	48.9	5%	Goethite
S2 – x >24.30 mm											
0.30	0.80	0.62		59%	para-Fe(III)	0.44	0.87	0.73		68%	para-Fe(III)
0.39	7.00	0.00		29%	para-Fe(III)	1.23	0.39	3.05		17%	para-Fe(II)
1.18	0.45	2.82		12%	para-Fe(II)	0.46	0.70	0.35	54.7	11%	Hematite
						0.49	0.50	-0.25	50.4	4%	Goethite

F.4.2. Experiment #1

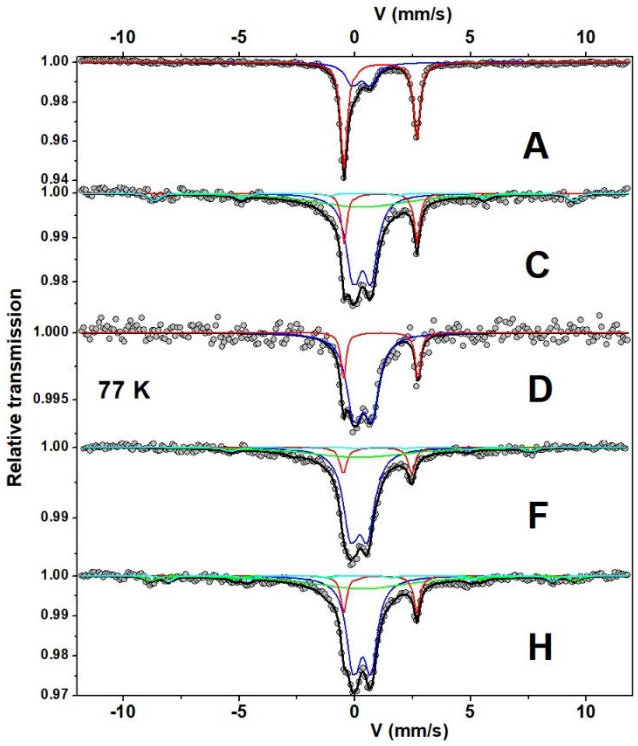

Figure F6 – 77 K Mössbauer spectra of samples from experiment #1.

Table F6 – Refined values of Mössbauer parameters and doublet structural attributions for samples from experiment #1. Spectra shown in Figure F-6, terminology and nomenclature described in section F-1.

300K – 12 mm · s^{-1}						77K – 12 mm · s-1					
Hyperfine parameters					Attribution	Hyperfine parameters					Attribution
I.S.	F.W. H.M.	Q.S. or 2ε	B_{hf}	Area (%)		I.S.	F.W. H.M.	Q.S. or 2ε	B_{hf}	Area (%)	
A (first slice) – x = 0.26 mm											
0.32	0.61	0.58		46%	para-Fe(III)	0.43	0.67	0.71		30%	para-Fe(III)
1.14	0.28	2.84		53%	para-Fe(II)	1.26	0.35	3.05		70%	para-Fe(II)
B – x = 1.03 mm											
C – x = 2.32 mm											
						0.47	0.87	0.70		72%	para-Fe(III)
						1.27	0.37	3.05		20%	para-Fe(II)
						0.48	0.50	0.38	55.7	8%	hematite
D – x = 3.83 mm											
						0.50	0.75	0.69		81%	para-Fe(III)
						1.27	0.26	3.12		19%	para-Fe(II)
F – x = 6.14 mm											
						0.34	0.76	0.65		57%	para-Fe(III)

	0.34	5.40	0.00		27%	para-Fe(III)
	1.13	0.37	2.85		10%	para-Fe(II)
	0.49	0.40	-0.25	45.9	3%	Hematite
	0.50	0.40	-0.25	64.2	3%	Goethite
H – x = 1.25 mm						
	0.46	0.71	0.70		41%	para-Fe(III)
	0.46	12.71	0.00		44%	para-Fe(III)
	1.25	0.32	3.06		8%	para-Fe(II)
	0.48	0.50	0.38	56.6	4%	Hematite
	0.50	0.40	-0.22	51.3	3%	Goethite

Appendix G Batch experiments data

G.1. Analytical results

Table G1 – Results of batch experiments with clay. Italicized values are calculated from mass of salts and or stock solutions used for solution preparation.

Exp.	L/S	$[Fe^{2+}]_{aq}$		Fe^{2+} uptake (sorption + precipitation)		pH		$[Na^{+}]_{aq}$	
		initial[a]	final[b]					initial[a]	final[b]
	(L·kg^{-1})	(mM)	(mM)	(%)	(mmol·kg^{-1})	initial[a]	final[b]	(mM)	(mM)
vary-pH&Na									
T1	52.2	10.0	3.0	69.9%	366.8	3.75	4.33	*0.0*	n.d.
T2	50.5	10.2	2.8	72.7%	374.1	5.11	4.47	*0.5*	n.d.
T3	50.7	10.0	2.1	78.8%	398.3	6.13	4.81	*2.5*	n.d.
T4	50.6	10.0	1.5	84.5%	426.4	6.50	5.26	*5.0*	n.d.
T5	51.1	10.0	1.1	88.9%	454.2	6.76	5.61	*7.5*	n.d.
T6	50.7	10.0	0.8	92.0%	464.4	6.94	5.87	*10.0*	n.d.
T7	51.4	10.1	0.7	93.0%	481.8	7.09	6.17	*12.5*	n.d.
T8	50.9	10.0	0.6	94.4%	479.2	7.27	6.37	*15.0*	n.d.
T9	51.0	10.0	0.5	95.2%	486.7	7.45	6.54	*17.5*	n.d.
T10	50.5	10.1	0.4	95.8%	489.9	7.67	6.67	*20.0*	n.d.
T11	51.4	10.0	0.4	96.3%	495.6	8.03	6.81	*22.5*	n.d.
T12	50.9	10.0	0.3	97.1%	492.9	8.39	6.91	*25.0*	n.d.
vary-Na									
T13	50.7	11.4	3.0	73.6%	423.5	8.24	6.55	249.7	n.d.
T14	49.2	15.8	3.1	80.5%	626.7	8.25	6.55	499.5	n.d.
T15	48.5	10.2	3.1	69.6%	343.7	8.25	6.49	999.7	n.d.
T16	47.0	10.2	3.0	70.6%	336.8	8.14	6.34	2000.3	n.d.
vary-Fe (high)									
T17	50.7	20.3	4.5	77.7%	801.4	8.10	6.37	25.0	n.d.
T18	50.4	30.0	12.6	58.1%	879.6	7.88	6.15	25.0	n.d.
T19	50.6	40.1	22.1	44.9%	912.0	7.75	6.05	25.0	n.d.
T20	50.9	50.1	31.6	37.0%	942.3	7.63	5.97	25.0	n.d.
vary-L/S									
T21	64.0	9.8	0.4	96.4%	605.6	8.27	6.91	25.0	n.d.
T22	85.9	9.8	0.5	94.7%	798.3	8.27	6.93	25.0	n.d.
T23	127.0	9.8	0.8	91.4%	1139.2	8.27	6.95	25.0	n.d.
T24	253.0	9.8	1.5	84.5%	2099.0	8.27	6.95	25.0	n.d.
vary-pH									
T25	51.2	*10.2*	4.1	60.0%	313.6	n.d.	4.32	*24.8*	38.4
T26	50.3	*10.1*	2.3	77.4%	392.2	n.d.	5.08	*24.9*	36.6
T27	51.2	*9.9*	1.3	86.7%	441.6	n.d.	5.87	*24.9*	34.9
T28	51.1	*9.8*	0.6	93.4%	468.4	n.d.	6.30	*24.9*	33.1
T29	51.1	*9.7*	0.5	95.3%	471.1	n.d.	6.67	*25.0*	33.0
vary-Fe (low)									
T30	52.6	*7.6*	0.1	98.8%	396.4	n.d.	7.06	25.0	23.0
T31	51.1	*5.7*	0.0	99.6%	291.8	n.d.	7.08	25.0	24.7
T32	51.0	*3.8*	0.0	99.5%	194.1	n.d.	7.32	25.0	24.8
T33	51.3	*1.9*	0.0	99.9%	97.8	n.d.	7.76	25.0	24.4
T35	50.9	*1.0*	0.0	100.0%	48.8	n.d.	8.10	25.0	25.2

a. in stock solution a few minutes after preparation

b. in supernatant after 48 hours

Table G2 – Results of batch experiments (blanks, without clay). Italicized values are calculated from mass of salts and or stock solutions used for solution preparation. Bracketed values are equivalent Fe uptake (per mass of clay) calculated with a S/L ratio of 51 L·kg^{-1}.

Exp.	L/S	$[Fe^{2+}]_{aq}$		Fe^{2+} uptake (sorption + precipitation)		pH		$[Na^{+}]_{aq}$	
		initial[a]	final[b]			initial[a]	final[b]	initial[a]	final[b]
	(L·kg^{-1})	(mM)	(mM)	(%)	(mmol·kg^{-1})			(mM)	(mM)
blank vary-Na&ph									
T1B	n.a.	10.0	10.0	0.6%	(3.3)	3.75	3.71	*0.0*	n.d.
T2B	n.a.	10.2	10.0	1.7%	(8.7)	5.11	5.12	*0.5*	n.d.
T3B	n.a.	10.0	9.8	1.5%	(7.7)	6.13	6.10	*2.5*	n.d.
T4B	n.a.	10.0	9.8	1.3%	(6.7)	6.50	6.45	*5.0*	n.d.
T5B	n.a.	10.0	9.9	1.0%	(4.9)	6.76	6.71	*7.5*	n.d.
T6B	n.a.	10.0	9.8	1.2%	(6.3)	6.94	6.88	*10.0*	n.d.
T7B	n.a.	10.1	9.9	2.0%	(10.1)	7.09	7.05	*12.5*	n.d.
T8B	n.a.	10.0	9.8	1.5%	(7.7)	7.27	7.22	*15.0*	n.d.
T9B	n.a.	10.0	9.5	5.4%	(27.4)	7.45	7.33	*17.5*	n.d.
T10B	n.a.	10.1	9.4	6.9%	(35.9)	7.67	7.56	*20.0*	n.d.
T11B	n.a.	10.0	9.2	7.8%	(39.7)	8.03	7.86	*22.5*	n.d.
T12B	n.a.	10.0	8.9	11.1%	(56.6)	8.39	8.20	*25.0*	n.d.
blank vary-ph									
T25B	n.a.	*10.2*	10.0	1.7%	(8.8)	n.d.	3.85	*24.8*	25.3
T26B	n.a.	*10.1*	9.9	1.3%	(6.7)	n.d.	6.45	*24.9*	25.1
T27B	n.a.	*9.9*	9.9	0.9%	(4.7)	n.d.	6.95	*24.9*	25.0
T28B	n.a.	*9.8*	9.6	2.5%	(12.7)	n.d.	7.20	*24.9*	25.1
T29B	n.a.	*9.7*	9.2	4.6%	(22.9)	n.d.	7.52	*25.0*	25.0
T30B	n.a.	*9.6*	8.6	10.0%	(48.5)	n.d.	7.94	*25.0*	25.5
blank vary-Fe (low)									
T31B	n.a.	*7.6*	7.0	8.5%	(32.9)	n.d.	8.02	*25.0*	25.8
T32B	n.a.	*5.7*	5.1	10.9%	(31.9)	n.d.	8.05	*25.0*	25.1
T33B	n.a.	*3.8*	3.2	17.6%	(34.4)	n.d.	8.09	*25.0*	24.9
T34B	n.a.	*1.9*	1.3	32.3%	(31.4)	n.d.	8.23	*25.0*	25.4
T35B	n.a.	*1.0*	0.5	43.1%	(21.1)	n.d.	8.48	*25.0*	25.0

a. in stock solution a few minutes after preparation

b. in supernatant after 48 hours

G.2. Example PhreeqC input file of sorption model for batch experiments

TITLE Equilibrium Sorption model for Batch experimental Series T25 to T30 using final solution composition

SURFACE_MASTER_SPECIES

Ss SsOH

Sw SwOH

Str StrOH #Site for Redox-sorption process, corresponding to structural Fe(III)

SURFACE_SPECIES

#Surface species on Strong and Weak 1 sites of Soltermann et al. 2014

SsOH = SsOH; log_k 0 # strong sites: high affinity, low capacity sites

SsOH + H+ = SsOH2+; log_k 4.5 #Bradbury & Baeyens 1997

SsOH = SsO- + H+; log_k -7.9 #

```
 SwOH = SwOH;                  log_k 0
 SwOH  + H+ = SwOH2+;          log_k 4.5
 SwOH = SwO- + H+;             log_k -7.9
 StrOH =  StrOH;               log_k 0      #site to represent Fe sequestration due to interaction with
structural Fe(III).

#Surface complexation reactions
 SsOH + Fe+2          = SsOFe++ + 1H+ +e- ;        log_k -1.4;  #Soltermann et al. 2014
 SsOH + Fe+2        = SsOFe+ + H+;                 log_k 1.9;   #Soltermann et al. 2014
 SwOH + Fe+2          = SwOFe++ + 1H+ +e-;         log_k -3.8;  #Soltermann et al. 2014
 SwOH + Fe+2          = SwOFe+ + H+;               log_k -1.7;   #Soltermann et al. 2014
#Addition of complex for Structural Fe reaction
StrOH + Fe+2          = StrOFe+ + H+;             log_k -3.1       #new included log K estimate

NAMED_EXPRESSIONS
# formation of O2 from H2O
 2H2O =  O2 + 4H+ + 4e-
    Log_K_O2
     log_k -85.980
     delta_H  559.526  kJ/mol
#
   -analytic 1.20446E+1 0E+0 -2.9226E+4 0E+0 0E+0

EXCHANGE_MASTER_SPECIES
     X     X-  # CEC
EXCHANGE_SPECIES #
   X- = X- ;        log_k 0.00
   X- + Na+ = NaX ; log_k 0.00
  2X- + Fe+2 = FeX2; log_k 0.8   #Soltermann et al. 2014

END

SOLUTION_SPREAD  1# Cells
units mmol/kgw
temp 25.0
```

Number	Description	pH	pe	Fe	Na	Cl
					charge	
1	T25	4.3	-4	4.09	38.36071574	20.00
2	T26	5.1	-4	2.27	36.64991586	20.00
3	T27	5.9	-4	1.33	34.89987881	20.00

```
4       T28     6.3     -4      0.65    33.05649989     20.00
5       T29     6.7     -4      0.46    33.04033914     20.00
6       T30     6.9     -4      0.26    30.2173643      20.00
END
SAVE solution 1-6
END
EXCHANGE 1
X 1.7E-02       #no. of CEC sites [eq/L_wat], 2.0E-02eq/kgw water
-equilibrate with SOLUTION 1

SURFACE 1
Ss      3.9E-05#strong site capacity in eq/L_wat, S/L: 1.7kg/L water
Sw      7.80E-04# Sw1 sites in eq/L_wat,
Str 9.95E-03#structural Fe in eq/L wat
-no_edl
-equilibrate with SOLUTION 1
END
```

Appendix H Diffusion experiments: reservoirs data

H.1. ^{56}Fe diffusion in experiment #1 and #2

H.1.1. Fe concentrations

Table H1 – Fe(II) concentration in bottom reservoirs (input) of experiments #1 and #2.

experiment #1		experiment #2	
time (day)	$[Fe^{2+}]$ mM	time (day)	$[Fe^{2+}]$ mM
-2.0	10.71 ±0.49	-2.0	10.54 ±0.05
-1.0	10.60 ±0.06	-1.0	10.40 ±0.12
0.0	10.51 ±0.01	-0.1	10.46 ±0.05
0.8	10.46 ±0.02	1.0	10.27 ±0.05
1.1	10.40 ±0.01	2.0	10.07 ±0.10
2.0	10.28 ±0.06	4.2	9.70 ±0.06
3.7	10.03 ±0.12	6.0	9.52 ±0.03
4.8	9.89 ±0.04	6.9	9.43 ±0.01
6.8	9.52 ±0.03	8.0	9.37 ±0.09
10.1	9.23 ±0.05	10.0	9.19 ±0.04
12.8	9.08 ±0.05	13.3	8.99 ±0.03
15.9	8.83 ±0.00	17.0	8.73 ±0.03
19.8	8.61 ±0.00	20.1	8.51 ±0.05
24.7	8.29 ±0.08	25.0	8.25 ±0.02
29.9	8.06 ±0.02	30.0	8.08 ±0.03
35.8	7.82 ±0.07	37.0	7.81 ±0.05
43.9	7.52 ±0.00	44.0	7.50 ±0.02
52.0	7.25 ±0.09	52.0	7.26 ±0.04
59.8	6.97 ±0.04	60.0	7.03 ±0.01
78.9	6.42 ±0.11	81.0	6.53 ±0.06
102.0	5.96 ±0.01	101.0	6.12 ±0.04
129.8	5.46 ±0.04	130.0	5.58 ±0.01
143.8	5.26 ±0.02	160.0	5.21 ±0.05
159.8	5.06 ±0.04	171.0	5.08 ±0.07
191.9	4.65 ±0.01	185.8	4.84 ±0.02
221.8	4.34 ±0.03		
251.8	4.14 ±0.03		
281.8	3.81 ±0.05		
297.9	3.69 ±0.07		
312.8	3.58 ±0.05		
344.9	3.41 ±0.04		
379.8	3.20 ±0.03		
391.7	3.16 ±0.01		

Table H2 – Fe(II) concentration in top reservoirs (output) of experiments #1 and #2.

experiment #1		experiment #2	
time (day)	$[Fe^{2+}]$ mM	time (day)	$[Fe^{2+}]$ mM
29.9	0.001	101.0	0.001
102.0	0.001	130.0	0.004 ±0.001
221.8	0.467 ±0.001	136.0	0.005 ±0.001
232.0	0.524 ±0.001	141.1	0.010 ±0.004
242.8	0.582 ±0.004	145.1	0.016 ±0.001
271.8	0.729 ±0.002	151.0	0.025 ±0.001
302.9	0.881 ±0.009	160.0	0.047 ±0.001
344.9	1.037 ±0.000	171.0	0.082 ±0.001
379.8	1.164 ±0.015	185.8	0.145 ±0.004
391.8	1.193 ±0.001		

H.1.2. Fe concentrations in out-diffusion experiment #1

Table H3 – Fe(II) concentration in bottom and top reservoirs of experiments #1 during Fe exfiltration sequence.

absolute time (day)	relative time (day)	bottom reservoir $[Fe^{2+}]$ mM	top reservoir $[Fe^{2+}]$ mM
reservoirs renewal #1			
406.8	0.0	0.004 ±0.002	0.004 ±0.002
411.8	5.0	0.274 ±0.006	0.148 ±0.003
416.7	10.0	0.392 ±0.004	0.219 ±0.001
423.9	17.1	0.512 ±0.001	0.302 ±0.001
430.8	24.1	0.594 ±0.001	0.356 ±0.002
445.8	39.0	0.717 ±0.004	0.462 ±0.005
467.8	61.0	0.819 ±0.001	0.555 ±0.000
476.8	70.0	0.838 ±0.008	0.582 ±0.004
reservoirs renewal #2			
476.9	70.2	0.003 ±0.001	0.003 ±0.001
483.8	77.0	0.130 ±0.001	0.115 ±0.002
490.8	84.0	0.209 ±0.000	0.185 ±0.000
500.8	94.0	0.285 ±0.001	0.245 ±0.003
523.8	117.1	0.391 ±0.001	0.327 ±0.016
545.7	139.0	0.444 ±0.002	0.392 ±0.014
567.8	161.0	0.475 ±0.004	0.416 ±0.005
573.7	166.9	0.479 ±0.001	0.424 ±0.002
reservoirs renewal #3			
573.8	167.1	0.004 ±0.008	0.004 ±0.008
587.8	181.1	0.120 ±0.003	0.114 ±0.003
616.9	210.1	0.217 ±0.013	0.191 ±0.006
626.6	219.8	0.249 ±0.009	0.204 ±0.004
406.8	0.0	0.004 ±0.002	0.004 ±0.002
411.8	5.0	0.120 ±0.006	0.114 ±0.003

416.7	10.0	0.217 ±0.004	0.191 ±0.001

H.1.3. Fe isotopic abundances

Table H4 – Isotopic abundances for $^{54/56/57}$Fe in reservoirs of the two diffusion experiments (determined by ICP-MS).

time (day)	^{54}Fe	^{56}Fe	^{57}Fe
Experiment #1 - input reservoir (volume = 1 L)			
0.0	0.084% ±0.000%	99.841% ±0.001%	0.076% ±0.001%
29.9	0.118% ±0.001%	99.794% ±0.001%	0.088% ±0.001%
59.8	0.121% ±0.001%	99.791% ±0.001%	0.088% ±0.000%
78.9	0.128% ±0.001%	99.780% ±0.001%	0.092% ±0.001%
102.0	0.140% ±0.001%	99.762% ±0.001%	0.098% ±0.001%
129.8	0.147% ±0.001%	99.752% ±0.001%	0.100% ±0.001%
143.8	0.154% ±0.001%	99.745% ±0.001%	0.101% ±0.001%
159.8	0.177% ±0.002%	99.714% ±0.002%	0.109% ±0.001%
191.9	0.177% ±0.001%	99.712% ±0.002%	0.110% ±0.001%
221.8	0.214% ±0.001%	99.660% ±0.002%	0.125% ±0.001%
312.8	0.267% ±0.004%	99.594% ±0.004%	0.138% ±0.001%
391.8	0.255% ±0.002%	99.604% ±0.003%	0.140% ±0.002%
Experiment #1 - output reservoir (volume = 0.2 L)			
242.8	0.908% ±0.009%	98.705% ±0.009%	0.369% ±0.002%
302.9	0.861% ±0.008%	98.774% ±0.012%	0.349% ±0.004%
391.8	0.712% ±0.006%	98.979% ±0.007%	0.299% ±0.002%
Experiment #2 - input reservoir (volume = 1 L)			
-0.1	0.086% ±0.001%	99.837% ±0.001%	0.078% ±0.001%
30.0	0.097% ±0.001%	99.822% ±0.001%	0.080% ±0.000%
60.0	0.113% ±0.001%	99.801% ±0.001%	0.086% ±0.001%
130.0	0.165% ±0.002%	99.733% ±0.004%	0.102% ±0.002%
185.8	0.191% ±0.003%	99.698% ±0.003%	0.111% ±0.001%

Table H5 – ICP-MS operating settings and data acquisition parameters for iron isotopic analyses in the solutions.

ICP-MS HR	Isotopic analyses of solutions
Operating settings	
RF power	1250 W
Auxiliary gas flow rate (Ar)	0.9 L.min^{-1}
Cool gas flow rate (Ar)	16.4 L.min^{-1}
Sample gas (Ar)	1.04 L.min^{-1}
Sampler and skimmer cones	Nickel
Introduction system	ESI SC-E2 fast/PC^{3} Peltier cooler MP^{2} Peristaltic pump/ GE micromist nebulizer (0.1 ml min^{-1})
Data acquisition parameters	

Isotopes	^{54}Fe, ^{56}Fe, ^{57}Fe, ^{53}Cr, ^{45}Sc
Mass resolution	MR (3000)
Mass window (%)	?
Dwell time/isotope	^{54}Fe, ^{56}Fe, ^{57}Fe (? ms)
Runs*Passes	?
Acquisition time	130 s
Detector mode	Analogous [Fe]=150 ppb/Pulse counting [Fe] = 25 ppb
Acquisition mode	E-Scan
[a]Detector dead time	4ns
Wash time	10 s with 2% (v/v) HNO_3

a. Only applied for pulse counting detector mode.

H.1.4. Tracers (D2O, Br), other solutes (Na, Cl) and pH

Table H6 – Tracer concentrations in reservoirs of experiments #1. Italicized values are calculated from the mass of chemicals employed for preparing the solutions.

time (day)	$[Na^+]$ mM	$[Cl^-]$ mM	$[Br^-]$ mM	$[D_2O]$ (‰ VSMOW)	pH
pre-equilibration – same reservoir (Fe-free, volume = 0.2 L)					
plan	*179.4*	*154.7*	*0*	*std*	*>7*
at day 0	175.5 ±1.07	152.4 ±2.3	b.d.	-80.2	7.23
input reservoir (volume = 1 L)					
plan	*159.6*	*142*	*10.0*	999.9	*7.23*
0.0	159.7 ±3.2	148.4 ±3.0	10.2 ±0.20	989.2 ±50.9	7.27
4.8	169.7 ±3.4	148.1 ±3.0	10.0 ±0.20	987.3 ±51.0	7.28
10.1	163.9 ±3.3	147.2 ±2.9	10.0 ±0.20	989.9 ±50.2	
19.8	163.7 ±3.3	148.0 ±3.0	10.3 ±0.21	989.2 ±51.5	7.27
29.9	165.4 ±3.3	151.0 ±3.0	10.1 ±0.20	985.6 ±50.3	
43.9	165.1 ±3.3	145.5 ±2.9	10.0 ±0.20	978.3 ±50.6	
59.8	164.8 ±3.3	147.1 ±2.9	10.3 ±0.21	972.7 ±51.1	7.25
78.9	168.7 ±3.4	153.7 ±3.1	9.9 ±0.20	970.6 ±95.6	7.24
102.0	165.8 ±3.3	154.2 ±3.1	9.9 ±0.20	963.1 ±97.7	7.25
129.8	168.5 ±3.4	153.8 ±3.1	10.0 ±0.20	958.4 ±96.1	
143.8	168.1 ±3.4	154.0 ±3.1	10.1 ±0.20	946.4 ±94.0	
159.8	168.6 ±3.4	152.8 ±3.1	10.0 ±0.20	943.4 ±96.8	
191.9	168.0 ±3.4	154.2 ±3.1	10.1 ±0.20	940.2 ±97.7	
221.8	168.5 ±3.4	146.8 ±2.9	9.7 ±0.19	938.6 ±96.1	7.25
251.8	170.2 ±3.4	145.6 ±2.9	9.3 ±0.19	942.4 ±49.9	
297.9	171.2 ±3.4	143.4 ±2.9	9.1 ±0.18	938.5 ±51.8	
344.9	172.1 ±3.4	143.4 ±2.9	9.5 ±0.19	921.0 ±52.1	
379.8	171.6 ±3.4	147.2 ±2.9	10.0 ±0.20	908.3 ±54.0	7.22
output reservoir (volume = 0.2 L)					
29.9	n.d.	n.d.	n.d.	n.d.	7.25
102.0	175.6 ±3.5	165.0 ±3.3	0.16 ±0.00	163.9 ±94.1	7.28
221.8	171.9 ±3.4	160.1 ±3.2	0.20 ±0.00	213.5 ±98.7	7.16

232.0	172.1 ±3.4	164.7 ±3.3	0.22 ±0.00	222.5 ±92.7	
242.8	171.8 ±3.4	166.4 ±3.3	0.23 ±0.00	237.1 ±97.4	
271.8	173.1 ±3.5	166.2 ±3.3	0.27 ±0.01	268.7 ±53.1	7.10
302.9	174.8 ±3.5	190.6 ±3.8	0.31 ±0.01	293.6 ±52.2	
344.9	174.1 ±3.5	184.1 ±3.7	0.36 ±0.01	329.4 ±49.5	6.97
379.8	173.8 ±3.5	181.3 ±3.6	0.37 ±0.01	376.2 ±51.6	6.97

n.d.: not determined

Table H7 – Tracer concentrations in reservoirs of experiments #2. Italicized values are calculated from the mass of chemicals employed for preparing the solutions.

time (day)	$[Na^+]$ mM	$[Cl^-]$ mM	$[Br^-]$ mM	$[D_2O]$ (‰ VSMOW)	pH
pre-equilibration – same reservoir (Fe-free, volume = 0.2 L)					
plan	*179.4*	*154.7*	*0*	*std*	*>7*
at day 0	180.9	151.0 ±3.0	b.d.	-80.2	7.13
output reservoir (volume = 1 L)					
plan	*159.6*	*142*	*10..00*	*999.9* ±96.0	*7.13*
-0.1	159.7 ±3.2	151.5 ±3.0	10.05 ±0.20	989.2 ±94.3	
6.9	160.1 ±3.2	151.0 ±3.0	9.91 ±0.20	980.6 ±94.4	
10.0	161.3 ±3.2	153.2 ±3.1	10.04 ±0.20	991.3 ±96.6	
20.1	160.7 ±3.2	151.8 ±3.0	10.03 ±0.20	983.6 ±98.7	
30.0	160.8 ±3.2	150.7 ±3.0	9.98 ±0.20	980.8 ±98.3	
44.0	162.4 ±3.2	150.2 ±3.0	9.91 ±0.20	956.6 ±96.9	
60.0	163.3 ±3.3	150.8 ±3.0	9.96 ±0.20	969.1 ±52.1	7.27
81.0	170.0 ±3.4	170.3 ±3.4	9.84 ±0.20	949.0 ±51.7	
101.0	169.7 ±3.4	152.8 ±3.1	10.54 ±0.21	965.4 ±52.5	7.28
130.0	173.5 ±3.5	150.3 ±3.0	10.08 ±0.20	942.0 ±52.7	
160.0	168.6 ±3.4	140.7 ±2.8	9.48 ±0.19	955.3 ±50.7	
171.0	170.8 ±3.4	145.1 ±2.9	9.61 ±0.19	953.6 ±50.0	
185.8	175.8 ±3.5	149.9 ±3.0	9.69 ±0.19	932.2 ±96.0	7.22
output reservoir (volume = 0.2 L)					
101.0	176.1 ±3.5	156.3 ±3.0	0.11 ±0.002	91.4 ±52.6	7.32
130.0	189.7 ±3.8	186.4 ±3.1	0.18 ±0.004	127.9 ±55.0	
160.0	179.5 ±3.6	119.3 ±3.7	0.21 ±0.004	140.9 ±53.0	7.28
171.0	194.6 ±3.9	190.0 ±2.4	0.22 ±0.004	169.1 ±54.8	7.25
185.8	178.7 ±3.6	180.3 ±3.8	0.26 ±0.005	174.3 ±49.9	7.19

Appendix I Diffusion experiments: clay core data

I.1. Water (gravimetric analysis) and Fe content (total digestion) in the two diffusion experiments.

Table I1 – Water content (gravimetric analysis) and Fe content (total digestion) in clay core of experiment #1 and pristine SWy-1 (control sample).

experiment #1			
distance (mm)[a]	H_2O (dry. wt.%)[b]	Total Fe	Fe(II)
		(mmole·kg^{-1})[c]	
0.27	54.36%	0.896 ±0.015	0.389 ±0.010
1.03	42.94%	0.612 ±0.001	0.146 ±0.007
2.32	45.12%	0.546 ±0.008	0.086 ±0.005
3.83	43.22%	0.515 ±0.037	0.074 ±0.000
5.13	46.10%	0.535 ±0.004	0.071 ±0.004
6.14	44.01%	0.538 ±0.017	0.072 ±0.003
7.10	44.45%	0.529 ±0.006	0.068 ±0.000
8.11	44.80%	0.557 ±0.018	0.075 ±0.003
9.14	43.69%	0.523 ±0.038	0.067 ±0.004
10.25	44.75%	0.534 ±0.006	0.071 ±0.001
11.38	45.04%	0.535 ±0.011	0.067 ±0.001
12.38	44.80%	0.536 ±0.003	0.066 ±0.003
13.54	43.59%	0.536 ±0.034	0.067 ±0.003
14.82	44.52%	0.533 ±0.007	0.068 ±0.000
16.22	44.20%	0.524 ±0.017	0.069 ±0.003
18.03	43.40%	0.548 ±0.020	0.081 ±0.025
19.78	49.62%	0.636 ±0.042	0.180 ±0.040
pristine	10.91%	0.498 ±0.016	0.020 ±0.0004

a. Distance at the middle of the analysed slice.
b. Content in the wet sample.
c. Content in the dry sample.

Table I2 – Water content (gravimetric analysis) and Fe content (total digestion) in clay core of experiment #2 and pristine SWy-1 (control sample).

experiment #2			
distance (mm)[a]	H_2O (wt.%)[b]	Total Fe	Fe(II)
		(mmole·kg^{-1})[c]	
1.26	53.08%	0.787 ±0.067	0.313 ±0.074
3.03	53.39%	0.640 ±0.007	0.163 ±0.006
4.35	54.12%	0.609 ±0.002	0.152 ±0.001
5.56	56.43%	0.619 ±0.025	0.146 ±0.006
6.48	59.14%	0.617 ±0.018	0.134 ±0.002
7.55	59.24%	0.601 ±0.010	0.130 ±0.011
8.57	57.19%	0.590 ±0.013	0.125 ±0.006
9.64	58.32%	0.581 ±0.006	0.116 ±0.005
10.76	59.02%	0.582 ±0.010	0.107 ±0.006
11.78	61.03%	0.580 ±0.019	0.105 ±0.013
12.88	58.72%	0.561 ±0.021	0.096 ±0.014

14.06	61.46%	0.563 ±0.017	0.092 ±0.006
15.17	62.61%	0.566 ±0.013	0.089 ±0.003
16.48	59.54%	0.539 ±0.002	0.076 ±0.006
17.78	61.34%	0.547 ±0.004	0.077 ±0.003
18.79	63.26%	0.549 ±0.012	0.070 ±0.011
19.73	63.44%	0.552 ±0.012	0.071 ±0.005
20.81	61.52%	0.535 ±0.022	0.065 ±0.009
22.90	60.02%	0.530 ±0.011	0.067 ±0.009
pristine	10.71%	0.497 ±0.007	0.020 ±0.004

a. Distance at the middle of the analysed slice.
b. Content in the wet sample.
c. Content in the dry sample.

I.2. Elemental analysis and Fe isotopic analysis (LA-ICP-MS)

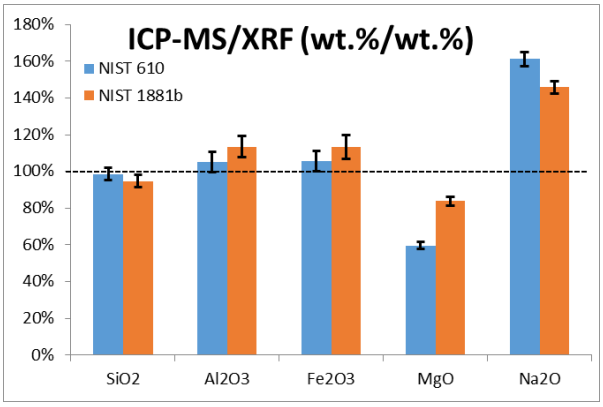

Figure I1 – Comparison between LA-ICP-MS (2 different calibrations) and XRF for the five main elements analysed in the pristine SWy-3 (renormalized to 100%).

Table I3 – Isotopic profiles for $^{54/56/57}Fe$ in clay core of experiment #2 (determined by LA-ICP-MS).

Experiment #2			
distance	**$^{54}Fe_2O_3$**	**$^{56}Fe_2O_3$**	**$^{57}Fe_2O_3$**
(mm)	**%oxides**		
0.27	0.240 ±0.041	7.081 ±1.067	0.092 ±0.022
1.03	0.210 ±0.049	4.654 ±1.030	0.078 ±0.022
2.32	0.228 ±0.055	5.041 ±1.186	0.085 ±0.024
3.83	0.242 ±0.039	5.223 ±0.771	0.090 ±0.021
5.13	0.246 ±0.040	5.196 ±0.750	0.100 ±0.023
6.14	0.249 ±0.040	5.191 ±0.739	0.094 ±0.021
7.10	0.238 ±0.037	4.779 ±0.675	0.089 ±0.020
8.11	0.254 ±0.040	5.072 ±0.729	0.095 ±0.021
9.14	0.245 ±0.038	4.788 ±0.672	0.096 ±0.021
10.25	0.221 ±0.035	4.274 ±0.621	0.086 ±0.019
11.38	0.235 ±0.035	4.188 ±0.585	0.091 ±0.020
12.38	0.220 ±0.031	4.757 ±0.632	0.084 ±0.018
13.54	0.209 ±0.032	3.943 ±0.580	0.082 ±0.018
14.82	0.222 ±0.032	4.186 ±0.560	0.086 ±0.018
16.22	0.230 ±0.032	4.183 ±0.520	0.086 ±0.018
18.03	0.227 ±0.031	4.142 ±0.545	0.085 ±0.018

19.78	0.236 ±0.033	4.273 ±0.550	0.090 ±0.019
pristine	0.246 ±0.034	4.423 ±0.569	0.095 ±0.020
pristine	0.235 ±0.031	4.244 ±0.525	0.091 ±0.019

Table I4 – Elemental profiles in experiment #2 (LA-ICP-MS)

Experiment #2

distance (mm)	SiO_2	Al_2O_3	Fe_2O_3	MgO	Na_2O	TiO_2
	%oxides					
0.27	63.99 ±8.88	23.22 ±3.37	7.41 ±1.13	2.59 ±0.44	1.58 ±0.30	0.14 ±0.02
1.03	64.11 ±12.55	25.42 ±5.15	4.94 ±1.10	2.59 ±0.57	1.66 ±0.39	0.13 ±0.03
2.32	64.03 ±13.43	25.11 ±5.60	5.35 ±1.26	2.72 ±0.63	1.78 ±0.44	0.14 ±0.03
3.83	65.23 ±7.62	22.21 ±3.13	5.56 ±0.83	2.59 ±0.41	1.78 ±0.34	0.15 ±0.02
5.13	64.59 ±8.58	24.17 ±3.49	5.54 ±0.81	2.81 ±0.44	1.92 ±0.36	0.16 ±0.03
6.14	65.12 ±7.88	23.62 ±3.35	5.53 ±0.80	2.75 ±0.41	1.83 ±0.34	0.15 ±0.02
7.10	63.76 ±7.77	25.45 ±3.61	5.11 ±0.73	2.78 ±0.41	1.99 ±0.36	0.14 ±0.02
8.11	65.29 ±8.94	23.64 ±3.53	5.42 ±0.79	2.74 ±0.42	2.04 ±0.39	0.16 ±0.02
9.14	64.54 ±8.58	24.54 ±3.62	5.13 ±0.73	2.85 ±0.44	2.06 ±0.39	0.16 ±0.02
10.25	65.38 ±7.30	24.31 ±3.26	4.58 ±0.68	2.75 ±0.37	2.09 ±0.37	0.15 ±0.02
11.38	66.40 ±7.29	23.32 ±3.11	4.51 ±0.64	2.88 ±0.39	2.07 ±0.37	0.16 ±0.02
12.38	64.76 ±6.71	24.45 ±3.17	5.06 ±0.68	2.77 ±0.35	1.92 ±0.33	0.14 ±0.02
13.54	67.21 ±7.21	22.97 ±3.04	4.23 ±0.63	2.65 ±0.34	2.03 ±0.35	0.13 ±0.02
14.82	66.25 ±7.28	23.84 ±3.39	4.49 ±0.61	2.73 ±0.36	2.00 ±0.34	0.14 ±0.02
16.22	65.60 ±6.47	23.32 ±3.01	4.50 ±0.57	2.72 ±0.33	2.03 ±0.34	0.16 ±0.02
18.03	65.41 ±6.51	24.39 ±3.25	4.45 ±0.59	2.75 ±0.33	2.09 ±0.35	0.15 ±0.02
19.78	65.52 ±8.15	23.73 ±3.56	4.60 ±0.60	2.84 ±0.39	2.37 ±0.43	0.16 ±0.02
pristine	64.74 ±7.76	24.26 ±3.54	4.76 ±0.62	2.90 ±0.37	2.27 ±0.40	0.15 ±0.03
pristine	65.22 ±7.32	24.03 ±3.43	4.57 ±0.57	2.87 ±0.35	2.40 ±0.42	0.15 ±0.02

distance (mm)[a]	SO_3	K_2O	CaO	P_2O_5	ZnO
	%oxides				
0.27	0.88 ±0.15	0.07 ±0.01	0.06 ±0.01	0.031 ±0.005	0.012 ±0.002
1.03	0.98 ±0.19	0.07 ±0.02	0.05 ±0.01	0.028 ±0.006	0.008 ±0.002
2.32	0.65 ±0.15	0.08 ±0.02	0.07 ±0.02	0.028 ±0.006	0.010 ±0.002
3.83	2.30 ±0.43	0.09 ±0.01	0.05 ±0.01	0.031 ±0.004	0.010 ±0.002
5.13	0.61 ±0.10	0.09 ±0.02	0.07 ±0.01	0.025 ±0.004	0.011 ±0.002
6.14	0.78 ±0.13	0.08 ±0.01	0.07 ±0.01	0.028 ±0.004	0.012 ±0.002
7.10	0.58 ±0.10	0.09 ±0.01	0.05 ±0.01	0.029 ±0.004	0.010 ±0.001
8.11	0.54 ±0.09	0.08 ±0.02	0.05 ±0.01	0.028 ±0.004	0.011 ±0.001
9.14	0.54 ±0.09	0.08 ±0.01	0.06 ±0.01	0.025 ±0.004	0.010 ±0.001
10.25	0.53 ±0.09	0.08 ±0.01	0.07 ±0.02	0.031 ±0.004	0.012 ±0.001
11.38	0.46 ±0.08	0.09 ±0.01	0.06 ±0.01	0.026 ±0.003	0.010 ±0.001
12.38	0.72 ±0.12	0.08 ±0.01	0.06 ±0.01	0.026 ±0.003	0.010 ±0.001
13.54	0.56 ±0.09	0.10 ±0.02	0.05 ±0.01	0.027 ±0.003	0.011 ±0.001
14.82	0.34 ±0.06	0.08 ±0.01	0.07 ±0.01	0.025 ±0.003	0.011 ±0.001
16.22	1.45 ±0.24	0.08 ±0.01	0.09 ±0.01	0.025 ±0.003	0.013 ±0.001
18.03	0.56 ±0.09	0.09 ±0.01	0.06 ±0.01	0.023 ±0.003	0.013 ±0.001
19.78	0.59 ±0.10	0.09 ±0.02	0.05 ±0.01	0.027 ±0.004	0.015 ±0.002
pristine	0.70 ±0.12	0.09 ±0.02	0.06 ±0.01	0.026 ±0.003	0.016 ±0.002
pristine	0.57 ±0.10	0.08 ±0.01	0.06 ±0.01	0.026 ±0.003	0.017 ±0.002

Table I5 – LA-ICP-MS acquisition parameters for elementary and isotopic analyses.

Analyses type	**Elementary**	**Isotopic**
Laser ablation device	NWR UP 213	
Wavelength	213 nm	
Pulse energy	0.5 mJ (50%)	
Fluence	22 J cm^{-2}	
Repetition rate	10 Hz	
Spot size 1diameter	55 µm	
Scanning speed	5 µm s^{-1}	
Ablation mode	Line (550 µm)	Line (600 µm)
Washout time	80 s	45 s
Ablation time	110 s	120 s
Carrier gas flow rate (He)	0.67 L min^{-1}	0.79 L min-1
Make-up gas flow rate (Ar)	0.73 L min^{-1}	0.76 L min-1
RF power	1250 W	
Auxiliary gas flow rate (Ar)	0.90 L min^{-1} (LA mode)	
Cool gas flow rate (Ar)	16 L min^{-1}	
Sampler and skimmer cones	Ni	
External standard	NIST 610 SRM, NIST 1881b	SWY-3 montmorillonite
Analysed Isotopes	^{7}Li,^{9}Be,^{11}B,^{23}Na,^{25}Mg,^{27}Al,^{29}Si,^{31}P,^{34}S,^{39}K,^{43}Ca,^{45}Sc,^{47}Ti,^{51}V,^{53}Cr,$^{54}Fe$$^{55}Mn$,$^{56}Fe$,$^{57}Fe$, ^{59}Co,^{60}Ni,^{63}Cu,^{66}Zn,^{69}Ga,^{75}As,^{77}Se,^{85}Rb,^{88}Sr,^{89}Y,^{90}Zr,^{93}Nb,^{95}Mo,^{107}Ag,^{111}Cd,^{115}In,^{118}Sn,^{121}Sb,^{133}Cs, ^{137}Ba,^{139}La,^{140}Ce,^{141}Pr,146Nd,^{147}Sm,^{153}Eu,^{157}Gd,^{159}Tb,^{163}Dy,^{165}Ho,^{166}Er,^{169}Tm,^{172}Yb, ^{175}Lu,^{178}Hf,^{181}Ta,^{182}W,^{197}Au,^{208}Pb,^{209}Bi,^{232}Th,^{238}U	^{53}Cr,^{54}Fe,^{56}Fe,^{57}Fe,^{58}Fe,^{60}Ni,$^{105}Pd^{++}$,$^{111}Cd^{+}$,$^{119}Sn^{++}$
Acquisition/counting time	180 s	205 s
Detector Mode	Triple	Analogical (sample), Pulse counting (blank)
Mass resolution mode	LR (300)	MR (3000)
Mass window	20%	Fe,Ni 100%, others 110%
Runs × passes	50 x 1	